Particle acceleration and synchrotron emission in blazars

Keith Richard Ballard

Presented for the Degree of Doctor of Philosophy

at the University of Edinburgh, 1991

This thesis is my own composition, except where specifically indicated in the text.

August, 1991.

Contents

Abstract

An optical and infrared observing programme which provides the most detailed information yet available for blazars is described. From this it is possible to make progress in understanding the physical processes which are occuring on the smallest scales within the emission region. Later theoretical calculations including a treatment of synchrotron emission incorporating losses and a realistic source geometry are presented together with a model of particle acceleration at relativistic shocks in disordered magnetic fields. The work contained in this thesis can explain the radiation and make predictions regarding future observations.

The conclusion is that the observations support the idea that the synchrotron emitting electrons are being accelerated at a collisionless shock front in a disordered field.

Introductory Comments

Throughout this thesis SI units will be employed, despite the fact that many textbooks presently being published still use cgs units. In many cases transposing between the two systems is trivial. It is not anticipated that this will cause too many difficulties. The exceptions to this are quantities such as days (dy).

Chapter 2 was the outcome of a collaboration with Drs Peter Brand and Andrew Mead of the University of Edinburgh, Drs Jim Hough and Chris Brindle of Hatfield Polytechnic, Dr Jeremy Bailey at the Anglo-Australian Observatory and Dr Bev Wills of the University of Texas at Austin. The material in this Chapter was published in a conference proceedings and in two refereed papers:

Ballard, K.R., Mead, A.R.G., Brand, P.W.J.L., Hough, J.H., Bailey, J.A. & Brindle, C., 1989, in *BL–Lac Objects: 10 Years After* Eds Maraschi et al. Springer-Verlag: Berlin. Simultaneous optical & IR polarimetric observations of blazars.

Mead, A.R.G., Ballard, K.R., Brand, P.W.J.L., Hough, J.H., Brindle, C. & Bailey, J.A., 1990. *Astronomy and Astrophysics Supplement*, **83**, 183–204. Optical & infrared polarimetry & photometry of blazars.

Ballard, K.R., Mead, A.R.G., Brand, P.W.J.L. & Hough, J.H., 1990. *Monthly Notices of the Royal Astronomical Society*, **243**, 640–655. The optical & infrared emission of blazars.

Chapter 3 is a report of a collaboration with Dr Alan Heavens. It is similar to the paper:

Ballard, K.R. & Heavens, A.F., 1991. *Monthly Notices of the Royal Astronomical Society*, **251**, 438–448. First order Fermi acceleration at oblique relativistic magnetohydrodynamic shocks.

The work for Chapter 4 is presented in two papers, a conference proceedings from the *"Variability in Active Galaxies"* conference in Heidelberg, September 1990, and a

refereed paper yet to be published:

Ballard, K.R., 1991, in *Variability in Active Galactic Nuclei* Eds Meisenheimer et al. Springer-Verlag: Heidelberg. The high frequency properties of synchrotron radiation.

Ballard, K.R., 1991. *Monthly Notices of the Royal Astronomical Society* A shock model for the optical emission of blazars.

Chapter 5 is a report of a collaboration with Dr Alan Heavens. It will be submitted to *Monthly Notices of the Royal Astronomical Society* in:

Ballard, K.R. & Heavens, A.F., 1991. *Monthly Notices of the Royal Astronomical Society* Fermi acceleration in a disordered magnetic field.

The material in Chapter 6 is a version of work carried out in collaboration with Dr Alan Heavens of Edinburgh University and Dr John Kirk of the Max Planck Institut für Astrophysics at Heidelberg. It was published in the paper:

Heavens, A.F., Ballard, K.R. & Kirk, J.G., 1990. *Monthly Notices of the Royal Astronomical Society*, **244**, 474–477. Relativistic particles in SS433.

Acknowledgements

The greatest acknowledgement goes to Alan Heavens for his help over the past few years. Without his wise guidance and attention to detail this thesis would be a lesser achievement. I am grateful to many others, most notably my other supervisor Peter Brand who asked lots of awkward questions and Lance Miller for a collaboration which would have formed Chapter 6 but for some bad weather at La Silla. Also, Jim Hough of Hatfield Polytechnic should be thanked for the use of his polarimeter and John Kirk and Bev Wills for useful discussions at various stages. In my first year Andrew Mead was an almost endless source of knowledge. The staff of Edinburgh University Computing Service and in particular Glenn Haworth are thanked for their efforts to produce a parallel version of the code which forms the centrepiece of Chapter 5.

I am grateful to the S.E.R.C. for financial support in the form of a studentship and the University of Edinburgh who funded a trip to Heidelberg.

Several of my fellow students who shared some enjoyable times should be mentioned. Claire Chandler and Steve Torchinsky were good friends throughout. I'd like to thank Paul Mitchell especially for typing the declaration on page ii for me and for pushing me off a chair once in return for a desperately sub-standard joke. Also: Stuart Lumsden for lots of lifts home; Karl Glazebrook for the supply of *Larson* cartoons; Andy Connolly for making me feel positively angelic when tackling on the football pitch; Bob Nichol for introducing me to some of the lesser subtleties of the language; Bob Mann for helping me with the spelling in Chapter 2; Pippa Goldschmidt for being willing to listen to me whinging in the office and Phil James who helped me find a useful phrase for section 5.2.5. I should apologise to Chris Collins for running him out when going for a quick third run during a cricket match a couple of years ago and to Brian Williams for dropping a sharp catch off his bowling earlier this season. The PATT committee are thanked for considering my applications for telescope time.

I am very grateful to Dad, Mum, Sue and Debbie for their continuous encouragement throughout my education. This thesis is dedicated to Judith for her support over the past year.

Chapter 1

Introduction

SUMMARY: The work for this thesis addresses several problems in the understanding of the emitting regions of blazars. Firstly, an observational study at optical and infra-red wavelengths is presented in Chapter 2. Chapters 3–5 deal with the acceleration of and emission from electrons at relativistic shock fronts. Accordingly, this chapter has been divided to a description of previous observations in Section 1.1 before going on to outline the theory of synchrotron radiation and Fermi acceleration in Section 1.2. Section 1.3 gives an outline of the rest of the thesis.

1.1 Observational properties of Blazars

1.1.1 Historical Background

Macleod & Andrew (1968) were the first to submit a paper showing the radio spectrum of the object VRO 42.22.01, together with an identification of its optical counterpart, and two measurements of the radio polarization which, on the basis of the rotation measure, indicated an extragalactic origin. Schmitt (1968) was the first to point out that the optical counterpart was in fact the "variable star" BL–Lacertae (hereafter BL–Lac), already known to exhibit extreme variability. Later, rapid variations in the radio flux (Biraud & Véron 1968) and polarization (Olsen 1969) were detected. In the optical Oke et al. (1969) measured a featureless spectrum and Visvanathan (1969) observed polarization. Strittmatter et al. (1972) investigated several other objects (OJ287, ON231, ON325 & PKS1514-241) and suggested a new class of objects, similar to quasars. A conference was held on the BL–Lac type objects at Pittsburgh in 1978 where their defining properties were the subject of much debate and their importance

to a full understanding of the Active Galactic Nuclei class was appreciated. It was at this conference that Blandford & Rees (1978) proposed the model which has formed the basis of current ideas of BL–Lacs, that the emission region is moving relativistically and is being observed at an angle close to the line of sight.

Since then the number of known BL–Lacs has grown steadily. In 1980, Angel & Stockman suggested a unification of BL–Lacs with highly polarized quasars (HPQ), on the basis that from radio to optical wavelengths the continuum properties are similar in all respects, save the emission lines in the spectrum of HPQ's. They gave a total of 57 "blazars" in their sample. Excellent current reviews of the present state of the understanding of blazars are given by Bregman (1990) or Altschuler (1989).

1.1.2 Definition of a blazar

For an object to be classified as a blazar it must display (Angel & Stockman 1980) a: an unresolved non-stellar continuum source at optical wavelengths, b: rapid and extreme optical variability, c: significant (>3%) optical and infrared polarization and d: core dominated, flat spectrum variable radio emission.

From each of these properties important conclusions regarding the nature of blazars can be drawn. There is a valid reason for using the value of 3% as a defining polarization level for blazars; that is the distribution of polarization levels appears to be bimodal with 3% separating the blazars and the rest of the (radio-loud) quasars (Moore & Stockman 1981; Stockman et al. 1984). All known blazars are also compact radio sources; there have been attempts to find radio quiet blazars, objects displaying only the optical characteristics of blazars, but these have proved negative to date (Impey & Brand 1982; Borra & Corriveau 1984).

To date, there are a total of 85 confirmed blazars and at least another 40 objects suspected of being blazars because of observations of high polarization or variability in one form or another. The full list is given in Mead (1988) although it should not be regarded as complete. There are several reasons for this, foremost among them being

the lack of a single coordinated observing programme to select objects. The detections were made with many telescopes operating at different wavelengths. There are, for example, large numbers of both radio and x-ray selected blazars. Similarly different surveys cover different areas of the sky and are complete to different limiting fluxes. Further observational problems arise because by their very nature blazars are highly variable and the question of a "duty cycle" occurs i.e. for what fraction of the time is a blazar in an active state. Thus many selection effects arise and any attempt to quantify them would encounter problems. Recently however authors such as Impey & Tapia (1988) and Fugmann (1988) have made repeated observations of complete samples of compact radio sources to determine the number of variable objects and estimate that a minimum of $\sim$ 70% are in fact blazars. One of the first major programmes which will achieve a high degree of completeness over the whole sky is the ROSAT survey at x-ray energies (0.1–2 keV).

1.1.3 Variability and periodicity

This term encompasses all detectable variations in the light output over time. As well as flux levels this includes changes in polarization and position angle of the radiation since from these important information about the alignment of the magnetic fields can be deduced. Generally observations point to shorter variability timescales at shorter wavelengths (e.g. Bregman 1990) which is consistent with emission with a synchrotron origin as the synchrotron electron lifetimes decrease with frequency. This has important consequences when planning an observing strategy; although it may be enough to observe only once every week at long (i.e. radio) wavelengths it is impossible to do the same in the optical and claim completeness as on occasions significant variations in the optical have been detected over a period of one hour or less (see e.g. Ballard et al. 1990 for 3C279).

It is important to determine the minimum timescale over which variations can occur as this gives details about the size of the emitting region. There are several possible ways to interpret the minimum timescales over which variations can be seen

which Elliot & Shapiro (1974) set equal to the light travel time across the Schwarzschild radius of a massive black hole. In this picture the variations would be the result of inhomogeneities in the flow of matter onto the black hole. As the emitting region may not be the central black hole then one should use the light crossing time of this instead (Fabian & Rees 1978).

Periodicity in the flux observed has been reported on several occasions but has not yet been shown to exist convincingly for any blazar. Doroshenko et al. (1986) found no significant periodicity in the range 8min.–2hr for BL–Lac and Moore et al. (1982) obtained the same result between 5hrs and 5 days. Both these results were obtained from data taken when BL–Lac was relatively faint so the conclusion does not preclude periodicity nearer maximum flux. Hagen-Torn et al. (1979) reported long term variability with an amplitude $0{\cdot}5^{m}$ for two periods, 47 days and 178 days. However, the observations were taken 6 months on/6 months off so perhaps one should be suspicious of the longer period. As with BL–Lac, OJ287 has been reported to have various periods between 15 & 40 mins (e.g. Carrasco et al. 1985) and similarly, negative results have also been published (e.g. Kiplinger 1974).

1.1.4 Optical Observations

Variations in the optical can occur on much shorter timescales than in the radio, ranging from a few hours (e.g. OJ287, Holmes 1985) up to years. Variations of up to 5 magnitudes have been seen for some objects (0235+164, 0829+046, 1156+295) over a period of months. There is occasional evidence for a correlation between luminosity and the spectral index, α (Smith et al. 1987). In objects such as 3C345, α reduces as the flux decreases, which can be explained in terms of an underlying constant thermal component – the "blue-bump". In others (1418+546) α is higher during quiescent periods which may be an indication that the electrons have a different energy distribution during outbursts whilst at later times synchrotron losses become important. In general, however the optical spectral index is independent of the luminosity, and this property has been used to reject models which predict spectral indices evolving during

flares although at longer wavelengths the spectral index does vary with flux (e.g. Gear et al. 1986a). Blazars have been shown to exhibit polarization changes at constant flux and also, flux fluctuations at essentially constant polarization and there appears to be no easily identifiable connection between the mean luminosity and mean polarization (Moore & Stockman 1981; Smith et al. 1987). In certain cases (e.g. Smith et al. for 3C345 and Marchenko (1985) for 1418+546) a relationship between source brightness and polarization has been claimed. Holmes (1985) found a correlation between luminosity in the near IR and the range of polarization position angle seen. If this is confirmed then the significance would be to the source alignment with respect to the line of sight (if there is beaming, then the closer a jet is to the line of sight the brighter it is and the greater the range of position angle). He warned however that this could be purely a selection effect as brighter sources are observed more often.

While some objects have position angles which vary greatly and appear to have no preferred position angle others are apparently restricted to a narrow range. On occasions rather exotic behaviour has been seen; Moore et al. (1982) reported an event in BL–Lac where the polarization vector traced a semi-circle in (Q,U) space, and then retraced its path. The whole event lasted around 2hrs and was interpreted as a result of two components with a constant polarization, one with a constant position angle, the other whose position angle rotated. Holmes et al. (1984b) observed a one-night-only 80° difference between 0.5 and $0.8\mu m$ also most readily interpreted in terms of two components. It has also been suggested (e.g. Marchenko 1985) that certain objects (0754+100 in this case) show preferred position angles when bright but no preferred orientation when faint. Alternatively Brindle et al. (1985) found an apparently constant component when faint which was tentatively ascribed to a jet.

1.1.5 Radio Observations

1.1.5.1 Single Dish

As in the optical, variability at radio wavelengths has been observed over a wide range of timescales (from under a week to several years, and typically a month or more e.g. Aller et al. 1985), and frequencies (0.61GHz→90GHz). Aller et al. (1985) found variations to be less at lower frequencies – most easily attributable to the effects of optical depth (i.e. synchrotron self-absorption at the lower frequencies), rather than Faraday rotation/depolarization (a λ^2 effect).

Altschuler & Wardle (1977) investigated the connection between radio luminosity and polarization. They concluded that polarization changes were on smaller timescales than the flux. Rapid flux changes are seen at constant polarization, and, perhaps of more interest, events where the polarization changes at roughly constant flux which in some cases yield (assuming a model with sub-components switching on and off) sub-components with polarizations greater than 100%. Altschuler & Wardle invoked changes in optical depth or increased ordering of the magnetic field to account for such extreme variations in the emission. They found no relation between the degree of variability and the mean polarization.

Aller et al. (1985) showed that the (derotated) position angles tend to align during periods of high flux, and also that most sources in their sample tend to have a preferred position angle persistent over several outbursts. There are several types of position angle events, ranging from "jumps" (Aller & Olsen 1971 for 3C279) where the variable position angle changed by up to 90° between observations, to "rotator" events. These occurrences, which have been seen in 5 blazars (0048-097, 0235+164, 1510-089, 1749+096, and BL–Lac) are events where the position angle appears to rotate, quasi-linearly with time, at varying rates (from 7° dy^{-1} to 15° y^{-1}), continuously for up to 2200°. On some occasions they occur differently at separate frequencies. An example to illustrate this point is that of Aller et al. (1985) who observed a steady position angle for BL–Lac at 4.8GHz, but a 440° rotation at 8.0GHz and 14.5GHz.

Several models have attempted to explain the phenomenon. Firstly, Faraday effects do not appear to be important because of those events which are independent of frequency. Ledden & Aller 1979 proposed rotations of the magnetic field within the compact object. Optical depth screening, whereby the inability to observe rotations within the source when it was optically thick could then be invoked to explain the apparent lack of low-frequency ($\leq$ 2.7GHz) rotator events. However, no rotator events have been recorded at millimetre wavelengths, or indeed in the optical and infrared. Blandford & Königl (1979) interpreted them as clumps of material being accelerated, and the rotation would then be a result of relativistic aberration effects. This could not explain events where the observed rotation was greater than 180°. Aller et al. (1981) suggested a cloud, asymmetrically positioned, spiraling around the jet axis. Jones et al. (1985) noted that during rotator events the polarization was usually low ($\leq$ 2%) and any "common" component would be small, or entirely absent. They used simulations to follow the path traced by randomly oriented vectors, each with a fixed lifetime being switched on and off and found the resultant random walk in (Q,U) space could generate apparent rotator events.

Although the optical and radio properties may not mimic each other precisely there are instances of behaviour which hint at a common origin. Aller et al. (1985) saw common preferred position angles in the optical and radio (out of a sample of 12, 7 were parallel and 3 perpendicular). This could be interpreted as similarly oriented magnetic-fields giving rise to the emission at the different wavelengths – with the perpendicular cases being an indication of optically thick emission. A further example is a synchronous PA rotation at 0·6μm and 3cm reported by Kikuchi et al. (1988).

1.1.5.2 VLBI

The study of the milliarcsecond radio structure of blazars began with the development of Very Long Baseline Interferometry during the late 1960's and 1970's (e.g. Broten et al. 1967; Moffet et al. 1972). It was soon noted that the structure of several objects was changing over time. After converting these motions on the sky into speeds it was found

that the apparent transverse velocities were greater than the speed of light. While this was taken by some as evidence against the cosmological interpretation of redshifts the general conclusion was that this was a manifestation of an effect noted by Rees (1966) whereby an object which is travelling at relativistic velocities ($v = \beta c$) at an angle θ to the line of sight of the observer will have an apparent transverse velocity:

$$\beta_{app} = \frac{\beta \sin\theta}{1 - \beta \cos\theta} \tag{1.1}$$

which has a maximum value of $\Gamma\beta$ at an angle $\sin\theta = 1/\Gamma$ where $\Gamma = (1-\beta^2)^{1/2}$ is the Lorentz factor of the material.

Superluminal radio sources were the subject of a workshop in 1987 and BL–Lacs were topics of several of the papers presented, e.g. Mutel & Phillips (1987). Of the eight BL–Lacs with single frequency multiple epoch maps only 1803 + 784 does not display superluminal motion. Comparing the spread in velocities of BL–Lacs with that of the other blazars, the HPQ's, one finds that the BL–Lacs have a wider range but a smaller mean velocity. A possible explanation for this was suggested by Roberts et al. (1987), that the BL–Lacs lie inside the maximal velocity cone, which reduces the apparent velocity whilst retaining the Doppler boosting of the flux. This would help to explain why emission lines are observed less frequently. However there are strong arguments against this explanation, the primary one being that the redshift distributions of the two samples should be identical, which they are not (Cohen 1989). Furthermore, to cite a particular example, the model of the emission of BL–Lac of Hughes et al. (1985) employs large viewing angles. As techniques have improved in recent years it has become apparent that the simple model of superluminal motions is not universally valid. For example in the object 3C345 the components appear to "speed up" as they move out from the stationary core (Biretta & Cohen 1987). There are possible explanations for this; Smith & Norman (1981) suggest that a relativistic equation of state would result in acceleration as the external pressure dropped. BL–Lac itself displays components apparently decelerating, it is tempting to associate this with material being slowed by some external material from the surrounding galaxy. On the parsec scale most jets appear to be collinear, although this may be a consequence of the

low dynamic range presently achievable with VLBI techniques, the bends in the jet of CTA102 (McGuinn et al. 1967; Wehrle et al. 1990) are only visible at a dynamic range greater than 50:1. However, nearly all BL–Lacs are misaligned between the parsec and kiloparsec scales. There is a reported bimodal distribution of bending angles around 0° and 90° (Pearson & Readhead 1988).

More recently methods of obtaining polarization information on VLBI maps have been developed. Data have been published for eight objects to date (Roberts et al. 1987; Gabuzda et al. 1989a,b). Polarization maps probe the structure of the magnetic field on the smallest scales yet accessible. Gabuzda et al. 1989b show that in sources with significant polarization the position angle of the knot is closely aligned with the jet i.e. the magnetic field lies across the jet. The knots have polarizations 2–10% and the cores 3–5%. VLBI maps of quasars (Wardle et al. 1989 for 3C273) have position angles perpendicular to the jet axis, suggestive of an intrinsic difference in the field structure within the two classes.

1.1.6 X-ray

Studies of the x-ray emission from blazars have been restricted because of the incomplete spectral coverage of the data available at present, which were taken with the EINSTEIN (0.1–10 keV) and EXOSAT (0.1–6 keV) satellites. A few objects have published data at higher energies, taken by the GINGA satellite (2–35 keV; Ohashi 1989). For blazars there is a wide range of spectral indices with a mean of $\langle \alpha_x \rangle = 1.0$ (Ghisellini et al. 1986; Worrall 1989). The origin and nature of the x-ray emission is still uncertain, but there do appear to be differences between objects. The first class appears to be those blazars which were detected by x-ray observations (e.g. $PKS2155-304$; Treves et al. 1989). In these objects the x-rays appear to form a continuation of the radio and optical radiation and it is generally supposed that one is indeed observing synchrotron radiation, although conclusive evidence such as polarization measurements are lacking. There are certain events where x-ray variations can be successfully correlated with optical variations (e.g. Treves et al. 1989 for $PKS2155-304$). Variations also tend

to be more rapid and have a greater amplitude at x-rays than at optical wavelengths. However, there are many objects where a simple extrapolation of the radio to optical radiation underestimates the flux of x-rays which is actually observed. In these objects the emission may have a different origin such as the Inverse Compton mechanism in which photons are scattered by the electrons in the emission region and gain enough energy to be observed as x-rays. On the basis of the identical spectral slope and correlated variability between optical and x-ray Bregman et al. 1986, Bregman et al. 1990 suggested the Inverse Compton effect for the x-rays from 3C345 and BL–Lac.

Resolving the question of the origin of the x-rays is a point of some importance. Under the assumption of spherical symmetry within the source Marscher (1987) used the radio emission to estimate the x-rays produced by the Inverse Compton effect. The predicted emission exceeds the observed flux for many objects. One solution is to allow the source to be in relativistic motion towards the observer, close to the line of sight. Thus one avoids the "Inverse Compton Catastrophe" by overestimating the low frequency flux due to beaming effects.

1.1.7 Unifying Schemes

The problem of relating blazars to other active galaxies has taxed many authors. In a previous subsection the observational evidence for superluminal motions was reviewed. The boosting of the flux from these moving components relative to the surrounding material gives us the appearance of a blazar. The aim of the various unifying schemes is to identify what a blazar which is not pointing towards us looks like. The original idea, due to Scheuer & Readhead (1979) was that the unaligned compact radio sources could be identified with radio quiet optically selected quasars. This scheme has since been rejected because of the steep spectrum radio emission which originates around compact sources (e.g. Perley et al. 1980; Antonucci & Ulvestad 1985) and which is presumed to be unbeamed i.e. it should be observed equally well in the parent class.

An important suggestion was made by Orr & Browne (1982) who proposed that all flat spectrum core dominated quasars are aligned counterparts of lobe dominated

quasars. They related a factor R, defined as the ratio of core to extended radio flux to the angle to the line of sight, jet Lorentz factor and the intrinsic value of R which would be seen by an observer perpendicular to the jet, and attempted to fit the numbers of the two populations. To support this Wills & Browne (1986) found an anti-correlation between R and the strength of the $H\beta$ line which they suggested originated in the disk, perpendicular to the jet axis. On the basis of the space density (Browne 1983) and the extended luminosities (Wardle et al. 1984) it has been suggested that more suitable candidates might be FRI type galaxies (Fanaroff & Riley 1974).

Potentially the most powerful diagnostics for investigating proposed schemes is to test for differences between samples using properties which are independent of orientation. Prestage & Peacock (1987) measured the cluster environments of radio sources simply by counting the observed galaxies around an object, this is one statistic which one might expect to be identical for beamed and unbeamed objects. Mead (1988) used this idea to test for a difference between lobe and core dominated quasars. He found a difference in the environments, but the result was significant at less than a 2σ level. However, as it might be more suitable to use the FRI's, which have comparable extended luminosities, a test using these objects is more appropriate. Indeed, a proposal for carrying out these observations was accepted by the European Southern Observatory at La Silla and would have formed a chapter in this thesis, but for foul weather at the site which made observing impossible.

The aim of unifying schemes is to find a parent population for blazars. However, it is not at all clear that blazars themselves are a single unified class which makes the task more difficult still. Ostriker & Vietri (1985) argued that the redshift distribution of BL–Lacs and HPQ's were different, the BL–Lacs being found preferentially in low redshift giant ellipticals. Also the x-ray spectral indices appear to be statistically different for the two samples (Worrall 1989). Finally, the speeds of superluminal components in HPQ's appears to be higher than for BL–Lacs. On the other hand Antonucci & Ulvestad (1985) argued that there were objects such as 3C446 and 3C279 which at times are observed with strong broad emission lines, as HPQ's, and yet at other periods the synchrotron emission flares up, swamping the lines and giving rise to classification

as a BL–Lac; they suggested that narrow lines should be used to discriminate between the two types. As often occurs when attempting to classify objects, there are objects which can span more than one category (Lawrence 1987). Recently, Impey et al. (1989) showed that the quasar 3C273, which has optical polarization $< 3\%$, contained a "mini-blazar" in that the emission could be decomposed so that emission could be seen with polarization behaviour like a blazar i.e. a random walk in (Q, U) space which was being diluted by the other emission features.

1.2 Theory of Blazars

This section will explore some current ideas regarding the physics responsible for the blazar phenomenon. Brief introductions to the theory of synchrotron radiation and Fermi acceleration are given alongside the evidence for these occurring in blazars.

1.2.1 Synchrotron Radiation

In blazars it is believed that the primary radiation mechanism is the synchrotron mechanism, and the evidence for this is compelling. As the spectrum of a blazar is generally devoid of any strong emission or absorption features a determination of the exact shape of the spectrum is of critical importance. It was reported by Landau et al. (1986) that in many cases the spectrum fits a parabola in $\log \nu F_\nu - \log \nu$ space, the width of which was too wide to be consistent in any way with a black body spectrum. Here F_ν is the flux and ν the frequency. Furthermore, the brightness temperature of the radio emission is of the order of 10^{12}K which immediately precludes a thermal origin. Edelson & Malkan (1986) used the infrared variability timescale to derive an infrared brightness temperature of 10^6K, again in conflict with black body radiation. It must therefore be acknowledged that it is impossible to reproduce the observations with a thermal source of radiation, a non-thermal mechanism is operative instead. The proposed mechanism is synchrotron radiation because of the high observed polarizations ($\simeq 10\%$ at radio wavelengths); the short variability timescales argue against it being produced by

secondary means e.g. by scattering. The smoothness of the spectrum suggests that the radiation mechanism is of the same origin at submillimetre, infrared and optical wavelengths.

A complete knowledge of the physical conditions present within blazars can only be achieved with a thorough understanding of the radiation mechanism operating within these sources. Synchrotron radiation is produced as a result of the acceleration of ultrarelativistic electrons (or positrons) in a magnetic field. This mechanism was first conceived of by Ginzberg (1951) and Shklovskii (1952) and has proved to be highly successful in interpreting the non-thermal emission from discrete radio sources (e.g. the Crab Nebula), diffuse radio emission in the Galaxy and also the extragalactic extended radio sources. The theory of the mechanism is well developed and detailed descriptions can be found in the works by Rybicki & Lightman (1979) in the first instance, and also Pacholczyk (1970; 1977). A brief derivation of the main equations can be found in Appendix A.

An electron in a magnetic field, B, will follow a helical path being accelerated and emitting radiation. For non-relativistic electron velocities the radiation has a frequency equal to the gyration frequency, ω_H and is termed cyclotron radiation. At ultrarelativistic velocities the electron emission is beamed into a cone, around the instantaneous velocity vector, of half angle γ_e^{-1}, γ_e being the electron Lorentz factor. If the angle, ε, between the velocity vector and the magnetic field direction is $> \gamma_e^{-1}$ the radiation will sweep the observer at intervals of $2\pi/\omega_H$, giving a pulse of duration $(\gamma_e^3 \omega_H \sin\varepsilon)^{-1}$. An electron of energy E loses energy at a rate given by:

$$\frac{dE}{dt} = -\frac{e^4 B^2 \sin^2\varepsilon\, E^2}{6\pi\varepsilon_0 m_e^4 c^5} \tag{1.2}$$

where m_e is the electron rest mass and the other symbols have their usual meanings. The spectrum of the radiation from a single electron is composed of the harmonics of ω_H, and has the form:

$$\frac{dW}{d\omega} = \frac{3\sqrt{3}\gamma_e e^2 B \sin\varepsilon}{32\pi c\varepsilon_0}\left[F(x) \pm G(x)\right] \tag{1.3}$$

where W is the power radiated per unit frequency, $x = \omega/\omega_H$ and $F(x)$ and $G(x)$ are defined to be:

$$F(x) = x \int_x^\infty K_{5/3}(\zeta) d\zeta \tag{1.4}$$

$$G(x) = x K_{2/3}(x) \tag{1.5}$$

where the K_i are the modified Bessel functions of fractional order i. These functions are plotted in Appendix A, where an algorithm for their generation is also described. Note that synchrotron losses from protons are a factor of $(m_p/m_e)^4$ smaller than those from electrons and are thus disregarded. Also note that this radiation is elliptically polarized, the major axis being perpendicular to the direction of the magnetic field projected onto the line of sight. In general, one is interested in the synchrotron radiation from a large ensemble of electrons. The total emission coefficient is then given by:

$$\epsilon(\nu) = c_3 B \sin\varepsilon \int_0^\infty N(E,\theta) F(x) dE \tag{1.6}$$

where c_3 is a constant given by Pacholczyk (1970). $N(E,\theta)dEd\theta$ describes the number density of electrons in an energy band dE and lying within a direction $d\theta$. The simplest distribution is that of an isotropic power law: $N(E,\theta) = N_0 E^{-\gamma}$ (γ here is the spectral index, it should not be confused with the electron Lorentz factor γ_e). Carrying out the integration one obtains:

$$\epsilon(\nu) = c_3 \left(\frac{3e}{2\pi m_e^4 c^5 \nu}\right)^{-\alpha} (B \sin\varepsilon)^{\frac{\gamma+1}{2}} \tag{1.7}$$

where α is defined as the spectral index such that $-2\alpha = \gamma - 1$ Taking optical depth effects into account the full equation for the intensity of the radiation can be shown to be:

$$I_\nu = \frac{\epsilon(\nu)}{\kappa(\nu)} (1 - e^{-\kappa_\nu s}) \tag{1.8}$$

under the assumptions of a constant absorption coefficient, κ_ν within the source and

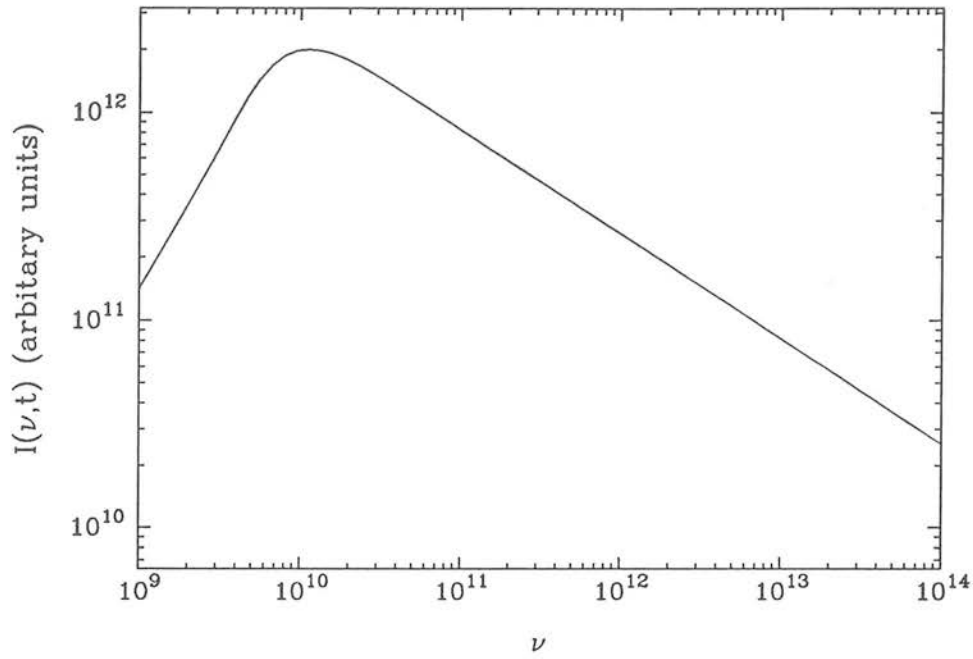

Figure 1.1: The synchrotron emission for a idealized power–law distribution of electron energies has a self-absorption turnover at low frequencies, below which $I(\nu,t) \propto \nu^{5/2}$ whereas in the optically thin regime $I(\nu,t) \propto \nu^{(1-\gamma)/2}$.

negligible incident radiation. The absorption coefficient is given by:

$$\kappa(\nu) = -c_3 \frac{c^2}{2\nu^2} B \sin\varepsilon \int_0^\infty \frac{d}{dE}\left(\frac{N(E,\theta)}{E^2}\right) F(x) dE \tag{1.9}$$

The resulting spectrum is shown in Fig. 1.1.

The appearance of a source can also be affected by the presence of a significant amount of plasma within the source, the most important mechanism being Faraday rotation of the position angle when a wave propagates through a magnetized plasma which arises as a result of the different propagation velocities of opposite circularly polarized waves. The degree of rotation is proportional to the square of the wavelength and so the mechanism is most important at long wavelengths. Another important consequence is that the medium can cause a decrease in the overall degree of polarization as radiation from different regions is rotated through different amounts and this can effectively cancel out the polarization. Faraday rotation and depolarization are important tools to probe the conditions within the sources but they are unlikely to be relevant to the high frequency work contained within this thesis, and consequently they

will not be considered further.

Another method of evaluating conditions within the source is to use minimum energy arguments. It can be shown that the internal magnetic energy of a source with given flux increases with B, while the energy density of the synchrotron emitting electrons increases with decreasing B. The total energy is a minimum at around the point where there is equipartition between these two forms of energy. This equipartition value of B is often relied upon in calculations of source properties, particularly for extended radio sources. However, estimates of B from minimum energy requirements could conceivably be wildly astray because of uncertainties in the fraction of the source volume which actually contains magnetic flux and electrons and also the unknown amount of energy contained in the (non-emitting) relativistic protons. Neither is there any guarantee that the electrons and fields should be at equipartition of energy.

The radiation from a single electron is elliptically polarized. When the radiation from left– or right–handed elliptically polarized radiation (determined by which side of the radiation cone the observer is situated) is integrated over the electron distribution, the circular polarization cancels out, leaving purely linearly polarized radiation. For a power law of index γ, the polarization from a uniform magnetic field is:

$$p_0 = \frac{\gamma + 1}{\gamma + 7/3} \times 100\% \tag{1.10}$$

This suggests that polarizations of the order of 70% should be observed. This may be contrasted with the levels of polarization actually seen, typically 10–30%. This feature of synchrotron sources is generally interpreted as meaning the assumption of a homogeneous, uniform field in the derivation of equation 1.10 is incorrect. A more realistic magnetic field structure can hopefully be inferred from the data. For example, one could envisage an idealized structure consisting of a number of identical cells containing magnetic flux emitting identical amounts of polarized flux with different position angles. If the position angles of N cells were randomly distributed in the plane of the sky the polarization would decrease as:

$$p = p_0 N^{-1/2}. \tag{1.11}$$

A model of this kind can explain some aspects of the polarization behaviour (Moore et al. 1982, Brindle et al. 1985), but runs into difficulties with large flaring events.

So far only the idealized case of isotropic power law distributions have been mentioned. In reality the overall form of the distribution may be dramatically modified by losses due to various mechanisms or the injection of additional electrons into the emission region and this in turn can modify the form of the radiation observed. The exact form of the distribution as a function of time may be obtained by solving the kinetic equation. This can modify the form and isotropy of the distribution. This is discussed in more detail by Kardaschev (1962) and in Chapter 4.

1.2.2 Source inhomogeneities, jets and shocks

1.2.2.1 Inhomogeneities

Having briefly discussed the properties of an ideal homogeneous synchrotron source, a comparison should be made with real sources. It has long been known that the spectrum of Fig 1.1 is a poor representation of blazar spectra, particularly at low frequencies. At the lowest frequencies the spectrum turns over and a power-law of the form $F_\nu \sim \nu^{5/2}$ is expected which is characteristic of self-absorption of synchrotron photons by the emitting medium (e.g. Rybicki & Lightman 1979). This is not at all what is observed where the spectrum below the self-absorption turnover is generally flat. This inconsistency is the origin of the "Cosmic Conspiracy". Cotton et al. (1980) showed conclusively that for the object $0735+178$ this is not the result of the superposition of a number of discrete synchrotron sources with different turnover frequencies as the spectra are too smooth; Cook & Spangler (1980) repeated this analysis for a larger sample of compact radio sources and arrived at the same conclusion. Instead the results are consistent with an inhomogeneous source structure. This is the prime piece of evidence for source inhomogeneity at low frequencies.

At higher frequencies there is also strong observational evidence that the emitting region is inhomogeneous and more particularly that the size of the emission region de-

creases with increasing energy. As already mentioned the typical variability timescale gives information on the size of the emitting region and the variability timescale decreases with increasing frequency. Broadly speaking this decrease is $\propto \nu^{-1/2}$ (Bregman et al. 1988 for 3C446 and also Celotti et al. 1989). Variability may have several origins but it is most likely that the short timescale variations are due to finite source size and the fact that this varies with frequency can be regarded as evidence for inhomogeneity. In principle one cannot say which mechanism is responsible for the variability however it must be true that it is radiative losses, e.g. synchrotron or inverse Compton emission which tend to dominate over losses caused by expansion of the source. This is because expansion losses are $dE/dt \sim -E$ which does not give rise to a steepening of the spectrum unlike radiative losses where $dE/dt \sim -E^2$ and where one has $\tau \propto \nu^{-1/2}$ and spectral curvature as observed.

1.2.2.2 Jets

The strongest single piece of evidence supporting the claim that jets are central to the blazar class is the motion of VLBI radio components, previously mentioned in Section 1.1.5.2. This is interpreted as superluminal motion of knots of material moving away from the central source at apparent velocities which may be as high as $10h^{-1}c$ (see Porcas 1987). This flow of material comprises a jet. The superluminal knots are known to be polarized (Roberts et al. 1987) and generally the position angle of the knots is aligned with the jet i.e. the dominant magnetic field lies across the jet. The second piece of evidence comes from the more detailed studies of time dependence from variability studies. The single dish radio observations of Aller et al. (1985) show that flux outbursts are associated with an alignment of the position angle with the jet. In the model of Hughes et al. (1985) a shock passes down the jet. As this encounters high density regions it compresses the fluid and magnetic field producing a flux outburst. This also aligns the field across the jet naturally as the field, assumed isotropic upstream, is enhanced parallel to the shock face. They obtained good fits to their monthly data using this picture of a shock causing flares and a piston which drives the shock together with quiescent jet component which has a steeper spectral index and which is seen

during less active periods. A shock in a jet was also the basis of the model of Marscher & Gear (1985) who included losses but did not use a particular magnetic field geometry. Both papers showed that variations could be well explained by a shock travelling along a jet whereas the "standard" isotropically expanding source model of Pauliny–Toth & Kellerman (1966) encountered severe difficulties, as had been known for some time (see e.g. Altschuler & Wardle 1977).

1.2.2.3 Shocks

An example of the emission from a shock model is shown in Fig. 1.2. This is similar to the model of Hughes et al. (1985) in that there is a slab of synchrotron emitting plasma moving along a jet. The width of the jet expands with time, $s \propto t$ and the magnetic field in the plasma decreases as the jet width increases $B \propto s^{-2}$. Three loss mechanisms have been taken into account in the analysis, adiabatic expansion, synchrotron and inverse Compton. The expansion of the source is responsible for the evolution of the self-absorption turnover to lower frequencies. Synchrotron and inverse Compton losses have the same qualitative effect upon the spectrum, they cause evolution of the sharp cutoff to lower energies, the difference is in the value of the cutoff as a function of time, the inverse Compton effect being more important at higher densities where the source is more compact. In the model spectra plotted in Fig 1.2, it was assumed that the photons being scattered were wholly from the emitting slab itself. Fig 1.2 also shows the effect of integrating along the line of sight through the jet where one observes radiation from electrons which were injected at earlier times. This gives rise to the spectral break seen in the integrated flux.

Prior to this thesis there have been no attempts to extend the shock model to optical frequencies. Indeed there are conflicting ideas on the point of whether the optical emission arises entirely within the superluminal components or in the core regions, unresolved even by VLBI observations. On the other hand, there are preferred optical position angles which align with the VLBI axis (Rusk & Seaquist 1985; Impey 1987) again implying a magnetic field across the jet and a shock origin for the radiation.

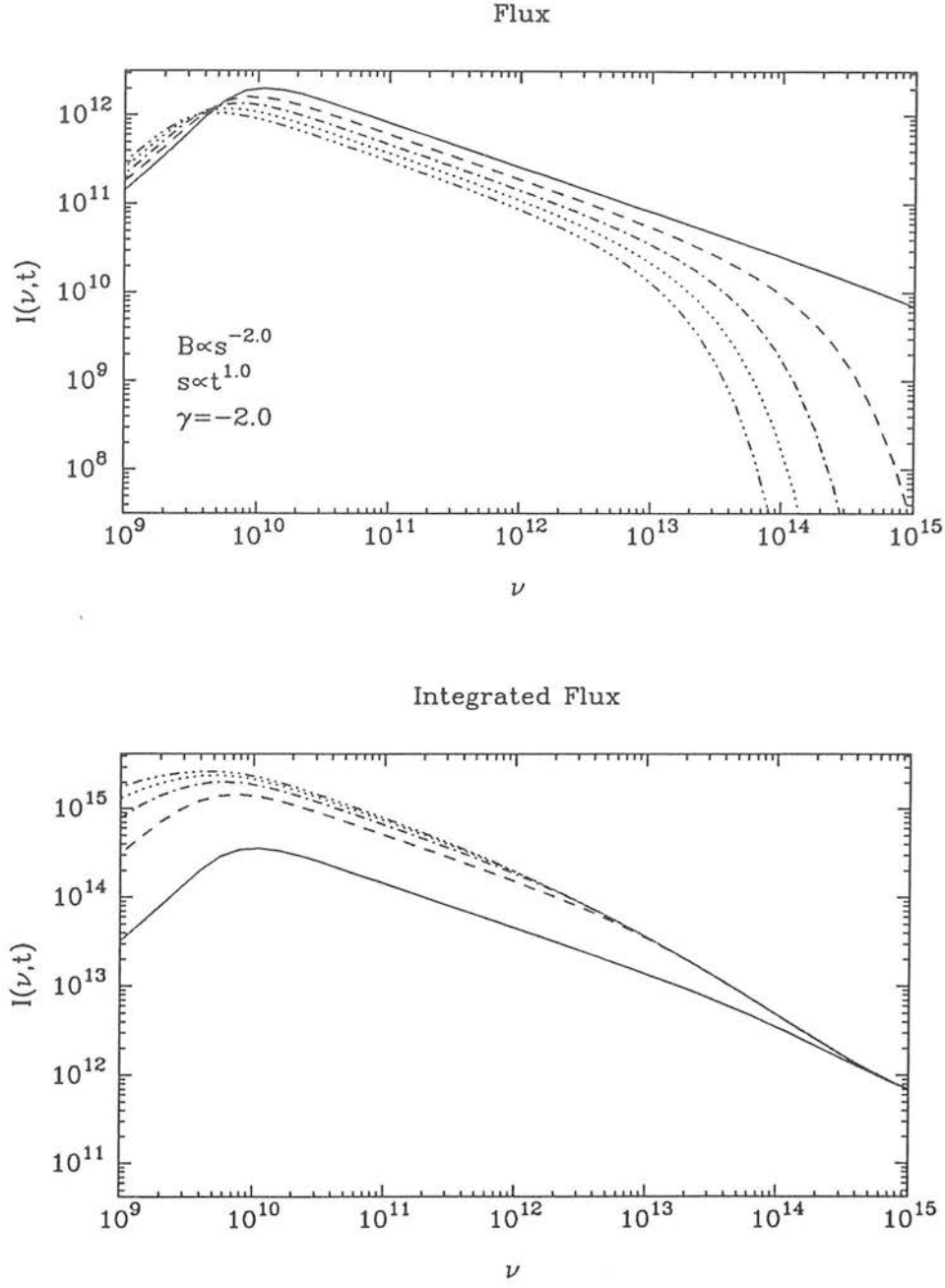

Figure 1.2: This shows the evolution of a slab of synchrotron emitting material passing along a jet which expands as $s \propto t$ and in a magnetic field which decreases with increasing jet width $B \propto s^{-2}$. The lower figure shows the integrated emission from a jet.

Also the work of Landau et al. (1986), mentioned previously, supports a common origin.

1.2.3 Particle acceleration

There are several arguments which advocate a localized form of particle acceleration operating within the source; primarily it is the short variability timescale which suggests electron lifetimes of the order of days. At present the most viable scheme for accelerating electrons to the high energies at which synchrotron emission is radiated at high frequencies is the first order Fermi mechanism which operates at the site of a converging fluid flow such as a shock front. The theory was developed almost simultaneously by Bell (1978a,b), Axford et al. (1977), Blandford & Ostriker (1978) and Krymsky (1977).

The principle behind the mechanism is extremely simple. Consider a shock front in a fluid where the thickness of the shock front is governed by the mean free path of the average particle. In the case of a collisionless shock this will effectively be the gyroradius of a thermal proton. A suprathermal particle, entering from the upstream region, with a gyroradius much greater than the shock thickness can pass through the shock front essentially unperturbed. In doing so the energy and pitch angle in the shock reference frame are conserved. The particle then moves into the downstream fluid where it can be scattered in pitch angle by the fluid. For magnetic interactions the particle maintains a constant energy as measured in the rest frame of the scattering medium. The scattered particle has a finite and energy-independent probability of crossing the shock again into the upstream fluid in which case eventually the fluid will advect the particle across the shock once more. If the particle is highly relativistic this cyclic process results, statistically, in a fractional gain in energy for each particle. The combination of a fractional energy gain and an energy-independent return probability results in a non-thermal power-law distribution of energies being manufactured. In the time since this was realized the original formulations have been considerably elaborated and widely applied, although the original principles remain unchanged. It has been observed by satellites at the Earth's bow shock and it is believed to be important for solar flares,

supernova remnants and extended radio sources. As the prime candidate for particle acceleration in blazars it is appropriate to discuss it further. Several good reviews of Fermi acceleration exist in the literature, for example those by Drury (1983), Blandford & Eichler (1987) and Decker (1988).

There are several approaches to tackling the problem which give varying degrees of insight into the microphysics taking place and which yield varying degrees of spectral accuracy; all will be employed at different points in this work. Firstly there are integrations of particle orbits which follow the particles through the fluid as they are scattered and cross the shock front (Chapter 5). Secondly there are Monte Carlo methods which utilize the stochastic nature of the process of the scattering process but which still follow individual particles (Chapter 3). Finally there are analytic treatments (Chapter 3) which obtain solutions to the transport equation at the shock front; these are quickest to evaluate in practice but at the expense of all information about individual particles.

The simplest approach is that of Bell (1978a), which is the method which best illustrates the microscopic nature of the mechanism. It was originally developed for non-relativistic shocks but the principles carry over to the relativistic regime. In it he assigns a probability η of a particle in the downstream region escaping from the shock $\eta = \frac{4u_2}{v}$, where u_2 is the downstream fluid speed and v is the particle velocity (η is simply the ratio of the flux of particles a long distance away from the shock to the flux of particles across a surface). Secondly one has to obtain the momentum gain when a particle completes a cycle. This is found by transforming the momentum, p, between frames, noting that at the shock crossing the momentum is unchanged in the shock frame. The average momentum gain will be:

$$\langle \Delta p \rangle = \frac{2p(u_1 - u_2)}{3v} \tag{1.12}$$

where $u_{1[2]}$ is the fluid speed on the upstream [downstream] side of the shock. The particle can thus repeatedly cross the shock each time with a finite chance of being lost. After n cycles it reaches a momentum:

$$p_n = \prod_{i=1}^{n} \left[1 + \frac{4(u_1 - u_2)}{3v_i}\right] p_0 \Rightarrow \ln\left(\frac{p_n}{p_0}\right) \sim \frac{4(u_1 - u_2)}{3} \sum \frac{1}{v_i} \tag{1.13}$$

and the probability of this occurring is:

$$P_n = \prod_{i=1}^{n} \left[1 - \frac{4u_2}{v_i}\right] \Rightarrow \ln P_n \sim 4u_2 \sum \frac{1}{v_i} \tag{1.14}$$

thus one obtains the probability of a particle being accelerated to momentum p. The number density of electrons with momenta greater than p is given by this probability multiplied by the total number of particles (r is the compression ratio):

$$N(> p_n) = N_0 r \left(\frac{p_n}{p_0}\right)^{-3/(r-1)} \tag{1.15}$$

This is the basic method for accelerating electrons. There are two modifications that will be considered in detail in this thesis. The first is that the shock at which the electrons are accelerated could be moving through the fluid at relativistic velocities. This is suggested by the observations of superluminal motions in BL–Lacs; if the moving components are associated with a shock front then the shock is moving relativistically. The non-relativistic approach outlined above is unsatisfactory at relativistic speeds. The treatment assumed that the electron velocity distribution remained isotropic at the shock front whereas it is actually impossible that an electron distribution can remain isotropic in both the upstream and downstream rest frames if the shock is moving at relativistic speeds. Thus it is necessary to introduce an extra parameter into the problem i.e. the pitch angle of the electron velocity. Peacock (1981) attempted solving the problem via the microphysics and derived spectral indices under certain conditions, but as recently as 1987 Blandford & Eichler stated that it was unlikely that an electron distribution close to isotropy in the downstream frame could be efficiently accelerated at a relativistic shock.

The major advance was made by Kirk & Schneider (1987a) who adapted the techniques of radiative transfer to the problem of electron scattering at ultrarelativistic energies. The key aspect of their approach was to note that one can mix reference frames. Thus certain properties are best expressed in the shock rest frame (such as the spatial and time dependence) while other quantities (the momentum and pitch angle) are more suitably measured in the frame in which the scattering takes place i.e. the fluid rest frame. Under the assumptions of a plane parallel shock, with a magnetic

field parallel to the shock normal, and a distribution which is independent of gyrophase they wrote down and solved the time-independent transport equation. After separating variables this reduces to an eigenvalue problem which is solved by expanding in terms of Legendre polynomials. The distribution can then be obtained under the assumption that it is continuous at the shock front and that the momentum distribution is a simple power law. The results of this "Q_J" method showed that relativistic shock fronts can indeed accelerate ultrarelativistic electrons and that the resulting spectra were often harder than those predicted by the simple non-relativistic approximation i.e. the mechanism was very efficient. The range of spectral indices which could be produced by relativistic shocks under a variety of conditions was summarized by Heavens (1988).

The second modification to the theory is due to the expectation that in a large proportion of cases the magnetic field will be inclined to the shock normal. The case for oblique shocks has already been stated, the effect that this has upon the process of Fermi acceleration is potentially quite drastic. This can be illustrated simply in the "superluminal" case where $u_{sh}/\cos\theta_{sh} > 1$ when the magnetic field intersects the shock front at a speed which is greater than that of light. u_{sh} is the shock speed and θ_{sh} is the angle between the shock normal and the magnetic field. In this case an electron, once having reached the downstream fluid can never return upstream as the shock is receding at faster than it can travel, the Fermi mechanism simply does not work under such conditions. For "subluminal" shocks Kirk & Heavens (1989) solved the problem in the limit of a dynamically unimportant magnetic field. The physics are complicated by a couple of extra features. Firstly, oblique shocks can accelerate electrons even during the course of a single shock crossing. This is the "shock drift" mechanism caused by the electric field which exists at the shock front in the shock frame (see Decker 1988). Secondly, if the particles are assumed to conserve magnetic moment upon crossing the shock then particles incident from the upstream region have the possibility of being reflected by the shock. The problem of the electric field at the shock is solved by transforming to a reference frame where the fluid flow is along the magnetic field on both sides of the shock front, a transformation which is always possible for subluminal shocks (de Hoffman & Teller 1948). Kirk & Heavens extended the work of Kirk & Schneider (1987) by modifying the transport equation to be solved to oblique shocks

and then expanding the distribution function in terms of Chebychev polynomials. They found that oblique subluminal shocks are extremely efficient at particle acceleration and that as the shock become more oblique more particles are trapped upstream and the spectral index becomes very hard, $\alpha \rightarrow 0$.

An alternative approach to solving the problem was presented in Kirk & Schneider (1987b) who used a Monte Carlo technique to follow particles through the plasma. The distribution function at the shock front is then built up as the individual particles make shock crossings. Monte Carlo methods had already been used to model Fermi acceleration for the non-relativistic limit (see e.g. Achterberg 1988; Decker & Vlahos 1988) but they had a poor reputation as an unwieldy method requiring a great deal of computing power to achieve reasonable signal to noise i.e. in order to accelerate a sufficient number of particles to high energies it was necessary to inject a prohibitively large number of low energy particles. Kirk & Schneider (1987b) overcame this problem by allowing particles at the shock front to split into a number of daughter particles, each weighted down accordingly. Thus the number of shock crossings can be made to stay approximately constant with energy although the distribution function itself decreases rapidly. This results in more potential power for the technique. To illustrate this Kirk & Schneider modelled the acceleration process allowing for synchrotron losses, something which is not possible with the analytic approach.

Thus relativistic shocks can be regarded as the site of efficient particle acceleration. It it quite feasible that the method is so efficient that the accelerated electrons may themselves have a high enough pressure to have a back-reaction upon the shock front itself. This effect has been investigated by a number of authors (e.g. Blandford 1980; Heavens 1983, 1984; Achterberg et al. 1984 for non-relativistic shocks; Schneider & Kirk 1989 for relativistic shocks). The effect of a non negligible pressure is to create a shock precursor which increases the width of the shock transition. The result is to decrease the efficiency of the acceleration process and steepen the power law. This possibility will be entirely ignored in this thesis.

Having stated a method for accelerating electrons to a power-law distribution in energy it is also worth mentioning that there must also be a cutoff to the distribution

either at low or high energies, otherwise the number density of electrons diverges. The method of injection of electrons is not at all well understood. At high energies there may be a number of physical restrictions to the acceleration process such as synchrotron losses or the finite scale of the perturbations.

The acceleration process will be examined in detail in Chapter 3 where oblique relativistic magnetohydrodynamic will be considered. The Q_J method of Kirk & Heavens (1989) and the Monte Carlo approach of Kirk & Schneider (1987b) will be used is this case. The subject of Chapter 5 will be Fermi acceleration at relativistic shocks in disordered magnetic fields where a technique of following particle trajectories exactly will be developed.

1.2.4 The role played by gravitational microlensing

As for any class of astronomical objects there are objects which do not fit into the scheme of things. There are several blazars which appear to be extraordinary in location. One of the more unusual properties of the class of blazars is the redshift distribution, which is difficult to understand unless we are located at a particularly high space density. To overcome this problem, Ostriker & Vietri (1985) put forward a suggestion that BL–Lacs might be gravitationally microlensed images of higher redshift HPQ's. The BL–Lacs would then be observed projected against normal elliptical galaxies at lower redshifts, the line emitting region is too large to be amplified and would therefore tend to be swamped by the continuum.

In addition to these arguments, one can also use observational oddities to support a claim for gravitational microlensing. Firstly there are three objects that Ostriker (1989) cites: $0235+15$, where a BL–Lac is seen with weak emission lines at $z = 1.75$ but also a strong absorption feature at $z = 1.345$, including ZnII, which would be unique among quasars, but which could also be indicative of cool gas in an intervening galaxy. $0846+51W1$, which when bright is classified as a BL–Lac, but which when faint is a normal quasar. On the plate there is a faint red nebulosity. Possibly, suggests Ostriker, the flare was caused by an intervening star in the foreground galaxy. Finally,

$0537-441$, at $z = 0.894$, is located in the centre of an elliptical of unknown redshift, but which is large enough to make a redshift of 0.9 unlikely.

Although it is possible that the effect could actually be present in a few objects, the original claim, that microlensing is occurring in a large proportion of objects has severe difficulties. In the first instance, the size of the radio emitting region, as inferred from variability is much larger than the optical emitting region, and so would not be amplified by the lensing object. It then follows that one would expect to see some radio-quiet BL–Lacs. Another argument against microlensing is that flare events often produce position angle rotations which cannot be explained by lensing. In the lensing scenario a flare takes place whenever a foreground star moves transverse to the line of sight. This boosts the Stokes parameters to give a flux flare but does not alter their relative values. If one sees a position angle rotation associated with a flare, then the flare is not the result of lensing. Finally, there are the suggested differences between BL–Lacs and HPQ's such as the fact that the VLBI polarization of BL–Lacs tends to be along the jet whereas in HPQ's it is perpendicular to the jet axis and also the difference in speeds of the superluminal components (reported by Gabuzda et al. 1989b). Given these objections, gravitational microlensing will not be considered again in this thesis.

1.3 Thesis Outline

The contents of this thesis are as follows. In Chapter 2 the observations obtained during a series of four nights monitoring the flux and polarization properties of a number of blazars are presented. These data are combined with past observations and the global properties of the whole sample are discussed, together with a few examples of unusual behaviour. The results are compared with what one would expect from a particular parameterization of the emission region. The results obtained in this Chapter are used as the observational base with which the theory of the subsequent chapters is compared. Chapter 3 concerns itself with oblique relativistic MHD shock fronts and Fermi acceleration and whether this mechanism can actually explain the range of spectral indices seen in blazars. Chapter 4 is more speculative and examines

the form of high frequency synchrotron emission and makes an attempt to explain the optical polarization of blazars in terms of a simple source structure. Chapter 5 develops the ideas expressed in the previous two chapters, exploring the possibility of Fermi acceleration at relativistic shocks with disordered magnetic fields by following the motion of individual electrons through the magnetic field exactly. Chapter 6 is something of a digression, proposing a model to explain the extent of the radio emission of the galactic object, SS433. Chapter 7 presents the conclusions of the work.

The work for this thesis will aim to present particular physical models of the emission region based upon what can be deduced from the optical data; it is arguable whether or not this is a suitable approach to the problem. Comparing the methods used for BL–Lacs with those used to understand the kiloparsec scale jets over a longer period of time is an instructive exercise. In the field of large scale jets those methods which relied upon simple physical arguments based upon unjustifiable assumptions such as minimum energy (originally due to Burbidge 1956) have lost favour and have in some cases been shown to be incorrect (e.g. Killeen et al. 1988). Instead numerical models of the flow patterns are currently the trend (e.g. Matthews & Scheuer 1989) as these give more insight into the physics. If one was to be prudent therefore and learn from past lessons, perhaps one could anticipate the best results coming from morphological studies of ever improving VLBI observations and more detailed numerical simulations of jets. However, this is not an option which is open in the present case, where the brief is to understand the emission without any spatial information and only unresolved optical data. Furthermore, although the present approach does not attempt to explain the location or origin of shocks, it does examine the processes which occur at shocks and the effect they have on the synchrotron emission which is a problem that numerical flow studies do not tackle.

Chapter 2

Multifrequency observations of blazars

2.1 Introduction

The optical radiation is important in trying to understand blazars because it probes the structure of sources on scales of the order of a single light day or less, corresponding to the light travel distance of the approximate variability timescale. Thus data taken at these frequencies yield information about the short timescale acceleration and loss mechanisms. The observations presented in this chapter were made at the United Kingdom Infrared Telescope (UKIRT) on Mauna Kea in Hawaii in February 1988. Data were obtained for fourteen objects over four nights, covering the UBVRIJHK wavebands. The data were taken simultaneously in the five optical and any one infrared waveband with the Mark II Hatfield Polarimeter and are appreciably more accurate than previous observations. This high degree of accuracy allows detailed analysis and critical examination of specific models of the emission region. Data from a further 30 objects taken prior to 1988 using the polarimeter, representing the full results of the programme, will be incorporated for the analysis, as this has the potential to strengthen considerably the conclusions drawn from the observations.

Several aspects of the data will be considered in turn. Firstly, the frequency dependence of the observed flux will be examined because of the information it yields about the value of the spectral index of the underlying non-thermal distribution of electrons. A rough estimate of the value of the magnetic field of B$\sim 10^{-5}$T (Gear et al. 1986) yields electron lifetimes of the order of days, implying that acceleration of electrons must take place *in situ*. To date, the most commonly advanced theory is first order Fermi acceleration at magneto-hydrodynamic collisionless shocks. The theory

has the advantage that it makes specific predictions of the spectral index which should be observed (e.g. Heavens 1988). The evidence for breaks or cutoffs having steepened the spectrum (Rieke et al. 1979; Bregman et al. 1981) will also be considered.

The polarization properties can yield important information about the structure of the source. The idealized polarization level ($\sim 70\%$), expected from a uniform magnetic field is not observed, so the magnetic field must be misaligned at some level when averaged over the source. In addition, if a cutoff is affecting the flux which is observed then this will in turn have a characteristic effect upon the polarization. Any preferred direction of position angle which is observed will indicate a preferred orientation of the magnetic field. Following Björnsson (1985), and the previous papers Mead et al. (1990, hereafter MEA90) and Ballard et al. (1990, hereafter BEA90) frequency dependence of polarization will be referred to as FDP, and frequency dependence of position angle as FDθ.

Variability can also play an important role in understanding the emission region, the most notable examples of this in the optical being the week long intensive monitoring programmes carried out on the object BL–Lac (Moore et al. 1982; Brindle et al. 1986) which, upon analysis, yielded source models consisting of randomly oriented components being switched on and off.

Before continuing with this chapter it is worth stating the context within which it is written. Long term status was granted for this programme by the PATT committee in 1986. The time allocated, 20 nights, was divided between four separate observing runs. The first three, 1986 July 31 – August 7, 1987 July 27–30 and 1987 September 18–21 were carried out by a team including Andrew Mead and the results, for a total of 37 blazars, formed the bulk of his thesis, which was published in September 1988. The author was present for the final observing run, 1988 February 15–18, during which 14 blazars were observed. Only the data from these 14 objects are presented here as it would be impractical to include the entire data set although these are included in the analysis. Thus, once the analysis of the data is considered, in Section 2.3, the two parts will be considered as one. This approach, using all the data available, is the same as in the two published papers from the programme, MEA90 and BEA90; it is unnecessary

to cover the same ground as these two works and therefore only a summary of their conclusions will be given, together with an updated analysis.

The layout of the remainder of this chapter is as follows: Section 2.2 describes the general observing strategy and includes a description of the instrument and the techniques used to reduce the data. Section 2.3 analyses the results of all the data which have been taken since 1986 and considers several different aspects such as the instances where dilution of the synchrotron component occurs, variability in the data and the properties of the flux and polarization. In Section 2.4 the observations are fitted with a specific parameterization and the implications this has for the source structure are discussed. In Section 2.5 the conclusions are presented.

2.2 Observational Techniques

2.2.1 The Hatfield Polarimeters

In this section a brief description of the procedure used to obtain the data is given. Throughout the observing programme two instruments were used, the MkI and MkII Hatfield polarimeters. These were both constructed by Dr J.H. Hough at Hatfield Polytechnic. The MkI instrument was described by Bailey & Hough (1982) and later modifications were described by Mead (1988). It was capable of simultaneous observations in any two optical and any one near infrared wavebands. It was only used for the initial observing run in August 1986 and will not be described further.

The MkII device was first employed in July 1987 and was described in detail in MEA90. This is a twin beam instrument which operates at the f/35 focus of UKIRT. The two beams are separated by 50.8mm in the focal plane which corresponds to an angular separation on the sky of 81.3 arcsec. The layout is shown in Fig. 2.1.

The infrared beam passes through a rotating IR-achromatic wave-plate (1–2.5μm) and then an IR/optical dichroic beamsplitter. The reflected IR beam passes through a

wire-grid analyser and into the observatory cryostat (UKT9). The transmitted optical beam is sent to the UKIRT TV camera and is used to aid acquisition and guidance. An efficiency correction must be applied to the infrared polarization measurements, due to inefficiencies which arise from the frequency response of the detector and the wire-grid analyser. The appropriate efficiency to use for correcting the measurements is the measured polarization of an unpolarized star with the Glan prism inserted into the IR beam. The wire grid indicated on the calibration slide in Fig. 2.1 is only used when calibration at wavelengths longer than K is required, where the Glan prism can no longer be used; no such observations are presented.

For the optical beam a super-achromatic wave plate is followed by a Foster prism which produces two orthogonally polarized beams. Dichroics are then used to split the beams into U and R channels, and the B,V and I beams channels with filters used in each beam to form the separate passbands. The polarimeter can thus measure the U,B,V,R,I wavebands and one IR waveband simultaneously. The filters quite closely reproduce the Cousins UBVRI system (Bessell 1979) and any differences have been ignored. The effective wavelengths of the filters are listed in Table 2.1.

Table 2.1: Effective wavelengths and zero-magnitude flux densities. These are taken from Bessell (1979) and Campins et al. (1985).

Filter	$\lambda/\,\mu$m	$\nu/10^{14}$ Hz	S_o/kJy
K	2.18	1.38	0.667
H	1.64	1.83	1.075
J	1.23	2.44	1.603
I	0.80	3.75	2.55
R	0.64	4.68	3.08
V	0.55	5.45	3.64
B	0.44	6.81	4.26
U	0.36	8.33	1.81

The polarimeter is operated as follows. A cycle consists of four rotations of the wave-plate with the object centred on the optical beam at the start of each cycle. At the end of the first rotation the telescope is nodded to bring the object into the IR beam and then nodded back after the third rotation. While not centred on the object, the beams are measuring the sky. On-line software updates the polarization and flux measurements and their combined errors – obtained from photon statistics – at the end

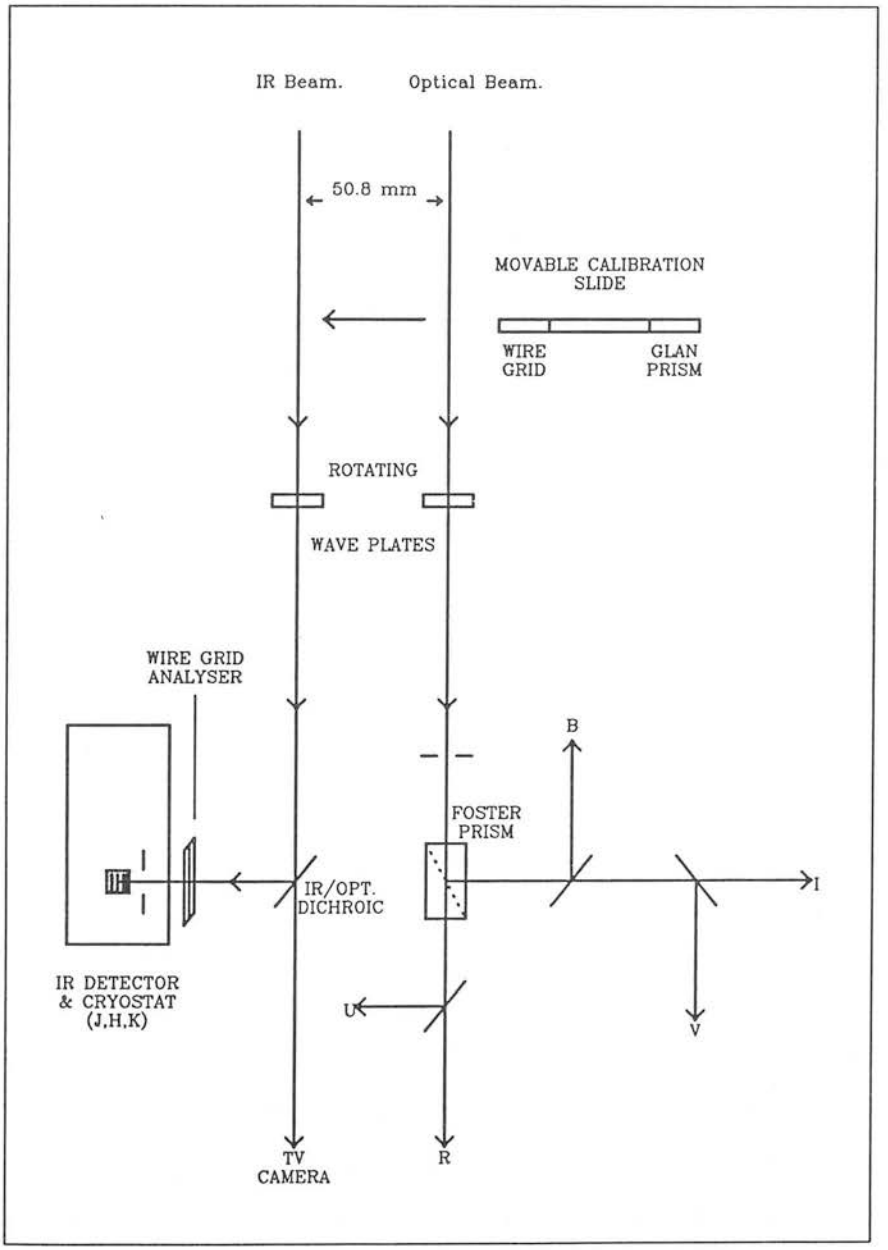

Figure 2.1: This figure illustrates the optical layout of the Mark II Hatfield Polarimeter. Taken from MEA90.

of each cycle.

2.2.2 Data Reduction

The polarimeter returns relative fluxes for each waveband, which are then calibrated by observations of standard stars. The infrared magnitudes were calibrated using stars from the UKIRT standards list and the optical standards were obtained from the catalogue of Landolt (1983). Airmass corrections were performed using observationally determined extinctions. The fluxes have all been corrected for interstellar extinction with the values of $E(B-V)$, taken from Burstein and Heiles (1982). The extinction curve is taken from Rieke and Lebofsky (1985).

The degree of polarization observed is subject to a statistical bias which must be corrected. This is inherent in the measurement of a directional quantity in the presence of noise. Wardle and Kronberg (1974) give the expression for the modal value, which is used to relate the true polarization p to the measured polarization p' for high signal to noise values.

$$p \simeq p' \sqrt{1 - \left(\frac{\sigma_p}{p'}\right)^2} \tag{2.1}$$

The best estimate of the error on p is the error on the measured polarization σ_p. The measured position angle is the best estimate of the true position angle, but the error is underestimated in the case of poor signal to noise (Wardle and Kronberg 1974).

The glan prism is used to measure the relative position angles in each band. The zero of position angle on the sky is determined by measurements of polarized standard stars taken from Serkowski (1974). These position angles are only quoted to one degree accuracy and no errors are given. Consequently for many of the measurements given, the absolute position angle error is dominated by the unknown error in these angles.

2.3 Results

The data obtained for the 14 objects observed in 1988 February are presented in full in Appendix B. Values of $E(B-V)$ are given for each object observed. Selection of the objects to be observed was made prior to the observing run and was modified as the run proceeded. The strategy which was adopted was to observe as many objects as possible and to concentrate on obtaining as much interesting behaviour as possible, where such behaviour was taken to include FDP, FDθ and large degrees of variability. The objects targeted initially were well known sources, such as OJ287, 3C279, OI 090.4 etc. Following the first night, objects showing more unusual properties were selected for repeat observations on later nights, whereas others were dropped and new objects observed to increase the chance of obtaining more unusual features. There are examples of objects (e.g. 1308+326) which were observed and found to be in a very faint state using the TV camera, after which observations were quickly terminated before any quantities could be determined accurately. This procedure is obviously heavily subjective and as a consequence the data obtained form an inhomogeneous set. No information regarding the duty cycle can be derived.

The shape of the spectrum will be characterised by the (local) spectral index which is obtained from the flux, $S(\nu)$ using;

$$\alpha(\nu) = -\frac{d\log_{10} S(\nu)}{d\log_{10}\nu}\,. \tag{2.2}$$

The condition of a frequency-dependent spectral index which results in curvature in the $\log S(\nu) - \log\nu$ plane will be referred to as spectral curvature.

The data are separated into polarized and unpolarized observations because it is only when polarizations in excess of the 3% limit are seen, that it is certain the observed flux contains a blazar contribution. The fits which are presented were all obtained by minimising the χ^2 statistic, using 5% as the critical level. The use of χ^2 is only valid if the errors concerned are distributed normally. Unfortunately, this is certainly not the case here. The errors on the photometry are not simply the random errors associated with photon counting, but include the systematic uncertainties in the

photometric calibration. It is most unlikely that these errors are distributed normally. The use of χ^2 here is justified as the aim is to obtain an approximate idea of the global properties of blazars rather than the exact frequency of the occurrence of spectral curvature within the population or to reject a power-law fit for any individual object. The use of this level of significance is rather lenient given the likely non-normal errors involved (it corresponds to a 1.96σ point of the normal distribution). To test for spectral curvature, a power-law was fitted to all the UKIRT photometric data. The Mark II data all have one infrared and at least four optical measurements and thus, all the data can be fitted by a power-law with at least two degrees of freedom. If a power-law was rejected at this level, then a parabola was fitted and the spectral flux distribution is characterised as having either a convex spectrum ($d\alpha/d\nu > 0$), a concave spectrum ($d\alpha/d\nu < 0$) or a "complex" spectrum.

All the data which had two or more polarization measurements were tested for FDP. The weighted mean of the measured polarizations was calculated and then tested against all the measured polarizations by use of the χ^2 statistic with the loss of one degree of freedom. In order to assign the FDP categories where a constant polarization level could not be fitted, a power-law polarization behaviour was fitted ($p(\nu) \propto \nu^{\beta}$). The form of this empirical fit was chosen because the polarization degree is fixed as positive and this allows an unconstrained minimisation to be performed with respect to $\log p_{14}$ and β. The two FDP categories ($dp/d\nu > 0$ and $dp/d\nu < 0$) were assigned on the basis of the sign of the fitted value of β. Those objects not fitted (at the 5% level) by this functional form, are described as having "complex" polarization behaviour. This procedure will flag behaviour, such as that seen in $1641+399$ and $2200+420$, where the FDP is only significant over a narrow range of the observed frequencies.

Similarly the data were tested for FDθ . The different categories were assigned using the same method as for FDP. Polarimetric errors should have an approximately normal distribution in the case of high signal to noise, and the position angle error distribution is also approximately normal in this regime (Wardle and Kronberg 1974).

In the following subsection a description of the individual objects which were observed is given.

2.3.1 Summary of the behaviour of individual objects

H0414 + 009

This object is an x-ray selected blazar, first detected by the HEAO–1 satellite. Ulmer et al. (1983) classified it as a candidate BL Lac object from x-ray, optical and radio data. Impey and Tapia (1988) reported an optical polarization of $2.76 \pm 0.29\%$. Recently a redshift of 0.287 has been reported by Halpern et al. (1991). On 1988 February 15 and February 16 the B polarization was 6.4 ± 0.8 % and therefore this object can be confirmed as a blazar. There was no evidence for FDP or FDθ on either night although significant spectral curvature was seen.

PKS 0422 + 004

This object was present in the catalogue of Angel & Stockman (1980; hereafter AS80). No redshift is available. It was observed twice, on 1988 February 16 and 18. Spectral curvature was observed on both occasions. There was no evidence for frequency dependent polarization, but the polarization decreased from 21.4 ± 0.3 to $12.4 \pm 0.2\%$ between these dates. The position angle behaviour was complex as there was a significant rotation between the infrared and optical wavebands.

PKS 0735 + 178

This blazar is known to display spectral curvature over a wide range of frequency (see Landau et al. 1986 for observations of this and the following objects: 0736 + 017, 0851 + 202, 1156 + 295, 1253 − 055, 1418 + 546, 1510 − 089, 1641 + 399). On 1988 February 16 there was evidence for $dp/d\nu > 0$. The object has a redshift of 0.424. VLBI polarization observations have been published by Gabuzda et al. (1989a) showing a position angle lying roughly along the jet axis, which lies at an angle of 14°. It has an outer knot which is more polarized than the unresolved core.

PKS 0736 + 017

This again is an AS80 blazar which has often been observed in the past. It was

observed on 1988 February 15, 16 when no significant polarization was detected at the 3% level. The flux behaviour was complex.

0754 + 100, OI 090.4

0754 + 100 is a well known AS80 blazar which was observed on 1988 February 15, 16, 17 and 18. The polarization showed $dp/d\nu > 0$, the degree of which decreased with time. On the last two nights the position angle was frequency independent at an average angle of 36.2°.

0818 – 128, OJ–131

This AS80 blazar was observed on 1988 February 15, 16 and 17. During the course of the observations FDP was seen with polarizations increasing to the blue and the degree of FDP increasing from night to night. The spectra tended to show spectral indices increasing with frequency. The position angle was frequency independent throughout, at an average angle of 81°.

0851 + 202, OJ287

This well known object was the subject of a previous paper (Holmes et al. 1984b), in which notable behaviour was interpreted in terms of a two-component model of the emission. It was observed on 1988 February 15, 16 and 17 to have a polarization around 10%. $dp/d\nu > 0$ was observed on February 16 and February 17. The data presented here for OJ287 are satisfactorily fitted by the two-component model. The VLBI polarization measurements of Roberts et al. (1987) indicated a position angle of −115°, implying a magnetic field lying perpendicular to the jet axis.

0906 + 015

This source has a single polarization measurement (Moore & Stockman 1984). It was observed as a candidate blazar on 1988 February 15 when at the 3% level no significant polarization was detected.

1101 + 384, Mkn 421

This is an AS80 object, located in an elliptical galaxy at redshift, z=0.0308. It was observed once, on 1988 February 15. The fact that the polarization showed complex behaviour and the curvature in the spectrum is in agreement with the hypothesis that the galactic flux significantly contaminates the blazar component.

1147 + 245

This was an AS80 blazar which displayed $dp/d\nu > 0$ and complex position angle behaviour on the single occasion on which it was observed (1988 February 18).

1156 + 295

On 1988 February 15, 16 and 17 this well studied AS80 blazar was observed to have frequency independent polarizations and position angles (frequency averaged) of 24% at 165°. It lies at a redshift of 0.729 and has been the subject of several intensive multifrequency monitoring programmes (see McHardy 1989).

1253 − 055, 3C 279

This object is a well studied superluminal radio source, which has long been known to be a blazar. The observations of 1986 August show a polarization flare, and a maximum U polarization of 45.92±0.98%, the largest polarization ever seen in the IR/optical for a blazar. In 1988 February the polarization rose throughout the observations from $19.6 \pm 0.8\%$ to $30.7 \pm 0.6\%$ in the U band.

1418 + 546, OQ 530

During the 1988 February run the position angle of this AS80 blazar was constant at 144° on the 16th and 17th. On the final night significant FDθ was observed, from $132.0 \pm 2.5°$ at H to $156.2 \pm 3.9°$ at U.

1424 + 240

This is a smooth spectrum radio source identification which was confirmed as a blazar by Impey and Tapia (1988). Frequency independent polarizations (19.6%) and position angles (116°) were recorded on 1988 February 16, 17 and 18.

PKS 1510 – 089

This object was confirmed to be a blazar by Moore and Stockman (1981) and Smith et al. (1987). It is one of the more violently variable HPQ's with recorded flux variations of 5.4 magnitudes (Moore and Stockman 1981). It was observed twice during 1988 February although the data obtained were not published in BEA90. They will be published in Wills et al. (in preparation). Complex polarization behaviour was observed.

1641 + 399 3C345

This frequently observed blazar was the subject of Mead et al. (1988). As with the data for 1520 – 089, those obtained in February 1988 will be published in the near future. The observations show polarization decreasing to the blue which, it is suggested, is caused by dilution by unpolarized optical light.

Hereafter these observations will be combined with the data obtained in the three previous observing runs and will be treated as a single data set, as was mentioned earlier. Table 2.2 summarizes all the results from the 14 clear nights when observing was possible, a total of 156 photometric data sets were obtained. Table 2.2 lists all the polarimetric observations of blazars and whether they were fitted (at the 5% level of significance) by a constant polarization or FDP (either with $dp/d\nu > 0$, $dp/d\nu < 0$ or with more complex behaviour). Also tabulated are the results of testing for frequency dependence of the position angle of polarization. FDθ is seen to be rarer than FDP. There is no evidence suggesting any preference for clockwise over counter-clockwise variations with frequency.

2.3.2 Contamination by unpolarized components

It is a matter of primary importance to establish whether or not the data presented can be taken as pure synchrotron sources, because, at later stages in this thesis models of the synchrotron emitting regions will be discussed and contamination of the source by unpolarized emission may severely affect the appearance of the source and, hence, the conclusions drawn.

There are two possible origins for contamination within the data set. The first is blue light. Excess flux was first noticed in highly polarized quasars by Shields (1978). Malkan & Sargent (1982) fitted this "blue-bump" emission with the black body spectrum which approximates the spectrum from a thermally radiating thin accretion disk. The clearest example of such contamination was seen in the observations of 3C345 (1641 + 399) which were the subject of a paper by Mead et al. (1988). The effect of unpolarized emission at the blue end of the spectrum is to produce a decreasing polarization and spectral index with frequency. If however, the underlying synchrotron source has a frequency independent spectral index and polarization, then by plotting the polarized flux, one can recover details about the non-thermal source from the resulting power-law. In order to select objects where this may have affected the spectra, objects showing either $d\alpha/d\nu < 0$ or not showing monotonic polarization variation were selected. These are listed in Table 2.3 and it might be noted that several of these showed little or no significant polarization.

The χ^2 levels of significance in Table 2.3 are quoted for a fit to a frequency-independent polarization for the FDP cases and to a power law flux distribution for the abnormal spectra cases. An alternative explanation of this polarization behaviour is a superposition of misaligned polarized components. This is equivalent to the Holmes et al. (1984b) two-component model, where two polarized components, of approximately equal polarized fluxes produce a polarization signature which decreases to zero at the frequency where the polarized fluxes are equal. This will also produce FDθ and indeed such behaviour was seen in 0109 + 224 on 1986 August 4 and 1418 + 546 on 1988 February 18.

Table 2.2: Summary of the observations. $\alpha_0(>0,<0)$ refers to the spectral index constant (increasing, decreasing) with frequency. This is also indicated for polarization and position angle. Those observations not satisfactorily fitted are labelled complex.

Object	E(B-V)	Date	Flux	Polarization	Position Angle
$0048-097OB-081$	0.00	86 Jul 31	α_0	$\Delta p>0$	θ_0
		86 Aug 3	$\Delta\alpha<0$	$\Delta p>0$	θ_0
		86 Aug 4	α_0	$\Delta p>0$	θ_0
		86 Aug 6	α_0	$\Delta p>0$	θ_0
		86 Aug 7	α_0	$\Delta p>0$	θ_0
		87 Jul 27	$\Delta\alpha<0$	p_0	θ_0
		87 Jul 29	α_0	p_0	θ_0
		87 Jul 30	α_0	p_0	θ_0
		87 Sep 18		p_0	θ_0
		87 Sep 19	α_0	p_0	θ_0
		87 Sep 20		p_0	θ_0
PKS $0106+013$	0.00	86 Aug 4	α_0	unpolarized	
		87 Jul 28	$\Delta\alpha<0$	p_0	θ_0
		87 Sep 21	α_0	unpolarized	
GC $0109+224$	0.06	86 Aug 1	α_0	p_0	θ_0
		86 Aug 4	α_0	$\Delta p<0$	$\Delta\theta<0$
		86 Aug 5		p_0	$\Delta\theta<0$
		86 Aug 6		$\Delta p>0$	θ_0
		86 Aug 7	α_0	$\Delta p>0$	θ_0
		87 Jul 27	α_0	p_0	θ_0
		87 Jul 30	$\Delta\alpha>0$	p_0	θ_0
		87 Sep 19	α_0	p_0	θ_0
		87 Sep 20		p_0	θ_0
		87 Sep 21	α_0	$\Delta p>0$	complex
$0118-272$	0.00	86 Aug 5	α_0	p_0	θ_0
		86 Aug 6		p_0	complex
		86 Aug 7	α_0	p_0	θ_0
		87 Jul 27	$\Delta\alpha<0$	$\Delta p>0$	θ_0
		87 Jul 30	α_0	$\Delta p>0$	θ_0
		87 Sep 20		complex	θ_0
		87 Sep 21	α_0	$\Delta p>0$	θ_0
$0138-097$	0.00	86 Aug 5	α_0	$\Delta p<0$	θ_0
		86 Aug 6		p_0	θ_0
		86 Aug 7	α_0	p_0	$\Delta\theta>0$
		87 Jul 28	α_0	p_0	θ_0
		87 Jul 30	α_0	p_0	θ_0
		87 Sep 19	α_0	$\Delta p>0$	θ_0
		87 Sep 20	α_0	$\Delta p>0$	θ_0
		87 Sep 21	α_0	p_0	θ_0
$0219-164$	0.00	87 Jul 28	α_0	p_0	θ_0
$0219+428$ 3C 66A	0.09	86 Aug 1		p_0	$\Delta\theta>0$
		86 Aug 4		$\Delta p>0$	θ_0
		86 Aug 6		p_0	θ_0
		86 Aug 7		p_0	θ_0
		87 Jul 27	α_0	p_0	θ_0
		87 Jul 30	α_0	p_0	θ_0
		87 Sep 18		complex	θ_0
		87 Sep 19		p_0	θ_0
		87 Sep 20	α_0	p_0	θ_0
		87 Sep 21		p_0	θ_0

Table 2.2: Summary of the observations contd.

Object	E(B-V)	Date	Flux	Polarization	Position Angle
AO 0235 + 164	0.15	87 Jul 28	$\Delta\alpha > 0$	p_0	θ_0
		87 Sep 20	$\Delta\alpha > 0$	complex	θ_0
0300 + 470 4C 47.08	0.15	87 Sep 20		p_0	θ_0
0323 + 022	0.06	86 Aug 1			
		87 Sep 21		p_0	θ_0
0336 − 019	0.06	86 Aug 5		unpolarized	
0338 − 214	0.00	86 Aug 6		p_0	θ_0
		87 Sep 19		p_0	θ_0
0414 + 009	0.12	88 Feb 15	$\Delta\alpha > 0$	p_0	θ_0
		88 Feb 16	$\Delta\alpha > 0$	p_0	θ_0
0422 + 004	0.12	88 Feb 16	$\Delta\alpha > 0$	p_0	complex
		88 Feb 18	$\Delta\alpha > 0$	p_0	complex
PKS 0735 + 178	0.03	87 Sep 19		p_0	$\Delta\theta < 0$
		88 Feb 15	complex	p_0	complex
		88 Feb 16	α_0	p_0	θ_0
		88 Feb 18	α_0	p_0	complex
0736 + 017	0.12	88 Feb 15	complex	unpolarized	
		88 Feb 16	complex	unpolarized	
0754 + 100	0.00	88 Feb 15	$\Delta\alpha > 0$	$\Delta p > 0$	$\Delta\theta > 0$
		88 Feb 16	$\Delta\alpha > 0$	$\Delta p > 0$	complex
		88 Feb 17	α_0	p_0	θ_0
		88 Feb 18	α_0	p_0	θ_0
0818 − 128 OJ-131	0.09	88 Feb 15	complex	$\Delta p > 0$	θ_0
		88 Feb 16	$\Delta\alpha > 0$	$\Delta p > 0$	θ_0
		88 Feb 17	$\Delta\alpha > 0$	$\Delta p > 0$	θ_0
0851 + 202 OJ287	0.00	88 Feb 15	$\Delta\alpha > 0$	p_0	θ_0
		88 Feb 16	α_0	$\Delta p > 0$	θ_0
		88 Feb 17	α_0	$\Delta p > 0$	$\Delta\theta > 0$
0906 + 015	0.00	88 Feb 15	α_0	unpolarized	
1101 + 384	0.00	88 Feb 15	$\Delta\alpha > 0$	complex	θ_0
1147 + 245	0.00	88 Feb 18	α_0	$\Delta p > 0$	$\Delta\theta < 0$
1156 + 295	0.00	88 Feb 15	α_0	p_0	θ_0
		88 Feb 16	α_0	p_0	θ_0
		88 Feb 17	α_0	p_0	θ_0
1253 − 055 3C 279	0.03	86 Aug 1	α_0	p_0	θ_0
		86 Aug 2	α_0	$\Delta p > 0$	$\Delta\theta < 0$
		86 Aug 4	α_0	$\Delta p > 0$	complex
		86 Aug 5	α_0	$\Delta p > 0$	$\Delta\theta < 0$
		86 Aug 6	α_0	$\Delta p > 0$	$\Delta\theta < 0$
		87 Jul 28	$\Delta\alpha > 0$	$\Delta p > 0$	θ_0
		88 Feb 16	α_0	p_0	complex
		88 Feb 17	α_0	p_0	complex
		88 Feb 18	α_0	$\Delta p > 0$	θ_0
1413 + 135	0.03	86 Aug 6	α_0	unpolarized	
1418 + 546 OQ 530	0.03	86 Aug 4		$\Delta p > 0$	θ_0
		86 Aug 5		$\Delta p > 0$	complex
		86 Aug 6		complex	θ_0
		87 Jul 30	α_0	$\Delta p > 0$	complex
		87 Sep 20		$\Delta p > 0$	θ_0
		87 Sep 21		$\Delta p > 0$	θ_0
		88 Feb 16	$\Delta\alpha > 0$	complex	θ_0
		88 Feb 17	$\Delta\alpha > 0$	complex	θ_0
		88 Feb 18	$\Delta\alpha > 0$	p_0	$\Delta\theta > 0$

Table 2.2: Summary of the observations contd.

Object	E(B-V)	Date	Flux	Polarization	Position Angle
1424 + 240	0.00	88 Feb 16	complex	p_0	θ_0
		88 Feb 17	$\Delta\alpha > 0$	p_0	θ_0
		88 Feb 18	α_0	unpolarized	
PKS 1510 − 089	0.06	86 Aug 1	α_0	p_0	
		88 Feb 15	$\Delta\alpha < 0$	complex	θ_0
		88 Feb 16	complex	complex	$\Delta\theta < 0$
1514 − 241 AP Libra	0.15	86 Aug 1		p_0	complex
		87 Jul 27	$\Delta\alpha > 0$	complex	θ_0
1538 + 149 4C 14.60	0.00	86 Aug 1	α_0	unpolarized	
1641 + 399 3C 345	0.00	86 Aug 1	$\Delta\alpha < 0$	complex	θ_0
		86 Aug 2	$\Delta\alpha < 0$	complex	θ_0
		86 Aug 4	$\Delta\alpha < 0$	complex	θ_0
		86 Aug 5	$\Delta\alpha < 0$	complex	θ_0
		86 Aug 6	complex	complex	θ_0
		86 Aug 7		$\Delta p < 0$	θ_0
		87 Jul 28	complex	unpolarized	
		87 Jul 30	$\Delta\alpha < 0$	unpolarized	
		87 Sep 19	$\Delta\alpha < 0$	unpolarized	
		88 Feb 15	complex	p_0	θ_0
		88 Feb 16	complex	p_0	θ_0
		88 Feb 17	complex	complex	θ_0
		88 Feb 18	complex	p_0	θ_0
1652 + 398 Mkn 501	0.00	87 Sep 21		complex	$\Delta\theta < 0$
1717 + 178 OT 129	0.06	86 Aug 6	α_0	p_0	θ_0
		86 Aug 7		$\Delta p < 0$	θ_0
		87 Jul 30	α_0	unpolarized	
1727 + 502 I Zw 186	0.00	86 Aug 6		p_0	$\Delta\theta < 0$
		86 Aug 7		$\Delta p > 0$	θ_0
		87 Sep 21		$\Delta p > 0$	θ_0
1749 + 096 OT 081	0.15	86 Jul 31		p_0	$\Delta\theta > 0$
		86 Aug 5		p_0	θ_0
		86 Aug 6		p_0	θ_0
		86 Aug 7		$\Delta p > 0$	θ_0
		87 Jul 27	α_0	$\Delta p > 0$	θ_0
1921 − 293 OV-236	0.12	86 Aug 3		p_0	$\Delta\theta > 0$
		86 Aug 6		$\Delta p < 0$	θ_0
		86 Aug 7		p_0	θ_0
		87 Jul 27	complex	unpolarized	
2032 + 107	0.12	87 Jul 27	complex	unpolarized	
PKS 2155 − 304	0.00	86 Aug 1	α_0	$\Delta p > 0$	complex
		86 Aug 5	α_0	p_0	θ_0
		86 Aug 6		p_0	$\Delta\theta > 0$
		86 Aug 7	α_0	p_0	θ_0
		87 Jul 27	α_0	$\Delta p > 0$	$\Delta\theta < 0$
		87 Sep 21		complex	θ_0
2200 + 420 BL Lacertae	0.15	86 Jul 31		$\Delta p > 0$	θ_0
		86 Aug 1		p_0	θ_0
		86 Aug 3	$\Delta\alpha > 0$	complex	$\Delta\theta > 0$
		86 Aug 4		complex	$\Delta\theta > 0$
		86 Aug 5		complex	$\Delta\theta > 0$
		86 Aug 6		complex	θ_0
		86 Aug 7		complex	$\Delta\theta > 0$
		87 Jul 27	$\Delta\alpha > 0$	$\Delta p < 0$	$\Delta\theta < 0$
		87 Jul 28	$\Delta\alpha > 0$	complex	$\Delta\theta < 0$
		87 Jul 30	$\Delta\alpha > 0$	$\Delta p < 0$	$\Delta\theta < 0$
		87 Sep 19	$\Delta\alpha > 0$	complex	complex
		87 Sep 20		complex	$\Delta\theta > 0$
		87 Sep 21		complex	$\Delta\theta > 0$

Table 2.2: Summary of the observations contd.

Object	E(B-V)	Date	Flux	Polarization	Position Angle
PKS 2208 – 137	0.00	86 Aug 3		unpolarized	
		86 Aug 4		unpolarized	
		86 Aug 6	α_0	unpolarized	
		86 Aug 7		unpolarized	
2223 – 052 3C 446	0.03	86 Aug 4	α_0	unpolarized	
		87 Jul 27	α_0	p_0	θ_0
		87 Jul 29	α_0	p_0	θ_0
		87 Jul 30	α_0	p_0	θ_0
		87 Sep 20		$\Delta p > 0$	θ_0
		87 Sep 21		p_0	θ_0
2230 + 114 4C 11.69	0.03	86 Aug 3	α_0	unpolarized	
		86 Aug 4	α_0	unpolarized	
2251 + 158	0.06	86 Aug 5	α_0	unpolarized	
		87 Jul 28	$\Delta\alpha > 0$	unpolarized	
		87 Sep 20		p_0	θ_0
2254 + 074 OY 091	0.06	86 Jul 31		$\Delta p > 0$	θ_0
		86 Aug 1		p_0	θ_0
		86 Aug 3	complex	$\Delta p > 0$	θ_0
		86 Aug 4	$\Delta\alpha > 0$	complex	θ_0
		86 Aug 5		$\Delta p > 0$	θ_0
		86 Aug 6		$\Delta p > 0$	θ_0
		86 Aug 7	α_0	p_0	complex
		87 Jul 28	$\Delta\alpha > 0$	complex	θ_0
		87 Jul 30	$\Delta\alpha > 0$	complex	θ_0
		87 Sep 18		p_0	complex
		87 Sep 21		$\Delta p > 0$	θ_0

Table 2.3: Objects possibly containing contaminating flux. The data for 3C345 has been excluded.

Object Name		Date of observation	Significance Level (%)
$0106+013$	(2)	1987 July 28	2.5
$0109+224$	(1)	1986 August 4	1.0
$0118-272$	(2)	1987 July 27	0.01
$0138-097$	(1)	1986 August 5	1.0
$0735+178$	(2)	1988 February 15	5.0
$0754+100$	(1)	1988 February 18	2.5
$0818-128$	(2)	1988 February 15,16	0.01
$1418+546$	(1), (2)	1986 August 6	0.01
$1418+546$	(2)	1988 February 18	0.01
$1424+240$	(2)	1988 February 16	0.01
$1510-089$	(2)	1988 February 15	1×10^{-4}
$1510-089$	(2)	1988 February 16	0.1
$1717+178$	(1)	1986 August 7	0.01
$1749+096$	(2)	1986 August 5	0.01
$1921-293$	(1)	1986 August 6	0.1
$1921-293$	(2)	1987 July 27	0.01
$2032+107$	(2)	1987 July 27	0.01
$2208-137$	(2)	1986 August 3,4 & 7	0.01
$2251+158$	(1)	1987 September 20	3.0

(1)$\equiv$ FDP with $dp/d\nu < 0$, (2)$\equiv$concave flux spectra ($d\alpha/d\nu < 0$)

Of greater importance is the possible contaminating flux originating in the starlight of the host galaxy. This emission would peak in the near infrared and drop off in the optical and hence the effect on the blazar spectra would be to produce artificial spectral curvature and FDP with the polarization increasing to the blue. Since, as will be seen, this is similar to the behaviour which is actually observed in blazars, it could cause confusion and those objects which are known to be situated in low redshift galaxies ($0521-365$, $0548-022$, $1101+384$, $1133+704$, $1514-241$, $1652+398$ and $2200+420$) should be treated with caution. In future they should be studied with multi-aperture photometry or imaging, in order to separate out the galaxy component (c.f. Kikuchi & Mikami 1987). However, in the case of the higher redshift sources, the fraction of observed flux which originates within galaxies is uncertain. It is unlikely, however, that there will be many galaxies at redshifts $z \simeq 1$ with K fluxes greater than those seen for blazars (Glazebrook, personal communication). A further objection to the

suggestion that the properties of blazars are heavily influenced by galactic flux is that many properties such as the level of FDP are independent of flux. A constant galactic flux will not be able to induce artificial FDP at all flux levels.

2.3.3 Flux and spectral index behaviour

In this and the following sections in this chapter several correlations between various aspects of the data will be considered. These will be calculated using a non-parametric Spearman rank correlation technique (see Conover 1980). A non-parametric test between properties is suitable because there is no obvious origin to the scatter in the data points. As was previously noted the selection of observations was highly subjective and so the data set obtained is inhomogeneous. Therefore, when calculating correlations between properties it would be inappropriate to treat each data point as independent. For example, many flux and polarization measurements remained constant from day to day or even in a few cases, between observing runs. To try to overcome such potential biases only one value from each object is employed in the correlations, either the maximum or the median value. This point was made in BEA90, but it is arguable whether the method used there was correct. This is because the points taken were, for example, maximum observed values in both quantities i.e. the procedure could lead to a point which had the maximum value in the first and second variables but the individual observations from which these values were taken could be different and comprise data taken anything up to 18 months apart. Therefore the results presented in this chapter have been corrected so that correlations are only examined between various quantities where each point consists of simultaneous data. It could, however, be argued that if any correlation is in fact present then it will make itself apparent because maximum values will be simultaneous anyway although since there will be scatter in the points it is more appropriate to alter the analysis. As will become apparent, this change of method does not greatly affect the conclusions drawn.

The shape of the spectrum is important because of its relevance to theories of acceleration mechanisms which provide specific predictions about the range of spectral

index. For all observations there are at least three flux points and, hence, an attempt was made to fit all the data points with a power law of constant spectral index. The technique employed was to minimise the χ^2 value which was carried out using a NAG minimization routine, E04FCF. In many cases a constant power law could not fit the data satisfactorily and, in those instances, an alternative form was tried, a parabola in $\log S - \log \nu_{14}$ space. ν_{14} is the frequency in units of 10^{14} Hz, a convenient reference frequency. This could only be attempted if there were four or more flux points, as a fit to only three points would be unique with zero degrees of freedom. The form of the parabola was:

$$\log_{10} S(\nu_{14}) = \log_{10} S(\nu = 10^{14} Hz) - a \log_{10} \nu_{14} + b(\log_{10} \nu_{14})^2 \tag{2.3}$$

and on this basis the spectral index could be estimated at any frequency. The degree of spectral curvature over the range of observations was calculated as:

$$\Delta\alpha_{B-H} = \alpha(\nu_B) - \alpha(\nu_H) \tag{2.4}$$

The resulting parabola could then be classified according to whether $\Delta\alpha > 0$ or $\Delta\alpha < 0$. If no satisfactory fit could be achieved again then the spectrum was classified as complex, although the best fit parabola was still used to derive $\Delta\alpha_{B-H}$. It should be stressed that the motivation for fitting parabolae to the data was solely to indicate the sense of spectral curvature, there was no theoretical motivation. The results of fitting the data are summarized in Table 2.4 and Fig. 2.2.

Another useful indicator of the properties of the synchrotron emitter is the polarized flux because synchrotron radiation is expected to be the sole source of polarized radiation. This quantity is calculated by multiplying the flux in a given waveband by the polarization value. The polarized flux spectral index and degree of polarized spectral curvature are then calculated in the same manner as the total flux parameters. The results are summarized in Table 2.4 and Fig. 2.3.

The results can now be compared with the predictions of spectral index obtained from particle acceleration theories. As can be seen by inspection of Table 2.4, many of

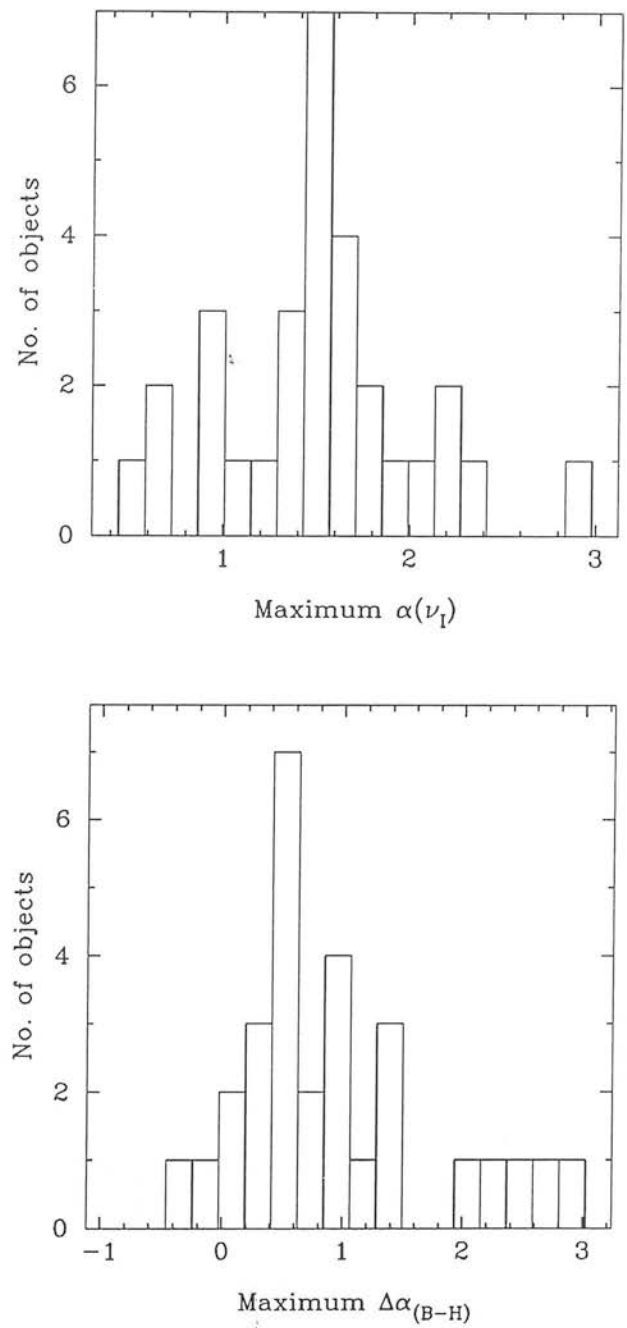

Figure 2.2: This shows histograms of the maximum values of $\alpha(\nu_B) - \alpha(\nu_H)$ and $\alpha(\nu_B)$.

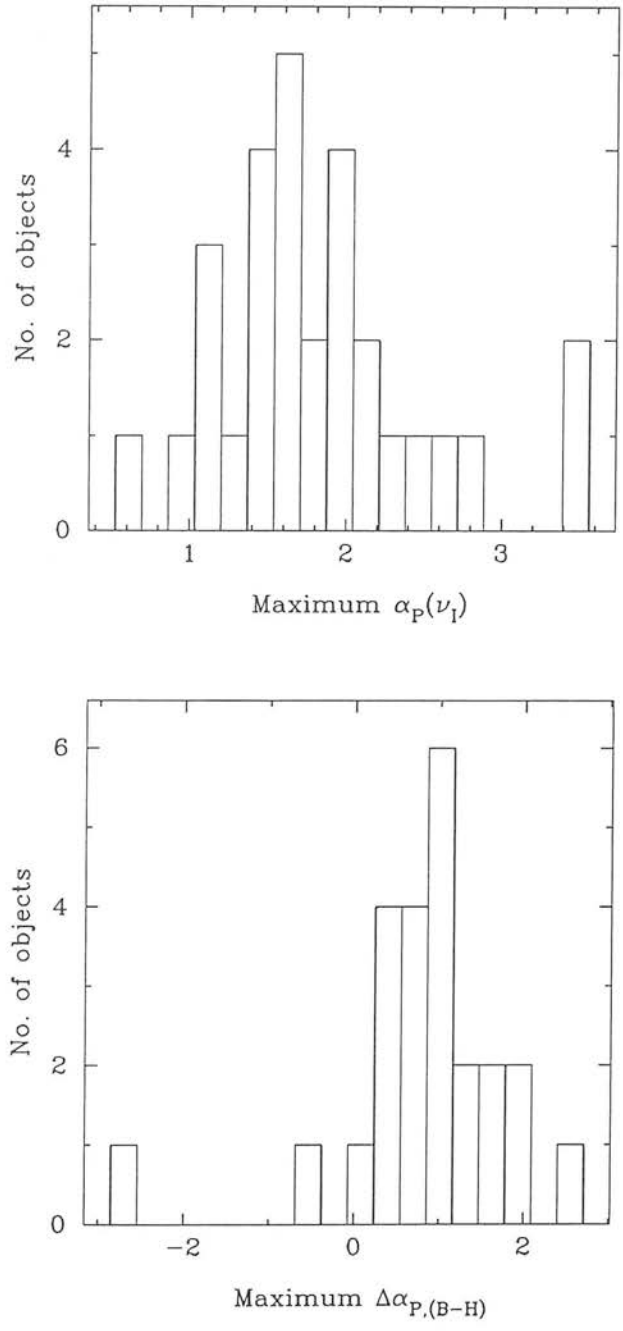

Figure 2.3: This shows histograms of the maximum values of $\alpha_p(\nu_B) - \alpha_p(\nu_H)$ and $\alpha_p(\nu_B)$.

the spectral indices are extremely steep, the maximum being $\alpha = 2.89$ for the object $1749 + 096$. Furthermore, the degree of spectral curvature is high in a large number of cases (e.g. $\Delta\alpha_{B-H} = 3.37$ for $0818 - 128$). As had been made clear, the prime candidate for producing the non-thermal spectra of blazars is Fermi acceleration. The spectral indices that this produces were summarized by Heavens (1988). To repeat, these are that a strong, non-relativistic shock can produce a spectral index $\alpha = 0.5$ (Bell 1978); strong, relativistic shocks can produce a wider range, between roughly $\alpha \sim 0.4 \rightarrow 0.63$ (Kirk & Schneider 1987a); weak shocks, where the energy gain per shock crossing is less, produce steeper spectral indices, any value greater than $\alpha = 0.5$ in fact. Synchrotron losses, combined with a finite emission region, produce a spectral break accompanied by a gradual increase of $\Delta\alpha = 0.5$, if the acceleration of electrons is steady (e.g. Bregman 1985; Heavens & Meisenheimer 1986). There is, in addition, the possibility of a high energy cutoff to the distribution (Blandford 1979). An upper energy cut-off in the electron energy distribution is an expected feature of particle acceleration at shocks because the acceleration timescale is longer than the energy loss timescale above certain energies. Biermann & Strittmatter (1987) derive a cut-off frequency between 3×10^{14} Hz and 2×10^{15} Hz. The value of the cutoff frequency is dependent on the assumptions made in its derivation, for example, a Kolmogorov spectrum ($\propto k^{-5/3}$) was used to model the spectrum of the turbulent magnetic energy density responsible for the scattering while Heavens (1984) showed that a k^{-1} spectrum can give rise to a cut-off at x-ray frequencies or higher.

Table 2.4: Flux and polarized flux spectral indices at I and spectral curvature parameters

Object Name	$\alpha(\nu_I)$ Med	Max	Obs.	$\Delta\alpha_{(B-H)}$ Med	Max	Obs.	$\alpha_p(\nu_I)$ Med	Max	Obs.	$\Delta\alpha_{p,(B-H)}$ Med	Max	Obs.
0048 − 097	1.32	2.29	9	0.02	0.42	7	1.16	1.27	9	1.28	1.68	7
0106 + 013	1.36	1.36	1	−0.43	−0.43	1	0.64	0.64	1	−2.67	−2.67	1
0109 + 224	1.24	1.55	7	0.42	0.85	5	1.40	1.59	5	−0.03	−0.03	4
0118 − 272	1.18	1.98	5	0.00	0.62	4	1.06	1.11	5	−0.39	1.08	4
0138 − 097	1.25	1.45	7	0.45	0.70	5	1.17	2.08	7	0.33	0.76	5
0219 − 164	1.00	1.00	1	0.35	0.35	1	1.07	1.07	1	0.04	0.04	1
0219 + 428	1.21	1.44	3	0.01	0.72	3	1.19	1.38	5	0.35	0.36	3
0235 + 164	1.84	2.23	2	2.44	2.49	2	2.32	3.41	2	1.60	2.50	2
0338 − 214	–	–	–	–	–	–	2.03	2.03	1	–	–	–
0414 + 009	1.01	1.03	2	1.09	1.09	2	1.71	2.19	2	−0.71	−0.38	2
0422 + 004	1.19	1.22	2	1.25	1.39	2	–	–	–	–	–	–
0735 + 178	1.55	1.62	3	0.41	0.47	3	1.50	1.50	1	0.74	0.74	1
0754 + 100	1.39	1.51	4	0.40	0.56	4	1.51	1.55	2	0.05	0.92	2
0818 − 128	1.20	1.52	3	1.29	3.37	3	1.63	1.92	3	1.32	3.38	3
0851 + 202	1.44	1.47	3	0.31	0.45	3	1.36	1.53	2	−0.24	0.53	2
1101 + 384	0.62	0.62	1	1.03	1.03	1	0.92	0.92	1	0.44	0.44	1
1147 + 245	1.36	1.36	1	0.27	0.27	1	–	–	–	–	–	–
1156 + 295	1.25	1.29	3	0.06	0.11	3	1.28	1.40	3	−0.08	0.34	3
1253 − 055	1.16	1.62	9	0.42	0.95	8	1.59	1.78	3	0.43	1.11	2
1418 + 546	1.15	1.59	4	0.80	1.28	4	1.35	1.61	3	0.43	0.82	2
1424 + 240	0.76	0.95	3	0.45	1.04	3	1.03	1.05	3	0.64	1.03	3
1510 − 089	1.58	1.68	2	−0.42	−0.18	2	2.01	2.01	1	0.66	0.66	1
1514 − 241	0.99	0.99	1	1.99	1.99	1	1.79	1.79	1	1.33	1.33	1
1641 + 399	1.70	2.07	10	−0.75	−0.11	10	1.76	2.29	11	0.06	1.53	10
1717 + 178	1.83	1.83	1	–	–	–	1.62	1.62	1	–	–	–
1727 + 502	–	–	–	–	–	–	3.45	3.45	1	–	–	–
1749 + 096	2.89	2.89	1	0.28	0.28	1	–	–	–	–	–	–
1921 − 293	–	–	–	–	–	–	2.57	2.77	3	–	–	–
2155 − 304	0.62	0.71	2	0.02	0.42	2	–	–	–	–	–	–
2200 + 420	1.38	1.52	5	2.73	2.87	5	2.66	2.66	1	–	–	–
2223 − 052	1.71	1.78	3	0.28	0.50	3	1.66	1.43	3	1.96	2.00	3
2254 + 074	0.92	2.23	5	2.39	2.69	4	1.68	1.96	6	0.59	0.93	3

Clearly, the only way the optical spectral indices can be explained in terms of Fermi acceleration is if there are weak shocks or, alternatively, if the spectral curvature is associated with a cutoff, as all other possibilities fail to explain the full range of spectral indices. Weak shocks can explain any spectral index and indeed the model of Hughes et al. (1985), where a shock is responsible for the flaring behaviour at radio wavelengths, employs "weak" shocks, with a compression ratio around three. It is interesting that later Hughes et al. (1990) discounted the possibility of particle acceleration occurring at their shocks because of the effect that it would have in altering the particle spectrum. However, arbitrarily weak shocks can produce arbitrarily steep spectral indices, greater than the range that is actually observed. This problem could be circumvented because there is an obvious selection effect, in that objects with extremely steep spectral indices will not be observed. Furthermore, the fact that the radio spectral indices tend to be fairly sharply peaked around $\alpha = 0.2$ (Valtaoja et al. 1991) suggests that weak shocks are not responsible for the steep spectral indices, but rather that there is some form of steepening of the spectrum which could be due to a variety of possible mechanisms.

Although a cutoff or synchrotron losses can reproduce spectral curvature, it cannot explain steep power-law spectra. For example the object 0219 + 428 which was observed three times, with spectral indices between $\alpha = 1.22$ and 1.44 with spectral curvatures $\Delta\alpha_{B-H} = 0.01 \rightarrow 0.72$. Spectral indices greater than $\alpha = 1.22$ need cutoffs to explain them if the simplest models of Fermi acceleration are relevant and yet in this object the spectral curvature is not severe enough. In order to underscore this point a search was made for a correlation between the spectral index and the degree of spectral curvature, using the Spearman rank correlation statistic, but no significant correlations were obtained. This does not, of course, rule out Fermi acceleration; it simply shows that there is not a universal low frequency spectral index in blazars and that the chosen model for the acceleration mechanism should have a degree of flexibility over the value of the spectral index.

It is also feasible that the structure of the optical emission region is not homogeneous and that there are more complicated processes occurring. Inhomogeneous source models give rise to steeper spectral indices (e.g. Königl 1981), but testing these models

is not possible here with only a limited frequency coverage. In conclusion, the spectral behaviour of blazars is inconsistent with the simplest acceleration models, although a cutoff can reproduce the spectral curvature often seen at optical wavelengths.

2.3.4 Polarization properties

All the observations have at least two data points and these were investigated for unusual polarization behaviour, using the method outlined in Section 2.3. The results are summarized in Table 2.5 and Fig. 2.5. As is clear from these, in the majority of cases the value of the ratio $p(\nu_B)/p(\nu_H)$ is greater than 1.0 i.e. the trend in blazars is generally for the polarization to increase towards the blue end of the spectrum. Indeed, only three objects have a median observed value of $p(\nu_B)/p(\nu_H)$ which is less than one (3C345, $1921-293$ and $2251+158$) and in each case one could attribute this to contamination by unpolarized optical flux.

This tendency for those objects with FDP to have polarizations increasing to the blue raises an interesting question, that of the existence or otherwise of a correlation between the degree of FDP and the level of polarization, in the sense that as $p(\nu_B)$ increases so does $p(\nu_B)/p(\nu_H)$. This is the "$p(\lambda)-p$" effect of Bailey et al. 1983; Holmes et al. 1984a; Holmes 1985; Brindle et al. 1986. Holmes (1985) found a correlation at a level of $> 99\%$; however, he also pointed out that his correlation may have been affected, at some unspecified level, by using his entire data set which included multiple observations of certain interesting objects with high polarizations and large degrees of FDP. Following on from Holmes, Mead (1988) used only median or maximum values and showed that in fact no correlations were present. The same result was later found for the enlarged data set (BEA90). Valtaoja et al. (1991) have since claimed to have found the correlation in a smaller data set, over a shorter frequency range, but they again used all the data available to them rather than selecting single points for each object. It might also be noted that the correlation is present in the data set of MEA90 when all the data are used. Valtaoja et al. also claimed the existence of a correlation in the opposite sense i.e. $p(\nu_U)/p(\nu_I)$ decreasing with increasing $p(\nu_U)$ at shorter wavelengths,

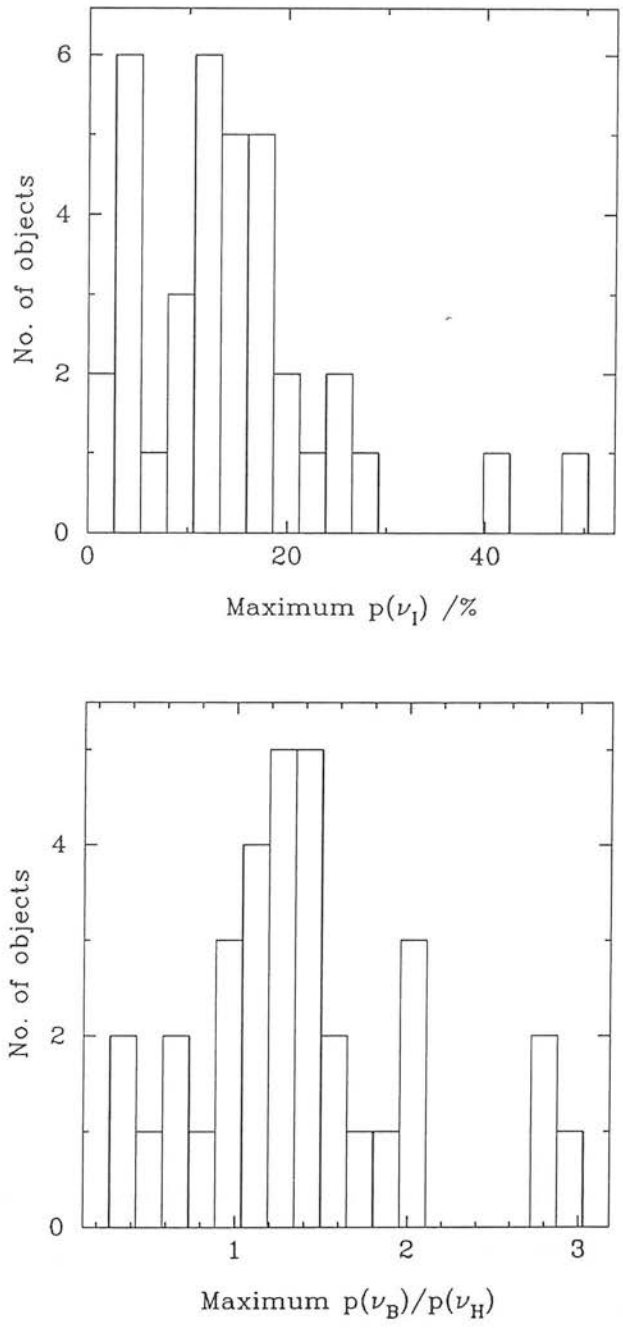

Figure 2.4: This shows histograms of the maximum values of $p(\nu_H)/p(\nu_B)$ and $p(\nu_B)$.

at a much lower significance level. This simply serves to strengthen the point that one cannot calculate correlations using data points which may not be independent. In this chapter it has been argued that one should combine single values, be they maxima or medians, with simultaneous values. Using this criterion for sorting the data a correlation was sought by two methods. The first was a Kolmogorov–Smirnov test (e.g. Conover 1980) which tests for the difference between the distributions using the maximum difference between the two cumulative distributions. Fig. 2.5 shows the distribution of all polarization values and all the observations which displayed significant FDP (the shaded parts) and the two distributions are different at the 75% confidence level. The lower figure repeats the analysis but for FDθ and again the distributions are different, but at the 50% level. The alternative is to use the Spearman rank correlation statistic as before. Plots of the maximum value of $p(\nu_B)/p(\nu_H)$ against the simultaneous value of $p(\nu_I)$ and the values of $p(\nu_B)/p(\nu_H)$ which were observed simultaneously with the maximum value of $p(\nu_I)$ are shown in Fig. 2.6. Neither yield correlations at the 95% level. There may be a number of reasons why this correlation is not apparent. Firstly it is possible that as the previous data sets were obtained with more primitive instruments, the observers missed cases of FDP at low polarization levels. Secondly the biasses introduced by observing some objects more than others could have affected the result. As the correlation is present if all the present data are employed, it is suggested that this is the most likely reason. To conclude, there is no evidence for the $p(\lambda) - p$ effect and caution should be exercised when selecting points to analyse for such a correlation.

2.3.5 Variability

Variability information can be extremely important because of its implications for models of the emission region and flaring events. There are several different timescale over which one can test for variability. Data were taken on successive nights during each observing run and, therefore, one can test for variability on inter-night timescales. In addition, there were four separate observing trips over a period of 18 months so that variability over a timescale of months could be investigated. There is also the question

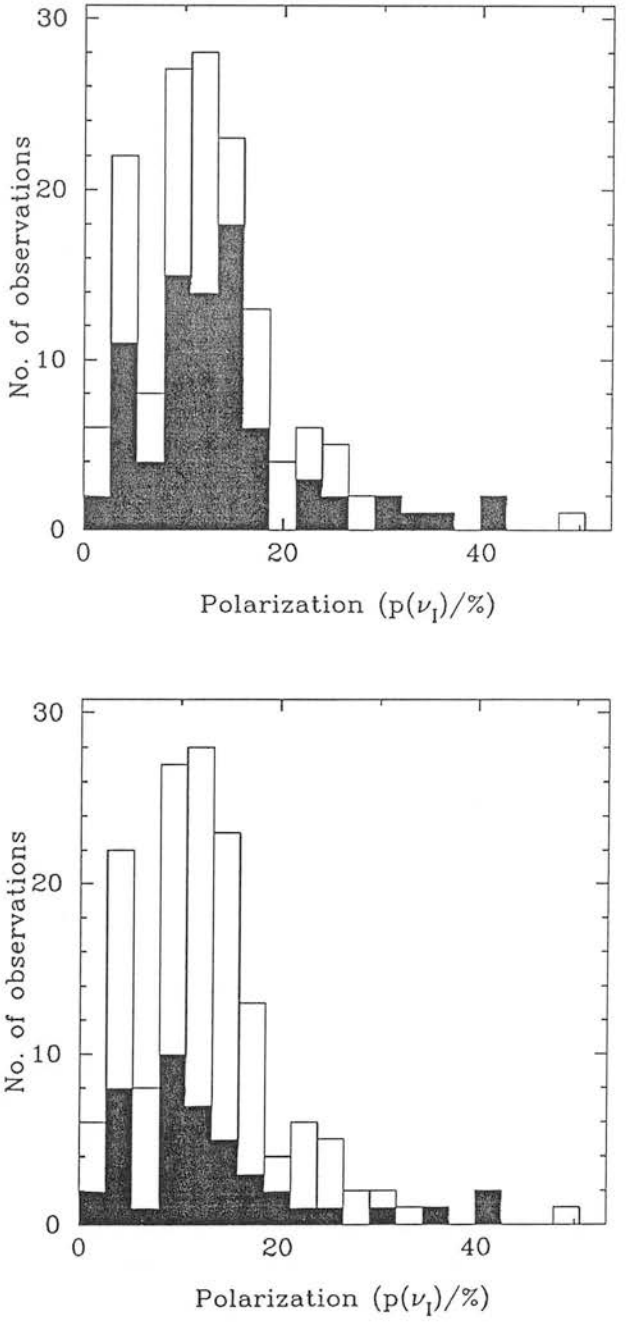

Figure 2.5: This shows the distributions of the polarization values at I. In the top figure those observations showing FDP are shaded, in the bottom figure those showing FDθ are shaded. The critical significance level is 5%. Using a Kolmogorov–Smirnov test the unshaded and shaded distributions are not significantly different.

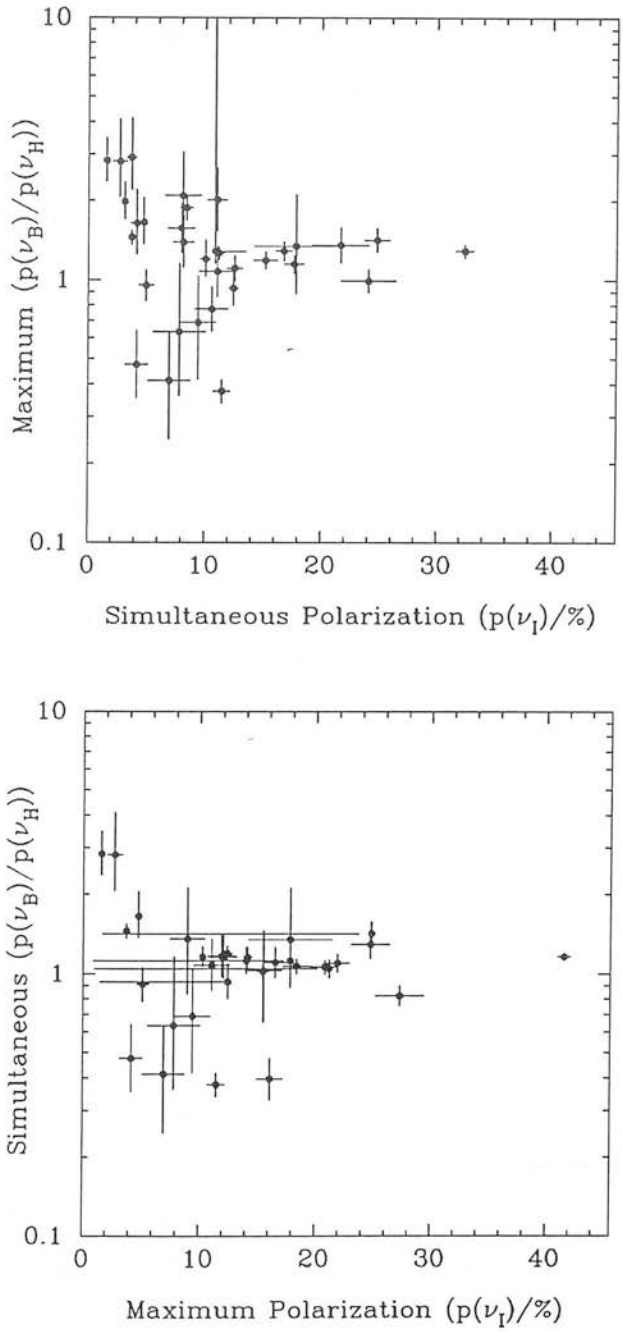

Figure 2.6: This shows plots of the maximum values of $p(\nu_B)/p(\nu_H)$ versus $p(\nu_I)$. No correlations are present at the level previously reported.

of variability on even shorter timescales i.e. tens of minutes corresponding to variability of the source parameters on timescales shorter than the integration times. There is a single example of this with the MKI data, taken in August 1986 for 3C279 (see BEA90 for details), but apart from this case, no information about variability on such timescales was available. The χ^2 statistic was again used to test for variability between individual observations. In this case the critical level was taken to be 1%, lower than previously because of possible systematic errors in the photometry.

Inter-epoch variability in the flux densities was seen in the majority of objects, and ranged from 1253−055 and 1749+096 which varied by a factor of almost three to 0118−272 and 0138−097 which remained constant between 1987 July and September. Night-to-night variations were also commonly seen, though exceptions were more common than above. One object, 2254 + 074, varied from 1.18mJy to 0.44mJy in one day at I, but this was atypical. Three objects (0109 + 224 in 1987 September, 1156 + 295 in 1988 February and 1253 − 055 in 1986 August) varied by up to 33% whilst retaining a constant spectral index. No observations were seen which repeated the pattern of Gear et al. (1986), where spectral indices decreased with increasing flux. Three objects showed steepening spectral indices with increasing flux (0048 − 097 and 0109 + 224, both in 1986 August and 1253 − 055 in 1988 February).

As with the flux variability, inter-epoch variations in the degree of polarization were seen in the majority of blazars, the only exception being 2254 + 074. In addition seven other objects failed to show any inter-night variations when repeat observations were performed: these were 0118 − 272, 0138 − 097, 1156 + 295, 1418 + 546, 1424 + 240, 1641 + 399 and 2223 − 052. Changes in the polarization did not necessarily coincide with significant changes in the observed flux. The variations in the polarization data were not all of a similar form; for example 1253 − 055 showed a generally increasing degree of polarization with the onset of FDP ($dp/d\nu > 0$) whereas 0109 + 224 showed (during 1986 August) FDP of both senses ($dp/d\nu < 0$ and $dp/d\nu > 0$).

Only one object (0235 + 164) was observed with a position angle constant over the inter-epoch timescale; only two high signal to noise observations of this object were made (in 1987 July and 1987 September). One of the more extreme cases was 1749+096

where the position angle varied from 5° to 35° in one day in 1986 August. Only six objects failed to show inter-night variations during any of the epochs. These were 0118−272, 0138−097, 0818−128, 1156+295, 1418+546 and 1424+240. Note that these objects also failed to display any inter-night variations of the degree of polarization. However the other objects which similarly failed to show inter-night changes in the polarization degree did show inter-night changes in position angle. Indeed, position angle variations were marginally more common than those in the degree of polarization.

2.4 Models of the emission region

In this section various mechanisms which may be responsible for FDP will be considered. The aim will be to obtain a simple description of the behaviour of the observed emission as the implications that this holds for the structure of the emission region will be discussed in more detail in Chapter 4. The possibility of a cutoff being responsible for the observed steep spectra and spectral curvature was discussed briefly in the previous section, a high energy cutoff would also have a dramatic effect upon the polarization properties of a source, the result being strong FDP. This is simply because above a cutoff the polarization from an isotropic distribution rises to 100% in a uniform magnetic field although there is no FDθ. Polarization behaviour associated with spectral curvature induced by various loss mechanisms will be considered in detail in Chapter 4. Anisotropic velocity distributions of electrons can produce strong FDP and FDθ in the synchrotron spectra as Björnsson (1985) showed. However, this explanation will not be explored in more detail because of the difficulty in determining realistic anisotropic distributions and because simpler pictures are sufficient to explain many of the observations.

Björnsson & Blumenthal (1982) set out a formalism whereby the polarization properties of an inhomogeneous source can be evaluated. Their result was:

$$p(\nu) = \Pi(\nu)\,\frac{\alpha(\nu)+1}{\alpha(\nu)+\frac{5}{3}}\;\times 100\%. \tag{2.5}$$

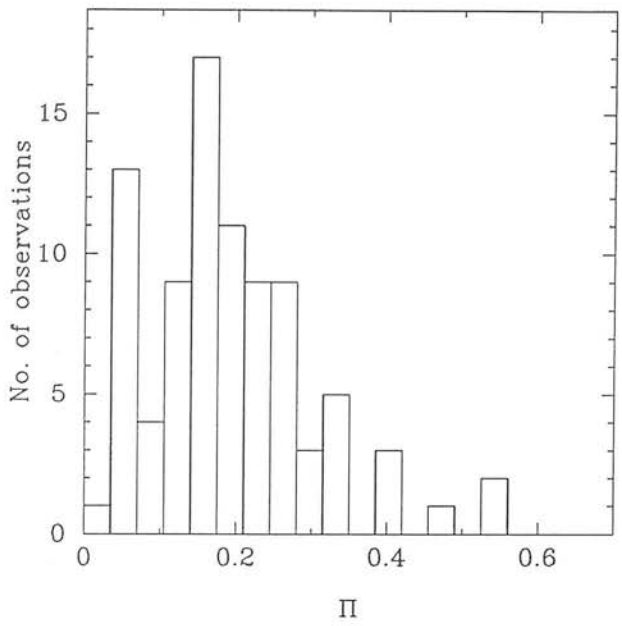

Figure 2.7: This shows a histogram of the fitted values of Π.

where $\Pi(\nu)$ is composed of integrals over the magnetic field geometry, and represents the degree of ordering of the magnetic field.

The Björnsson & Blumenthal (1982) formalism (hereafter the α-parameterization) will be used as an initial parameterization of the radiation. In BEA90, this parameterization was first developed to explain the emission from a single object (3C279) where there was only a single observation with FDθ, which means, in effect, that a frequency independent form of $\Pi(\nu)$ can be employed. In the present chapter, this parameterization will be applied to all data. There are four parameters in this description, $\log_{10} S_{14}$, the flux at 10^{14}Hz, a and b, the spectral index parameters using the parabolic form from equation 2.3 which are use to determine the value of $\alpha(\nu)$. Finally Π, the degree of magnetic field ordering is used to normalize the polarization to the observed values. The α-parameterization was fitted to all observations which were significantly polarized and had five or more data points. Observations which had FDθ were included in the analysis, although the parameterization with a constant value of Π was not strictly valid in this case. The observations of 3C345 were not included because an alternative explanation of the FDP seen in this object, that of dilution by unpolarized flux, has

been put forward. The model was only fitted to the flux and polarization data, the position angle data were disregarded. The distribution of the fitted values of Π are shown in Fig. 2.7. In total, the model was fitted to 84 individual sets of data, yielding satisfactory fits in 58 cases. The fits are summarized in Table 2.6.

It is worthwhile considering the objects where the parameterization failed because in several instances they shed light on the limit of applicability of the formalism. Six of the fits are not rejected at the 1% level, so it is probably acceptable to consider these to be broadly consistent with the α-parameterization. The observations of $0109+224$ and $1418+546$ exhibited dramatic increases in polarization with frequency. Indeed, $0109+224$ had previously shown FDP both increasing and decreasing with frequency so it is possible that for this object a two component model or a model similar to that of Section 4.3.2, may be more suitable. The observations of $0118-272$ and $0818-128$ showed possible signs of containing unpolarized contaminating flux, as was discussed in Section 2.3.2. Along similar lines, $1101+384$, $1514-241$ and $2200+420$ are BL–Lac objects situated within nearby giant elliptical galaxies and dilution by unpolarized starlight may well have invalidated an attempt to fit data using an approach developed to explain intrinsic FDP. In the cases of $1147+245$ and $2155-304$ the observations showed FDθ and this implies the assumption of a frequency independent form of $\Pi(\nu)$ is inappropriate. The polarization behaviour of $2254+074$ was unusual, it was frequency independent between H and B and then rose steeply to the U band value. This may explain why the α-parameterization did not work well for this object, although it is hard to explain why the polarization behaved as it did. Finally, there are no readily apparent reasons why the parameterization should have failed with the data from $0048+097$ (1986 August 3) and $0754+100$ (1988 February).

Thus, it has been shown that the α-parameterization is a valid first description of the radiation, since it adequately fits the data in the majority of observations. However, the α-parameterization simply shows that the polarization behaviour is usually a consequence of the spectral properties; it does not explain the spectral curvature, for which a particular model of the emission region must be used. In BEA90, the authors follow up the work on the α-parameterization with a specific model where the emission came

from an unpolarized power-law of constant spectral index, combined with a second polarized component which had a cutoff at a frequency around 10^{15} Hz. The combination of these two components could explain the polarization and flux properties in a number of objects although in a substantial fraction it failed. The polarization around a cutoff in a uniform magnetic field increases to 100% from the polarized component, but as this is diluted by the unpolarized component, the overall polarization decreases, as the flux from the polarized component drops off above the cutoff frequency. Hence, FDP with polarizations both increasing and decreasing to the blue can be produced. The model cannot, however, explain FDθ as only one component is polarized. In BEA90 it was envisaged that the polarized component was restricted at high energies by some unspecified loss process during the acceleration of electrons and could be associated with the emission from the downstream region of a shock while the steeper spectrum component was attributed to an inhomogeneous jet component. A model similar to this has recently been proposed for radio observations (Qian et al. 1991) of a single object, $0917+624$.

The two component model presented in BEA90 will not be repeated here for a number of reasons. It must be stressed that it is only a particular model which can explain certain features of the polarization behaviour; it cannot explain the lack of FDP with decreasing polarization, which it also predicts, nor can it explain FDθ without recourse to the use of a polarized second component. When this restriction is lifted, its status is reduced to that of the two component model of Holmes et al. 1984b, an empirical description of unusual features which does not give insight to the underlying physics and which must be finely tuned to work – in other words it fails to explain features that occur at all levels of flux and predicts decreasing spectral indices. Finally, it cannot explain the results of intensive monitoring campaigns which suggest multi-component descriptions of the radiation are more appropriate. The aim of this work is to try to deduce some principles of the emission, rather than to explain a particular set; enough one-off models have already been proposed to explain observations.

Table 2.5: Summary of the polarization data. Numbers in brackets are 1σ errors.

Object Name	$p(\nu_I)$/% Median		$p(\nu_I)$/% Maximum		No. of Obs.	$p(\nu_B)/p(\nu_H)$ Median		$p(\nu_B)/p(\nu_H)$ Maximum		No. of Obs.
0048 − 097	14.55	(0.61)	21.17	(1.02)	11	1.24	(0.13)	1.64	(0.17)	10
0109 + 224	8.91	(0.85)	14.04	(0.90)	9	1.09	(0.10)	1.20	(0.05)	7
0118 − 272	16.49	(0.68)	17.82	(0.58)	7	1.17	(0.04)	1.29	(0.08)	7
0138 − 097	22.16	(1.13)	24.80	(1.08)	6	1.09	(0.15)	1.42	(0.05)	8
0219 − 164	12.45	(0.42)	12.45	(0.42)	1	0.93	(0.04)	0.93	(0.04)	1
0219 + 428	11.46	(0.84)	15.46	(0.55)	10	1.08	(0.13)	1.29	(0.06)	10
0235 + 164	13.28	(0.90)	15.52	(1.59)	2	1.52	(0.38)	2.02	(0.24)	2
0300 + 470	9.44	(1.52)	9.44	(1.52)	1	0.69	(0.52)	0.69	(0.52)	1
0323 + 022	3.84	(1.02)	3.84	(1.02)	1	–	–	–	–	–
0338 − 214	10.76	(1.05)	11.07	(1.56)	2	1.00	(0.25)	1.08	(0.13)	2
0414 + 009	7.82	(2.25)	7.82	(2.25)	1	0.63	(0.42)	0.63	(0.42)	1
0422 + 004	16.67	(0.65)	20.79	(1.12)	2	1.08	(0.13)	1.11	(0.05)	2
0735 + 178	16.57	(0.65)	21.90	(0.98)	4	1.07	(0.11)	1.15	(0.06)	4
0754 + 100	11.16	(0.39)	12.39	(0.48)	4	1.10	(0.08)	1.27	(0.03)	4
0818 − 128	23.32	(1.33)	24.73	(1.66)	2	1.29	(0.05)	1.29	(0.05)	1
0851 + 202	18.06	(0.66)	18.36	(1.22)	3	1.07	(0.05)	1.19	(0.06)	3
1101 + 384	3.73	(0.13)	3.73	(0.13)	1	1.45	(0.03)	1.45	(0.03)	1
1147 + 245	2.71	(0.67)	2.71	(0.67)	1	2.82	(0.21)	2.82	(0.21)	1
1156 + 295	26.42	(2.87)	27.27	(2.08)	3	0.91	(0.08)	0.99	(0.05)	3
1253 − 055	31.30	(0.36)	41.58	(0.55)	9	1.08	(0.01)	1.29	(0.06)	9
1418 + 546	4.62	(0.31)	15.37	(2.82)	9	1.51	(0.09)	2.93	(0.16)	7
1424 + 240	4.98	(0.66)	5.14	(0.55)	3	0.91	(0.09)	0.95	(0.09)	3
1510 − 089	11.13	(0.10)	11.49	(0.72)	2	0.37	(0.20)	0.38	(0.16)	2
1514 − 241	3.31	(0.21)	4.76	(0.30)	2	1.53	(0.14)	1.66	(0.07)	2
1641 + 399	14.39	(0.81)	16.09	(1.14)	9	0.50	(0.07)	0.77	(0.14)	9
1652 + 398	1.56	(0.16)	1.56	(0.16)	1	2.85	(0.11)	2.85	0.11	1
1717 + 178	16.11	(1.85)	17.82	(3.62)	2	0.93	(0.50)	1.35	(0.27)	2
1727 + 502	2.48	(0.49)	2.51	(0.82)	2	–	–	–	–	–
1749 + 096	8.89	(0.58)	16.53	(0.95)	4	1.21	(0.21)	1.39	(0.13)	4
1921 − 293	7.56	(1.23)	8.13	(1.65)	2	0.41	(0.79)	0.41	(0.79)	1
2155 − 304	3.10	(0.12)	10.29	(0.23)	5	1.14	(0.06)	1.99	(0.04)	6
2200 + 420	12.02	(0.50)	14.15	(0.37)	13	1.21	(0.06)	1.88	(0.13)	13
2223 − 052	11.64	(1.87)	11.90	(1.21)	3	1.12	(0.23)	1.57	(0.14)	4
2251 + 158	4.18	(0.96)	4.18	(0.96)	1	0.47	(0.29)	0.47	(0.29)	1
2254 + 074	9.65	(1.45)	12.06	(1.26)	11	1.82	(0.16)	2.09	(0.19)	6

Table 2.6: Summary of the fits to the polarization behaviour using the α-parameterization.

Name	U.T. Date	χ^2	$P(\chi^2)$	Π
$0048-097$	1986 Aug. 3	27.40	0.0006	0.20
$0048-097$	1986 Aug. 4	15.98	0.014	0.22
$0048-097$	1986 Aug. 6	12.63	0.125	0.23
$0048-097$	1987 Jul. 27	7.09	0.527	0.21
$0048-097$	1987 Jul. 29	5.44	0.860	0.28
$0048-097$	1987 Jul. 30	4.33	0.931	0.17
$0048-097$	1987 Sep. 19	8.20	0.609	0.07
$0109+224$	1986 Aug. 7	45.77	2.6×10^{-7}	0.09
$0109+224$	1987 Jul. 27	4.26	0.833	0.18
$0109+224$	1987 Jul. 30	3.15	0.925	0.11
$0109+224$	1987 Sep. 19	0.94	0.998	0.05
$0109+224$	1987 Sep. 21	8.87	0.181	0.19
$0118-272$	1986 Aug. 5	7.80	0.453	0.22
$0118-272$	1987 Jul. 27	38.27	6.7×10^{-6}	0.19
$0118-272$	1987 Jul. 30	11.15	0.346	0.18
$0118-272$	1987 Sep. 21	9.18	0.164	0.21
$0138-097$	1987 Jul. 28	5.26	0.729	0.26
$0138-097$	1987 Jul. 30	5.23	0.732	0.27
$0138-097$	1987 Sep. 19	13.90	0.177	0.33
$0138-097$	1987 Sep. 20	13.93	0.030	0.32
$0138-097$	1987 Sep. 21	3.45	0.750	0.32
$0219-164$	1987 Jul. 28	4.35	0.976	0.17
$0219+428$	1987 Jul. 27	13.72	0.089	0.17
$0219+428$	1987 Jul. 30	6.64	0.575	0.17
$0219+428$	1987 Sep. 20	7.79	0.254	0.19
$0235+164$	1987 Jul. 28	11.11	0.519	0.15
$0235+164$	1987 Sep. 20	27.27	0.002	0.12
$0414+009$	1988 Feb. 15	45.56	1.7×10^{-6}	0.07
$0414+009$	1988 Feb. 16	11.59	0.170	0.06
$0422+004$	1988 Feb. 16	3.24	0.918	0.26
$0422+004$	1988 Feb. 18	5.34	0.867	0.15
$0735+178$	1988 Feb. 15	8.76	0.363	0.21
$0735+178$	1988 Feb. 16	9.34	0.314	0.21
$0735+178$	1988 Feb. 18	1.95	0.983	0.27
$0754+100$	1988 Feb. 15	65.80	2.8×10^{-10}	0.15
$0754+100$	1988 Feb. 16	26.76	0.003×10^{-3}	0.15
$0754+100$	1988 Feb. 17	8.81	0.358	0.14
$0754+100$	1988 Feb. 18	17.67	0.061	0.10
$0818-128$	1988 Feb. 15	18.74	0.044	0.28
$0818-128$	1988 Feb. 16	25.80	0.004	0.28
$0818-128$	1988 Feb. 17	13.90	0.084	0.26
$0851+202$	1988 Feb. 15	8.265	0.408	0.22

Table 2.6: Summary of the fits to the polarization behaviour using the α-parameterization contd.

Name	U.T. Date	χ^2	$P(\chi^2)$	Π
$0851+202$	1988 Feb. 16	14.06	0.080	0.21
$0851+202$	1988 Feb. 17	11.84	0.295	0.25
$1101+384$	1988 Feb. 15	67.8	8.2×10^{-10}	0.05
$1147+245$	1988 Feb. 18	43.32	4.4×10^{-6}	3.72
$1156+295$	1988 Feb. 15	6.06	0.641	0.31
$1156+295$	1988 Feb. 16	8.46	0.390	0.30
$1156+295$	1988 Feb. 17	13.39	0.099	0.32
$1253-055$	1986 Aug. 2	2.96	0.814	0.39
$1253-055$	1986 Aug. 4	11.67	0.308	0.48
$1253-055$	1986 Aug. 5	9.60	0.476	0.54
$1253-055$	1986 Aug. 6	12.04	0.282	0.55
$1253-055$	1987 Jul. 28	19.52	0.077	0.40
$1253-055$	1988 Feb. 16	10.72	0.218	0.26
$1253-055$	1988 Feb. 17	7.28	0.507	0.33
$1253-055$	1988 Feb. 18	9.27	0.320	0.38
$1418+546$	1987 Jul. 30	62.93	1.0×10^{-9}	0.07
$1418+546$	1988 Feb. 16	31.85	1.4×10^{-3}	0.04
$1418+546$	1988 Feb. 17	54.71	2.0×10^{-7}	0.06
$1418+546$	1988 Feb. 18	8.21	0.413	0.04
$1424+240$	1988 Feb. 16	19.64	0.012	0.06
$1424+240$	1988 Feb. 17	4.73	0.786	0.06
$1424+240$	1988 Feb. 18	3.96	0.861	0.06
$1510-089$	1988 Feb. 15	222.8	0.00	0.11
$1510-089$	1988 Feb. 16	306.2	0.00	0.12
$1514-241$	1987 Jul. 27	24.44	0.018	0.06
$2155-304$	1986 Aug. 1	30.96	2.6×10^{-5}	0.05
$2155-304$	1986 Aug. 7	2.22	0.973	0.03
$2155-304$	1987 Jul. 27	5.11	0.954	0.14
$2200+420$	1986 Aug. 3	57.43	1.48×10^{-9}	0.16
$2200+420$	1987 Jul. 27	124.5	7.69×10^{-21}	0.11
$2200+420$	1987 Jul. 28	91.85	2.2×10^{-14}	0.14
$2200+420$	1987 Jul. 30	41.40	1.7×10^{-6}	0.16
$2200+420$	1987 Sep. 19	54.83	4.75×10^{-9}	0.11
$2223-052$	1987 Jul. 27	8.90	0.351	0.15
$2223-052$	1987 Jul. 29	14.10	0.079	0.12
$2254+074$	1986 Aug. 3	30.04	2.1×10^{-4}	0.16
$2254+074$	1986 Aug. 4	75.67	3.5×10^{-12}	0.14
$2254+074$	1987 Jul. 28	28.87	3.3×10^{-4}	0.15
$2254+074$	1987 Jul. 30	16.94	0.031	0.15

Explanations for the observations from a more theoretical viewpoint will be the subject of Chapter 4. It will suffice for the present to conclude that the α-parameterization works well in describing many observations whilst recalling its limitations. This simple result, although it does not in itself give detailed information about the detailed nature of the emission, does provide strong constraints on any physical model which aims to explain the emission.

2.5 Conclusions

This Chapter has analysed the results of a programme of multi-frequency polarimetric observations of blazars. A total of 157 observations of 44 blazars were obtained during four separate observing runs in 1986 August, 1987 July, 1987 September and 1988 February. The data consist of simultaneous observations using up to 8 different filters at infrared and optical frequencies. The conclusions that have been reached may be summarized as follows:

- In many cases the spectrum could be represented as a power law over the full range of observed frequencies, but significant spectral curvature was common. The behaviour of the polarized flux density was similar to that of the total flux density whose properties could be assumed to be representative of the synchrotron component. The spectral indices were too steep to be consistent with particle acceleration at relativistic shocks unless the observations were made in the region of a high-frequency cut-off. Inhomogeneous source models can also explain the observed behaviour.

- Frequency dependence of the degree of polarization was seen in many cases, generally with $dp/d\nu > 0$. The counter examples were often associated with the "blue bumps" discussed in Section 2.3.2. Frequency dependence of the polarization position angle was a less common feature of blazar behaviour. No evidence was found to support claims that frequency dependence is associated with high levels of polarization.

- Variability was a common feature of the observations. No simple characteristics have yet been found to describe all the variations.

- Most of the observed frequency dependence of polarization in blazars is linked to the intrinsic curvature in the blazar flux spectrum. This suggests an inhomogeneous model for the emission region is required.

The later chapters in this thesis will concentrate upon the theoretical explanations for the characteristic observational properties of blazars, the determination of which was the subject of this chapter. Further observational work must provide a rigorous test of the models. The fits would be better constrained if flux information were available from higher and lower frequencies than those observed. This would make the empirical determination of the spectral index more secure at K, H & J and B & U. This, in turn, would more severely test the observed polarization behaviour at these frequencies. Polarization information at lower frequencies where the spectral curvature would be less, and, hence, the polarization lower, and closer to a value which can constrain the degree of magnetic field ordering, would be particularly important.

Chapter 3

Oblique Relativistic Magnetohydrodynamic Shocks

3.1 Introduction

The theory of first order Fermi acceleration (Bell 1978a; Drury 1983; Section 1.3.3), whereby electrons are accelerated to large energies through scattering off magnetic irregularities on either side of a collisionless shock front predicts a power-law spectral index for the accelerated electrons which is a decreasing function of the compression ratio at the shock. In the non-relativistic limit the spectral index is independent of shock obliquity for low obliquity (Bell 1978a; Drury 1983; Ostrowski 1988). The relativistic case was solved by Kirk & Heavens (1989; hereafter KH). In order to make the problem tractable they neglected the possibility of cross-field wandering of the electrons, assuming all particles are tied to the magnetic field lines so that the particles were only scattered in pitch angle. Furthermore, a particle's magnetic moment was assumed to be conserved during an encounter with the shock. Their result was that the spectrum hardens with increasing shock obliquity. All the work was carried out for "subluminal" shocks where the shock front intersects the magnetic field lines at a speed less than the speed of light. In such a case it is always possible to transform to a frame where the material moves along the magnetic lines (de Hoffman & Teller 1950; hereafter deHT). This chapter investigates the consequence of incorporating a dynamically important magnetic field into the problem which will reduce the compression ratio. The spectral indices of the electrons accelerated at such shocks will then be calculated. A similar approach to KH will be used here with dynamically important magnetic fields i.e. transform to the deHT frame, solve the jump conditions and then

evaluate the spectral index. However, in this chapter, the semi-analytic method of KH will be tested by employing a Monte Carlo technique to obtain particle distributions. This study is limited to the test particle case where the pressure of the accelerated particles is very much less than the pressures which determine the compression ratio of the shock.

Previous studies of oblique relativistic MHD shocks (Webb et al. 1987; Appl & Camenzind 1988) have worked in the shock frame where the fluid moves parallel to the shock normal and where there exists an electric field ($\mathbf{u} \wedge \mathbf{B} \neq \mathbf{0}$) which must be included in the expressions for the jump conditions. This leads to seventh order polynomials to be solved. The method given here, by transforming to the deHT frame is considerably simpler, but is only applicable to subluminal shocks. This is not a serious restriction because the problem is only of interest when particles can be accelerated, which they cannot be at a superluminal shock. However the present work allows for the introduction of various downstream conditions. As one is concerned primarily with collisionless shocks the assumption of full local thermodynamic equilibrium downstream of the shock is not necessarily valid; in addition to this possibility it may be that full pressure is provided purely by the ions, the electrons or indeed electron/positron pairs in the case where this is the composition of the fluid.

The layout of the remainder of this chapter is as follows. In Section 3.2 the equation of state is derived. In Section 3.3 the jump conditions are written down and a method for their solution described. Section 3.4 discusses the results in terms of the compression ratio and in Section 3.5 the spectral index of the accelerated electrons are obtained. Section 3.6 discusses results and applies them to the emission from extragalactic hotspots. The following two simplifications have been made: the Boltzmann constant $k_B = 1$ and the speed of light $c = 1$. Otherwise, SI units are used throughout.

3.2 Equation of state

The jump conditions which will be derived in Section 3.3 must be accompanied by an equation of state to describe the gas. Here the assumption will be that the fluid behaves according to the Synge equation of state (Synge 1957) i.e. that of a classical ideal gas composed of fully ionized hydrogen and electrons plus any electron/positron pairs produced downstream of the shock front. Summing over the different species (subscript i) the pressure, energy density (including rest mass) and mass density in terms of the number density n_i, the particle rest mass m_i and temperature T_i can be expressed as:

$$P = \sum_i n_i T_i \tag{3.1}$$

$$e = \sum_i m_i n_i R(m_i/T_i) \tag{3.2}$$

$$\rho = \sum_i m_i n_i \tag{3.3}$$

These quantities are defined in the respective fluid rest frames. In SI units m/T is equivalent to $mc^2/k_B T$. $R(z)$ is defined in terms of the modified Bessel functions of order n, $K_n(z)$:

$$R(z) = \frac{3}{z} + \frac{K_1(z)}{K_2(z)} \tag{3.4}$$

The enthalpy is then defined as:

$$w = e + P \tag{3.5}$$

and setting the specific enthalpy $\overline{w} = w/\rho$ etc,

$$\begin{aligned} \overline{w} &= \overline{e} + \overline{p} \\ &= \left(\textstyle\sum_i m_i n_i R\left(\frac{m_i}{T_i}\right) + \sum_i n_i T_i\right) / \left(\sum_i m_i n_i\right). \end{aligned} \tag{3.6}$$

Now set $n_e = n_i \equiv n$ assuming overall electrical neutrality. It is not possible to state the exact conditions downstream of the shock because details of the process by which

individual species are thermalized are uncertain. However, three particular cases will be described.

Case 1. The fluid is in local thermodynamic equilibrium, where $T_e = T_i \equiv T$. The temperature and enthalpy can then be written:

$$T = \frac{(m_p + m_e)}{2}\overline{p} \tag{3.7}$$

$$\overline{w} = \frac{m_e R\left(\frac{m_e}{T}\right) + m_p R\left(\frac{m_p}{T}\right) + 2T}{m_e + m_p} \tag{3.8}$$

For low temperatures the expressions for $\overline{w}$ reduce to the asymptotic expansions of $R(z)$, $z \to \infty$, $R(z) \to 1 + 3/2z$ and one obtains the non-relativistic equation of state:

$$e_i \to n_i m_i + \frac{3P_i}{2} \tag{3.9}$$

For high temperatures $z \to 0$ and $R(z) \to 1 + 3/z$ and $e_i \to 3P_i$, the ultra-relativistic equation of state.

Case 2. Ion pressure only. This case also essentially describes a shock through an electron-positron plasma apart from corrections of order m_e/m_p and a rescaling of the temperature. In this case,

$$T = (m_p + m_e)\overline{P} \tag{3.10}$$

$$\overline{w} = \frac{m_e + m_p R\left(\frac{m_p}{T}\right) + T}{m_e + m_p} \tag{3.11}$$

Case 3. Electron pressure only.

$$T = (m_p + m_e)\overline{P} \tag{3.12}$$

$$\overline{w} = \frac{m_p + m_e R\left(\frac{m_e}{T}\right) + T}{m_e + m_p} \tag{3.13}$$

3.3 The jump conditions

At first consider the situation as seen from the rest frame of the upstream fluid. Without loss of generality assume that the shock front lies in the yz plane and the magnetic field in the xy plane. In order to derive a simple set of jump conditions a transformation is made from this upstream fluid frame to a frame of reference where the magnetic field lies along the streamlines. Assuming infinite conductivity the electric field then vanishes everywhere, as $\mathbf{u} \wedge \mathbf{B} = \mathbf{0}$. The transformation involves a boost along the magnetic field direction of speed $\beta = \beta_s / \cos\theta$; note that β will refer to a speed throughout and $c = 1$. β_s is the speed of the shock with respect to the upstream plasma and θ is the angle between the field and direction of the shock velocity. The two-dimensional Lorentz transformation from the upstream frame to the deHT frame (see Fig 3.1) is given by:

$$L_{\alpha\beta} = \begin{pmatrix} \gamma & \gamma\beta_s & \gamma\beta_s \tan\theta & 0 \\ \gamma\beta_s & 1 + \frac{(\gamma-1)\beta_s^2}{\beta^2} & \frac{(\gamma-1)\beta_s^2 \tan\theta}{\beta^2} & 0 \\ \gamma\beta_s \tan\theta & \frac{(\gamma-1)\beta_s^2 \tan\theta}{\beta^2} & 1 + \frac{(\gamma-1)\beta_s^2}{\beta^2} & 0 \\ 0 & 0 & 0 & 1 \end{pmatrix} \tag{3.14}$$

(see Jackson 1975, p541). $\gamma = (1 - \beta^2)^{-1/2}$. Such a transformation can only be made if $\beta_s < \cos\theta$, the condition for a subluminal shock. This changes the reference frame into the deHT frame. Here the direction and magnitude of the magnetic field remains unchanged and the shock front is stationary but no longer lies in the yz plane. The rotation of the shock face can be obtained by transforming the position of shock face in the upstream frame using the above Lorentz transform. The shock is rotated through an angle α, given by:

$$\tan\alpha = \frac{\gamma\beta_s^2 \tan^4\theta + \beta_s^2 \tan^2\theta - (1 - \beta_s^2)(1 + \gamma \tan^2\theta)}{(\gamma - 1)\beta_s^2 \tan^3\theta - (\gamma - 1)(1 - \beta_s^2)\tan\theta} \tag{3.15}$$

The fluid velocities in the deHT frame are then:

$$\beta_{1x} = \beta_s \cos\alpha \sec\theta \tag{3.16}$$

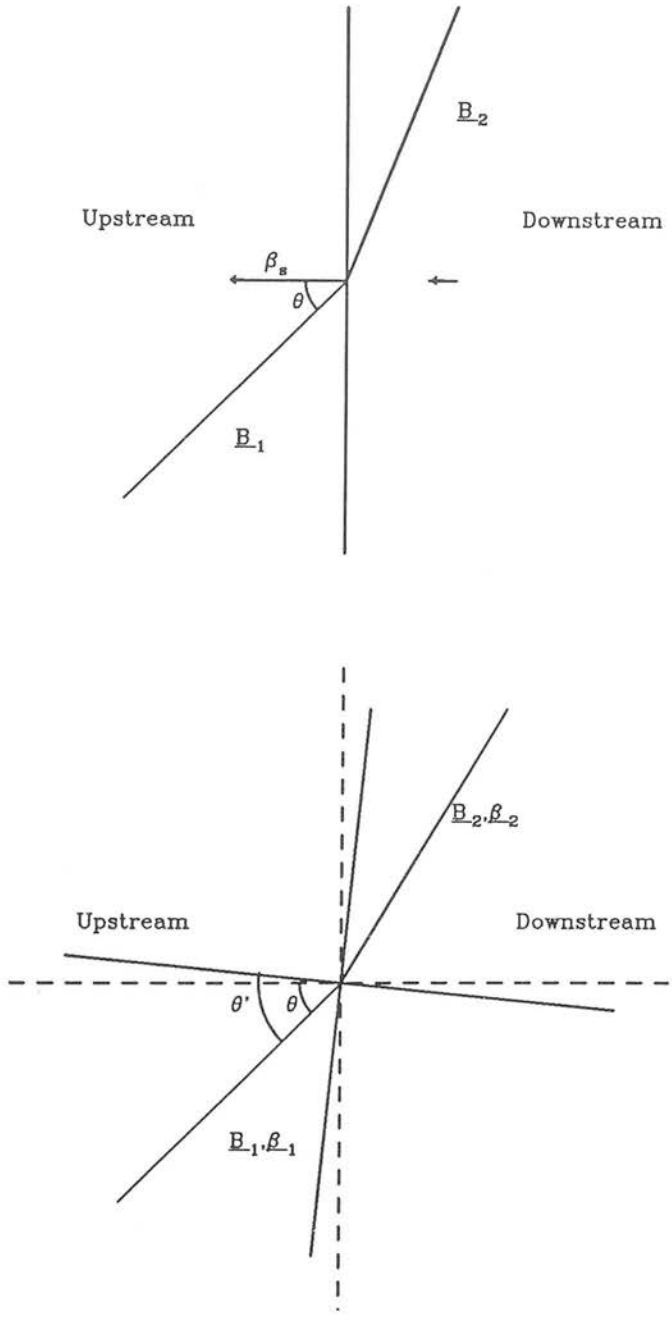

Figure 3.1: Fig 3.1a shows the upstream reference frame. Fig 3.1b shows the deHT frame.

$$\beta_{1y} = \beta_s \sin\alpha \sec\theta \tag{3.17}$$

Next, the jump conditions are obtained from the conservation equations (Licnerowicz 1967):

$$\nabla_\mu(\rho u^\mu) = 0 \tag{3.18}$$

$$\nabla_\mu(B^\mu u^\nu - u^\mu B^\nu) = 0 \tag{3.19}$$

$$\nabla_\mu(T^{\mu\nu}) = 0 \tag{3.20}$$

where Greek indices run from 0–3 and $T^{\mu\nu}$ is the stress-energy tensor including electromagnetic terms, given by:

$$T^{\mu\nu} = (e+P)u^\mu u^\nu + Pg^{\mu\nu} + \frac{1}{\mu_0}(F^{\mu\lambda}F^\nu_\lambda - \frac{1}{4}g^{\mu\nu}F^{\lambda\sigma}F_{\lambda\sigma}) \tag{3.21}$$

e is the energy density (including rest mass energy), P is the plasma pressure, $g^{\mu\nu}$ is the metric tensor, u_ν is the four-velocity and $F_{\mu\nu}$ is the covariant electromagnetic field tensor:

$$F_{\mu\nu} = \begin{pmatrix} 0 & -B_z & B_y & -E_x \\ B_z & 0 & -B_x & -E_y \\ -B_y & B_x & 0 & -E_z \\ E_x & E_y & E_z & 0 \end{pmatrix}. \tag{3.22}$$

Note that the components of the electric field E_i can be set to zero because $\mathbf{u} \wedge \mathbf{B} = \mathbf{0}$. The jump equations were written down by deHT. Conservation of mass gives

$$\rho_1\beta_{1x}\gamma_1 = \rho_2\beta_{2x}\gamma_2 \tag{3.23}$$

where $\gamma_i = (1-\beta_i^2)^{-1/2}$. From the stress–energy tensor conservation of momentum parallel and perpendicular to the shock normal and conservation of energy give:

$$w_1\beta_{1x}\gamma^2 = w_2\beta_{2x}\gamma^2 \tag{3.24}$$

$$w_1\beta_{1x}^2\gamma^2 + P_1 + \frac{B_{1y}^2}{2\mu_0} = w_2\beta_{2x}^2\gamma^2 + P_2 + \frac{B_{2y}^2}{2\mu_0} \tag{3.25}$$

$$w_1 + \beta_{1x}\beta_{1y}\gamma^2 - \frac{B_{1x}B_{1y}}{\mu_0} = w_2 + \beta_{2x}\beta_{2y}\gamma^2 - \frac{B_{2x}B_{2y}}{\mu_0} \tag{3.26}$$

In the deHT frame the fluid flows along the magnetic field on both sides of the shock. Hence:

$$\frac{B_{1x}}{B_{1y}} = \frac{\beta_{1x}}{\beta_{1y}} \tag{3.27}$$

$$\frac{B_{2x}}{B_{2y}} = \frac{\beta_{2x}}{\beta_{2y}}. \tag{3.28}$$

Finally, from $\nabla \cdot \mathbf{B} = 0$:

$$B_{1x} = B_{2x} \equiv B_x \tag{3.29}$$

Then substitute equations (3.27–3.29) into (3.24–3.26) and divide throughout by equation (3.23), setting $\overline{B_x^2} = B_x^2/\rho$, $\overline{w_1} = w_1/\rho$ etc. Defining the following constants:

$$A = \overline{w_1}\gamma_1 \tag{3.30}$$

$$C = \frac{\overline{B_x^2}}{\mu_0\gamma_1\beta_{1x}} \tag{3.31}$$

One obtains an expression for β_{2y}:

$$\beta_{2y} = \frac{\beta_{2x}\beta_{1y}}{\beta_{1x}}\left(\frac{A\beta_{1x} - C}{A\beta_{2x} - C}\right). \tag{3.32}$$

The following equations are the result:

$$A\beta_{1x} + \frac{\overline{P_1}}{\gamma_1\beta_{1x}} + \frac{C\beta_{1y}^2}{2\beta_{1x}^2} = A\beta_{2x} + \frac{\overline{P_2}\,\overline{w_2}}{A\beta_{2x}} + \frac{C}{2}\left(\frac{\beta_{1y}}{\beta_{1x}}\right)^2\left(\frac{A\beta_{1x} - C}{A\beta_{2x} - C}\right)^2 \tag{3.33}$$

$$A = \overline{w_2}(1 - \beta_{2x}^2 - \beta_{2y}^2)^{-1/2} \tag{3.34}$$

Thus there are two simple simultaneous equations which express the results so far and which have to be solved to obtain the two unknowns (β_{2x}, $\overline{P_2}$), given the upstream

conditions. β_{2y} is estimated from (3.34), using (3.32) and $\overline{w_2}$ is a function of $\overline{P_2}$ which depends on the thermodynamic state of the downstream gas via equations (3.7, 3.8), (3.10, 3.11) or (3.12, 3.13) for the three cases considered. In practice these were solved numerically. The starting point was to take the shock speed, angle θ, between the magnetic field and shock normal, (relativistic) Alfvénic Mach number, the pressure and the composition as seen from the upstream frame, Fig 3.1a. These were then transformed to the deHT frame using the two dimensional Lorentz transformation, allowing for the rotation of the shock front that results from this transformation. Then from $\overline{P_1}$ we can obtain $\overline{w_1}$ using equations(3.7–3.13). Through equations (3.33 & 3.34), using the equation for $\overline{w_1}(\overline{P_1})$ these can be solved for $\overline{P_2}$ and hence β_{2x}. These are then transformed back into the upstream reference frame using the two dimensional Lorentz velocity transform, again taking account of the rotation of the shock front. Finally, these were transformed back to the shock frame and the compression ratio, pressure, and temperature obtained. The results are outlined below.

3.4 Solutions to the jump conditions

Throughout the following discussion attention is restricted to the fast magnetosonic solutions to the above equations. The results of solving the jump conditions in the purely hydrodynamical limit (see Kirk 1987) are shown in Fig 3.2, which plots the downstream fluid speed, the shock compression ratio and temperature as a function of the shock speed. The pre-shock pressure has been set to zero in order to obtain the strongest possible shock. The three cases illustrated correspond to full local thermodynamic equilibrium (solid line), ion pressure only (dashed line) and electron pressure only, where the ions are still present and contribute to the mass density (dot-dashed line). As is clear from Fig. 3.2, in both the low and high velocity limits, where the equations of state are fully non-relativistic and ultra-relativistic respectively, there is little difference between the compression ratios as each case is described by essentially the same equation of state with adiabatic index equal to 5/3 or 4/3 in the respective limits. The difference between the three cases considered is most apparent at intermediate velocities. This is because electrons, with less mass, are thermalized to relativistic

velocities at much lower temperatures than ions which are only relativistic for high shock velocities, as $\beta_s \rightarrow 1.0$. Hence, there can exist states with non-relativistic shock velocities, with relativistic electrons (an adiabatic index of 13/9, and a compression ratio, 5.5).

The remainder of this chapter will be concerned primarily with the Fermi shock acceleration mechanism. Therefore it is useful to define the following parameters, of use in calculating particle pitch angles. Firstly, the compression ratio as seen in the deHT frame,

$$r = \frac{\beta_{1x}}{\beta_{2x}} \tag{3.35}$$

and secondly, the ratio of the magnitudes of the upstream and downstream magnetic fields,

$$b = \frac{B_1}{B_2} = \frac{\beta_1}{r\beta_2}. \tag{3.36}$$

Note, however, that it is no longer possible to write down a simple expression for b, as in equation (4) of KH; this is because the component of fluid velocity perpendicular to the shock normal, β_y, is no longer continuous at the shock.

In Figs 3.3–3.5 the effects of increasing the magnetic pressure are displayed for a series of differing angles between the magnetic field direction and the shock normal (as seen from the upstream frame). The figures have different assumed thermodynamic states downstream, as outlined in Section 3.2. The quantities plotted are the compression ratio, r, against shock speed, the downstream fluid temperature, T_2 in degrees Kelvin as a function of shock speed, and finally, b as a function of shock speed for several cases, as labelled. Note that the curves do not extend to $\beta = 1$ as the shock becomes superluminal when $\beta_s > \cos\theta$. All these figures have Alfvén Mach number, $M_A \equiv \beta_s/(B^2/\rho\mu_0)^{1/2} = \sqrt{5}$.

As the magnetic field and θ become larger, the shock becomes weaker in the sense that the compression ratio decreases (Kundt & Krotschek 1980), although it is apparent that the temperature is not greatly affected by these changes. As the field becomes

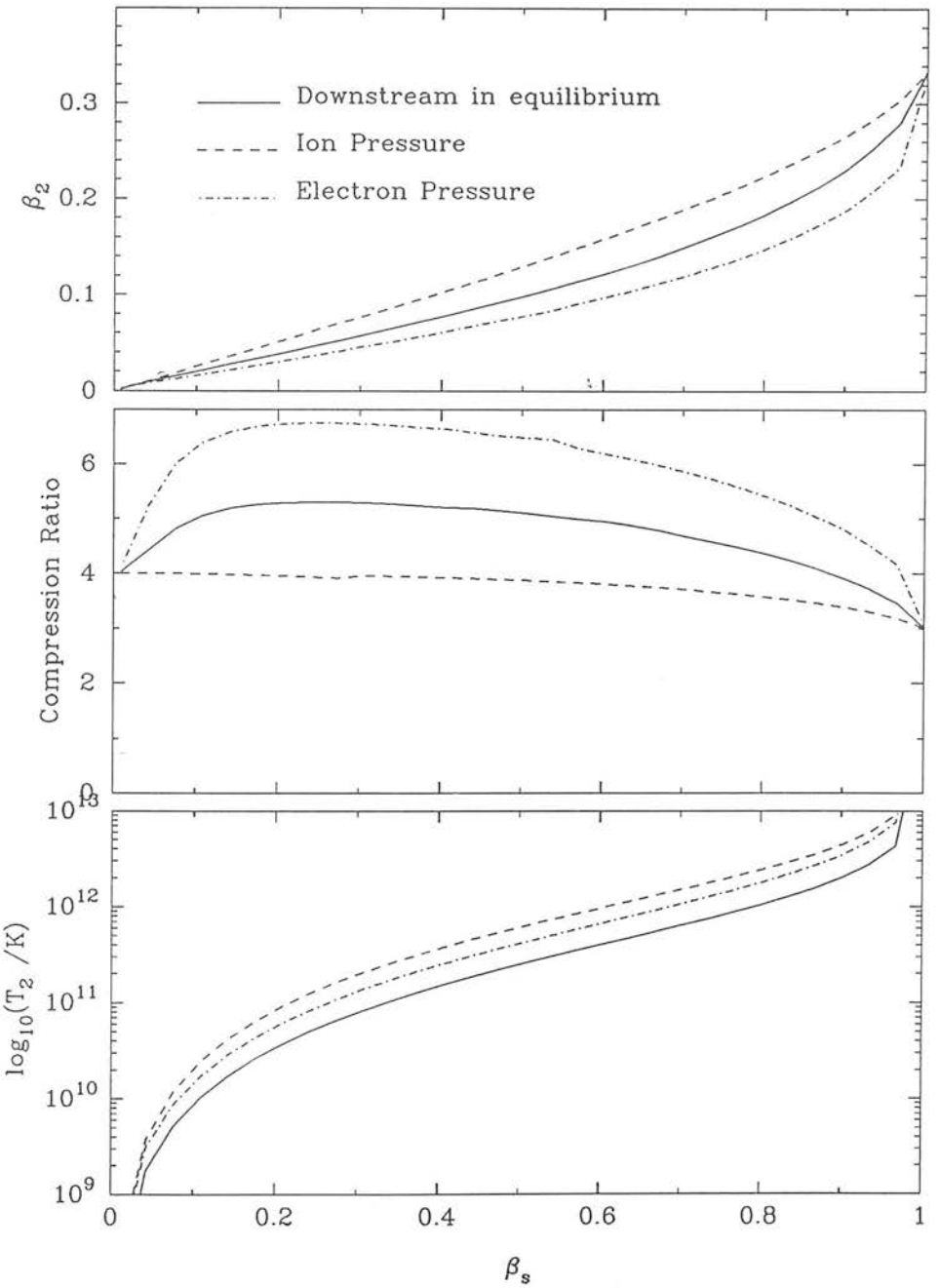

Figure 3.2: This shows the solutions to the jump conditions at a relativistic strong shock in the hydrodynamic limit. The three cases of interest are with the downstream fluid in local thermodynamic equilibrium (solid line), ion pressure dominating (dashed line) and electron/positrons dominating (dot–dashed line).

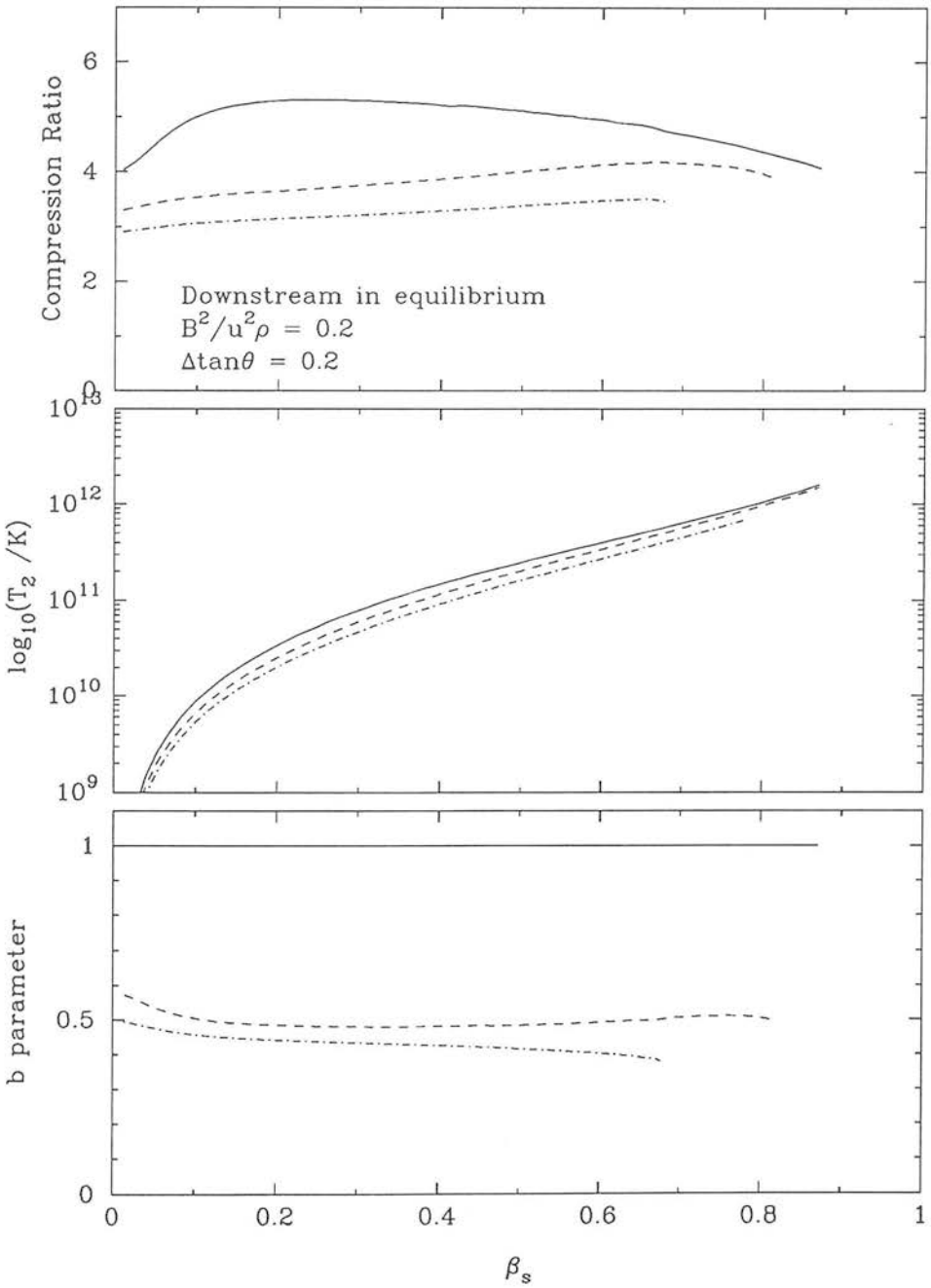

Figure 3.3: This shows the solutions to the jump conditions as a function of shock speed with a dynamically important magnetic field. The downstream fluid is in equilibrium between electrons and ions. The five curves plotted correspond to different values of $\tan\theta$, as $\tan\theta$ increases so the compression ratio decreases. Also shown are the downstream temperatures and b parameter.

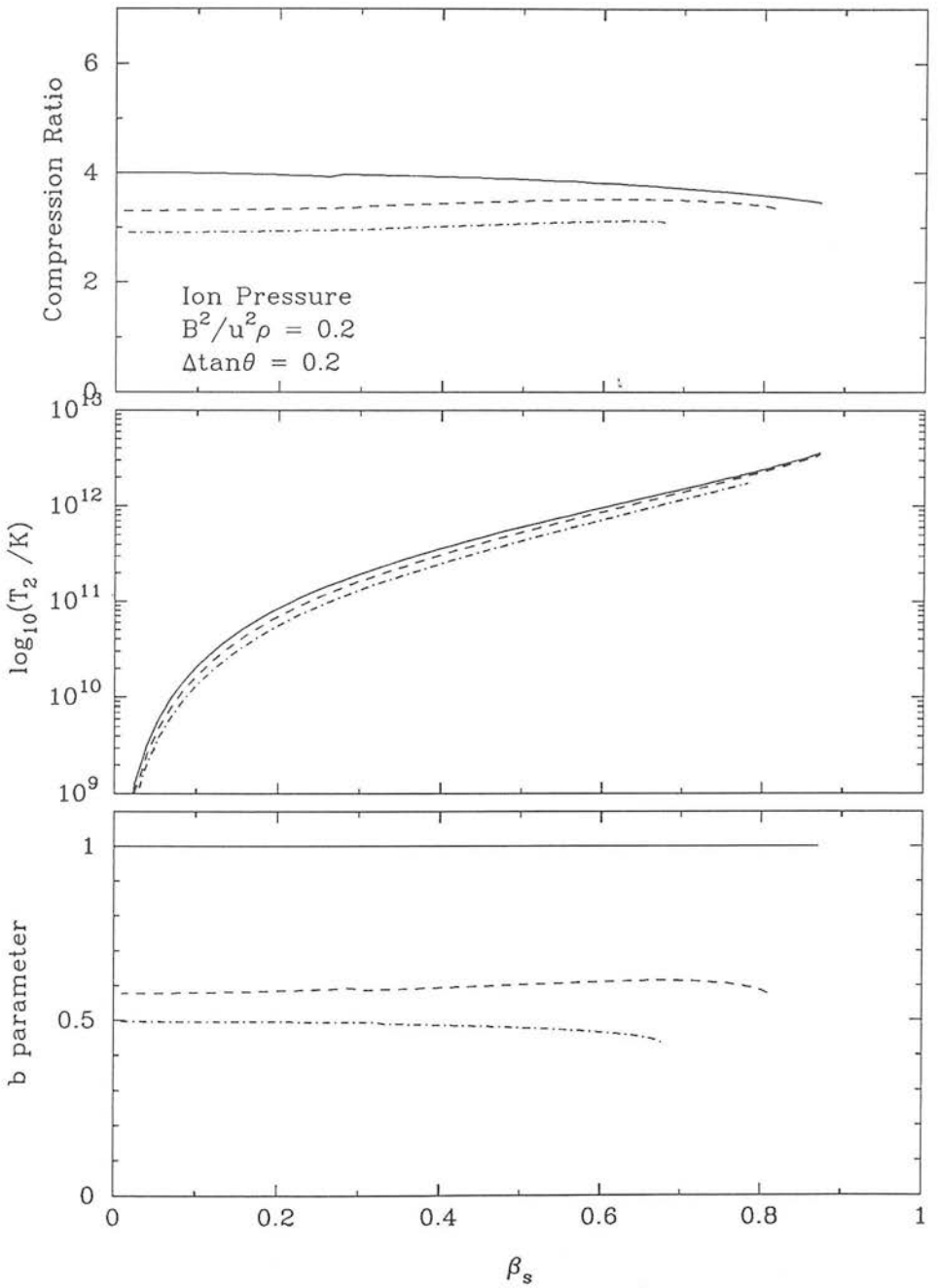

Figure 3.4: This shows the solutions to the jump conditions as a function of shock speed with a dynamically important magnetic field. The downstream pressure is provided entirely by ions. The compression ratio, downstream temperatures and b parameter are plotted and the five curves plotted correspond to different values of $\tan\theta$.

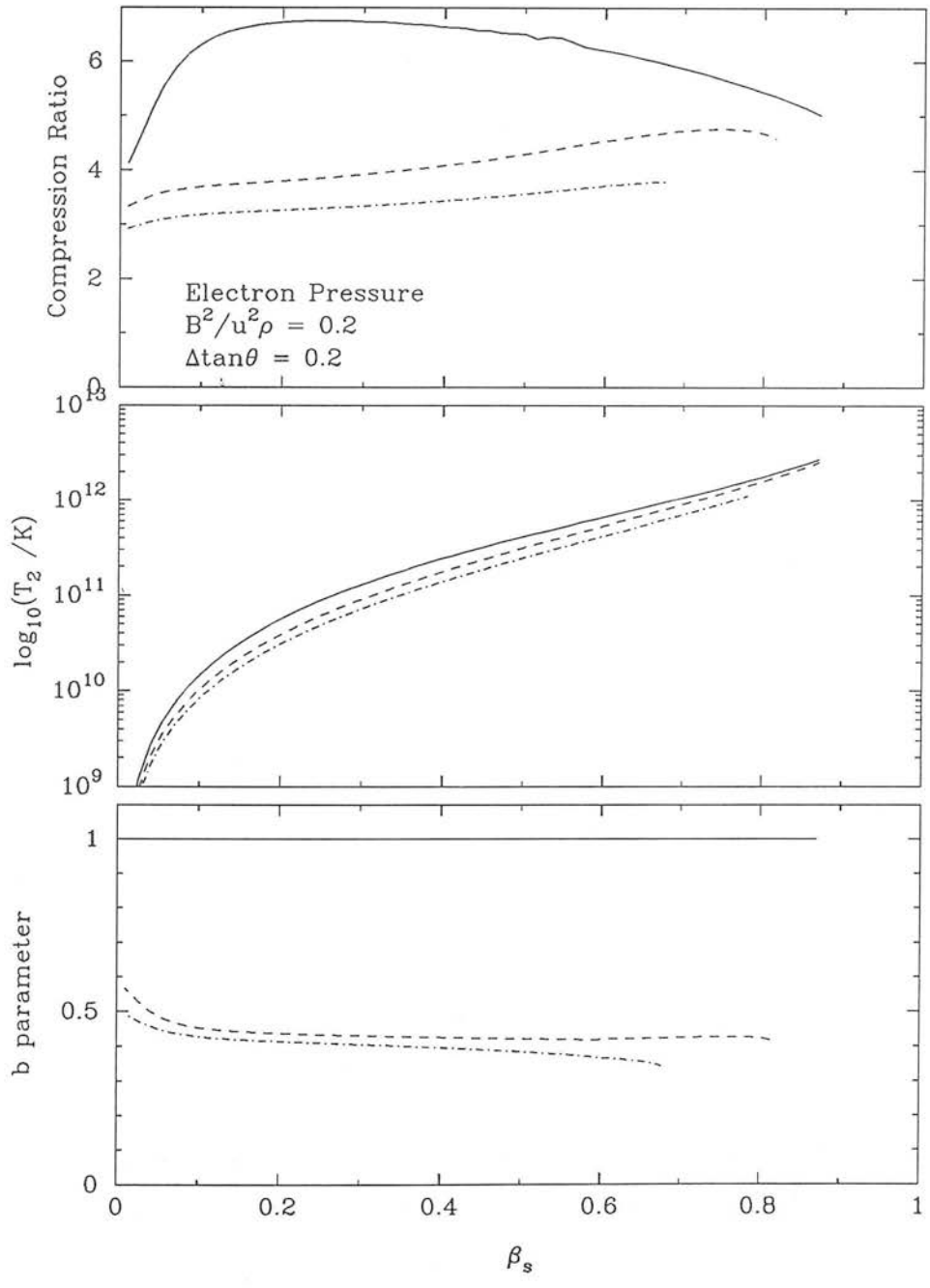

Figure 3.5: This shows the solutions to the jump conditions as a function of shock speed with a dynamically important magnetic field. The downstream pressure is provided entirely by electrons. The compression ratio, downstream temperatures and b parameter are plotted and the five curves plotted correspond to different values of $\tan\theta$.

more oblique at a given speed the compression ratio decreases; however the component of the field perpendicular to the shock normal increases and hence the field is boosted by an increased factor. The parameter b thus decreases with increasing shock obliquity.

3.5 Particle acceleration

The jump conditions at a relativistic oblique shock have been solved for a variety of possible downstream conditions and it has been shown that increasing the magnetic pressure can significantly reduce the compression ratio at the shock. This is of manifest relevance to the process of Fermi acceleration of particles at a shock front where the spectral index of the accelerated particles is a strong function of the compression ratio. The process of acceleration of electrons at a shock front is considered next. In calculating spectral indices it will be assumed that the suprathermal component has no significant back reaction upon the shock. The effect of the non-thermal component upon the shock structure has been discussed by e.g. Blandford 1980; Heavens 1983; Achterberg et al. 1984; Heavens 1984; Drury 1989 in the limit of negligible magnetic pressure and a non-relativistic shock front. Two methods are presented in the following subsections so that the semi-analytic calculations of KH can be tested by a numerical simulation of the scattering process. Clearly, as the compression ratio is a function of shock speed and magnetic pressure, one would expect a range of spectral indices.

3.5.1 Q_J Method

The theory of particle acceleration at a relativistic oblique shock front was developed by KH, again in the case where the magnetic pressure was negligible. This chapter uses the technique of KH, and the reader is referred to that paper for details. Their method was similar to that of Kirk & Schneider (1987a) in that the problem is solved by expanding the distribution function in terms of the eigenfunctions of the scattering operator. There are however additional points to be taken into account for the oblique case. Firstly the possibility of the electrons making multiple shock crossings at the

shock front has to be allowed for. This "shock drift" mechanism was noted by Jokipii (1982). Secondly it is not always the case that a particle incident from the upstream side of the shock front will cross though to the downstream region. By employing conservation of magnetic moment KH showed that the downstream pitch angle μ_s of a particle is related to its upstream value by:

$$1 - \mu_s^2 = b(1 - \overline{\mu}_s^2) \tag{3.37}$$

Thus there is a critical pitch angle cosine:

$$\mu_0 \equiv \sqrt{1 - b} \tag{3.38}$$

Particles incident with $|\mu_s| < \mu_0$ cannot penetrate downstream, and are reflected by the shock front. Particles with $|\mu_s| > \mu_0$ are transmitted to the downstream side. The method assumed that electrons do not drift across magnetic field lines. The spectrum is determined by the shock speed, compression ratio and obliquity. The distribution is obtained by solving the relativistic transport equation at the shock front; in an electromagnetic field the scattering is governed by:

$$\hat{L}^\mu_\nu \hat{p}^b \frac{\partial F_o}{\partial x^\mu} + \frac{e}{m} \hat{\mathcal{F}}^a_\lambda \hat{p}^\lambda \frac{\partial F_o}{\partial p^a} = \hat{p}^0 \hat{\mathcal{C}} \tag{3.39}$$

(e.g. Riffert 1986), where F_0 is the distribution function, $\hat{\mathcal{F}}^a_\lambda$ is the electromagnetic field tensor, p is the momentum , $\mathcal{C}$ is the collision term, Latin indices run $1 - 3$. Reference frames are mixed so that spatial coordinates are measured in the deHT shock frame, but momentum is measured in the fluid frames. $\hat{L}^\mu_\nu$ is then the Lorentz transformation from the fluid frame to the de Hoffman–Teller frame. Terms measured in the fluid frame are marked with a circumflex. If one assumes that the distribution function is independent of the gyrophase, ϕ, and defines a phase-averaged distribution function f, then the transport equation reduces to:

$$\gamma \cos\theta (u + v\mu) \frac{\partial f}{\partial x} = D_{\mu\mu} \frac{\partial}{\partial \mu} (1 - \mu^2) \frac{\partial f}{\partial \mu} \tag{3.40}$$

(KH) where an isotropic pitch angle scattering operator has been employed as the simplest case. The particle speed, v is taken to be unity. The distribution function

$f(p)$ is a power-law in momentum $f(p) \propto p^{-s}$ and the spectral index s is calculated by the method. The energy spectral index, $s-2$ is shown in Figs 3.8–3.10 for the three thermodynamic cases under consideration, for a range of values of M_A^{-2}. Also shown are the synchrotron spectral indices, $\alpha = (s-3)/2$. For values $M_A > 10$, the effect of the magnetic field strength is negligible.

3.5.2 Monte Carlo Method

Rather than relying upon the semi-analytic treatment of the problem the solutions were tested additionally using a numerical approach, following the propagation of individual particles on either side of the shock front by a Monte Carlo method. This will allow confirmation of the results of KH in the limit of a low magnetic field. The present approach however makes the same physical assumptions as KH, in particular that the magnetic moment is conserved upon crossing the shock, and so is not truly independent. Note however that the assumption of magnetic moment conservation has been shown to be a valid approximation by Ostrowski (1991) in the case of diffusion in pitch angle only.

The method chosen here is similar to that of Kirk & Schneider (1987b). First a particle is injected at one side of the shock front, the upstream region was chosen in order to ensure that each particle crosses the shock front at least once, thus benefitting the efficiency of the method. The particle is injected with an initial momentum p_0 and random pitch angle μ_0. The particle is then followed as it scatters off magnetic irregularities. The equation which governs its motion is:

$$\gamma \cos\theta (u + v\mu)\frac{\partial f}{\partial x} = D_{\mu\mu}\frac{\partial}{\partial \mu}(1-\mu^2)\frac{\partial f}{\partial \mu} \tag{3.41}$$

note that to obtain such an equation it has been necessary to assume the electron distribution function is independent of the gyrophase of the electrons and also that the interactions can be described via an isotropic pitch angle scattering operator; in order to examine this assumption one would have to follow the orbits. The use of this form, rather than the large angle scattering operator usually employed in the non-

relativistic limit is necessary to describe the expected scattering by small scale magnetic irregularities. This gives rise to the expected anisotropy in the distribution function in the relativistic case.

The method simulates particle acceleration by following individual particles as they cross and re-cross the shock front. Each particle is injected into the fluid and as it moves through the fluid it undergoes scattering in pitch angle until it is either returned to the shock front or lost; the latter can only occur if the particle is in the downstream region. To try to treat the problem fully one would have to follow the very large number of small pitch angle deflections that a particle undergoes each time it crosses the shock front. Instead the lead of Kirk & Schneider (1987b) is followed and it is noted that in a time Δt the particle will travel a distance $\Delta s = v\Delta t$, Δt being measured in the fluid frame; this leads to a change in position in the shock frame,

$$\Delta x = \gamma(u + \mu)\Delta t \tag{3.42}$$

and thus one can write the transport equation as

$$\frac{\cos\theta}{D_{\mu\mu}}\frac{\partial f}{\partial \Delta t} = \frac{\partial}{\partial \mu}(1-\mu^2)\frac{\partial f}{\partial \mu} \tag{3.43}$$

The propagation is followed by making a rotation, where the pitch angle, μ_0' is zero the azimuthal angle ϕ, is introduced, whence equation (3.41) becomes:

$$\frac{\cos\theta}{D_{\mu\mu}}\frac{\partial f}{\partial \Delta t} = \left[\frac{\partial^2}{\partial \mu'^2} + \frac{\partial^2}{\partial \phi^2}\right] f \tag{3.44}$$

The probability distribution of the pitch angle after the scattering event is then given by the Green's function,

$$P(\mu', \phi' \mid \mu_0' = 0, \phi_0' = 0) = \frac{\cos\theta}{4\pi\Delta t D_{\mu\mu}} \exp\left[\frac{-(\mu'^2 + \phi'^2)\cos\phi}{4\pi\Delta t D_{\mu\mu}}\right] \tag{3.45}$$

and the new μ' and ϕ' are random values taken from this probability distribution. This is then transformed back to the shock frame to find the new μ,

$$\mu = (1-\mu'^2)^{-1/2}\mu_0\cos\phi' + \mu'(1-\mu_0'^2)^{-1/2} \tag{3.46}$$

Finally, note that one must set a downstream boundary (it is clear that all particles in the upstream region must return to the shock front). From KH we note that the spatial part of the distribution is separable and decays as $\exp(-\lambda_i x/\gamma\cos\theta)$, so that at large x the distribution function decays to its isotropic value and there is little chance of a particle returning to the shock, rather it is more likely to be advected away. The position of the downstream boundary is chosen to be ($\lambda_0 = 0$)

$$d = \frac{10\gamma}{D_{\mu\mu}\lambda_1} \tag{3.47}$$

From KH $\lambda_1 = 6u\gamma$. Thus, the method adopted is as follows. A particle is injected with momentum p_0 and pitch angle μ_0. After a time Δt it will have travelled a distance Δx, given by equation (3.42). At this point it is scattered to a new μ, chosen as described. This procedure is repeated for the next Δt and continued until either:

1. The particle crosses the downstream boundary at which point it is regarded as having no chance of returning to cross the shock front and is 'lost'. It takes no further part in the simulation.

2. Or it returns to the shock front after a finite number of scattering events. Upon reaching the shock it is added to the distribution function at its present momentum and pitch angle (in the shock frame). What happens next depends upon the value of the pitch angle. It is assumed that as a particle crosses the shock front its magnetic moment is conserved. Thus all particles incident from the downstream region pass into the upstream region with a new pitch angle – measured now in the upstream frame. On the other hand, in crossing from the upstream region, a particle may be reflected by the shock and returned to the upstream region. In this case the simulation continues as before with a reflected pitch angle.

An important point to note is use of the technique of particle splitting when a particle returns to the shock (Kirk & Schneider 1987b). In order to achieve a high signal-to-noise ratio in the distribution function over a large enough range of momentum it is apparent that an impractically large number of particles, each with a finite escape probability, would have to be injected into the simulation at momentum p_0. To

circumvent this problem any particle which reaches the shock is split. This creates a number of daughter particles, N_D, with the parent's momentum and pitch angle. This process allows one to achieve enough high energy particles to achieve the desired accuracy in the simulations. Each of the daughter particles is assigned a weighting of $1/N_D$ and is then followed throughout the simulation until it is subsequently lost. In order to retain roughly constant numbers of particles throughout the simulation the number of daughters is chosen to be an integer from a Poissonian distribution with mean $\overline{N_D} = p_{esc}/(1 - p_{esc})$ (p_{esc} is the escape probability, $\sim 4u_2$ in the parallel non-relativistic limit). The value of $\overline{N_D}$ does not affect the spectral index if the particles are weighted appropriately, but it does affect the efficiency of the simulation. The weight associated with each particle as it crosses the shock is w. The increment to the distribution function at p and μ is $w/\mid \mu_s \mid$. This is because the weight w refers to the flux of particles (i.e. w particles have crossed the shock front), whereas the purpose of the simulation is to obtain the distribution function, $f(p, \mu)$.

3.5.3 Particle distributions

The Monte Carlo method described above returns the distribution function in a series of pitch angle and momentum bins, and this can then be plotted as a function of either. Fig. 3.6 shows the standard non-relativistic result, obtained with $\beta_{1x} = 0.2$, $\beta_{2x} = 0.05$, $\beta_{iy} = 0.0$. Fig. 3.7 shows the distribution obtained for a shock with $\beta_{1x} = 0.4$, $r = 4$, and $\theta = 45°$. The spectral index is $s = 3.17$, in good agreement with the result of KH. However, as can be seen from the figures, the distributions are noisy as a consequence of employing a Monte Carlo method; a large amount of computer time is required to reduce the noise to a satisfactory level. From these distributions the spectral indices of the electron distributions are obtained by simply fitting the weighted least squares best straight line to the plot of $\log_{10}(fp^2)$ against $\log_{10} p$. The question of weighting the points correctly was one of some importance because of the large amount of computer time necessary to generate reliable spectra if the error weighting procedure was not optimized. It is not obvious what the correct weighting method should be; one cannot simply assume the errors should all be weighted equally because it is clear the low

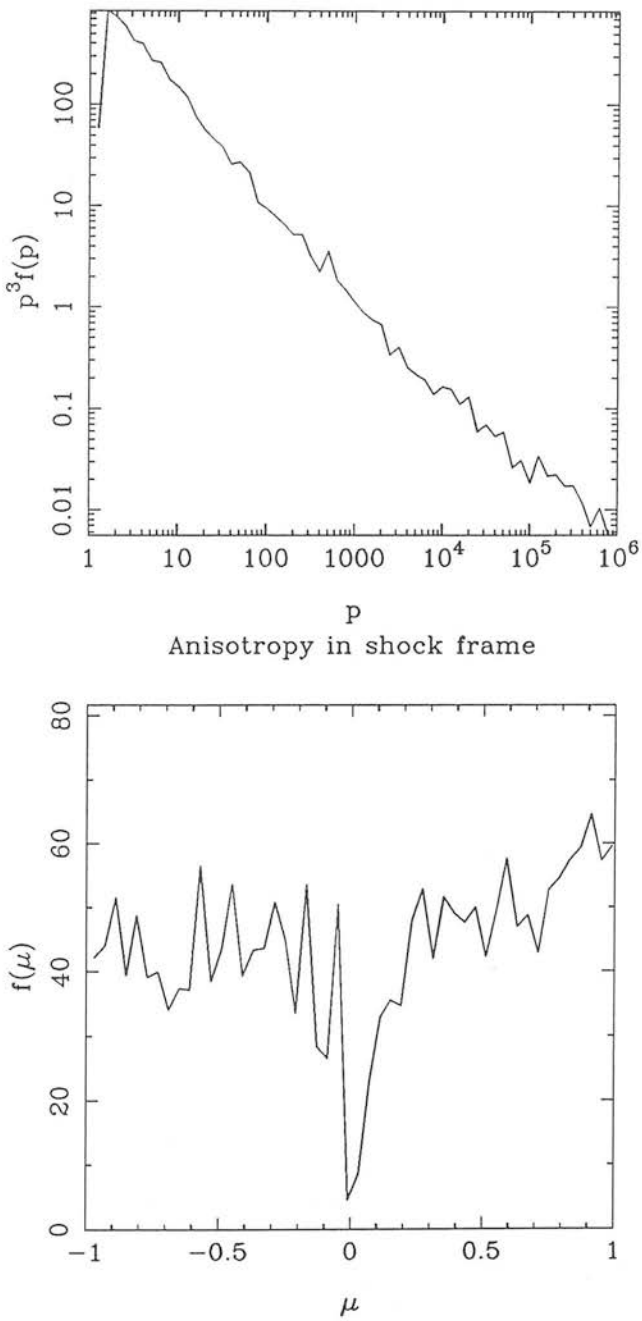

Figure 3.6: This shows the distribution function at an parallel shock with speed $u_{sh} = 0.2$, compression ratio 4. The spectral index is $\alpha = 0.5$.

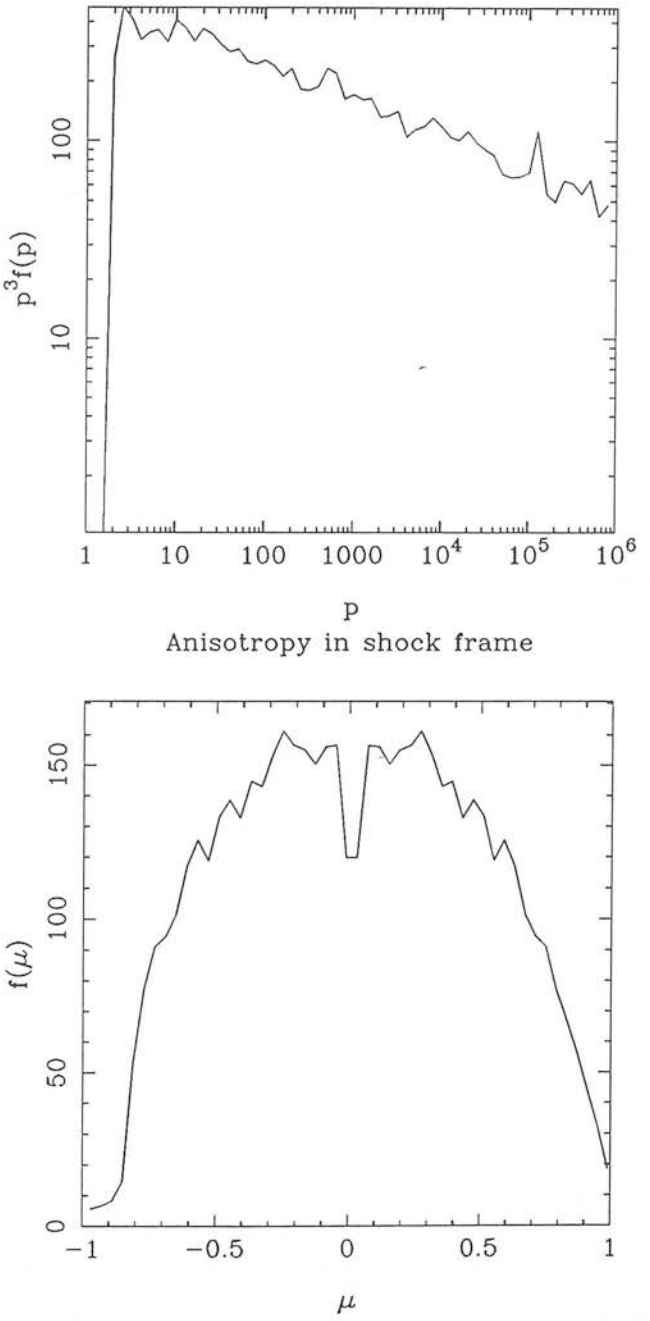

Figure 3.7: This shows the distribution function at an oblique shock with speed $u_{sh} = 0.4$, compression ratio 4 and a magnetic field at 45° to the shock normal. The spectral index is $\alpha = 0.057$.

momentum bins, with a higher number of particles are more accurate than the higher valued bins. The assumption that the errors in $f(p)$ decrease roughly as $f(p)^{-1/2}$ is not valid because of the splitting of particles which tends to have the opposite effect i.e. to increase the number of shock crossing events at high p and consequently increase the signal-to-noise ratio at high p (which is after all the purpose for which it was introduced). If the technique worked perfectly then one would have a situation where the errors were indeed equal in each bin, but it did not, the simulations all ended when the particles were exhausted (in practice this was partially caused by a fixed minimum weighting below which particles were "lost"). In the end it was decided to weight the bins by the number of shock crossing events occurring within each bin; it is hard to see how to better this method although it should be recognized that each entry is not of equal value, rather being weighted by the number of splittings it has experienced and the pitch angle cosine. The simulations were terminated after obtaining the desired accuracy in the spectral index. This method was used to obtain Figures 3.8–3.10 where spectral indices are plotted as a function of β_{1x}, the parallel shock speed for a series of differing magnetic field strengths. Having shown that the method of KH agrees well with a number of numerical results, the lines on Figs 3.8–3.10 were obtained using their method. The points superimposed upon these plots correspond to specific numerical calculations with identical physical conditions. The error on the best straight line is plotted as an error bar. The upper limit to the shock speed of $\beta_{1x} = 1/\sqrt{2}$ is a result of a fixed β_s, above which the shock becomes superluminal, and the method we have described is unsuitable to provide solutions to the jump conditions and consequently the Monte Carlo method cannot accelerate particles in this regime. Although it is outside the scope of this work, it is not without interest; Jokipii (1982) has shown that superluminal shocks can accelerate particles and Begelman & Kirk (1990) have shown that, even assuming the particles do not drift across field lines and thus cannot return to the shock after having travelled further than one gyroradius away from it, the adiabatic energy gain from the shock crossings may be up to a factor of 4γ per particle.

The results of these simulations show that for values of the Alfvénic Mach number of $M_A^{-2} \sim 0.05$ or larger the compression ratio of the shock may be significantly altered. This weakening of the shock strength can lead in turn to steeper spectral indices. Thus

by employing realistic jump conditions synchrotron spectral indices as high as $\alpha \simeq 2.0$ can be obtained and the problem of unphysical spectral indices obtained by KH can be circumvented. The flat spectral indices in KH were caused by the fact that at a highly oblique shock most of the particles incident upon the shock from upstream are reflected and hence particles tend to be trapped upstream. This also happens with a larger magnetic field, only here the energy gain is reduced by the reduced compression ratio which acts to steepen the spectral index. As high spectral indices are associated with the higher magnetic fields, the synchrotron emissivities are also high ($\propto B^2$) and one might expect regions with these magnetic fields to dominate, particularly at lower frequencies. On the other hand synchrotron lifetimes also are proportional to B^2 so that the source evolves more rapidly.

It is notable that at low shock speeds there is a greater range of spectral indices than at higher speeds. This is possibly a result of particles being reflected more often at higher shock speeds. At the highest speeds the compression ratio at the shock decreases as the equation of state becomes fully relativistic and as a consequence of this there is a slight increase in the spectral index observed. The nature of the scattering centres should also be discussed. In general it is assumed that electrons scatter in pitch angle by collision with resonant Alfvén waves moving much more slowly than the electrons upstream of the shock, and turbulence downstream. Despite increasing the Alfvén wave speed in these simulations, it is assumed that it will still be much less than the ultrarelativistic speeds at which the electrons are moving and thus the Alfvén waves are retained as scattering centres.

3.6 Discussion

The results may be applied to those environments where synchrotron emission, the astrophysical signature of high energy electrons in a magnetic field has been observed. The most likely applications are to the hotspots of extragalactic radio sources. The best studied example is that of 3C273. Flatters & Conway (1985) describe the radio structure of the jet and hotspot and suggest an oblique shock in the hotspot because

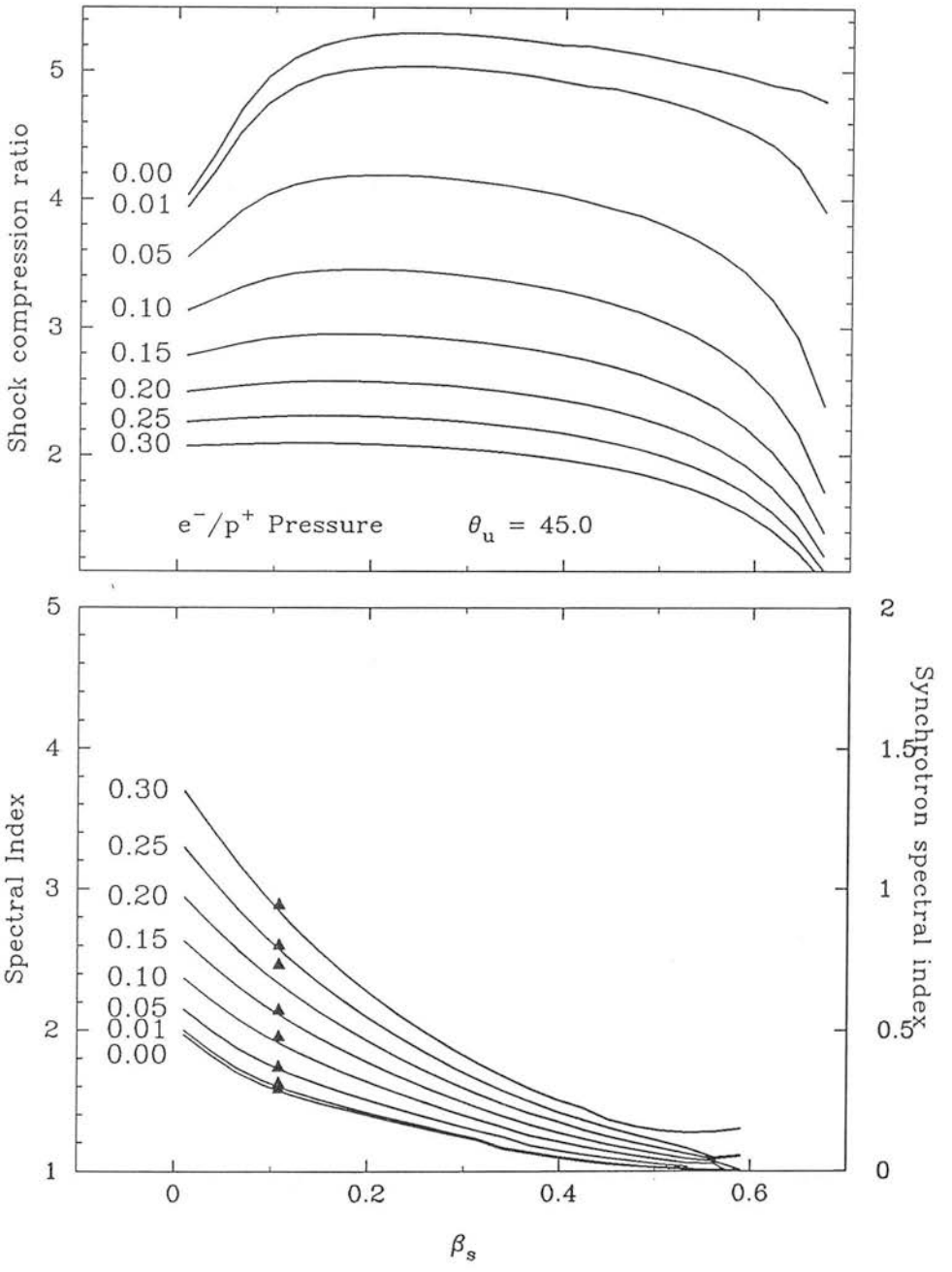

Figure 3.8: This shows a comparison between the analytically derived spectral indices and the numerical results for a shock with a magnetic field at an angle $\theta = 45°$ and the downstream fluid in local thermodynamic equilibrium. The different lines correspond to different values of M_A^{-2} as labelled.

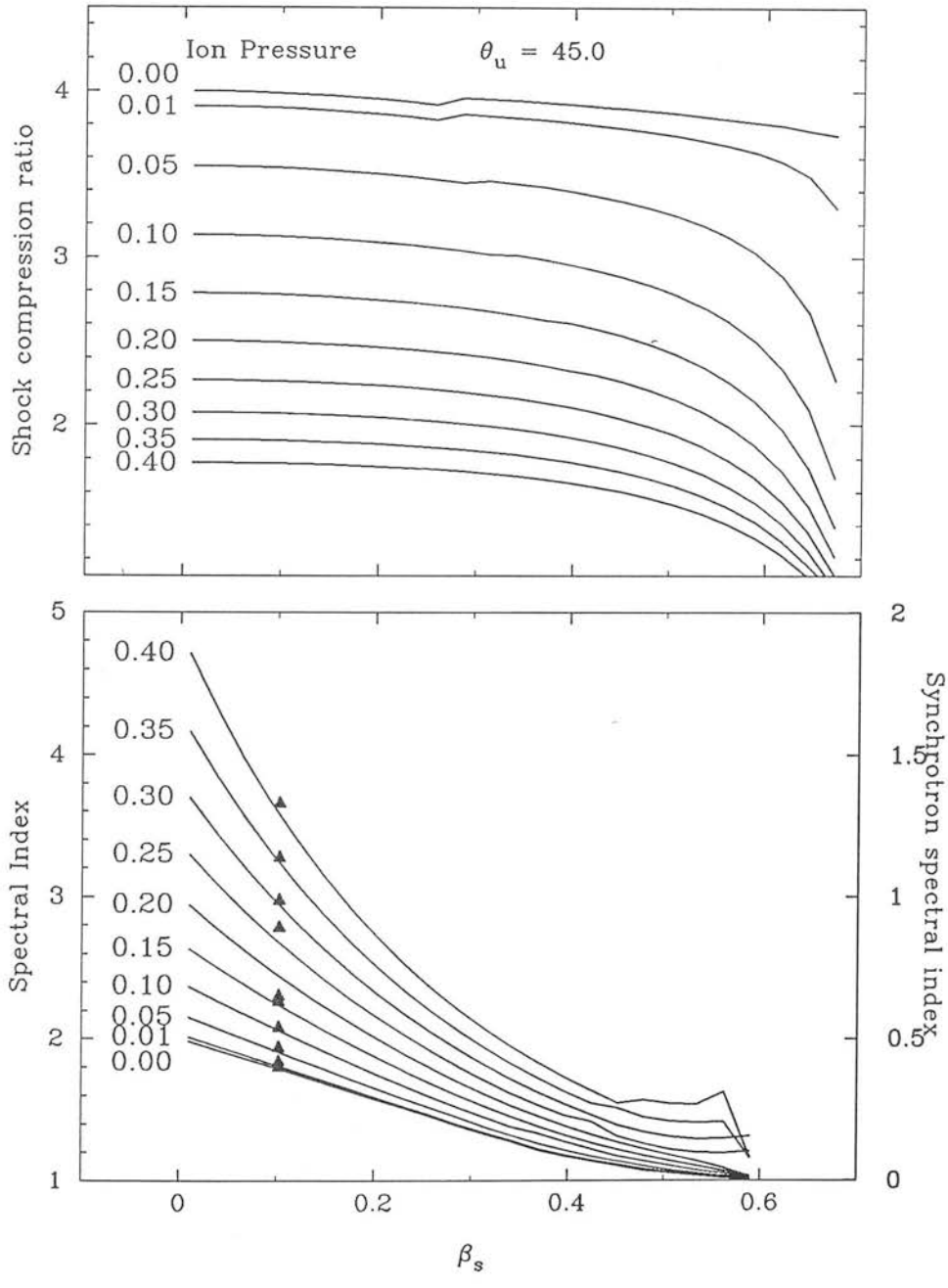

Figure 3.9: This shows a comparison between the analytically derived spectral indices and the numerical results for a shock with a magnetic field at an angle $\theta = 45°$ and the downstream fluid pressure provided entirely by ions.

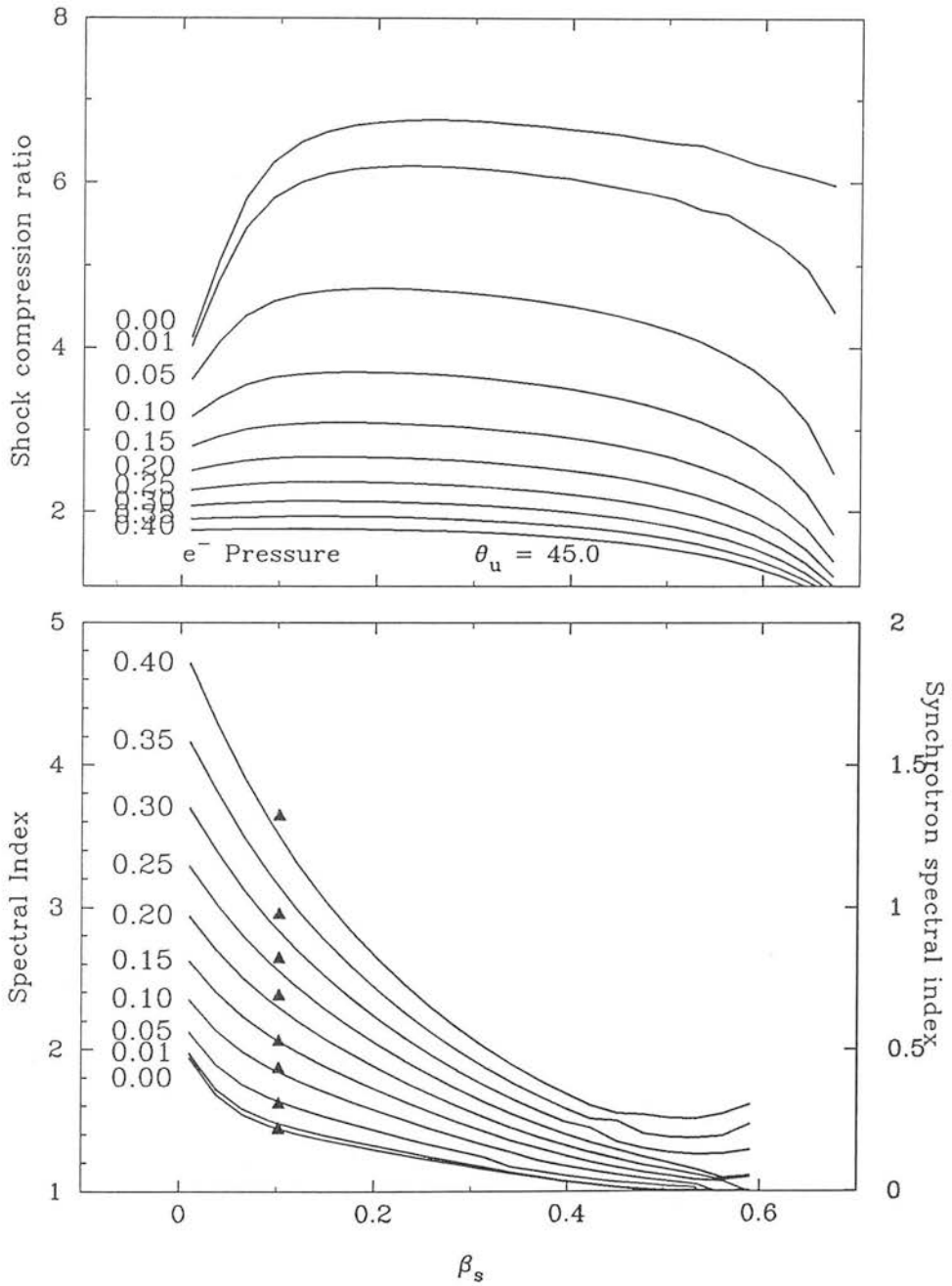

Figure 3.10: This shows a comparison between the analytically derived spectral indices and the numerical results for a shock with a magnetic field at an angle $\theta = 45°$ and the downstream pressure provided by electrons.

the dominant magnetic field lies transverse to the jet. This is a result which is repeated at optical wavelengths (Scarrott & Rolph 1989). Meisenheimer et al. (1989) recently published observations of spectral indices for a number of sources. They showed that in those cases where there is an optical counterpart to the radio source, spectral indices are around $\alpha \sim 0.5$ in agreement with the classical result of Bell (1978a). Furthermore, they used the observed frequencies at which the synchrotron break and cutoff appeared and a simple Fermi acceleration model to derive shock speeds between $\beta \sim 0.15$ and $\beta \sim 0.5$. However, this suggests an inconsistency because as both this work and that of KH have shown, at these shock speeds a simple oblique shock with a dynamically unimportant field and a compression ratio of around 4 (as Meisenheimer et al. derived) would produce a spectrum of exceptional hardness. However, they had to make certain assumptions about the shock in order to derive a value for the field so that their results are not exact. Although it is not possible to argue for particular values of the Alfvénic Mach number for the shocks, it is likely that dynamically unimportant fields would produce unrealistically hard spectra. To circumvent this, it is suggested that the magnetic field may be important in reducing the shock compression ratio to a value where the spectral index is more representative of that which is actually observed; it is a more attractive line to take than that which starts with conventional weak shocks where there is some upstream pressure because such shocks can produce any spectral index, including any value greater than those observed.

It is also possible that these results are applicable to blazars. Again one has oblique shocks and steep spectral indices, so that by the same logic, dynamically important fields could be responsible for spectral steepening. The problem with this is the supposition that the shocks are relativistic, in which case they would be superluminal for quite low angles of the field to the shock normal. It is quite possible that the more realistic modelling of the Fermi process which is carried out in Chapter 5 is more relevant to both blazars and hotspots.

This chapter has presented solutions to the jump conditions at a subluminal oblique relativistic magnetohydrodynamic shock employing a Synge equation of state using a simple method involving a single two-dimensional Lorentz transformation to a

reference frame where the fluid moves parallel to the magnetic field on either side of the shock front. This can provide solutions while the speed of intersection of the shock and magnetic field is less than the speed of light. This is not a restriction because we are interested in the process of the first order Fermi acceleration of electrons, which can only occur under these conditions. This aspect of oblique shocks was investigated using a Monte Carlo method for comparison with earlier analytic work in the weak field limit; the agreement between the two was good. Increasing the magnetic field reduces the compression ratio at the shock. This reduces the energy gain experienced by a particle upon completing a cycle of crossing and recrossing the shock. This acts to steepen the spectral index. This may be able to explain why objects where the magnetic field is expected to be perpendicular to the shock front have synchrotron spectral indices considerably steeper than those expected in the weak field limit.

Chapter 4

Shock models of blazars

4.1 Introduction

Shocks are attractive elements in any model which purports to explain the blazar phenomenon because they can explain many of the features of variability in blazars and also, under certain conditions, they provide a ready made explanation of the non-thermal spectrum of the electron distribution. However, to date the properties of shock models have not been applied to the optical data; this is the aim of the present chapter. In this chapter only the properties of BL–Lacs will be considered i.e. there is no suspicion that the optical light has been diluted by unpolarized emission of a non-synchrotron origin. Before making a detailed calculation it is worth restating the high frequency properties of the emission, as stated in Chapter 2. These are:

- Although in many cases the spectrum was a power-law of constant slope, there were a significant number of observations where the spectrum steepened with increasing frequency. The fact that generally spectral indices in the optical are greater than in the radio (where $\alpha \simeq 0.2$, Valtaoja et al. 1988) suggests losses may have modified the spectrum. Synchrotron or inverse Compton losses can steepen the spectral index by 0.5 if there is a continuous injection of electrons. The gradually increasing spectra of blazars (Landau et al. 1986) from the radio to the optical strongly supports the form of steepening produced by losses.
- With only a couple of exceptions, in the case of the BL–Lacs the polarization always increased towards the blue end of the spectrum. The level of polarization was indicative of a partially ordered magnetic field when averaged over the entire emission region – although it is possible that it could be almost uniform in regions

of smaller extent than the optical emitting volume. Frequency dependence of position angle was less common than frequency dependence of polarization. Most of the frequency dependence of polarization was associated with the intrinsic curvature of the flux via the simple parameterization of Björnsson & Blumenthal (1982) i.e. as the spectral index increased so did the polarization according to the relationship:

$$\mathrm{pol}(\nu) = \Pi \frac{\alpha(\nu) + 1}{\alpha(\nu) + 5/3} \times 100\% \tag{4.1}$$

where $\alpha(\nu)$ is the spectral index and Π is a constant representing the degree of ordering in the magnetic field.

These are the principal characteristics of BL–Lacs deduced from a large number of observations and any model must be able to explain these in order to be taken seriously; it is upon this premise that the work in this chapter will be based. This approach is different from others, where individual events from a single object are understood and then applied to other objects. By concentrating on a few properties which are true for a large number of objects it is to be hoped that some general conclusions about the sources can be drawn. Having achieved that, a good model should also allow for the more occasional extreme events such as those seen by Holmes et al. (1984b) or Moore et al. (1982).

There are two main motivations for a study of this kind. The first is simply an attempt to plug a gap in the knowledge of the properties of a simple synchrotron source. Kardaschev (1962) presented results for the evolution of a synchrotron source, as the electrons lost or gained energy to various mechanisms, such as synchrotron emission, adiabatic expansion or the inverse Compton effect. Implicit in this work however, was the assumption that as the electrons lose energy they maintain their initial pitch angle with respect to that magnetic field element. As effects such as synchrotron losses are pitch angle dependent this naturally leads to anisotropies in the distribution. The only specific source fields considered were isotropic and as there was no preferred direction to the field, there was no overall polarization. An initial aim is to investigate the effect

on the polarization of any anisotropies which might develop in a more realistic field geometry.

The second motivation arises from observational studies and the necessity to adapt present ideas to observations of blazars which may be possible in the future. The dominant model of blazar emission is a shock in a jet. Groups such as those in Michigan (see Aller et al. (1985) and references therein) at centimetre wavelengths or Preston (see Brown et al. 1989a) at submillimetre and infrared wavelengths have used their data to model the variability convincingly using a shock in a jet. A randomly-oriented field compressed by a weak shock front was employed in the model of Hughes et al. (1985), together with a driving piston and the integrated flux from a quiescent jet. They had data for BL–Lac over a period of four years (from 1981 to 1985) taken at three frequencies (4, 8 & 14.5 Ghz) with full polarization information and they obtained good fits to their data over this period. However the emission at radio frequencies arises from electrons not affected significantly by losses which accordingly were not included in their analysis. Of more relevance to their work were optical depth effects; throughout this chapter it will be assumed that the source is optically thin as the work is primarily concerned with high frequency emission for which this should be a reasonable assumption.

The effect on the electron distribution of inverse Compton scattering, synchrotron radiation and adiabatic expansion were included in the analysis of Marscher & Gear (1985) who modelled the data for a dramatic flare in the millimetre emission of 3C273. 3C273 is not strictly speaking a blazar, as the optical emission is not dominated by synchrotron emission but the model was later applied to several blazars (Gear et al. 1986) with favourable results. However, polarization data for the millimetre wavelengths was not available at the time and consequently the only field that was specified was "nearly random" upstream and compressed by the shock.

The properties of synchrotron emission from partially ordered magnetic fields were discussed by Björnsson & Blumenthal (1982) who, with some restrictions, evaluated the flux and polarization expected from a number of possible magnetic field and electron pitch angle distributions. However the Björnsson & Blumenthal (1982) parameteriza-

tion of the radiation does not give any insight into the origin of the electron spectrum in blazars; it is simply a technique for calculating polarization features given certain field and electron distributions.

Finally, the connection between the optical and radio emitting regions has not yet been established conclusively, although there are several pieces of evidence which favour their being related. Events such as that reported by Kikuchi et al. (1988) for OJ287 of a position angle rotation, simultaneous at both radio and optical wavelengths, are highly suggestive. Position angle rotations such as this may be a result either of an actual rotation of the magnetic field within the source, or of aberration effects, where the speed of the jet itself changes (Blandford & Königl 1979). However the mere fact that they occur suggests that the optical light is originating in the same region in space as the radio emission. Support comes from the work of Landau et al. (1986) who found the radio to optical spectra to change smoothly. If the emission in the two wavebands arose in separate regions and varied independently then the spectra would not be so smooth. The fact that Landau et al. fitted their spectra with parabolæ is not in conflict with sharp breaks in the underlying energy distribution because of the broad nature of the synchrotron Green functions; any sharp breaks tend to be washed out, giving a smoother flux distribution. Finally there is the work of Impey (1987) who has shown that the distribution of the difference between VLBI structure axis and preferred optical position angle tends to be peaked around 90°, again suggestive of underlying source structure. This assumption is implicit in this work, the model is known to be successful in the radio, the question is, how relevant is it to the optical.

The layout is as follows: Section 4.2 describes the construction of a model for the optical radiation, in Section 4.3 the results for a source decaying, and having a constant injection are presented and discussed under the assumption that the individual electrons maintain a constant pitch angle. Section 4.4 examines the opposite limit where the electrons maintain isotropy. Section 4.5 describes an alternative model, one which includes a number of randomly oriented subcomponents. Section 4.6 presents the conclusions and discusses how to improve the model.

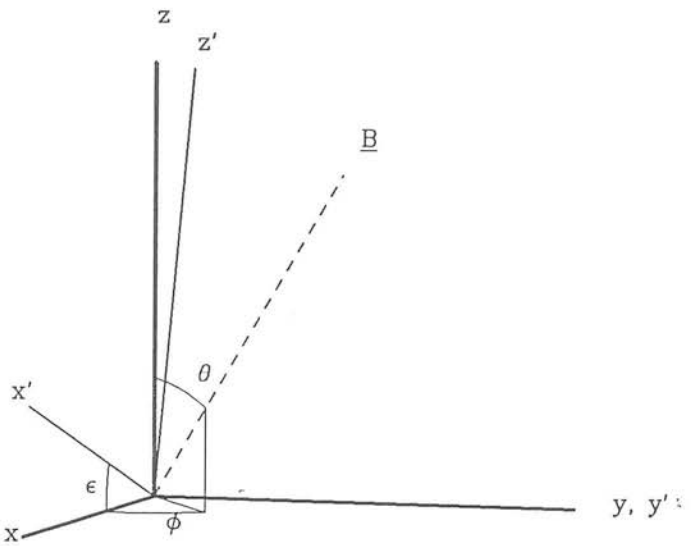

Figure 4.1: The shock face lies in the xy plane, the magnetic field components lying in this plane are enhanced by a factor r at the shock. The observer [electron velocity] lies at an angle ϵ to the x axis, the field distribution is axisymmetric around the z axis.

4.2 The Model

In this section a calculation of the emission from an ensemble of electrons emitting synchrotron radiation in a compressed random magnetic field downstream of a shock front will be made. The assumed source geometry is shown in Fig. 4.1. This is essentially identical to that of Hughes et al. (1985). The shock front lies in the xy plane, that is the z axis is parallel to the shock normal. The velocity compression ratio at the shock front, β_1/β_2 is given by r. Thus by conservation of magnetic flux density the magnetic field, assumed isotropic upstream, is compressed at the shock front. Note that this has assumed that the magnetic field is dynamically unimportant in determining the jump conditions at the shock front i.e. $v_A^2 << v_S^2$ downstream. This will enable a simple treatment of the magnetic field so that the geometry is dependent only upon the shock compression ratio and is independent of the magnetic field magnitude.

It is necessary to evaluate $B \sin\varepsilon$ for the source geometry shown by Fig. 4.1 i.e. to find the projected magnetic field distribution. B is the isotropic magnetic field strength upstream of the shock and ε is the angle between the line of sight and an

element of the field downstream. This work makes use of the fact that the emission from a single electron is concentrated within a narrow cone of half angle γ_e^{-1}. This is because the dipole radiation from an accelerated charge is beamed into a narrow angle when seen from a stationary frame in which the electron is moving relativistically (e.g. Rybicki & Lightman 1979). This considerably simplifies any calculations, one is not observing synchrotron emission from electrons with a distribution of velocity directions, only those electrons which are moving directly towards the observer. The angle ε, the pitch angle between the observed electron's velocity and the element of magnetic field is equal to the angle between the line of sight and the magnetic field. $B\sin\varepsilon$ is the projection of the magnetic field onto the plane of the sky. Without loss of generality, due to axial symmetry, the electron's velocity vector lies in the xz plane and makes an angle ϵ to the x axis. A second Cartesian coordinate system $x'y'z'$ as shown in Fig. 4.1 is defined so that the electron's velocity lies along the x' axis and the y' axis lies parallel to the y axis. An element of the magnetic field of magnitude B at an angle θ, ϕ before being compressed has the following components after compression:

$$\begin{aligned} B_x &= Br\sin\theta\cos\phi \\ B_y &= Br\sin\theta\sin\phi \\ B_z &= B\cos\theta \end{aligned} \tag{4.2}$$

in the xyz system. In the $x'y'z'$ system these can be rotated to give:

$$\begin{aligned} B_{x'} &= B(r\sin\theta\cos\phi\cos\epsilon + \cos\theta\sin\epsilon) \\ B_{y'} &= Br\sin\theta\sin\phi \\ B_{z'} &= B(\cos\theta\cos\epsilon - r\sin\theta\cos\phi\sin\epsilon) \end{aligned} \tag{4.3}$$

and thus one can evaluate $B^2\sin^2\varepsilon$, the component perpendicular to the x' axis:

$$\begin{aligned} B^2\sin^2\varepsilon &= B_{y'}^2 + B_{z'}^2 \\ &= B^2(r^2\sin^2\theta\sin^2\phi + r^2\sin^2\theta\cos^2\phi\sin^2\epsilon \\ &\quad + \cos^2\theta\cos^2\epsilon - 2r\sin\theta\cos\theta\cos\phi\sin\epsilon\cos\epsilon) \end{aligned} \tag{4.4}$$

The position angle of a field element is also required. This is given by:

$$\tan\chi = \frac{B_{z'}}{B_{y'}} = \frac{\cos\theta\cos\epsilon - r\sin\theta\cos\phi\sin\epsilon}{r\sin\theta\sin\phi} \tag{4.5}$$

where χ is measured from the y' projected axis. Having evaluated the magnetic field geometry in which the electrons emit, it is possible to write down expressions for the Stokes parameters of the emission from this region. Specific electron distributions will be evaluated in following sections under various conditions. It is assumed that the electron distribution depends upon only three parameters: the electron energy, E, the time t, and ε, the pitch angle – the angle between the velocity vector and the element of magnetic field. Standard synchrotron theory (e.g. Pacholczyk, 1970) then gives the expressions for the Stokes parameters for an element of magnetic field. These are stated in Appendix A. To evaluate the total emission it is necessary to integrate over the full field distribution. Thus the following expressions for the radiation are obtained:

$$\begin{aligned}
I(t,\nu) &= LB\int_E\int_\theta\int_\phi \sin\varepsilon F(\tfrac{\nu}{\nu_c})N(E,\varepsilon,t)d\phi\sin\theta d\theta dE \\
Q(t,\nu) &= LB\int_E\int_\theta\int_\phi \sin\varepsilon G(\tfrac{\nu}{\nu_c})\cos 2\chi N(E,\varepsilon,t)d\phi\sin\theta d\theta dE \\
U(t,\nu) &= LB\int_E\int_\theta\int_\phi \sin\varepsilon G(\tfrac{\nu}{\nu_c})\sin 2\chi N(E,\varepsilon,t)d\phi\sin\theta d\theta dE \\
V(t,\nu) &= 0
\end{aligned} \tag{4.6}$$

where L is the line of sight depth of the source, χ is the position angle, ν_c is a critical frequency ($= (3\pi\gamma_e^2 eB\sin\varepsilon)/m_e$) and $\sin\varepsilon$ is given by equation 4.4. F and G are synchrotron Green's function given in Appendix A. From the expressions for the individual Stokes parameters, the observational characteristics of the synchrotron radiation can be obtained. The flux spectral index is given by:

$$\alpha(\nu,t) = -\frac{d\log_{10}I(\nu,t)}{d\log_{10}\nu} \tag{4.7}$$

which is obtained by numerically differentiating $\log_{10}I(\nu,t)$. The degree of linear polarization is given by:

$$p(\nu,t) = \frac{(Q^2(\nu,t)+U^2(\nu,t))^{\frac{1}{2}}}{I(\nu,t)} \times 100\% \tag{4.8}$$

Finally, the position angle is obtained from:

$$\tan 2\zeta = \frac{U(\nu,t)}{Q(\nu,t)} \tag{4.9}$$

which is degenerate for $\zeta = 0, \pi/2$. In order to differentiate between these the sign of $Q(\nu,t)$ is taken into account; $Q(\nu,t)$ is positive at $\zeta = 0$ and negative at $\zeta = \pi/2$.

The Stokes parameters calculated are the expressions for the emitting frame, in this case the frame downstream of the shock front. This may be in relativistic motion relative to an observer. The downstream region is assumed to be moving at a velocity β, at an angle η' in the observers frame corresponding to an angle $\eta \equiv (90 - \epsilon)$ in the emitting frame. The Doppler boost is given by

$$\delta = \frac{1}{\Gamma(1-\beta\cos\eta')} \tag{4.10}$$

where Γ is the Lorentz factor of the source. The Stokes parameters transform as:

$$\begin{aligned} I'(t,\nu) &= I(t,\nu)\delta^{2+\alpha} \\ Q'(t,\nu) &= Q(t,\nu)\delta^{2+\alpha} \\ U'(t,\nu) &= U(t,\nu)\delta^{2+\alpha} \\ V'(t,\nu) &= 0 \end{aligned} \tag{4.11}$$

The value 2 in the exponent is appropriate for a stream of knots with finite lifetimes and α is the spectral index taken from equation 4.7. The requirement that the source be in relativistic motion will introduce an extra parameter into the model. In order to maintain clarity all results are presented for sources with identical velocities with $\Gamma = 2.0$. η' will be determined by the chosen value at η.

In the previous section, Björnsson & Blumenthal's (1982) work on the properties of inhomogeneous synchrotron sources was mentioned. In their paper they evaluated the following integrals for the Stokes parameters (see also Korchakov & Syrovatskii

1962):

$$\begin{aligned} I(t,\nu) &= \int_{\gamma_e}\int_{\chi}\int_{b} b^2 H(b,\chi,\gamma_e) F(\tfrac{\nu}{\nu_c}) db d\chi d\gamma_e \\ Q(t,\nu) &= \int_{\gamma_e}\int_{\chi}\int_{b} b^2 H(b,\chi,\gamma_e) \cos 2\chi G(\tfrac{\nu}{\nu_c}) db d\chi d\gamma_e \\ U(t,\nu) &= \int_{\gamma_e}\int_{\chi}\int_{b} b^2 H(b,\chi,\gamma_e) \cos 2\chi G(\tfrac{\nu}{\nu_c}) db d\chi d\gamma_e \\ V(t,\nu) &= 0 \end{aligned} \tag{4.12}$$

here b is the projected magnetic field ($\equiv B \sin\varepsilon$), χ is the position angle of an element of the field on the sky and γ_e is the electron Lorentz factor. The function $H(b,\chi,\gamma_e)$ is defined as "the trivariate probability density of finding an electron with Lorentz factor γ_e radiating in a magnetic field specified by b and χ". The equations can be written in this form after a transformation between the frames; the integrals over χ and b are equivalent to the integrals over θ and ϕ and the integral over γ_e is equivalent to the integral over E. They use the function $H(b,\chi,\gamma_e)$ to describe the entire source structure, considering several arbitrary parameterizations where $H(b,\chi,\gamma_e)$ is separable in each of the variables. They show that the polarization can be written as:

$$\mathrm{pol}(\nu) = \left[q^2(\nu) + u^2(\nu)\right]^{1/2} \frac{\alpha(\nu)+1}{\alpha(\nu)+5/3} \times 100\% \tag{4.13}$$

where q and u are stated integrals over the magnetic field geometry and which are frequency independent in the case where the electron distribution is independent of position within the source. While a parameterization such as this provides an analytic description of the radiation, it is not based upon any particular physical model. The present approach is to calculate the emission from a particular model.

4.3 Results

4.3.1 No scattering, no injection

In a sense this is the least relevant case for understanding blazars. In practice there is likely to be some level of injection of electrons into the source, particularly for flares; this will be neglected. Secondly, it will be assumed that the electrons have a pitch

angle which is constant in time for their particular element of field and this precludes the possibility of Fermi acceleration operating. Finally the possibility of a relativistic shock will be ignored. A Lorentz transformation of an isotropic electron distribution results in anisotropies. All these assumptions may be incorrect and attempts will be made to drop them in later sections. However the present case does illustrate several of the properties of synchrotron emission downstream of a shock.

Only synchrotron losses will be considered in detail. This makes the calculations simple but again it may be unrealistic; it is likely that other loss mechanisms play a role in the variability. Adiabatic losses are important in the later stages of radio flares (Marscher & Gear 1985) but as $-dE/dt \propto E$ it is more likely that it will be either synchrotron or inverse Compton losses (for which $-dE/dt \propto E^2$) which will dominate at high energies. Inverse Compton losses act isotropically i.e. they are independent of pitch angle. Hence later sections where electron isotropy is maintained by scattering are relevant if this loss mechanism is operating.

If the initial energy of an electron is E_0 at time $t = 0$, then in a time t the energy will reduce to:

$$\frac{1}{E} - \frac{1}{E_0} = \sigma t \tag{4.14}$$

where:

$$\sigma = \frac{e^4 B^2 \sin^2 \varepsilon}{6\pi \epsilon_o c^5 m_e^4} \equiv 1.31 \times 10^{12} B^2 \sin^2 \varepsilon \tag{4.15}$$

The solution to the kinetic equation is (Kardaschev, 1962):

$$N(E, \varepsilon, t) = kE^{-\gamma}(1 - \sigma t E)^{\gamma - 2} \Theta \left(\frac{E_c}{1 + \sigma t E_c} - E \right) \tag{4.16}$$

where $N(E, \varepsilon, 0) = kE^{-\gamma}$ is the initial distribution. In the integrations the distribution has been assumed to have both an upper cutoff at E_c and a lower cutoff. Both are assumed to be initially sharp i.e. $N(E, \varepsilon, t) = 0$ above or below the cutoff energies. Finally note the presence of the step function Θ in the electron distribution. Electrons at the cutoff energies will experience a loss of energy as all the electrons do, governed

by equation 4.14. Care must therefore be taken when integrating over the energy distribution not to extend the integration to the constant initial cutoffs but rather only to the correctly evolved cutoff energy. This point is important when deriving the form of the distribution when a constant injection of electrons is included, later on. However as this chapter is concerned principally with the high energy effects, the low energy cutoff will be ignored. This does not cause any extra electrons to be included in the integration which are not actually present, and furthermore the low energy cutoff is set to a value corresponding to a frequency lower than that shown on the plots, which are not therefore invalidated.

Fig. 4.2 illustrates several features of the electron distribution which have been discussed. Fig. 4.2a shows the basic form of equation 4.16, an evolving cutoff with constant energy spectral index $\gamma = 2.0$, Fig. 4.2b shows what happens for different values of the spectral index. It is notable that whenever the spectral index is harder than $\gamma = 2.0$ a hump appears in the distribution. This appears as Kardaschev (1962) pointed out because there are more electrons losing energy into an energy band ΔE than from ΔE. Fig. 4.2c shows how the value of $B \sin\varepsilon$ changes with θ (the angle between the field element and the shock normal) for a series of different viewing angles. Clearly it will increase as the field becomes more tangential to the shock and hence more compressed. Fig. 4.2d shows how the cutoff energy changes, again with θ, for these last two plots ϕ has been assumed constant and set to $\pi/2$.

The multiple integrals stated in the previous section were carried out for a series of shock compression ratios (r), spectral indices (γ) and viewing angles (ϵ) for an electron distribution with both an upper and lower cutoff for a range of 5 decades of frequency from the radio to the optical/UV. The integrals were evaluated using the NAG routines D01BBF/D01FBF which utilise normal Gaussian weights using a Gauss-Legendre method. This does not give an estimate of the error in the calculation but in practice the integrands were divided until further subdivisions yielded similar answers. The amount of CPU time required for the integrations was considerable so that only a series of the most notable limits was taken. The technique for evaluating the integrand was as follows. For a given run fixed values of r and ϵ were taken together with the

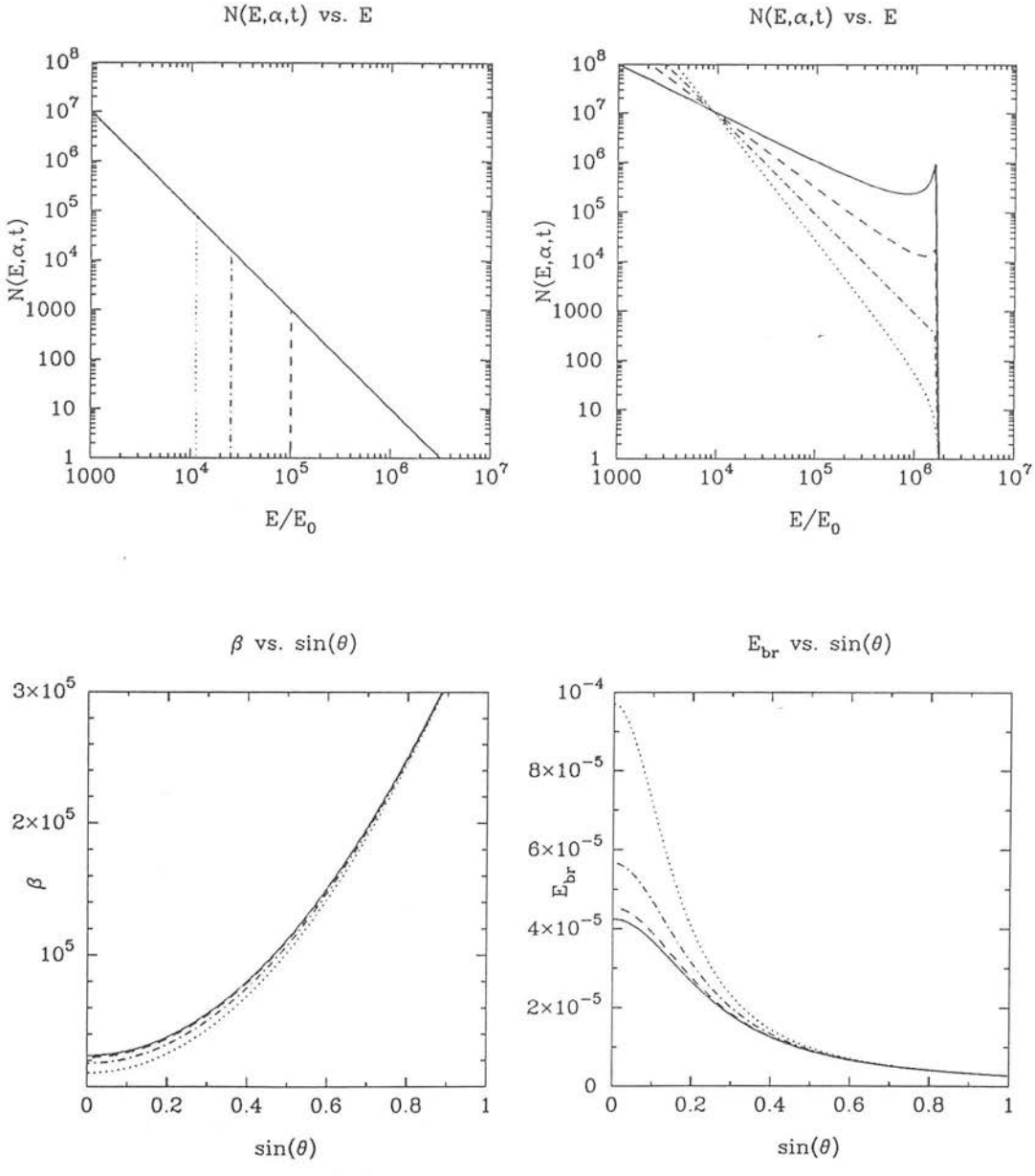

Figure 4.2: Fig4.2a shows the electron distribution for $\sin\varepsilon = 0.0$ (solid line), 0.2 (dashed line), 0.4 (dot-dashed line) and 0.6 (dotted line). Fig4.2b shows the distribution for a series of different spectral indices ($\gamma = 1.0, 1.5, 2.0, 2.5$). Fig 4.2c and Fig4.2d show $B^2 \sin^2\varepsilon$ and the break energy as a function of $\sin\theta$ for different viewing angles, $\eta = 0.0, 0.25, 0.50, 0.75$.

values of θ and ϕ for the element of field. From this $B \sin \varepsilon$ and $N(E, \varepsilon, t)$ can be obtained from equations 4.4 and 4.16 respectively. Similarly ν_c, the critical frequency for a given value of E and $B \sin \varepsilon$ can be obtained. At the fixed observing frequency ν, a value for $F(\nu/\nu_c)$ or $G(\nu/\nu_c)$ could be obtained by linear interpolation within a look-up table of values. Finally, the position angle of the element was referred to the z' axis and setting $\tan \chi = B_{z'}/B_{y'}$ one obtains: $\cos 2\chi = (B_{y'}^2 - B_{z'}^2)/(B_{y'}^2 + B_{z'}^2)$.

The results of a sample run with an electron spectral index of $\gamma = 2.0$ and a compression ratio of 4.0, corresponding to the non-relativistic shock limit are shown in Fig. 4.3. The three curves shown correspond to three equally spaced times. The time intervals (in the emitting frame) are $\delta t = 3$hours between the individual spectra. The flux decays with time. The flux spectral index is shown in Fig. 4.3b. This is calculated numerically using equation 4.7. This confirms the results of Kardaschev (1962) where the spectrum steepens from $\alpha = (\gamma - 1)/2$ to $\alpha = (2\gamma + 1)/3$ at the break frequency ν_B which moves to a lower frequency as time progresses. The spectrum steepens again at the sharp upper cutoff to take an exponential form. The break is not sharp but is smoothed out over several decades of frequency by the finite width of the function $F(x)$. The polarization properties are of more interest, the most striking feature is the dip in polarization accompanied by a subsequent rise at higher frequencies. At the zero polarization point there is a swing in position angle by 90°. An explanation for this behaviour is as follows. Behind a shock front with a moderate or large compression ratio the magnetic field will be dominated by the component which lies along the shock front. The electrons tied to magnetic lines lying along the shock front will dominate the emission at early times as this contributes most to the polarized flux. The result will be a position angle parallel to the shock normal. However, these electrons will quickly lose energy. At later times, after the initially dominant flux has died off, it is the electrons tied to weaker field lines along the shock normal which will dominate the emission at a much lower level and this will have a position angle at 90° to the initial position angle i.e. along the shock face; hence the position angle rotation. The zero polarization occurs at a frequency where the polarized fluxes from the two parts cancel out. Note that due to the symmetry of the problem, there are only two possible position angles.

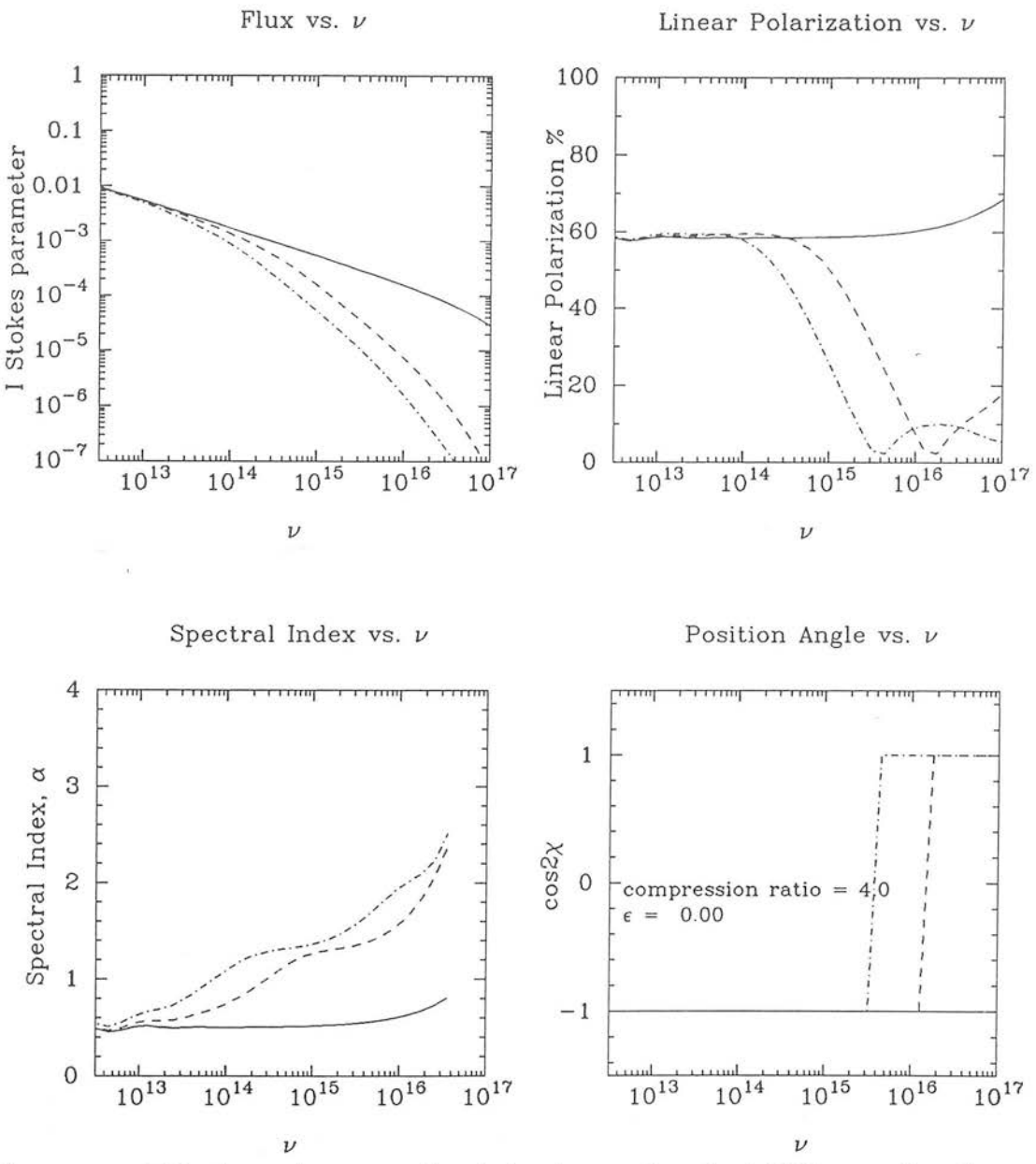

Figure 4.3: This shows the expected emission from a decaying initial power-law distribution. Fig 4.3a and b show the flux and polarization as a function of frequency. Note the dramatic drop in polarization as the spectrum breaks. Fig 4.3c shows the spectral index, derived as in equation 4.5. Fig 4.3d shows the cosine of the position angle, illustrating the flip in position angle at the frequency where the polarization reaches zero.

A summary of the general properties of decaying synchrotron sources is shown in Figs 4.4–4.7. These illustrate the change in the intensity and polarization of the emission as ϵ and t vary for a series of differing spectral indices and compression ratios. Each are shown at two frequencies, $\nu = 10^{12.5}$Hz, where losses have not affected the spectrum and $\nu = 10^{15}$Hz where the spectrum has steepened due to losses. The low frequency results are equivalent to those given in Hughes et al. (1985). They will not be discussed in full here, but are used to verify the method. Fig. 4.4 shows the intensity and polarization plotted against time for differing spectral indices ($\gamma = 2, 3, 4$) at a constant $\epsilon = 30°$. The flux increases with spectral index, at low frequencies staying constant with time, at high frequencies evolving. The initial polarizations are $\sim (\gamma + 1)/(\gamma + 5/3)$ (this is not exact because there is some degree of disorder in the field distribution). Note that distributions with higher spectral indices appear to decay in polarization more rapidly than lower spectral indices. Also because $\epsilon = 30°$ the polarization does not rise again after dropping to zero as the difference between the break energy at different values of $\sin\theta$ is less marked than for $\epsilon = 0$. Fig. 4.5 shows the variation in properties with time for differing angles to the shock face at a constant compression ratio ($r = 4$) and spectral index ($\gamma = 2.0$). These are fairly self-explanatory; at low frequency with no evolution, the flux increases and the polarization decreases with increasing ϵ, due to the dominant emission from larger and more disordered magnetic field lines along the shock face. When the source has evolved, at high frequency the polarization drops and then rises at a different position angle for $\varepsilon = 0$ as discussed earlier. At larger viewing angles the polarization does not rise at later times. Fig. 4.6 shows the change with ϵ for $\gamma = 2.0$ and increasing compression ratios ($r = 4, 5, 6$) at a time $t = 50$. At low frequencies the flux increases with compression ratio due to the increased emission at increased magnetic field values. The polarization drops as ϵ increases as the emission becomes dominated by radiation from more disordered fields. At high frequencies the flux decreases as the compression ratio increases, due to the fact that at higher compression ratios the flux evolves more rapidly and hence at later times there are fewer high energy electrons left and therefore less emission. The polarization is low due to the evolution at high frequencies and does not rise at larger values of ϵ. Fig. 4.7 plots the change in intensity and polarization with ϵ for differing spectral indices ($\gamma = 2, 3, 4$) at $t = 50$ and $r = 4$. The flux increases with increasing γ

and the polarization decreases with ϵ.

4.3.2 Applications

The results obtained so far for a decaying source may not be entirely realistic, but it would be unwise to proceed further without reference to a particular set of data obtained by Holmes et al. (1984b). In 1983 January they observed the BL–Lac object 0851 + 202 (OJ287) at near-infrared to optical frequencies (K–U wavebands) and recorded a low but varying degree of polarization. The spectral index increased with frequency. The polarization decreased with frequency in the near-infrared at a low level and had a position angle of 100° on the sky. Observations at higher frequencies showed a dramatic shift in the position angle to around 20° and the degree of polarization, after having dropped to a minimum of 0.4% in the R waveband, increased to 2.5% at U. The data on other nights showed constant position angles and larger polarizations. Holmes et al. interpreted this behaviour as the result of two polarized components at differing position angles each having different, curved spectra. At the frequency where the polarized fluxes are equal they cancel out to produce zero overall polarization, accompanied by a position angle swing. This is qualitatively similar to the properties of a decaying synchrotron source, described above and is probably the most dramatic single observation of a position angle rotation with frequency. Consequently an attempt was made to fit the model to these data. The parameters used to fit the data were: (low frequency) electron energy spectral index, shock compression ratio, time of observation (or age of the source), ϵ the line of sight to the shock normal, the low frequency position angle and the flux at 10^{14} Hz, a convenient frequency for normalization of the optical flux. The computer time necessary to achieve an accurate and complete search of parameter space was considerable and the limited search which was possible did not find a satisfactory fit. However, this is only the most obvious example and it is possible that a fit could be obtained for other data. In this case it would be most likely that the break frequency occurs at lower frequencies. Then the observed increase in polarization with frequency would always be the consequence of an evolved source. However the position angle alignment would then indicate that the field lies along the jet, contrary

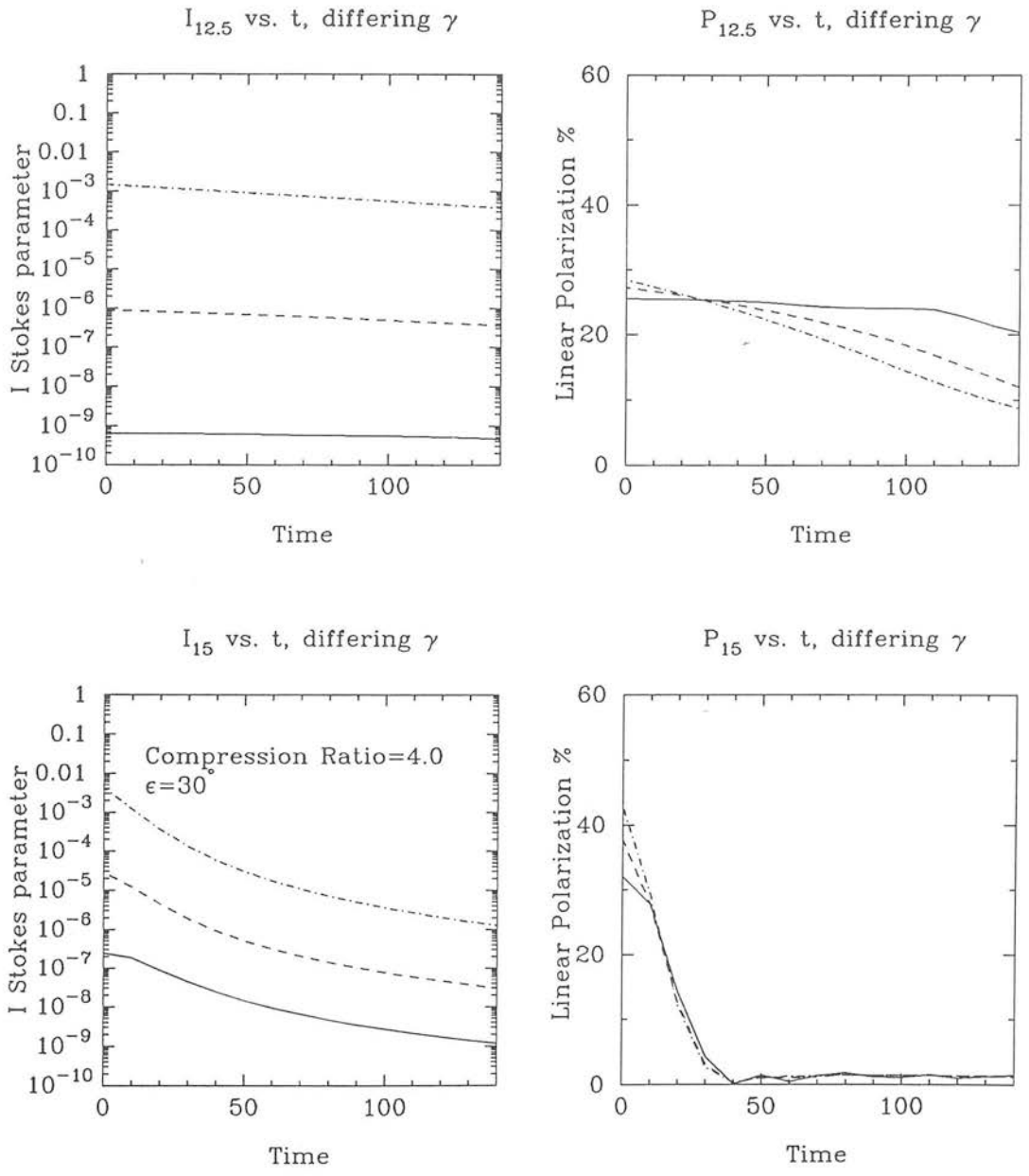

Figure 4.4: This shows the behaviour of a decaying synchrotron source for increasing time. Figs 4.4a & b show the flux and polarization at a low frequency where losses have not yet affected the distribution. Figs 4.4c & d are the same plots at a higher frequency. The lines refer to differing spectral indices; $\gamma = 2(,3,4)$ for the filled (dashed, dot-dashed) line.

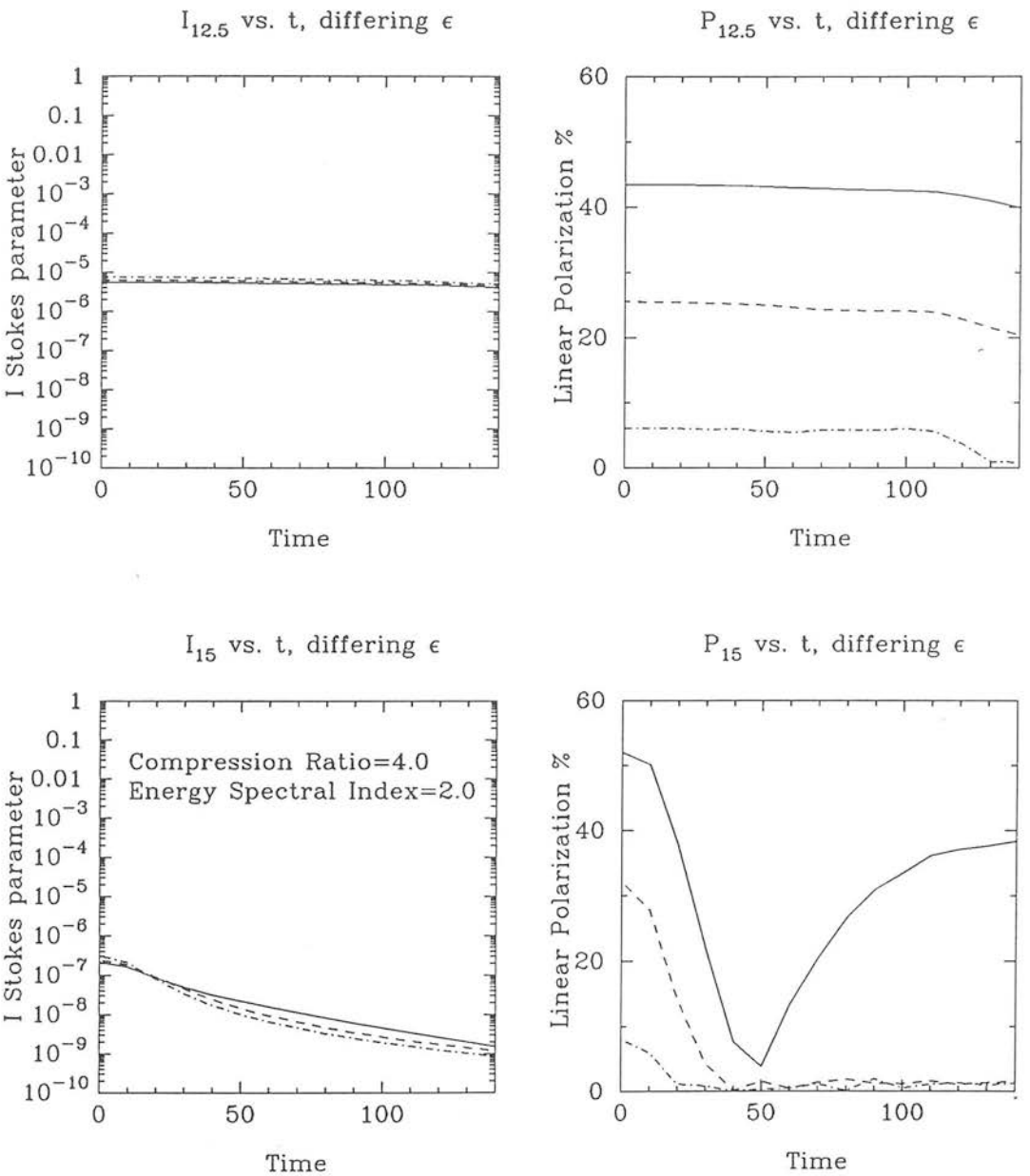

Figure 4.5: This shows the behaviour of a decaying synchrotron source for increasing time. Figs 4.5a & b show the flux and polarization at a low frequency where losses have not yet affected the distribution. Figs 4.5c & d are the same plots at a higher frequency. The lines refer to differing viewing angles; $\epsilon = 0(, 30, 60)$ for the filled (dashed, dot-dashed) line.

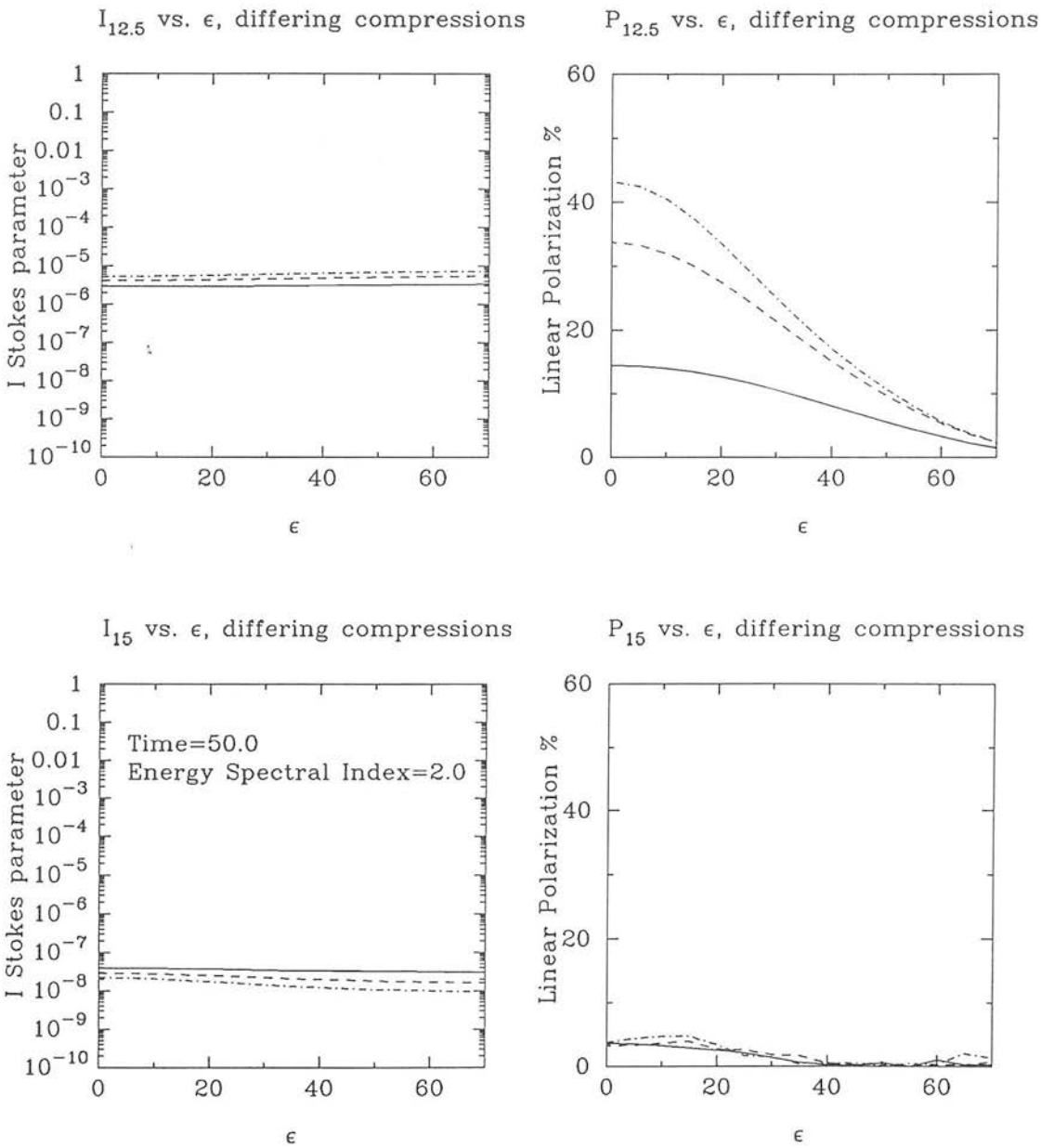

Figure 4.6: This shows the behaviour of a decaying synchrotron source for increasing time. Figs 4.6a & b show the flux and polarization at a low frequency where losses have not yet affected the distribution. Figs 4.6c & d are the same plots at a higher frequency. The lines refer to differing compression ratios; $r = 2(,3,4)$ for the filled (dashed, dot-dashed) line.

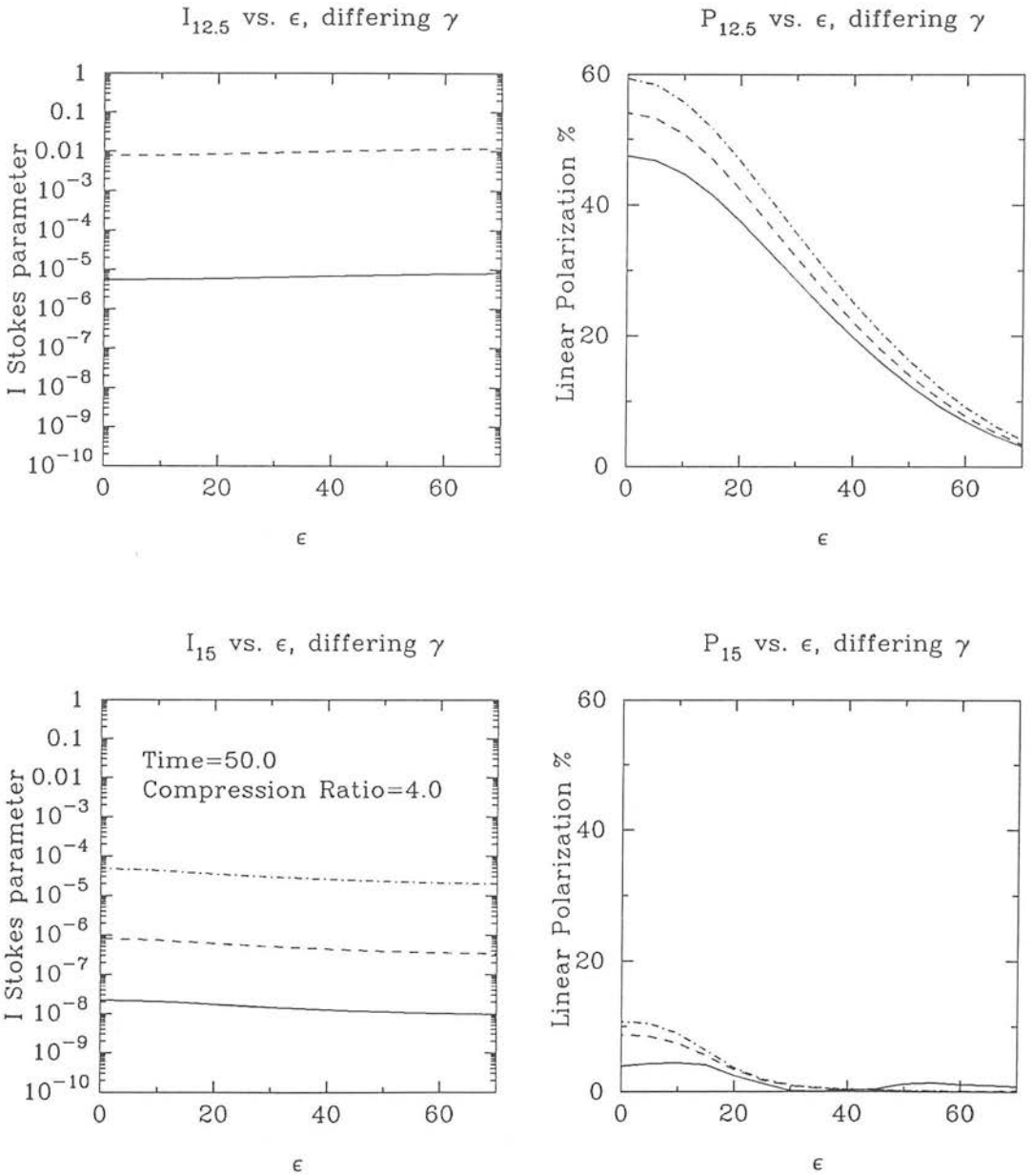

Figure 4.7: This shows the behaviour of a decaying synchrotron source for increasing time. Figs 4.7a & b show the flux and polarization at a low frequency where losses have not yet affected the distribution. Figs 4.7c & d are the same plots at a higher frequency. The lines refer to differing spectral indices; $\gamma = 2(, 3, 4)$ for the filled (dashed, dot-dashed) line.

to what is observed. Thus the predictions of the calculation are inconsistent with the observations.

It is not yet known how exactly the polarization behaves around the break frequency, as at present there are no observations between 2cm and the K waveband ($2.18\mu m$) in the near-infrared. Clearly the above demonstrates that such observations are highly desirable. If the model is justified by future measurements then there are a number of properties of the emission region which could be deduced in a straightforward manner. By fitting the model to data, parameters such as shock speed, compression ratio and orientation can be determined. The absolute value of the scattering timescale could also be found as a function of the loss timescale at the frequency of observation; after the loss time exceeds the scattering timescale the model breaks down.

4.3.3 The case of a relativistic shock

Several blazars display apparent superluminal motion (e.g. Impey 1987). If an association is made between these superluminally moving (milli-arcsec) features and the synchrotron emitting region downstream of the shock, then one is lead to the conclusion that the shock is moving at relativistic velocities. If this is the case then the previous assumption of an isotropic distribution in the upstream rest frame will, if there is no scattering of the electrons as they cross the shock front, lead to a significantly anisotropic distribution downstream. In this part an estimation of the initial degree of anisotropy introduced by a relativistic transformation and the effect this has upon the results is presented.

By Liouville's theorem the phase space distribution function of the electrons, $f(p,\mu)$, is Lorentz invariant. The relative velocity of the downstream region (subscript 2) to the upstream region (1), is given by:

$$\beta_r = \frac{\beta_1 - \beta_2}{1 - \beta_1\beta_2} \tag{4.17}$$

Then, as seen from the downstream frame the initial distribution has the form:

$$N(E,\mu_d)dEd\mu_d = kE^{-\gamma}\left(\Gamma(1-\beta_r\mu_d)\right)^{-\gamma-2}\Theta\left(\frac{E_c}{\Gamma(1-\beta_r\mu_d)}-E\right)dEd\mu_d \quad (4.18)$$

The step function was introduced this time to account for the fact that the cutoff energy which was constant in the upstream frame is transformed to a value which is a function of μ_d. Having been injected into the emission region with this distribution, the source decays and takes the form:

$$\begin{aligned} N(E,\varepsilon,\mu_d,t)dEd\mu_d &= kE^{-\gamma}\left(\Gamma(1-\beta_r\mu_d)\right)^{-\gamma-1}(1-\sigma tE)^{-\gamma-2} \\ &\quad \times\Theta\left(\frac{E_c}{\Gamma(1-\beta_r\mu_d)+\sigma tE_c}-E\right)dEd\mu_d \end{aligned} \quad (4.19)$$

The form of this distribution function is such that the electrons are effectively beamed forwards into the downstream region. This produces an anisotropic distribution in the downstream fluid which can be integrated to yield a series of spectra, an example of which is shown by Fig. 4.8. This was obtained for a hydrodynamic strong shock with $\beta_1 = 0.96$, $\beta_2 = 0.347$, corresponding to a fully relativistic equation of state with adiabatic index $\Gamma = 4/3$. These are the appropriate speeds for a shock where the downstream pressure is provided by electrons and ions in local thermodynamic equilibrium (see chapter 3 for details). The viewing angle is perpendicular to the shock in the emission frame. Inspection reveals the spectra are quite dissimilar to those previously obtained. The polarization has a lower level than before, around 30%. As time passes the spectrum evolves, although there is no evidence for a break to the spectral index. The low frequency polarization remains low but at high frequencies the polarization increases dramatically to a maximum value of $> 80\%$. This feature moves to lower frequencies as time progresses. The position angle of the radiation lies along the shock face indicating that in this case the dominant emission originates from electrons moving along field lines parallel to the shock normal. An explanation for this behaviour can be obtained by reference to the form of the electron distribution function. Most of the electrons at any given energy lie within a narrow cone concentrated in the forward direction i.e. along the shock normal, and at energies where the initial cutoff is important the actual value of the cutoff is higher for those electrons lying along the shock normal. It is apparent that although the greater number of electrons lie in

the weaker magnetic field along the shock normal the electrons tied to field elements perpendicular to the shock normal which radiate in the stronger magnetic field also contribute a significant amount of flux. The result is a low polarization. At later times, when the electrons along the stronger field lines have decayed, the radiation comes predominantly from the electrons in the weak magnetic field and the overall level of polarization rises. The position angle remains aligned with the shock face.

Comparisons with the observations are favourable in this case as the polarization increases with frequency and clearly this behaviour could be utilized in the form of a diagnostic of the shock velocity. However, it is not the case that the model gives complete agreement with the observations. The primary objection is based upon the position angles which are observed. It has been mentioned before that several authors have found that position angles tend to indicate dominant magnetic fields perpendicular to the VLBI structure i.e. along the shock face. This contrasts with that found above. Also, as will be apparent from the next subsection, injection would cause the level of polarization to decrease. The conclusion must be that although this cannot be firmly rejected it does run into severe difficulties with certain aspects of the observations.

4.3.4 Injection of electrons

Now consider the case where fresh electrons are injected at a constant rate into the emission region downstream of the shock front. Assume that these electrons have an isotropic power-law distribution between the two cutoff energies and an energy spectral index γ. This is clearly more relevant than the previous case if the aim is to provide a description of variability. The injection allows the flux to increase steadily at low frequencies although at high frequencies the injection will be balanced by the losses. The form of the distribution can be found by integrating equation 4.16 using the variable t as a dummy variable t' between 0 & t. It yields

$$\begin{aligned} N(E,\varepsilon,t)dE &= \frac{qE^{-(\gamma+1)}}{\sigma(\gamma-1)}\left\{\left[1-(1-\sigma tE)^{\gamma-1}\right]\Theta\left(\frac{E_c}{1+\sigma tE_c}-E\right)\right. \\ &+ \left.\left[1-\left(\frac{E}{E_c}\right)^{\gamma-1}\right]\Theta\left(E-\frac{E_c}{1+\sigma tE_c}\right)\Theta(E_c-E)\right\}dE \end{aligned} \tag{4.20}$$

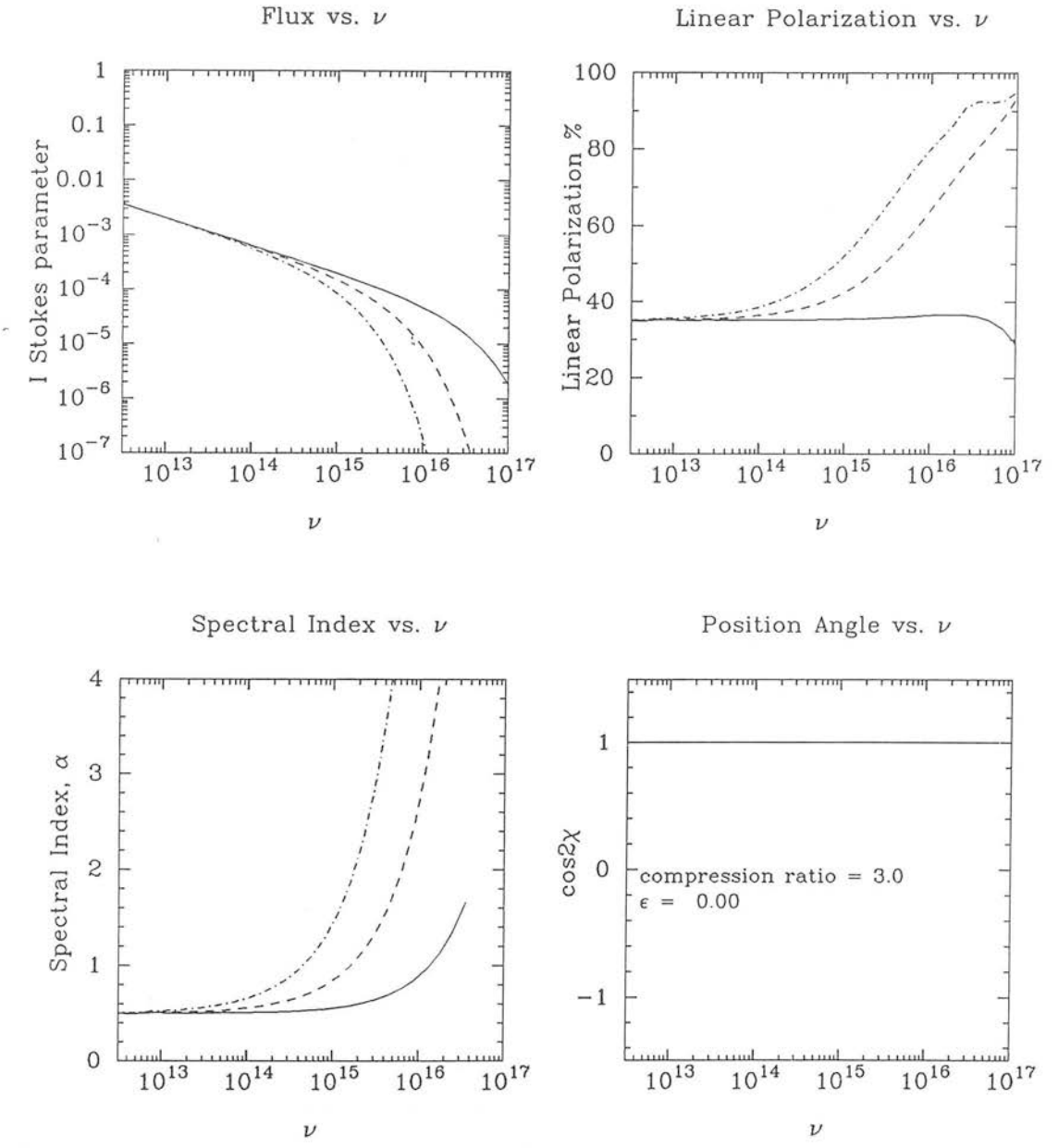

Figure 4.8: This shows the expected emission from a initially power-law distribution of electrons. These are then advected into the downstream region without experiencing any scattering. Fig 4.8a and b show the flux and polarization as a function of frequency. Note the rise in polarization. Fig 4.8c shows the spectral index, and Fig 4.8d shows the cosine of the position angle, which remains fixed and along the shock face.

Care must be taken when evaluating this integral as the effect of the finite energy cutoff must be included, as mentioned in Section 4.3.1. At low energies the initial cutoff will not have evolved into the energy range and equation 4.16 can be integrated directly. At higher energies where the cutoff has had time to evolve before the time $t' = t$ one must truncate the integration after a time, t_c;

$$t_c = \frac{1}{\sigma}\left(\frac{1}{E} - \frac{1}{E_c}\right) \tag{4.21}$$

hence one obtains equation 4.20. As a check, the high and low energy terms match at the evolved cutoff energy. As noted by Kardaschev (1962) at low energies the number increases linearly with time. At high energies it reduces to a time independent form, with injection balanced by losses to lower energies.

The results of a sample integration using this electron distribution are presented in Fig. 4.9 where $\gamma = 2$. The three curves again correspond to three equally spaced times. The low frequency flux increases linearly with time, then breaks and the spectral index increases by 0.5 until at the highest frequencies it is independent of time. The low frequency polarization is the same as in the decaying case, as one would expect. At high frequencies the polarization drops, but not to zero as before; this is due to the fact that fresh electrons are always being injected onto field lines along the shock face which dominate the emission. Hence the polarization level stays relatively high while the position angle remains fixed.

4.3.5 Switching off the injection

A final case shall now be considered, that is, the form of the spectrum if the initial burst of injected electrons is not instantaneous, but takes place on a longer timescale, comparable to the synchrotron loss timescale. Alternatively, this may be considered to be what happens after the injection is terminated after a prolonged burst. The behaviour of the source is then identical to that obtained in the previous subsection during the constant injection period, taking into account the energy losses. If the injection is then abruptly terminated at a time t_0, one can then use exactly the same

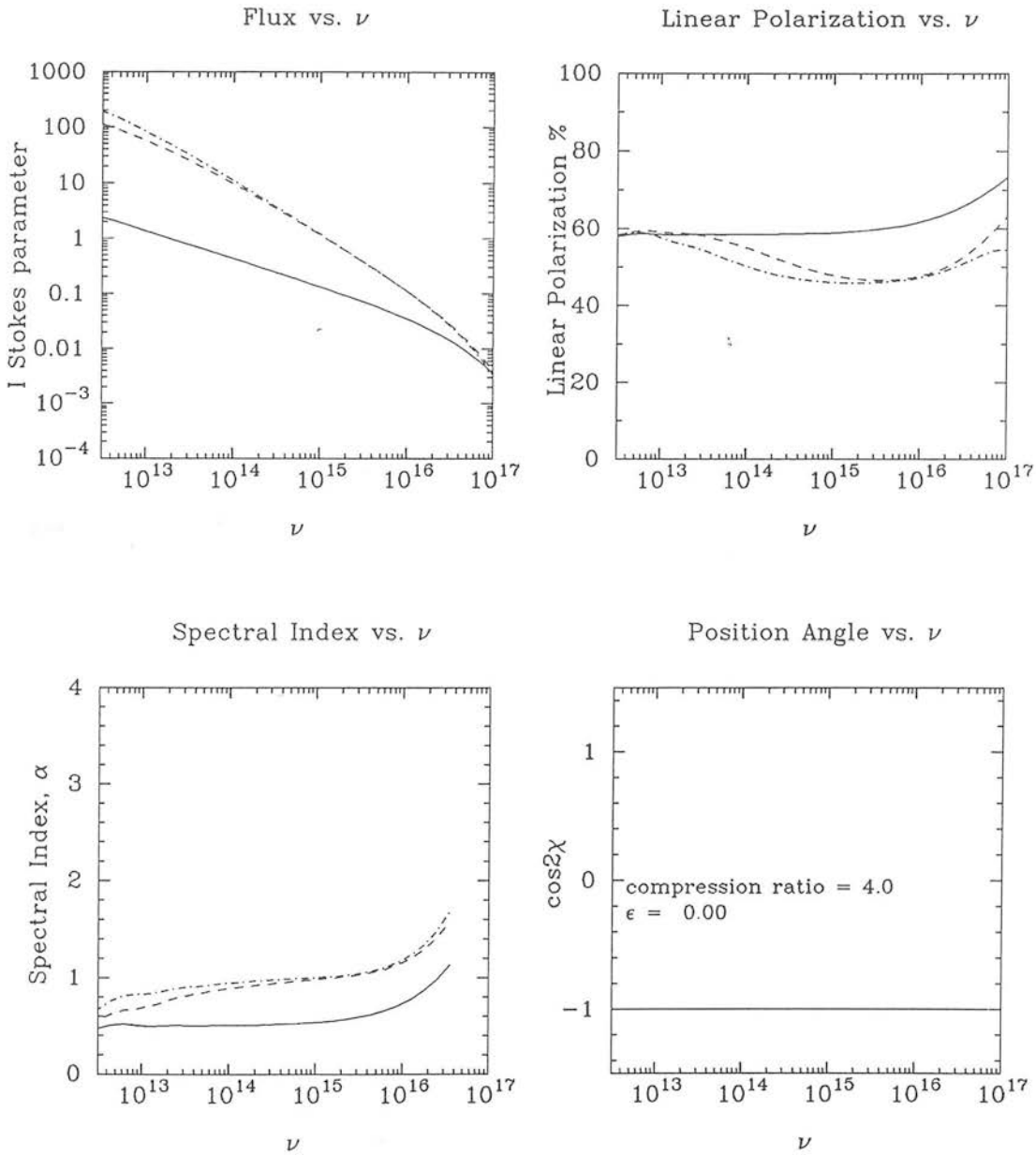

Figure 4.9: This shows the expected emission from a initially power-law distribution with continuous injection of electrons. Fig 4.9a and b show the flux and polarization as a function of frequency. Note the drop in polarization as the spectrum breaks. Fig 4.9c shows the spectral index, derived as in equation 4.5. Fig 4.9d shows the cosine of the position angle, which remains fixed.

procedure as used for the decaying source to obtain the form of the distribution at a later time t. Setting $\Delta t = t - t_0$:

$$\begin{aligned} N(E,\varepsilon,t)dE &= \tfrac{qE^{-\gamma-1}}{\sigma(\gamma-1)}(1-\sigma E\Delta t)^{\gamma-1} \\ &\times \left\{ \left[1 - \left(1 - \tfrac{\sigma t_0 E}{1-\sigma\Delta t E} \right)^{\gamma-1} \right] \Theta\left(\tfrac{E_c}{1+\sigma t E_c} - E \right) \right. \\ &+ \left. \left[1 - \left(\tfrac{E}{E_c(1-\sigma\Delta t E)} \right)^{\gamma-1} \right] \Theta\left(E - \tfrac{E_c}{1+\sigma t E_c} \right) \Theta\left(\tfrac{E_c}{1+\sigma\Delta t E_c} - E \right) \right\} dE \end{aligned} \tag{4.22}$$

A sample spectrum is shown in Fig. 4.10. The initial (solid) line is set to the time t_0, after which the source decays as normal.

4.3.6 Discussion

The results showing the appearance of a simple synchrotron source situated behind a strong hydrodynamic shock have been presented. These correspond to the simplest extrapolation of the model of Hughes et al. (1985) to optical wavelengths. In all cases the agreement between the model and the observational data has been poor. At frequencies around the break the polarization starts to decrease with frequency; even if one is always observing well aged sources to allow increasing polarizations, the polarization position angles then tend to align perpendicular to the shock normal, contrary to observations. The only case where the polarization increases with frequency is if there is a relativistic shock so that the distribution is initially anisotropic, although position angles again argue against this being the case.

4.4 Scattering limit

4.4.1 Introduction

It is apparent that restricting the motion of an electron to a single pitch angle produces unsatisfactory results, there is therefore a need to calculate the results in the case where the electrons are allowed to change pitch angle. It is envisaged that this is effected by the scattering by the inhomogeneity of the magnetic field.

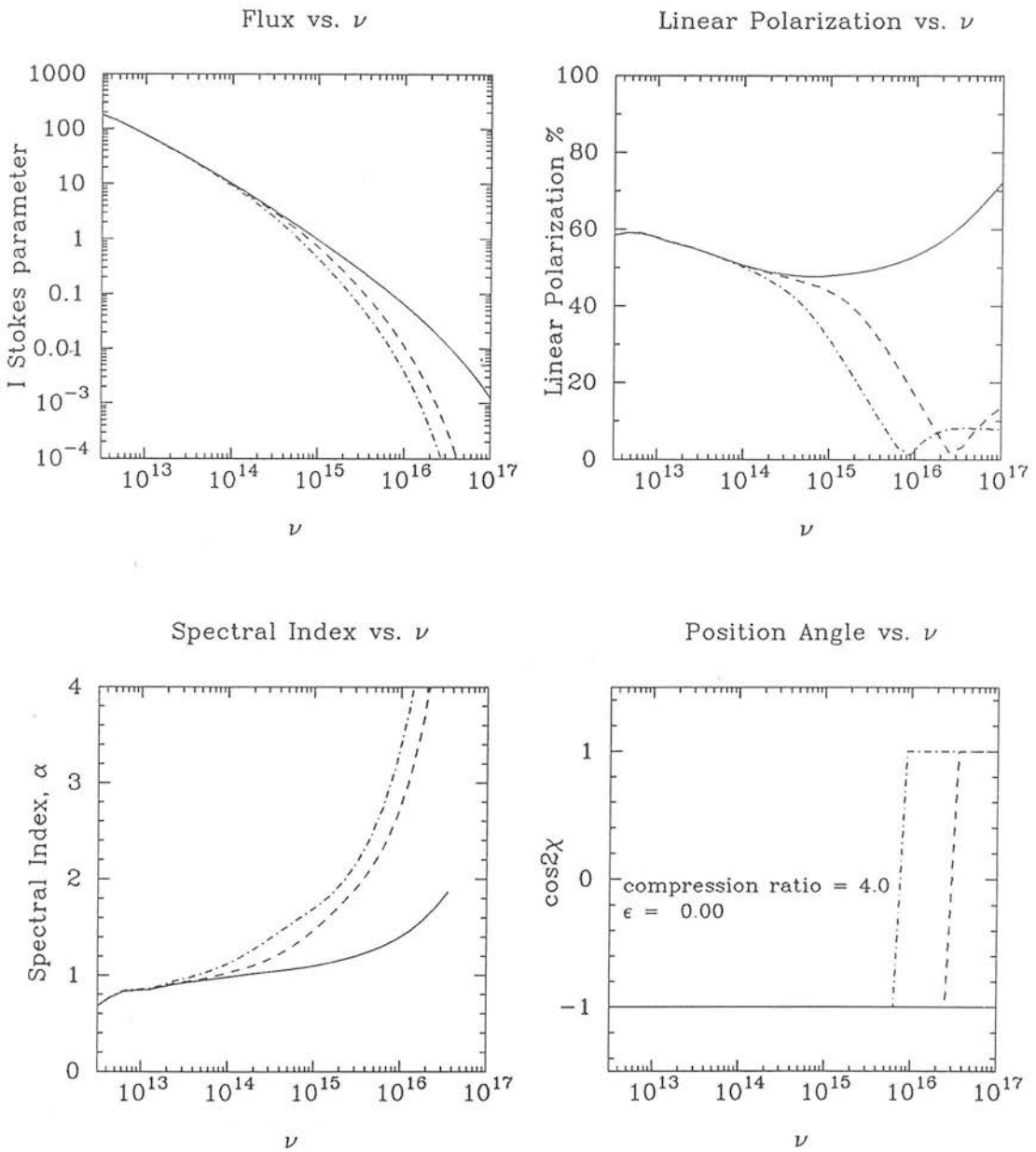

Figure 4.10: This shows the expected evolution of the source when the injection is terminated after the final plot in the previous section. Fig 4.10a and b show the flux and polarization as a function of frequency. Note the drop in polarization as the spectrum breaks. Fig 4.10c shows the spectral index, derived as in equation 4.5. Fig 4.10d shows the cosine of the position angle, which flips. Overall the emission reverts to that seen for a decaying source.

One advantageous by-product of allowing the electrons to scatter is that the Fermi mechanism can operate. In the previous section there was no way that an electron, with constant pitch angle, having once crossed the shock front could ever recross it. If, on the other hand the electrons can change pitch angle in the vicinity of a shock then Fermi acceleration may take place. This can in itself produce the initial power law distribution of energies, thus effectively removing the difficulty of the origin of the non-thermal spectrum from the problem.

If the electrons are being accelerated at a shock then the assumption of a simple distribution with a sharp cutoff may be unrealistic. Taking synchrotron losses into account during the acceleration process in the steady state limit Heavens & Meisenheimer (1987) found that the spectrum around a cutoff is more curved as the acceleration to the highest energies is limited by the losses although the exact form depends upon the diffusion operator. Meisenheimer et al. (1989) applied this to differentiate between models of the conditions in radio hotspots and found this shock acceleration model gave good agreement with the observations. However, this possible feature is ignored. In order to obtain an isotropic electron distribution decaying in energy it is envisaged that the synchrotron loss time is much greater than the acceleration time. Thus what limits the distribution is not the synchrotron losses but rather the amount of time the electrons are accelerated for before they are advected away from the shock and uniformly lose energy. Furthermore, there is no clear alternative to employing sharp cutoffs. The work of Heavens & Meisenheimer (1987) was under the assumption of a uniform magnetic field, lying along the shock normal, behind a non-relativistic shock. There is not yet a model which predicts distributions around the cutoff at shocks with randomly varying magnetic fields, although Achterberg (1988) has published simulations of the effects of a perturbed magnetic field upon the acceleration process. As there is no viable alternative, it is probably wise to use the simplest, an initially isotropic power law form with sharp cutoffs. The exact form of the cutoff is not reflected sensitively in the polarization properties, discussed below.

The possibility of a relativistic shock velocity being responsible for an initial anisotropy in the distribution which affects the form of the spectrum, as discussed

in Section 4.3.3 is not relevant here. This is because the electrons are continually re-isotropized in the downstream region. The speed of the shock is of less importance in the present case.

The next step will be to evaluate the form of the distribution with losses and a variable pitch angle. Simply assuming that the coherence length of the magnetic field divided by c is very much less than the loss timescale then each electron loses energy to all the field elements equally. In this case the equation for the loss of energy can be written:

$$\frac{dE}{dt} = -\sigma' E^2 \tag{4.23}$$

where σ' is the integral of σ – the constant for a single element of the field – over the entire distribution. One obtains $\sigma' = (2/3)(\pi r^2 + 2)bB^2$. Having obtained this the appropriate electron distributions can be found by substituting σ' for σ in equations 4.16, 4.20 and 4.22. It is the results from these distributions that will now be considered in turn.

4.4.2 Decaying source

Again, although this is not the most relevant case because of the neglect of injection of any fresh electrons, it does serve to illustrate the processes which occur when the electrons are allowed to scatter. The results of a sample integration are shown in Fig. 4.11 and are relatively straightforward to explain. The chosen values are $\gamma = 2$, $r = 4$, corresponding to a non-relativistic strong shock and $\epsilon = 0$, looking along the shock face. The three curves correspond to three equally spaced times, commencing at time $t = 0$. The flux decays with time from the initial power-law, however no break to the spectral index appears. As the electron distribution is isotropic and has a cutoff at the same energy, independent of ε, there is no break. The position angle remains constant as the emission is always dominated by the component perpendicular to the shock normal, as the distribution remains isotropic.

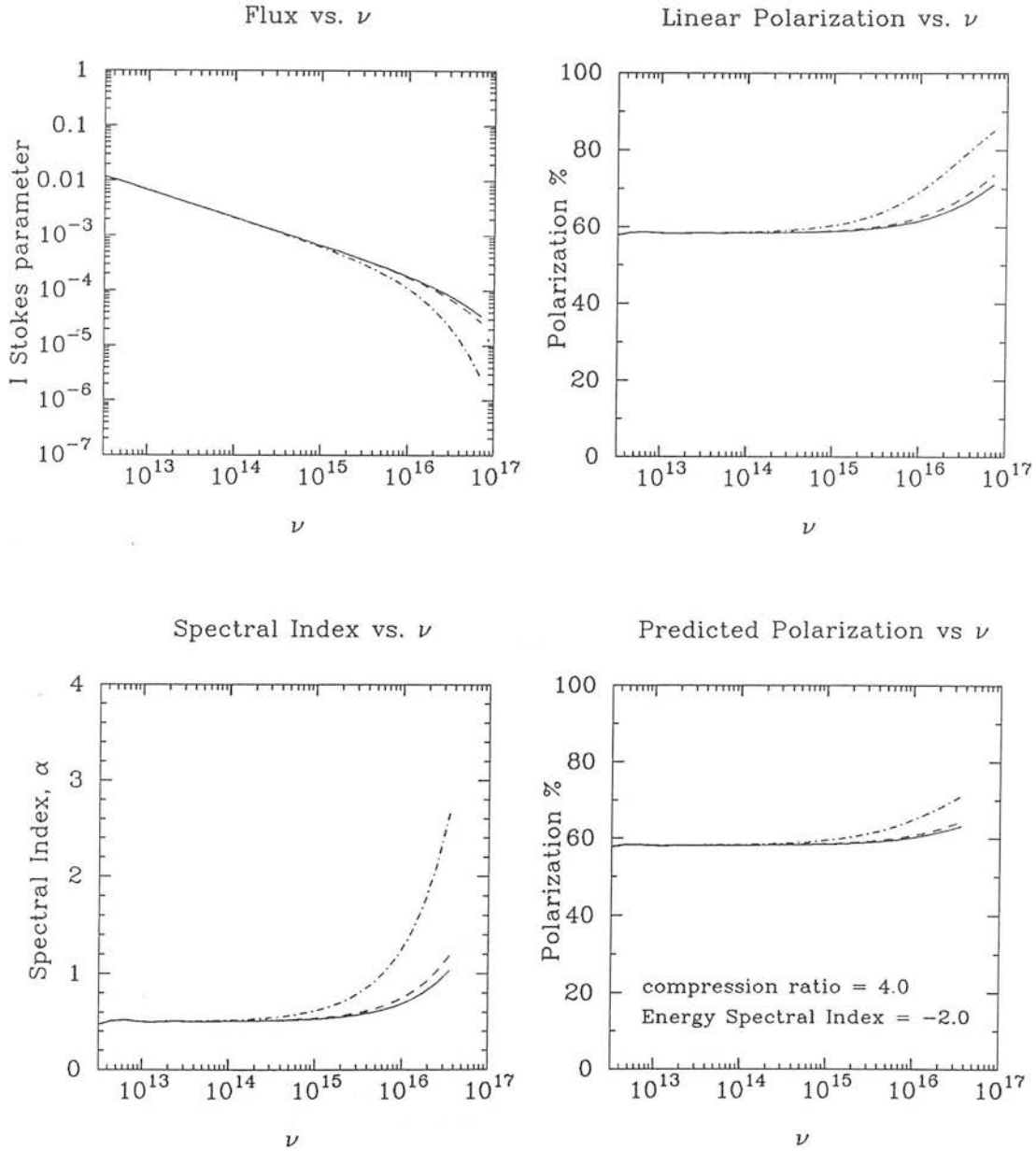

Figure 4.11: This shows the expected emission from a initially power-law distribution with continual scattering of electrons. Fig 4.11a and b show the flux and polarization as a function of frequency. Note the gradual rise in polarization as the spectrum breaks. Fig 4.11c shows the spectral index, derived as in equation 4.5. Fig 4.11d shows the expected polarization, in agreement with the model value.

Finally, note that the electron distribution has now been defined to be isotropic and hence independent of position. The is precisely the condition required for the polarization to reduce to the form of equation 4.1 (Björnsson & Blumenthal 1982). Accordingly, in addition to plotting the spectral index in Fig 4.11, the polarization as predicted by this parameterization has been plotted. The spectral index, derived from the differentiated $\log_{10} F_\nu - \log_{10} \nu$ graph was calculated and hence the polarization was found from equation 4.1, deducing a value of Π obtained by normalizing the expected value to the low-frequency model value. Qualitatively there is good agreement, confirming the model polarizations by comparison with an analytic result.

4.4.3 Injection

This case is of most relevance to the early stages of flares. The distribution of electrons is given by equation 4.20 with σ' again substituted for σ. Model plots for the flux, polarization, spectral index and expected polarization are shown in Fig 4.12. The position angle remains aligned with the shock normal throughout and is not plotted. At low frequencies the flux increases linearly with time, there is a break of 0.5 in $\alpha(\nu)$ and at the highest frequencies the flux becomes time independent. The polarization is constant at both low and high frequencies where the spectral index is unchanging while around the break frequency there is a gradual increase in polarization with frequency. It might be noted that at a given frequency as the flare progresses the flux and polarization both increase while the degree of frequency dependence of polarization at a given frequency increases and then decreases as the break frequency evolves.

4.4.4 Switching off the injection

This case is important once a period of injection has ceased. The distribution is given by equation 4.22 with σ' substituted for σ. The plots of flux, polarization, spectral index and predicted polarization are presented in Fig 4.13. Once more a cutoff develops at high frequencies, moving to lower frequencies with time.

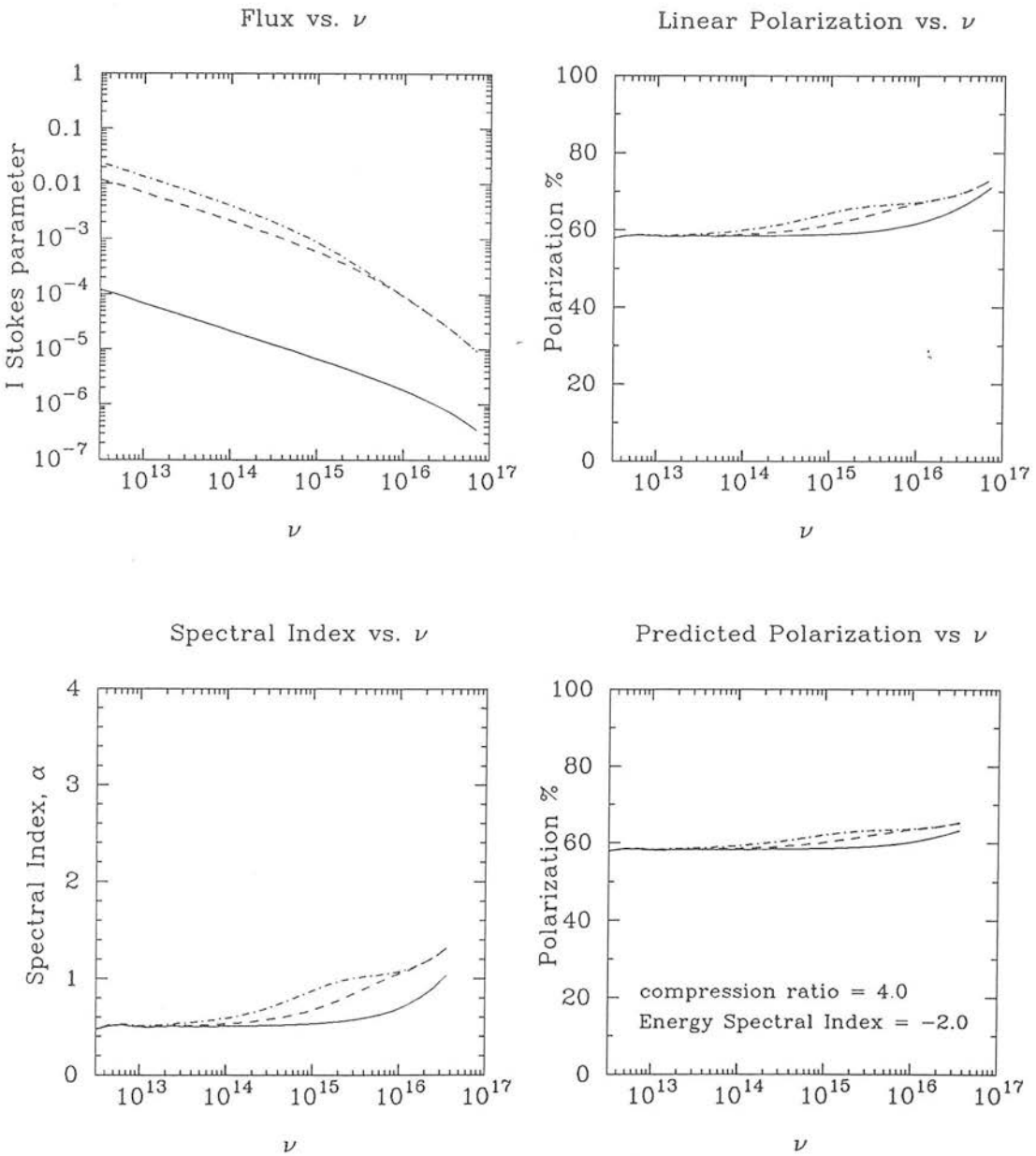

Figure 4.12: This shows the expected emission from a initially power-law distribution with continuous injection of electrons. Fig 4.12a and b show the flux and polarization as a function of frequency. Note the gradual rise in polarization as the spectrum breaks. Fig 4.12c shows the spectral index, derived as in equation 4.5. Fig 4.12d shows the expected polarization, in agreement with the model value.

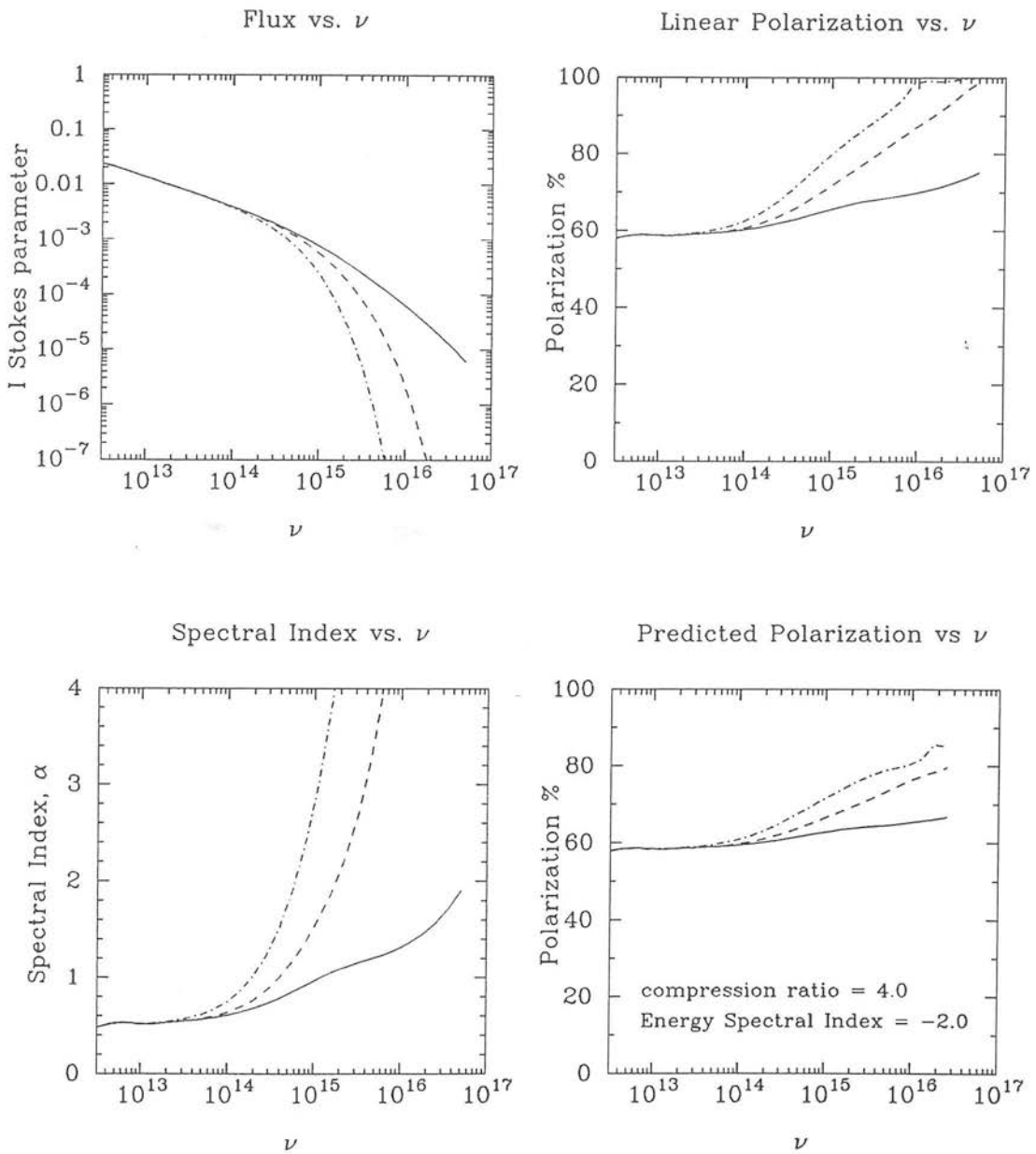

Figure 4.13: This shows the expected emission from the previous source after the injection of electrons has been terminated. Fig 4.13a and b show the flux and polarization as a function of frequency. Note the gradual rise in polarization as the spectrum breaks. Fig 4.13c shows the spectral index, derived as in equation 4.5. Fig 4.13d shows the expected polarization, in agreement with the model value.

4.4.5 Discussion

The spectra of synchrotron sources in three cases of interest to flaring BL–Lac objects have been calculated in the limit where the electrons are scattered by irregularities in the magnetic field structure, the assumption being that the pitch angle of an electron changes on a much smaller timescale than it takes the electron to lose energy via the synchrotron mechanism and that an average energy loss rate can be defined. This maintains isotropy of the electron distribution in the fluid frame, and hence the parameterization of Björnsson & Blumenthal (1982) is valid. Plots of the polarization predicted by this parameterization were also presented, which are in good agreement with the calculated values. These plots are closer to that which is actually observed at single epochs, the polarization generally increases with frequency. As the Björnsson & Blumenthal (1982) parameterization is known to be successful in a large number of cases at optical frequencies the conclusion to be drawn is that the shock model can reproduce the high frequency observations when scattering is included. If the shock model is correct and one has electrons scattering in the vicinity of a shock front then Fermi acceleration of electrons will take place, producing a non-thermal distribution of energies. Thus this result provides circumstantial evidence that the Fermi mechanism is operating in BL–Lacs. The Fermi mechanism also makes specific predictions of the actual value of the spectral index although spectral indices have not been found for disordered magnetic fields. This problem is the subject of the next Chapter.

The inverse Compton effect may well be important in governing the form of the distribution. In the model of Marscher & Gear (1985) it was this mechanism which was responsible for all the early evolution of the source. Inverse Compton losses arise when a synchrotron photon collides with an electron; clearly the stronger the field and the more compact the source, the stronger this effect will be. A simple treatment of the effect (e.g. Rybicki & Lightman 1979) shows that if the radiation field is isotropic and unpolarized then the loss mechanism will be independent of the direction of the electron velocity. Therefore, in their simplest form inverse Compton losses produce the same effects as synchrotron losses with scattering. Note that in the present case the source is assumed to be stationary on the timescales over which the calculations are

made, expansion of the source changes the relative strengths of the two effects and is discussed in Appendix A.

It has been shown that at a qualitative level the shock model can reproduce certain features of the high frequency emission when scattering is included, most notably the high levels of polarization and the preferred position angles. However, it is not successful when the details of the data are examined which suggests that, as it stands, this model is inapplicable to the optical data. Primarily, this is because the variability between individual nights does not follow any simple patterns (see Chapter 2), although this discrepancy between the model and the data can perhaps be put down to the rather artificial assumptions of the steady injection of electrons with sharp cutoffs.

The increase in spectral index caused by a break due to losses is $\Delta\alpha \sim 0.5$ if the electrons are continually injected. If the electrons are allowed to scatter then the polarization is well described by equation 4.1. Denoting the polarizations above and below the break frequency by $p_{H[L]}$ and the low frequency spectral index by α then the ratio of the high frequency polarization to that at low frequencies is given by:

$$\frac{p_H}{p_L} = \frac{(9+6\alpha)(5+3\alpha)}{3(13+6\alpha)(1+\alpha)} \tag{4.24}$$

which is plotted in Fig 4.14. This ratio is quite small for reasonable values of the spectral index, for $\alpha = 0.5$ it is 13/12. This may be contrasted with those ratios actually observed over the range of the U to H wavebands which are shown in Fig 2.4, some of which are as high as 3. Therefore it is not possible that the frequency dependent polarization and spectral curvature observed at optical wavelengths originates with a spectral break. Of course it is quite possible that the observational features arise because of the high frequency cutoff instead. This work on breaks is more relevant to longer wavelength work than the near infrared and optical data.

There are also considerable problems with position angles. In the calculations the only case where frequency dependent position angles were found was rejected on the basis of the unlikely polarization behaviour accompanying it. In the most likely case, where scattering was included, the position angle was both constant and frequency

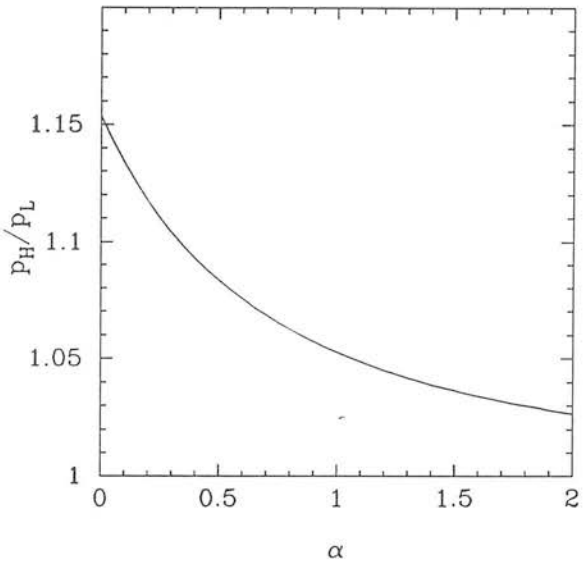

Figure 4.14: This shows the ratio of the high to low frequency polarizations at a synchrotron break when injection is included.

independent. Position angle variations are often explained in terms of acceleration of the emission region (e.g. Blandford & Königl 1979; Björnsson 1982). This does not alleviate the problem of frequency dependent position angles, which were actually detected in around 25% of the observations presented in Chapter 2. There are two main opinions on the origin of the phenomenon. Firstly Björnsson (1985) attributed it to anisotropic pitch angle distributions, the work of Section 4.3 is of course a particular example of the anisotropies which can develop in a more realistic model. Secondly, it may be caused by multiple components i.e. there are two or more synchrotron sources with different spectral indices and position angles, as the frequency changes so the relative strengths change and the position angle rotates (e.g. Holmes et al. 1984b). Furthermore, models with a larger number of components have been suggested by Moore et al. (1982,1987) and Brindle et al. (1986) to account for the apparently stochastic variations in position angle. The difficulty with interpreting all observations in this light is that if one wishes to explain large flares as simply the superposition of a large number of components the polarization becomes vanishingly small, which is not the case. The next section will examine whether a modified version of this simple multicomponent model can explain

the more detailed features of the optical observations and discuss how it could be placed within the framework of the shock model so far developed.

4.5 A multi-component model of blazar emission

4.5.1 Introduction

The week of intensive monitoring of BL–Lac itself which was carried out by Moore et al. (1982) showed that the variations in optical polarized flux appear to describe a random walk in (Q,U) space. This they interpreted as being due to randomly orientated sub-components being switched on at a rate of approximately 10 per day, each decaying over a period of about five days. In a following programme, again monitoring the single object, BL–Lac in the optical, Brindle et al. (1986) obtained different results when the flux was at a much lower level. In their case they found behaviour which was consistent with a random walk in (Q,U) space superimposed upon a single underlying, time-invariant polarized component. This, they speculated, was possibly due to a fixed jet component. In addition to BL–Lac, a model involving two or more components has been able to account for many other examples of extreme behaviour, see for example Holmes et al. (1984b) and Meisenheimer (1991). It is not possible to compare the polarization behaviour of each object in the large sample in Chapter 2 with a random walk as many observations were not repeated and of those that were, many were at irregular intervals so that proper time coverage is not available. Whilst it would be impractical to attempt fitting all the individual simultaneous spectra with a multi-component model involving an unnecessarily large number of free parameters it is interesting to examine a wider question; by simulating a series of optical spectra one can compare the general properties of the sample with those of the data obtained during the observing programme. The approach will be to generate a series a randomly oriented synchrotron emitters of differing strengths and then to calculate the combined Stokes parameters to yield a number of simulated observations which will then be compared with observations.

4.5.2 The simulations

The model that will be considered is similar to that of Moore et al. It will be more realistic to include a high energy cutoff to each component; this is because any acceleration mechanism can only accelerate electrons to a finite energy, even in the absence of radiation losses. Also, the effect of radiation losses have been included in the analysis. The problem, mentioned previously of the inverse correlation between the number of components and the overall polarization has been circumvented by employing the shock front to compress the field, altering it's orientation and hence providing a preferred field alignment. The result is to allow a large number of components without reducing the polarization. As in Moore et al. each cell has been assumed to have a perfectly aligned magnetic field; although this may be a rather artificial assumption it will not greatly affect the results and does considerably ease the problem of computation. Further, it is assumed that the entire source of the emission is unresolved and that the radiation that is observed is purely the summation of the radiation from these independent regions.

In the simulations, the magnetic fields for each component were chosen to be randomly oriented in space upstream and with a Gaussian distribution of strengths. Although previously the upstream field was considered to have a constant strength, it might be more general to allow it to vary in this manner between components. The number density of electrons was then fixed at a random value taken from a Gaussian distribution as was the upper energy cutoff, again to make the problem as general as possible. The electrons were allowed to radiate and lose energy, giving distributions for the ith component of:

$$N(E,\varepsilon,t) = k_i E^{-\gamma}(1-\sigma_i'\Delta t_i E)^{\gamma-2}\Theta\left(\frac{E_{ci}}{1+\sigma_i'\Delta t_i E_{ci}} - E\right) \tag{4.25}$$

e.g. Kardaschev (1962), where k_i is a constant, $\sigma' = b^2(4\pi/9)(5r^2+1)$, ε being the angle between the line of sight and the magnetic field. The step function is included to take account of the fact that electrons at the cutoff energy will decay in energy with time. The subscript i denotes the ith synchrotron component. It is further assumed that the electrons are allowed to scatter, thus maintaining the original isotropy of the

distribution. The expressions for the Stokes parameters are then given by:

$$\begin{aligned} I(\varepsilon,t,\nu) &= \textstyle\sum_i LB\sin\varepsilon\int_E F(x)N(E,\varepsilon,t)dE \\ Q(\varepsilon,t,\nu) &= \textstyle\sum_i LB\sin\varepsilon\int_E G(x)\cos 2\chi N(E,\varepsilon,t)dE \\ U(\varepsilon,t,\nu) &= \textstyle\sum_i LB\sin\varepsilon\int_E G(x)\sin 2\chi N(E,\varepsilon,t)dE \\ V(\varepsilon,t,\nu) &= 0 \end{aligned} \tag{4.26}$$

e.g. Pacholczyk (1970). Thus one can obtain the evolving spectrum of a single cell. A mean magnetic field strength of B$\sim 10^{-4}$ Gauss was chosen, so that one obtains an approximate synchrotron lifetime of $\tau_{1/2} \sim 5$ days at a frequency of $\nu \sim 10^{14}$Hz. Having obtained this the angle between the field and the line of sight could be found and one can evaluate the emission from each cell. The next stage is to construct the overall signature from a series of such cells. The rate of injection was fixed to give a mean of 10 new subcomponents each day. Having obtained the multifrequency spectrum it is straightforward to add a nominal 1σ error bar of 5% to the flux, the purpose of which was purely to cast the output from the simulations in a similar form to the observational data. A sample spectrum is shown to illustrate the simulated spectra in Fig. 4.15.

Having obtained a series of 50 such spectra, comparable to the number obtained during the observing, it was then possible to test for correlations between various observational features e.g. spectral index, spectral curvature, polarization etc. for comparison with the actual data.

4.5.3 Discussion

After running the simulations it was found that many of the results summarized in Chapter 2 could be reproduced by the simulations with a few notable exceptions. In the first instance it was found that the simulations produced a tight correlation between the degree of spectral curvature and the spectral index. It is straightforward to explain this; all the components in the simulations had identical low frequency spectral indices ($\gamma = 2$ was chosen) and as the basic form of the flux was the same i.e. increasing curvature with spectral index, a correlation emerged. Relaxing this constraint on the model by allowing

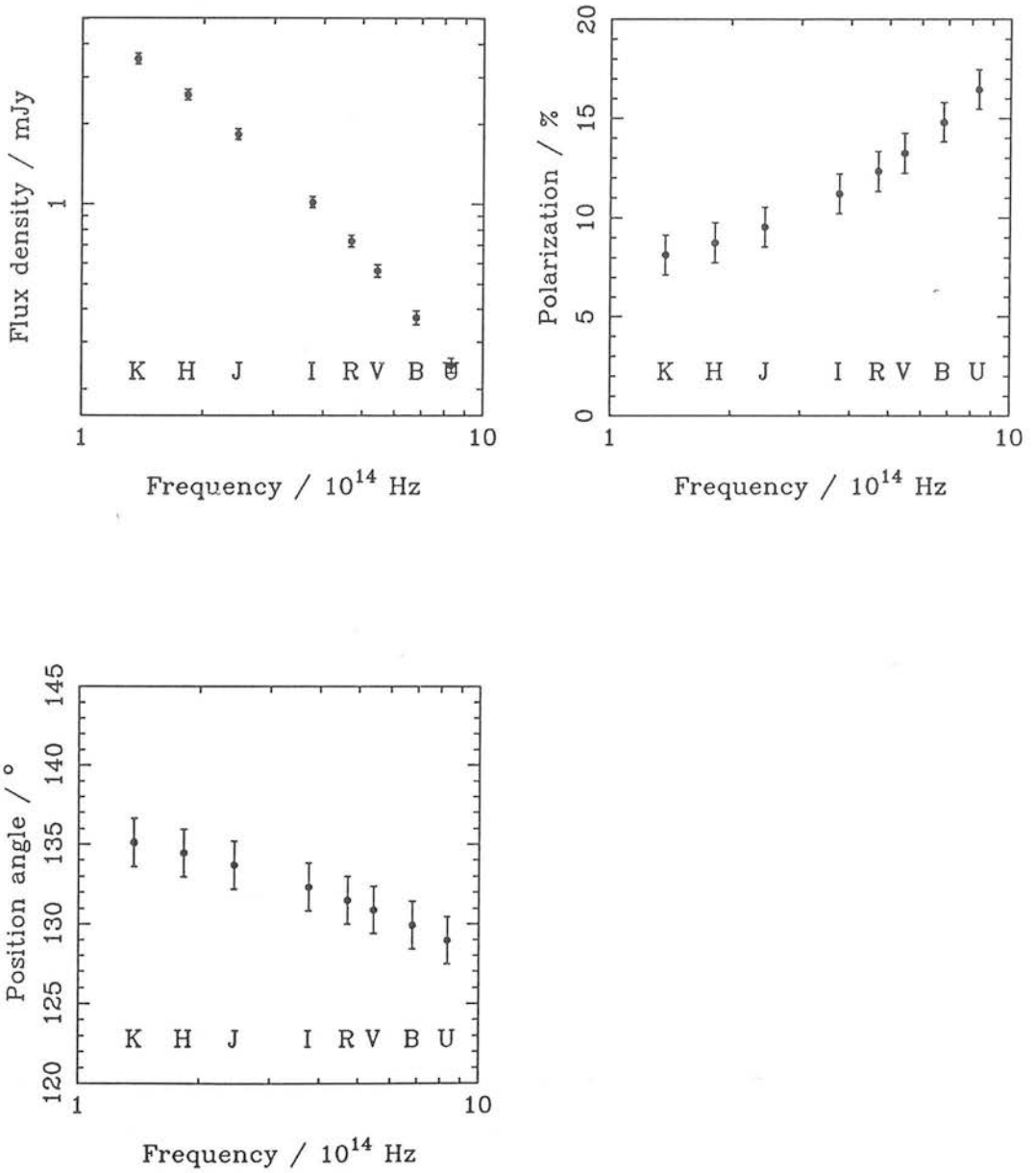

Figure 4.15: This shows an example of a simulated blazar spectrum. The nominal error bars are set at 5% of the flux.

some degree of spectral index variation removed the effect, which is more in line with the observations. A second correlation found was between the frequency dependence of polarization (FDP) and the polarization in the sense that as the polarization increased so did the degree of FDP. Again it is straightforward to attribute this behaviour to a feature of the simulations, in this case by increasing the number of components the expected polarization will decrease. Thus by reducing the number of subcomponents, each of which displays FDP, one would expect the polarization to increase and as fewer components dominate the degree of FDP to increase. Previous authors (Holmes et al. 1984a; Brindle et al. 1986) found such a correlation, but it was not evident within the new data, for which a more careful analysis was employed. Nevertheless it is possible to circumvent this problem in a number of ways. For example, by using a less well ordered variable magnetic field in each of the cells it would be possible to produce lower polarizations with a smaller number of sub-components, yet these components could still effect appreciable FDP. It would not be feasible to include arbritrary magnetic field distributions without a gross increase in the amount of computing time as it would then require integrations over the chosen field geometry.

With the exception of these two points, both of which can be overcome by minor, more realistic modifications, it is apparent that the predictions of a simulated sample can reproduce many of the global properties of the observations. While this cannot be regarded as conclusive support of a model involving many components, the general result does indicate that as a class, blazars often behave in a manner similar to what one would expect from this model.

There are problems when this model is applied to all observational results, although these problems are fewer than in Section 4.4. Hagen-Torn et al. (1979) undertook a monitoring program and obtained data at all levels of brightness. In their published conclusions for the objects BL–Lac and OJ287 they showed that the degree of variability generally increased with source brightness; this manifested itself by a preferred position angle when the objects were in a faint state. This is similar to the result obtained by Brindle et al. (1986), who attributed the preferred position angle to a jet component. Unless this is the case, this is contrary to what would be expected in a multicomponent

model where the greatest changes in the emission are expected at the lowest flux levels where the relative contribution of each component is greater.

It could be argued that the inclusion of a shock front to compress the magnetic field is unnecessary. By removing the shock (setting $r = 1$) all the correlations mentioned can still be produced. In a sense then the extra two parameters introduced because of the shock (r, ϵ) are superfluous. The shock however was included to allow preferred position angles and to place the multicomponent model in the context of the shock model which is successful at longer wavelengths.

A further point is that the model consists of a combination of pure synchrotron sources, whereas in reality the blazar class contains objects where contamination by unpolarized light cannot be neglected. It is possible that these objects could have affected the correlations to such a marked extent as to mask other properties only apparent in the BL–Lacs. In Chapter 2 it was noted that contamination could be indicated by $dp/d\nu < 0$ or $d\alpha/d\nu < 0$ and a list of objects where this was the case was compiled. Removing these objects had no effect upon the conclusions drawn from the correlation analysis, so one is lead to accept the fact that the behaviour is indeed characteristic of BL–Lacs. To summarize, the observations expected from a series of random synchrotron emitters were simulated and found to be broadly in agreement with that which is actually observed in blazars.

4.6 Conclusions

This Chapter has investigated several aspects of synchrotron emission arising from electrons in the magnetic field downstream of a shock front. There are good reasons to suppose that this is a valid starting point for any model of BL–Lacs. The aim was to investigate whether such a model which explains well the radio properties can be applied directly to higher frequencies where losses complicate the source structure. Overall an attempt has been made to bring together the understanding of the emission from BL–Lacs in two wavebands. The work was necessarily rather speculative because of the

current lack of polarization data at intervening wavelengths. Several new points have been made, notably that by including polarization calculations the power of models is greatly increased. The conclusions that can be drawn strengthen the case that can be made for in-situ acceleration of electrons.

The approach that was adopted was to try to explain the features that occur most frequently in BL–Lacs, for example spectral curvature, the high levels of polarization and the fact that when frequency dependence of polarization is observed, the polarization increases towards the blue in the majority of cases. It was shown that extrapolating the shock model of Hughes et al. (1985) to energies where losses play a significant role produces polarizations which are unlike those seen. In fact, above the break frequency in a field where one might expect some polarization, the polarization decreases to low values because of anisotropies that develop in the distribution of electrons. If instead the distribution maintains isotropy then spectral curvature is accompanied by an increase in polarization. The results in this case are more in accordance with observations of BL–Lacs. If the electrons are being scattered by some mechanism in the vicinity of a shock over a timescale much less than the loss timescale then the first order Fermi mechanism will operate and the problem of the production of the non-thermal energy distribution is overcome. It is not likely that the optical properties are governed purely by a break because both the spectral curvature and the degree of frequency dependence of polarization observed are in excess of those allowed by a model break. Instead it is more likely that, in the optical, spectral curvature is the result of a cutoff to the electron distribution.

Having obtained broad agreement between the model and the most general observational features the problem of detailed observational features were considered. There have been many attempts made in the literature to explain particular observations and rather than trying to develop any new model, an attempt was made to place an existing model within the context of the shock model. It was shown that apart from a correlation between polarization and frequency dependence all the optical properties of BL–Lacs could be reproduced by simulating a large data set.

The prospects for future multifrequency optical observations, of the type described

in Chapter 2 should be mentioned. One could crudely describe the multicomponent model as weather in the sense that making ever more observations will not reveal any more of the physics, all one is observing is a number of random synchrotron emitters switching on and off at random. However, it is not certain that this picture is valid for more than two or three objects. The place for future optical observations can only be as part of a large collaboration involving simultaneous observations at longer wavelengths in order to determine how the wavebands are related.

An outstanding observational restriction is the present lack of polarization data for BL–Lacs between the near infrared K waveband and 14.5 GHz. The spectra obtained by Landau et al. (1986) are consistent with a break in this frequency range. Thus there are no data available in the frequency range which is of most interest. This however was one of the prime motivations for this work as an instrument which is capable of the observations is soon to become available. This is the UKT14 polarimeter on the James Clerk Maxwell Telescope in Hawaii. This instrument was built by Murray & Flett at Aberdeen University and in principle is extremely simple as it consists of a quarter waveplate which is rotated in front of the UKT14 detector at the focus of the telescope and which can operate at two frequencies ($800\mu m$ and $1100\mu m$). The instrument has undergone tests at the telescope in July 1990 and has detected levels of polarization in two of the brighter extragalactic radio sources (3C273 & 3C446). It should therefore soon be possible to detect the presence or absence of polarization in BL–Lacs which although generally fainter do have much higher levels of polarization.

Chapter 5

Fermi Acceleration In Disordered Magnetic Fields

SUMMARY: Previous chapters have shown the need for disordered magnetic fields and shocks in the emission regions of blazars. This chapter addresses the processes which occur as the electrons interact with the shock and tackles the problem of Fermi acceleration at relativistic shock fronts in disordered magnetic fields. A method for constructing a suitable magnetic field is given. The process is simulated by following particle trajectories exactly. The spectral indices of the resulting electron distributions are presented and discussed. It is shown that power-law distributions with synchrotron spectral indices $\alpha \simeq 0.5 \pm 0.1$ are produced. This provides a good description of the region close to shocks in blazars.

5.1 Introduction

The question of the origin of the non-thermal electron distribution which gives rise to the characteristic emission patterns of blazars and other radio sources is one of fundamental importance to obtaining a clear understanding of these objects. The Fermi mechanism which produces such spectra must be a strong candidate for several reasons. The fact that the spectral indices produced are in rough agreement with those observed in itself supports the case. Also, one expects the shocks which would be the sites of Fermi acceleration to arise naturally. Finally, as was shown in Chapter 4, shocks can explain the observed polarization behaviour only if the electrons are allowed to scatter in the vicinity of the shock and this in itself provides further evidence. Having stated all this, the first order mechanism in its simplest form is severely lacking in several

important respects.

The original theory was developed with the assumptions of a non-relativistic parallel shock. Later extensions to this work have examined the process when the more realistic conditions of relativistic fluid motion (Kirk & Schneider 1987a), oblique magnetic fields (Kirk & Heavens 1989; this work) or the back-reaction of the accelerated particles on the flow (Drury & Völk 1981) are added. The details of the predictions that these latter works make are in disagreement with the observations in that, for configurations where acceleration is possible, they produce spectral indices which are flatter than generally seen. In addition to this problem, it might be expected that in many cases the shock will be moving superluminally with respect to the magnetic field i.e. the point at which the magnetic field intersects the shock front moves faster than the speed of light. A superluminal shock front cannot repeatedly accelerate electrons unless the electrons diffuse across the field (Jokipii 1982); this is a more serious drawback for the Fermi mechanism.

A further drawback to the theory of the Fermi process is that almost all treatments deal with the diffusive limit where the perturbations to the magnetic field which act to scatter the particles are small i.e. $\delta B/B \ll 1$. At some level this is in conflict with the observations because the polarizations seen are lower than one might expect for uniform fields. Elementary synchrotron theory shows that one expects radiation which is approximately 70% polarized in a uniform magnetic field which compares with the maximum observed value of 46.9% (MEA90). The obvious conclusion, that there is some degree of field disordering, was investigated in the previous chapter. In particular it was shown that a fully disordered pre-shock magnetic field, with an isotropic distribution of directions, can reproduce polarizations of the correct magnitude and showing the observed behaviour. One motivation for the work in this chapter is to attempt to apply these constraints from observations to the theory of the Fermi mechanism to examine whether these more realistic source conditions remain conducive to acceleration.

In Chapter 4 it was assumed implicitly that the particle acceleration mechanism produced simple isotropic power-law distributions, there being no viable model of par-

ticle acceleration in such magnetic field distributions. This Chapter simulates the acceleration process in a different magnetic field structure to find the exact distribution functions. This is not a restriction on the previous work, as the distributions tend to become isotropic quite close to the shock front as the electrons are scattered and the aim was to find the effect of losses upon the polarization. Synchrotron losses will not be included in the present analysis, the aim will simply be to simulate the acceleration.

The layout of the remainder of this chapter is as follows: Section 5.2 describes the construction of the magnetic field in which the acceleration is to be simulated and the method by which the shock passes through the fluid. The equations of motion are described together with the tests which were used to check the computer code and the resulting particle trajectories. The results, represented by the final electron distributions are the subject of Section 5.3 and in Section 5.4 the conclusions are presented.

The work for this chapter is not quite complete owing to the large amount of computer time which was required in order to obtain meaningful conclusions. A great deal of effort was invested in constructing a realistic model which works correctly. It will be necessary therefore to include details of the computing techniques used and the methods used to check the program. The results which will be presented in Section 5.4 will be limited to a few specific restricted cases although there will of course be suggestions for more wide-ranging continuing work in future.

5.2 The Model

5.2.1 Assumptions

The problem to be considered, that of acceleration in a disordered magnetic field, will not be tackled analytically because it might be difficult. Furthermore, for shock speeds close to the speed of light the trajectory of a particle is critically dependent upon the exact field structure it moves through rather than any space-averaged properties of the field. There are several stages in constructing a model of acceleration. The track taken

was to simulate particle trajectories and hence construct particle distribution functions. The first step, which will be the subject of the following section, was to construct a magnetic field. It was assumed that this had an isotropic distribution upsteam of the shock front. At the shock this field was compressed perpendicular to the shock normal; a new magnetic field structure was not generated. It was assumed that the magnetic field did not affect the shock structure. The jump conditions at hydrodynamical shocks were solved in Chapter 3. The compression of the field gives rise to the polarizations which are observed.

The work employed a box with periodic boundary conditions containing a grid of points at which the field was determined precisely; it could not be constructed at an infinite number of points because of the limitation of finite computer memory; the technique was to build a three dimensional box containing the magnetic field. The size of the box was limited, by the computer, to a cubic grid of side 64 making a total of 262144 grid points. The construction of the field was not trivial, one cannot simply generate a random vector at each grid point within the box because one is constrained by the requirement that $\nabla.B = 0$ be satisfied. However, once the field was constructed, the next stage was to simulate the particle acceleration process by following trajectories. In the individual fluid frames on either side of the shock front an electron moves in response to the acceleration on the magnetic field. The particle trajectories are extremely complex and the electrons cross and recross the shock, being accelerated. As a particle crosses the shock the distribution function is built up in an analogous way to the construction of distributions in the Monte Carlo simulations of particle acceleration in Chapter 3. It is a significant achievement to explicitly model the whole process of Fermi acceleration.

The model which is described here took the form of a piece of FORTRAN code. This was implemented on a VAX3800, from which all the results presented here were taken. The code was adapted, by Glenn Haworth, to run in a parallel version on a MEIKO computing surface. This version was tested but was not used to produce the results here owing to the memory limitations of each transputer, a larger box of magnetic field could be built on the VAX.

5.2.2 Construction of the magnetic field

There are various forms that the magnetic field structure could assume, however the one that was chosen was one that had a random distribution of directions upstream and a normal distribution of strengths. As mentioned previously, the constraint that $\nabla.\mathrm{B} = 0$ over the box meant that setting up the field structure within the box was not a simple operation. There was however a method of solving the problem by generating the vector potential, $\mathrm{A(x)}$, over the grid and then, by evaluating $\mathrm{B(x)}$ using $\mathrm{B(x)} = \nabla \wedge \mathrm{A(x)}$, one automatically satisfied $\nabla.\mathrm{B(x)} = 0$; thus the problem reduced to that of generating $\mathrm{A(x)}$. Next the form of $\mathbf{A(x)}$ had to be decided. The aim of the work was to achieve a realistic picture of the Fermi process occurring over the widest possible range of particle momentum. Electrons tend to be most efficiently scattered by disturbances in the magnetic field which have wavelengths comparable to their gyroradii (see e.g. Blandford & Eichler 1987). The gyroradius of a particle is proportional to the particle momentum (and inversely proportional to the magnetic field) so that one would clearly wish to create a magnetic field structure containing a range of wavelengths and strengths which yield appropriate gyroradii. However, just as it was not possible to generate the magnetic field at an infinite number of grid points, neither was it possible to generate a magnetic field which had a very large number of wavelength components. The largest wavelength which the disturbances could have was equal to the size of the box, i.e. 64 (the grid size was be employed as a unit of length). The smallest wavelength to be used was more debatable; however throughout this work wavelengths less than 4 grid points were not used, the point to make is that the field is interpolated linearly between the grid points and one wished to obtain an accurate value of the magnetic field. Using shorter wavelengths would have lead to variations on a smaller scale so that the field could not be accurately determined. Thus there was a vector field with a range of wavelengths between 4 and 64 grid points. It was assumed that the wavelengths of the disturbances had a power-law form; if the spectral index of the magnetic field disturbances is defined as n then $A(\mathrm{k})$ was obtained using the form:

$$A(\mathrm{k}) = |\mathrm{k}|^{-n} e^{i\psi(\mathbf{k})} \tag{5.1}$$

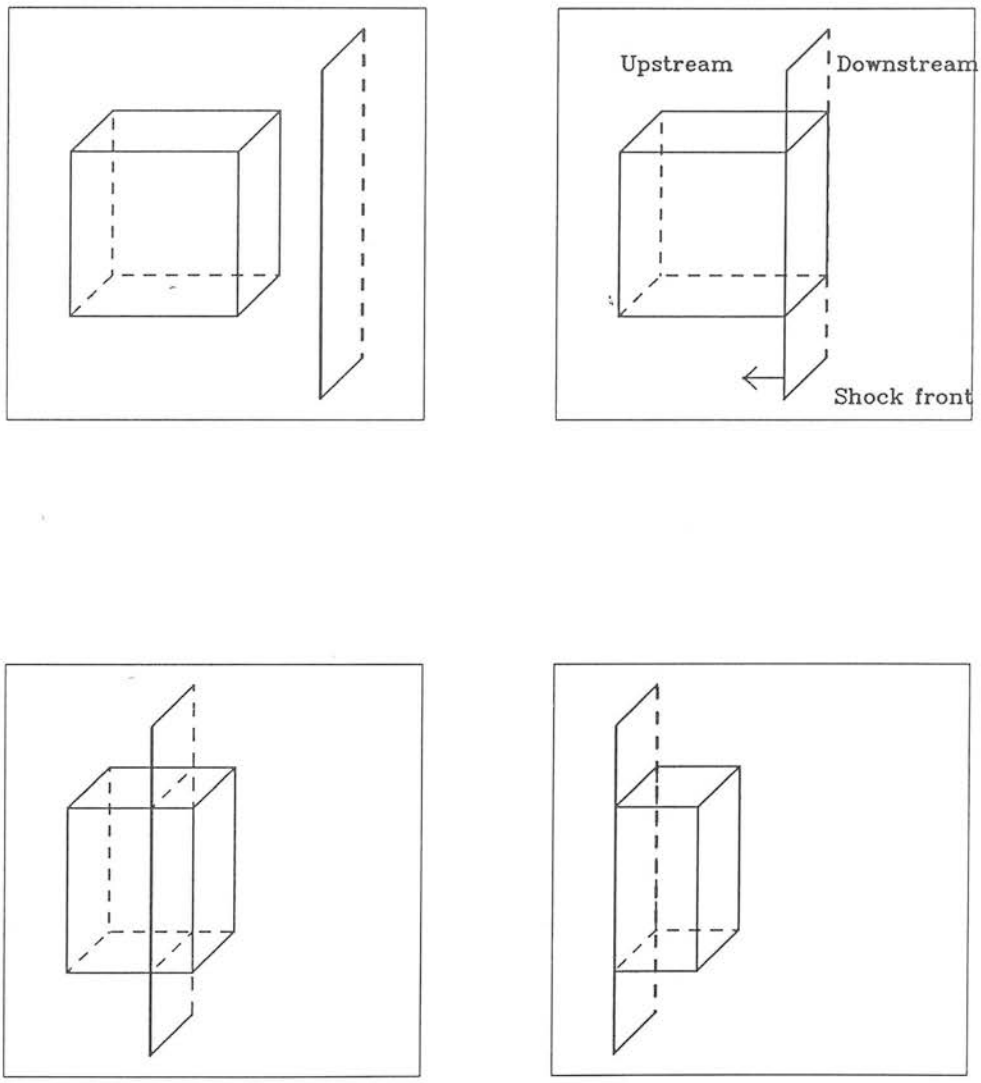

Figure 5.1: This figure illustrates the principle of the acceleration method. The particle moves around within the box, or adjacent boxes, as the shock passes through the fluid.

The term $\psi(\mathbf{k})$ represents the phase of the waves, chosen randomly between 0 and 2π for each value of the wavenumber k. $\hat{\mathbf{k}}$ is a unit vector in the direction of k. This ensured the random direction of the field. Thus the technique was to generate an array of $\mathbf{A}(\mathbf{k})$ values within a box in k space and then carry out a Fast Fourier transform (FFT) to generate the form of $\mathbf{A}(\mathbf{x})$. This was done using the multi-dimensional NAG library routine *C06FJF*. Rather than solving for each dimension simultaneously, the method used was to calculate each component in sequence, A^x then A^y and then A^z and construct the contribution to the $\mathbf{B}(\mathbf{x})$ array after each run before resetting the array (this was the most memory efficient method of solving the problem). An array containing the projected components of $\mathbf{A}(\mathbf{k})$ values was filled up for each point in k space using equation (5.1). Finally, note that a real magnetic field was required i.e. all the complex values of $\mathbf{A}(\mathbf{x})$ were zero. To ensure this the $\mathbf{A}(\mathbf{k})$ were forced to satisfy:

$$\mathbf{A}(-\mathbf{k}) = \mathbf{A}^*(\mathbf{k}) \tag{5.2}$$

The NAG routine was then required to evaluate:

$$\mathbf{A}(\mathbf{x}) = \sum_{j=-L}^{L-1} \mathbf{A}(\mathbf{k}) e^{i\mathbf{k}.\mathbf{x}} \tag{5.3}$$

There is an important remark to make at this point. The NAG routine in practice only evaluates the summation between $j = 0 \rightarrow 2L - 1$ whereas the summation required was that given by equation (5.3). The problem is to translate the three dimensional FFT from a grid on the positive x octant to one centred on the origin and is treated by Nussbaumer (1981). The problem is solved by simply multiplying each element in the $\mathbf{A}(\mathbf{x})$ array by

$$(-1)^{l+m+n} \tag{5.4}$$

and the k vectors are measured from a grid point in the centre of the box. Having thus created an array of A^i values and carried out the FFT, using this last equation to correct the values, an array of values for $A^i(\mathbf{x})$ was obtained within the box. The next stage was to obtain the contribution to the magnetic field strength by evaluating the curl of the A terms. There are three components of $\mathbf{B}$, each of which had to be

evaluated at 64^3 points. The method used in practice was a linear difference method, using the change in A between the appropriate points. The relevant equations are:

$$\begin{aligned} B^x_{lmn} &= \frac{A^y_{lmn+1} - A^y_{lmn-1}}{2\Delta z} - \frac{A^z_{lm+1n} - A^z_{lm-1n}}{2\Delta y} \\ B^y_{lmn} &= \frac{A^z_{l+1mn} - A^z_{l-1mn}}{2\Delta x} - \frac{A^x_{lmn+1} - A^x_{lmn-1}}{2\Delta z} \\ B^z_{lmn} &= \frac{A^x_{lm+1n} - A^x_{lm-1n}}{2\Delta y} - \frac{A^y_{l+1mn} - A^y_{l-1mn}}{2\Delta x} \end{aligned} \tag{5.5}$$

where $\Delta x, \Delta y, \Delta z$ is the grid spacing $(= 1)$. The problem was easily solved except at the edges of the box where use was made of the periodic structure of the field to obtain values from the other end of the box e.g. the (9,0,10) component of B^z was made up from the difference between the (9,1,10) and (9,63,10) elements in the A^x array and the corresponding difference in the A^z array. This procedure was employed for all points in the A^x array. Having done this the array was emptied and used to calculate all the components of A^y and finally the same procedure was followed for A^z. This gave the three components of $\mathbf{B(x)}$ at all grid points within the box. To illustrate the magnetic field structures which were generated a sample of the magnetic field components in a single plane cut through the box is shown in Fig 5.2. For the purposes of clarity, the box used in this example has a side of only 32 and only a quarter of the field elements within this plane are actually plotted. Each realization of the magnetic field took a large amount of memory to store so that instead of storing very large arrays, each time a run was made a new magnetic field was generated. Finally, note that as mentioned previously, the magnetic field had to be real with all complex values of $\mathbf{B(x)}$ equal to zero, consequently a check was added to the code to ensure that this was always so.

An additional question is that of the spectral index of the disturbances. For the present, a Kolmogorov spectrum will be assumed. The energy in an interval of wavenumber, dk is then $I(k)dk \propto k^{-5/3}dk$. For a magnetic field one has:

$$I(k)dk \propto |B(k)|^2 k^2 dk \tag{5.6}$$

but one also has:

$$B(r) \propto \sum B(k) e^{-i\mathbf{k}.\mathbf{r}} = \sum (-i\mathbf{k} \wedge \mathbf{A}) e^{-i\mathbf{k}.\mathbf{r}} \tag{5.7}$$

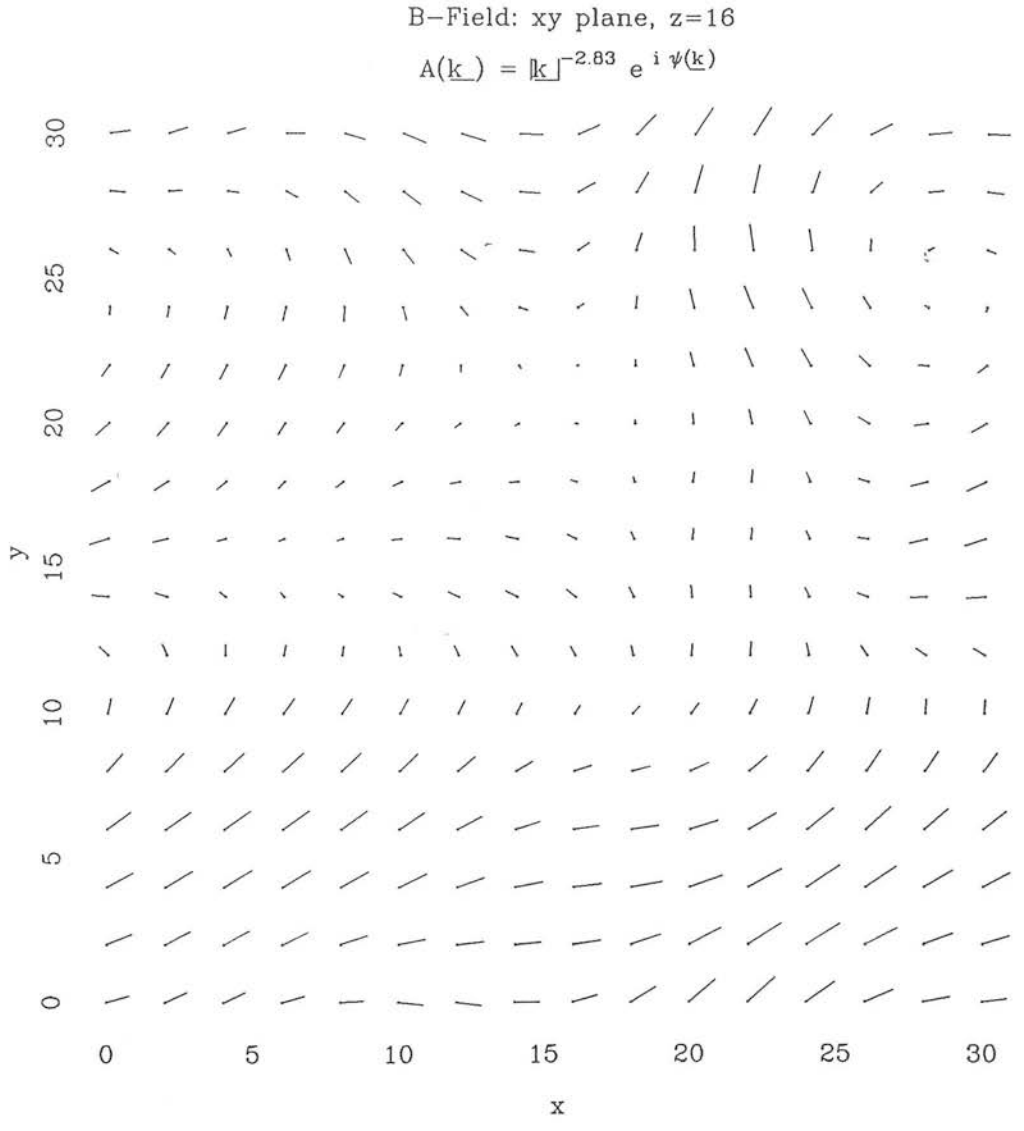

Figure 5.2: This figure shows a slice through the fluid showing the magnetic field structure in the xy plane. The box in this illustrative case was 32 grid points per side. Only a quarter of the points within the plane are plotted.

so that $I(k)dk \propto k^4|A(k)|^2 dk$. For a Kolmogorov spectrum one thus has $n = 2.833$ which is the value used in Fig. 5.2. Note that, as Alfvén (1981) stated the disturbances are not strictly turbulence in the sense that what one usually means by turbulence is a process involving collisions between particles whereas in a collisionless plasma like this the disturbances are caused by a series of plasma waves.

The magnetic fields which were calculated should have approximately Gaussian distributions for each component. This is essentially due to the central limit theorem; as a large number of waves of differing wavenumbers with random phases are added together in a box, one obtains a normal distribution of strengths. The distribution of B^x for the previously calculated magnetic field is shown in Fig. 5.3 and it is indeed approximately Gaussian. The best fit Gaussian is also plotted, as a solid line. In the lower plot, the distribution of field strengths $|B|$ is shown.

Finally, the magnitude of the magnetic field had to be scaled so that the particles resonated with the magnetic field disturbances. The gyroradius of a particle of momentum p moving at a pitch angle θ is:

$$r_g = \frac{p \sin\theta}{zeB} \tag{5.8}$$

Units were chosen such that the charge ze was unity. As a particle was accelerated the gyroradius increased. The acceleration was efficient over the widest possible range if the minimum gyroradius corresponded approximately to the minimum wavelength of the disturbances i.e. 4 grid points. Therefore, in the simulations, once the magnetic field was generated at each point, the mean value was calculated and then each value was scaled by a fixed value so that disturbances with a wavelength of 4 resonated with momenta around the injection value and those with a wavelength 16 times larger resonated with momenta roughly 16 times the injection value.

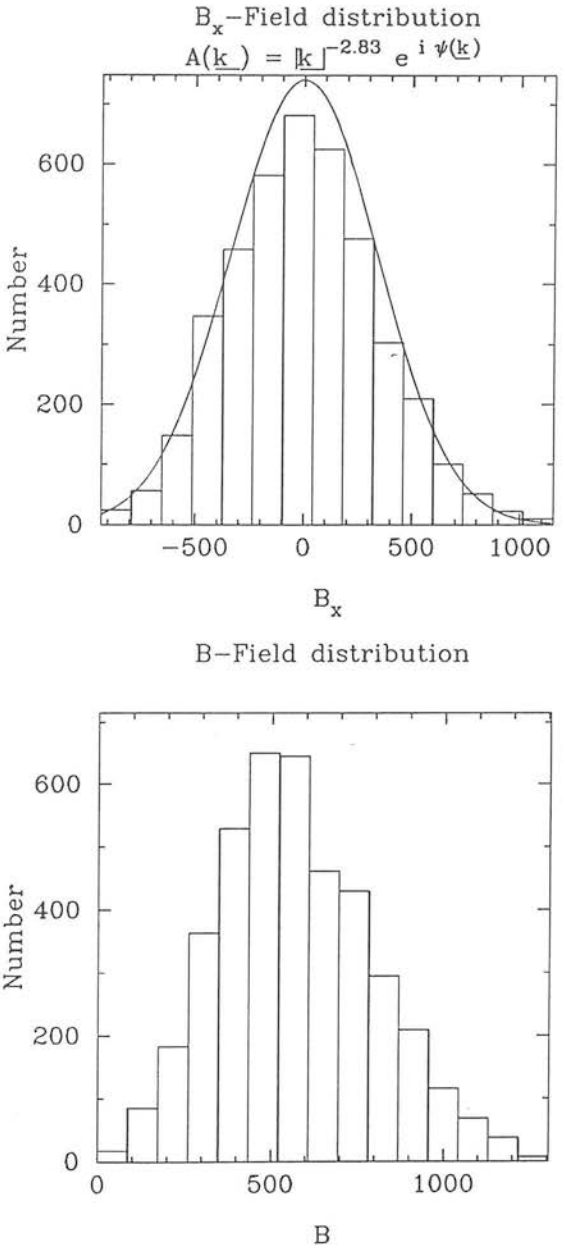

Figure 5.3: This figure shows the distribution of magnetic field strengths for a box of side 32. The top figure shows the distribution of a single component and has a Gaussian form. The lower figure shows the distribution over total strengths.

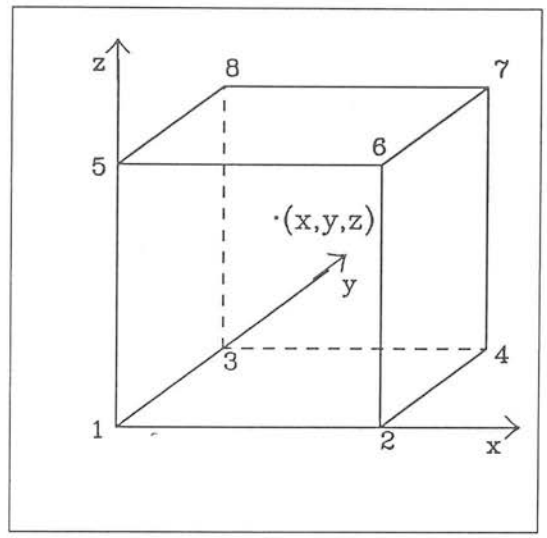

Figure 5.4: Given the particle's position within a gridpoint at (x, y, z), the magnetic field is calculated using three dimensional linear interpolation.

5.2.3 Determining the magnetic field

The next stage of the problem was one of the practicalities of the acceleration process. When eventually the point was reached where the particles were accelerated, the method used was to obtain exact particle trajectories. The motion of the electrons was governed by the magnetic field. Hence there was a clear need for constructing a technique for evaluating the magnetic field which a particle experienced given its position. It was realistic to allow the field to vary gradually within the grid. One possible method is to obtain the exact position of the particle and interpolate linearly to obtain an approximation to the field. Again, this was only an approximation to the field but as the field doesn't vary too wildly between grid points, it is probably a reasonable guess at what the field actually is. The principle of three dimensional linear interpolation is illustrated by Fig. 5.4. Note that throughout this chapter all distances and times are measured in the shock frame, the same as in Chapter 3, as this makes identifying which side of the shock a particle is located trivial. In order to find the field a particle experiences it is necessary to transform the position of the particle into the fluid frame.

This is carried out using:

$$x_i = \gamma_i(x_s - u_i t_s) \tag{5.9}$$

where $\gamma_i = (1 - u_i^2)^{-1/2}$ is the Lorentz factor corresponding to the flow speed and $x_s[t_s]$ is the position [time] in the shock frame. Note that in the shock frame both fluids are flowing in the same direction so the equation is in the same form in each case. However, as was noted before, it was assumed that, at the shock front, the component of the magnetic field perpendicular to the shock normal was enhanced by a factor of the shock compression ratio. For particles in the downstream field there was therefore a need to find their position within the (compressed) box and then make an appropriate correction to the perpendicular components of the field. If the field is to be linearly interpolated and if the particle has coordinates (x, y, z) then one can define three weights:

$$\begin{aligned} wt &= \tfrac{x-x_1}{x_2-x_1} \\ wu &= \tfrac{y-y_1}{y_3-y_1} \\ wv &= \tfrac{z-z_1}{z_5-z_1} \end{aligned} \tag{5.10}$$

where the subscripts refer to the vertices of the grid as labelled on Fig. 5.4. Then if the known value of the ith component of the field at the jth vertex was given by B_j^i, one could approximate the field by:

$$\begin{aligned} B^i(x,y,z) = \; & (1-wt)(1-wu)(1-wv)\,B_1^i + wt\,(1-wu)(1-wv)\,B_2^i \\ & +(1-wt)\,wu\,(1-wv)\,B_4^i + wt\,wu\,(1-wv)\,B_3^i \\ & +(1-wt)(1-wu)\,wv\,B_5^i + wt\,(1-wu)\,wv\,B_6^i \\ & +(1-wt)\,wu\,wv\,B_8^i + wt\,wu\,wv\,B_7^i \end{aligned} \tag{5.11}$$

and this procedure was carried out for each of the three components. Each particle was flagged according to which side of the shock it lay. If it lay upstream then its position within the box was found, the weights calculated and the approximate field determined. If it was downstream, its position within the box was found and account was be taken of the reduced grid spacing owing to the compression; this gives the weights. The field was then calculated using equation (5.11) but the perpendicular components were

boosted by a factor of the compression ratio.

5.2.4 Particle trajectories

The next stage was to accelerate the particles by following the particle trajectories; this was carried out in either fluid frame where the fact that $\mathbf{u} \wedge \mathbf{B} = \mathbf{0}$ and the assumption of infinite conductivity means that the electric field was zero. The equations of motion of the electrons are then:

$$\dot{\mathrm{p}}(t) = \frac{q\mathrm{p}(t)}{mc} \wedge \mathrm{B}(\mathrm{x}, t) \tag{5.12}$$

$$\dot{\mathrm{x}}(t) = \frac{\mathrm{p}(t)}{m} \tag{5.13}$$

where $m = \gamma_e m_e$ is the electron mass, γ_e being the electron Lorentz and m_e the rest mass and $\mathrm{B}(\mathrm{x}, t)$ is the magnetic field. t and x in these equations are measured in the local fluid frames which were obtained from the values in the shock frame through the appropriate transformations. The aim of this experiment was to solve these equations to find values of $\mathrm{p}(t)$ and $\mathrm{x}(t)$ for all times to yield the points where the electrons cross the shock front in order to construct the particle distributions. The method that was actually used to integrate these differential equations was a fourth order Runge Kutta method, with adaptive stepsize control. It was important to find the fastest available routine for this. Several different numerical methods for carrying out these integrations were tested to determine the most efficient technique. The two relevant routines were *D02BAF* from the NAG library and ODEINT from Numerical Recipes (Press et al. 1989). The latter was used for the integrations at the shock front where the ability to handle a variable integration range was required and for all the work on the MEIKO machine where NAG was unavailable but otherwise the NAG routine was used for all the integrations as it proved to be considerably faster. Needless to say, the two routines were tested to ensure they gave identical trajectories.

The aim was to integrate equations (5.12) and (5.13) between t and $t+\delta t$ given $\mathrm{p}(\mathrm{t})$ and $\mathrm{x}(\mathrm{t})$ where δt is a fixed timestep. Each particle was allowed to set off from the shock,

moving upstream, at time $t = 0$. After integration the new position and momentum were obtained and this process was repeated giving the particle trajectory until the particle crossed the shock. In practice the time of a shock crossing was not an integer multiple of the timestep, so having determined that a crossing event was occurring, the shock crossing was achieved by moving back a step and then integrating using the alternative routine, ODEINT, which has a variable endpoint. Thus the exact value of momentum and time at the crossing could be determined. The particle distribution as a function of momentum and pitch could then be constructed by adding in $1/\cos\theta$ to the appropriate bin. This factor of $1/\cos\theta$ was used in Chapter 3 for the same reason i.e. the computer program measured the flux of particles crossing the plane shock front, yet the aim was to find the particle distribution function. The integration of the particles motion was then continued. A stopping point was fixed in the downstream fluid and when a particle passed this point it was regarded as lost and the next particle was followed. The ability to plot exact particle trajectories was used in checking the program, a couple of examples are shown in Fig. 5.5.

Now consider the downstream boundary, the point at which particles were lost from the simulations. It was important to get this approximately correct as underestimating this quantity means that particles would be lost which could still return to the shock, and this would affect the distribution functions. This may in fact be energy dependent as higher momenta particles require higher wavelength disturbances to scatter and hence may travel further before being returned to the shock. On the other hand, overestimating the boundary could mean that a great deal of computing power was wasted in calculating particle trajectories which were being advected away from the shock with little chance of returning. To test for the ideal position of the boundary, a series of runs were carried out with identical starting conditions ($u_1 = 0.4$ and compression ratio $r = 4$, and a spectral index for the fluctuations of $n = 2.833$) apart from the value of the boundary, x_d. Each run started with 100 particles and the total number of shock crossing events was recorded. The results are summarized in Fig. 5.6 where the number of crossing events is shown plotted against $1/x_d$. The line plotted is the best fit straight line through the points. There appears to be no absolute value of x_d which is best, as the boundary is moved downstream so more crossings are

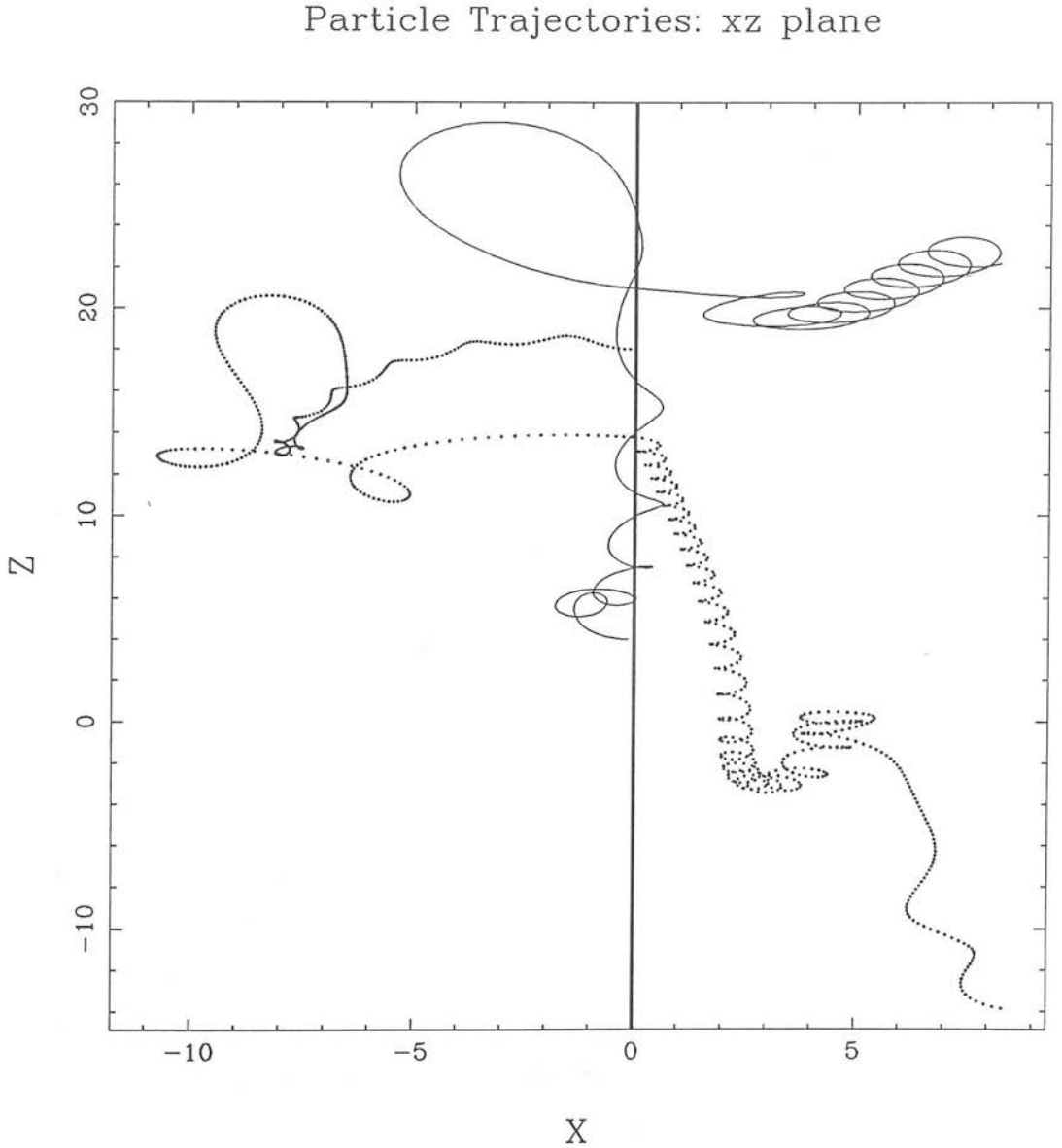

Figure 5.5: This shows the trajectories of two particles with different starting positions along the shock front. The paths follow the magnetic field and cross the shock front (at $x = 0$) several times. In this case the assumed shock speed was $0.4c$ and the compression ratio was 4.

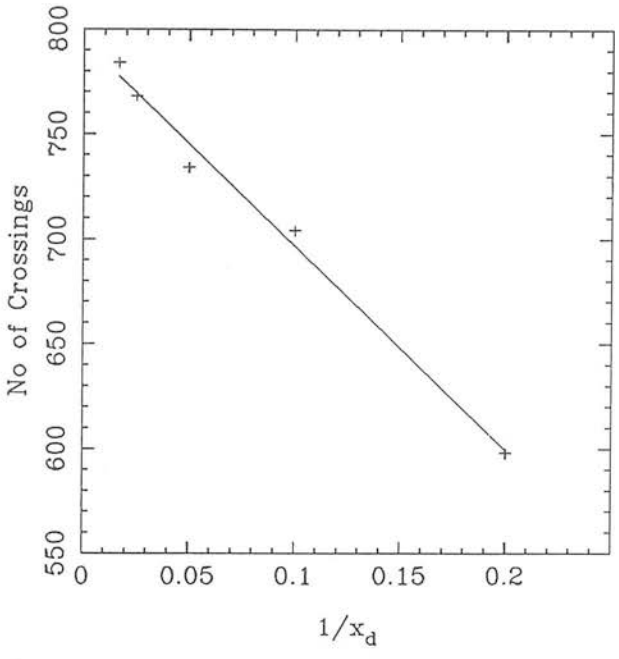

Figure 5.6: This figure shows the change in the number of shock crossing events as the downstream boundary (x_d) is moved away from the shock.

recorded. It has to be accepted therefore that some crossing events are going to be missed and that this effect will increase as time goes on and the momentum gets larger. There will unavoidably be some error introduced into the spectral index although this could be treated by using a roulette technique described below.

It is perhaps worth pointing out that the technique of particle splitting which was used to great effect in Chapter 3 could not be employed in the present work where individual motions were followed exactly; if a particle was split split into two halves, both would subsequently follow the same paths, making the exercise pointless. This means that all the advantages of particle splitting (i.e. maintaining a high signal-to-noise at high momenta without injecting an excessively large number of particles) were lost.

Although splitting could not be used to reduce the noise on the distribution functions, by combining particles it was possible to probe further into the downstream fluid. The technique used was that of playing Roulette with individual particles. A

particle was followed until it reached the pre-determined downstream boundary. It was then discarded or not on the basis of a random number. It if was not discarded its weight was increased by the inverse of its probability of being selected, the downstream boundary was extended by a fixed length (in practice the length of the original boundary) and it was followed as before. The aim of this was simply to obtain extra shock crossing events from particles which would have been lost otherwise particularly at higher momenta where otherwise the gyroradius would be too large for the particle to be scattered before reaching the boundary. It was, of course, a noisy technique as a very few particles, with unnaturally large weights, were added in to the distribution function. However, it did detect shock crossings which would otherwise be missed. It was not used in any of the plots which are presented in this chapter for consistency between the various shock speeds. As the code was improved to run faster it was found that the downstream boundary could be extended to an acceptable length without increasing the computing time excessively. Thus using the roulette technique would not have increased significantly the number of crossings recorded.

5.2.5 Time reversal

It is amusing to note that this technique for accelerating particles was completely reversible in time, although this is of course an unphysical situation with the entropy decreasing at the shock front. In this case the fluid flow upstream of the shock was moving slower than the downstream fluid in the shock frame. The technique used was to follow a particle orbit with time increasing, terminating the trajectory after several shock crossing events. The final position, time and momentum components of the particle were then recorded and entered back into the program as starting points. Time was then allowed to decrease back to zero when the trajectories were printed out and compared. They are shown in Fig. 5.7. Clearly they agree fairly well, similar features in the motion can be observed in both cases although they do diverge slightly; this was presumably due to high-order errors when the orbits were computed. This work was carried out purely as part of testing the code, apart from that it has no significance.

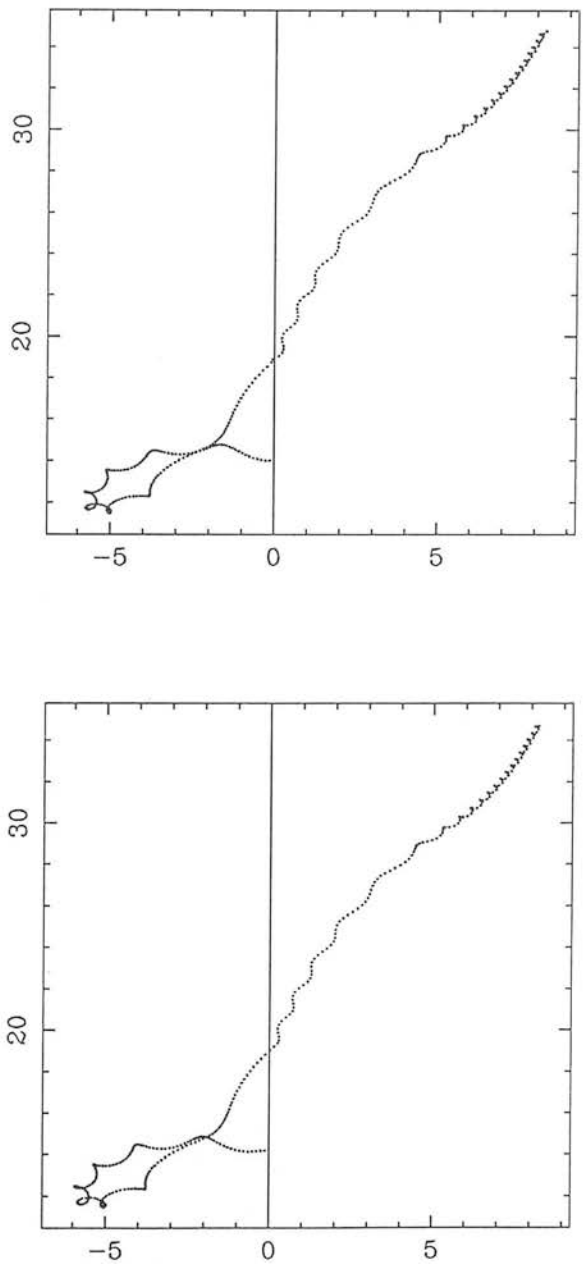

Figure 5.7: In the top figure a particle starts from the shock front and is accelerated. Its final position is recorded and used as the starting point in the lower figure, where time is run backwards.

5.2.6 Discussion

Before the results of the simulations are presented in the following section, there are a few further points that the reader should be aware of. The first is regarding the way the spectra were constructed; that is they should only be regarded as time averaged spectra. When an electron crossed the shock front it made a contribution to the distribution function. It may have crossed the shock again, but at a later time when it made a further contribution to the distribution; the consequence of this is that the spectra presented are from shock crossings at many different times. Neither is it possible to regard the distributions as snapshots, assuming shock crossings to have been due to particles which originated at different times simply because the electron motion was being followed through a particular magnetic field.

The second point to note is that since the particle splitting technique could not be used, a very large number of particles were accelerated in order to obtain realistic spectra and this required a lot of computer time. It would have been both impractical and unsociable to carry out these integrations on a single occasion so a method was devised to accelerate a few hundred particles, write out the results and have them read in before starting on the next run. Between runs the magnetic field realization was changed (by using a non-repeatable random number generator). The purpose of this was to ensure that the resulting spectra were not particular to a specific field realization, but rather they were an attempt to obtain an average for a variety of field structures.

Finally, the simulations that were carried out were Monte Carlo simulations only to the extent that the field configurations were random. In the present work the electron trajectories were exact although they may not have been exhaustive because only a restricted number of particles were accelerated. The particles were not even located at random positions and with random motions as they all started off moving upstream along the shock normal and were placed down on a grid to try and simulate an even injection pattern rather than allowing any chance bottling up of the electrons to take place.

5.3 Results

Having outlined the construction of the model in the previous section, this section will be concerned with the results that were obtained. These are expressed as spectra, examples of which are shown in Figs 5.8-5.11. Unless otherwise stated the conditions which were assumed for the shock compression ratio were at all times those expected for a purely hydrodynamical shock where the downstream fluid reaches full local thermodynamic equilibrium, although as mentioned in Chapter 3 this is only one of several possible downstream states which are feasible and which give different compression ratios. In all cases a Kolmogorov spectrum for the magnetic field was assumed.

The spectra shown clearly illustrate the fact that using a monoenergetic injection spectrum, a shock and disordered magnetic field are the site of Fermi acceleration and over a restricted range of momentum a power-law distribution is the result. In Fig. 5.8 there is a recognisable power-law over two decades of momentum before the spectra begin to steepen with an apparent cutoff. The origin of this cutoff will be the subject of a later subsection. For the faster shocks in Fig. 5.10 and 5.11, the power-law is less certain although more particles were injected initially. For the faster shock each particle made fewer crossings of the shock front before being lost (on average approximately 1.5, as opposed to around 5 per particle for the slower shock).

An additional feature which is present in all the spectra is the spike in the angular distribution of the particles. This is measured relative to the shock normal, there being no preferred magnetic field direction to measure pitch angles relative to. There are several possible origins of this spike, the most likely being that the weight given to any particle which crosses the shock at a direction to place it in this bin will be very large producing a large value in this bin. Another feature is the increasing degree of anisotropy as the shock gets faster, which can be seen by comparing the two spectra reproduced here. The distribution is more heavily weighted towards particles crossing from the upstream to the downstream region for the faster shock. This is due to particles which tend to cross the shock only once before being immediately lost from the shock region. In this sense the distribution function represents all particles and not

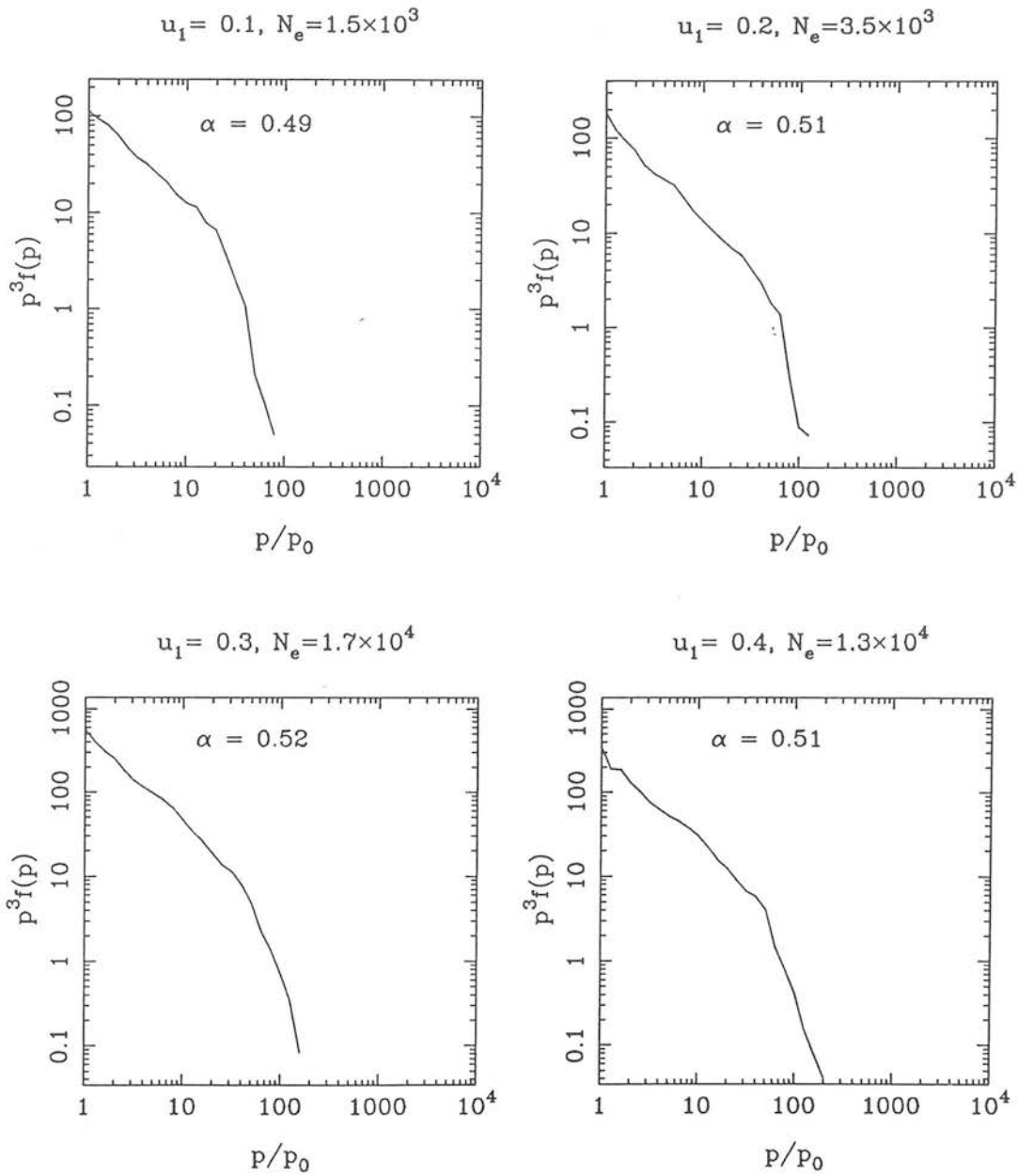

Figure 5.8: This figure shows the spectra obtained for shocks moving at 0.1, 0.2, 0.3 and 0.4.

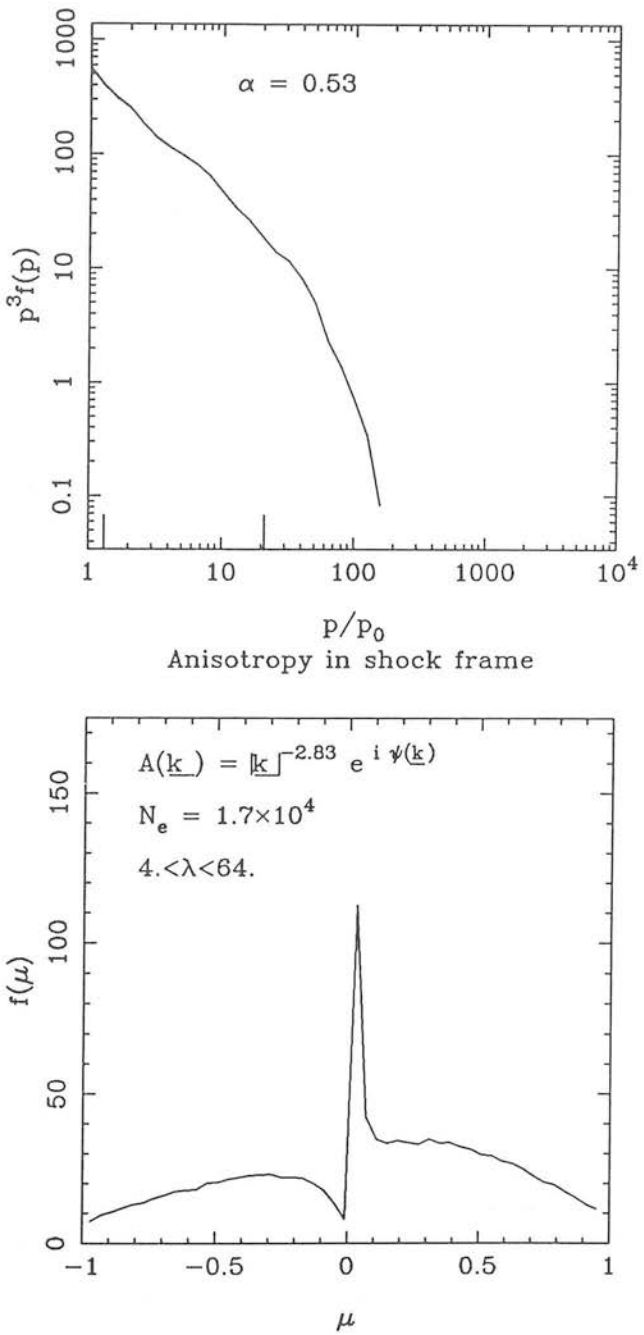

Figure 5.9: This figure shows an example of the spectra which could be obtained using the method described in this chapter. The top figure shows the momentum distribution and the bottom figure shows the angular distribution. The shock speed was $u_1 = 0.3$ and the compression ratio was $r = 3.95$.

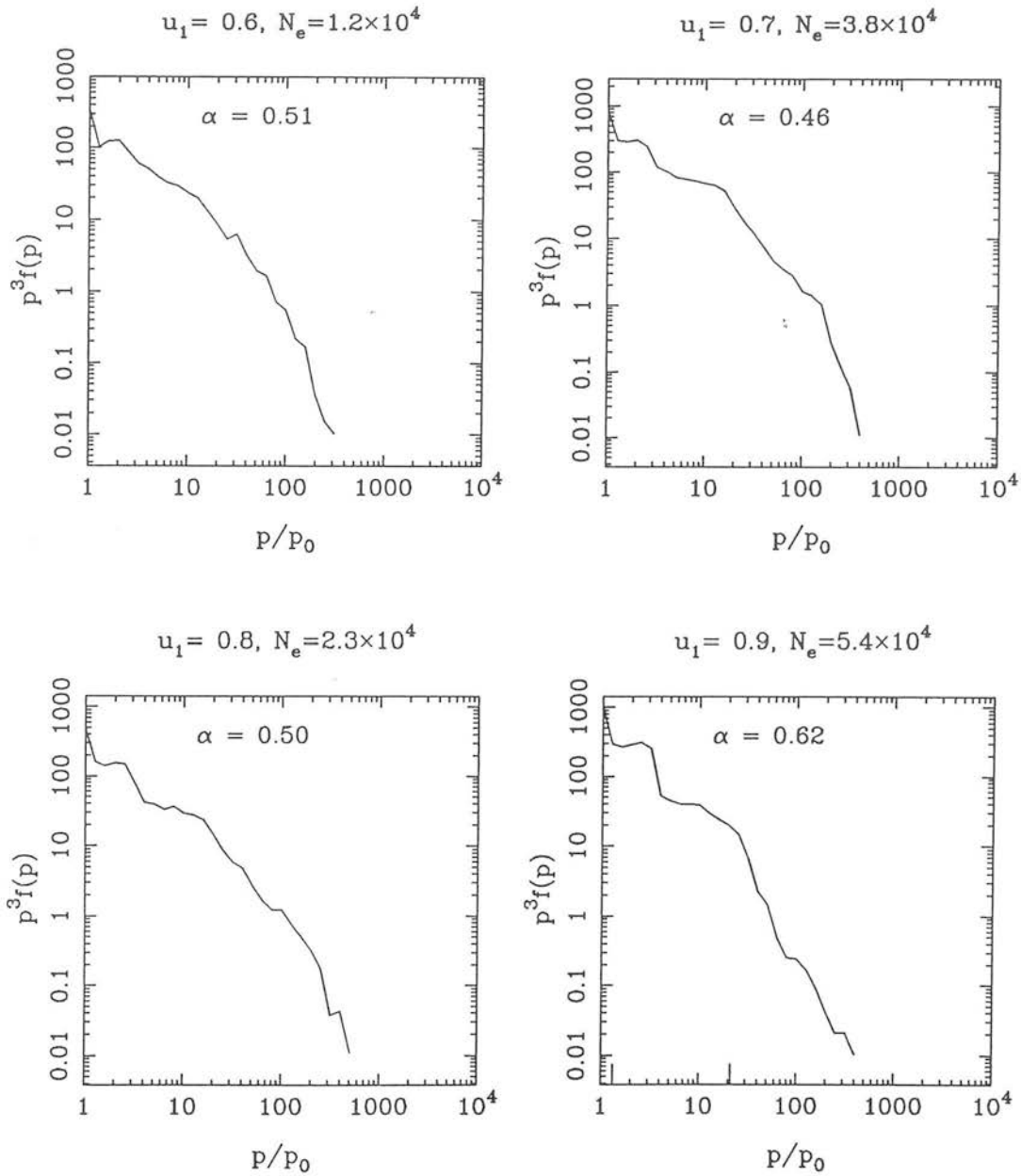

Figure 5.10: This figure shows the spectra obtained for shocks moving at 0.6, 0.7, 0.8 and 0.9.

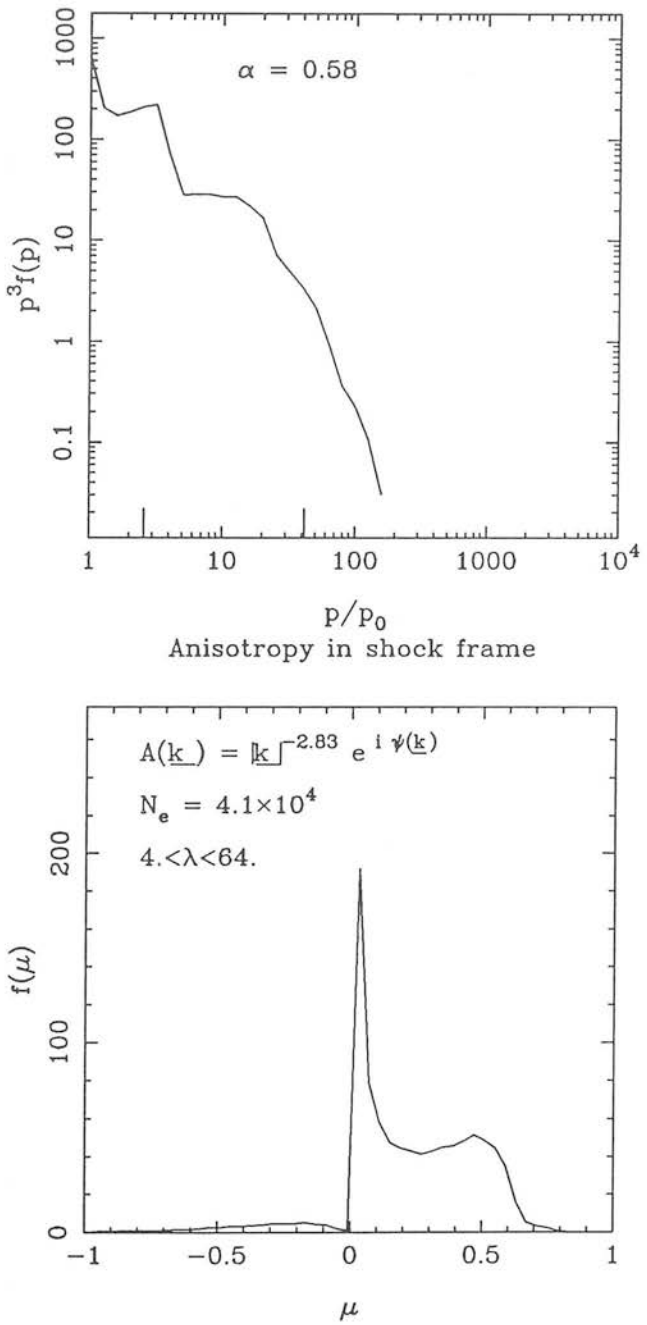

Figure 5.11: This figure shows an example of the spectra which could be obtained using the method described in this chapter. The top figure shows the momentum distribution and the bottom figure shows the angular distribution. The shock speed was $u_1 = 0.98$ and the compression ratio was $r = 3.58$.

simply those that have been accelerated by repeated shock crossings. However this is a true picture of what occurs in practice, electrons being injected into the upstream region will always cross once more from upstream to downstream than vice versa. It simply expresses the fact that the acceleration process is less efficient at high shock speeds in the sense of the ability to return particles to the shock, although the energy gain on completing a cycle is correspondingly larger.

5.3.1 Determining spectral indices

The spectral indices of the particle distribution have to be found. As with the spectral indices of the distributions in Chapter 3, this is not a simple matter. Particles are not split so the errors increase at high momenta. Although, each bin contains contributions with different weights it was decided to weight each bin by the number of particles. The slope could then be estimated using a least squares technique (see e.g. Barford 1967). From this the synchrotron spectral index could be obtained. However, it is clear that not all points in the spectra should be used in deriving the spectral index, at momenta just above the injection point there were spikes in some distributions; therefore the first three bins were ignored. At high momenta, the spectra steepen to a cutoff. Whatever the reason for this it will bias the spectral index. In practice each point was tested as the endpoint, the point giving the lowest error estimate was chosen as the best guess.

5.3.2 Particle diffusion

In this subsection the evidence that the process occurring is similar to diffusive acceleration will be presented. By monitoring the progress of a number of particles their diffusion in direction could be followed. The standard definition of pitch angle is with respect to a particular magnetic field direction. As there is no fixed magnetic field direction the pitch is defined with respect to the shock normal. To test this a run was carried out with 100 particles all injected directly upstream. After each integration the particles pitch angle was recorded together with details of the time in the shock frame. This was continued until the particle moved into the downstream region when

it was lost from the simulation. The details of the overall pitch angle distributions were then calculated to give the mean pitch angle as a function of time $\langle \mu(t) \rangle$. This is plotted in Fig. 5.12 and shows the mean pitch angle moving away from the upstream direction. It is also instructive to examine the spread in this distribution with time, the standard deviation from the mean was also calculated and is shown as an error bar on Fig. 5.12. The spread in pitch angles increases with time, as one would expect for simple pitch angle diffusion. When particles are lost they have large pitch angles and the distribution of the remaining pitch angles should get narrower, and this is also seen.

5.3.3 The origin of the high energy cutoff

In the previous subsections, spectra for the accelerated electrons were presented. These quite clearly have a power-law form at momenta in the first two decades above the injection energy. At higher momentum progressively fewer particles should reach a given momentum in line with the appropriate spectral index. This is not the case, the spectra all steepen significantly. It is not evident from the data whether the high energy spectra are all steep power-laws or whether there is a quasi-exponential cutoff. The origin of this steepening should be discussed although there is a fairly straightforward explanation. Recall that the magnetic field amplitude was "tuned" to give a mean value which resulted in electron gyroradii comparable with the wavelength of the field perturbations so that the electrons would tend to resonate with the magnetic field and optimize the acceleration process. If this is the case at around the injection energy, then it follows that as the particles are accelerated gaining momentum and increasing the gyroradius the wavelengths they interact with increases. The maximum possible wavelength of any disturbance is 64, the size of the box, and once the gyroradius has exceeded this they will be scattered to a much lesser extent and will tend to escape the shock vicinity. Allowing for some scatter about this because the gyroradius is determined by the local value of magnetic field and pitch angle rather than mean values, one can understand that the acceleration process will only be efficient over a couple of decades in momentum. The momentum value where the gyroradius in the mean magnetic field and pitch angle 90° exceeds the box size is marked on the spectra

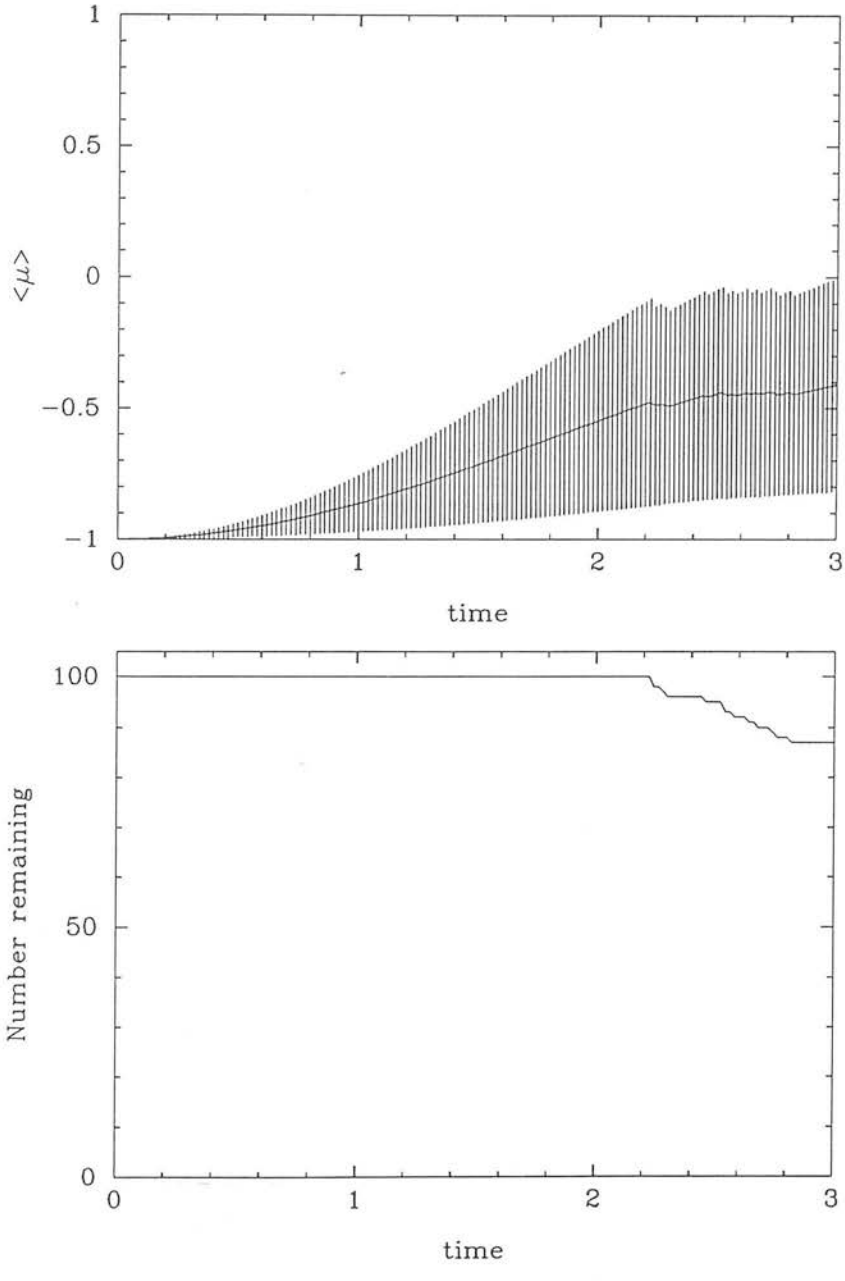

Figure 5.12: This figure shows the change in mean pitch angle with time for 100 particles injected directly upstream, the standard deviation being plotted as an error bar. The lower figure shows the total number of particles which remain upstream of the shock.

as a tick mark.

5.3.4 Synchrotron emission

In this subsection a brief description of the form of the emission expected from the electrons as they are accelerated will be given. Part of the motivation for this was the work of Ostrowski (1991) who simulated particle motions with an oblique magnetic field and showed that the number density of electrons tends to be higher in the upstream fluid, although this is perhaps the natural conclusion to be drawn from the fact that most particles are reflected at a highly oblique shock front (Kirk & Heavens 1989). To plot the distribution of electrons the motions of 100 particles were followed and after each integration the particles were binned in position. The synchrotron emission from the particles was also evaluated in a rather simple manner, the energy emitted in this form being $\propto E^2 B^2 \sin^2 \varepsilon$. The synchrotron emission does not correspond to what one would actually observe i.e. an unresolved spectrum from a selected number of electrons, but rather it is the total energy emitted. Care was required around the shock front where the actual time interval at the crossing point can vary, thus particles were weighted by the appropriate timestep. The results are plotted in Fig. 5.13 where the number of particles and total synchrotron power emitted are plotted as a function of position in the shock frame.

An interesting conclusion that could be drawn from the steepening of the sample spectra is that the observed spectral steepening at high frequencies could be explained in these terms rather than employing radiation losses as was the case in Chapters 2 and 4 and as was first suggested by Blandford (1979) or any of the other mechanism which have been suggested to suppress the acceleration process. In this case the cutoff would be the result of gyroradii larger than the largest perturbations in the magnetic field. This would not really give much more insight to the actual conditions within the source as this can only constrain a combination of the magnetic field scale and magnitude. It is however an interesting possibility for the origin of the steep spectral indices. An example synchrotron spectrum which could be obtained is shown in Fig. 5.14. It can

be seen that the energy spectrum has been noticably smoothed and there exists a steep high frequency portion caused purely by the finite size of the box.

A summary of the results presented is shown in Fig. 5.15 and Table 5.1. A number of acceleration runs were carried out at shock speeds ranging from $0.1c$ to $0.98c$ using shock compression ratios appropriate for shocks where full local thermodynamic equilibrium is reached downstream. Apart from this all the simulations were identical. The spectra that resulted have synchrotron indices which are all approximately $\alpha \simeq 0.5$.

Table 5.1: Summary of the spectral index behaviour

Shock speed	Compression Ratio	Number of particles	Spectral Index
0.1	3.988	1500	0.480
0.2	3.953	3500	0.502
0.3	3.956	17000	0.506
0.4	3.920	12500	0.504
0.5	3.870	17500	0.509
0.6	3.806	12000	0.505
0.7	3.708	38000	0.500
0.8	3.580	23000	0.608
0.9	3.388	54500	0.726
0.98	3.388	40500	0.726

5.4 Conclusions

In this chapter numerical simulations of particle acceleration in a disordered magnetic field have been presented for a range of shock speeds between the non-relativistic and highly relativistic regimes. Particles were injected into the fluid and by the simple task of repeatedly solving the equations of motion for the particles, the acceleration process could be explicitly monitored. The details of the acceleration method were described in Section 5.2. Adding all the particles together gave a momentum distribution. From these distributions, synchrotron spectral indices could be calculated as was discussed in Section 5.3. It was found that these tend to be around $\alpha \simeq 0.5$ which is close to the classical non-relativistic results. If anything, there is a slight trend for steeper spectral indices as the shock gets faster although there is not convincing evidence of a power law

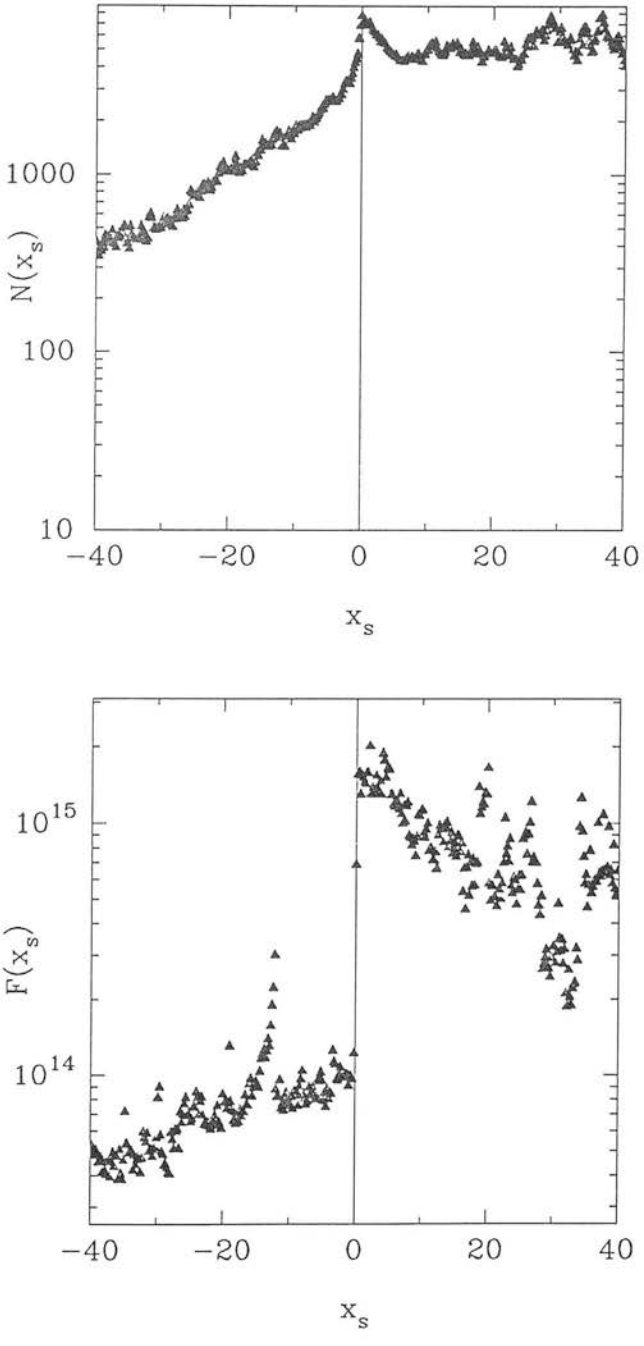

Figure 5.13: The top figure shows the number of electrons as a function of position in the shock frame, the upstream portion being to the left. The lower figure shows how the synchrotron emission changes with position; here there is a decrease in flux as one moves away from the shock although it will eventually level off.

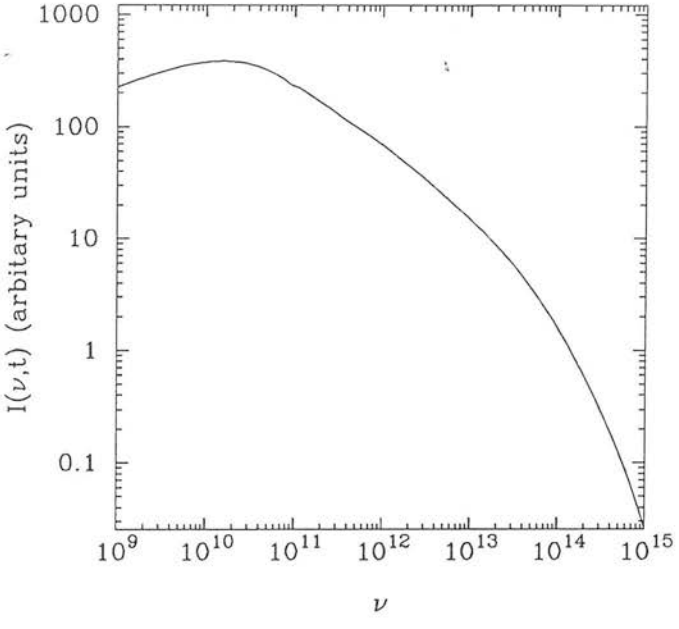

Figure 5.14: This figure shows the spectrum of the radiation from a shock of speed $u_1 = 0.3$. The electron distribution is assumed to be isotropic in the fluid frame and, for simplicity, the magnetic field structure is assumed uniform in strength. The curvature in the spectrum is the result of the cutoff to the electron distribution caused by gyroradii larger than the box.

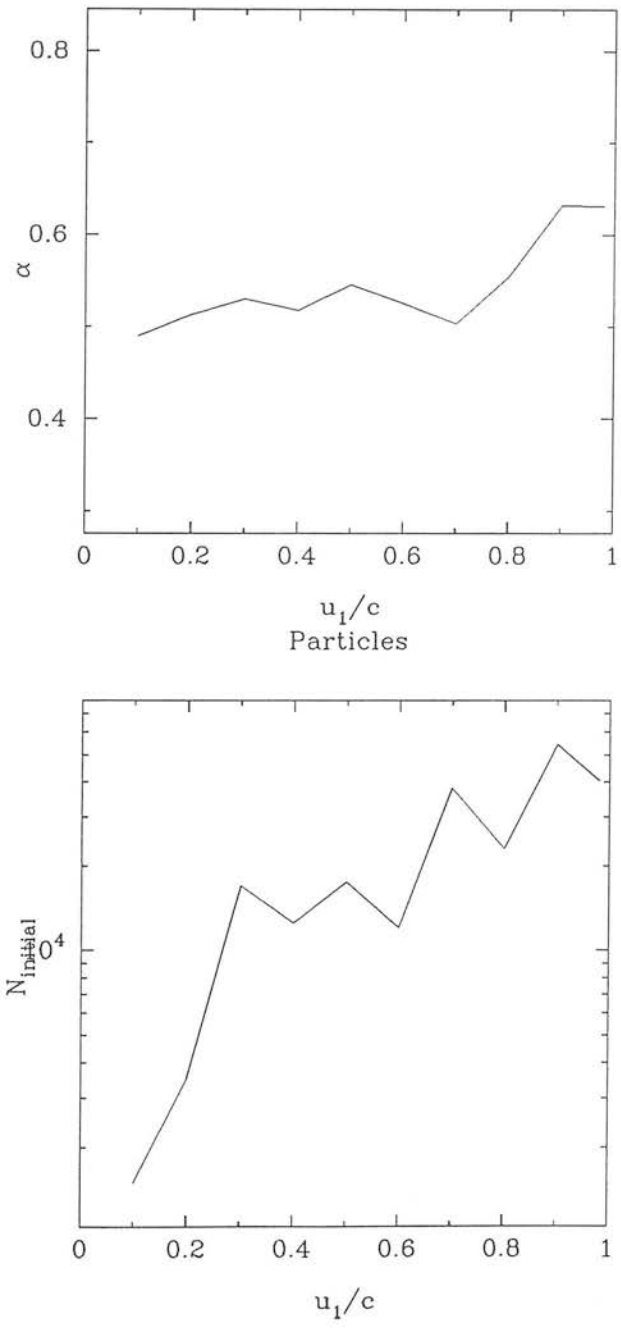

Figure 5.15: In the top figure are shown the spectral indices obtained for a range of shock speeds, where error bars are marked for each point. The spectrum of the turbulence employed was $n = 2.833$. In the lower figure the number of particles which were used in each simulation is shown.

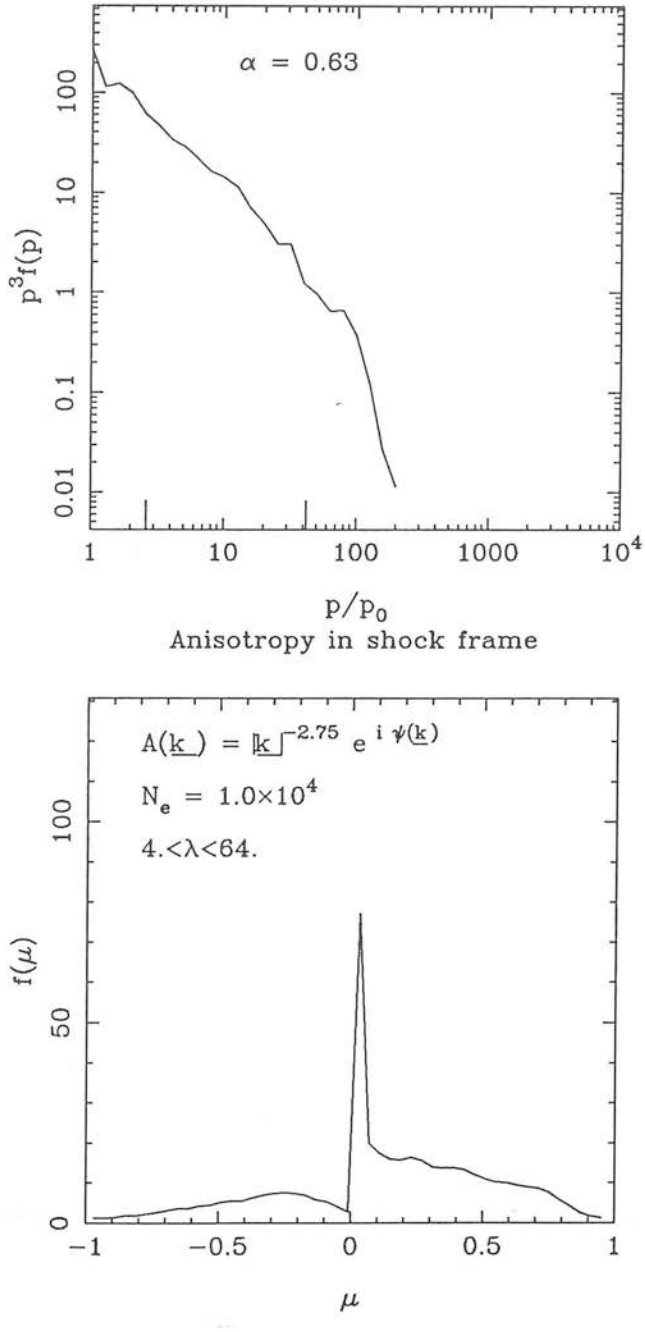

Figure 5.16: This figure shows an example of the spectra which could be obtained using a Kraichnan spectral index. The top figure shows the momentum distribution and the bottom figure shows the angular distribution. The shock speed was $u_1 = 0.5$ and the compression ratio was $r = 3.62$. The spectral index is slightly steeper than in the case where a Kolmogorov spectral index was assumed.

at the fastest shocks. The principal reason for this is that nearly all the particles are lost after a single crossing. Those that do return all receive a large boost in energy and hence the spectra have a more lumpy nature. Acceleration at shocks through disordered fields give rise to polarized emission as the post shock field is compressed. The degree of polarization was not calculated for these distributions but the work of Chapter 4 has shown that these should be quite high (perhaps up to 60%) looking perpendicular to the shock normal dropping to lower values as one looks face on.

There are many possibilities for further work. So far the model has only been constructed and run on a few problems and there are still many unresolved questions. These are primarily because of lack of time, it takes a considerable amount of time to obtain a reasonable spectrum from which conclusions can be drawn. A further limitation is provided by the amount of core memory available on computer. A cube of side 64 is the largest that can be generated at present, more memory could extend this and hence particles could be accelerated to higher energies in the simulations before being lost. This would then make determining accurate spectral indices more precise. All the results presented here were for a Kolmogorov spectral index for the magnetic field disturbances, it would be interesting to see if changing this altered the resulting spectral index. A single example, in Fig. 5.16, is presented with a Kraichnan spectral index. It might also be interesting to calculate the polarization expected from these particle distributions for comparison with the polarizations which were calculated in the previous Chapter.

Finally, the relevance to blazars should be mentioned. To date it has often been supposed that the high energy particles which emit in a disordered magnetic field in these objects could originate by being accelerated through the Fermi mechanism at a relativistic shock although it had not been shown that the Fermi mechanism could operate under such conditions. This work has shown that it can. Furthermore, the spectral indices are consistent with the observed spectral indices particularly if allowance is made for a possible steepening at high frequencies.

Chapter 6

Particle Acceleration in SS433

6.1 Introduction

Every so often a single object temporarily diverts the attention of a large proportion of the astronomical community and remains in vogue for a short while before the majority return to other interests. SS433 is one such object. At its peak in popularity, during 1981, one paper was published on average every 3 days. An account of the discovery of the object is given in Clark's book "The Quest for SS433" (1984). Thorough reviews of the state of observational and theoretical knowledge are given by Margon (1984) and Zwitter et al. (1989). The first optical position of the "star" was as an object in the catalogue of bright emission line sources by Stephenson & Sanduleak (1977). The first radio observations showed a compact source surrounded by an extended source, W50, believed to be a supernova remnant. At x-ray wavelengths Seward et al. (1976) noted a source, A1909+04 – later identified with SS433 – which appeared to vary with time and suggested an unusual origin.

The exceptional nature of this object became apparent as optical spectra were published. There appeared to be two sets of emission lines, one stationary and consisting of H and He from the central source, and a further set whose wavelength appeared to be changing with time. These are H Balmer and HeI lines and occur in pairs, equally red and blue-shifted. The origin of this behaviour is the Doppler shifting of a pair of lines because of the precession of a pair of jets. Several authors contributed to this conclusion (e.g. Fabian & Rees 1979; Milgrom 1979). The form of the Doppler shifting of the lines, expressed in terms of the red/blue shift was finally stated by Abell &

Margon (1979) as:

$$1 + z = \gamma(\pm v \sin\theta \sin\psi \cos(2\pi\phi) \pm v \cos\theta \cos\psi + 1) \tag{6.1}$$

where z is the redshift, $\gamma = (1 - v^2)^{-1/2}$, $v = 0.2601 \pm 0.0014$ is the speed of the jet in units of the speed of light, $\theta = 19.8° \pm 0.18°$ is the opening angle of the cone of precession, $\psi = 78.82° \pm 0.11°$ is the angle between the axis of symmetry of the cone and the line of sight, and $\phi = (t - t_0)/\tau)$ is the phase ($t_0 = JD2443505.6 \pm 0.5$, and the period, $\tau = 164$ days). Notice that the redshift is degenerate in ψ & θ, the opening angle and the angle of the jet to the line of sight. Neither is it apparent in which sense the jets are precessing. These uncertainties were finally fixed with the publication of radio maps of the jets showing the extended structure (Hjellming & Johnston 1981), although Begelman et al. (1980) had previously used the elliptical structure of the surrounding nebula to determine that the jet lay on a cone of half angle 17°, rather than on one of half angle 78°. The radio data were also used to determine the distance to SS433 as 5.1 kpc, through comparisons of the observed proper motion of clouds of radio emitting material with the known jet speeds of 0.26, from the kinematic model, assuming the radio emitting material has the same speed as the optically emitting material.

The kinematic model is a simple device which yields an explanation for the observations of moving emissions lines within the spectrum; it does not explain the physical mechanisms for producing the radiation, nor the origin of the precession of the beams, nor does it give any information on the nature of the central source. Fairly early on it was concluded that the motion of the beams was due to precession of an accretion disk from an orbiting companion star, surrounding a massive compact central object (Abell & Margon 1979). Alternatives such as rotation of the central source itself were dismissed as the energy carried by the jet is very much greater than that held by the rotating compact star. Although the kinematic model is very successful in explaining the basic motion of the lines, there are several deviations from the shifts that it predicts. Firstly there is a 6.28 day period oscillation superimposed upon the 164 day period with an amplitude $\sim$ 10% of the total amplitude (Katz et al. 1982). This is a consequence of the precession of the disk. The orbital period of the binary companion

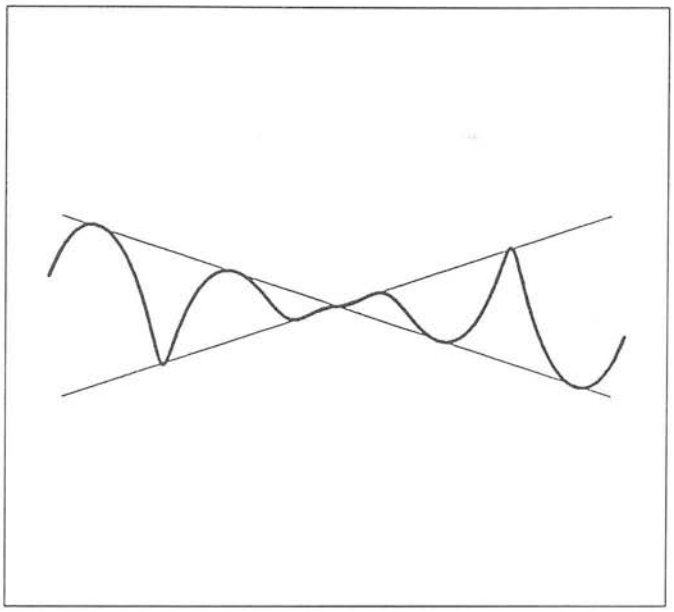

Figure 6.1: The kinematic Model of Abell & Margon (1979).

is 13.5 days and this will apply a torque, producing a periodic modulation of the signal at half the orbital period i.e. 6.28 days. Katz et al. also found a 5.8 day period within their data at a lesser amplitude. Finally Katz & Piran (1982) found an apparently random "jitter" which was independent of the phase of the observation. This implies that it is not a systematic variation of speed, but rather is a variation in the pointing of the jet. The amplitude of the variation of angle is of the order of the opening angle of each jet. It is seen simultaneously in both jets which implies that the beams are always in opposing directions within the motion.

The presence of jets in SS433 can be inferred from optical data, and the kinematic model. The extent of this line emitting optical part of the jet is of the order of a light hour ($\sim 10^{12}$m) which represents the typical timescales over which the radiation varies (Kopylov et al. 1986). Also changes in the line features are synchronous to within one day in the red-shifted and blue-shifted spectra (Margon 1984) putting an upper limit on the extent of this region. Furthermore, the line profiles can be exceedingly complex, which has been interpreted as being the result of a "clumpy" jet structure.

Authors such as Murdin et al. (1980) have described in detail events where individual lines appear to grow and then fade, being overtaken by another line at the frequency corresponding to the later velocity. Fabrika & Borisov (1987) followed the decay of a single component and deduced a length of 7×10^{12}m over which a component survives before being lost in the observational noise. One of the most convincing manifestations of the jets are the radio maps made with the VLA and MERLIN arrays (see e.g. Hjellming & Johnston 1981; Spencer 1984), which show extended radio knots. These appear to describe a corkscrew-like motion with time which agrees with the kinematic model. The agreement is startling, as the corkscrew motion was predicted two years prior to these maps in a different waveband. The radio emission from the jets is non-thermal with a spectral index $\alpha \simeq 0.65$ and is probably synchrotron in origin, as the polarizations are high ($\simeq 10\%$: Hjellming & Johnston 1981). The source varies over a period of 1–5 days (Johnston et al. 1981, 1984) but does not show periodicity, as the radio emission is extended and comes from all phases of the cycle. There is no evidence for correlated optical/radio variability (Ciatti et al. 1981).

The main mechanism for accelerating the jets to their speed of 0.26c which is discussed in the literature is radiative acceleration, the prime one being the "line-locking" mechanism of Milgrom (1979) whereby momentum from a continuum source is absorbed by the jet material. This method is only efficient up to momenta corresponding to the Lyman α limit, which results in jet speeds ~ 0.26. There are problems with this particular scheme, for example the jet material has to be cooler than 10^4K.

The nature of the central object is not yet entirely clear. It is expected that there is a compact object, either a neutron star or a black hole, because of the presence of x-ray emission. The main method used to choose between the possibilities is based on determining the central mass, M. Numerous authors have attempted this problem and have obtained varying results because of the various assumptions about the accretion disk, that are employed in their models. A detailed critique of these is given by Zwitter et al. (1989). The values the various authors find range from $1.4\,\mathrm{M}_\odot < M < 84\,\mathrm{M}_\odot$.

The central point of SS433 is situated near to the centre of a radio emitting nebula, W50 (Ryle et al. 1978). This emission is plerionic and has been classified as a supernova

remnant (Clark & Caswell 1976). Begelman et al. (1980) pointed out the alignment between the symmetry axis of the kinematic model and the major axis of the elliptical source structure, which established the connection with SS433. Furthermore, the kinetic energy output from the central source could be large enough to influence the evolution of the structure of W50. Königl (1983) has speculated that the strength of the energy output from the jet might in fact obviate the need for a supernova event to produce the nebula.

Many authors have speculated on there being some form of relationship between SS433 and extragalactic jets; that SS433 is a prototype of larger scale outflows (Davidson & McCray 1980). This hypothesis is appealing because of the information one could then obtain on the small scale details of jet production, acceleration and collimation. Indeed SS433 is the only such source which has admitted unambiguous determination of such parameters as jet speed and distance. There are several examples where the superluminal sources show motion which imply the direction of ejection is variable (e.g. Biretta et al. 1986). Rees (1982) has argued that the flow onto a compact object is governed by two parameters – the ratio of the luminosity to the Eddington luminosity, and the ratio of the cooling time to the dynamical timescale – and both these ratios are independent of the central mass; then one can simply scale down the flows. However, arguments about the central source do not mean that the jets are similar. As Zwitter et al. (1989) have pointed out, there are several important differences. For example, the optical radiation from SS433 is dominated by thermal emission, in extragalactic jets the emission is non-thermal in origin; the jets of SS433 are quite possibly ballistic, in extragalactic jets the opening angle can vary (and may well decrease) with distance from the central object. The synchrotron lifetime of the radiating electrons is much greater than the source lifetime in SS433, whereas in extragalactic sources the opposite applies. Thus, although the analogy between SS433 and the extragalactic sources is intriguing it is probably unwise to take it too far.

The synchrotron emission originates in a non-thermal distribution of electrons. From equipartition energy arguments, Hjellming & Johnston (1981) find an electron density $\sim 10^2 \mathrm{m}^{-3}$ in the extended radio components and a B-field of $10^{-6} - 10^{-7}$T, in-

dicating electron lifetimes of the order of $10^9 - 10^{11}$ secs. Clearly therefore synchrotron losses will not be important in influencing the radio flux, expansion losses will be the dominant loss mechanism and consequently these will be most relevant in modelling the distribution of the radio flux. When this is done it appears that simple two-dimensional expansion losses cause the flux to decay too rapidly. Spencer (1984) proposed two alternatives, either one-dimensional adiabatic expansion which requires an unusual source structure or, alternatively, a form of localized particle injection. Hjellming & Johnston (1988) also modelled the brightness distribution in detail and found that allowing continuous slowed expansion caused the jets to extend further out than is actually the case. The best fit came from a model with "slowed expansion" out to 10^{15}m, followed by conical free expansion; this is clearly rather ad hoc. It is the aim of this chapter to try to explain this behaviour in terms of the injection of fresh energetic electrons, and then to suggest several mechanisms which naturally account for the extent of the jets.

6.2 The Model

In this section a model of the radio jets in SS433 will be discussed. Material is ejected from the central object at a speed of $0.26c$. As the material moves away it expands in the two dimensions perpendicular to its direction of motion. It is assumed that its thickness remains constant. The direction in which materials is ejected continuously changes direction as was discussed in Section 6.1 and when the material from all elements is integrated it produces the characteristic helical pattern which is observed. In order to maintain the emission out to the observed distance with the assumed expansion some form of particle acceleration must take place within the jet. In this model, the acceleration takes place at a shock which propagates into the jet material driven by the density discontinuity. This is illustrated in Fig.6.2 where a portion of the jet is shown.

A preliminary result, the angle β, that the front surface of the jet makes with respect to the direction of flow of the jet is necessary. This is obtained by considering the relative positions of two elements of the jet emitted a small time, Δt, apart. It is

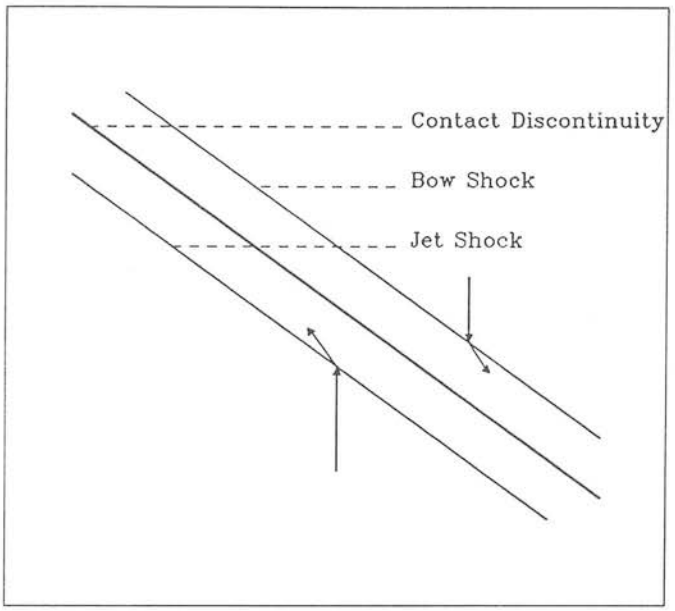

Figure 6.2: This shows the flow of fluid around the shocks, the bow shock which propagates out and the jet shock which moves back into the jet. The two regions are separated by a contact discontinuity.

then straightforward to show that:

$$\tan\beta = \frac{2\pi R \sin\psi}{v_j \tau} \tag{6.2}$$

where R is the distance from the source and $v_j = 0.26c$ is the jet velocity, shown in Fig 6.2. Hence the angle β increases as one moves away from the central source, and the front surface becomes progressively less oblique.

Next it is postulated that a shock is driven through the jet material and this shock acts as a site for particle acceleration. In order to find the point where the process of particle acceleration ceases it is necessary to obtain expressions for the speed of the shock into the jet in terms of the density of the fluids. What follows is a simple analysis of the jump conditions at an oblique, non-relativistic hydrodynamic shock. This may oversimplify the problem, but it does at least result in relatively simple conclusions. The jump conditions are:

$$[\rho v_x] = 0.0 \tag{6.3}$$

$$\left[P + \rho v_x^2\right] = 0.0 \tag{6.4}$$

$$[\rho v_x v_y] = 0.0 \tag{6.5}$$

$$\left[w + v^2/2\right] = 0.0 \tag{6.6}$$

v_x is the fluid velocity parallel to the shock normal, v_y is the velocity perpendicular to the normal, P is the pressure, ρ the density and w the enthalpy. Furthermore it is assumed that the material, both ahead of the bow shock and inside the jet is relatively cold and has an adiabatic index $\Gamma = 5/4$ throughout.

The next stage is to solve the jump conditions. Assuming a strong hydrodynamical shock then in the shock frame one has $v_{1x} = 4v_{2x}$, $\rho_1 = \rho_2/4$, $v_{1y} = v_{2y}$ and $P_2 = 3v_{2x}^2\rho_2$, where the subscript 1[2] refers to the upstream [downstream] region and x[y] to components of velocity parallel [perpendicular] to the shock normal. From now on denote quantities measured in the external, ambient medium with a subscript e, and quantities measured in the jet frame with a subscript j. At the contact discontinuity the pressure and parallel component of velocity is continuous while there may be an arbitrary velocity jump perpendicular to the contact discontinuity normal (see e.g. Courant & Friedrichs 1948). The problem is solved by relating these known velocities and noting that in the frame of the ambient medium the jet material is moving at $0.26c$. From the frame of the ambient medium there is a bow shock (subscript b) propagating at $\mathbf{v_4} = (v_{bx}, v_{by})$ and a region downstream of this moving at $\mathbf{v_3} = (3v_{bx}/4, 0)$ (n.b. the perpendicular velocity is continuous in the hydrodynamical limit). At the contact discontinuity material on the jet side will be moving at $\mathbf{v_2} = (3v_{bx}/4, v_y)$, the perpendicular velocity being unknown for the reason given above. At the jet shock the pressure can be eliminated as it is assumed constant at the contact discontinuity. Employing the superscript j to refer to quantities measured in the frame of the jet shock the jump conditions at the shock can be solved to give $\mathbf{v_1^j} = (v_{bx}(\rho_e/\rho_j)^{1/2}, v_{1y}^j)$ and $\mathbf{v_2^j} = (0.25v_{bx}(\rho_e/\rho_j)^{1/2}, v_{2y}^j)$. One can now simply add the velocities to find that the velocity of the material upstream of the jet shock i.e. the jet material has a velocity $\mathbf{v} = \mathbf{v_1^j} - \mathbf{v_2^j} + \mathbf{v_2}$. It is known that this is equal to 0.26. These are used to obtain v_{bx}

and hence the speed of the jet shock through the jet:

$$v_{1x}^{j} = \frac{4v\sqrt{\frac{\rho_e}{\rho_j}}\sin\beta}{3\left(1+\sqrt{\frac{\rho_e}{\rho_j}}\right)} \tag{6.7}$$

and similarly the unknown velocity v_y above. This quantity increases with distance out from the central source, as $\sin\beta$ also varies according to equation 6.2. As the jet material moves out the shock becomes less oblique. Another factor which will influence the shock velocity is the variation of density, either of the ambient or jet material. Expansion of the jet, if it occurs, will cause ρ_j to decrease and hence v_{1x} will increase. In order to include density changes in the work, the quantity $\sqrt{(\rho_e/\rho_j)}$ will be replaced by $r \equiv R^a\sqrt{(\rho_{e0}/\rho_{j0})}$.

This value for the shock speed will not be exactly correct for a number of reasons. The assumption that the shock is strong may not be valid; this is most likely to be the case in the inner regions of the jet where there is x-ray emission from an accretion disk to heat the jet material. It is in this region ($\leq 10^{13}$m from the centre) that the Balmer and HeI emission lines originate, from the shocked ambient medium in the model of Begelman et al. (1980). Observations show that the material is likely to be clumpy, thus the shock will not be steady. Whether or not this clumpiness affects the problem to any marked extent is uncertain as evidence for clumps in the outer regions of the source is lacking owing to the fact that the optical emission dies away after approximately 1 light day (Fabrika & Borisov 1987). Secondly, even if the shock settles down to a steady state, the jet surface is not planar, but curved, as is the shock front. These factors affect the shock speed and structure but it is assumed that they result in minor corrections and that equation 6.7 is still valid, at least in the extended parts of the source, $\sim 10^{15}$m away from the central object.

Thus it has been shown that a shock can propagate through the jet, possibly acting as a site for Fermi acceleration. In the inner regions, where the shock is highly oblique, but not moving relativistically, the electrons will produce synchrotron radiation with a spectrum $\alpha \simeq 0.5$ (Bell 1978), although this will be subject to the provisos mentioned above; a weaker shock is less efficient in accelerating electrons and would therefore

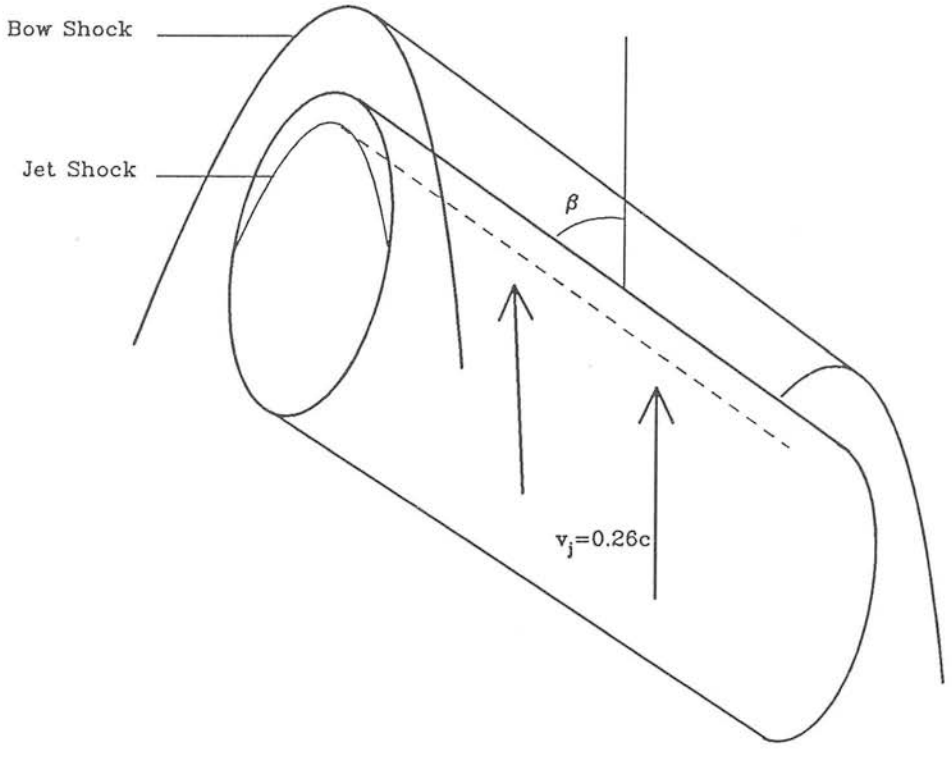

Figure 6.3: Schematic representation of the model for SS433. The bow shock propagates into the interstellar medium. Fermi acceleration occurs at the inner shock, propagating back into the jet. β is the angle between the direction of motion of the jet and the front surface of the jet.

result in a steeper spectral index. This value for the spectral index is close to that which is actually observed ($\alpha \simeq 0.65 \pm 0.1$ Hjellming & Johnston 1981), which changes with time. This could be a consequence of inhomogeneities in the ambient medium, although it is usually interpreted as being independent optically thick flaring events (Seaquist et al. 1982). Secondly, it can also account for the decay in brightness of the jet without it being necessary to appeal to unusual geometries. Fermi acceleration provides a method of extending the range of the source because it effectively acts to inject fresh electrons continuously. Having provided a natural method of extending the source radiation, the problem of cutting off the jets remains; this will be addressed in the following section.

Finally, note that it is only the jet shock which will act as the site of particle acceleration because the synchrotron radiation defines a corkscrew motion. If there were synchrotron emitting electrons in the ambient medium which had been accelerated by the bow shock this would not be observed because the synchrotron lifetimes are considerably greater than the 164 day period of the precessional motion. One can then conclude that in this model the fluid must flow around the jet downstream of the bow shock without having time to be accelerated.

6.3 Limitations on the extent of the Jets

In the previous section it was shown that the jets in SS433 could plausibly act as a site for first order Fermi acceleration of electrons and these could give rise to the observed radio emission. It has already been noted however that, at some point, it is necessary to incorporate some mechanism whereby the emission can drop off more rapidly than would be predicted with acceleration included i.e. a method of disrupting the acceleration process must also be found; this is the purpose of this present section where three possible alternatives will be considered separately.

6.3.1 Superluminal Shocks

Superluminal shocks cannot accelerate electrons. In this model of SS433 the parallel shock speed increases with distance from the central source and therefore there will be a point where the velocity through the jet increases to a value where the point of intersection of a field line and the shock front moves at a speed greater than c if the magnetic field parallel to the motion decreases as the jet expands. At this point the electrons located downstream of the shock will be unable to recross the shock and further particle acceleration will be suppressed. An estimate of the distance at which the shock becomes superluminal can be obtained by assuming that as the jet moves outwards it expands so that the magnetic field parallel to the direction of motion drops off as R^{-2}, while the magnetic field perpendicular to the motion, i.e. along the jet, drops off as R^{-1} under the assumption that the flux is frozen-in. Thus, far away from the centre it is the field along the jet which dominates. The angle between this direction and the shock velocity along the shock normal is β and then the point at which the shock becomes superluminal can be obtained by setting the shock speed equal to $c\cos\beta$. One obtains:

$$R_s = \frac{3\tau(1+r)}{8\pi r \sin\psi} \tag{6.8}$$

r can be a function of R. For the case where the density of the ambient medium drops off as R^{-2} with the jet expansion, r is constant and equation 6.8 is correct as it stands, but if it is constant with R, equation 6.8 reduces to a quadratic. The points at which this occurs are illustrated in Fig 6.4 and Fig 6.5, together with the variation in the superluminal point as a function of the density ratio for the two possibilities for the change of density with R considered here.

6.3.2 Shock passing through the jet

A second method which may suppress the acceleration mechanism is if the shock passes through the jet entirely, at which point there will be no more electrons to accelerate. In trying to obtain an estimate of the distance from the central source at which this

occurs, it will be necessary to make a number of assumptions about the thickness of the jets. The first requirement is an estimate of the opening angle of the jet. The jitter in the optical lines reported by Katz & Piran (1982), has an r.m.s. amplitude which corresponds to a variation in opening angle of $\simeq 0.05$ radians. Secondly, there is other optical data from authors such as Murdin et al. (1980) that suggests new optically emitting clouds appear roughly once a day. Thus they will subtend an angle $2\pi/164 \sim 0.04$ radians $\equiv \alpha$ at the source and the number of clouds emitted over an entire period will be $2\pi \sin\psi/\alpha$. Thus one estimate of the jet thickness will be simply the distance a cloud travels during the period it dominates the emission $L = v_j \tau \alpha / 2\pi \sin\psi$. It is now assumed that these inferences from the optical data can be applied directly to the radio jets. To obtain a distance at which the shock passes through the jet, one must satisfy the condition that $L = \int_0^t v_{1x}^j(t')dt'$. In the case where r is constant, one obtains $R_c = 3(1+r)L/(4r)$, otherwise the appropriate distance can be found numerically. The points at which this occurs are illustrated in Fig 6.4 and Fig 6.5 together with the variation in the shock passage point as a function of the density ratio for the two possibilities for the change of density with R considered here. This point generally occurs much nearer the central source than the point at which the shock becomes superluminal.

6.3.3 Kelvin–Helmholtz Instabilities

The fact that there is a contact discontinuity in the problem means that there is a possibility of Kelvin–Helmholtz instabilities being important. These occur whenever there is a boundary between two fluids, moving with different transverse velocities. An introduction to the role they play in astrophysical jets is given by Begelman et al. (1984). The topic of Kelvin–Helmholtz instabilities has received most attention from those attempting to understand extragalactic radio jets (e.g. Norman et al. 1983). In the linear regime (Blake 1972) the relative motion of two fluids results in transverse waves in the jet material. As the instability develops, the amplitudes of the waves grow until they become comparable with their wavelength and the nonlinear regime is reached. Whether or not the instability disrupts the jet is not clear. In order for the

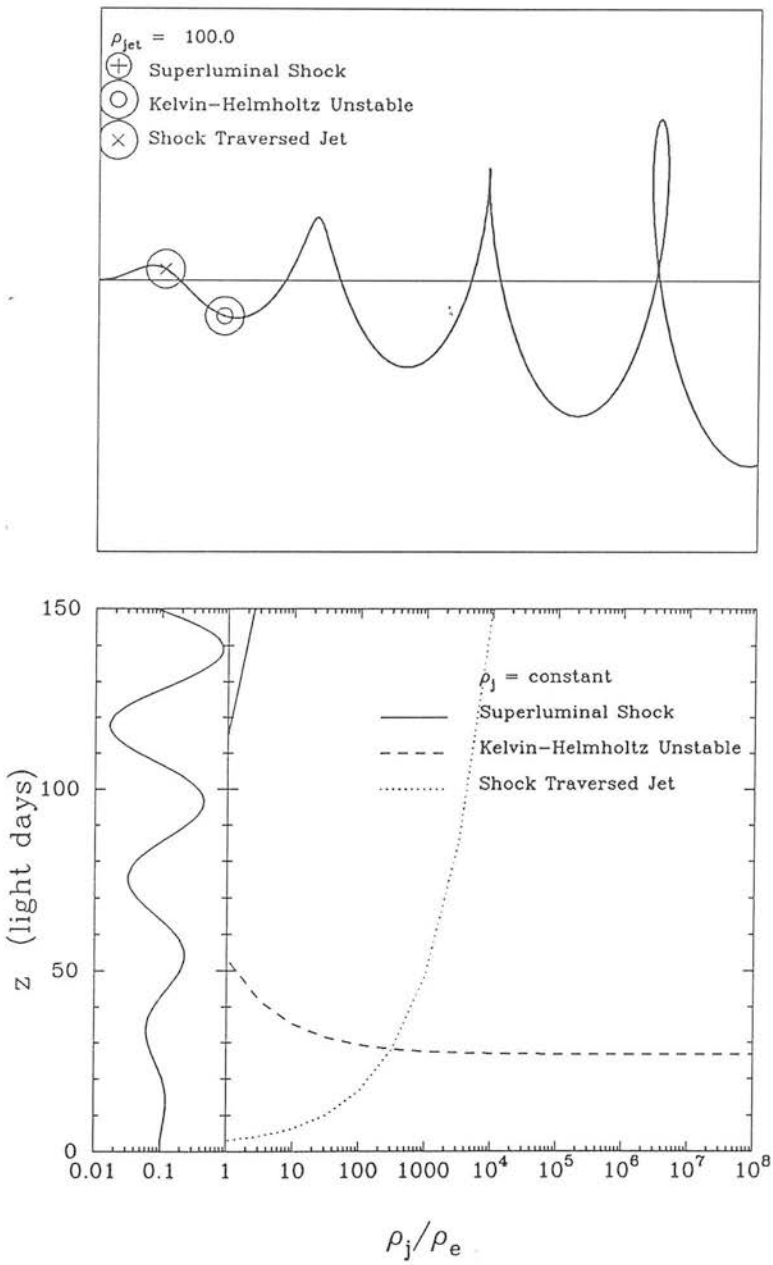

Figure 6.4: This shows the points where the three possible mechanisms discussed in the text come into operation. The density is assumed constant with distance from the source.

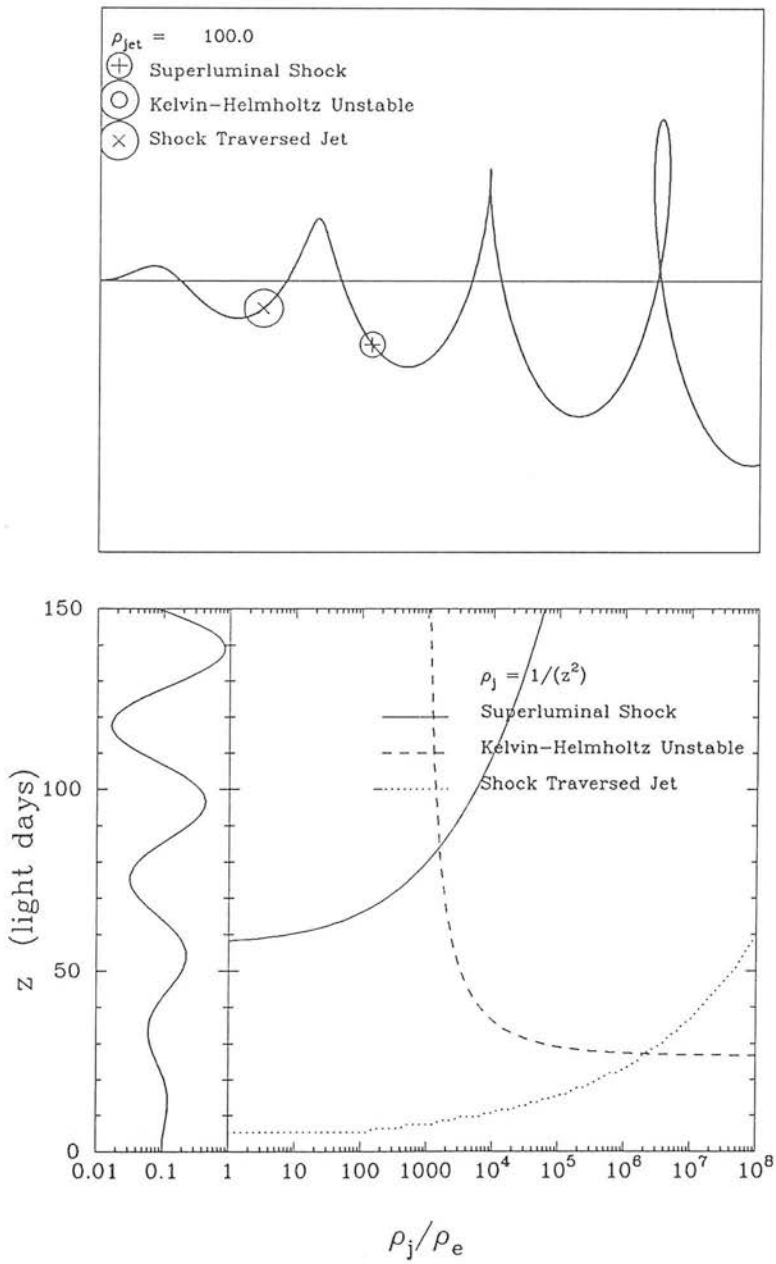

Figure 6.5: This shows the points where the three possible mechanisms discussed in the text come into operation. The density is assumed to decay with distance squared from the source.

instability to be allowed to grow perturbations must occur at a boundary where the relative transverse velocity is subsonic in the less dense fluid. In the model here the transverse velocity is initially supersonic until a point, R_{KH} where it becomes subsonic. This point can be estimated as follows: the sound speed in the shocked ambient medium is $c_s = \sqrt{5}v_{bx}/4$ and the relative transverse velocity is $v_j \cos\beta$ (the transverse velocity of the fluid is zero on the ambient side). Thus, equating $v_j \cos\beta$ to c_s, one obtains:

$$R_{KH} = \frac{3(1+r)v_j\tau}{\sqrt{52}\pi \sin\psi} \tag{6.9}$$

Again, the problem is straightforward for the alternative case where the density ratio, r, is a function of R. The points where the instability may occur are marked on Figs 6.4 and 6.5. Although this is where the instability may first occur, Begelman et al. (1984) make the point that if there is a high density ratio, the waves will move with the denser fluid, in this case the jet. Thus the waves could travel with the jet even further out before growing large enough to affect particle acceleration.

6.4 Discussion

It has been shown that a shock propagating through a jet could be the site of Fermi acceleration of electrons and the resulting spectrum can explain the non-thermal radio emission from the object SS433. In the picture of the jets presented here there are at least three mechanisms which may act to suppress the particle acceleration. It has been shown that these can occur at distances from the central source comparable in scale to those at which the radio knots commence a more rapid expansion according to Hjellming & Johnston (1988). Firstly, there is the point where the shock becomes superluminal and electrons can no longer make repeated shock crossings. This occurs at large distances from the source, farther out than the other two mechanisms considered here. An assumption was made in deriving this distance, that the magnetic field perpendicular to the motion of the jet dominates at large distances from the source; the results are not heavily dependent upon this assumption because if the magnetic field were more isotropically distributed then the angle between the shock normal and the

magnetic field would decrease in general and the superluminal point would be pushed still further out.

Secondly, the possibility that the shock passes completely through the jet was considered. A value for the jet opening angle, taken from optical data, was assumed for this section. If this upper limit is reduced then so is the jet thickness and the point at which the shock passes through the jet moves towards the central source. In any case, this effect occurs closer to the centre than a superluminal shock. Exactly what happens when the shock passes through the jet is open to speculation. The acceleration mechanism will cease whilst the jet continues expanding so that the emission dies off rapidly, in common with Hjellming & Johnston (1988). However the non-luminous material carrying kinetic energy will continue to move outwards and will eventually interact with the W50 nebula, as mentioned in the introduction, which is on a much larger scale ($\sim 2 \times 10^{18}$m, Geldzahler et al. 1980).

Finally, the possibility of Kelvin–Helmholtz instabilities being important in disrupting the jet structure was mentioned. The problem was simplified by the assumption that the instability does not grow for supersonic relative transverse velocities and the point where the transverse velocity becomes subsonic was derived as the point where the instability may start to grow. This point depends upon the density ratio in a different form to those mechanisms discussed previously, and as the jet density increases the distance at which this occurs lessens. The question of the ultimate fate of the jet was left open as it will depend upon the behaviour of the instability in the non-linear regime.

It should be noted that the results are a function of the density ratio. Several estimates of the jet or ambient number densities have been made in the literature. In the external medium, estimates of the density have been based upon different techniques. Spencer (1984) determined it to be $\leq 10^4 \mathrm{m}^{-3}$, by balancing the ram pressure with the internal pressure of the jet. On the other hand Faraday depolarization measurements within the remnant as a whole suggest a higher density, $3 \times 10^5 \mathrm{m}^{-3}$ (Downes et al. 1981) or Hjellming & Johnston (1981) find $3 \times 10^6 \mathrm{m}^{-3}$ on the evidence of a 90° Faraday rotation measure between the lobes of SS433. Assuming the density in the external

medium declines proportional to R^{-2}, then this implies a density $\sim 10^4$ times greater at 10^{13}m from the core. Determinations of the internal density at this distance are based upon optical observations and these depend upon whether one includes the effects of the denser clumps. Begelman et al. (1980) use an average density of $10^{14}\mathrm{m}^{-3}$. This yields an estimate of the jet–ambient density ratio of the order of 10^4.

From Fig. 6.5, one can see that a jet–ambient density ratio $> 10^3$ is required in order to maintain the particle acceleration out to the observed distance of approximately one wavelength of the oscillation, assuming an ambient density which decreases $\propto R^{-2}$. To summarize then, it is possible that the brightness of the jet in SS433 is sustained by a shock acting as a site of rapid particle acceleration, which acts to inject fresh electrons continuously and, after employing parameters derived from radio and optical observations, the observed brightness decrease is most probably due to the shock having passed completely through the jet.

Chapter 7

Summary

7.1 Conclusions

The aim of this thesis was to present a study of what is known at present of the emission properties of blazars and to produce feasible methods for combining the theory with observations which are, or will shortly be possible. A series of observations of blazars were presented in Chapter 2. These were taken during 1988 and were combined with the data taken during three previous observing runs in 1986 and 1987. All observations were made using the Hatfield polarimeters (Mk I & II), the Mk II version being capable of taking simultaneous photometric and polarimetric measurements in five optical and a single infra-red wavebands; this is the best instrument currently available for such observations. The data displayed rapid variability of flux, polarization and position angle, high and frequency dependent polarizations. This is the largest single data set yet constructed at these wavelengths and allows the properties of the sample as a whole to be deduced. The results showed that several correlations between observational properties which had previously been reported were in fact actually consequences of selection effects. In general the observations can be summarized by stating that no correlations were found. This, together with the characteristic timescales of variability, the range of spectral indices observed, and the degree of frequency dependence of polarization can act as useful constraints for blazar models.

Throughout the remainder of the thesis more theoretical work was presented. In Chapter 3 the process of Fermi acceleration was introduced. In many cases the magnetic field at the shock front is expected to be oblique to the shock normal. This can severely modify the compression ratio at the shock front if the jump conditions are solved

correctly, and this in turn can affect the spectral index of the accelerated electrons (or positrons). In that chapter a method was employed which allowed for considerable simplification in solving the jump conditions i.e. the problem was transformed to the "de Hoffmann–Teller" frame where the fluid runs parallel to the magnetic field at all points. This method has the advantage that it naturally eliminates the electric field from the problem and the disadvantage that it cannot provide solutions in the case where the magnetic field lines intersect the shock front at a speed greater than the speed of light. The method is justified however as one is interested in Fermi acceleration, a process which can only occur at subluminal shock fronts. The jump conditions were then solved using an equation of state corresponding to a variety of downstream conditions. From the results of this the spectral indices of the accelerated electrons were calculated using two methods, the Q_J method of Kirk & Heavens (1989) and a Monte Carlo method. There was good agreement between the two methods and this can be regarded as independent confirmation of Kirk & Heavens' result although it does not go so far as to question their initial assumption of conservation of the magnetic moment of the electron as it crosses the shock front. The work assumed throughout that the electron spectrum is generated within the compact source despite the suggestion of some authors that superluminal shocks could also be important in boosting the energy of a pre-existing power law electron distribution. Oblique shocks were seen to have the ability to produce a wide range of spectral indices according to value of the Alfvénic Mach number. This is in accordance with the observations particularly when losses to the spectrum are taken into account. It is important that it can explain the range of spectral indices seen, although it does not necessarily imply a simple observational test because the relationship between the shock obliquity (position angle), electron number density, field strength (luminosity) and spectral index is not a simple one.

Chapter 4 presented a study of the high frequency polarization of synchrotron radiation. At optical frequencies the variability timescales suggest radiative lifetimes of the order of days for the emitting electrons so that radiative losses may well modify the naïve assumption of a simple power law distribution. The form of the polarization expected as a result of these losses was calculated numerically by integrating the expected radiation from an element over magnetic flux over a chosen field geometry. Two as-

sumptions about the electrons were examined in turn, in the first case it was assumed that as the spectrum evolves the distribution becomes anisotropic and it was found that this can cause quite large position angle rotations. Secondly the opposite extreme was taken i.e. that the electron changes pitch angle on a timescale much less than the radiative lifetime and the electron distribution remains isotropic as losses progressively alter the spectrum. This leads to frequency dependent polarization as in the first case but not to any dependence of the position angle upon frequency. It may well be that a true picture is some way intermediate between the two limits but the aim was to illustrate the extremes so this possibility was not explored further. Several predictions were made about the polarization around the break. However no observations have yet been made which can serve as useful constraints to the model although on occasions position angle swings which are qualitatively similar have been observed. This is quite promising for future observations at submillimetre wavelengths and also suggests the model could progress further by allowing for the possibility of a less homogeneous field structure. An example of an oft cited ad hoc model for the optical emission – the multi-component model of Moore et al. (1982) was discussed in this chapter. It was logically developed by including a form of a high frequency cutoff to the electron number density. Then it was shown that broadly speaking such a model could qualitatively reproduce the observations of a large sample of blazars such as had been presented.

Chapter 5 looked at the important problem of Fermi acceleration in an inhomogeneous magnetic field. This was constructed from vector potentials in a box consisting of 64 grid points on each side. The large angle scattering of electrons in the magnetic field was followed by monitoring particle trajectories on either side of the shock front. Despite the limitations of finite computing time spectra were produced with satisfactory signal to noise over two or more decades in momentum. A strong hydrodynamic shock front could produce a range of spectral indices for varying shock speeds. Overall it was found that without the general assumption of a preferred magnetic field orientation the Fermi mechanism is an efficient method for the production of non-thermal power law electron distributions. An obvious question is whether this could be combined with the work of Chapter 4 to obtain the expected modifications to the spectrum as electrons were accelerated. One could then obtain distributions with the correct degree of

anisotropy. However this is not a realistic proposition at present owing to the rather limited dynamic range of the spectra.

Chapter 6 was concerned with the well known Galactic object SS433. This is an object which has been widely regarded as a key to an understanding extragalactic jets. It shows a precessing jet which is visible at radio wavelengths out to approximately 1.2λ from the central source. An oblique shock of the type mentioned in chapter 3 was suggested as providing the necessary site for acceleration in the jet. From this one can deduce various other properties of the jet such as where one would would expect the acceleration to cease due to various mechanisms which may be operative to quash the particle reacceleration. It was found that by employing a $\rho \sim r^{-2}$ density law and a jet opening angle obtained from observations, that a shock will have propagated though the width of the jet. This can then provide a natural explanation for the extent of the radio emission without recourse to "slowed expansion" as had previously been suggested.

7.2 Further Work

As with any research, questions remain to be answered, assumptions challenged and observations completed. Despite the fact that this is the final in a succession of four theses to have been presented on the topic of blazars at Edinburgh in the past ten years there is still more work than ever to be done, both theoretically and observationally.

An example of the theoretical work to be completed is to explore the assumption that the distribution of electrons is independent of gyrophase in the work on the Fermi acceleration mechanism at an oblique shock in Chapter 3. As was discussed at the time this assumption is known to be valid only for nearly parallel shocks, at more oblique orientations of the magnetic field it breaks down and at this point the Monte Carlo simulation method presented in that chapter becomes incorrect as it no longer treats the shock crossing correctly. In that situation, one finds it necessary to follows the particle trajectories exactly – the behaviour of the particle at the shock depends upon

it's gyrophase. A possible method of tackling this problem was produced in Chapter 5, except in that case the field had no preferred direction. A solution is trivial, reducing the value of the magnetic field at each grid point in these simulations and adding a constant oblique component of the desired magnitude allows one to investigate the problem directly. Using such a method loses accuracy in the spectrum, following each particle in detail requires more computing time, and this means fewer particles take part in the simulation in practice.

In the limit where the Monte Carlo technique is still valid it can be a very powerful tool. In the field of relativistic shocks there are many problems yet to be solved. An example is time dependent acceleration. By injecting the particles into the simulation at a random time up to some given maximum value, and generalizing the method given in Chapter 3 by using the full, time-dependent transport equation, the problem can be solved for injection with a step function profile at a fixed initial momentum. The solution is shown in Fig 7.1a. This compares with the non-relativistic case of step function injection which can be solved analytically and which is shown in Fig 7.1b. Employing a little more CPU time and binning the particles in time as they cross the shock front, one could solve the problem with a δ function injection, and any given initial energy spectrum.

Regarding the work in Chapter 5, more computing power would be useful in extending the dynamic range of the simulations, presently little more than two orders of magnitude and also the size of the box, which acts to effectively limit the maximum momentum gain during the process. This would put the conclusions, particularly those based on determinations of spectral indices on a more secure basis. It would also be desirable to have a greater physical basis on which to make the assumptions employed in constructing the realizations of the magnetic field.

The basic first order Fermi mechanism has remained essentially unchanged since its elucidation 13 years ago. Though the spectral indices or the form of the distribution function obtained may change as each approach to the problem is developed, what one is endeavouring to do is to show that in each new, hopefully more realistic situation, the Fermi mechanism does indeed still operate and remains (or must be challenged as)

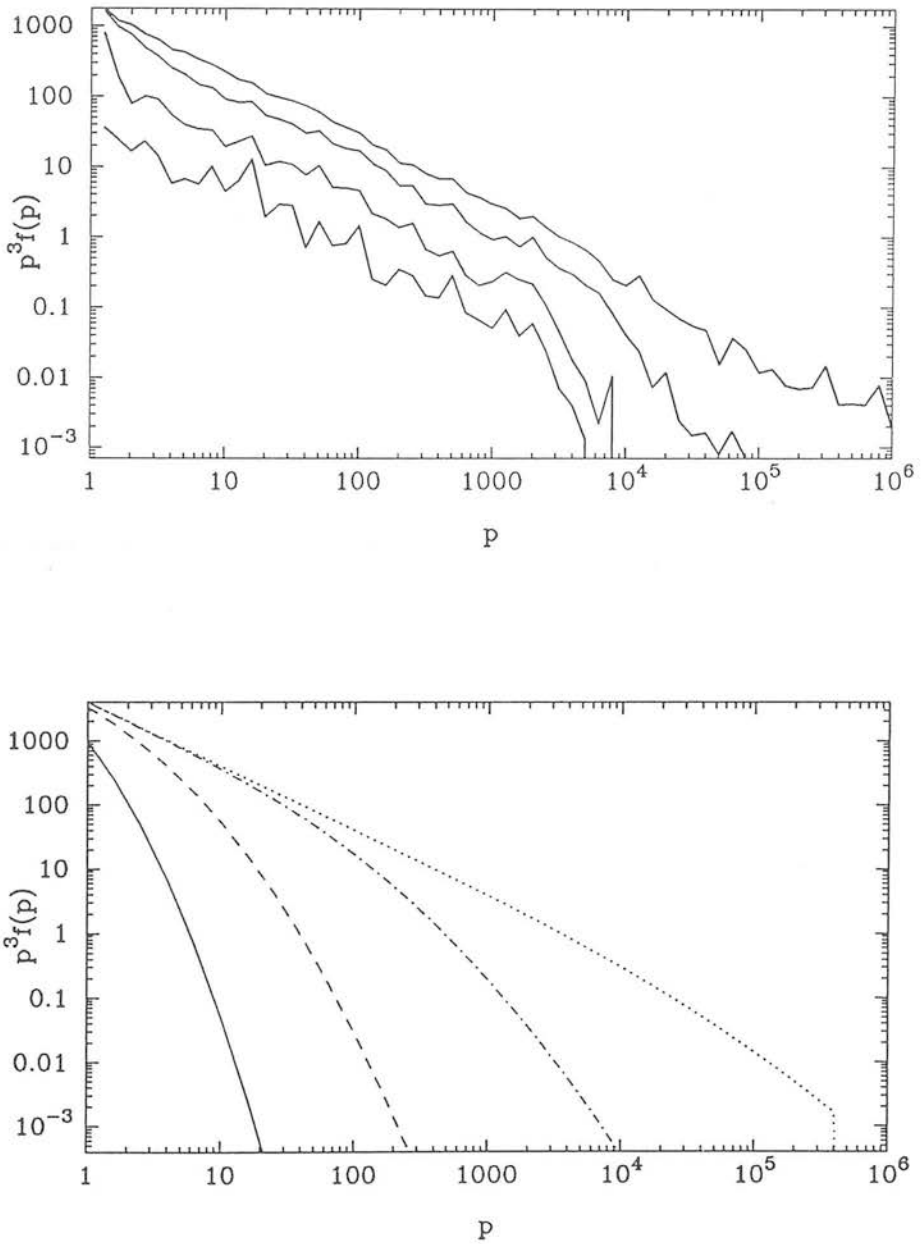

Figure 7.1: Time dependent Fermi acceleration. The top figure show the results for a shock of speed $\beta = 0.4$, compression ratio 4, using the Monte Carlo method outlined in Chapter 3, the bottom figure shows the non-relativistic result for a shock speed $\beta = 0.1$ with the assumption that κ_i/u_i^2 is constant where κ is the spatial diffusion coefficient (Drury 1983).

the prime candidate for providing an origin for the non-thermal electrons or positrons responsible for the synchrotron emission. The work of Chapter 5 shows that this position remains unchallenged even though the magnetic field may have no preferred direction ahead of the shock.

Observationally the future could be equally promising. The work of Chapter 4 showed that the high frequency polarization and in particular its variability properties could in principle tell one much about the emission region and the timescales over which the electrons are re-isotropized. In that chapter a single, rather speculative model was developed for the high frequency polarization of these sources. The conclusion seemed to be that one could not differentiate between the two possibilities put forward there without observation of the polarization at wavelengths longer than K, around the break frequency. These observations have not yet been made, but the "Aberdeen polarimeter", at present undergoing final tests on the JCMT could make such observations to determine the submillimetre polarization around the break. Detailed observations of a single flaring event could then yield invaluable information on the form and evolution of the electron distribution. These observations would be co-ordinated with simultaneous optical/infra-red measurements by prudent observers since this is where one would expect the evolution to be fastest. One could also obtain information on the relationship between the radio and optical emitting regions quite apart from testing specific models such as that which was the subject of Chapter 4.

References

Abell, G.O. & Margon, B., 1979. *Nature,* **279**, 701.

Abromowicz, M. & Stegun, I.A., 1965. *Handbook of Mathematical Functions*, National Bureau of Standards: Washington, DC.

Achterberg, A., 1988. *Mon. Not. R. astr. Soc.,* **232**, 323.

Achterberg, A., Blandford, R.D. & Periwal, V., 1984. *Astr. Astrophys.,* **132**, 97.

Alfvén, H., 1981. *Cosmic Plasma*, Dordrecht: Reidel.

Aller, H.D., Aller, M.F., Latimer, G.E. & Hodge, P.E., 1985. *Astrophys. J. Suppl.,* **59**, 513.

Aller, H.D., Hodge, P.E. & Aller, M.F., 1981. *Astrophys. J.,* **248**, L5.

Aller, H.D. & Olsen, E.T., 1971. *Astron. J.,* **76**, 671.

Altschuler, D.R. 1989. *Fund. Cosmic Phys,* **14**, 37.

Altschuler, D.R. & Wardle, J.F.C., 1977. *Mon. Not. R. astr. Soc.,* **179**, 153.

Angel, J.R.P. & Stockman, H.S., 1980. *Ann. Rev. Astron. Astrophys.,* **18**, 321.

Antonucci, R.R.J. & Ulvestad, J.S., 1985. *Astrophys. J.,* **294**, 158.

Appl, S. & Camenzind, M., 1988. *Astr. Astrophys.,* **206**, 258.

Axford, W.I., Leer, E. & Skadron, G., 1977. *Proc. 15th Int. Cosmic Ray Conf.*, Plovdiv.

Bailey, J.A. & Hough, J.H., 1982. *Publs astr. Soc. Pacif.,* **94**, 618.

Bailey, J.A., Hough, J.H. & Axon, D.J., 1983. *Mon. Not. R. astr. Soc.,* **203**, 339.

Ballard, K.R., 1989. *Variability of Active Galaxies*, Ed Meisenheimer, K., Springer–Verlag: Heidelberg.

Ballard, K.R. & Heavens, A.F., . *Mon. Not. R. astr. Soc.,* **1991**, in press.

Ballard, K.R., Mead, A.R.G., Brand, P.W.J.L., Hough, J.H., Bailey, J.A. & Brindle, C., 1989. *BL–Lac Objects: 10 Years After*, Eds Maraschi, L., Maccaro, T. & Ulrich, M–H. Springer–Verlag: Berlin.

Ballard, K.R., Mead, A.R.G., Brand, P.W.J.L. & Hough, J.H., 1990. *Mon. Not. R. astr. Soc.,* **243**, 640.

Barford, N.C., 1967. *Experimental Measurements: Precision, Error & Truth*, Addison–Wesley: London.

Begelman, M.C., Blandford, R.D. & Rees, M.J., 1984. *Rev Modern Physics,* **56**, 255.

Begelman, M.C. & Kirk, J.G., 1990. *Astrophys. J.,* **353**, 66.

Begelman, M.C. Sarazin, C.L., Hatchett, S.F. & McKee, C.F., 1980. *Astrophys. J.,* **238**, 722.

Bell, A.R., 1978a. *Mon. Not. R. astr. Soc.,* **182**, 147.

Bell, A.R., 1978b. *Mon. Not. R. astr. Soc.,* **182**, 443.

Bessell, M.S., 1979. *Pub. A.S.P.,* **91**, 589.

Biermann, P.L. & Strittmatter, P.A., 1987. *Astrophys. J.,* **322**, 643.

Biraud, F. & Véron, P., 1968. *Nature,* **219**, 254.

Biretta, J.A. & Cohen, M., 1987. *Superluminal Radio Sources*, Eds Zensus, J.A. & Pearson, T.J. Cambridge University Press.

Biretta, J.A., Moore, R.L. & Cohen, M.H., 1986. *Astrophys. J.*, **308**, 93.

Björnsson, C.-I., 1982. *Astrophys. J.*, **260**, 855.

Björnsson, C.-I., 1985. *Mon. Not. R. astr. Soc.*, **216**, 241.

Björnsson, C.-I. & Blumenthal, G.R., 1982. *Astrophys. J.*, **259**, 805.

Blake, G.M., 1972. *Mon. Not. R. astr. Soc.*, **156**, 67.

Blandford, R.D., 1979. *Particle Acceleration Mechanisms in Astrophysics, Proc. A.I.P. Conf.*, No. 56, p. 335.

Blandford, R.D., 1980. *Astrophys. J.*, **238**, 410.

Blandford, R.D. & Eichler, D., 1987. *Phys. Reports.* , **154**, 1.

Blandford, R.D. & Königl, A., 1979. *Astrophys. J.*, **232**, 34.

Blandford, R.D. & Ostriker, J.P., 1978. *Astrophys. J.*, **221**, L29.

Blandford, R.D. & Rees, M.J., 1978. *Pittsburgh Conference on BL-Lac Objects*, Eds Wolfe, A.M. University of Pittsburgh Press.

Borra, E.F. & Corriveau, G., 1984. *Astrophys. J.*, **276**, 449.

Bregman, J.N., 1985. *Astrophys. J.*, **288**, 32.

Bregman, J.N., 1990. *Astron. Astrophys. Rev.*, **2**, 125.

Bregman, J.N., Lebofsky, M.J., Aller, M.F., Rieke, G.H., Aller, H.D., Hodge, P.E., Glassgold, A.E. & Huggins, P.J., 1981. *Nature*, **293**, 714.

Bregman, J.N., Glassgold, A.E., Huggins, P.J., Neugebauer, G., Soifer, B.T., Matthews, K., Elias, J.H., Webb, J.R., Pollock, J.T., Pica, A.J., Leacock, R.J., Smith, A.G., Aller, H.D., Aller, M.F., Hodge, P.E., Dent, W.A., Balonek, T.J., Barvainis, R.E., Roellig, T.P.L, Wisniewski, W.Z., Rieke, G.H., Lebofsky, M.J., Wills, B.J., Wills, D., Ku, W.H.M., Bregman, J.D., Witteborn, F.C., Lester, D.F., Impey, C.D. & Hackwell, J.A., 1986. *Astrophys. J.*, **301**, 708.

Bregman, J.N., Glassgold, A.E., Huggins, P.J., Kinney, A.L., McHardy, I., Webb, J.R., Pollock, J.T., Leacock, R.J., Smith, A.G., Pica, A.J., Aller, H.D., Aller, M.F., Hodge, P.E., Miller, J.S., Stephens, S.A., Dent, W.A., Balonek, T.J., Barvainis, R.E., Neugebauer, G., Impey, C.D., Soifer, B.T., Matthews, K., Elias, J.H. & Wisniewski, W.Z., 1988. *Astrophys. J.*, **331**, 746.

Bregman, J.N., Glassgold, A.E., Huggins, P.J., Neugebauer, G., Soifer, B.T., Matthews, K., Elias, J.H., Webb, J.R., Pollock, J.T., Leacock, R.J., Smith, A.G., Aller, H.D., Aller, M.F., Hughes, PA., Maccagni, D., Garilli, B., Giommi, P., Miller, J.S., Stephens, S., Balonek, T.J., Dent, W.A., Kinsel, W., Wisniewski, W.Z., Williams, P.W., Brand, P.W.J.L. & Ku, W.H.M., 1990. *Astrophys. J.*, **352**, 574.

Brindle, C., Hough, J.H., Bailey, J.A., Axon, D.J., Schulz, H., Kikuchi, S., McGraw, J.T., Wisniewski, W.J., Fontaine, G., Nadesu, D., Clayton, G., Anderson, E., Jameson, R.F., Smith, R. & Wallis, R.E., 1985. *Mon. Not. R. astr. Soc.*, **214**, 619.

Broten, N.W., Legg, T.H., Locke, J.L., McLeish, C.W., Richards, R.S., Chisholm, R.M., Gush, H.P., Yen, Y.L. & Galt, J.A., 1967. *Nature*, **215**, 38.

Brown, L.M.J., Robson, E.I., Gear, W.K., Hughes, D.H., Griffin, M.J., Geldzahler, B.J., Schwartz, P.R., Smith, M.G., Smith, A.G., Shepherd, D.W., Webb, J.R.,

Valtaoja, E., Terasranta, H. & Salonen, E., 1989a. *Astrophys. J.*, **340**, 129.

Browne, I.W.A., 1983. *Mon. Not. R. astr. Soc.*, **204**, 23p.

Burbidge, G.R., 1956. *Astrophys. J.*, **124**, 416.

Burstein, D. & Heiles, C., 1982. *Astron. J.*, **87**, 1165.

Campins, H., Rieke, G.H. & Lebofsky, M.J., 1985. *Astron. J.*, **90**, 896.

Carrasco, L., Dultzin–Hacyon, D. & Cruz–Gonzalez, I., 1985. *Nature*, **314**, 146.

Celotti, A., Maraschi, L. & Treves, A., 1989. *BL–Lac Objects: 10 Years After*, Eds Maraschi, L., Maccaro, T. & Ulrich, M–H. Springer–Verlag: Berlin.

Ciatti, F., Mammano, A., Bartolini, C., Guarnieri, A. & Picconi, A., 1981. *Astr. Astrophys.*, **95**, 177, **100**, 330.

Clark, D.H., 1984. *The Quest For SS433*, Penguin Books.

Clark, D.H. & Caswell, J.L., 1976. *Mon. Not. R. astr. Soc.*, **174**, 267.

Cohen, M., 1989. *Parsec Scale Radio Jets*, Eds Zensus, J.A. & Pearson, T.J. Cambridge University Press.

Conover, W.J., 1980. *Practical Nonparametric Statistics*, Wiley, New York.

Cook, D.B. & Spangler, S.R., 1980. *Astrophys. J.*, **240**, 751.

Cotton, W.D., Wittels, J.J., Shapiro, I.I., Marcaide, J., Owen, F.N., Spangler, S.R., Rius, A., Angulo, C., Clark, T.A. & Knight, C.A., 1980. *Astrophys. J.*, **238**, L123.

Courant, R. & Friedrichs, K.O., 1948. *Supersonic Flow & Shock Waves*, Springer–Verlag: New York.

Davidson, K. & McCray, R. 1980. *Astrophys. J.*, **241**, 1082.

Decker, R.B., 1988. *Space Science Reviews*, **48**, 195.

Decker, R.B. & Vlahos, L., 1986. *Astrophys. J.*, **306**, 710.

de Hoffman, F. & Teller, E., 1950. *Phys. Rev.* , **80**, 692.

Doroshenko, V.T., Lyuty, V.M., Terebizh, V.Y., Efimov, Y.S., Shakhovskoy, N.M., Piirola, V., Haarola, S., Korhonen, T., Silanpää, V. & Valtaoja, E., 1986. *Astr. Astrophys.*, **163**, 321.

Downes, A.J.B., Pauls, T. & Salter, C.J., 1981. *Astr. Astrophys.*, **103**, 277.

Drury, L.O'C., 1983. *Rep. Progr. Phys*, **46**, 973.

Drury, L.O'C., 1989. *Magnetic Fields and Extragalactic Objects.*, Eds Asseo, E. & Grésillon, D.

Edelson, R.A. & Malkan, M.A., 1987. *Astrophys. J.*, **323**, 516.

Elliot, J.L. & Shapiro, S.L., 1974. *Astrophys. J.*, **192**, L3.

Fabian, A.C. & Rees, M.J., 1978. *X–Ray Astronomy; Proceedings of 21st COSPAR meeting*, Eds Baity, W.E. & Peterson, L. Pergamon Press.

Fabian, A.C. & Rees, M.J., 1979. *Mon. Not. R. astr. Soc.*, **187**, 13p.

Fabrika, S.N. & Borisov, N.V., 1987. *Sov. Astron. Lett.*, **13**, 279.

Fanaroff, B.L. & Riley, J.M., 1974. *Mon. Not. R. astr. Soc.*, **167**, 31p.

Flatters, C. & Conway, R.G., 1985. *Nature*, **314**, 425.

Fugmann, W., 1988.. *Astr. Astrophys.*, **205**, 86.

Gabuzda, D.C., Wardle, J.F.C. & Roberts, D.H., 1989a. *Astrophys. J.*, **338**, 743.

Gabuzda, D.C., Cawthorne, T.W., Roberts, D.H. & Wardle, J.F.C., 1989b. *Astrophys. J.*, **347**, 701.

Gear, W.K., Brown, L.M.J., Robson, E.I., Ade, P.A.R., Griffin, M.J., Smith, M.G., Nolt, I.G., Radostitz, J.V., Veeder, G. & Lebofsky, L., 1986. *Astrophys. J.*, **304**, 295.

Geldzahler, B.J., Pauls, T. & Salter, C.J., 1980. *Astr. Astrophys.*, **84**, 237.

Ghisellini, G., Maraschi, L., Tanzi, E.G. & Treves, A., 1986. *Astrophys. J.*, **310**, 317.

Ginzberg, V.L., 1951. *Sov. Phys Dokl. (translation of Dokl. Akad. Nauk. SSSR)*, **76**, 377.

Hagen–Torn, V.A., Perevozchikoa, A.I., Érshtadt, S.G. & Yakoleva, V.A., 1979. *Sov. Astron. Lett.* , **5**, 217.

Halpern, J.P., Chen, V.S., Madejski, G.M. & Chanan, G.A., 1991. *Astron. J.*, **101**, 818.

Heavens, A.F., 1983. *Mon. Not. R. astr. Soc.*, **204**, 699.

Heavens, A.F., 1984. *Mon. Not. R. astr. Soc.*, **211**, 195.

Heavens, A.F., 1988. *Hotspots in Extragalactic Objects*, Eds Meisenheimer, K. & Röser, H-J., Springer–Verlag.

Heavens, A.F., Ballard, K.R. & Kirk, J.G., 1990. *Mon. Not. R. astr. Soc.*, **244**, 474.

Heavens, A.F. & Meisenheimer, K., 1987. *Mon. Not. R. astr. Soc.*, **225**, 335.

Hjellming, R.M. & Johnston, K.J. 1981. *Nature*, **290**, 100.

Hjellming, R.M. & Johnston, K.J. 1988. *Astrophys. J.*, **328**, 600.

Holmes, P.A., 1985. *PhD Thesis*, University of Edinburgh.

Holmes, P.A., Brand, P.W.J.L., Impey, C.D. & Williams, P.M., 1984a. *Mon. Not. R. astr. Soc.*, **210**, 961.

Holmes, P.A., Brand, P.W.J.L., Impey, C.D., Williams, P.M., Smith, P., Elston, R., Balonek, T., Zeilik, M., Burns, J., Heckert, P., Barvainis, R., Kenny, J., Schmidt, G. & Puschell, J., 1984b. *Mon. Not. R. astr. Soc.*, **211**, 497.

Hughes, P.A., Aller, H.D. & Aller, M.F., 1985. *Astrophys. J.*, **298**, 301.

Hughes, P.A., Aller, H.D. & Aller, M.F., 1989. *Astrophys. J.*, **341**, 54.

Impey, C.D., 1987. *Superluminal Radio Sources*, Eds Zensus, J.A. & Pearson, T.J., Cambridge University Press, Cambridge.

Impey, C.D. & Brand, P.W.J.L., 1982. *Mon. Not. R. astr. Soc.*, **201**, 849.

Impey, C.D., Malkan, M. & Tapia, S., 1989. *Astrophys. J.*, **347**, 96.

Impey, C.D. & Tapia, S., 1988. *Astrophys. J.*, **333**, 666.

Jackson, J.D., 1975. *Classical Electrodynamics.*, John Wiley, New York.

Jokipii, J.R., 1982. *Astrophys. J.*, **255**, 716.

Johnston, K.J., Santini, N.J., Spencer, J.H., Klepczynski, W.J., Kaplan, G.H., Josties, R.J., Angerhofer, P.E., Florkowski, D.R. & Matsakis, D., 1981. *Astron. J.*, **86**, 1377.

Johnston, K.J., Geldzahler, B.J., Spencer, J.H., Waltman, E.B., Klepczynski, W.J., Josties, R.J., Angerhofer, P.E., Florkowski, D.R., McCarthy, D.D. & Matsakis,

D., 1984. *Astron. J.*, **89**, 509.

Jones, T.W., Rudnick, L., Aller, H.D., Aller, M.F., Hodge, P.E. & Fielder, R.L., 1985. *Astrophys. J.*, **290**, 627.

Kardashev, N.S., 1962. *Sov. Astron. - A.J.*, **6**, 317.

Katz, J.I., Anderson, S.F., Margon, B. & Grandi, S.A., 1982. *Astrophys. J.*, **260**, 780.

Katz, J.I. & Piran, T., 1982. *Astrophys. Lett.*, **23**, 11.

Kikuchi, S. & Mikami, Y., 1987. *Publs astr. Soc. Japan*, **39**, 237.

Kikuchi, S., Inoue, M., Mikami, Y., Tabara, H. & Kato, T., 1988. *Astr. Astrophys.*, **190**, L8.

Killeen, N.E.B., Bicknell, G.V. & Ekers, R.D., 1988. *Astrophys. J.*, **325**, 180.

Kiplinger, A.L., 1974. *Astrophys. J.*, **191**, L109.

Kirk, J.G., 1987. *Particle Acceleration at Relativistic Shock Fronts*, Max–Planck Institut für Astrophysik preprint No. 345.

Kirk, J.G. & Heavens, A.F., 1989. *Mon. Not. R. astr. Soc.*, **239**, 995.

Kirk, J.G. & Schneider, P., 1987a. *Astrophys. J.*, **315**, 425.

Kirk, J.G. & Schneider, P., 1987b. *Astrophys. J.*, **322**, 256.

Königl, A., 1981. *Astrophys. J.*, **243**, 700.

Königl, A., 1983. *Mon. Not. R. astr. Soc.*, **205**, 471.

Kopylov, I.M., Kumaĭgorodskaya, R.N., Somov, N.N., Somova, T.A. & Fabika, S.N., 1986. *Sov. Astron. - A.J.*, **30**, 408.

Korchakov, A.A. & Syrovatskii, S.I., 1962. *Sov. Astron. - A.J.*, **5**, 678.

Krymsky, G.F., 1977. *Sov. Phys Dokl. (translation of Dokl. Akad. Nauk. SSSR)*, **23**, 327.

Kundt, W. & Krotschek, E., 1980. *Astr. Astrophys.*, **83**, 1.

Landau, R., Grolsch, B., Jones, T.J., Jones, T.W., Pedelty, J., Rudnick, L., Sitko, M.L., Kenney, J., Roellig, T., Salonen, E., Urpo, S., Schmidt, G., Neugebauer, G., Matthews, K., Elias, J.H., Impey, C.D., Clegg, P. & Harris, S., 1986. *Astrophys. J.*, **308**, 78.

Landolt, A.U., 1983. *Astron. J.*, **88**, 439.

Lawrence, A., 1987. *Publs astr. Soc. Pacif.*, **99**, 309.

Ledden, J.E. & Aller, H.D., 1979. *Astrophys. J.*, **229**, L1.

Licnerowicz, A., 1967. *Relativistic Hydrodynamics and Magnetohydrodynamics*, Benjamin Press, New York.

Macleod, J.M. & Andrew, B.H., 1968. *Astrophys. Lett.*, **1**, 243.

Malkan, M.A. & Sargent, W.L.W., 1982. *Astrophys. J.*, **254**, 22.

Marchenko, S.G., 1985. *Astrophysics (translation of Astrofizika)*, **22**, 15.

Margon, B., 1984. *Ann. Rev. Astron. Astrophys.*, **22**, 507.

Marscher, A.P., 1987. *Superluminal Radio Sources*, Eds Zensus, J.A. & Pearson, T.J. Cambridge University Press.

Marscher, A.P. & Gear, W.K., 1985. *Astrophys. J.*, **298**, 114.

Matthews, A.P. & Scheuer, P.A.G., 1989. *Mon. Not. R. astr. Soc.*, **242**, 616.

McGuinn, J., Clarke, M, Crosby, D. & Hillman, C., 1967. *Younger Than Yesterday*, The Byrds.

McHardy, I., 1989. *BL–Lac Objects: 10 Years After*, Eds Maraschi, L., Maccaro, T. & Ulrich, M–H. Springer–Verlag: Berlin.

Mead, A.R.G., 1988. *PhD Thesis*, University of Edinburgh.

Mead, A.R.G., Ballard, K.R., Brand, P.W.J.L., Hough, J.H., Bailey, J.A. & Brindle, C., 1990. *Astr. Astrophys. Suppl. Ser.*, **83**, 183.

Mead, A.R.G., Brand, P.W.J.L., Hough, J.H. & Bailey, J.A., 1988. *Mon. Not. R. astr. Soc.*, **233**, 503.

Meisenheimer, K., Röser, H.-J., Hiltner, P.R., Yates, M.G., Longair, M.S., Chini, R & Perley, R.A., 1989. *Astr. Astrophys.*, **219**, 63.

Milgrom, A.A., 1979. *Astr. Astrophys.*, **78**, L9.

Moffet, A.T., Gubbay, J., Robertson, D.S. & Legg, A.J., 1972. *IAU Symposium 44, External Galaxies and Quasi–Stellar Objects*, Ed Evans, D.S. Dordrecht: Reidel.

Moore, R.L. & Stockman, H.S., 1981. *Astrophys. J.*, **243**, 60.

Moore, R.L., McGraw, J.T., Angel, J.R.P., Duerr, R., Lebofsky, M.J., Rieke, G.H., Wiśniewski, W.Z., Axon, D.J., Bailey, J.A., Hough, J.H., Thompson, I., Breger, M., Schulz, H., Clayton, G.C., Martin, P.G., Miller, J.S., Schmidt, G.D., Africano, J. & Miller, H.R., 1982. *Astrophys. J.*, **260**, 415.

Moore, R.L., Schmidt, G.D. & West, S.C., 1987. *Astrophys. J.*, **314**, 176.

Murdin, P., Clark, D.H. & Martin, P.G., 1980. *Mon. Not. R. astr. Soc.*, **193**, 135.

Mutel, R.L. & Phillips, R.B., 1987. *Superluminal Radio Sources*, Eds Zensus, J.A. & Pearson, T.J. Cambridge University Press.

Norman, M.L., Winkler, K-H.A. & Smarr, L., 1983. *Astrophysical Jets*, Eds Ferrari, A. & Pacholczyk, A.G. Reidel Publishing Company: New York.

Nussbaumer, H.J., 1981. *Fast Fourier transforms & convolution algorithms*, Springer–Verlag: Berlin.

Ohashi, T., 1989. *BL–Lac Objects: 10 Years After*, Eds Maraschi, L., Maccaro, T. & Ulrich, M–H. Springer–Verlag: Berlin.

Oke, J.B., Neugebauer, G. & Becklin, E.E., 1969. *Astrophys. J.*, **156**, L41.

Olsen, E.T., 1969. *Nature*, **224**, 1008.

Orr, M.J.L. & Browne, I.W.A., 1982. *Mon. Not. R. astr. Soc.*, **200**, 1067.

Ostriker, J.P., 1989. *BL–Lac Objects: 10 Years After*, Eds Maraschi, L., Maccaro, T. & Ulrich, M–H. Springer–Verlag: Berlin.

Ostriker, J.P. & Vietri, M., 1985. *Nature*, **318**, 446.

Ostrowski, M., 1988. *Mon. Not. R. astr. Soc.*, **233**, 257.

Pacholczyk, A.G., 1970. *Radio Astrophysics*, Freeman: San Francisco.

Pacholczyk, A.G., 1977. *Radio Galaxies*, Pergammon Press: Oxford.

Panofsky, W.K.H. & Phillips, M., 1964. *Classical Electricity & Magnetism*, Addison–Wesley: Reading, Massachusetts.

Pauliny–Toth, I.I.K. & Kellerman, K.I., 1966. *Astrophys. J.*, **146**, 634.

Peacock, J.A., 1981. *Mon. Not. R. astr. Soc.*, **196**, 135.

Pearson, T.J. & Readhead, A.C.S., 1988. *Astrophys. J.*, **328**, 114.

Perley, R.A., Fomalont, E.B. & Johnston, K.J., 1980. *Astron. J.*, **85**, 649.

Porcas, R.W., 1987. *Superluminal Radio Sources*, Eds Zensus, J.A. & Pearson, T.J. Cambridge University Press.

Press, W.H., Flannery, B.P., Teukolsky, S.A. & Vetterling, W.T., 1989. *Numerical Recipes*, Cambridge University Press.

Prestage, R.M. & Peacock, J.A., 1988. *Mon. Not. R. astr. Soc.*, **230**, 131.

Qian, S.J., Quirrenbach, A., Witzel, A., Krichbaum, T.P., Hummel, C.A. & Zensus, J.A., 1991. *Astr. Astrophys.*, **241**, 15.

Rees, M.J., 1966. *Nature*, **211**, 468.

Rees, M.J., 1982. *Extragalactic Radio Sources, IAU Symp. No. 97, Ed. D.S. Heeschen, C.M. Wade,*, Dordrecht: Reidel.

Rieke, G.H. & Lebofsky, M.J., 1985. *Astrophys. J.*, **288**, 618.

Rieke, G.H., Lebofsky, M.J. & Kinman, T.D., 1979. *Astrophys. J.*, **232**, L151.

Riffert, H., 1987. *Astrophys. J.*, **310**, 729.

Roberts, D.H., Gabuzda, D.C. & Wardle, J.F.C., 1987. *Astrophys. J.*, **323**, 536.

Rusk, R. & Seaquist, E.R., 1985. *Astron. J.*, **90**, 30.

Rybicki, G.B. & Lightman, A.P., 1979. *Radiative Processes in Astrophysics*, Wiley: New York.

Ryle, M., Caswell, J.L., Hine, G. & Shakeshaft, J., 1978. *Nature*, **276**, 571.

Scarrott, S.M. & Rolph, C.D., 1989. *Mon. Not. R. astr. Soc.*, **238**, 348.

Scheuer, P.A.G. & Readhead, A.C.S., 1979. *Nature*, **277**, 182.

Schmitt, J., 1968. *Nature*, **218**, 663.

Schneider, P. & Kirk, J.G., 1989. *Astr. Astrophys.*, **217**, 344.

Seaquist, E.R., Gilmore, W.S., Johnston, K.J. & Grindlay, J.E., 1982. *Astrophys. J.*, **260**, 220.

Serkowski, K., 1974. *Methods Exp. Phys*, **12**, (Academic Press, New York), p361.

Seward, F.D., Page, C.G., Turner, M.J. & Pounds, K.A., 1976. *Bull. Am. Astr. Soc.*, 8, 443.

Shields, G., 1978. *Nature*, **272**, 706.

Shklovskii, I.S., 1952. *Astr. Zh.*, 29, 418.

Singal, A.K., 1986. *Astrophys. J.*, **310**, 733.

Smith, M.D. & Norman, C.A., 1981. *Mon. Not. R. astr. Soc.*, **194**, 771.

Smith, P.S., Balonek, T.J., Elston, R. & Heckert, P.A., 1987. *Astrophys. J. Suppl.*, **64**, 459.

Spencer, R.E., 1984. *Mon. Not. R. astr. Soc.*, **209**, 869.

Stephenson, C.B. & Sanduleak, N. 1977. *Astrophys. J. Suppl.*, **33**, 459.

Stockman, H.S., Moore, R.L. & Angel, J.R.P., 1984. *Astrophys. J.*, **279**, 485.

Strittmatter, P.A., Serkowski, K., Carswell, R., Stein, W.A., Merrill, K.M., Burbidge, E.M., 1972. *Astrophys. J.*, **175**, L7.

Synge, J.L., 1957. *The Relativistic Gas*, North Holland.

Treves, A., Chiapetti, L., Fabian, A., Falomo, R., Maccagni, D., Maraschi, L., Morini, M., Tanzi, E.G. & Tagliatelle, G., 1989. *Astrophys. J.*, **341**, 733.

Valtaoja, E., Haarala, S., Lehto, H., Valtaoja, L., Valtonen, M., Moiseev, I.G., Nesterov, N.S., Salonen, E., Teräsranta, H., Urpo, S. & Tiuri, M., 1988. *Astr. Astrophys.*, **203**, 1.

Valtaoja, L., Valtaoja, E., Shakhovskoy, N.M., Efimov, Y.S. & Sillanpää, A., 1991. *Astron. J.*, **101**, 78.

Visvanathan, N., 1969. *Astrophys. J.*, **155**, L133.

Wardle, J.F.C. & Kronberg, P.P., 1974. *Astrophys. J.*, **194**, 249.

Wardle, J.F.C., Moore, R.L. & Angel, J.R.P., 1984. *Astrophys. J.*, **279**, 93.

Wardle, J.F.C., Roberts, D.M., Brown, L.F., Koogaard, R.I. & Gabuzda, D.C., 1990. *Parsec Scale Radio Jets*, Zensus, J.A. & Pearson, T.J. Cambridge University Press.

Webb, G.M., Zank, G.P. & Mackenzie, J.F., 1987. *J. Plasma Physics*, **37**, 117.

Wehrle, A.E., Cohen, M.H. & Unwin, S.C., 1990. *Parsec Scale Radio Jets*, Zensus, J.A. & Pearson, T.J. Cambridge University Press.

Westfold, K.C., 1959. *Astrophys. J.*, **130**, 241.

Wills, B.J. & Browne, I.W.A., 1986. *Astrophys. J.*, **302**, 56.

Worrall, D., 1989. *BL-Lac Objects: 10 Years After*, Eds Maraschi, L., Maccaro, T. & Ulrich, M-H. Springer-Verlag: Berlin.

Zwitter, T., Calvani, M., Bodo, G. & Massaglia S., 1989. *Fund Cosmic Phys*, **13**, 309.

Appendix A

Synchrotron Radiation.

A.1 Basic Derivations

In this appendix a brief summary of the derivation of the equations of synchrotron emission and source evolution is given. There are several textbooks published which give detailed derivations of these equations (e.g. Rybicki & Lightman 1979; Pacholczyk 1970; 1977) all in cgs units. However, the work within this thesis is carried out in SI units, so that a statement of the relevant equations is desirable.

An accelerated electronically-charged particle will radiate; when this acceleration is caused by the Lorentz force experienced by a particle in a stationary magnetic field, **B**, the resulting emission is termed synchrotron radiation. A primary objective is to determine the energy loss rate of an electron in a magnetic field. The situation is shown in Fig. A1. In the frame where the magnetic field is at rest and there is no electric field, $\mathbf{E} = \mathbf{0}$, the equations of motion reduce to:

$$\frac{d}{dt}(\gamma_e m_e \mathbf{v}) = e(\mathbf{v} \wedge \mathbf{B}) \tag{A.1}$$

$$\frac{d}{dt}(\gamma_e m_e c^2) = e(\mathbf{v}.\mathbf{E}) = 0 \tag{A.2}$$

which are the equations for helical motion at a constant speed $|\ \mathbf{v}\ |$, the acceleration being perpendicular to the velocity perpendicular to the field; along the field there is zero acceleration. The total energy loss rate of a relativistically charge moving of energy E in an electromagnetic field is:

$$-\frac{dE}{dt} = \frac{e^2\gamma_e^4}{6\pi\epsilon_0 c^3}(\gamma_e^2\dot{v}_{\|}^2 + \dot{v}_{\perp}^2) \tag{A.3}$$

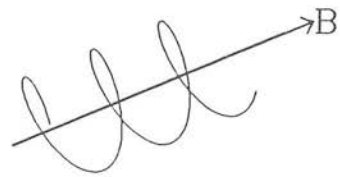

Figure A1: This shows the helical motion of an electron placed in a magnetic field.

where $\dot{v}_{\|[\perp]}$ refer to the acceleration parallel [perpendicular] to the field. Upon substitution:

$$-\frac{dE}{dt} = \frac{e^2\gamma_e^4}{6\pi\epsilon_0 c^3}\left(\frac{eBv\sin\varepsilon}{m_e\gamma_e}\right)^2 \tag{A.4}$$

where ε is the pitch angle, equal to the angle between the instantaneous velocity vector and the magnetic field. The next goal is to obtain the spectrum of the radiation from a single electron. The energy per unit time and per unit solid angle can be obtained from the Poynting flux. After Fourier transforming this is given by:

$$\frac{d^2W}{d\Omega d\omega} = \frac{\epsilon_0 c}{\pi}\left|\int R\mathbf{E}(t)e^{i\omega t}dt\right|^2 \tag{A.5}$$

where $\mathbf{E}(t)$ is the electric field at time t and distance R from an electric charge. Now, from Panofsky & Phillips (1964, section 20.1) this is given by:

$$\mathbf{E}(t) = \frac{e}{4\pi\epsilon_0(1-\boldsymbol{n}.\boldsymbol{\beta})^3}\left[\frac{(\mathbf{n}-n\beta)\,(1-\beta^2)}{R^2} + \frac{(\mathbf{n}\wedge(\mathbf{n}-n\beta))\wedge\dot{\beta}}{R}\right] \tag{A.6}$$

where $\mathbf{n}$ is a unit vector along the line of sight from the particle to the observer at the retarded time $t' = t - \frac{R(t')}{c}$. Similarly the velocity, β and the position $\mathbf{R}(t')$ are evaluated at the retarded time. The first term in equation (A.6) is simply the generalization of Coulomb's law to a moving charge, it is only the second, radiation term which arises from the acceleration which will be considered further, the R^{-1} form of the field allowing radiation energy to be lost by the electron. Substituting equation (A.6) into (A.5) and

integrating by parts once, one obtains:

$$\frac{d^2W}{d\Omega d\omega} = \frac{e^2\omega^2}{16\pi^3\epsilon_0 c}\left|\int \{\mathbf{n}\wedge(\mathbf{n}\wedge\beta)\}\exp\left(i\omega\left(t'-\frac{\mathbf{n}.\mathbf{r}(t)}{c}\right)\right)dt'\right|^2 \tag{A.7}$$

For high γ_e one can approximate the term in the exponential by:

$$t'-\frac{\mathbf{n}.\mathbf{r}(t)}{c} \simeq (2\gamma_e^2)^{-1}\left[(1+\gamma_e^2\theta^2)t'+\frac{c^2\gamma_e^2 t'^3}{3a^2}\right] \tag{A.8}$$

and the outer term:

$$\mathbf{n}\wedge(\mathbf{n}\wedge\beta) = -\varepsilon_\perp \sin\left(\frac{vt}{a}\right)+\varepsilon_{||}\cos\left(\frac{vt}{a}\right)\sin\theta \tag{A.9}$$

where a is the radius of curvature of the electron path (which differs from the gyroradius by a factor $1/\sin\varepsilon$), and θ is the angle between the instantaneous velocity vector and the line of sight. Upon substituting this into equation (A.7), one obtains two terms for the emission parallel and perpendicular to the magnetic field. The following substitutions are then made:

$$y = \frac{\gamma_e c t'}{a(1+\gamma_e^2\theta^2)^{1/2}} \qquad \eta = \frac{\omega a(1+\gamma_e^2\theta^2)^{3/2}}{3c\gamma_e^3} \tag{A.10}$$

and equations 10.4.26, 10.4.31 & 10.4.32 of Abramowicz & Stegun (1965) are then utilized to yield finally:

$$\frac{d^2W_\perp}{d\Omega d\omega} = \frac{e^2\omega^2}{16\pi^3\epsilon_0 c}\left(\frac{a(1+\gamma_e^2\theta^2)}{\gamma_e^2 c}\right)^2 K_{2/3}^2(\eta) \tag{A.11}$$

$$\frac{d^2W_{||}}{d\Omega d\omega} = \frac{e^2\omega^2\theta^2}{16\pi^3\epsilon_0 c}\left(\frac{a(1+\gamma_e^2\theta^2)^{1/2}}{\gamma_e^2 c}\right)^2 K_{1/3}^2(\eta) \tag{A.12}$$

where K_i are the modified Bessel functions of order i. Next, one integrates over solid angle $d\Omega = 2\pi\sin\varepsilon d\theta$. This form can be used because the radiation lies in a narrow cone of half angle γ_e^{-1}, and this effectively sweeps out a narrow cone of half angle ε and thickness γ_e^{-1} on the sky, centred upon the magnetic field. The limits of the integration can be extended to infinity with little error. These integrals are carried out by Westfold

(1959) (note also the corrections of Singal 1986) to yield:

$$\frac{dW_{\perp}}{d\omega} = \frac{3\sqrt{3}\gamma_e e^2 \sin\varepsilon}{32\pi c\epsilon_0}(F(x) - G(x)) \tag{A.13}$$

$$\frac{dW_{\parallel}}{d\omega} = \frac{3\sqrt{3}\gamma_e e^2 \sin\varepsilon}{32\pi c\epsilon_0}(F(x) + G(x)) \tag{A.14}$$

where $x = \omega/\omega_c = 2a\omega/3c\gamma_e^3$ and where the functions $F(x)$ and $G(x)$ are defined for use throughout the thesis as:

$$F(x) = x\int_{-} K_{5/3}(\zeta)d\zeta \tag{A.15}$$

$$G(x) = xK_{2/3}(x) \tag{A.16}$$

Modified Bessel functions of fractional order occur at several points in this thesis, either in the chapters on synchrotron radiation, or in relation to the equation of state of a relativistic gas in Chapter 3. In order to satisfactorily carry out the numerical integrations, the functions themselves were generated at a large number of points to a high accuracy. In order evaluate the functions at arbitrary values the series supplied in Abramowicz & Stegun (1965) were employed. The modified Bessel functions $K_{1/3}(z)$ and $K_{2/3}(z)$ were generated from the series for the Airy functions given by equations 10.4.3 of Abramowicz & Stegun and then 10.4.26 & 10.4.31. One then uses the recurrence relation 9.6.26, $K_{5/3}(z) = K_{1/3}(z) + (4/3z)K_{1/3}(z)$, to obtain $K_{5/3}(z)$. Then the necessary integral was carried out numerically to obtain $F(x)$. The form of the function is plotted in Fig. A2.

Thus one obtains finally expressions for the energy emitted by a single electron parallel to and perpendicular to the magnetic field. However, it is generally the case that one observes radiation from an ensemble of electrons with an electron distribution which is not simply monoenergetic, but which is a function of energy, pitch angle, time, and position, $N(E, \varepsilon, t, R)$. Under the assumption that the source is both stationary and small, the emission coefficient becomes:

$$\varepsilon_{\perp} = \frac{3\sqrt{3}e^3}{64\pi^2 m_e c\epsilon_0}\int_{\Omega}\int_{E} B\sin\varepsilon(F(x) - G(x))N(E, \varepsilon, t)dEd\Omega \tag{A.17}$$

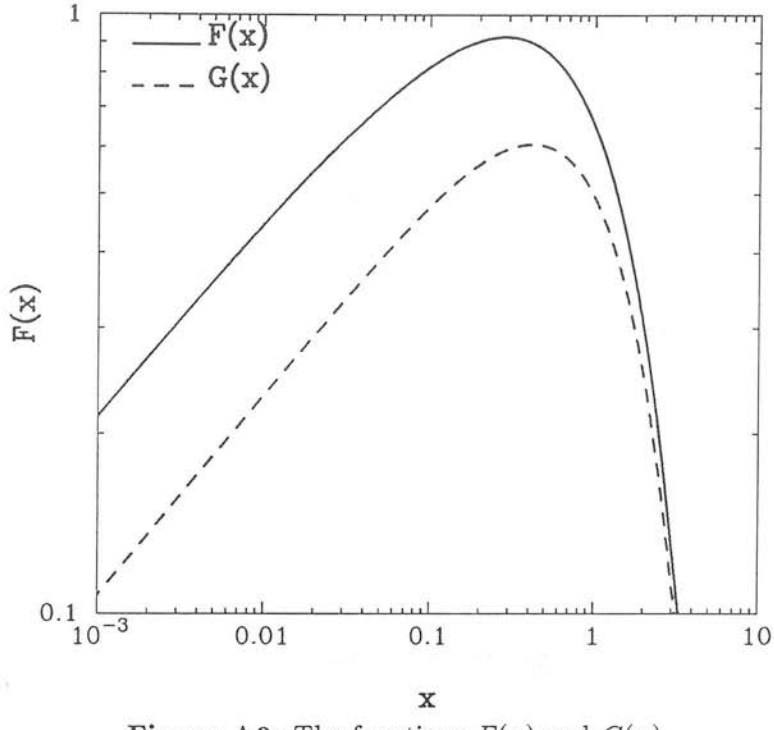

Figure A2: The functions $F(x)$ and $G(x)$.

$$\varepsilon_{\parallel} = \frac{3\sqrt{3}e^3}{64\pi^2 m_e c\epsilon_0} \int_{\Omega}\int_{E} B \sin\varepsilon (F(x) + G(x)) N(E,\varepsilon,t) dE d\Omega \tag{A.18}$$

By referring these to a fixed position angle projected on the sky χ from the magnetic field, one obtains the Stokes parameters:

$$I(\nu,t) = \frac{3\sqrt{3}e^3}{32\pi^2 m_e c\epsilon_0} \int_{\Omega}\int_{E} B \sin\varepsilon F(x) N(E,\varepsilon,t) dE d\Omega \tag{A.19}$$

$$Q(\nu,t) = \frac{3\sqrt{3}e^3}{32\pi^2 m_e c\epsilon_0} \int_{\Omega}\int_{E} B \sin\varepsilon \cos 2\chi G(x) N(E,\varepsilon,t) dE d\Omega \tag{A.20}$$

$$U(\nu,t) = \frac{3\sqrt{3}e^3}{32\pi^2 m_e c\epsilon_0} \int_{\Omega}\int_{E} B \sin\varepsilon \sin 2\chi G(x) N(E,\varepsilon,t) dE d\Omega \tag{A.21}$$

$$V(\nu,t) = 0 \tag{A.22}$$

The circular polarization approximates to zero in the case where the electron distribution does not change over an angle γ_e^{-1} i.e. when the electron velocity is ultra-relativistic, or when the distribution is nearly isotropic. In the simplest case one takes

an isotropic power law distribution of electron energies $N(E) \sim E^{-\gamma}$ and obtains a power-law distribution of flux, $I(\nu) \sim \nu^{-\alpha}$, where $\alpha = (\gamma - 1)/2.0$. This radiation is linearly polarized:

$$P = \frac{(Q^2 + U^2)^{1/2}}{I} \times 100\% = \frac{\gamma + 1}{\gamma + 7/3} \times 100\% \tag{A.23}$$

A.2 Effect of losses

Quite often however a simple power-law is an incorrect description of the radiation, either because the field is not perfectly aligned, or the form of the distribution is more complicated than a simple power law. In this section the effect that losses can have will be considered. To illustrate this, the most general case is considered, although this may be applied to any of the cases considered in Chapter 4 with more specific magnetic fields.

The following is a method for obtaining the number density of electrons as a function of energy and time in a slab of width $s(t)$ and constant thickness which evolves as the electrons lose energy. It is taken from Kardaschev (1962), who considered losses and Hughes et al. (1985), who only considered adiabatic expansion, but who employed a more general source geometry in principle. There are three separate mechanisms which will be discussed.

- Adiabatic expansion losses as a result of the transverse expansion of the slab; as it expands the volume increases, $V \propto s^2$ (constant thickness) and the electrons lose energy. Assuming the plasma can be described as a relativistic gas of adiabatic index $\Gamma = 4/3$, then the energy of an electron decreases as $E \propto s^{-2/3}$. Further assuming that in the general case the jet expands $s \propto t^m$. Thus:

$$\frac{dE}{dt} = -\frac{2E}{3s}\frac{ds}{dt} = -\frac{2mE}{3t} \tag{A.24}$$

- Synchroton losses as a result of the radiation emitted by the non-thermal plasma. Equation A.4 gives the rate at which an electron loses energy; again, for the sake

of generality consider a magnetic field which decays with jet width as $B \propto s^{-n} \propto t^{-x}, x = mn$. Thus:

$$\frac{dE}{dt} = bB^2 \sin^2 \varepsilon E^2 \propto b_1 B_0^2 t^{-2x} \sin^2 \varepsilon E^2 \tag{A.25}$$

where $b =$ is a constant.

- Inverse Compton losses which are caused by photons scattered by the radiating electrons. In the simplest treatment the energy boost given to the photon is proportional to γ_e^2 but it is also proportional to U_{ph}, the energy density of the incident photons. There are two possible origins of these photons, either the microwave background, or the synchrotron radiated photons from the slab. It is this second source that will be assumed to dominate. In what follows, assume that the spectrum of incident radiation is that of a source which has suffered purely adiabatic losses. The energy density of synchrotron radiation is given by:

$$U \propto r \int_{E_{min}}^{E_{max}} \left(\frac{dE}{dt}\right)_{synch} N(E)dE \propto r\kappa B^2 E_{max}^{3-\gamma} \tag{A.26}$$

Overall then the equation for the loss of energy by a single electron can be written:

$$\frac{dE}{dt} + \frac{2mE}{3t} = \left\{-A_1 t^{-2x} - A_2 t^{-7m/3-2x}\right\} E^2 \tag{A.27}$$

In order to solve equation A.28 note that it is cast in the form of a Bernoulli equation, and that by the substitution $u = E^{-1}$ it can be re-written as a linear ordinary differential equation.

$$\frac{du}{dt} - \frac{2m}{3t}u = \left[A_1 t^{-2x} + A_2 t^{-7m/3-2x}\right] \tag{A.28}$$

and then that this can be solved in the usual manner. The consequence is that an electron with energy E_0 at time t_0 has energy $E(t)$ given by:

$$\frac{1}{E} - \frac{1}{E_0} = \left(\frac{t}{t_0}\right)^{2m/3} \left[\frac{A_1 t^{y_1}}{y_1} + \frac{A_2 t^{y_2}}{y_2}\right] \tag{A.29}$$

where

$$y_1 = 1 - 2x - \frac{2m}{3} \qquad y_2 = 1 - 3m - 2x \tag{A.30}$$

Before obtaining the energy distribution note that the total number density decreases as $N \sim s^2$, and hence that the constant in the power law $N(E, t_0) = N_0 E^{-\gamma}$ decreases as:

$$N_0 \propto t^{-2m/3(\gamma+2)} \tag{A.31}$$

Then from this point one uses conservation of the total number of particles to obtain:

$$N(E,\varepsilon,t) = N_0 E^{-\gamma} \left(\frac{t}{t_0}\right)^{2m/3(\gamma+2)} \left\{1 + \frac{EA_1 t^{2m/3}}{y_1}\left[\frac{1}{t_0^{y_1}} - \frac{1}{t^{y_1}}\right] + \frac{EA_2 t^{2m/3}}{y_2}\left[\frac{1}{t_0^{y_2}} - \frac{1}{t^{y_2}}\right]\right\}^{\gamma-2} \tag{A.32}$$

cf Kardaschev (1962, equation 11).

Appendix B

Multifrequency data

The UKIRT data, taken on 1988 February 15 - 18. These are tabulated by increasing Right Ascension. The figures in brackets are the 1σ errors in the measured quantities. Following on from this table, Figs B1–11 provide plots of all the data, showing flux density, polarization and position angle in each waveband.

Filter	Flux density (mJy)		Polarization (%)		Position angle (deg)	
0414+009			E(B-V) = 0.12			
15th. Feb 1988						
H	1.63	(0.15)	2.29	(2.07)	158.56	(24.65)
J	1.19	(0.04)	4.14	(1.92)	174.45	(10.58)
I	0.68	(0.02)	4.24	(1.64)	159.87	(9.55)
R	0.46	(0.01)	3.87	(0.66)	153.22	(4.61)
V	0.32	(0.01)	5.08	(1.43)	170.57	(7.70)
B	0.23	(0.01)	6.41	(0.79)	157.69	(3.60)
U	0.15	(0.01)	4.94	(1.08)	153.76	(6.11)
16th. Feb 1988						
H	1.56	(0.12)	6.20	(2.01)	146.42	(1.38)
I	0.70	(0.03)	7.82	(2.25)	154.03	(8.43)
R	0.45	(0.02)	5.72	(1.08)	155.71	(5.44)
V	0.33	(0.01)	4.73	(1.89)	151.40	(9.96)
B	0.23	(0.01)	3.93	(0.97)	157.80	(7.44)
U	0.15	(0.01)	7.38	(1.44)	159.53	(6.16)
0422+004			E(B-V) = 0.12			
16th. Feb 1988						
H	7.47	(0.28)	20.27	(0.64)	155.80	(1.04)
I	2.60	(0.10)	20.79	(1.12)	148.91	(1.38)
R	1.71	(0.06)	21.84	(0.65)	151.77	(0.81)
V	1.22	(0.05)	23.30	(1.07)	153.20	(1.50)
B	0.78	(0.04)	21.47	(0.75)	151.76	(0.91)
U	0.47	(0.03)	22.14	(0.97)	150.93	(1.47)
18th. Feb 1988						
K	10.56	(1.07)	12.32	(0.73)	147.60	(1.09)
H	7.75	(1.15)	11.25	(0.87)	148.00	(1.38)
I	2.93	(0.19)	12.55	(0.67)	141.90	(1.51)
R	1.74	(0.07)	12.25	(0.34)	140.42	(0.69)
V	1.25	(0.08)	12.93	(0.69)	140.24	(1.34)
B	0.79	(0.06)	12.48	(0.48)	136.95	(0.96)
U	0.44	(0.03)	13.69	(0.83)	141.36	(1.44)
0735+178			E(B-V) = 0.03			
15th. Feb 1988						
H	7.96	(0.22)	16.24	(0.54)	131.37	(1.06)
I	2.40	(0.07)	15.48	(1.02)	125.56	(1.64)
R	1.84	(0.05)	17.17	(0.47)	130.41	(0.65)
V	1.33	(0.04)	18.05	(1.00)	127.83	(1.71)
B	0.96	(0.04)	16.80	(0.56)	130.68	(1.15)
U	0.62	(0.03)	17.57	(1.03)	136.73	(1.90)

Appendix A. Continued.

Filter	Flux density (mJy)		Polarization (%)		Position angle (deg)	
16th. Feb 1988						
H	8.41	(0.31)	15.23	(0.61)	130.73	(0.94)
I	2.73	(0.11)	17.66	(0.82)	132.51	(1.44)
R	2.00	(0.07)	17.90	(0.51)	129.97	(0.79)
V	1.46	(0.06)	17.19	(1.06)	130.60	(1.32)
B	1.05	(0.05)	17.49	(0.73)	130.98	(0.99)
U	0.67	(0.04)	17.94	(1.26)	132.36	(1.66)
18th. Feb 1988						
H	8.65	(1.36)	20.50	(0.89)	127.25	(0.78)
I	3.14	(0.44)	21.90	(0.98)	126.70	(1.14)
R	2.19	(0.31)	21.15	(0.68)	126.60	(0.73)
V	1.66	(0.27)	22.50	(1.00)	128.80	(1.11)
B	1.21	(0.20)	22.50	(0.82)	124.00	(0.89)
U	0.80	(0.14)	21.80	(0.93)	125.90	(1.11)
0736+017			E(B-V) = 0.12			
15th. Feb 1988						
J	2.20	(0.06)	1.53	(0.93)	105.58	(17.81)
I	1.66	(0.05)	2.98	(1.24)	172.76	(9.01)
R	0.96	(0.03)	0.77	(0.67)	7.56	(18.61)
V	0.75	(0.03)	0.49	(1.00)	152.87	(64.32)
B	0.60	(0.03)	0.22	(0.64)	73.87	(83.42)
U	0.46	(0.03)	1.28	(0.78)	107.22	(19.18)
16th. Feb 1988						
J	2.16	(0.10)	4.43	(2.04)	171.13	(11.22)
I	1.50	(0.05)	0.53	(1.39)	46.94	(83.32)
R	0.82	(0.03)	1.53	(0.93)	91.61	(16.10)
V	0.67	(0.03)	2.89	(1.92)	9.21	(18.86)
B	0.52	(0.02)	0.77	(0.81)	15.05	(28.29)
U	0.40	(0.02)	0.96	(1.25)	56.86	(40.83)
0754+100			E(B-V) = 0.00			
15th. Feb 1988						
K	14.33	(0.40)	8.58	(0.49)	40.50	(1.37)
H	10.17	(0.29)	10.56	(0.42)	41.31	(0.81)
I	4.08	(0.09)	11.22	(0.51)	43.20	(1.00)
R	2.89	(0.08)	12.33	(0.24)	44.15	(0.58)
V	2.15	(0.07)	12.22	(0.43)	46.12	(0.92)
B	1.62	(0.07)	13.39	(0.29)	46.39	(0.66)
U	1.07	(0.06)	14.39	(0.48)	48.43	(0.87)
16th. Feb 1988						
K	13.81	(0.38)	10.34	(0.38)	34.40	(1.28)
H	9.63	(0.27)	10.96	(0.42)	35.20	(1.23)
I	3.62	(0.08)	12.39	(0.48)	30.20	(1.23)
R	2.27	(0.08)	12.59	(0.32)	34.74	(0.76)
V	1.86	(0.06)	13.22	(0.57)	35.45	(1.24)
B	1.36	(0.06)	13.10	(0.42)	35.69	(0.81)
U	0.91	(0.05)	13.25	(0.62)	38.54	(1.30)

Appendix A. Continued.

Filter	Flux density (mJy)		Polarization (%)		Position angle (deg)	
17th. Feb 1988						
H	9.71	(0.36)	11.41	(0.51)	34.80	(1.67)
I	3.69	(0.24)	11.09	(0.59)	34.60	(1.95)
R	2.36	(0.12)	11.80	(0.39)	34.70	(1.23)
V	1.88	(0.10)	10.07	(0.58)	37.20	(2.27)
B	1.40	(0.07)	11.52	(0.54)	36.30	(1.27)
U	0.93	(0.06)	12.09	(0.77)	39.60	(2.27)
18th. Feb 1988						
K	14.73	(1.22)	8.67	(0.69)	36.20	(1.41)
H	10.75	(1.59)	8.17	(0.67)	39.00	(1.25)
I	3.75	(0.12)	9.28	(0.67)	32.33	(2.06)
R	2.73	(0.14)	8.65	(0.32)	36.67	(0.93)
V	2.08	(0.13)	8.43	(0.62)	36.40	(1.34)
B	1.55	(0.12)	6.95	(0.40)	36.35	(1.49)
U	1.03	(0.08)	7.56	(0.63)	38.28	(2.36)
0818-128 OJ-131			E(B-V) = 0.09			
15th. Feb 1988						
K	3.02	(0.14)	17.13	(1.60)	82.16	(2.81)
H	2.19	(0.10)	18.66	(1.72)	85.68	(2.15)
I	0.84	(0.03)	24.73	(1.66)	79.09	(1.92)
R	0.47	(0.02)	22.45	(0.72)	80.44	(1.01)
V	0.34	(0.01)	25.33	(1.81)	82.30	(1.85)
B	0.23	(0.01)	24.09	(0.86)	79.49	(1.04)
U	0.13	(0.01)	24.92	(1.66)	81.51	(1.99)
16th. Feb 1988						
K	3.16	(0.15)	15.48	(1.82)	79.61	(2.72)
J	1.32	(0.07)	21.87	(1.88)	83.54	(2.54)
I	0.68	(0.03)	21.92	(2.07)	88.24	(2.70)
R	0.38	(0.01)	22.22	(1.02)	81.56	(1.23)
V	0.28	(0.01)	25.68	(2.32)	81.85	(2.44)
B	0.19	(0.01)	26.75	(1.45)	80.49	(1.56)
U	0.11	(0.01)	27.67	(2.29)	81.59	(2.27)
17th. Feb 1988						
H	2.23	(0.10)	17.41	(1.62)	78.40	(2.33)
I	0.71	(0.03)	21.66	(2.43)	83.30	(3.20)
R	0.46	(0.02)	19.54	(1.21)	79.86	(1.85)
V	0.32	(0.01)	23.19	(2.78)	85.80	(3.03)
B	0.22	(0.01)	23.65	(1.55)	81.00	(1.83)
U	0.13	(0.01)	27.24	(2.37)	79.10	(2.41)

Appendix A. Continued.

Filter	Flux density (mJy)		Polarization (%)		Position angle (deg)	
0851+202 OJ287			E(B-V) = 0.00			
15th. Feb 1988						
H	6.60	(0.19)	17.33	(0.59)	61.99	(0.96)
I	2.50	(0.08)	18.36	(1.22)	57.81	(1.91)
R	1.65	(0.06)	17.20	(0.59)	60.17	(0.99)
V	1.26	(0.05)	17.80	(1.13)	60.25	(1.53)
B	0.96	(0.04)	18.49	(0.65)	59.57	(0.88)
U	0.63	(0.04)	15.90	(1.06)	63.12	(2.07)
16th. Feb 1988						
H	6.54	(0.30)	15.62	(0.64)	60.40	(1.12)
I	2.50	(0.12)	15.20	(1.02)	66.07	(1.90)
R	1.65	(0.08)	15.55	(0.63)	61.96	(1.22)
V	1.31	(0.06)	17.38	(0.99)	63.58	(1.53)
B	1.00	(0.06)	18.55	(0.72)	62.56	(1.16)
U	0.70	(0.04)	17.65	(1.02)	64.89	(1.54)
17th. Feb 1988						
K	10.10	(0.28)	18.81	(0.50)	64.20	(0.77)
H	6.85	(0.19)	18.90	(0.58)	64.80	(0.88)
I	2.60	(0.08)	18.06	(0.66)	63.88	(1.08)
R	1.82	(0.09)	19.72	(0.33)	65.78	(0.48)
V	1.37	(0.05)	18.43	(0.74)	67.90	(1.17)
B	1.05	(0.05)	20.14	(0.44)	66.77	(0.65)
U	0.71	(0.04)	20.83	(0.76)	69.26	(0.99)
0906+015			E(B-V) = 0.00			
15th. Feb 1988						
H	0.48	(0.42)	51.43	(51.89)	142.20	(16.30)
I	0.37	(0.04)	48.40	(13.40)	49.50	(10.30)
R	0.36	(0.02)	2.08	(3.92)	6.20	(56.00)
V	0.35	(0.02)	8.33	(5.13)	73.90	(14.90)
B	0.31	(0.02)	2.16	(2.90)	35.50	(47.30)
U	0.24	(0.02)	10.10	(5.38)	135.10	(10.20)
1101+384			E(B-V) = 0.00			
15th. Feb 1988						
K	50.13	(0.94)	3.64	(0.30)	43.91	(2.17)
H	46.07	(1.29)	3.22	(0.14)	40.85	(1.19)
J	36.72	(0.74)	3.50	(0.20)	44.60	(1.09)
I	22.83	(0.90)	3.73	(0.13)	42.21	(0.90)
R	18.22	(0.63)	3.86	(0.08)	42.12	(0.55)
V	13.97	(0.55)	3.82	(0.11)	40.55	(0.82)
B	11.31	(0.53)	4.68	(0.10)	41.83	(0.58)
U	7.55	(0.43)	4.64	(0.13)	42.26	(0.83)

Appendix A. Continued.

Filter	Flux density (mJy)		Polarization (%)		Position angle (deg)	
1147+245			E(B-V) = 0.00			
18th. Feb 1988						
H	8.62	(0.16)	1.52	(0.40)		
J	6.04	(0.12)	1.82	(0.54)	177.50	(8.05)
I	3.33	(0.10)	2.71	(0.67)	168.71	(6.70)
R	2.52	(0.11)	2.50	(0.26)	162.87	(3.05)
V	1.91	(0.10)	2.99	(0.46)	160.49	(4.41)
B	1.52	(0.09)	4.29	(0.32)	150.46	(2.08)
U	1.02	(0.07)	4.34	(0.52)	153.51	(3.62)
1156+295			E(B-V) = 0.00			
15th. Feb 1988						
H	2.35	(0.13)	23.04	(1.63)	168.83	(1.86)
I	0.97	(0.05)	24.07	(2.38)	162.06	(2.82)
R	0.77	(0.03)	24.37	(0.90)	164.87	(1.11)
V	0.62	(0.02)	24.76	(1.66)	166.81	(1.85)
B	0.53	(0.02)	22.83	(0.80)	164.20	(1.00)
U	0.35	(0.02)	24.25	(1.33)	163.78	(1.55)
16th. Feb 1988						
H	2.49	(0.21)	24.15	(2.53)	164.95	(1.55)
I	1.01	(0.05)	26.42	(2.87)	168.59	(3.25)
R	0.77	(0.03)	23.85	(1.02)	164.46	(1.16)
V	0.63	(0.03)	19.35	(2.46)	161.88	(3.68)
B	0.54	(0.03)	21.88	(1.24)	164.78	(1.64)
U	0.35	(0.02)	25.06	(2.17)	168.22	(2.41)
17th. Feb 1988						
H	2.37	(0.11)	28.06	(1.58)	166.80	(1.55)
I	0.88	(0.04)	27.27	(2.08)	161.20	(2.32)
R	0.71	(0.02)	24.99	(0.99)	164.90	(1.02)
V	0.57	(0.02)	22.54	(2.12)	162.20	(2.44)
B	0.48	(0.02)	23.08	(0.82)	164.60	(1.07)
U	0.31	(0.02)	24.87	(1.78)	168.10	(2.02)
1226+023 3C273			E(B-V) = 0.00			
15th. Feb 1988						
K	51.07	(0.95)	1.78	(0.08)	165.85	(1.28)
H	29.07	(0.55)	2.03	(0.11)	166.38	(2.16)
J	19.81	(0.57)	1.30	(0.71)	152.89	(15.92)
I	37.20	(1.46)	0.73	(0.10)	165.32	(4.53)
R	28.61	(0.80)	0.44	(0.07)	168.55	(4.49)
V	27.61	(1.09)	0.28	(0.09)	178.94	(9.06)
B	26.88	(1.25)	0.27	(0.06)	173.83	(7.29)
U	23.21	(1.32)	0.16	(0.09)	33.13	(14.48)

Appendix A. Continued.

Filter	Flux density (mJy)		Polarization (%)		Position angle (deg)	
16th. Feb 1988						
K	48.32	(1.79)	1.11	(0.09)	167.56	(2.07)
H	29.07	(0.55)	0.95	(0.08)	171.38	(2.05)
J	18.92	(0.38)	0.83	(0.11)	174.38	(6.91)
I	37.20	(1.15)	0.40	(0.09)	34.16	(7.99)
R	28.09	(0.98)	0.08	(0.07)	18.63	(18.47)
V	27.87	(1.10)	0.30	(0.08)	69.80	(7.60)
B	27.63	(1.45)	0.27	(0.06)	65.47	(6.84)
U	24.30	(1.38)	0.31	(0.08)	50.76	(6.48)
17th. Feb 1988						
K	98.20	(1.84)	2.06	(0.06)	151.50	(0.91)
H	56.42	(1.08)	2.46	(0.16)	153.80	(1.93)
J	38.10	(0.77)	1.99	(0.10)	148.10	(1.20)
I	36.19	(0.83)	0.78	(0.08)	150.63	(2.72)
R	29.41	(0.83)	0.63	(0.06)	137.80	(2.72)
V	28.13	(0.95)	0.31	(0.08)	134.55	(7.29)
B	27.13	(1.13)	0.29	(0.05)	113.04	(5.22)
U	24.30	(1.15)	0.18	(0.08)	111.42	(11.17)
17th. Feb 1988						
K	51.54	(1.43)	1.93	(0.06)	146.30	(0.98)
H	30.16	(0.58)	2.07	(0.07)	144.20	(0.87)
J	20.37	(0.41)	1.73	(0.11)	137.50	(2.77)
I	43.11	(0.99)	0.48	(0.08)	120.38	(4.96)
R	31.09	(1.08)	0.56	(0.05)	119.60	(2.75)
V	30.84	(1.67)	0.32	(0.07)	96.70	(7.05)
B	30.86	(2.06)	0.25	(0.05)	83.45	(6.56)
U	27.14	(1.91)	0.37	(0.08)	107.52	(5.64)
1253-055			E(B-V) = 0.00			
16th. Feb 1988						
H	29.07	(1.35)	21.36	(0.70)	114.44	(0.79)
I	12.55	(0.94)	20.94	(0.70)	110.07	(0.97)
R	9.22	(0.63)	20.08	(0.59)	111.38	(0.83)
V	7.00	(0.49)	19.58	(0.64)	109.58	(0.91)
B	5.17	(0.39)	19.47	(0.66)	109.65	(0.65)
U	3.29	(0.26)	19.65	(0.81)	112.30	(1.15)
17th. Feb 1988						
H	28.80	(0.55)	26.10	(0.20)	113.60	(0.24)
I	9.78	(0.30)	26.30	(0.42)	111.90	(0.46)
R	6.49	(0.23)	26.30	(0.36)	112.10	(0.39)
V	5.17	(0.20)	26.40	(0.53)	112.40	(0.58)
B	3.74	(0.17)	25.70	(0.42)	110.20	(0.38)
U	2.30	(0.12)	25.50	(0.67)	112.60	(0.69)

Appendix A. Continued.

Filter	Flux density (mJy)		Polarization (%)		Position angle (deg)	
18th. Feb 1988						
H	32.17	(0.61)	30.12	(0.21)	113.80	(0.21)
I	10.53	(0.24)	31.30	(0.36)	113.70	(0.33)
R	7.12	(0.25)	31.30	(0.33)	113.30	(0.30)
V	5.56	(0.22)	31.50	(0.39)	114.10	(0.36)
B	3.96	(0.17)	30.70	(0.33)	113.30	(0.30)
U	2.57	(0.13)	30.70	(0.58)	114.90	(0.53)
1418+546			E(B-V) = 0.00			
16th. Feb 1988						
K	19.96	(1.11)	2.49	(0.37)	134.85	(4.33)
H	16.88	(0.63)	2.90	(0.30)	142.21	(4.51)
J	12.27	(0.25)	3.57	(0.29)	143.80	(2.48)
I	7.49	(0.36)	3.12	(0.31)	146.58	(3.09)
R	5.25	(0.27)	3.06	(0.18)	140.00	(1.87)
V	3.64	(0.20)	3.31	(0.39)	146.85	(3.50)
B	2.59	(0.15)	4.38	(0.23)	143.90	(1.55)
U	1.49	(0.10)	4.89	(0.50)	147.29	(2.56)
17th. Feb 1988						
K	17.38	(0.48)	4.09	(0.48)	142.10	(3.71)
H	12.92	(0.36)	4.04	(0.32)	145.50	(1.85)
J	8.97	(0.18)	4.06	(0.29)	138.90	(3.07)
I	4.81	(0.11)	4.48	(0.27)	142.63	(1.88)
R	3.38	(0.09)	4.51	(0.18)	142.82	(1.09)
V	2.34	(0.08)	5.05	(0.35)	146.93	(1.91)
B	1.70	(0.07)	6.28	(0.23)	144.21	(1.11)
U	0.96	(0.05)	5.88	(0.43)	147.41	(1.86)
18th. Feb 1988						
H	14.43	(0.41)	3.38	(0.25)	132.01	(2.63)
I	5.68	(0.13)	3.56	(0.51)	140.80	(4.60)
R	4.25	(0.12)	3.11	(0.25)	146.20	(2.27)
V	2.97	(0.10)	2.96	(0.55)	142.80	(5.86)
B	2.34	(0.10)	3.20	(0.38)	150.00	(3.49)
U	1.49	(0.08)	4.05	(0.64)	156.20	(3.86)
1424+240			E(B-V) = 0.00			
16th. Feb 1988						
H	9.28	(0.26)	4.86	(0.36)	119.82	(2.12)
I	5.74	(0.28)	4.98	(0.66)	121.54	(3.78)
R	4.21	(0.12)	4.70	(0.36)	113.04	(2.18)
V	3.81	(0.21)	3.46	(0.50)	116.21	(4.07)
B	3.17	(0.15)	4.63	(0.30)	113.05	(1.95)
U	1.81	(0.09)	4.32	(0.48)	115.97	(3.12)

Appendix A. Continued.

Filter	Flux density (mJy)		Polarization (%)		Position angle (deg)	
17th. Feb 1988						
H	9.19	(0.26)	4.92	(0.40)	123.82	(2.24)
I	4.95	(0.11)	4.24	(0.53)	114.60	(3.52)
R	3.84	(0.13)	4.48	(0.31)	119.20	(1.86)
V	3.26	(0.13)	4.36	(0.38)	114.20	(2.33)
B	2.76	(0.13)	4.45	(0.24)	117.80	(1.88)
U	1.91	(0.11)	4.35	(0.58)	116.60	(3.38)
18th. Feb 1988						
H	9.36	(0.35)	5.01	(0.44)	122.58	(2.21)
I	4.95	(0.11)	5.14	(0.55)	120.30	(3.00)
R	4.06	(0.11)	4.93	(0.30)	118.30	(1.65)
V	3.38	(0.11)	4.99	(0.49)	116.30	(2.87)
B	2.87	(0.12)	4.56	(0.30)	114.20	(1.90)
U	2.12	(0.10)	4.42	(0.58)	113.20	(3.85)
1510-089			E(B-V) = 0.06			
15th. Feb 1988						
K	7.31	(0.20)	13.45	(0.70)	147.31	(1.65)
H	4.55	(0.17)	15.11	(0.74)	148.32	(1.50)
J	2.83	(0.08)	12.25	(1.06)	143.62	(3.56)
I	1.39	(0.05)	10.77	(0.92)	145.63	(2.50)
R	1.14	(0.03)	8.54	(0.37)	144.49	(1.26)
V	0.88	(0.04)	7.17	(0.75)	148.88	(3.48)
B	0.78	(0.03)	5.44	(0.41)	146.52	(2.29)
U	0.58	(0.03)	4.16	(0.51)	145.56	(3.83)
16th. Feb 1988						
K	7.94	(0.22)	13.51	(0.63)	153.29	(1.35)
H	4.90	(0.14)	14.72	(0.70)	152.79	(1.34)
J	3.22	(0.09)	13.97	(0.88)	152.60	(1.79)
I	1.87	(0.11)	11.49	(0.72)	148.93	(1.70)
R	1.27	(0.04)	9.22	(0.33)	149.18	(1.01)
V	1.13	(0.06)	7.81	(0.64)	150.66	(2.36)
B	0.95	(0.04)	5.54	(0.34)	148.32	(1.64)
U	0.52	(0.03)	4.40	(0.54)	155.59	(3.35)
1641+399 3C345			E(B-V) = 0.00			
15th. Feb 1988						
H	2.85	(0.24)	15.08	(5.23)	59.83	(7.30)
I	0.98	(0.06)	10.91	(3.77)	77.89	(10.51)
R	0.67	(0.03)	14.00	(2.67)	63.66	(5.48)
V	0.55	(0.03)	1.86	(5.13)	85.98	(66.60)
B	0.54	(0.03)	13.47	(1.98)	71.37	(4.04)
U	0.34	(0.02)	9.83	(4.06)	45.09	(15.69)

Appendix A. Continued.

Filter	Flux density (mJy)		Polarization (%)		Position angle (deg)	
16th. Feb 1988						
H	2.78	(0.10)	10.64	(1.08)	62.00	(2.93)
I	1.04	(0.07)	6.44	(2.07)	54.16	(10.29)
R	0.69	(0.02)	9.15	(1.35)	72.41	(4.23)
V	0.63	(0.04)	9.49	(2.24)	71.84	(6.73)
B	0.59	(0.03)	7.74	(1.05)	66.14	(4.35)
U	0.27	(0.02)	8.94	(1.81)	68.31	(6.09)
17th. Feb 1988						
K	4.41	(0.16)	10.38	(1.00)	61.77	(2.75)
H	2.78	(0.10)	9.64	(1.02)	61.30	(2.96)
J	1.73	(0.07)	14.20	(1.74)	63.00	(3.48)
I	0.99	(0.04)	12.06	(1.25)	66.98	(2.91)
R	0.73	(0.02)	9.27	(0.88)	66.39	(2.69)
V	0.62	(0.02)	8.07	(1.32)	62.67	(4.62)
B	0.55	(0.03)	5.66	(0.82)	59.75	(3.97)
U	0.25	(0.01)	5.72	(1.31)	65.61	(5.91)
18th. Feb 1988						
H	2.93	(0.14)	9.80	(1.05)	62.70	(2.99)
J	1.82	(0.09)	9.26	(1.16)	64.90	(3.62)
I	1.01	(0.03)	10.61	(1.41)	65.50	(3.72)
R	0.76	(0.02)	9.61	(0.91)	58.60	(2.46)
V	0.66	(0.03)	6.89	(1.59)	71.95	(6.57)
B	0.63	(0.03)	7.59	(0.70)	66.15	(2.91)
U	0.28	(0.02)	7.09	(1.19)	66.87	(4.89)

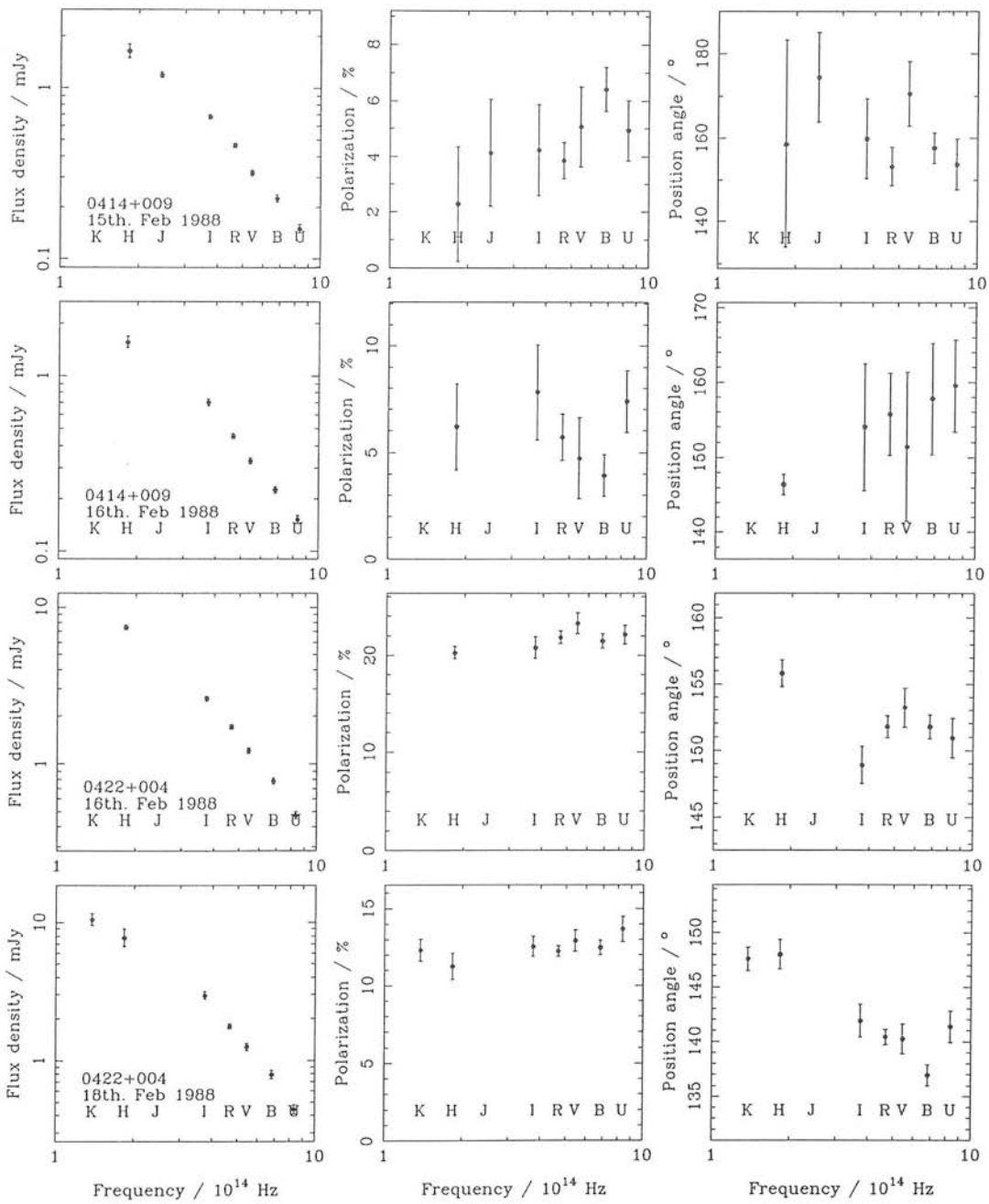

Figure B1: Multifrequency data from UKIRT 1988 February 15-18

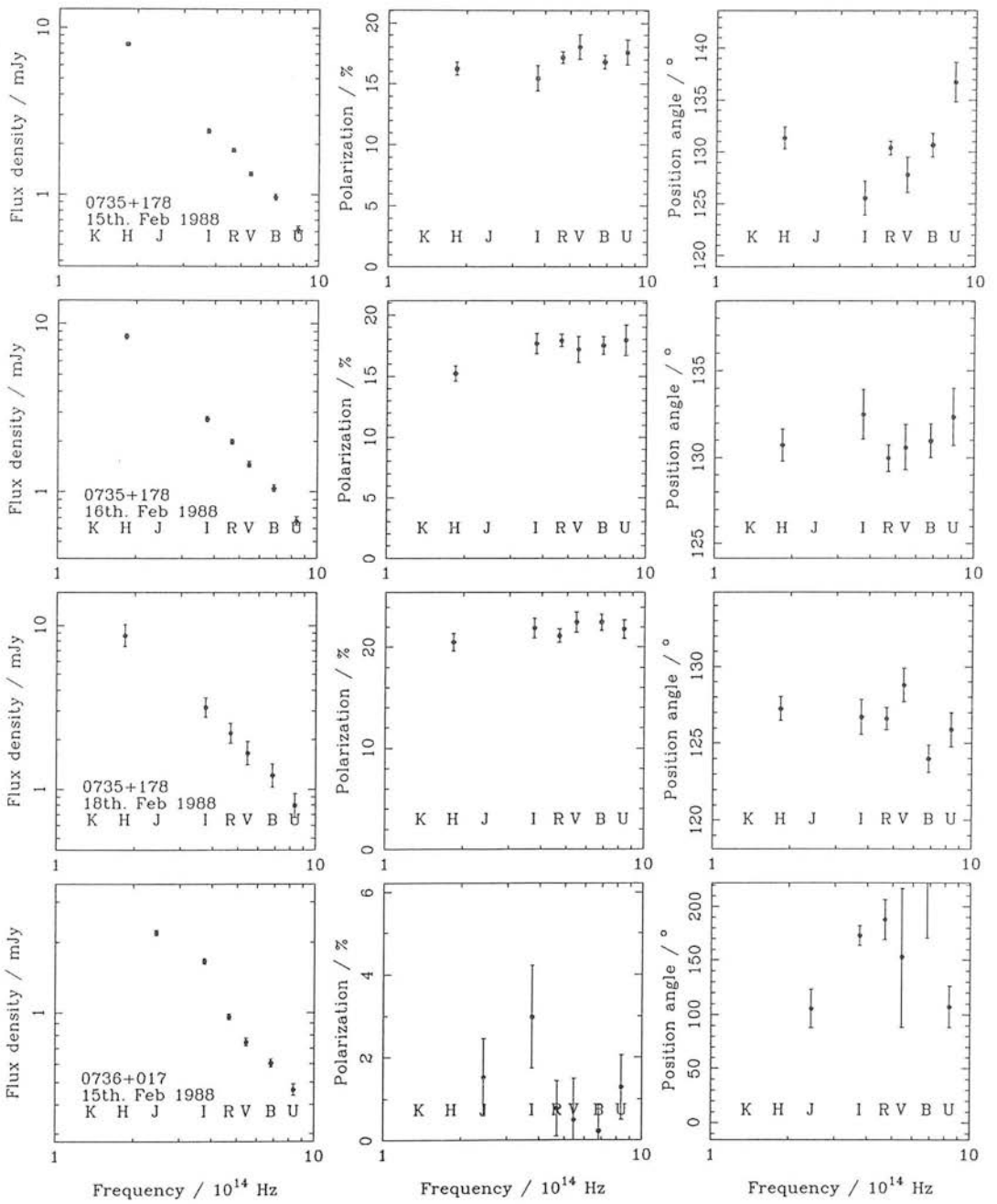

Figure B2: Multifrequency data continued

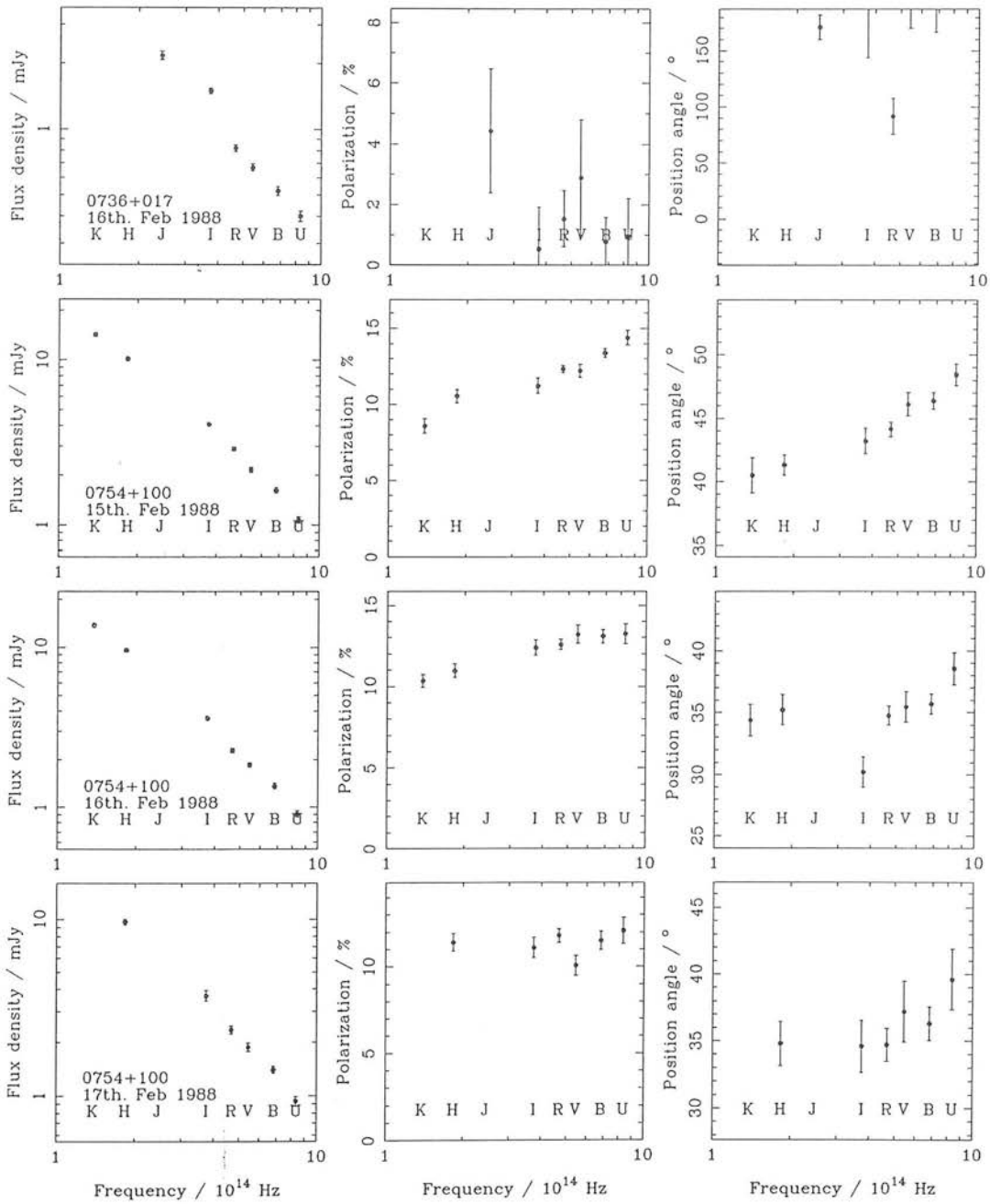

Figure B3: Multifrequency data continued

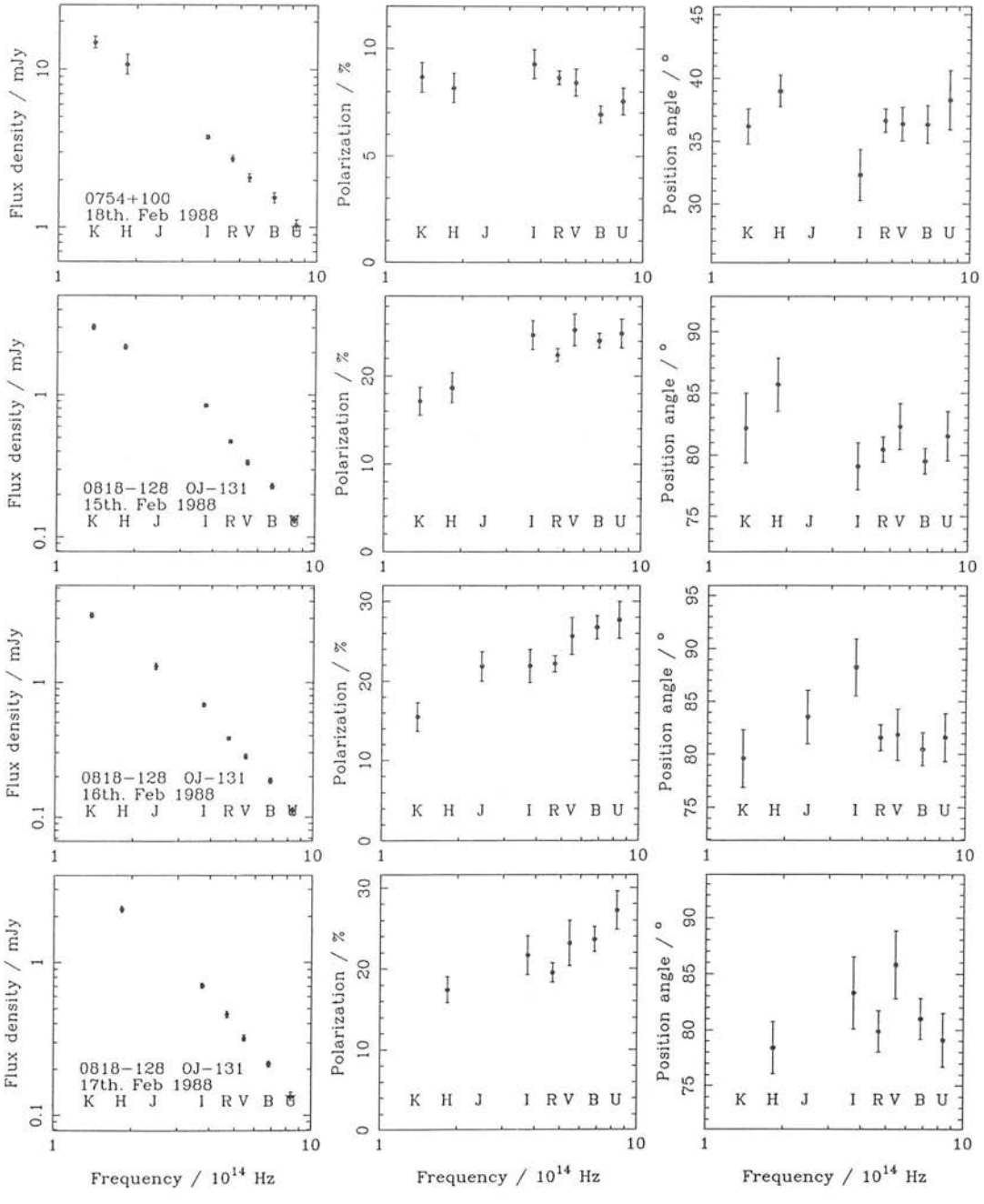

Figure B4: Multifrequency data continued

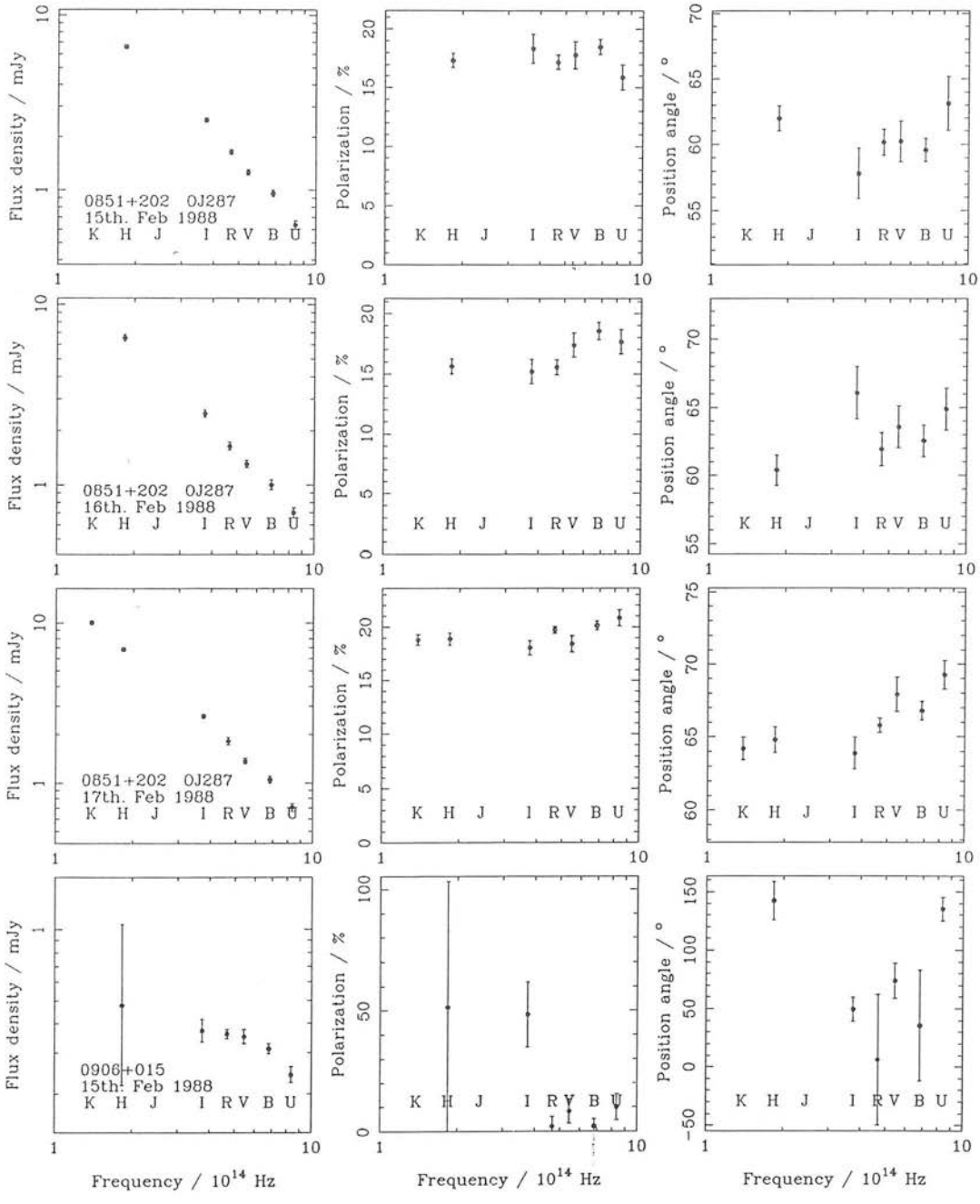

Figure B5: Multifrequency data continued

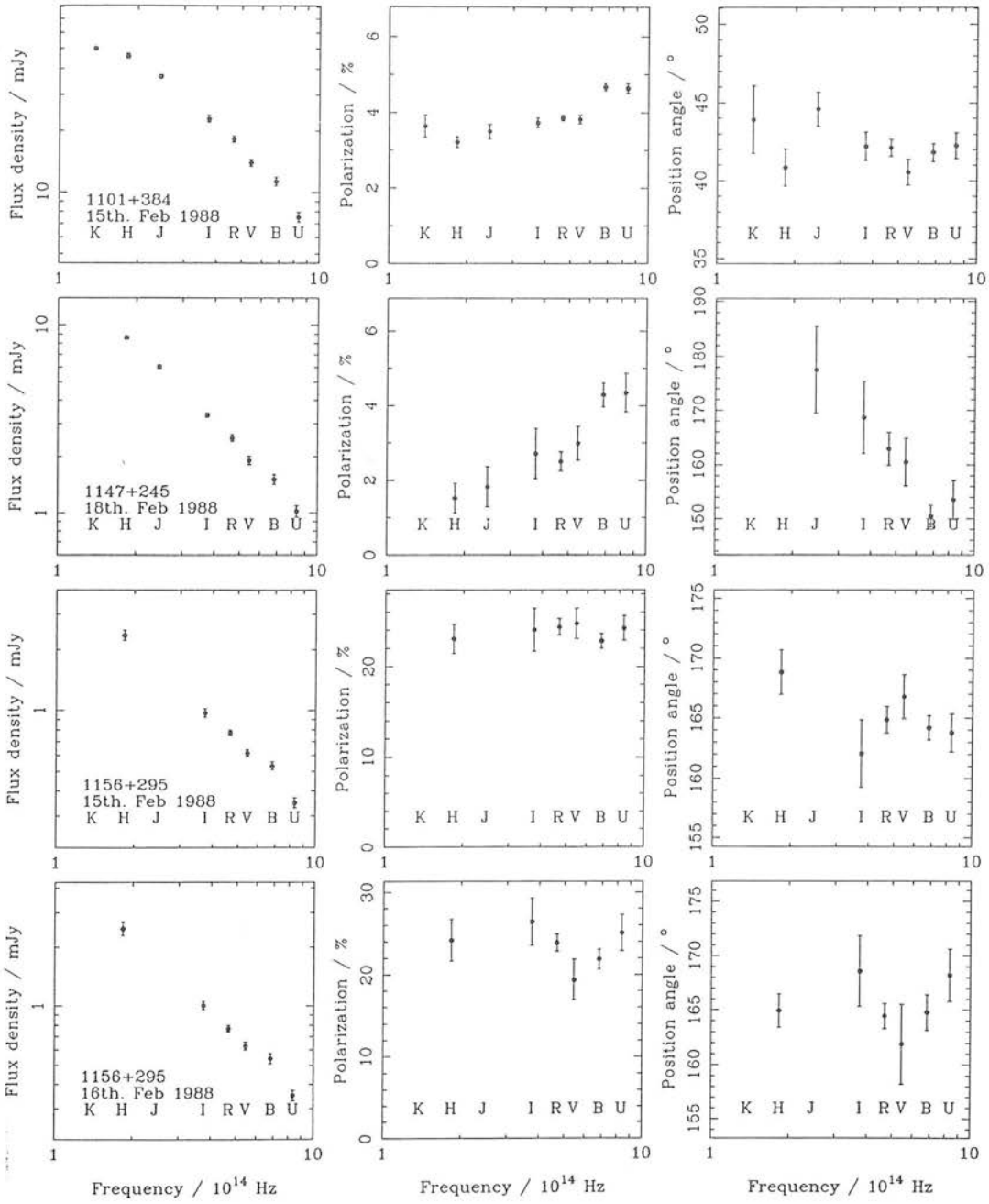

Figure B6: Multifrequency data continued

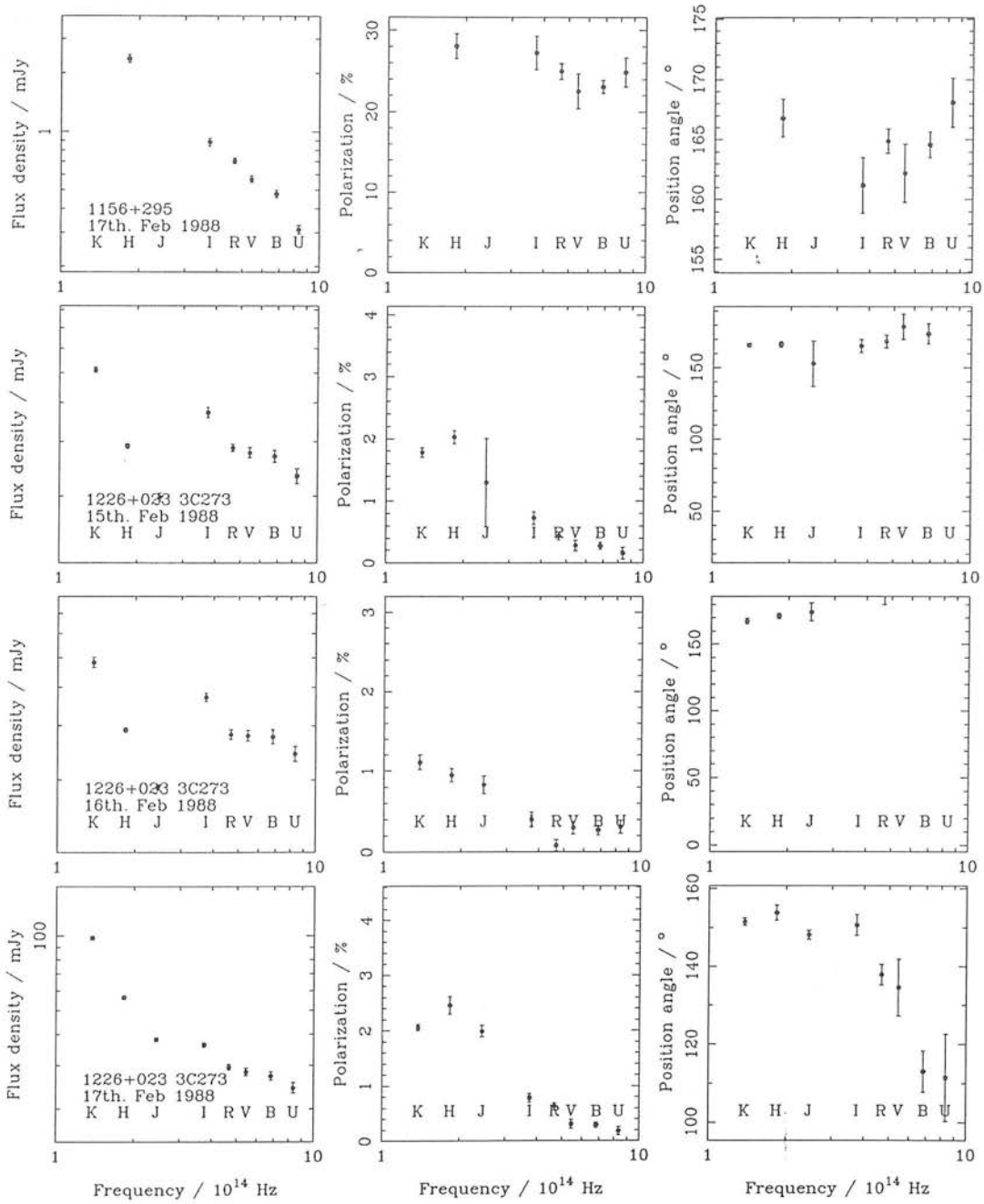

Figure B7: Multifrequency data continued

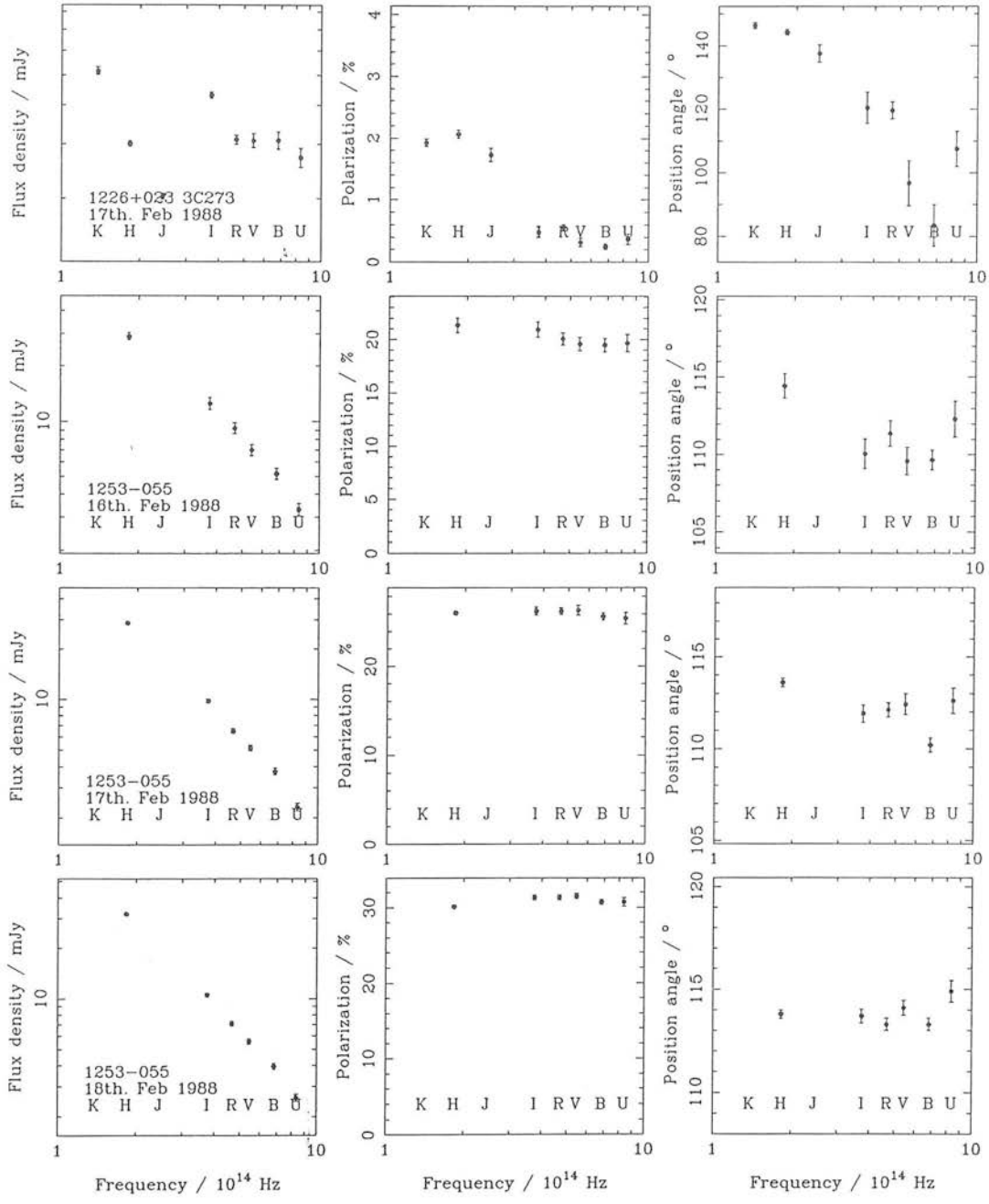

Figure B8: Multifrequency data continued

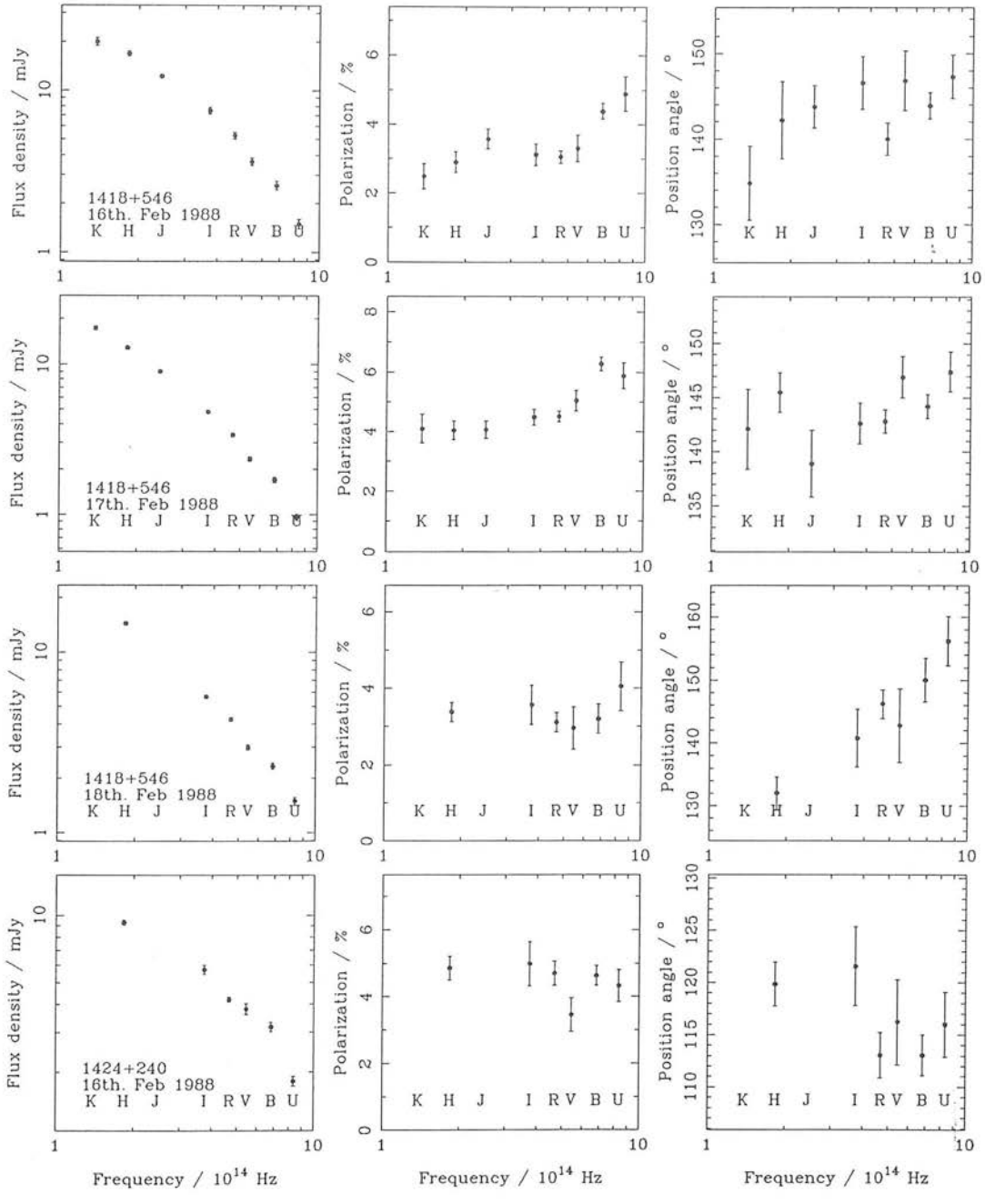

Figure B9: Multifrequency data continued

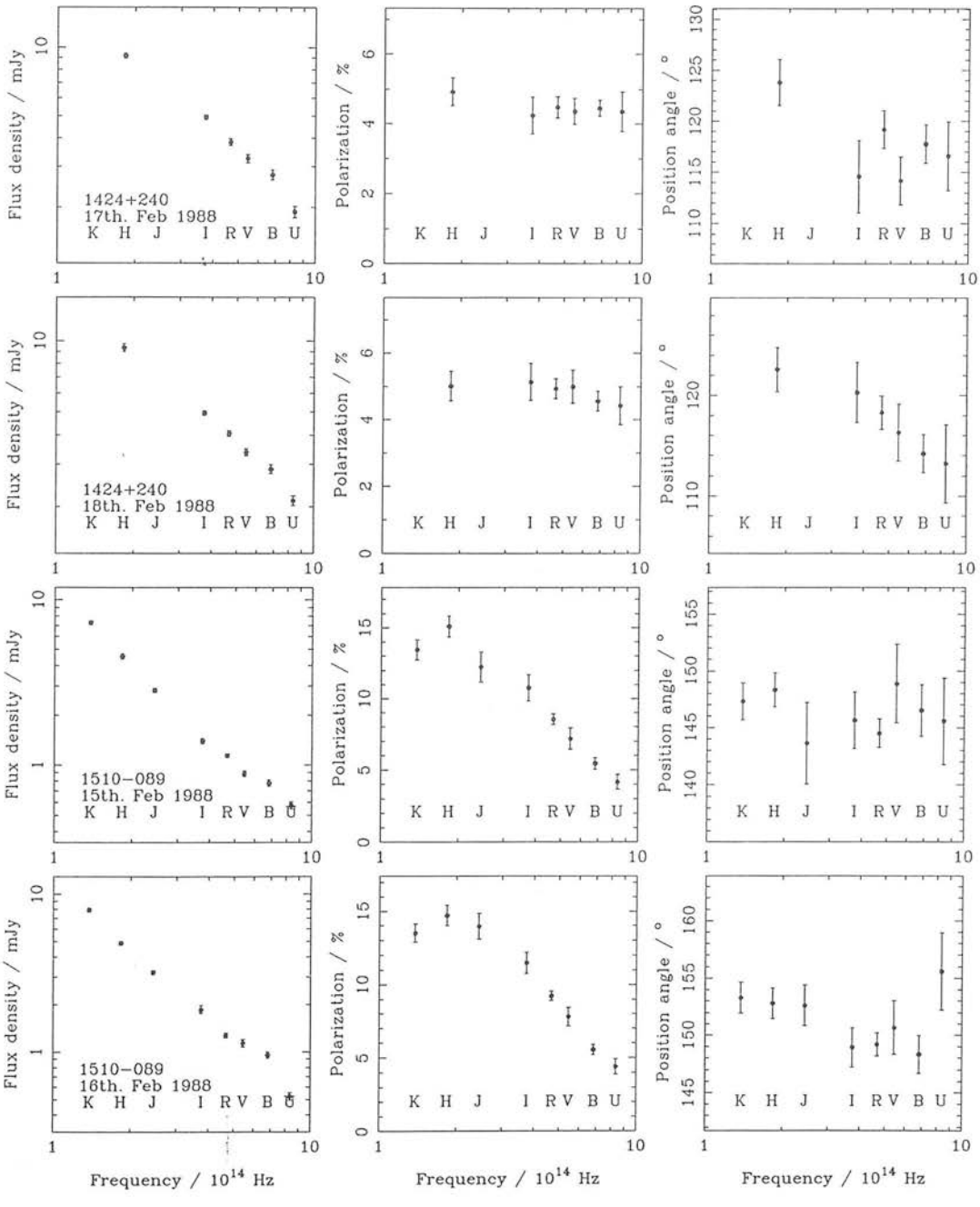

Figure B10: Multifrequency data continued

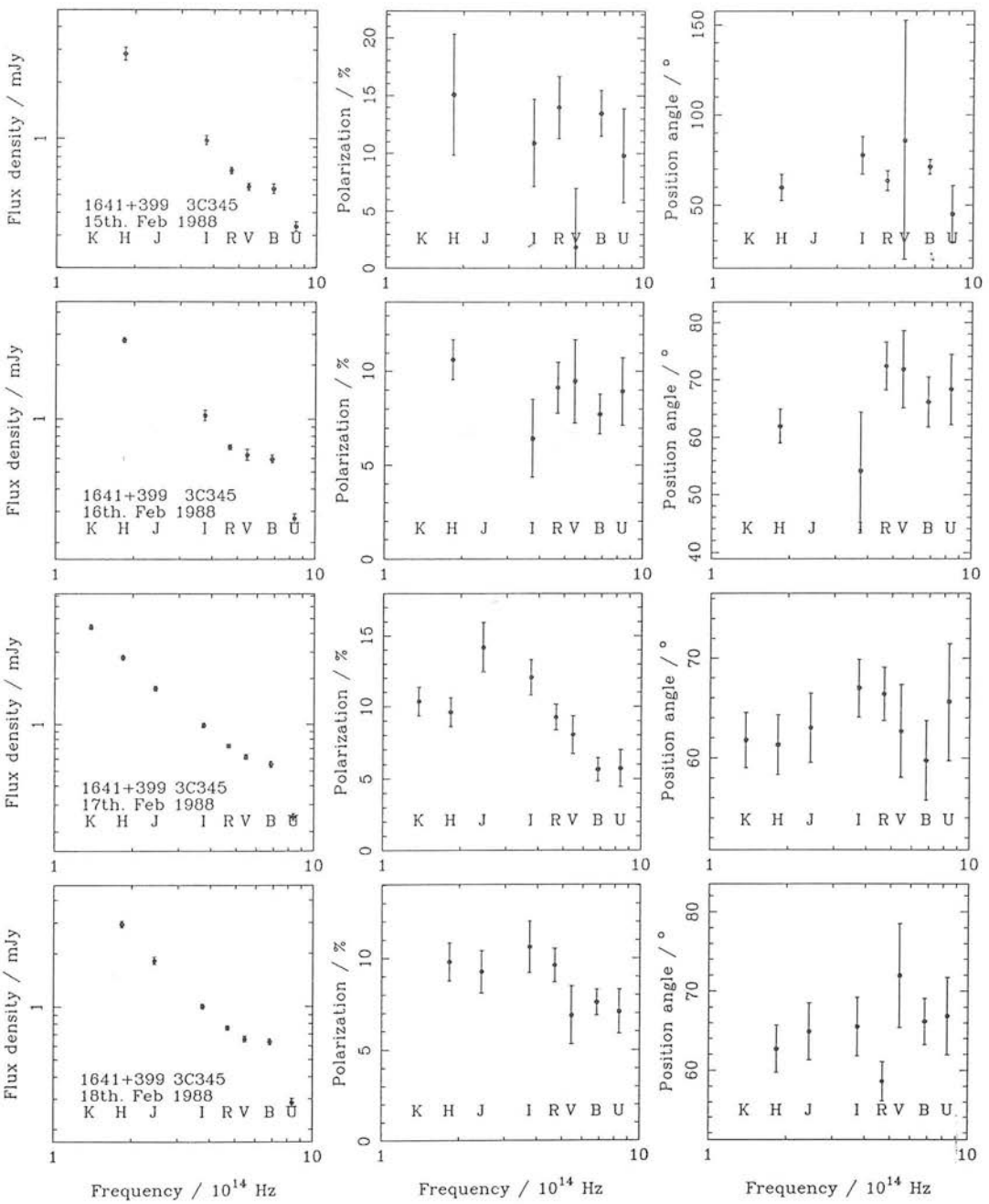

Figure B11: Multifrequency data continued

The following pages contain copies of the four Edinburgh Astronomy Preprints and the two unrefereed contributions to conference proceedings which are related to the work contained in this thesis.

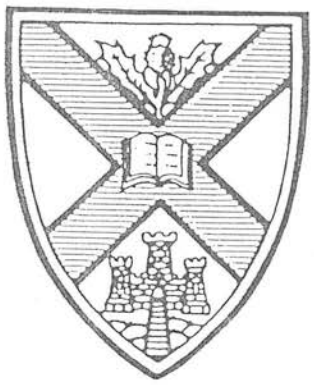

Edinburgh Astronomy Preprint

Number 28/89

December 1989

Optical and infrared polarimetry and photometry of blazars

A.R.G. Mead
K.R. Ballard
P.W.J.L. Brand
J.H. Hough
C. Brindle
J.A. Bailey

University of Edinburgh Department of Astronomy
Royal Observatory, Blackford Hill, Edinburgh EH9 3HJ, Scotland
Telephone: 031-668 8100 Telex 72383

Accepted for publication in *Astr. Astrophys. Suppl.*

Optical and infrared polarimetry and photometry of blazars

A.R.G. Mead[1] , K.R. Ballard[1], P.W.J.L. Brand[1], J.H. Hough[2],
C. Brindle[2], J.A. Bailey[3]

Summary. – We have carried out a polarization study of 44 blazars and candidate blazars at optical and near-infrared frequencies covering the period 1986 August to 1988 February. The data show flux and polarization properties changing on internight timescales, and commonly exhibit frequency dependence of spectral index, polarization and polarization position angle. The observations of the quasar 1253 – 055 (3C 279) showed a U-band polarization of $45.5 \pm 0.9\%$, the highest ever seen in a blazar. The interpretation of the data is the subject of a further paper (Ballard *et al.* 1989).

Key Words. – BL Lacertae Objects.

1. Introduction.

We present the results of a continuing programme of simultaneous measurements of the linear Stokes parameters in optical and near-infrared wavebands. This is the fourth paper in the series (see Impey *et al.* 1982; Impey *et al.* 1984; Holmes *et al.* 1984a). The observations, described in Sect. 2, are tabulated in Table 3. In all 44 objects were observed at the 3.8m United Kingdom Infrared Telescope (UKIRT) during four observing runs from 1986 July 31 to August 7, from 1987 July 27 to 30, from 1987 September 18 to 21 and from 1988 February 15 to 18. This yielded 135 sets of simultaneous photometric and polarimetric data, 23 sets

[1] *Dept of Astronomy, Edinburgh University, Scotland, EH9 3HJ.*

[2] *Division of Physical Sciences, Hatfield Polytechnic, Hatfield, Herts, AL10 9AB.*

[3] *Joint Astronomy Center, 665, Komohana St, Hilo, Hawaii 96720, USA.*

of polarimetric data without photometric calibration and 23 sets of photometric data with no significant polarization at the 3 σ level. The data which lack photometric calibration come from poor observing conditions during the 1987 September run. Consequently, for those objects where no polarization was detected (at 3 σ), some of the upper limits are quite high. These data constitute the largest such set of observations yet obtained.

2. Observational techniques.

Two instruments were used to obtain the data presented in this paper. The Mark I Hatfield Polarimeter (as described by Brindle *et al.*(1986), with the addition of an extra optical channel) was used for the observations of 1986. The Mark II instrument, described below, was used for the observations of 1987 and 1988. Both operate at the $f/35$ Cassegrain focus of UKIRT. All the observations were taken with an 8 arcsec aperture.

2.1 THE MARK II HATFIELD POLARIMETER.

The Mark II Hatfield Polarimeter was constructed at the Hatfield Polytechnic and was first used in 1987 July at UKIRT. Its optical layout is shown in Fig. 1. It is a twin-beam instrument with two beams separated by 50.8 mm., which corresponds to an angular separation on the sky of 81.3 arcsec at the $f/35$ focus of UKIRT. The advantage of this set-up over the Mark I polarimeter is that the optical and infrared measurements are now performed on separate beams so that the wave-plates and other optics have been optimised for the appropriate wavelength ranges.

The infrared beam passes through an IR-achromatic wave-plate (1–2.5μm) and then an IR/optical dichroic. The reflected IR beam passes through a wire-grid analyser and into the observatory cryostat (UKT9). The transmitted optical beam is sent to the UKIRT TV

camera for acquisition and guiding. An efficiency correction must be applied to the infrared polarization measurements, due to inefficiencies which arise from the frequency response of the detector and the wire-grid analyser. The appropriate efficiency to use for correcting the measurements is the measured polarization of an unpolarized star with the Glan prism inserted into the IR beam. The wire grid indicated on the calibration slide in Fig. 1 is only used if calibration at longer wavelengths than K is required, where the Glan prism can no longer be used. No such observations are presented in this paper.

The optical beam is measured in a similar way to the Mark I device. A superachromatic wave plate is followed by a Foster prism which produces two orthogonally polarized beams. Dichroics are then used to split the beams into U and R channels, and the B,V and I beams channels with filters used in each beam to form the separate passbands. The polarimeter can thus measure the U,B,V,R,I wavebands and one IR waveband simultaneously. The filters quite closely reproduce the Cousins UBVRI system (Bessell, 1979) and any differences have been ignored. The effective wavelengths of the filters are listed in Table 1.

The polarimeter is operated in a similar manner to the Mark I device. A cycle consists of four rotations of the wave-plate. At the start of the cycle the object is centred on the optical beam. At the end of the first rotation the telescope is nodded to bring the object into the IR beam and then nodded back after the third rotation. While not centred on the object, the beams are measuring the sky. As for the Mark I device, on-line software updates the polarization and flux measurements and their combined errors — obtained from photon statistics — at the end of each cycle.

The polarimeter returns relative fluxes for each waveband, which are then calibrated by observations of standard stars. The infrared magnitudes were calibrated by observations of stars from the UKIRT standards list and the optical standards were obtained from the

catalogue of Landolt (1983). Airmass corrections were performed using observationally determined extinctions. The fluxes have all been corrected for interstellar extinction with the values of $E(B-V)$, taken from Burstein and Heiles (1982), given in Table 5. The extinction curve is taken from Rieke and Lebofsky (1985).

The degree of polarization observed is subject to a statistical bias which must be corrected. This is inherent in the measurement of a vector quantity in the presence of noise. Wardle and Kronberg (1974) give the expression for the modal value, which is used to relate the true polarization p to the measured polarization p'.

$$p = p'\sqrt{1-\left(\frac{\sigma_p}{p'}\right)^2} \tag{1}$$

The best estimate of the error on p is the error on the measured polarization σ_p. The measured position angle is the best estimate of the true position angle, but the error is underestimated in the case of poor signal-to-noise (Wardle and Kronberg, 1974).

The glan prism is used to measure the relative position angles in each band. The zero of position angle on the sky is determined by measurements of polarized standard stars taken from Serkowski (1974). These position angles are only quoted to one degree accuracy and no errors are given. Consequently for many of the measurements given, the position angle error is dominated by the unknown error in these angles.

3. Results.

3.1 Individual Objects.

The shape of the spectrum will be characterised by the use of the (local) spectral index;

$$\alpha(\nu) = -\frac{d\log S_\nu(\nu)}{d\log\nu}\,. \tag{2}$$

The condition of a frequency-dependent spectral index which results in curvature in the $\log S_\nu(\nu) - \log \nu$ plane is referred to as spectral curvature.

To test for spectral curvature, a power-law was fitted to all the UKIRT photometric data. All the Mark I Hatfield Polarimeter data consist of measurements at H, I and B at least. The Mark II data all have one infrared and at least four optical measurements. For some high airmass ($\sec z > 1.5$) observations, the U data had to be rejected because atmospheric refraction makes the photometry unreliable. Consequently all the data can be fitted by a power-law with at least one degree of freedom. These fits were achieved by minimising the χ^2 statistic, the use of which is only valid if the errors concerned are distributed normally. Unfortunately, this is certainly *not* the case here. The errors on the photometry are not simply the random errors associated with photon counting, but include the systematic uncertainties in the photometric calibration. It is most unlikely that these latter errors are distributed normally. However its use here is justified as the aim is to obtain an idea of the frequency of spectral curvature within the blazar population rather than to reject a power-law fit for any one individual object.

All the data which had two or more polarization measurements were tested for frequency dependence of the degree of polarization (hereafter FDP). The weighted mean of the measured polarizations was calculated and then tested against all the measured polarizations by use of the χ^2 statistic with the loss of one degree of freedom. Similarly the data were also tested for frequency dependence of the position angle of polarization (hereafter FDθ). Polarimetric errors should have an approximately normal error distribution in the case of high signal-to-noise, and the position angle error distribution is also approximately normal for high signal-to-noise observations (Wardle and Kronberg, 1974).

We now give a brief description of the observations of each object.

0048 – 097, OB–081

This object was confirmed as a blazar by Angel and Stockman (1980) (hereafter AS80). 0048 – 097 was observed extensively in the 1986 August, 1987 July and 1987 September runs. It consistently showed FDP, but not FDθ , in 1986 August. No such behaviour was observed in 1987 July or September. Typically the position angle changed from night to night by a few degrees.

PKS 0106 + 013

This highly polarized quasar, HPQ, (confirmed by Moore and Stockman, 1984) was observed on one night in each of the first three runs. No significant polarizations were recorded during the 1986 July/August and the 1987 September runs. The only significant polarization measured was the U polarization of 1987 July 28 ($p(U) = 14.37 \pm 2.39\,\%$).

GC 0109 + 224

An AS80 blazar, 0109 + 224 was observed during all three runs. The polarization in 1986 August was highly variable and displayed both FDP and FDθ . Both $dp/d\nu > 0$ and $dp/d\nu < 0$ were observed on successive nights. The polarization observed in 1987 July was $\sim 10\%$ but essentially constant. The 1987 September data showed more variation but only one case of FDP.

PKS 0118 – 272

This object was a radio source identification with a smooth IR/optical spectrum (Wilkes *et al.* 1983). Impey and Tapia (1988) measured one significant (i.e. $> 3\%$) polarization. The observations presented here confirm that this object is a blazar. The polarization was high ($p \sim 17\%$) but constant through 1987 August. FDP was seen in 1987 July with $dp/d\nu > 0$.

0138 – 097

This was another radio source identification with a smooth IR/optical spectrum (Fricke *et al.* 1983), which was confirmed as a blazar by Impey and Tapia (1988). The polarization in 1986 August was $\sim 6\%$ with marginal indications of $dp/d\nu < 0$. The 1987 July data showed higher polarization ($\sim 20\%$) without FDP, while the 1987 September polarizations were of similar amplitude but with $dp/d\nu > 0$.

PKS 0219 – 164

This object was identified as a blazar by Meisenheimer and Röser (1984). It was observed only once (1987 July 28), when it had (frequency averaged) polarization of $12.63 \pm 0.18\%$ at a position angle of $160.9 \pm 0.5\,°$. This position angle is consistent with the range predicted by the 'oblique rotator' model of Meisenheimer and Röser, though of course this model cannot be confirmed without some data on variability.

0219 + 428, 3C 66A

An AS80 blazar which was observed in all three runs. The polarization behaviour in 1986 August was fairly constant with no marked frequency dependence, and this was also the case in 1987 July. Marginal evidence for FDP was seen in 1987 September. Inoue (personal communication) reports 10 GHz observations of this object on 1987 September 17 which show 2.8% polarization at 5°.

AO 0235 + 164

This is the object for which Impey, Brand and Tapia (1982) measured their record polarization of $p(V) = 43.9 \pm 1.4\,\%$. Two photometric observations of this object were made. The spectrum was very steep $\alpha(B) = 4.61$, but the polarizations were always of the order of 10%. Inoue (personal communication) reports 10 GHz observations on 1987 September 17 which show 1.5% polarization at 14°. This position angle is consistent with the IR/optical data.

0300 + 470, 4C 47.08

This AS80 blazar was observed only once on 1987 September 20 in poor photometric conditions. The data were consistent with $p = 8.91 \pm 0.64\%$ and $\theta = 9.42 \pm 1.92°$, independent of frequency.

1H 0323 + 022

This X-ray selected object was classified as a blazar by Feigelson *et al.* (1986) who, in particular, noted its extremely rapid X-ray variability. They observed it to be optically polarized (2 – 9%) in 1983 and 1984. No significant polarization was observed on 1986 August 1 ($p < 6.3\%; 3\sigma$ upper limit at I). Polarization was measured on 1987 September 21, with the average over all wavebands being 3.56 ± 0.45 %.

0336 – 019, CTA 26

This HPQ (Moore and Stockman, 1981) was observed only once on 1986 August 5, and no significant polarization was measured as the object was faint and the integration was accordingly terminated early.

0338 – 214

This is a smooth optical spectrum radio source identification (Wilkes *et al.* 1983). The polarization was observed to be $\sim 10\%$ in both 1986 August and 1987 September with no frequency dependence.

1H 0414 + 009

This X-ray selected object is a candidate blazar. Ulmer *et al.* (1983) classified it as a BL Lac object and Impey and Tapia (1988) reported an optical polarization of $2.76 \pm 0.29\%$. On 1988 February 15 and February 16 the B polarization was 6.4 ± 0.8 %. There was no

evidence for frequency dependent polarization on either night.

PKS 0422 + 004

This AS80 blazar was observed on 1988 February 16 and 18. There was no evidence for frequency dependent polarization, but the polarization decreased from 21.4 ± 0.3 to $12.4 \pm 0.2\%$ between these dates.

PKS 0735 + 178

This well known blazar was observed on 1987 September 19 in poor photometric conditions. The measured polarization was frequency independent ($p = 6.9 \pm 0.4$ %) but the position angle was marginally frequency dependent (average value 136°). On 1988 February 16 there was evidence for $dp/d\nu > 0$.

PKS 0736 + 017

This AS80 blazar was observed on 1988 February 15, 16 when no significant polarization was detected at the 3% level.

0754 + 100, OI 090.4

0754 + 100 is a well known AS80 blazar which was observed on 1988 February 15, 16, 17 and 18. The polarization showed $dp/d\nu > 0$, the degree of which decreased with time. On the last two nights the position angle was frequency independent at an average angle of 36.2°.

0818 − 128, OJ−131

This AS80 blazar was observed on 1988 February 15, 16 and 17. During the course of the observations the degree of frequency dependence of the polarization increased. The

position angle was frequency independent throughout at an average angle of 81°.

0851 + 202, OJ287

This well known object was the subject of a previous paper (Holmes *et al.* 1984b), when it displayed notable behaviour, interpreted in terms of a two-component model for the emission. It was observed on 1988 February 15, 16 and 17 to have a polarization around 10%. $dp/d\nu > 0$ was observed on the February 16 and February 17. The data presented here for OJ287 are satisfactorily fitted by the two-component model.

0906 + 015

0906 + 015 is an AS80 blazar which was observed once in February 1988. At the 3% level no significant polarization was detected.

1101 + 384, Mkn 421

This is an AS80 object, located in a galaxy at redshift, z=0.0308. It was observed once, on 1988 February 15. The fact that the polarization showed complex behaviour and the curvature in the spectrum is in agreement with the hypothesis that the galactic flux significantly contaminates the blazar component.

1147 + 245

This AS80 blazar displayed $dp/d\nu > 0$ and complex position angle behaviour on the single occasion on which it was observed (1988 February 18).

1156 + 295

On 1988 February 15, 16 and 17 this well studied AS80 blazar was observed to have frequency independent polarizations and position angles (frequency averaged) of 24% at

165°.

1253 − 055, 3C 279

This object is a well studied superluminal radio source, which has long been known to be a blazar. The observations of 1986 August show a polarization flare, with the degree of polarization increasing during the course of the run, and consistently showing $dp/d\nu > 0$. The U data of 1986 August 5 show a polarization of $45.92 \pm 0.98\%$. This is the largest polarization ever seen in the IR/optical for a blazar (c.f. 0235 + 164; Impey, Brand and Tapia 1982). On 1987 July 28 the polarization was still high, but not at the record level. In 1988 February the polarization rose throughout the observations from $19.6 \pm 0.8\%$ to $30.7 \pm 0.6\%$ in the U band.

1413 + 135, OQ 122

This is a radio source with a very steep IR/optical spectrum (Beichman *et al.* 1981; Bregman *et al.* 1981). The latter gives the only recorded significant polarization of $19 \pm 3\%$ at H. This object was observed in 1986 August, but was too faint for IR polarimetry to be feasible in the time available. The spectrum was so steep that only an upper limit is available for the optical flux.

1418 + 546, OQ 530

This AS80 blazar was observed during all four runs. In 1986 August the polarization showed FDP with $dp/d\nu > 0$, which was repeated in the measurements of 1987 July 30, where the polarization increased from 2.5% at H to 8.7% at U. This latter was accompanied by significant FDθ . The data of 1987 September were all obtained in poor photometric conditions. However the polarization data still showed FDP but no FDθ . During the 1988 February the position angle was constant at 144° on the 16th and 17th. On the final night significant $FD\theta$ was observed, from $132.0 \pm 2.5°$ at H to $156.2 \pm 3.9°$ at U.

1424 + 240

This is a smooth spectrum radio source identification which was confirmed as a blazar by Impey and Tapia (1988). Frequency independent polarizations (19.6%) and position angles (116°) were recorded on 1988 February 16, 17 and 18.

PKS 1510 – 089

This object was confirmed to be a blazar by Moore and Stockman (1981) and Smith *et al.* (1987). It is one of the most violently variable HPQ's with $\Delta m = 5.4$ (Moore and Stockman, 1981). It was observed only once on 1986 August 1. The 3σ upper limit to the the I polarization was 6.3 %.

1514 – 241, *AP Lib*

One of the original BL Lac objects, 1514 – 241 was observed only twice (1986 August 1 and 1987 July 27). The polarization of this object is typically quite low compared to most other blazars (e.g. AS80). Our observations are consistent with this. FDP was seen on 1987 July 27.

1538 + 149, 4C 14.60

An AS80 blazar which was observed on 1986 August 1 when no significant polarization was observed. The 3 σ upper limit was high (27 %) as the object was faint.

1641 + 399, 3C 345

The behaviour of this object was the subject of a recent paper (Mead *et al.* 1988).

1652 + 398, Mkn. 501

This BL Lac object was observed only once on 1987 September 21. Both the degree and position angle of polarization were observed to be frequency dependent (at the 0.5 % level of significance).

1717 + 178, OT 129

This AS80 blazar was observed twice in 1986 August with strong $dp/d\nu < 0$ on the second night. No significant polarization was measured on 1987 July 30 ($p < 21\%$) (upper limit at R).

1727 + 502, I Zw. 186

An AS80 blazar which was observed twice in 1986 August, when it showed variable FDP and FDθ . It was also observed on 1987 September 21 when $dp/d\nu > 0$ was observed (without FDθ).

1749 + 096, OT 081

An AS80 blazar which was extensively observed in 1986 August. No FDP was seen but significant variations were seen in the polarization. FDθ was seen on 1986 July 31. On 1987 July 27, 1749 + 096 was faint but $dp/d\nu > 0$ was seen.

1921 − 293, OV−236

This blazar was first classified as such by Wills and Wills (1981). Confirmation of it being polarized was provided by Impey *et al.* (1982). The observations of 1986 August indicate appreciable photometric variability (a factor of two from 1986 August 6 to August 7). Appreciable FDP was seen on 1986 August 6.

2032 + 107 MC

This candidate blazar was first classified by Zotov and Tapia (1979), who have published the only polarization measurement. Antonucci *et al.* (1987) have confirmed its extragalactic nature. One observation of this object was made on 1987 July 27. Significant polarization was not detected. The 3 σ upper limit was 1.32% at R.

PKS 2155 – 304

This is one of the brightest of the AS80 BL Lac objects, and was observed as a part of the 1986 August and 1987 July and September runs, but its polarization is typically quite low (3 – 7%; AS80). The data of 1986 August showed polarization at about this level and exhibited variability in both amplitude and frequency dependence. The data of 1987 July 27 showed a higher polarization ($\sim$ 10%) and both FDP and FDθ . The data of 1987 September 21 were obtained in poor conditions, but the polarization showed FDP.

2200 + 420, *BL Lac*

BL Lac was observed more often than any other object in this programme. Photometric variability was small over the 1986 August and 1987 July and September runs. Instances of both FDP and FDθ were observed in all three periods. The position angle of the polarization was in the range 10–40° for all the observations. This is essentially the same position angle seen by Brindle *et al.* (1985). Inoue (personal communication) reports a high 10 GHz polarization of 9.2% at 21° on 1987 September 17. This position angle is somewhat different from that seen in the IR/optical on 1987 September 19 ($\sim$ 40°).

PKS 2208 – 137

This is an AS80 blazar which was observed four times in the 1986 August run. On each occasion it was observed to have an abnormally flat IR/optical spectrum and no polarization. The lowest 3σ upper limit was 1.78% at B on 1986 August 4.

2223 – 052, 3C 446

This is a violently variable HPQ. During the 1986 August observations the object was faint and no reasonable limits on the optical polarization were obtained. In 1987 July frequency independent polarization was seen varying from 12% to 8%. The observations of 1987 September were obtained in poor photometric conditions. The noisy data showed some evidence for FDP. The 10 GHz polarization data of 1987 September 17 ($p \approx 4\%$ and $\theta \approx 2°$), showed a position oriented roughly at 90° from the IR/optical data (Inoue, personal communication).

2230 + 114, CTA 102

This object is an AS80 blazar and a well known superluminal radio source. It was observed twice in 1986 August and no polarization was detected, the upper limits at B being 3.6% and 5.7%.

2251 + 158, 3CR 454.3

Another superluminal radio source and AS80 blazar, this object was observed once in 1986 August, 1987 July and 1987 September. No polarization was observed in the first two runs, but frequency independent polarization was observed on 1987 September 20 of $p = 3.8 \pm 0.3\%$. This position angle was oriented somewhat differently from the 10 GHz data of Inoue (personal communication) who measured $p \approx 3.2\%$ and $\theta \approx 11°$, on 1987 September 1987.

2254 + 074, OY 091

This AS80 blazar was extensively observed in 1986 August, 1987 July and 1987 September . The polarization behaviour was characterised by strong FDP with little evidence for FDθ in all three runs. On all dates except for 1986 August 6, the FDP was such that

$dp/d\nu > 0$.

3.2 Discussion.

The fits to the spectra of the 156 photometric data sets are shown in Table 2. These fits are separated into polarized and unpolarized samples. This is because it is only when polarizations in excess of the 3% limit are seen, that it is certain the observed flux contains a blazar contribution. The fits were all tested at the 5% significance level. If a power-law was rejected at this level, then the spectral flux distribution is characterised as having either a convex spectrum ($d\alpha/d\nu > 0$), a concave spectrum ($d\alpha/d\nu < 0$) or a 'complex' spectrum. The use of this level of significance is very lenient given the likely non-normal errors involved (it corresponds to a 1.96σ point of the normal distribution).

Table 2 lists all the polarimetric observations of blazars and whether they were fitted (at the 5% level of significance) by a constant polarization or FDP (either with $dp/d\nu > 0$, $dp/d\nu < 0$ or with more complex behaviour). In order to assign the FDP categories, a power-law polarization behaviour was fitted to these data ($p(\nu) \propto \nu^{\beta}$). This was an empirical fit whose form was chosen as the polarization degree is constrained to be positive definite and this form allows an unconstrained minimisation to be performed with respect to $\log p_{14}$ and β. The two FDP categories ($dp/d\nu > 0$ and $dp/d\nu < 0$) were assigned on the basis of the sign of the fitted value of β. Those objects not fitted (at the 5% level) by this functional form, are described as having 'complex' polarization behaviour. This procedure will flag behaviour, such as that seen in $1641+399$ and $2200+420$, where the FDP is only significant over a narrow range of the observed frequencies.

Table 2 also presents the results of testing for frequency dependence of the position angle of polarization. The different categories were assigned using the same method as for FDP. FDθ is seen to be rarer than FDP. There is no evidence suggesting any preference for

clockwise over counter-clockwise variations with frequency.

We have presented the results of our observing programme and described the operation of the MkII Hatfield polarimeter. Detailed discussion of individual events and the implications of the statistical properties of the sample is deferred to a further paper (Ballard *et al.* 1989).

Acknowledgements

We would like to thank the PATT committee for the generous allocation of telescope time awarded to this project and to the staff of UKIRT for their assistance during the observing program. K. Ballard and A. Mead wish to acknowledge the receipt of SERC studentships.

References

ANGEL J.R.P., STOCKMAN H.S. (AS80): 1980, *Ann. Rev. Astron. Astrophys.* **18**, 321.

ANTONUCCI R.R.J., HICKSON P., MILLER J.S., OLSZEWSKI E.W.: 1987, *Astron. J.* **93**, 785.

BALLARD K.R., MEAD A.R.G., BRAND P.W.J.L., HOUGH J.H.: 1989, *Mon. Not. R. Astron. Soc. submitted.*

BEICHMAN C.A., NEUGEBAUER G., SOIFER B.T., WOOTTEN H.A., ROELLIG T., HARVEY P.M.: 1981, *Nature* **293**, 711.

BESSEL M.S.: 1979, *Publs. astr. Soc. Pacif.* **91**, 589.

BREGMAN J.N., LEBOFSKY M.J., ALLER M.F., RIEKE G.H., ALLER H.D., HODGE P.E., GLASSGOLD A.E., HUGGINS P.J.: 1981, *Nature* **293**, 714.

BRINDLE C., HOUGH J.H., BAILEY J.A., AXON D.J., SCHULZ H., KIKUCHI S., MCGRAW J.T., WISNIEWSKI W.J., FONTAINE G., NADESU D., CLAYTON G., ANDERSON E., JAMESON R.F., SMITH R., WALLIS R.E.: 1985, *Mon. Not. R. Astron. Soc.* **214**, 619.

BRINDLE C., HOUGH J.H., BAILEY J.A., AXON D.J., HYLAND A.R.: 1986, *Mon. Not. R. Astron. Soc.* **221**, 739.

BURSTEIN D., HEILES C.: 1982, *Astron. J.* **87**, 1165.

FEIGELSON E.D., BRADT H., MCCLINTOCK J., REMILLARD R., URRY C.M., TAPIA S., GELDZAHLER B., JOHNSTON K., ROMANISHIN W., WEHINGER P.A., WYCKOFF S., MADEJSKI G., SCHWARTZ D.A., THORSTENSEN J., SCHAEFER B.E.: 1986, *Astrophys. J.* **302**, 337.

FRICKE K.J., KOLLATSCHNY W., WITZEL A.: 1983, *Astron. Astrophys.* **117**, 60.

HOLMES P.A., BRAND P.W.J.L., IMPEY C.D., WILLIAMS P.M.: 1984a, *Mon. Not. R. Astron. Soc.* **210**, 961.

HOLMES P.A., BRAND P.W.J.L., IMPEY C.D., WILLIAMS P.M., SMITH P., ELSTON R., BALONEK T., ZEILIK M., BURNS J., HECKERT P., BARVAINIS R., KENNY J., SCHMIDT G., PUSCHELL J.: 1984b, *Mon. Not. R. Astron. Soc.* **211**, 497.

IMPEY C.D., BRAND P.W.J.L., WOLSTENCROFT R.D., WILLIAMS P.M.: 1982, *Mon. Not. R. Astron. Soc.* **200**, 19.

IMPEY C.D., BRAND P.W.J.L., TAPIA S.: 1982, *Mon. Not. R. Astron. Soc.* **198**, 1.

IMPEY C.D., BRAND P.W.J.L., WOLSTENCROFT R.D., WILLIAMS P.M.: 1984, *Mon. Not. R. Astron. Soc.* **209**, 245.

IMPEY C.D., TAPIA S.: 1988, *Astrophys. J.* **333**, 666.

LANDOLT A.U.: 1983, *Astron. J.* **88**, 439.

MEISENHEIMER K., RÖSER H.–J.: 1984, *Astrophys. J.* **279**, L39.

MEAD A.R.G., BRAND P.W.J.L., HOUGH J.H., BAILEY J.A.: 1988, *Mon. Not. R. Astron. Soc.* **233**, 503.

MOORE R.L., STOCKMAN H.S.: 1981, *Astrophys. J.* **243**, 60.

MOORE R.L., STOCKMAN H.S.: 1984, *Astrophys. J.* **279**, 465.

RIEKE G.H., LEBOFSKY M.J.: 1985, *Astrophys. J.*, **288**,618.

SERKOWSKI K.: 1974, *Methods of Experimental Physics* **12 A**, 361, Academic Press, New York.

SMITH P.S., BALONEK T.J., ELSTON R., HECKERT P.A.: 1987, *Astrophys. J. Suppl.* **64**, 459.

ULMER M.P., BROWN R.L., SCHWARTZ D.A., PATTERSON J., CRUDDACE R.G.: 1983, *Astrophys. J.* **270**, L1.

WARDLE J.F.C., KRONBERG P.P.: 1974, *Astrophys. J.* **194**, 249.

WILKES B.J., WRIGHT A.E., JAUNCEY D.L., PETERSON B.A.: 1983, *Proc. astr. Soc. Austr.*, **5**, 2.

WILLS D., WILLS B.J.: 1981, *Nature* **289**, 384.

ZOTOV N.V., TAPIA S.: 1979, *Astrophys. J.* **229**, L5.

Table 1: Effective wavelengths and zero-magnitude flux densities.

Filter	$\lambda/\,\mu$m	$\nu/10^{14}$ Hz	S_o/kJy
K	2.18	1.38	0.667
H	1.64	1.83	1.075
J	1.23	2.44	1.603
I	0.80	3.75	2.55
R	0.64	4.68	3.08
V	0.55	5.45	3.64
B	0.44	6.81	4.26
U	0.36	8.33	1.81

Table 2: Summary of the observations. $\alpha_0(>0,<0)$ refers to the spectral index constant (increasing, decreasing) with frequency. This is also indicated for polarization and position angle. Those observations not satisfactorily fitted are labelled complex.

Object	E(B-v)	Date	Flux	Polarization	Position Angle
$0048-097OB-081$	0.00	86 Jul 31	α_0	$\Delta p>0$	θ_0
		86 Aug 3	$\Delta\alpha<0$	$\Delta p>0$	θ_0
		86 Aug 4	α_0	$\Delta p>0$	θ_0
		86 Aug 6	α_0	$\Delta p>0$	θ_0
		86 Aug 7	α_0	$\Delta p>0$	θ_0
		87 Jul 27	$\Delta\alpha<0$	p_0	θ_0
		87 Jul 29	α_0	p_0	θ_0
		87 Jul 30	α_0	p_0	θ_0
		87 Sep 18		p_0	θ_0
		87 Sep 19	α_0	p_0	θ_0
		87 Sep 20		p_0	θ_0
PKS $0106+013$	0.00	86 Aug 4	α_0	unpolarized	
		87 Jul 28	$\Delta\alpha<0$	p_0	θ_0
		87 Sep 21	α_0	unpolarized	
GC $0109+224$	0.06	86 Aug 1	α_0	p_0	θ_0
		86 Aug 4	α_0	$\Delta p<0$	$\Delta\theta<0$
		86 Aug 5		p_0	$\Delta\theta<0$
		86 Aug 6		$\Delta p>0$	θ_0
		86 Aug ?	α_0	$\Delta p>0$	θ_0
		87 Jul 27	α_0	p_0	θ_0
		87 Jul 30	$\Delta\alpha>0$	p_0	θ_0
		87 Sep 19	α_0	p_0	θ_0
		87 Sep 20		p_0	θ_0
		87 Sep 21	α_0	$\Delta p>0$	complex
$0118-272$	0.00	86 Aug 5	α_0	p_0	θ_0
		86 Aug 6		p_0	complex
		86 Aug 7	α_0	p_0	θ_0
		87 Jul 27	$\Delta\alpha<0$	$\Delta p>0$	θ_0
		87 Jul 30	α_0	$\Delta p>0$	θ_0
		87 Sep 20		complex	θ_0
		87 Sep 21	α_0	$\Delta p>0$	θ_0
$0138-097$	0.00	86 Aug 5	α_0	$\Delta p<0$	θ_0
		86 Aug 6		p_0	θ_0
		86 Aug 7	α_0	p_0	$\Delta\theta>0$
		87 Jul 28	α_0	p_0	θ_0
		87 Jul 30	α_0	p_0	θ_0
		87 Sep 19	α_0	$\Delta p>0$	θ_0
		87 Sep 20	α_0	$\Delta p>0$	θ_0
		87 Sep 21	α_0	p_0	θ_0
$0219-164$	0.00	87 Jul 28	α_0	p_0	θ_0
$0219+428$ 3C 66A	0.09	86 Aug 1		p_0	$\Delta\theta>0$
		86 Aug 4		$\Delta p>0$	θ_0
		86 Aug 6		p_0	θ_0
		86 Aug 7		p_0	θ_0
		87 Jul 27	α_0	p_0	θ_0
		87 Jul 30	α_0	p_0	θ_0
		87 Sep 18		complex	θ_0
		87 Sep 19		p_0	θ_0
		87 Sep 20	α_0	p_0	θ_0
		87 Sep 21		p_0	θ_0

Table 2: Summary of the observations contd.

Object	E(B-v)	Date	Flux	Polarization	Position Angle
AO 0235 + 164	0.15	87 Jul 28	$\Delta\alpha > 0$	p_0	θ_0
		87 Sep 20	$\Delta\alpha > 0$	complex	θ_0
0300 + 470 4C 47.08	0.15	87 Sep 20		p_0	θ_0
0323 + 022	0.06	86 Aug 1			
		87 Sep 21		p_0	θ_0
0336 − 019	0.06	86 Aug 5		unpolarized	
0338 − 214	0.00	86 Aug 6		p_0	θ_0
		87 Sep 19		p_0	θ_0
0414 + 009	0.12	88 Feb 15	$\Delta\alpha > 0$	p_0	θ_0
		88 Feb 16	$\Delta\alpha > 0$	p_0	θ_0
0422 + 004	0.12	88 Feb 16	$\Delta\alpha > 0$	p_0	complex
		88 Feb 18	$\Delta\alpha > 0$	p_0	complex
PKS 0735 + 178	0.03	87 Sep 19		p_0	$\Delta\theta < 0$
		88 Feb 15	complex	p_0	complex
		88 Feb 16	α_0	p_0	θ_0
		88 Feb 18	α_0	p_0	complex
0736 + 017	0.12	88 Feb 15	complex	unpolarized	
		88 Feb 16	complex	unpolarized	
0754 + 100	0.00	88 Feb 15	$\Delta\alpha > 0$	$\Delta p > 0$	$\Delta\theta > 0$
		88 Feb 16	$\Delta\alpha > 0$	$\Delta p > 0$	complex
		88 Feb 17	α_0	p_0	θ_0
		88 Feb 18	α_0	p_0	θ_0
0818 − 128 OJ-131	0.09	88 Feb 15	complex	$\Delta p > 0$	θ_0
		88 Feb 16	$\Delta\alpha > 0$	$\Delta p > 0$	θ_0
		88 Feb 17	$\Delta\alpha > 0$	$\Delta p > 0$	θ_0
0851 + 202 OJ287	0.00	88 Feb 15	$\Delta\alpha > 0$	p_0	θ_0
		88 Feb 16	α_0	$\Delta p > 0$	θ_0
		88 Feb 17	α_0	$\Delta p > 0$	$\Delta\theta > 0$
0906 + 015	0.00	88 Feb 15	α_0	unpolarized	
1101 + 384	0.00	88 Feb 15	$\Delta\alpha > 0$	complex	θ_0
1147 + 245	0.00	88 Feb 18	α_0	$\Delta p > 0$	$\Delta\theta < 0$
1156 + 295	0.00	88 Feb 15	α_0	p_0	θ_0
		88 Feb 16	α_0	p_0	θ_0
		88 Feb 17	α_0	p_0	θ_0
1253 − 055 3C 279	0.03	86 Aug 1	α_0	p_0	θ_0
		86 Aug 2	α_0	$\Delta p > 0$	$\Delta\theta < 0$
		86 Aug 4	α_0	$\Delta p > 0$	complex
		86 Aug 5	α_0	$\Delta p > 0$	$\Delta\theta < 0$
		86 Aug 6	α_0	$\Delta p > 0$	$\Delta\theta < 0$
		87 Jul 28	$\Delta\alpha > 0$	$\Delta p > 0$	θ_0
		88 Feb 16	α_0	p_0	complex
		88 Feb 17	α_0	p_0	complex
		88 Feb 18	α_0	$\Delta p > 0$	θ_0
1413 + 135	0.03	86 Aug 6	α_0	unpolarized	
1418 + 546 OQ 530	0.03	86 Aug 4		$\Delta p > 0$	θ_0
		86 Aug 5		$\Delta p > 0$	complex
		86 Aug 6		complex	θ_0
		87 Jul 30	α_0	$\Delta p > 0$	complex
		87 Sep 20		$\Delta p > 0$	θ_0
		87 Sep 21		$\Delta p > 0$	θ_0
		88 Feb 16	$\Delta\alpha > 0$	complex	θ_0
		88 Feb 17	$\Delta\alpha > 0$	complex	θ_0
		88 Feb 18	$\Delta\alpha > 0$	p_0	$\Delta\theta > 0$

Table 2: Summary of the observations contd.

Object	E(B-v)	Date	Flux	Polarization	Position Angle
1424 + 240	0.00	88 Feb 16	complex	p_0	θ_0
		88 Feb 17	$\Delta\alpha > 0$	p_0	θ_0
		88 Feb 18	α_0	unpolarized	
PKS 1510 − 089	0.06	86 Aug 1	α_0	p_0	
1514 − 241 AP Libra	0.15	86 Aug 1		p_0	complex
		87 Jul 27	$\Delta\alpha > 0$	complex	θ_0
1538 + 149 4C 14.60	0.00	86 Aug 1	α_0	unpolarized	
1641 + 399 3C 345	0.00	86 Aug 1	$\Delta\alpha < 0$	complex	θ_0
		86 Aug 2	$\Delta\alpha < 0$	complex	θ_0
		86 Aug 4	$\Delta\alpha < 0$	complex	θ_0
		86 Aug 5	$\Delta\alpha < 0$	complex	θ_0
		86 Aug 6	complex	complex	θ_0
		86 Aug 7		$\Delta p < 0$	θ_0
		87 Jul 28	complex	unpolarized	
		87 Jul 30	$\Delta\alpha < 0$	unpolarized	
		87 Sep 19	$\Delta\alpha < 0$	unpolarized	
1652 + 398 Mkn 501	0.00	87 Sep 21		complex	$\Delta\theta < 0$
1717 + 178 OT 129	0.06	86 Aug 6	α_0	p_0	θ_0
		86 Aug 7		$\Delta p < 0$	θ_0
		87 Jul 30	α_0	unpolarized	
1727 + 502 I Zw 186	0.00	86 Aug 6		p_0	$\Delta\theta < 0$
		86 Aug 7		$\Delta p > 0$	θ_0
		87 Sep 21		$\Delta p > 0$	θ_0
1749 + 096 OT 081	0.15	86 Jul 31		p_0	$\Delta\theta > 0$
		86 Aug 5		p_0	θ_0
		86 Aug 6		p_0	θ_0
		86 Aug 7		$\Delta p > 0$	θ_0
		87 Jul 27	α_0	$\Delta p > 0$	θ_0
1921 − 293 OV-236	0.12	86 Aug 3		p_0	$\Delta\theta > 0$
		86 Aug 6		$\Delta p < 0$	θ_0
		86 Aug 7		p_0	θ_0
		87 Jul 27	complex	unpolarized	
2032 + 107	0.12	87 Jul 27	complex	unpolarized	
PKS 2155 − 304	0.00	86 Aug 1	α_0	$\Delta p > 0$	complex
		86 Aug 5	α_0	p_0	θ_0
		86 Aug 6		p_0	$\Delta\theta > 0$
		86 Aug 7	α_0	p_0	θ_0
		87 Jul 27	α_0	$\Delta p > 0$	$\Delta\theta < 0$
		87 Sep 21		complex	θ_0
2200 + 420 BL Lacertae	0.15	86 Jul 31		$\Delta p > 0$	θ_0
		86 Aug 1		p_0	θ_0
		86 Aug 3	$\Delta\alpha > 0$	complex	$\Delta\theta > 0$
		86 Aug 4		complex	$\Delta\theta > 0$
		86 Aug 5		complex	$\Delta\theta > 0$
		86 Aug 6		complex	θ_0
		86 Aug 7		complex	$\Delta\theta > 0$
		87 Jul 27	$\Delta\alpha > 0$	$\Delta p < 0$	$\Delta\theta < 0$
		87 Jul 28	$\Delta\alpha > 0$	complex	$\Delta\theta < 0$
		87 Jul 30	$\Delta\alpha > 0$	$\Delta p < 0$	$\Delta\theta < 0$
		87 Sep 19	$\Delta\alpha > 0$	complex	complex
		87 Sep 20		complex	$\Delta\theta > 0$
		87 Sep 21		complex	$\Delta\theta > 0$

Table 2: Summary of the observations contd.

Object	E(B-v)	Date	Flux	Polarization	Position Angle
PKS 2208 – 137	0.00	86 Aug 3		unpolarized	
		86 Aug 4		unpolarized	
		86 Aug 6	α_0	unpolarized	
		86 Aug 7		unpolarized	
2223 – 052 3C 446	0.03	86 Aug 4	α_0	unpolarized	
		87 Jul 27	α_0	p_0	θ_0
		87 Jul 29	α_0	p_0	θ_0
		87 Jul 30	α_0	p_0	θ_0
		87 Sep 20		$\Delta p > 0$	θ_0
		87 Sep 21		p_0	θ_0
2230 + 114 4C 11.69	0.03	86 Aug 3	α_0	unpolarized	
		86 Aug 4	α_0	unpolarized	
2251 + 158	0.06	86 Aug 5	α_0	unpolarized	
		87 Jul 28	$\Delta\alpha > 0$	unpolarized	
		87 Sep 20		p_0	θ_0
2254 + 074 OY 091	0.06	86 Jul 31		$\Delta p > 0$	θ_0
		86 Aug 1		p_0	θ_0
		86 Aug 3	complex	$\Delta p > 0$	θ_0
		86 Aug 4	$\Delta\alpha > 0$	complex	θ_0
		86 Aug 5		$\Delta p > 0$	θ_0
		86 Aug 6		$\Delta p > 0$	θ_0
		86 Aug 7	α_0	p_0	complex
		87 Jul 28	$\Delta\alpha > 0$	complex	θ_0
		87 Jul 30	$\Delta\alpha > 0$	complex	θ_0
		87 Sep 18		p_0	complex
		87 Sep 21		$\Delta p > 0$	θ_0

Table 3 UKIRT data:1986 July 31 - August 7, 1987 July 27 - 30, 1987 September 18 - 21, 1988 February 15 - 1

Filter	Flux density (mJy)		Polarization (%)		Position angle (deg)	
0048-097 OB-081			E(B-V) = 0.00			
1986 Jul. 31						
H	6.78	(0.63)	11.50	(1.80)	112.29	(4.85)
I	3.69	(0.34)	12.05	(0.52)	118.09	(1.28)
B	1.70	(0.24)	13.91	(0.44)	117.15	(0.83)
1986 Aug. 3						
H	9.63	(0.45)	13.17	(0.78)	116.34	(1.70)
J	5.26	(0.25)	15.09	(1.00)	117.58	(1.68)
I	3.01	(0.23)	14.55	(0.61)	118.13	(1.33)
R	2.34	(0.22)	16.02	(0.52)	116.38	(1.07)
V	1.74	(0.17)	16.59	(0.64)	118.54	(1.34)
B	1.62	(0.16)	16.90	(0.32)	116.45	(0.60)
1986 Aug 4						
H	6.54	(0.18)	14.80	(0.79)	111.71	(1.26)
J	4.71	(0.22)	14.31	(0.74)	112.37	(1.73)
I	3.12	(0.15)	15.67	(0.60)	111.29	(1.13)
V	1.86	(0.15)	17.42	(0.52)	113.68	(1.28)
B	1.73	(0.14)	17.85	(0.35)	111.50	(0.73)
1986 Aug. 6						
H	6.48	(0.30)	12.08	(0.88)	103.04	(1.75)
J	4.84	(0.23)	16.24	(0.68)	102.62	(1.39)
I	3.69	(0.34)	17.98	(0.60)	104.89	(1.02)
R	2.40	(0.23)	18.76	(0.49)	105.90	(0.78)
V	1.95	(0.15)	18.75	(0.57)	107.14	(1.32)
B	1.62	(0.16)	19.39	(0.38)	106.02	(0.57)
1986 Aug. 7						
H	6.60	(0.31)	12.89	(1.15)	106.69	(2.85)
I	3.15	(0.15)	15.79	(0.81)	107.36	(1.31)
B	1.66	(0.10)	18.12	(0.51)	108.82	(0.85)
1987 Jul. 27						
J	4.98	(0.32)	15.53	(1.30)	107.73	(1.95)
I	2.30	(0.11)	17.25	(0.82)	104.74	(1.27)
R	1.68	(0.09)	16.50	(0.80)	104.89	(1.22)
V	1.48	(0.08)	16.12	(0.86)	105.73	(2.43)
B	1.30	(0.08)	16.76	(0.71)	102.56	(1.04)
U	0.95	(0.10)	14.56	(0.75)	102.90	(1.46)
1987 Jul. 29						
K	9.64	(0.89)	19.34	(1.83)	117.44	(2.80)
H	6.24	(0.58)	21.72	(1.13)	117.82	(1.71)
I	2.55	(0.24)	21.17	(1.02)	116.85	(1.45)
R	1.94	(0.18)	21.32	(0.70)	118.82	(1.38)
V	1.59	(0.15)	20.54	(1.41)	118.50	(2.39)
B	1.17	(0.12)	22.69	(0.66)	118.26	(1.14)
U	0.79	(0.08)	23.03	(0.81)	117.66	(1.30)

Table 5 Continued.

Filter	Flux density (mJy)		Polarization (%)		Position angle (deg)	
1987 Jul. 30						
K	8.02	(0.44)	12.08	(1.53)	115.22	(3.67)
H	5.80	(0.11)	11.72	(0.98)	115.47	(2.50)
I	2.33	(0.11)	12.92	(0.59)	115.59	(1.71)
R	1.63	(0.08)	13.55	(0.57)	117.00	(1.32)
V	1.38	(0.07)	13.65	(0.86)	118.35	(2.12)
B	1.05	(0.06)	13.56	(0.57)	113.95	(1.56)
U	0.68	(0.07)	14.48	(1.16)	111.16	(2.42)
1987 Sep. 18						
H			5.40	(0.84)	81.26	(4.09)
I			3.64	(0.76)	78.81	(5.89)
R			4.52	(0.50)	88.50	(3.03)
V			3.60	(1.26)	87.11	(6.75)
B			4.09	(0.41)	94.10	(3.04)
U			3.12	(0.73)	95.17	(9.28)
1987 Sep. 19						
H	8.15	(0.75)	4.52	(0.60)	94.86	(4.07)
J	5.31	(0.49)	4.50	(0.75)	90.39	(4.22)
I	2.80	(0.26)	5.35	(0.50)	97.69	(5.21)
R	2.34	(0.22)	5.93	(0.30)	90.39	(1.37)
V	1.91	(0.18)	6.18	(0.70)	94.85	(2.29)
B	1.55	(0.15)	5.76	(0.44)	92.14	(1.76)
U	0.95	(0.10)	5.71	(0.51)	92.43	(2.25)
1987 Sep. 20						
H			3.18	(0.60)	90.70	(4.31)
I			4.17	(0.54)	86.53	(3.93)
R			4.15	(0.41)	89.69	(2.50)
V			2.46	(0.90)	83.31	(9.45)
B			5.23	(0.50)	88.92	(2.50)
U			4.08	(0.72)	94.61	(5.36)
PKS 0106+013			E(B-V) = 0.00			
1986 Aug. 4						
H	0.43	(0.06)	33.15	(18.62)	127.96	(15.16)
I	0.23	(0.02)	0.00	(7.84)		
B	0.20	(0.02)	12.28	(5.26)	122.37	(8.54)
1987 Jul. 28						
H	0.65	(0.03)	0.00	(13.02)		
I	0.29	(0.02)	17.44	(5.83)	138.64	(8.52)
R	0.19	(0.01)	11.30	(5.55)	146.86	(15.43)
V	0.17	(0.02)	0.00	(8.75)		
B	0.16	(0.01)	7.12	(3.39)	146.48	(9.67)
U	0.11	(0.01)	14.37	(2.39)	130.09	(5.03)

Table 5 Continued.

Filter	Flux density (mJy)		Polarization (%)		Position angle (deg)	
1987 Sep. 21						
H	0.43	(0.10)	36.73	(13.65)	119.33	(9.98)
I	0.28	(0.04)	0.00	(40.86)		
R	0.19	(0.02)	5.64	(4.43)	95.11	(24.59)
V	0.21	(0.03)	0.00	(10.99)		
B	0.15	(0.01)	0.54	(4.57)	56.51	(29.35)
U			0.00	(7.61)		
GC 0109+224			E(B-V) = 0.06			
1986 Aug. 1						
H	7.09	(0.33)	9.06	(1.20)	40.95	(3.55)
I	3.10	(0.29)	10.05	(0.43)	35.64	(1.30)
B	2.14	(0.21)	10.88	(0.34)	34.36	(1.04)
1986 Aug. 4						
H	7.02	(0.26)	5.66	(0.51)	54.70	(4.63)
I	3.07	(0.15)	3.81	(0.50)	42.74	(5.81)
B	1.26	(0.13)	4.13	(0.37)	31.15	(3.22)
1986 Aug. 5						
H	6.96	(0.32)	4.80	(1.90)	61.81	(7.07)
I	3.07	(0.15)	2.70	(0.45)	48.36	(4.71)
B	1.13	(0.07)	1.64	(0.49)	29.07	(7.95)
1986 Aug. 6						
H	6.58	(0.31)	0.00	(1.17)		
I	3.18	(0.15)	0.96	(0.63)	24.63	(3.43)
B	1.35	(0.08)	3.74	(0.47)	13.16	(3.96)
1986 Aug. 7						
H	6.58	(0.31)	1.58	(0.87)	4.06	(8.23)
J	4.70	(0.22)	3.41	(1.06)	22.18	(8.68)
I	2.90	(0.14)	4.95	(0.64)	17.54	(3.90)
R	2.13	(0.16)	6.35	(0.58)	20.31	(2.50)
V	1.61	(0.16)	7.53	(0.59)	21.90	(2.14)
B	1.29	(0.08)	8.63	(0.30)	17.20	(1.03)
1987 Jul. 27						
H	4.81	(0.22)	13.63	(1.10)	100.66	(2.25)
I	1.77	(0.08)	14.04	(0.90)	103.58	(1.57)
R	1.19	(0.06)	13.79	(0.60)	104.61	(1.74)
V	0.94	(0.05)	15.04	(1.67)	107.92	(2.04)
B	0.73	(0.04)	15.24	(0.60)	105.83	(1.48)
U	0.51	(0.05)	14.15	(0.99)	107.34	(2.19)
1987 Jul. 30						
H	4.86	(0.23)	9.37	(1.12)	109.42	(3.73)
I	1.92	(0.09)	8.91	(0.85)	108.91	(2.25)
R	1.29	(0.07)	9.51	(0.49)	109.15	(2.28)
V	1.01	(0.05)	9.08	(0.94)	104.22	(3.96)
B	0.72	(0.04)	9.12	(0.57)	110.09	(1.60)
U	0.43	(0.03)	8.35	(1.04)	113.16	(4.37)

Table 5 Continued.

Filter	Flux density (mJy)		Polarization (%)		Position angle (deg)	
1987 Sep. 19						
H	7.22	(0.67)	4.12	(0.70)	117.86	(5.10)
I	2.58	(0.24)	3.92	(0.69)	124.48	(3.95)
R	1.88	(0.18)	4.02	(0.40)	115.87	(2.84)
V	1.34	(0.13)	3.89	(1.22)	123.55	(8.53)
B	1.03	(0.10)	3.66	(0.54)	121.28	(4.32)
U	0.67	(0.07)	3.88	(0.81)	123.90	(5.81)
1987 Sep. 20						
H			13.16	(1.03)	107.82	(2.92)
I			11.64	(1.16)	105.58	(2.25)
R			15.01	(0.98)	107.98	(1.41)
V			15.90	(1.66)	110.97	(3.01)
B			14.37	(0.98)	112.02	(1.39)
U			17.26	(1.81)	109.32	(1.80)
1987 Sep. 21						
H	5.48	(0.51)	13.87	(0.74)	105.70	(1.51)
I	1.95	(0.18)	13.81	(0.57)	103.46	(1.54)
R	1.36	(0.13)	15.29	(0.50)	100.78	(0.76)
V	1.02	(0.10)	17.27	(1.37)	98.60	(2.35)
B	0.71	(0.07)	16.44	(0.64)	105.38	(1.14)
U			16.14	(0.82)	102.34	(1.79)
0118-272			E(B-V) = 0.00			
1986 Aug. 5						
H	8.15	(0.38)	15.37	(0.77)	147.79	(1.46)
J	5.98	(0.28)	16.26	(0.91)	148.01	(1.75)
I	4.00	(0.19)	17.82	(0.58)	147.24	(0.97)
R	2.81	(0.14)	17.87	(0.47)	149.97	(0.81)
V	2.19	(0.12)	17.33	(0.63)	149.19	(1.49)
B	1.86	(0.19)	17.21	(0.35)	149.90	(0.59)
1986 Aug. 6						
H	8.08	(0.37)	16.63	(1.02)	148.71	(1.85)
I	3.97	(0.19)	17.50	(0.53)	148.14	(0.89)
B	1.49	(0.09)	17.56	(0.76)	154.44	(1.33)
1986 Aug. 7						
H	8.38	(0.39)	15.96	(1.42)	149.48	(1.89)
I	3.90	(0.19)	16.49	(0.68)	148.94	(1.20)
B	2.06	(0.12)	17.74	(0.65)	151.60	(1.01)
1987 Jul. 27						
H	9.02	(0.42)	12.53	(0.71)	25.62	(1.73)
I	2.65	(0.13)	12.96	(1.15)	29.58	(2.29)
R	2.25	(0.11)	13.92	(0.98)	27.80	(1.83)
V	2.09	(0.11)	14.18	(0.86)	24.41	(1.92)
B	1.89	(0.11)	15.90	(0.57)	26.59	(1.23)
U	1.37	(0.14)	16.02	(1.08)	28.05	(1.97)

Table 5 Continued.

Filter	Flux density (mJy)		Polarization (%)		Position angle (deg)	
1987 Jul. 30						
K	11.48	(0.53)	12.31	(1.15)	28.51	(2.85)
H	8.62	(0.40)	12.82	(0.86)	29.04	(2.20)
I	3.62	(0.17)	14.19	(0.53)	30.66	(1.19)
R	2.68	(0.14)	13.58	(0.50)	30.47	(1.36)
V	2.25	(0.12)	13.94	(0.64)	27.20	(1.85)
B	1.78	(0.11)	15.03	(0.39)	28.54	(1.08)
U	1.44	(0.15)	15.01	(0.39)	27.58	(1.48)
1987 Sep. 20						
H			14.68	(0.54)	150.70	(1.26)
I			16.77	(0.68)	150.14	(1.04)
R			16.21	(0.56)	150.42	(0.73)
V			18.69	(1.01)	151.92	(1.37)
B			18.92	(0.99)	149.22	(0.72)
U			15.23	(1.37)	150.95	(1.84)
1987 Sep. 21						
H	7.44	(0.69)	15.25	(0.66)	148.50	(1.39)
I	3.07	(0.29)	16.00	(0.72)	149.91	(1.30)
R	2.34	(0.22)	15.81	(0.47)	150.33	(0.79)
V	1.91	(0.18)	17.94	(0.96)	152.33	(1.42)
B	1.48	(0.15)	17.95	(0.53)	151.56	(0.64)
U			16.54	(0.88)	150.45	(1.57)
0138-097			E(B-V) = 0.00			
1986 Aug. 5						
H	2.96	(0.22)	10.06	(2.02)	66.88	(6.31)
I	1.18	(0.06)	6.00	(1.08)	63.95	(4.93)
B	0.45	(0.04)	4.24	(1.02)	72.79	(6.52)
1986 Aug. 6						
H	2.82	(0.16)	7.68	(2.25)	64.73	(7.67)
I	1.16	(0.06)	7.63	(3.62)	73.96	(3.67)
B	0.30	(0.02)	5.31	(1.21)	76.10	(6.29)
1986 Aug. 7						
H	3.13	(0.14)	10.35	(2.65)	61.06	(5.41)
I	1.14	(0.05)	3.67	(1.38)	70.41	(8.77)
B	0.46	(0.03)	4.45	(1.24)	92.49	(7.18)
1987 Jul. 28						
H	3.49	(0.16)	14.76	(3.03)	104.72	(3.90)
I	1.34	(0.06)	19.09	(1.33)	103.14	(3.28)
R	1.03	(0.05)	20.56	(1.24)	107.72	(1.83)
V	0.87	(0.05)	19.95	(1.65)	104.91	(2.60)
B	0.71	(0.04)	19.99	(1.01)	104.83	(1.33)
U	0.50	(0.05)	20.88	(1.41)	103.47	(1.92)

Table 5 Continued.

Filter	Flux density (mJy)		Polarization (%)		Position angle (deg)	
1987 Jul. 30						
H	3.07	(0.14)	21.05	(2.94)	104.76	(3.58)
I	1.35	(0.06)	22.86	(2.04)	99.90	(2.08)
R	1.01	(0.05)	18.38	(1.81)	106.11	(2.08)
V	0.85	(0.05)	20.71	(2.38)	105.77	(2.19)
B	0.69	(0.05)	22.29	(1.45)	102.91	(2.26)
U	0.43	(0.04)	20.18	(1.73)	106.91	(2.83)
1987 Sep. 19						
K	4.21	(0.39)	21.61	(2.98)	74.36	(2.34)
H	3.40	(0.31)	20.60	(1.62)	73.96	(2.26)
I	1.34	(0.12)	24.80	(1.08)	71.11	(1.29)
R	1.02	(0.10)	25.86	(0.67)	72.81	(0.77)
V	0.83	(0.08)	26.04	(1.22)	74.30	(1.39)
B	0.62	(0.06)	29.25	(0.92)	71.62	(0.83)
U	0.38	(0.04)	26.81	(1.35)	74.89	(1.49)
1987 Sep. 20						
H	2.96	(0.27)	22.23	(1.34)	70.40	(1.66)
I	1.61	(0.15)	21.45	(0.99)	74.33	(1.34)
R	1.23	(0.12)	24.51	(0.66)	73.32	(0.81)
V	1.00	(0.10)	27.33	(1.59)	73.54	(1.66)
B	0.81	(0.08)	27.07	(0.87)	73.53	(0.89)
U			27.05	(1.48)	74.69	(1.58)
1987 Sep. 21						
H	2.96	(0.27)	23.95	(1.44)	72.70	(1.72)
I	1.47	(0.14)	23.53	(1.41)	73.40	(1.80)
R	1.12	(0.11)	24.75	(0.96)	72.79	(1.12)
V	0.91	(0.09)	23.08	(1.82)	71.63	(2.31)
B	0.71	(0.07)	26.63	(1.07)	73.13	(1.13)
U			24.95	(1.47)	76.01	(1.70)
0219-164			E(B-V) = 0.00			
1987 Jul. 28						
K	13.31	(0.61)	14.83	(2.46)	160.96	(4.55)
H	11.15	(0.52)	13.67	(1.84)	170.47	(3.04)
J	7.67	(0.71)	12.85	(1.06)	159.53	(1.54)
I	5.48	(0.26)	12.45	(0.42)	159.96	(1.21)
R	4.14	(0.21)	12.65	(0.34)	161.33	(1.07)
V	3.64	(0.20)	12.37	(0.50)	160.92	(1.52)
B	3.00	(0.18)	12.70	(0.33)	161.16	(1.14)
U	2.10	(0.13)	12.83	(0.68)	160.19	(1.29)
0219+428 3C 66A			E(B-V) = 0.09			
1986 Aug. 1						
H	12.13	(0.56)	8.29	(0.71)	41.07	(2.60)
I	5.66	(0.53)	9.59	(0.24)	43.29	(0.69)
B	1.75	(0.17)	10.05	(0.31)	47.83	(0.78)

Table 5 Continued.

Filter	Flux density (mJy)		Polarization (%)		Position angle (deg)	
1986 Aug 4						
H	9.91	(0.37)	9.57	(0.60)	33.03	(1.75)
I	4.29	(0.21)	10.86	(0.38)	35.17	(0.84)
B	1.51	(0.12)	12.32	(0.53)	35.26	(1.13)
1986 Aug. 6						
H	9.91	(0.46)	9.41	(1.01)	30.80	(3.16)
I	4.80	(0.23)	9.24	(0.43)	34.25	(1.18)
B	1.95	(0.12)	10.85	(0.64)	35.60	(1.45)
1986 Aug. 7						
H	10.47	(0.49)	11.08	(0.74)	30.28	(1.90)
I	4.54	(0.22)	10.19	(0.34)	32.79	(1.05)
B	1.80	(0.11)	10.51	(0.33)	34.41	(1.07)
1987 Jul. 27						
H	11.17	(0.52)	12.53	(0.61)	164.20	(1.65)
I	3.92	(0.19)	11.20	(1.02)	162.63	(1.93)
R	2.47	(0.15)	12.52	(0.72)	162.87	(1.98)
V	2.34	(0.13)	14.25	(0.69)	161.93	(1.70)
B	1.81	(0.14)	13.16	(0.62)	163.65	(1.63)
U	1.34	(0.14)	14.47	(1.02)	165.89	(2.02)
1987 Jul. 30						
H	9.55	(0.44)	13.30	(0.99)	159.89	(2.39)
I	4.58	(0.22)	11.72	(1.34)	158.10	(2.97)
R	3.29	(0.17)	12.54	(0.88)	159.94	(2.13)
V	2.64	(0.14)	13.93	(0.76)	164.56	(1.63)
B	2.02	(0.12)	14.39	(0.50)	162.82	(1.20)
U	1.34	(0.14)	12.15	(1.53)	158.73	(2.19)
1987 Sep. 18						
H			14.80	(0.49)	22.16	(0.98)
I			13.38	(0.78)	22.86	(1.71)
R			13.49	(0.43)	24.04	(0.89)
V			15.43	(0.73)	24.19	(0.37)
B			14.59	(0.73)	23.28	(1.17)
U			12.15	(1.07)	22.06	(2.16)
1987 Sep. 19						
H			14.11	(0.53)	22.86	(1.06)
I			14.19	(0.80)	24.47	(1.69)
R			13.73	(0.38)	24.06	(0.76)
V			15.14	(0.74)	26.87	(1.48)
B			15.29	(0.53)	24.75	(0.95)
U			13.98	(0.61)	24.79	(1.18)

Table 5 Continued.

Filter	Flux density (mJy)		Polarization (%)		Position angle (deg)	
1987 Sep. 20						
H	11.27	(1.04)	14.11	(0.43)	23.50	(0.95)
I	4.71	(0.44)	15.46	(0.55)	26.52	(1.05)
R	3.68	(0.35)	14.30	(0.37)	25.95	(0.76)
V	3.09	(0.30)	15.94	(0.69)	25.80	(1.35)
B	2.30	(0.23)	14.38	(0.46)	26.50	(0.96)
U			14.25	(0.64)	28.47	(1.39)
1987 Sep. 21						
H			12.50	(0.55)	24.90	(1.25)
I			12.82	(0.69)	27.53	(1.54)
R			13.31	(0.37)	27.40	(0.84)
V			14.26	(0.60)	28.07	(1.21)
B			13.43	(0.35)	28.92	(0.73)
U			12.10	(0.68)	30.04	(1.64)
AO 0235+164			E(B-V) = 0.15			
1987 Jul. 28						
K	11.79	(0.54)	12.05	(1.04)	42.55	(2.92)
H	6.97	(0.32)	11.77	(1.02)	45.41	(3.25)
J	3.26	(0.30)	14.73	(4.42)	33.01	(9.88)
I	0.96	(0.05)	15.52	(1.59)	49.44	(3.04)
R	0.41	(0.02)	10.18	(1.58)	56.00	(3.80)
V	0.22	(0.01)	14.52	(3.67)	50.30	(9.31)
B	0.09	(0.01)	12.08	(3.73)	43.43	(8.36)
U	0.03	(0.00)	33.02	(10.17)	47.91	(8.59)
1987 Sep. 20						
K	5.80	(0.54)	1.66	(1.90)	47.71	(18.00)
H	3.97	(0.37)	5.78	(0.95)	52.70	(4.58)
J	2.47	(0.23)	8.59	(1.26)	56.59	(4.42)
I	0.99	(0.09)	11.04	(0.83)	55.91	(1.59)
R	0.56	(0.05)	10.10	(0.70)	55.26	(1.84)
V	0.31	(0.03)	10.00	(2.24)	57.95	(5.46)
B	0.14	(0.01)	11.65	(1.34)	60.67	(3.26)
U			8.28	(3.42)	68.16	(9.88)
0300+470 4C 47.08			E(B-V) = 0.15			
1987 Sep. 20						
H			9.55	(1.16)	9.00	(3.39)
I			9.44	(1.52)	1.76	(4.48)
R			8.69	(1.02)	13.96	(2.97)
V			5.05	(4.91)		
B			6.58	(2.12)	8.84	(8.92)
U			7.53	(5.37)	4.07	(11.70)

Table 5 Continued.

Filter	Flux density (mJy)		Polarization (%)		Position angle (deg)	
0323+022			E(B-V) = 0.06			
1986 Aug. 1						
H	2.16	(0.14)	0.00	(7.42)		
I	1.03	(0.10)	0.00	(2.09)		
B	0.31	(0.03)	0.00	(2.25)		
1987 Sep. 21						
H			4.65	(1.63)	8.60	(6.61)
I			3.84	(1.02)	3.53	(8.40)
R			3.78	(0.70)	14.46	(5.13)
V			0.00	(1.84)		
B			3.49	(0.90)		
U			5.27	(0.86)	11.59	(6.65)
0336-019			E(B-V) = 0.06			
1986 Aug. 5						
H	0.76	(0.13)				
I	0.32	(0.02)				
B	0.10	(0.01)				
0338-214			E(B-V) = 0.00			
1986 Aug. 6						
H	4.01	(0.22)	11.39	(1.92)	31.92	(4.61)
I	1.47	(0.07)	10.45	(1.40)	29.31	(3.75)
B	0.29	(0.03)	10.60	(1.47)	37.32	(7.71)
1987 Sep. 19						
H			11.48	(1.60)	70.46	(3.69)
I			11.07	(1.56)	62.59	(3.88)
R			10.62	(0.95)	65.86	(2.00)
V			15.58	(2.90)	65.05	(6.33)
B			12.37	(1.13)	64.02	(3.21)
U			8.15	(3.39)	60.82	(11.61)
0414+009			E(B-V) = 0.12			
15th. Feb 1988						
H	1.63	(0.15)	2.29	(2.07)	158.56	(24.65)
J	1.19	(0.04)	4.14	(1.92)	174.45	(10.58)
I	0.68	(0.02)	4.24	(1.64)	159.87	(9.55)
R	0.46	(0.01)	3.87	(0.66)	153.22	(4.61)
V	0.32	(0.01)	5.08	(1.43)	170.57	(7.70)
B	0.23	(0.01)	6.41	(0.79)	157.69	(3.60)
U	0.15	(0.01)	4.94	(1.08)	153.76	(6.11)
16th. Feb 1988						
H	1.56	(0.12)	6.20	(2.01)	146.42	(1.38)
I	0.70	(0.03)	7.82	(2.25)	154.03	(8.43)
R	0.45	(0.02)	5.72	(1.08)	155.71	(5.44)
V	0.33	(0.01)	4.73	(1.89)	151.40	(9.96)
B	0.23	(0.01)	3.93	(0.97)	157.80	(7.44)
U	0.15	(0.01)	7.38	(1.44)	159.53	(6.16)

Table 5 Continued.

Filter	Flux density (mJy)		Polarization (%)		Position angle (deg)	
0422+004			E(B-V) = 0.12			
16th. Feb 1988						
H	7.47	(0.28)	20.27	(0.64)	155.80	(1.04)
I	2.60	(0.10)	20.79	(1.12)	148.91	(1.38)
R	1.71	(0.06)	21.84	(0.65)	151.77	(0.81)
V	1.22	(0.05)	23.30	(1.07)	153.20	(1.50)
B	0.78	(0.04)	21.47	(0.75)	151.76	(0.91)
U	0.47	(0.03)	22.14	(0.97)	150.93	(1.47)
18th. Feb 1988						
K	10.56	(1.07)	12.32	(0.73)	147.60	(1.09)
H	7.75	(1.15)	11.25	(0.87)	148.00	(1.38)
I	2.93	(0.19)	12.55	(0.67)	141.90	(1.51)
R	1.74	(0.07)	12.25	(0.34)	140.42	(0.69)
V	1.25	(0.08)	12.93	(0.69)	140.24	(1.34)
B	0.79	(0.06)	12.48	(0.48)	136.95	(0.96)
U	0.44	(0.03)	13.69	(0.83)	141.36	(1.44)
PKS 0735+178			E(B-V) = 0.03			
1987 Sep. 19						
H			6.64	(0.68)	144.76	(2.88)
I			8.08	(0.88)	132.34	(3.03)
R			6.77	(0.61)	137.22	(2.85)
V			7.44	(1.52)	131.02	(5.49)
B			6.59	(0.93)	130.39	(3.66)
U			5.68	(1.59)	129.65	(8.10)
15th. Feb 1988						
H	7.96	(0.22)	16.24	(0.54)	131.37	(1.06)
I	2.40	(0.07)	15.48	(1.02)	125.56	(1.64)
R	1.84	(0.05)	17.17	(0.47)	130.41	(0.65)
V	1.33	(0.04)	18.05	(1.00)	127.83	(1.71)
B	0.96	(0.04)	16.80	(0.56)	130.68	(1.15)
U	0.62	(0.03)	17.57	(1.03)	136.73	(1.90)
16th. Feb 1988						
H	8.41	(0.31)	15.23	(0.61)	130.73	(0.94)
I	2.73	(0.11)	17.66	(0.82)	132.51	(1.44)
R	2.00	(0.07)	17.90	(0.51)	129.97	(0.79)
V	1.46	(0.06)	17.19	(1.06)	130.60	(1.32)
B	1.05	(0.05)	17.49	(0.73)	130.98	(0.99)
U	0.67	(0.04)	17.94	(1.26)	132.36	(1.66)
18th. Feb 1988						
H	8.65	(1.36)	20.50	(0.89)	127.25	(0.78)
I	3.14	(0.44)	21.90	(0.98)	126.70	(1.14)
R	2.19	(0.31)	21.15	(0.68)	126.60	(0.73)
V	1.66	(0.27)	22.50	(1.00)	128.80	(1.11)
B	1.21	(0.20)	22.50	(0.82)	124.00	(0.89)
U	0.80	(0.14)	21.80	(0.93)	125.90	(1.11)

Table 5 Continued.

Filter	Flux density (mJy)		Polarization (%)		Position angle (deg)	
0736+017			E(B-V) = 0.12			
15th. Feb 1988						
J	2.20	(0.06)	1.53	(0.93)	105.58	(17.81)
I	1.66	(0.05)	2.98	(1.24)	172.76	(9.01)
R	0.96	(0.03)	0.77	(0.67)	7.56	(18.61)
V	0.75	(0.03)	0.49	(1.00)	152.87	(64.32)
B	0.60	(0.03)	0.22	(0.64)	73.87	(83.42)
U	0.46	(0.03)	1.28	(0.78)	107.22	(19.18)
16th. Feb 1988						
J	2.16	(0.10)	4.43	(2.04)	171.13	(11.22)
I	1.50	(0.05)	0.53	(1.39)	46.94	(83.32)
R	0.82	(0.03)	1.53	(0.93)	91.61	(16.10)
V	0.67	(0.03)	2.89	(1.92)	9.21	(18.86)
B	0.52	(0.02)	0.77	(0.81)	15.05	(28.29)
U	0.40	(0.02)	0.96	(1.25)	56.86	(40.83)
0754+100			E(B-V) = 0.00			
15th. Feb 1988						
K	14.33	(0.40)	8.58	(0.49)	40.50	(1.37)
H	10.17	(0.29)	10.56	(0.42)	41.31	(0.81)
I	4.08	(0.09)	11.22	(0.51)	43.20	(1.00)
R	2.89	(0.08)	12.33	(0.24)	44.15	(0.58)
V	2.15	(0.07)	12.22	(0.43)	46.12	(0.92)
B	1.62	(0.07)	13.39	(0.29)	46.39	(0.66)
U	1.07	(0.06)	14.39	(0.48)	48.43	(0.87)
16th. Feb 1988						
K	13.81	(0.38)	10.34	(0.38)	34.40	(1.28)
H	9.63	(0.27)	10.96	(0.42)	35.20	(1.23)
I	3.62	(0.08)	12.39	(0.48)	30.20	(1.23)
R	2.27	(0.08)	12.59	(0.32)	34.74	(0.76)
V	1.86	(0.06)	13.22	(0.57)	35.45	(1.24)
B	1.36	(0.06)	13.10	(0.42)	35.69	(0.81)
U	0.91	(0.05)	13.25	(0.62)	38.54	(1.30)
17th. Feb 1988						
H	9.71	(0.36)	11.41	(0.51)	34.80	(1.67)
I	3.69	(0.24)	11.09	(0.59)	34.60	(1.95)
R	2.36	(0.12)	11.80	(0.39)	34.70	(1.23)
V	1.88	(0.10)	10.07	(0.58)	37.20	(2.27)
B	1.40	(0.07)	11.52	(0.54)	36.30	(1.27)
U	0.93	(0.06)	12.09	(0.77)	39.60	(2.27)

Table 5 Continued.

Filter	Flux density (mJy)		Polarization (%)		Position angle (deg)	
18th. Feb 1988						
K	14.73	(1.22)	8.67	(0.69)	36.20	(1.41)
H	10.75	(1.59)	8.17	(0.67)	39.00	(1.25)
I	3.75	(0.12)	9.28	(0.67)	32.33	(2.06)
R	2.73	(0.14)	8.65	(0.32)	36.67	(0.93)
V	2.08	(0.13)	8.43	(0.62)	36.40	(1.34)
B	1.55	(0.12)	6.95	(0.40)	36.35	(1.49)
U	1.03	(0.08)	7.56	(0.63)	38.28	(2.36)
0818-128 OJ-131			E(B-V) = 0.09			
15th. Feb 1988						
K	3.02	(0.14)	17.13	(1.60)	82.16	(2.81)
H	2.19	(0.10)	18.66	(1.72)	85.68	(2.15)
I	0.84	(0.03)	24.73	(1.66)	79.09	(1.92)
R	0.47	(0.02)	22.45	(0.72)	80.44	(1.01)
V	0.34	(0.01)	25.33	(1.81)	82.30	(1.85)
B	0.23	(0.01)	24.09	(0.86)	79.49	(1.04)
U	0.13	(0.01)	24.92	(1.66)	81.51	(1.99)
16th. Feb 1988						
K	3.16	(0.15)	15.48	(1.82)	79.61	(2.72)
J	1.32	(0.07)	21.87	(1.88)	83.54	(2.54)
I	0.68	(0.03)	21.92	(2.07)	88.24	(2.70)
R	0.38	(0.01)	22.22	(1.02)	81.56	(1.23)
V	0.28	(0.01)	25.68	(2.32)	81.85	(2.44)
B	0.19	(0.01)	26.75	(1.45)	80.49	(1.56)
U	0.11	(0.01)	27.67	(2.29)	81.59	(2.27)
17th. Feb 1988						
J	3.47	(0.16)	17.41	(1.62)	78.40	(2.33)
R	0.97	(0.04)	21.66	(2.43)	83.30	(3.20)
V	0.66	(0.04)	19.54	(1.21)	79.86	(1.85)
B	0.48	(0.03)	23.19	(2.78)	85.80	(3.03)
U	0.13	(0.01)	23.65	(1.55)	81.00	(1.83)
0851+202 OJ287			E(B-V) = 0.00			
15th. Feb 1988						
H	6.60	(0.19)	17.33	(0.59)	61.99	(0.96)
I	2.50	(0.08)	18.36	(1.22)	57.81	(1.91)
R	1.65	(0.06)	17.20	(0.59)	60.17	(0.99)
V	1.26	(0.05)	17.80	(1.13)	60.25	(1.53)
B	0.96	(0.04)	18.49	(0.65)	59.57	(0.88)
U	0.63	(0.04)	15.90	(1.06)	63.12	(2.07)

Table 5 Continued.

Filter	Flux density (mJy)		Polarization (%)		Position angle (deg)	
16th. Feb 1988						
H	6.54	(0.30)	15.62	(0.64)	60.40	(1.12)
I	2.50	(0.12)	15.20	(1.02)	66.07	(1.90)
R	1.65	(0.08)	15.55	(0.63)	61.96	(1.22)
V	1.31	(0.06)	17.38	(0.99)	63.58	(1.53)
B	1.00	(0.06)	18.55	(0.72)	62.56	(1.16)
U	0.70	(0.04)	17.65	(1.02)	64.89	(1.54)
17th. Feb 1988						
K	10.10	(0.28)	18.81	(0.50)	64.20	(0.77)
H	6.85	(0.19)	18.90	(0.58)	64.80	(0.88)
I	2.60	(0.08)	18.06	(0.66)	63.88	(1.08)
R	1.82	(0.09)	19.72	(0.33)	65.78	(0.48)
V	1.37	(0.05)	18.43	(0.74)	67.90	(1.17)
B	1.05	(0.05)	20.14	(0.44)	66.77	(0.65)
U	0.71	(0.04)	20.83	(0.76)	69.26	(0.99)
0906+015			E(B-V) = 0.00			
15th. Feb 1988						
H	0.48	(0.42)	51.43	(51.89)	142.20	(16.30)
I	0.37	(0.04)	48.40	(13.40)	49.50	(10.30)
R	0.36	(0.02)	2.08	(3.92)	6.20	(56.00)
V	0.35	(0.02)	8.33	(5.13)	73.90	(14.90)
B	0.31	(0.02)	2.16	(2.90)	35.50	(47.30)
U	0.24	(0.02)	10.10	(5.38)	135.10	(10.20)
1101+384			E(B-V) = 0.00			
15th. Feb 1988						
K	50.13	(0.94)	3.64	(0.30)	43.91	(2.17)
H	46.07	(1.29)	3.22	(0.14)	40.85	(1.19)
J	36.72	(0.74)	3.50	(0.20)	44.60	(1.09)
I	22.83	(0.90)	3.73	(0.13)	42.21	(0.90)
R	18.22	(0.63)	3.86	(0.08)	42.12	(0.55)
V	13.97	(0.55)	3.82	(0.11)	40.55	(0.82)
B	11.31	(0.53)	4.68	(0.10)	41.83	(0.58)
U	7.55	(0.43)	4.64	(0.13)	42.26	(0.83)
1147+245			E(B-V) = 0.00			
18th. Feb 1988						
H	8.62	(0.16)	1.52	(0.40)		
J	6.04	(0.12)	1.82	(0.54)	177.50	(8.05)
I	3.33	(0.10)	2.71	(0.67)	168.71	(6.70)
R	2.52	(0.11)	2.50	(0.26)	162.87	(3.05)
V	1.91	(0.10)	2.99	(0.46)	160.49	(4.41)
B	1.52	(0.09)	4.29	(0.32)	150.46	(2.08)
U	1.02	(0.07)	4.34	(0.52)	153.51	(3.62)

Table 5 Continued.

Filter	Flux density (mJy)		Polarization (%)		Position angle (deg)	
1156+295			E(B-V) = 0.00			
15th. Feb 1988						
H	2.35	(0.13)	23.04	(1.63)	168.83	(1.86)
I	0.97	(0.05)	24.07	(2.38)	162.06	(2.82)
R	0.77	(0.03)	24.37	(0.90)	164.87	(1.11)
V	0.62	(0.02)	24.76	(1.66)	166.81	(1.85)
B	0.53	(0.02)	22.83	(0.80)	164.20	(1.00)
U	0.35	(0.02)	24.25	(1.33)	163.78	(1.55)
16th. Feb 1988						
H	2.49	(0.21)	24.15	(2.53)	164.95	(1.55)
I	1.01	(0.05)	26.42	(2.87)	168.59	(3.25)
R	0.77	(0.03)	23.85	(1.02)	164.46	(1.16)
V	0.63	(0.03)	19.35	(2.46)	161.88	(3.68)
B	0.54	(0.03)	21.88	(1.24)	164.78	(1.64)
U	0.35	(0.02)	25.06	(2.17)	168.22	(2.41)
17th. Feb 1988						
H	2.37	(0.11)	28.06	(1.58)	166.80	(1.55)
I	0.88	(0.04)	27.27	(2.08)	161.20	(2.32)
R	0.71	(0.02)	24.99	(0.99)	164.90	(1.02)
V	0.57	(0.02)	22.54	(2.12)	162.20	(2.44)
B	0.48	(0.02)	23.08	(0.82)	164.60	(1.07)
U	0.31	(0.02)	24.87	(1.78)	168.10	(2.02)
1253-055 3C 279			E(B-V) = 0.03			
1986 Aug. 1						
H	25.17	(1.17)	28.19	(0.55)	120.52	(0.72)
I	11.71	(1.09)	29.17	(0.76)	120.62	(0.37)
B	6.03	(0.60)	30.03	(0.96)	119.88	(0.76)
1986 Aug. 2						
H	25.64	(1.42)	28.71	(0.59)	121.63	(0.60)
J	17.32	(1.28)	28.18	(1.06)	120.15	(0.39)
I	12.84	(1.20)	29.88	(0.36)	118.44	(0.47)
V	6.67	(0.64)	30.46	(0.79)	117.47	(0.55)
B	5.50	(0.55)	30.91	(0.28)	116.94	(0.28)
1986 Aug. 4						
H	23.82	(0.67)	33.22	(0.26)	125.35	(0.25)
J	17.64	(1.31)	34.66	(0.33)	126.97	(0.28)
I	12.15	(0.58)	36.57	(0.30)	125.01	(0.26)
R	8.49	(0.65)	37.70	(0.29)	127.32	(0.19)
V	7.38	(0.71)	38.17	(0.44)	126.12	(1.05)
B	5.55	(0.41)	39.24	(0.18)	126.09	(0.18)
U	3.64	(0.37)	41.30	(1.09)	127.66	(0.51)

Table 5 Continued.

Filter	Flux density (mJy)		Polarization (%)		Position angle (deg)	
1986 Aug. 5						
H	21.52	(1.00)	37.87	(0.60)	133.34	(0.40)
J	14.81	(0.69)	39.80	(0.54)	132.65	(0.28)
I	10.68	(1.00)	41.58	(0.55)	131.92	(0.30)
R	6.44	(0.61)	43.67	(2.02)	130.75	(0.52)
V	5.30	(0.51)	44.28	(0.97)	131.99	(1.05)
B	4.57	(0.46)	43.95	(0.78)	131.63	(0.31)
U	2.76	(0.40)	45.92	(0.98)	131.77	(0.62)
1986 Aug. 6						
H	17.10	(0.64)	38.13	(0.60)	136.70	(0.47)
J	12.09	(0.57)	38.53	(0.77)	136.30	(0.45)
I	8.10	(0.61)	40.51	(0.89)	136.29	(0.74)
R	6.15	(0.47)	43.07	(0.48)	135.52	(0.31)
V	5.75	(0.56)	43.31	(0.64)	136.14	(0.80)
B	3.70	(0.37)	44.36	(0.64)	134.73	(0.32)
U	2.68	(0.27)	45.47	(0.89)	135.51	(0.48)
1987 Jul. 28						
K	21.88	(2.02)	26.69	(0.77)	108.71	(1.15)
H	13.96	(1.29)	27.53	(0.68)	109.21	(1.12)
J	7.77	(0.72)	31.01	(0.84)	108.87	(1.17)
I	4.45	(0.42)	32.43	(0.77)	110.57	(0.95)
R	2.89	(0.27)	34.10	(0.61)	110.90	(0.94)
V	1.92	(0.19)	34.78	(1.14)	106.41	(1.14)
B	1.26	(0.13)	35.56	(1.43)	109.41	(1.11)
U	0.63	(0.06)	35.43	(2.29)	107.74	(1.50)
16th. Feb 1988						
H	29.07	(1.35)	21.36	(0.70)	114.44	(0.79)
I	12.55	(0.94)	20.94	(0.70)	110.07	(0.97)
R	9.22	(0.63)	20.08	(0.59)	111.38	(0.83)
V	7.00	(0.49)	19.58	(0.64)	109.58	(0.91)
B	5.17	(0.39)	19.47	(0.66)	109.65	(0.65)
U	3.29	(0.26)	19.65	(0.81)	112.30	(1.15)
17th. Feb 1988						
H	28.80	(0.55)	26.10	(0.20)	113.60	(0.24)
I	9.78	(0.30)	26.30	(0.42)	111.90	(0.46)
R	6.49	(0.23)	26.30	(0.36)	112.10	(0.39)
V	5.17	(0.20)	26.40	(0.53)	112.40	(0.58)
B	3.74	(0.17)	25.70	(0.42)	110.20	(0.38)
U	2.30	(0.12)	25.50	(0.67)	112.60	(0.69)
18th. Feb 1988						
H	32.17	(0.61)	30.12	(0.21)	113.80	(0.21)
I	10.53	(0.24)	31.30	(0.36)	113.70	(0.33)
R	7.12	(0.25)	31.30	(0.33)	113.30	(0.30)
V	5.56	(0.22)	31.50	(0.39)	114.10	(0.36)
B	3.96	(0.17)	30.70	(0.33)	113.30	(0.30)
U	2.57	(0.13)	30.70	(0.58)	114.90	(0.53)

Table 5 Continued.

Filter	Flux density (mJy)		Polarization (%)		Position angle (deg)	
1413+135			E(B-V) = 0.03			
1986 Aug. 6						
H	0.75	(0.11)				
I	0.06	(0.01)				
B	0.00	(0.01)				
1418+546 OQ 530			E(B-V) = 0.03			
1986 Aug. 4						
H	9.40	(0.26)	3.56	(0.64)	138.41	(3.62)
I	4.02	(0.19)	4.62	(0.31)	142.15	(2.03)
B	1.18	(0.10)	5.82	(0.46)	138.46	(2.28)
1986 Aug. 5						
H	9.48	(0.44)	4.55	(0.60)	140.42	(3.95)
I	3.23	(0.30)	4.83	(0.52)	149.43	(3.03)
B	2.89	(0.29)	6.41	(0.39)	138.75	(2.24)
1986 Aug. 6						
H	8.65	(0.40)	1.73	(0.78)	122.26	(11.51)
I	3.29	(0.16)	4.94	(0.64)	134.68	(3.63)
B	0.91	(0.05)	5.09	(0.70)	134.51	(3.88)
1987 Jul. 30						
H	8.49	(0.39)	2.50	(0.64)	54.32	(7.65)
J	5.79	(0.27)	4.12	(2.29)	41.04	(5.74)
I	2.94	(0.04)	3.69	(0.44)	52.71	(3.63)
R	2.00	(0.19)	5.17	(0.39)	64.37	(2.02)
V	1.46	(0.14)	5.71	(0.71)	64.43	(3.86)
B	1.05	(0.10)	7.31	(0.41)	65.58	(1.86)
U	0.69	(0.07)	8.68	(0.96)	60.93	(2.70)
1987 Sep. 20						
H			8.21	(0.99)	3.96	(2.42)
I			15.37	(2.82)	3.45	(4.35)
R			11.30	(2.23)	15.26	(5.02)
V			17.53	(4.76)	−0.66	(12.40)
B			0.00	(6.11)		
U			0.00	(35.16)		
1987 Sep. 21						
H			7.22	(1.46)	15.39	(7.78)
I			8.99	(1.48)	7.56	(5.26)
R			12.83	(1.12)	3.12	(2.95)
V			13.13	(3.13)	14.46	(4.09)
B			9.78	(2.52)	8.53	(6.39)
U			12.93	(7.57)	19.81	(15.08)

Table 5 Continued.

Filter	Flux density (mJy)		Polarization (%)		Position angle (deg)	
16th. Feb 1988						
K	19.96	(1.11)	2.49	(0.37)	134.85	(4.33)
H	16.88	(0.63)	2.90	(0.30)	142.21	(4.51)
J	12.27	(0.25)	3.57	(0.29)	143.80	(2.48)
I	7.49	(0.36)	3.12	(0.31)	146.58	(3.09)
R	5.25	(0.27)	3.06	(0.18)	140.00	(1.87)
V	3.64	(0.20)	3.31	(0.39)	146.85	(3.50)
B	2.59	(0.15)	4.38	(0.23)	143.90	(1.55)
U	1.49	(0.10)	4.89	(0.50)	147.29	(2.56)
17th. Feb 1988						
K	17.38	(0.48)	4.09	(0.48)	142.10	(3.71)
H	12.92	(0.36)	4.04	(0.32)	145.50	(1.85)
J	8.97	(0.18)	4.06	(0.29)	138.90	(3.07)
I	4.81	(0.11)	4.48	(0.27)	142.63	(1.88)
R	3.38	(0.09)	4.51	(0.18)	142.82	(1.09)
V	2.34	(0.08)	5.05	(0.35)	146.93	(1.91)
B	1.70	(0.07)	6.28	(0.23)	144.21	(1.11)
U	0.96	(0.05)	5.88	(0.43)	147.41	(1.86)
18th. Feb 1988						
H	14.43	(0.41)	3.38	(0.25)	132.01	(2.63)
I	5.68	(0.13)	3.56	(0.51)	140.80	(4.60)
R	4.25	(0.12)	3.11	(0.25)	146.20	(2.27)
V	2.97	(0.10)	2.96	(0.55)	142.80	(5.86)
B	2.34	(0.10)	3.20	(0.38)	150.00	(3.49)
U	1.49	(0.08)	4.05	(0.64)	156.20	(3.86)
1424+240			E(B-V) = 0.00			
16th. Feb 1988						
H	9.28	(0.26)	4.86	(0.36)	119.82	(2.12)
I	5.74	(0.28)	4.98	(0.66)	121.54	(3.78)
R	4.21	(0.12)	4.70	(0.36)	113.04	(2.18)
V	3.81	(0.21)	3.46	(0.50)	116.21	(4.07)
B	3.17	(0.15)	4.63	(0.30)	113.05	(1.95)
U	1.81	(0.09)	4.32	(0.48)	115.97	(3.12)
17th. Feb 1988						
H	9.19	(0.26)	4.92	(0.40)	123.82	(2.24)
I	4.95	(0.11)	4.24	(0.53)	114.60	(3.52)
R	3.84	(0.13)	4.48	(0.31)	119.20	(1.86)
V	3.26	(0.13)	4.36	(0.38)	114.20	(2.33)
B	2.76	(0.13)	4.45	(0.24)	117.80	(1.88)
U	1.91	(0.11)	4.35	(0.58)	116.60	(3.38)

Table 5 Continued.

Filter	Flux density (mJy)		Polarization (%)		Position angle (deg)	
18th. Feb 1988						
H	9.36	(0.35)	5.01	(0.44)	122.58	(2.21)
I	4.95	(0.11)	5.14	(0.55)	120.30	(3.00)
R	4.06	(0.11)	4.93	(0.30)	118.30	(1.65)
V	3.38	(0.11)	4.99	(0.49)	116.30	(2.87)
B	2.87	(0.12)	4.56	(0.30)	114.20	(1.90)
U	2.12	(0.10)	4.42	(0.58)	113.20	(3.85)
PKS 1510-089			E(B-V) = 0.06			
1986 Aug. 1						
H	2.26	(0.13)	9.07	(5.34)	177.65	(7.87)
I	1.23	(0.11)	1.65	(2.09)		
B	0.71	(0.03)	0.00	(2.32)		
1514-241 AP Libra			E(B-V) = 0.15			
1986 Aug. 1						
H	15.96	(0.74)	1.70	(0.44)	177.65	(7.87)
I	6.87	(0.64)	1.86	(0.28)	3.27	(3.94)
B	1.16	(0.12)	2.38	(0.37)	170.79	(4.07)
1987 Jul. 27						
K	23.09	(0.07)	5.11	(0.72)	19.56	(4.28)
H	19.01	(1.76)	3.70	(0.62)	16.72	(3.85)
J	14.21	(1.32)	5.42	(0.44)	14.28	(2.05)
I	6.87	(0.64)	4.76	(0.30)	12.37	(1.61)
R	4.07	(0.39)	5.12	(0.24)	15.40	(1.35)
V	2.86	(0.28)	4.83	(0.34)	18.72	(2.25)
B	1.39	(0.14)	6.13	(0.23)	17.41	(1.22)
U	0.86	(0.04)	6.92	(0.65)	16.50	(2.56)
1538+149 4C 14.60			E(B-V) = 0.00			
1986 Aug. 1						
H	0.90	(0.14)	0.00	(16.62)		
I	0.34	(0.03)	10.99	(9.54)		
B	0.13	(0.01)	4.97	(7.54)		
1641+399 3C 345			E(B-V) = 0.00			
1986 Aug. 1						
H	4.40	(0.20)	16.37	(1.24)	51.41	(1.82)
J	2.43	(0.20)	14.52	(2.64)	43.60	(5.34)
I	1.45	(0.11)	13.85	(0.73)	54.84	(1.60)
R			12.80	(0.98)	55.96	(2.17)
V	0.91	(0.09)	11.32	(0.79)	52.63	(2.02)
B	0.98	(0.10)	7.85	(0.30)	52.76	(1.04)

Table 5 Continued.

Filter	Flux density (mJy)		Polarization (%)		Position angle (deg)	
1986 Aug. 2						
H	4.16	(0.23)	17.23	(0.95)	52.15	(1.35)
J	2.56	(0.14)	17.24	(1.02)	55.10	(1.39)
I	1.49	(0.11)	15.83	(0.82)	53.83	(1.46)
R	1.06	(0.08)	14.96	(0.66)	51.63	(1.40)
V	0.92	(0.07)	12.57	(0.79)	55.55	(1.72)
B	0.90	(0.05)	8.70	(0.29)	52.48	(0.90)
1986 Aug 4						
H	4.12	(0.19)	17.87	(0.78)	55.65	(0.99)
J	2.59	(0.12)	16.27	(0.79)	53.01	(1.35)
I	1.43	(0.07)	15.01	(0.68)	55.18	(1.34)
R	1.07	(0.04)	12.87	(0.51)	56.74	(1.13)
V	0.97	(0.09)	11.83	(0.46)	53.85	(1.36)
B	0.85	(0.07)	8.61	(0.57)	56.64	(1.67)
U	0.60	(0.06)	7.92	(0.67)	58.14	(1.13)
1986 Aug. 5						
K	8.02	(0.74)	17.93	(1.57)	63.05	(2.51)
H	4.16	(0.19)	19.56	(1.91)	55.29	(2.64)
I	1.39	(0.13)	16.09	(1.14)	59.64	(2.03)
B	0.89	(0.09)	7.73	(0.68)	57.20	(2.57)
1986 Aug. 6						
H	3.98	(0.18)	20.27	(1.30)	57.17	(1.96)
J	2.52	(0.12)	20.03	(1.23)	62.31	(1.75)
I	1.44	(0.07)	14.98	(0.72)	57.00	(1.39)
V	0.87	(0.03)	11.14	(0.81)	60.17	(2.30)
B	0.90	(0.04)	8.65	(0.38)	57.24	(1.22)
1986 Aug. 7						
H	4.05	(0.19)	18.59	(1.55)	60.72	(2.06)
I	1.45	(0.07)	14.39	(0.81)	58.34	(1.61)
B	0.91	(0.05)	9.60	(0.71)	58.48	(2.48)
1987 Jul. 28						
K	2.66	(0.12)	1.52	(2.19)	179.39	(17.65)
H	1.92	(0.09)	0.00	(1.93)		
J	1.15	(0.05)	2.32	(3.51)	72.37	(23.98)
I	0.58	(0.03)	2.32	(1.28)	50.69	(13.47)
R	0.47	(0.02)	3.41	(0.95)	123.12	(7.39)
V	0.43	(0.02)	3.47	(1.24)	119.39	(9.18)
B	0.44	(0.03)	1.76	(0.46)	131.81	(7.22)
U	0.25	(0.02)	2.62	(0.81)	127.29	(8.41)

Table 5 Continued.

Filter	Flux density (mJy)		Polarization (%)		Position angle (deg)	
1987 Jul. 30						
H	1.69	(0.08)	2.74	(1.78)	30.62	(13.86)
I	0.58	(0.05)	0.86	(1.97)	131.75	(26.86)
R	0.47	(0.04)	1.61	(1.29)	127.34	(16.72)
V	0.44	(0.04)	0.00	(3.39)		
B	0.43	(0.04)	1.38	(0.77)	123.69	(12.96)
U	0.24	(0.02)	1.99	(1.09)	73.13	(13.91)
1987 Sep. 19						
H	1.55	(0.14)	4.02	(3.28)	169.86	(18.80)
I	0.49	(0.05)	11.15	(3.89)	82.71	(8.74)
R	0.37	(0.04)	0.00	(1.62)		
V	0.36	(0.04)	0.00	(1.47)		
B	0.39	(0.04)	0.00	(1.41)		
U	0.24	(0.03)	1.49	(2.13)	138.80	(26.06)
1652+398 Mkn 501			E(B-V) = 0.00			
1987 Sep. 21						
K			1.34	(0.26)	138.09	(4.81)
H			1.24	(0.19)	125.70	(4.83)
J			1.57	(0.20)	124.98	(3.85)
I			1.56	(0.16)	126.94	(2.52)
R			1.95	(0.11)	122.09	(1.55)
V			2.50	(0.18)	124.08	(2.06)
B			3.53	(0.14)	124.06	(1.18)
U			3.76	(0.22)	119.20	(1.62)
1717+178 OT 129			E(B-V) = 0.06			
1986 Aug. 6						
H	1.34	(0.06)	15.55	(3.97)	39.16	(8.07)
I	0.39	(0.02)	17.82	(3.62)	45.33	(5.08)
B	0.12	(0.01)	20.92	(3.67)	45.37	(4.54)
1986 Aug. 7						
H	1.13	(0.05)	18.59	(1.55)	60.72	(2.06)
I	0.37	(0.02)	14.39	(0.81)	58.34	(1.61)
B	0.10	(0.01)	9.60	(0.71)	58.48	(2.48)
1987 Jul. 30						
H	0.55	(0.10)	16.85	(11.90)	103.02	(13.86)
I	0.16	(0.02)	0.00	(11.88)		
R	0.10	(0.01)	6.33	(7.03)	150.64	(19.41)
V	0.08	(0.01)	10.37	(11.63)	34.78	(20.79)
B	0.04	(0.01)	7.11	(7.81)	134.50	(21.14)
U	0.02	(0.00)	0.00	(16.81)		

Table 5 Continued.

Filter	Flux density (mJy)		Polarization (%)		Position angle (deg)	
1727+502 I Zw 186			E(B-V) = 0.00			
1986 Aug. 6						
H	4.16	(0.19)	2.36	(1.55)	142.17	(15.26)
I	1.80	(0.09)	2.51	(0.82)	91.15	(7.55)
B	0.23	(0.01)	4.16	(0.88)	78.49	(6.95)
1986 Aug. 7						
H	4.20	(0.19)	0.43	(0.98)	56.35	(31.99)
I	2.08	(0.10)	2.44	(0.54)	91.88	(6.24)
B	0.65	(0.04)	4.67	(0.59)	92.73	(3.94)
1987 Sep. 21						
H			1.55	(1.62)	118.80	(20.70)
I			0.00	(0.84)		
R			0.92	(0.41)	95.85	(12.45)
V			1.10	(1.92)	126.27	(25.93)
B			3.14	(1.02)	96.91	(6.26)
U			5.96	(1.30)	110.38	(6.50)
1749+096 OT 081			E(B-V) = 0.15			
1986 Jul. 31						
H	4.35	(0.40)	16.70	(1.49)	153.42	(2.43)
I	1.44	(0.13)	16.53	(0.95)	165.69	(1.31)
B	0.32	(0.03)	18.41	(0.88)	169.93	(1.39)
1986 Aug. 5						
H	4.64	(0.22)	5.66	(1.85)	16.41	(8.04)
I	1.31	(0.06)	6.64	(1.13)	5.80	(4.53)
B	0.71	(0.04)	7.42	(1.18)	6.29	(4.29)
1986 Aug. 6						
H	5.00	(0.23)	10.92	(1.35)	27.54	(6.42)
I	1.48	(0.07)	9.62	(0.72)	35.81	(1.89)
B	0.38	(0.04)	9.76	(0.85)	34.36	(2.87)
1986 Aug. 7						
H	4.16	(0.19)	7.80	(1.15)		
I	1.27	(0.06)	8.16	(0.90)	3.99	(2.90)
B	0.30	(0.02)	10.87	(0.89)	1.85	(2.69)
1987 Jul. 27						
J	1.34	(0.09)	4.06	(2.23)	18.99	(16.94)
I	0.41	(0.02)	9.96	(3.87)	35.57	(12.25)
R	0.22	(0.01)	9.71	(4.01)	13.91	(10.32)
V	0.14	(0.01)	18.96	(6.76)		
B	0.07	(0.00)	23.85	(3.78)	0.71	(5.88)
U	0.04	(0.00)	13.87	(7.20)		

Table 5 Continued.

Filter	Flux density (mJy)		Polarization (%)		Position angle (deg)	
1921-293 OV-236			E(B-V) = 0.12			
1986 Aug. 3						
H	1.33	(0.12)	9.78	(3.71)	104.12	(12.02)
I	0.57	(0.05)	6.34	(4.13)	100.10	(17.85)
B	0.11	(0.02)	16.89	(4.53)	160.42	(7.29)
6th. Aug 1986						
H	5.08	(0.24)	13.94	(1.91)	126.06	(4.92)
I	1.54	(0.07)	6.98	(1.82)	117.72	(6.59)
B	0.43	(0.04)	5.76	(1.85)	109.18	(8.79)
1986 Aug. 7						
H	2.52	(0.12)	7.10	(2.03)	119.56	(7.91)
I	0.54	(0.03)	8.13	(1.65)	135.93	(6.78)
B	0.08	(0.01)	5.97	(3.04)	111.08	(13.03)
1987 Jul. 27						
J	1.11	(0.06)	6.01	(3.86)	85.18	(15.94)
I	0.79	(0.05)	3.91	(2.92)	130.94	(17.44)
R	0.69	(0.07)	5.60	(2.26)	105.55	(10.49)
V	0.19	(0.02)	0.00	(5.44)		
B	0.15	(0.01)	0.00	(3.32)		
2032+107			E(B-V) = 0.12			
1987 Jul. 27						
J	8.61	(0.40)	0.56	(0.47)		
I	4.36	(0.21)	0.86	(0.40)		
R	1.98	(0.19)	1.08	(0.44)		
V	1.03	(0.06)	1.38	(1.08)		
B	0.28	(0.02)	0.00	(1.15)		
U	0.04	(0.00)	0.00	(7.18)		
PKS 2155-304			E(B-V) = 0.00			
1986 Aug. 1						
H	27.76	(1.29)	2.03	(0.30)	148.06	(3.24)
J	21.72	(1.02)	3.11	(0.36)	149.47	(4.93)
I	21.02	(1.58)	3.10	(0.12)	141.54	(1.18)
R	14.74	(1.40)	3.62	(0.08)	137.15	(0.76)
B	14.11	(1.41)	4.03	(0.07)	138.80	(0.53)
1986 Aug. 5						
H	30.44	(1.41)	1.24	(0.35)		
I	20.63	(0.99)	0.72	(0.19)	3.60	(8.10)
B	13.23	(0.79)	0.80	(0.19)	13.33	(7.97)
1986 Aug. 6						
H	28.02	(1.30)	0.73	(0.21)		
I	26.70	(2.49)	0.45	(0.16)	21.52	(9.23)
B	14.11	(1.41)	0.69	(0.21)	75.08	(7.70)

Table 5 Continued.

Filter	Flux density (mJy)		Polarization (%)		Position angle (deg)	
1986 Aug. 7						
H	29.88	(1.38)	1.85	(0.19)	147.57	(1.89)
J	26.12	(1.22)	1.67	(0.17)	149.75	(3.11)
I	20.82	(1.00)	1.94	(0.16)	149.14	(2.42)
R	18.90	(1.45)	2.03	(0.18)	145.32	(2.46)
V	15.60	(1.51)	2.06	(0.18)	146.78	(2.63)
B	13.47	(1.12)	2.11	(0.12)	142.71	(1.36)
1987 Jul. 27						
K	67.94	(3.14)	9.16	(0.24)	175.89	(1.11)
H	60.73	(2.81)	9.40	(0.70)	176.16	(1.51)
J	55.58	(3.61)	10.14	(0.97)	172.93	(1.01)
I	36.52	(2.74)	10.29	(0.23)	171.83	(1.07)
R	27.07	(2.56)	10.46	(0.23)	171.20	(1.07)
V	26.13	(2.06)	10.69	(0.21)	170.48	(1.03)
B	24.29	(1.81)	10.91	(0.15)	169.39	(0.94)
U	18.10	(1.85)	10.93	(0.16)	169.14	(0.96)
1987 Sep. 21						
K			7.14	(0.42)	170.19	(1.82)
H			7.60	(0.21)	170.00	(0.75)
I			8.33	(0.17)	170.41	(0.62)
R			8.52	(0.12)	169.67	(0.41)
V			9.05	(0.18)	169.96	(0.60)
B			8.61	(0.10)	169.91	(0.44)
U			8.35	(0.16)	171.62	(0.58)
2200+420 BL Lacertae			E(B-V) = 0.15			
1986 Jul. 31						
H	19.01	(1.76)	11.83	(0.48)	30.74	(1.17)
I	5.21	(0.49)	12.02	(0.50)	33.50	(0.76)
B	0.73	(0.07)	14.03	(0.65)	35.33	(1.14)
1986 Aug. 1						
H	21.04	(0.97)	12.52	(0.73)	26.56	(1.37)
I	3.96	(0.37)	11.36	(0.43)	27.93	(1.03)
B	0.61	(0.06)	12.57	(0.53)	30.78	(1.24)
1986 Aug. 3						
H	19.54	(0.91)	12.36	(0.24)	20.87	(0.81)
J	11.93	(0.56)	12.49	(0.24)	21.63	(0.57)
I	4.46	(0.33)	12.93	(0.34)	22.46	(0.72)
R	2.04	(0.19)	12.80	(0.42)	25.87	(1.06)
V	1.37	(0.13)	14.24	(0.45)	24.56	(1.32)
B	0.55	(0.06)	16.70	(0.39)	26.09	(0.71)
1986 Aug. 4						
H	18.32	(0.51)	12.24	(0.44)	17.50	(1.09)
I	4.54	(0.22)	13.34	(0.40)	19.62	(0.85)
B	0.61	(0.05)	17.17	(0.71)	22.74	(1.19)

Table 5 Continued.

Filter	Flux density (mJy)		Polarization (%)		Position angle (deg)	
1986 Aug. 5						
H	19.01	(0.88)	14.33	(0.36)	15.36	(0.58)
I	4.42	(0.21)	14.00	(0.43)	18.43	(0.94)
B	0.54	(0.03)	17.52	(0.74)	23.13	(1.22)
1986 Aug. 6						
H	15.96	(0.74)	14.92	(0.72)	19.39	(1.29)
I	5.21	(0.49)	14.15	(0.37)	22.31	(0.85)
B	0.63	(0.06)	17.24	(0.71)	23.17	(1.22)
1986 Aug. 7						
H	18.83	(0.87)	13.95	(0.38)	22.59	(0.83)
I	4.63	(0.22)	13.81	(0.40)	22.51	(0.89)
B	0.60	(0.04)	16.88	(0.68)	25.91	(1.12)
1987 Jul. 27						
K	28.53	(1.32)	10.42	(0.26)	16.50	(1.11)
H	20.84	(1.35)	9.60	(0.35)	16.44	(1.44)
J	13.32	(0.62)	8.52	(0.40)	16.12	(1.74)
I	5.12	(0.25)	7.83	(0.35)	15.57	(1.41)
R	3.12	(0.16)	8.40	(0.23)	14.93	(1.12)
V	1.60	(0.11)	8.50	(0.56)	10.96	(1.96)
B	0.67	(0.07)	8.30	(0.44)	10.56	(1.57)
U	0.30	(0.03)	8.32	(1.05)	11.59	(2.99)
1987 Jul. 28						
K	32.76	(1.51)	13.23	(0.42)	22.96	(1.24)
H	23.49	(1.09)	11.93	(0.19)	19.73	(0.91)
J	14.88	(1.10)	12.12	(0.41)	17.12	(1.31)
I	5.36	(0.31)	10.26	(0.40)	16.80	(1.16)
R	2.55	(0.13)	10.56	(0.41)	14.99	(1.12)
V	1.55	(0.08)	9.77	(0.70)	9.98	(1.82)
B	0.69	(0.04)	12.27	(0.59)	9.47	(1.46)
U	0.28	(0.02)	11.42	(1.20)	5.74	(2.79)
1987 Jul. 30						
H	23.28	(1.08)	13.85	(0.32)	18.81	(1.25)
I	5.56	(0.27)	12.57	(0.62)	16.96	(1.29)
R	2.84	(0.14)	12.01	(0.55)	12.54	(1.16)
V	1.60	(0.09)	10.36	(1.10)	15.46	(2.48)
B	0.74	(0.04)	13.25	(0.60)	10.06	(1.34)
U	0.29	(0.02)	13.04	(1.54)	4.75	(1.96)
1987 Sep. 19						
H	13.15	(1.21)	8.35	(0.61)	31.50	(2.36)
I	3.00	(0.28)	8.11	(0.59)	40.95	(1.84)
R	1.70	(0.16)	8.37	(0.35)	38.41	(1.38)
V	0.95	(0.09)	8.35	(1.24)	45.04	(3.82)
B	0.38	(0.04)	14.04	(0.69)	37.46	(1.42)
U	0.18	(0.02)	10.53	(1.60)	37.37	(4.74)

Table 5 Continued.

Filter	Flux density (mJy)		Polarization (%)		Position angle (deg)	
1987 Sep. 20						
H			6.96	(0.29)	25.96	(1.21)
I			8.43	(0.55)	32.97	(1.87)
R			9.07	(0.39)	31.05	(1.24)
V			10.52	(0.94)	38.75	(3.07)
B			13.09	(0.87)	38.30	(2.03)
U			19.57	(2.06)	31.48	(3.00)
1987 Sep. 21						
K			8.56	(0.51)	20.69	(1.59)
H			8.44	(0.40)	24.40	(1.26)
I			9.34	(0.50)	31.11	(1.52)
R			9.88	(0.36)	33.51	(0.97)
V			12.19	(1.44)	32.25	(3.41)
B			13.90	(0.82)	33.18	(1.71)
U			18.59	(2.31)	35.95	(3.53)
PKS 2208-137			E(B-V) = 0.00			
1986 Aug. 3						
H	1.87	(0.09)	4.11	(4.16)	152.96	(15.06)
I	0.89	(0.07)	1.40	(1.55)	51.88	(20.48)
B	1.07	(0.11)	0.00	(0.74)		
1986 Aug. 4						
H	1.82	(0.08)	0.00	(3.20)		
I	0.97	(0.05)	1.95	(1.00)	114.07	(15.56)
B	1.10	(0.09)	0.39	(0.56)	66.94	(23.78)
1986 Aug. 6						
H	1.70	(0.13)	9.32	(4.21)	157.41	(12.16)
I	1.19	(0.11)	0.00	(2.28)	109.04	(30.02)
B	1.17	(0.12)	0.99	(0.74)	77.88	(13.63)
1986 Aug. 7						
H	1.35	(0.09)	2.62	(5.23)	74.70	(31.35)
I	0.87	(0.04)	1.31	(1.67)	45.38	(20.74)
B	1.00	(0.06)	0.31	(0.75)	132.34	(21.31)
2223-052 3C 446			E(B-V) = 0.03			
1986 Aug. 4						
H	0.58	(0.08)	3.65	(20.99)	116.30	(28.41)
I	0.27	(0.02)	2.80	(7.93)	105.49	(23.25)
B	0.15	(0.01)	0.75	(5.65)	142.91	(28.84)
1987 Jul. 27						
J	1.38	(0.09)	12.99	(3.11)	76.27	(6.18)
I	0.65	(0.03)	11.64	(1.87)	70.41	(4.34)
R	0.47	(0.02)	13.21	(1.24)	76.03	(2.95)
V	0.33	(0.02)	17.42	(2.35)	75.44	(4.28)
B	0.22	(0.01)	11.59	(1.20)	68.41	(2.77)
U	0.16	(0.02)	9.75	(1.84)	71.52	(6.29)

Table 5 Continued.

Filter	Flux density (mJy)		Polarization (%)		Position angle (deg)	
1987 Jul. 29						
H	2.06	(0.19)	9.29	(1.48)	88.83	(5.65)
I	0.61	(0.06)	5.87	(2.05)	87.07	(9.47)
R	0.44	(0.04)	7.90	(1.35)	82.59	(4.89)
V	0.33	(0.03)	7.35	(2.75)	73.49	(7.78)
B	0.24	(0.02)	9.57	(1.15)	73.00	(4.41)
U	0.17	(0.02)	8.34	(2.17)	78.73	(6.83)
1987 Jul. 30						
H	1.98	(0.11)	9.04	(1.83)	77.89	(5.61)
I	0.64	(0.03)	7.23	(2.44)	55.10	(8.95)
R	0.45	(0.02)	7.02	(1.88)	71.52	(7.08)
V	0.31	(0.02)	7.80	(3.33)	84.66	(11.35)
B	0.22	(0.01)	9.77	(1.88)	68.42	(5.38)
U	0.15	(0.01)	6.08	(2.51)	60.98	(10.71)
1987 Sep. 20						
H			6.55	(0.91)	92.16	(3.88)
I			7.98	(1.12)	91.95	(3.90)
R			9.03	(0.59)	94.03	(1.77)
V			12.35	(2.00)	97.50	(4.37)
B			10.30	(0.86)	92.58	(2.30)
U			8.89	(1.24)	99.50	(4.12)
21st. Sep 1987						
H			9.29	(1.09)	97.70	(3.28)
I			11.90	(1.21)	98.72	(2.58)
R			9.76	(0.59)	101.84	(2.04)
V			11.64	(2.03)	106.59	(3.92)
B			10.86	(0.83)	100.67	(2.06)
U			8.92	(1.19)	103.30	(4.37)
2230+114 4C 11.69			E(B-V) = 0.03			
1986 Aug. 3						
H	1.18	(0.10)	8.29	(4.76)	154.21	(14.60)
I	0.64	(0.05)	3.77	(1.97)	52.35	(12.08)
B	0.42	(0.04)	0.00	(1.20)		
1986 Aug. 4						
H	1.02	(0.05)	7.70	(7.49)	136.84	(23.37)
I	0.64	(0.03)	3.86	(2.13)	109.45	(16.37)
B	0.39	(0.03)	0.00	(1.89)	100.39	(34.85)
2251+158			E(B-V) = 0.06			
1986 Aug. 5						
H	1.97	(0.16)	6.40	(2.91)	152.90	(14.99)
I	1.12	(0.05)	1.11	(1.31)	27.84	(19.01)
B	0.65	(0.04)	0.00	(0.68)		

Table 5 Continued.

Filter	Flux density (mJy)		Polarization (%)		Position angle (deg)	
1987 Jul. 28						
H	2.41	(0.16)	4.62	(2.06)	10.28	(9.32)
I	1.16	(0.06)	0.55	(1.18)	61.84	(22.04)
R	0.98	(0.05)	1.38	(0.87)	24.86	(14.17)
V	0.85	(0.05)	0.00	(1.21)		
B	0.60	(0.04)	0.00	(0.63)		
U	0.36	(0.03)	1.17	(0.97)	155.83	(24.63)
1987 Sep. 20						
H			7.35	(1.22)	161.96	(4.66)
I			4.18	(0.96)	160.62	(6.32)
R			3.92	(0.45)	162.27	(3.31)
V			3.72	(1.10)	159.21	(7.36)
B			3.49	(0.47)	161.95	(4.52)
U			2.37	(0.79)	163.02	(9.09)
2254+074 OY 091			E(B-V) = 0.06			
1986 Jul. 31						
H	2.08	(0.19)	7.06	(4.13)	46.26	(12.00)
I	0.93	(0.09)	10.09	(1.30)	57.36	(3.64)
B	0.20	(0.03)	18.91	(2.53)	57.23	(3.77)
1986 Aug. 1						
H	1.78	(0.12)	7.90	(5.62)	45.31	(12.85)
I	0.85	(0.08)	10.77	(1.48)	52.72	(4.24)
B	0.16	(0.02)	14.75	(1.57)	43.95	(3.99)
1986 Aug. 3						
H	2.50	(0.12)	10.54	(1.37)	52.66	(4.66)
J	1.75	(0.08)	12.91	(1.55)	41.11	(5.37)
I	0.84	(0.06)	11.80	(1.08)	47.70	(2.50)
R	0.52	(0.05)	12.28	(0.93)	43.97	(2.91)
V	0.23	(0.02)	15.40	(1.93)	45.59	(4.41)
B	0.18	(0.02)	18.71	(1.12)	42.44	(1.48)
1986 Aug. 4						
H	2.30	(0.06)	10.31	(1.15)	44.45	(3.18)
J	1.72	(0.08)	9.03	(1.30)	43.38	(3.54)
I	0.85	(0.04)	8.99	(0.90)	48.91	(2.77)
R	0.52	(0.03)	10.27	(0.63)	45.69	(1.84)
V	0.36	(0.03)	10.92	(0.87)	47.60	(2.92)
B	0.18	(0.02)	19.17	(0.95)	44.17	(1.40)
U	0.12	(0.01)	18.36	(4.04)	47.46	(5.98)
1986 Aug. 5						
H	2.39	(0.11)	7.69	(2.40)	55.64	(6.75)
I	0.90	(0.04)	8.44	(1.31)	40.39	(3.05)
B	0.20	(0.01)	15.80	(1.33)	48.81	(2.32)

Table 5 Continued.

Filter	Flux density (mJy)		Polarization (%)		Position angle (deg)	
1986 Aug. 6						
H	2.48	(0.11)	4.22	(2.19)	59.06	(14.98)
I	1.18	(0.11)	7.38	(0.98)	57.42	(3.80)
B	0.21	(0.01)	11.63	(1.21)	55.39	(3.22)
1986 Aug. 7						
H	2.01	(0.11)	7.91	(4.38)	60.36	(11.00)
I	0.44	(0.02)	10.74	(3.18)	4.26	(7.83)
B	0.11	(0.01)	2.30	(3.42)	54.50	(26.31)
1987 Jul. 28						
H	2.46	(0.11)	11.55	(1.19)	136.59	(3.17)
I	1.04	(0.05)	9.07	(0.94)	138.02	(3.07)
R	0.67	(0.03)	11.87	(0.83)	142.79	(2.18)
V	0.45	(0.02)	13.76	(1.51)	148.83	(2.17)
B	0.24	(0.01)	17.40	(1.16)	141.65	(2.19)
U	0.12	(0.01)	14.28	(1.82)	146.91	(4.89)
1987 Jul. 30						
H	2.74	(0.13)	13.62	(1.48)	139.19	(2.72)
I	1.06	(0.05)	12.06	(1.26)	143.84	(3.05)
R	0.67	(0.03)	9.89	(1.09)	142.96	(2.96)
V	0.47	(0.03)	12.09	(1.72)	141.55	(4.19)
B	0.24	(0.01)	15.76	(1.30)	148.76	(2.21)
U	0.13	(0.01)	17.52	(2.94)	139.69	(4.49)
1987 Sep. 18						
H			3.34	(3.89)	45.57	(22.10)
I			9.65	(1.45)	47.85	(4.14)
R			11.81	(0.75)	38.76	(1.82)
V			14.12	(2.43)	58.38	(5.14)
B			14.26	(1.13)	39.71	(2.57)
U			13.74	(2.16)	56.63	(4.34)
1987 Sep. 21						
H			7.01	(1.83)	50.27	(6.09)
I			8.10	(1.55)	42.91	(5.73)
R			9.76	(0.85)	42.30	(2.62)
V			14.37	(3.06)	30.83	(5.90)
B			14.63	(1.31)	38.52	(2.67)
U			13.47	(2.73)	40.60	(6.88)

Figure 1: *The Mark II Hatfield Polarimeter.*

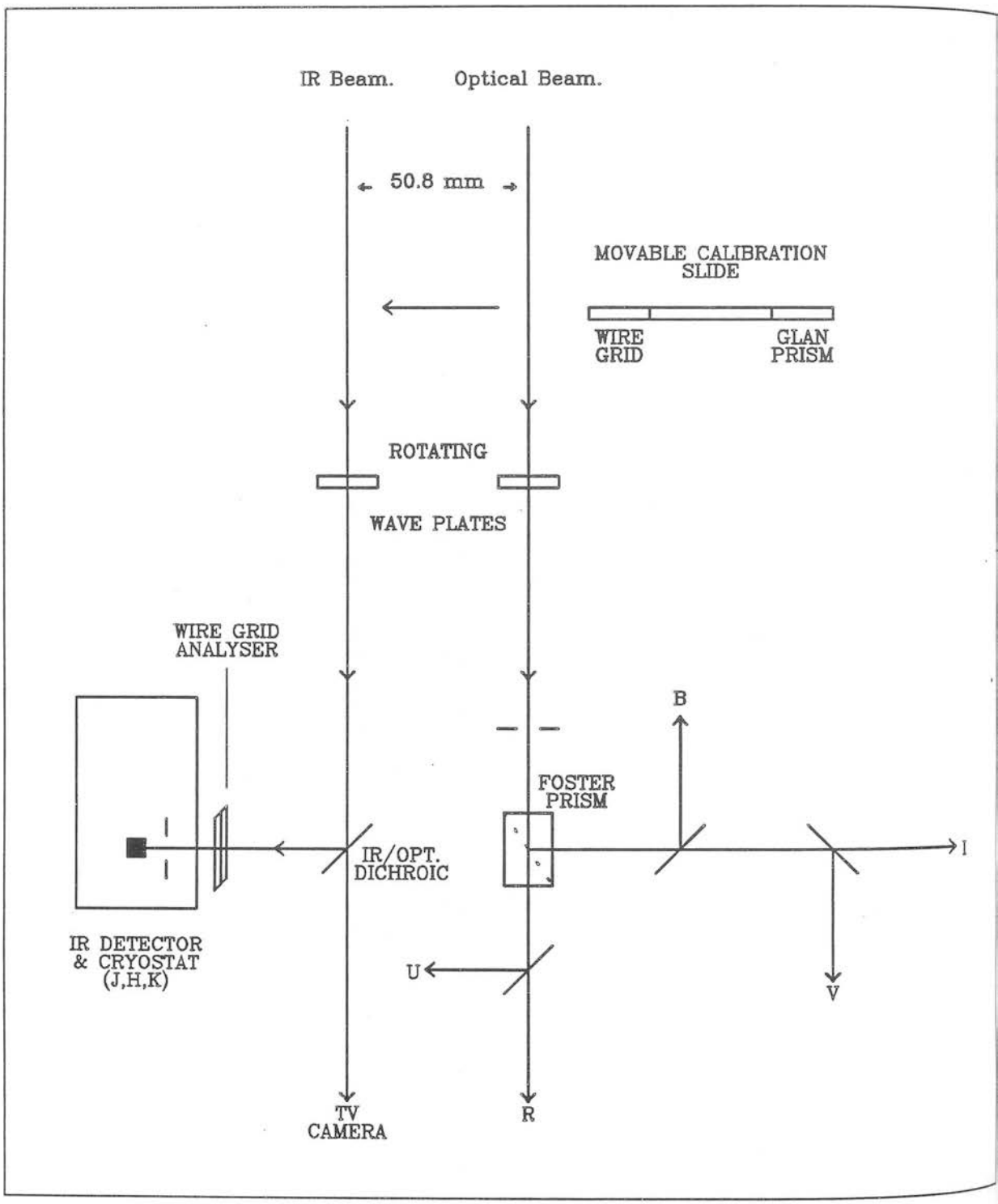

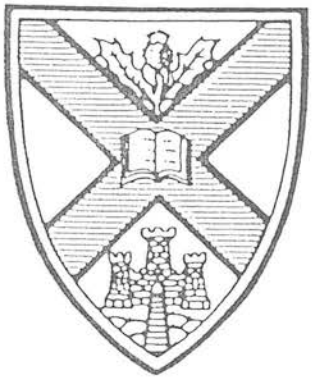

Edinburgh Astronomy Preprint

Number 27/89

December 1989

The optical and infrared emission of blazars

K.R. Ballard
A.R.G. Mead
P.W.J.L. Brand
J.H. Hough

University of Edinburgh Department of Astronomy
Royal Observatory, Blackford Hill, Edinburgh EH9 3HJ, Scotland
Telephone: 031-668 8100 Telex 72383

Accepted for publication in

Monthly Notices of the Royal Astronomical Society

The optical and infrared emission of blazars

K.R. Ballard, A.R.G. Mead, P.W.J.L. Brand

Dept of Astronomy, Edinburgh University, Scotland, EH9 3HJ.

J.H. Hough

Division of Physical Sciences, Hatfield Polytechnic, Hatfield, Herts, AL10 9AB.

Summary. We have carried out a polarization study of 44 blazars and candidate blazars observed at optical and near-infrared frequencies (Mead *et al.* 1989). The spectrum of the radiation is discussed in terms of shock acceleration models. Frequency dependence is a common feature of the polarization behaviour, with the polarization and spectral index generally increasing towards higher frequencies in those BL Lac objects which were observed. No evidence was found to support the previous claim that frequency dependence is related to high levels of polarization. No characteristic form of blazar variability was evident from the data. The intrinsic frequency-dependent polarization of the BL Lac objects is the result of spectral curvature, due to source inhomogeneity. We suggest that the observed spectral, temporal and polarization behaviour is the result of a polarized cut-off component, tentatively identified with emission from a shock and an unpolarized steep spectrum component. This can explain the observations of 1253 – 055 (3C 279) and many of the other observed cases of frequency-dependent polarization.

1 Introduction

In a previous paper (Mead *et al.* 1989; hereafter MEA) we presented the results of a programme to monitor the flux and polarization behaviour of a sample of blazars. The observations were made at the United Kingdom Infrared Telescope during four observing runs (1986 August, 1987 July, 1987 September and 1988 February). The observations, covering the UBVRIJHK frequency range were carried out simultaneously at one infrared and all five optical wavebands. A summary of the observations is given in Table 1. These data significantly enlarge the database of infrared polarimetry and photometry established by the observations of Impey *et al.* (1982), Impey *et al.* (1984), Holmes *et al.* (1984a, b) and Brindle *et al.* (1986). The data were collected with the MKI and MKII Hatfield

polarimeters (see MEA for a description of the instruments) and have smaller polarimetric errors than previous data; they allow statistical analysis at unprecedented levels.

This paper will address the interpretation of the observed optical emission of the 44 blazars in terms of specific models of the compact emission region. The term blazar will be taken to include BL Lac. objects and also highly polarized quasars which exhibit strong emission line spectra. The optical continua of both can usually be regarded together, since both contain synchrotron emission from relativistic charged particles. A full treatment of this process is given by e.g. Pacholczyk (1970, 1977). The canonical synchrotron model, which has had considerable success in explaining the emission of extended radio sources, consists of a uniform magnetic field, a power law distribution of electron energies and an isotropic distribution of electron velocities. This predicts a frequency-independent form of the polarization. It is well established (see Puschell & Stein 1980, Holmes *et al.* 1984a, Brindle *et al.* (1986), Smith *et al.* 1987 etc.) that frequency dependence of both polarization and position angle is a common occurrence among the BL Lac objects, dominated by synchrotron emission. These properties of blazar emission indicate that a more complicated, inhomogeneous model for the emission region is required. The polarization of inhomogeneous sources has been the subject of works by Nordsieck (1976), Björnsson & Blumenthal (1982) and Björnsson (1985); their results will be applied in detail in this paper.

The frequency distribution of the radiation has received much attention. Due to the fact that variability is observed at all wavelengths, accurate multifrequency spectra can only be obtained through simultaneous observations. At radio frequencies blazars generally have flat spectra, and the optically thick synchrotron spectral index of -2.5 is not seen – the 'Cosmic Conspiracy' of Cotton *et al.* (1980). At higher frequencies the spectrum is steep ($\alpha \sim 1.0$) and is often of a power law form (Allen, Ward & Hyland 1982). There has been some discussion as to whether the spectrum is best described by a power law with breaks (e.g. Gear *et al.* 1985 who have breaks in their 1μm–2mm spectra at 10μm). Breaks at 3. 10^{14}Hz are suggested by Cruz-Gonzalez & Huchra (1984). In contrast Landau *et al.* (1986) fit all their (1400Å– 20cm) multifrequency spectra with parabolæ. There is some observational evidence for a cutoff to the infrared/ optical spectrum (e.g. Rieke, Lebofsky & Kinman 1979, Bregman *et al.* 1981). Evidently, the origin of the non-thermal distribution of particle energies is a question of crucial importance. A rough estimate of the magnetic field ($B \sim 10^{-5}T$; Gear *et al.* 1985) yields electron lifetimes of the order of days at optical frequencies, implying that *in situ* acceleration of electrons must take place. To date the most commonly advanced theory is first-order Fermi acceleration at magneto-

hydrodynamic shocks. The basic process is outlined by Longair (1981). At a non-relativistic strong shock front this process yields a spectral index of $\alpha = 0.5$. The spectral index can steepen by 0.5 when electron losses become important (Kardashev 1962) and a cutoff is present at a frequency where the synchrotron loss time becomes equal to the acceleration time (Blandford 1979). Meisenheimer & Heavens (1986) use shock acceleration to model multifrequency spectra of 3C273. The arguments for relativistic motion in blazars were reviewed by Impey (1987). On the basis that many superluminal sources are blazars, he argues for a connection between superluminal motion and the blazar phenomenon, which suggests that if the acceleration is due to a shock then it is relativistic.

Flux variability can be an important tool in understanding the emission region. For example, Marscher & Gear (1985) showed that the mm behaviour of 3C273 could be understood by a simple model of a shock passing along a jet close to the line of sight, characterizing the evolution in terms of the energy loss mechanism (Compton, synchrotron and 'adiabatic'). On the basis of a week of monitoring of BL Lac, Moore *et al.* (1982) advocated a model of randomly oriented sub-components turning on at a rate of about 10 per day and decaying over about 5 days. Brindle *et al.* (1985), reporting observations of the same object when fainter, proposed a fixed underlying component with superimposed sub-components.

Alternative models for the emission region are summarized by Begelman, Blandford & Rees (1984); these include the possibility that the emission may be associated with orbiting hotspots on an accretion disk. It should be noted that thick accretion disks, like relativistic flows, may be able to radiate at super-Eddington luminosities (Abramowicz, Calvani & Nobili 1980). However, given the uncertainty as to whether such disks are stable (Rees 1984), these ideas will not be developed here.

The layout of the paper is as follows: §2 will discuss the possibility that the emission from several objects may be contaminated by unpolarized emission, in particular the 'blue bump' emission reported for several quasars. §3 discusses the properties of the data; this has been partitioned into three subsections, discussing the spectral index, the frequency dependence of the polarization and the variability, each of which is a theoretically separable area. §4 presents a model to explain the observed phenomena of spectral curvature and frequency dependent polarizations. §5 presents the conclusions of the paper.

Following Björnsson (1985), frequency dependence of the degree of polarization will be referred to as FDP and frequency dependence of the polarization position angle as FDθ . As with MEA the shape of the spectrum will be characterised by use of the (local) spectral

index;

$$\alpha(\nu) = -\frac{d\log S_\nu(\nu)}{d\log \nu} . \qquad (1)$$

A frequency-dependent spectral index is referred to as spectral curvature.

2 Contamination by unpolarized components

As was first noted by Shields (1978) several notable highly polarized quasars have excess flux at optical and ultraviolet frequencies, which takes the form of contamination of the optical emission by unpolarized flux. This results in either FDP with $dp/d\nu < 0$ or spectral curvature with $d\alpha/d\nu < 0$. Malkan & Sargent (1982) fitted this 'blue-bump' emission by black-body radiation, associated with radiating accretion disks in the centre of active galactic nuclei. The observations of $1641+399$, described in a previous paper, Mead *et al.* (1988), represent the most extreme example of contamination of the synchrotron component seen in the UKIRT data set. There exists the possibility that other data may similarly contain 'non-blazar' emission. In order to select objects where this may have affected the spectra, objects showing either $d\alpha/d\nu < 0$ or not showing monotonic polarization variation were selected, and are listed in Table 2. They represent a very small subset of the observations of blazars in MEA. Several of these showed little or no significant polarization.

The χ^2 levels of significance in Table 2 are quoted for a fit to a frequency-independent polarization (for the FDP cases) and to a power law flux distribution (for the abnormal spectra cases). An alternative explanation of this behaviour is superposition of misaligned polarized components. This is equivalent to the Holmes *et al.* (1984b) two-component model, where two polarized components, of approximately equal polarized fluxes produce a polarization signature which decreases to zero at the frequency where the polarized fluxes are equal. This will also produce FDθ , and indeed the FDθ seen in the behaviour of $0109+224$ on 1986 August 4 and $1418+546$ on 1988 February 18 could lend weight to this explanation.

One of the important potential causes of contaminating flux is the starlight of the host galaxy. Since this will be expected to peak in the near IR, such emission would be similar to that observed for blazars, being curved ($d\alpha/d\nu > 0$), very steep and showing FDP with $dp/d\nu > 0$ although largely unpolarized. Consequently care must be taken to ensure that behaviour which will be interpreted as being characteristic of the blazar emission process

is not the result of contaminating starlight. This implies that all those blazars known to be located in low-redshift galaxies ($0521-365$, $0548-022$, $1101+384$, $1133+704$, $1514-241$, $1652+398$ and $2200+420$) must be studied with multi-aperture photometry or imaging, in order to separate out the galaxy component (c.f. Kikuchi & Mikami 1987). Other objects may also exhibit continuum properties affected by their relatively weaker underlying galaxies.

3 The data

Three aspects of the data will be considered in turn. First the shape of the spectrum which can be related to current models of shock acceleration and energy losses will be discussed. The polarization behaviour and the correlations derived from the polarization can provide evidence on magnetic field geometry. Finally, variability will be considered as this can provide limits to the size of the emission region, and can be used to constrain models of the emission region.

There are a number of points about the nature of the data which are studied in this and the following sections. The UKIRT data form an inhomogeneous sample, subject to known (but unquantifiable) selection effects. The strategy adopted was to observe as many blazars as possible. Repeat observations were made for those objects which showed variability, high polarizations, FDP or FDθ . Consequently there are in-built biasses in this sample of observations which will necessarily affect the conclusions if each observation were to be treated as an independent point. Even if the observing strategy had avoided these problems, it would still be questionable whether the individual observations were independent. This problem is related to the timescales associated with variations in the flux and polarization properties. It is known these properties can be constant over periods of several nights, so that observations over one run would not be independent. To try to avoid the effects of these biasses, the following results refer to the median and maximum values of the parameters for each object although this loses some information. In these sections ν_f will refer to the effective frequency of the waveband f, quoted in the observer's frame. The lack of complete redshift information for the blazar sample makes it impossible to transform these measurements to the emission frame.

3.1.1 Spectral Curvature and the Distribution of Spectral Index

The results presented in this and following sections are obtained by testing the data against a variety of null hypotheses (e.g. a power law flux distribution). The fits were achieved by minimising the χ^2 statistic, the use of which is valid if the errors concerned are distributed normally. The errors on the photometry, however, include systematic uncertainties in the photometric calibration. Consequently, where the data concerned include flux information the true level of the significance is likely to be different from that calculated in the case of normally distributed errors. The use of the χ^2 statistic is justified on the basis that the aim is to obtain some idea of the relative goodness of fit between observations rather than to reject a power law fit for an individual object.

The distribution of spectral indices at waveband I are tabulated in Table 3 and shown in Fig. 1. Both median and maximum values for each object are shown. The data used are all the observations in the sample for which polarized observations with calibrated flux data were obtained. These are the objects given in Tables 3 and 4. The fits are separated into polarized and unpolarized samples, because only when polarizations in excess of the 3% limit (used to distinguish highly polarized objects from low polarizations, e.g. Moore & Stockman 1984), are seen, is it certain the observed flux contains a synchrotron contribution. If the spectrum is fitted by a power law at the 5% level, then the value of the frequency-independent spectral index is used. Otherwise, a parabola in the $\log S_\nu(\nu) - \log \nu$ plane is fitted, and is used to derive the spectral index at I.

$$\log S_\nu(\nu) = \log S_{14} - a \log \nu_{14} + b(\log \nu_{14})^2 \, . \qquad (2)$$

S_{14} is the flux at $10^{14} Hz$. There is no theoretical justification for choosing such a form, it is simply an empirical fit to the data. There is a problem with those observations made with the Mark I Hatfield polarimeter at H, I and B only. Three-point data sets are fitted with zero degrees-of-freedom for a three-parameter fit, and as the data are subject to observational errors the fitted parabolæ may be quite different from the true flux distribution. Consequently, if a power law fit to a three-point data set was rejected, then no information from this data set was included in Fig. 1. Fig. 2 shows the degree of spectral curvature for all the UKIRT data, again showing the median and maximum values for each object. The statistic used, $\Delta\alpha_{(B-H)}$, is the difference in the spectral indices at B and H;

$$\Delta\alpha_{(B-H)} = \alpha(\nu_B) - \alpha(\nu_H)\,. \qquad (3)$$

This quantity is estimated using the aforementioned parabolic fits.

3.1.2 The Distribution of Polarized Flux

A partial indication of whether the range of spectral indices given in the previous section is truly representative of the synchrotron components can be obtained from polarized flux distributions. The polarized spectral indices α_p and the degree of curvature, $\Delta\alpha_{p,(B-H)}$ (analogous to $\Delta\alpha_{(B-H)}$ in the previous section) are shown in Table 4. The distributions of these quantities are shown in Figs 3 and 4. These are calculated in an exactly analogous way to the similar quantities of the previous section. The spectral parameters so derived represent the behaviour of the synchrotron component, as no other sources of polarized flux are thought to be present. Only in the case of frequency-independent polarization will the polarized flux spectral index be equal to the flux spectral index. For an object displaying convex curvature in its total flux spectrum, the polarized flux spectral index $\alpha_p(\nu)$ will be marginally smaller than $\alpha(\nu)$.

3.1.3 The Interpretation of the Spectral Flux Distribution

It is useful to discuss the implications of the observations described in the above sections, although to a certain extent a discussion of the flux distribution cannot be held independently of a discussion of any FDP, as this constrains most explanations of the origin of the continuum flux properties of blazars. The primary candidate for the process whereby the electrons (or positrons) are accelerated, first-order particle acceleration at shock fronts, makes specific predictions about the observed spectrum. In summary, strong non-relativistic shocks with the magnetic field parallel to the shock normal produce observed spectra of 0.5. Kirk & Schneider (1987) expanded the distribution function in terms of the eigenfunctions of the scattering equation to solve the problem at a relativistic shock front which yields spectra between 0.4 and 0.65, while weak shocks can produce any spectral index greater than 0.5. The spectral indices expected from oblique shocks have been calculated (Kirk & Heavens 1989) when the shock is 'subluminal' *ie.* the magnetic field lines intersect the shock front at a velocity less than c. For shock speeds v$\geq 0 \cdot 1c$ they find spectral indices harder than in the parallel shock case, tending to an unphysical value of $\alpha \sim 0$ as v increases. These spectral indices should be constant over many decades of frequency. In the high

frequency domain, synchrotron energy losses cause the observed spectral index to increase by 0.5 (Kardashev 1962), with a high energy cut-off beyond which the Fermi process cannot accelerate electrons (Blandford 1979).

Weak shocks can explain any spectral index, but such shocks are generally rejected for two reasons. First, the observed spectral index is a strong function of shock speed; this implies that even the large range of spectral indices shown in Fig. 1 corresponds to a narrow range of shock speeds, and it is unlikely that the range of speeds should be small. Second, strong shocks are expected to be a common feature of the hydrodynamic flows which are thought to be the origin of the blazar emission. As these amplify the emissivity of the fluid, by accelerating particles and compressing the magnetic field, it may be reasonable to expect such shocks to play an important part in the origin of the observed emission. As most blazar identifications are made on the basis of their optical emission, this objection can be overcome if selection effects are important; there is an obvious bias against very steep optical spectra. To resolve this question a complete survey of a sample of compact radio sources is needed.

If arbitrarily weak shocks are rejected, then the range of spectral indices observed is not consistent with the power law spectra predicted by Fermi acceleration at strong shocks. Spectral indices of order 3 are too large.

The high energy cutoff inherent in acceleration models implies a steepening of the spectrum over a relatively small frequency interval, where the models have steep spectra and spectral curvature but not steep ($\alpha > 1.2$) *power law* spectra. Such curvature *is* observed but is not limited to sources with the steepest spectra. For example the spectral index (at I) of the observation of 0818−128 is high (1.52) but not extreme, but the curvature ($\Delta\alpha_{(B-H)} = 3.37$) is the highest seen. Checking for a correlation (using the Spearman rank correlation statistic) between either the median or maximum spectral indices and curvature parameters produced no result which was significant even at the 10% level.

Heavens (1988) considers advection of electrons away from a shock front where the magnetic field decays arbitrarily with distance from the shock. He shows that the resulting spectrum may have spectral indices higher than those predicted by the simple shock theory and gradually curved though approximately described by a power law for single decades of frequency if these are well below the cut-off. This is not the only inhomogeneous source model which produces spectral indices much higher than that derived from the electron spectral index. For example, the synchrotron-self-Compton (SSC) model of

Ghisellini, Maraschi & Treves (1985) gives rise to steep optical-IR continua as a result of the integration of the luminosity of an inhomogeneous jet. There exist a series of inhomogeneous models, including those of Marscher (1980) and Königl (1981) with steep power law flux distributions. However, there are a large number of free parameters which go into determining the spectral index. Ghisellini, Maraschi & Treves (1985) attempt fits to the IR/optical continua of two blazars ($2155-304$ and $0537-441$) using this model by varying some of these parameters. Fitting such models to the UKIRT data is not possible, given the limited number of frequency points.

We conclude that the spectral indices shown in Fig. 1 are too high to be consistent with a simple model of shock acceleration at a strong shock with a parallel, or oblique, homogeneous magnetic field. The fact that position angles tend to align with the VLBI axis (Impey, 1987) suggests the oblique case may be more realistic. Inhomogeneous jet models produce higher spectral indices although, given the restricted frequency range, these cannot be tested fully here. Alternatively a cutoff to the spectrum can produce a greater range of spectral indices. All the data were obtained with simultaneous polarimetry and, as this strongly constrains models of the emission region, we postpone further discussion until after the polarization properties have been considered.

3.2 ANALYSIS OF THE POLARIZATION PROPERTIES

3.2.1 Frequency Dependence of the Degree of Polarization

All data with two or more polarization measurements were tested for frequency dependence of polarization and polarization position angle. Power law forms ($p(\nu) \propto \nu^{\beta}$) were fitted to the data using the χ^2 statistic to test the goodness of fit. This empirical fit allows an unconstrained minimization to be performed with respect to $\log p_{14}$ (p_{14} is the polarization at $10^{14} Hz$) and β. Those objects not fitted (at the 5% level) by a constant polarization are described as showing FDP; those not fitted by a power law with constant β at the 5% level are described as having 'complex' polarization behaviour. This procedure will flag behaviour, such as that seen in $2200+420$, where the FDP is only significant over a narrow range of the observed frequencies. Fig. 5 shows the distribution of the median and maximum degrees of polarization at I and Fig. 6 the median and maximum changes in polarization over the observed frequency range, expressed in terms of the ratio of the B polarization to the H polarization ($p(\nu_B)/p(\nu_H)$). The data displayed in these figures are listed in Table 5.

Fig. 5 shows a wide range of both median and maximum polarizations, the largest being the series of observations of $1253-055$ (3C 279) (see §4.2). There is a common tendency for the B polarization to be higher than that at H. Indeed, only three objects have a median value of $(p(\nu_B)/p(\nu_H))$ significantly less than one (the highly polarized quasars $1641+399$ (3C 345), $1921-293$ and $2251+158$). The probable reason for this is contamination of the blazar flux by unpolarized optical components, discussed previously. The data were also tested for FDθ which is much rarer than FDP (see MEA, Table 4). There is no evidence suggesting any preference for clockwise over counter-clockwise variations with frequency.

3.2.2 Correlation of Frequency Dependence with Other Properties

It has been suggested (Bailey, Hough & Axon 1983, Holmes *et al.* 1984a, Holmes 1985, Brindle *et al.* 1986) that there is a tendency for frequency dependence to be associated with high polarization (the '$p(\lambda)-p$' effect). The appearance of this effect has been approached in two ways. Fig. 7 shows histograms of the I polarizations wherein objects displaying either FDP (Fig. 7a) or FDθ (Fig. 7b) have been flagged. The distributions of the two samples were then tested using the Kolmogorov-Smirnov test (e.g. Conover 1980) under the null hypothesis that the frequency-independent data had the same distribution as the frequency-dependent data. When considering FDP, the Kolmogorov-Smirnov statistic was $T = 0.112$, which corresponds to the 75.2% level of significance. When considering FDθ , the Kolmogorov-Smirnov result was $T = 0.150$, which corresponds to the 50.0% level of significance. An alternative is to use non-parametric correlation tests to test directly for a correlation between the amount of frequency dependence and the polarization. Fig. 8 shows plots of $\log(p(\nu_B)/p(\nu_H))$ versus the I polarization. Whereas all the observations were plotted in Fig. 7, only median or maximum values for each object are shown in Fig. 8. Neither was significant at the 5% level. We conclude there is no evidence that the amount of frequency dependence is dependent on the degree of polarization.

This data set is larger and covers a wider frequency range than those for which the $p(\lambda)-p$ effect was claimed; thus it is surprising that, if real, this effect does not appear. A possible explanation is provided by a selection effect, given that the polarimetric errors obtained on these data are certainly smaller than those on the data of Bailey, Hough & Axon (1983), Holmes *et al.* (1984a) and Holmes (1985). It seems possible that these authors simply missed examples of FDP (and FDθ) in objects of moderately low polarization that would have been detected in this work. Further, Holmes (1985) notes that, in some of his

sample, this correlation is markedly affected by specific blazars observed more frequently than others. This indicates that his result may be susceptible to the kinds of systematic biasses discussed earlier.

In §3.1.3 cut-offs were mentioned as a possible explanation for the steep and curved spectra observed in blazars. If this were generally so for blazars, then a correlation between the steepness of the spectrum and the occurrence of FDP should be observed. This has been tested using the Spearman rank correlation test statistic for the correlation between $\alpha(\nu_I)$ and $(p(\nu_B)/p(\nu_H))$. Also tested for were correlations between $\alpha(\nu_I)$ and $p(\nu_I)$, $\Delta\alpha_{(B-H)}$ and $p(\nu_I)$ and $\Delta\alpha_{(B-H)}$ and $(p(\nu_B)/p(\nu_H))$. No correlations were found at the 5% level.

3.3 VARIABILITY

3.3.1 Variability in the Flux Densities

Before discussing variability it is necessary to differentiate between the different timescales being tested. Data were taken over several nights at four epochs (1986 August, 1987 July, 1987 September and 1988 February). As a consequence there are three inter-epoch and numerous inter-night timescales to be considered. The χ^2-statistic was used to test the null hypothesis that there was no difference between measurements for any pair of observations. The critical level of significance used was 1.0%, any lower value being regarded as evidence for variability. Again it must be stressed that possible systematic errors may compromise the assumption of normal errors in the photometry.

Inter-epoch variability in the flux densities was seen in the majority of objects, and ranged from $1253-055$ and $1749+096$ which varied by a factor of almost three to $0118-272$ and $0138-097$ which remained constant between 1987 July and September. Night-to-night variations were also commonly seen, though exceptions were more common than above. One object, $2254+074$, varied from 1.18mJy to 0.44mJy in one day at I, but this was atypical. Three objects ($0109+224$ in 1987 September, $1156+295$ in 1988 February and $1253-055$ in 1986 August) varied by up to 33% whilst retaining a constant spectral index. No observations were seen which repeated the pattern of Gear, Robson & Brown (1986), where spectral indices decreased with increasing flux. Three objects showed *steepening* spectral indices with increasing flux ($0048-097$ and $0109+224$, both in 1986 August and $1253-055$ in 1988 February).

As with the flux variability, inter-epoch and inter-night variations in the degree of polarization were seen in the majority of blazars. The only example of a polarized object displaying constant inter-epoch polarization degree was $2254+074$. In addition seven other objects failed to show any inter-night variations when repeat observations were performed. These were $0118-272$, $0138-097$, $1156+295$, $1418+546$, $1424+240$, $1641+399$ and $2223-052$. Changes in the polarization did not always coincide with significant changes in the observed flux of these objects. The variations in the polarization data were not all of a similar form; for example $1253-055$ showed a generally increasing degree of polarization with the onset of FDP ($dp/d\nu > 0$) whereas $0109+224$ showed (during 1986 August) FDP of both senses ($dp/d\nu < 0$ and $dp/d\nu > 0$).

There is evidence for variability on timescales of tens of minutes in the polarization position angle in the data of 1253–055 (3C 279) during 1986 August. All these data were collected with the Mark I instrument where the flux and polarization spectrum was constructed from a series of simultaneous measurements at three frequencies. Only on 1986 August 2 did the individual sets show strong evidence for FDθ , on all other nights during this period the data were consistent with frequency-independent position angles but with variations of order half a degree over the approximately ten minute timescale of the integrations. Table 6 shows the averaged position angle for each run during this period. Inspection shows that for any pair of runs the evidence for variability is marginally significant. Nevertheless this was capable of inducing artificial FDθ in the summed data. The data given in MEA are the summed values which are the best estimates of the position angle during the whole series of observations, although the errors are underestimated. There was no evidence for similar rapid changes in the polarization degree nor did any other object show such rapid variability of the position angle.

Only one object ($0235+164$) was observed with a polarization position angle constant over the inter-epoch timescale. Only two high signal-to-noise observations of this object were made (in 1987 July and 1987 September). One of the more extreme cases was $1749+096$ where the position angle varied from 5° to 35° in one day in 1986 August. Only six objects failed to show inter-night variations during any of the epochs. These were $0118-272$, $0138-097$, $0818-128$, $1156+295$, $1418+546$ and $1424+240$. Note that these objects also failed to display any inter-night variations of the degree of polarization. However the other objects which similarly failed to show inter-night changes in the polarization degree did show inter-night changes in position angle. Indeed, position angle variations were marginally more common than variations in the degree of polarization.

The fact that variability in the position angle is the rule rather than the exception should not be taken as invalidating the results of Rusk & Seaquist (1985) and Impey (1987) who showed that preferred polarization position angles were generally along the milliarcsecond radio-structure axis. Impey (1987) regarded any object where two-thirds of the position angles were consistent to within 40° as having a preferred (range of) position angle. The variations which were detected in the UKIRT data were generally of a few to ten degrees in amplitude, but six objects exhibited variability around or in excess of the 40° limit. These were $0109+224$, $0118-272$, $0219+428$, $1418+546$, $1749+096$ and $2254+074$. Three other objects ($0138-097$, $1727+502$ and $2155-304$) showed FDθ which came close to violating the limit. Since the majority of the detected variations were of much smaller amplitude, this data set should not invalidate Impey's result.

4 Models of the frequency dependence of polarization

4.1 Theoretical Background

Björnsson & Blumenthal (1982) set out a formalism whereby the polarization properties of an inhomogeneous source can be evaluated. Their result was:

$$p(\nu) = \Pi(\nu)\,\frac{\alpha(\nu)+1}{\alpha(\nu)+\frac{5}{3}}\,. \tag{4}$$

where $\Pi(\nu)$ is composed of integrals over the magnetic field geometry, and represents the degree of ordering of the magnetic field. This provides a description of the properties of an inhomogeneous synchrotron source. There are several possible specific models of the emission region which are summarized below.

Section 3.1.3 discussed the effect of cut-offs in the energy spectrum of the radiating electrons on the total flux spectrum. Such a cut-off would also have a dramatic effect on the observed polarization behaviour. Strong FDP occurs around the cut-off frequency but no FDθ is seen. Fig. 9 shows the expected polarization signature of an *ad hoc* two-component model consisting of a polarized cut-off component and an unpolarized power law component. The cut-off was assumed to be a sharp upper limit in the electron energy distribution. The rise in polarization results from the fact that synchrotron emission from an isotropic electron distribution tends to 100% polarization above the critical frequency, the fall-off in polarization resulting from the dominance of the unpolarized emission at high frequencies.

Björnsson (1985) considers the effect of anisotropic particle velocity distributions on the polarization behaviour of the synchrotron radiation which can result in significant FDP and FDθ . This explanation for the observed FDθ has not been pursued, as the naïve two-component model can adequately explain the observations. Nevertheless relativistic shock acceleration models do produce anisotropic particle distributions (e.g. Kirk & Schneider 1987, Heavens & Drury 1988) and shock acceleration is implicitly assumed in the cut-off models applied in §4.2 and §4.3.

4.2 APPLICATION TO THE OBSERVATIONS OF $1253-055$

The best example of FDP in the UKIRT data is $1253-055$ (3C 279) which was extremely polarized and was observed at high signal-to-noise ratios. The fluxes were fitted by power laws on all nights in 1986 August. The fluxes decreased from 1986 August 4 to August 6, but were otherwise constant. The photometric errors were too large to permit any description of the spectral index behaviour during the latter period. The flux varied by a factor of almost three between 1986 August and 1987 July 28 when the flux could again be expressed as a power law. Finally, it was observed three times during 1988 February. On February 16 and February 18 the flux could be described as a power law, while on February 17 a parabola gave the best fit. There was a decrease in the observed flux, followed by an increase in flux and spectral index. In the following discussion the data obtained on the night of 1986 August 1 will be excluded as these consist of only three frequency points. The polarization varied more often than the flux, between 45.92 ± 0.98 % (the highest optical polarization yet seen in a blazar) on 1986 August 5 to 19.65 ± 0.81 % on 1988 February 16. During 1986 August FDP developed with $dp/d\nu > 0$ as the polarization rose to a maximum. The frequency dependence of position angle was subject to the systematic errors discussed in §3.3.2. The significant FDθ seen on 1986 August 2 appears to be real. Otherwise the data appear to be consistent with variable but frequency-independent position angles and so the explanation of the behaviour on these nights is much easier. The 1987 July 28 data showed FDP ($dp/d\nu > 0$) but no FDθ . The polarization rose each night in 1988 February. Significant FDP with $dp/d\nu > 0$ was present on the final night only, while FDθ was present on the first two nights.

The Björnsson & Blumenthal (1982) formalism (hereafter the α-parameterisation) will be used to parameterise the emission initially. The lack of any FDθ on most nights justifies a frequency-independent form of $\Pi(\nu)$ as an initial approximation. This has been used

to fit all the data of 1253 − 055 (including the data of 1986 August 2, 1988 February 16 and 1988 February 17 for which it is not strictly applicable). Table 7 shows the results of these fits. The spectral flux distribution has been fitted using the parabolic form of equation 2. Fig. 10 shows the application of this parameterisation to the 1986 August 5 data. The α-parameterisation essentially separates the polarization behaviour into two parts i.e. the degree of magnetic field ordering and the (potentially coupled) distribution of the projected magnetic field and electron Lorentz factor. The former factor determines the *degree* of polarization while the latter determines the spectral flux distribution. This in turn determines the FDP through the spectral index. Consequently the FDP supplies no more information about the nature of the source than is contained in the spectral flux distribution and the level of polarization. This has no relation to any physical model of the emission region. The α-parameterisation implies that the FDP is entirely a result of the process which produces the spectral shape of the continuum flux, which remains unexplained. The α-parameterisation cannot account for the FDθ of 1986 August 2 or 1988 February 16 and 17. FDθ implies that the functions $q(\nu)$ and $u(\nu)$ in Björnsson & Blumenthal (1982) are frequency-dependent. This gives rise to a potentially frequency-dependent form of $\Pi(\nu)$. Despite this the α-parameterisation is still able to fit the observed FDP on this night, and so, although not strictly valid, it is a reasonable first approximation, suggesting that the frequency dependence due to $\Pi(\nu)$ was small compared to that arising from the α term. The change in position angle over the observed frequency range is consistent with this hypothesis.

In addition, the cut-off polarization model was fitted to these data. Again it was assumed that the magnetic field in the region was partially ordered and was such that no FDθ would result. It was not possible to fit the data using a single cut-off component. Therefore the cut-off model fits presented in Table 7 include unpolarized power-law components which permit reasonable fits. The observed FDP results from a combination of the intrinsic FDP of the cut-off component and the dilution of the polarized flux by an unpolarized component of differing spectral shape. The fits are characterised by the following parameters: the 10^{14} Hz flux densities of the cut-off and power law components (S_1 and S_2 respectively in units of mJy), the two spectral indices (α_1 and α_2), the cut-off frequency (ν_c in units of 10^{14} Hz) and the polarization parameter (Π). This latter is defined such that at low frequencies the polarization is $\Pi\,(1+\alpha_1)/(\frac{5}{3}+\alpha_1)$. All the frequencies are measured in the observer's frame. Fig. 11 shows the best fit to the 1986 August 5 data. In contrast to the α-parameterisation, the cut-off explanation appears to be more complicated as it requires an extra unpolarized component, and an extra parameter is needed to fit the data. However

it has a number of advantages over the α-parameterisation. In the cut-off picture the FDP results from the intrinsic properties of the synchrotron process and from the relative spectral indices of the two components. The spectral index parameter (α_1) appears to be consistent with relativistic strong shocks and synchrotron losses. The unpolarized component appears to have a higher spectral index which is inconsistent with current estimates of those obtainable from shock acceleration, but which is well within the range of spectral indices that can be predicted by the SSC models. This leads to a tentative identification of this component with the integrated emission of the quiescent jet, while the cut-off would arise from a shock in this flow. Hence, the cut-off model contains more information about the physical nature of the source than the α-parameterisation. Those observations which displayed FDθ could be interpreted similarly to the explanation given for the α-parameterisation. Alternatively, if the second component had a small polarization at a slightly different position angle to that of the cut-off component, then the observed FDθ could result without requiring intrinsic FDθ in the cut-off polarization behaviour. This is, of course, the explanation used by Holmes *et al.* (1984b) to describe their data. This would introduce extra parameters, reducing the degrees of freedom to the fits which, in themselves, would make more likely a satisfactory fit to the limited number of points available.

Even assuming normal statistics neither the α-parameterisation nor the cutoff model can be rejected on the basis of the χ^2 value at the 1% level. An important question is the constancy of these parameters as the source varies. Can the observed variations be characterised as simple changes in a small subset of parameters in either of these pictures? In the α-parameterisation the fitted flux parameters appear to change markedly from 1986 August 2 to 1986 August 6. However it was stated above that the spectral index did not change significantly during the observing period. If the parameters in Table 7 are used to calculate the spectral index at I (which is the best constrained part of the fit), then the calculated spectral indices remain essentially constant over the period of the 1986 August observations. The variability arises from changes in $\log S_{14}$ and Π. In the cut-off model the situation is more complicated. The variations in ν_c, α_1 and α_2 in 1986 August are within the uncertainties in these parameters. The observed variations, in this picture, result from a complicated mix of variations in $\log S_1$, $\log S_2$ and Π.

The α-parameterisation was fitted to all polarized observations with four or more flux points, excluding the observations of $1641+399$, for which an alternative explanation of dilution by unpolarized flux was advanced in Mead *et al.* (1988). There were 81 sets of observations satisfying this criterion, of which 52 were successfully fitted at the 5% level. No allowance was made for the presence of FDθ . The fitted values of the B-field ordering parameter are displayed in Fig. 12. This confirms that in many cases the radiation can be modelled in terms of a simple inhomogeneous source. The rejected fits are summarised in Table 8. As six of the rejected fits are not significant at the 1% level, it is probably reasonable to consider these consistent with the α-parameterisation. The remaining cases in Table 8 are worthy of discussion. There was no *a priori* reason to expect that the α-parameterisation would not have been able to fit the data of $0048-097$ (1986 Aug. 3), $0754+100$ (1988 Feb. 15, 16), or $0818-128$ (1988 Feb. 16, 17). The observations of $0109+224$ and $1418+546$ were characterised by sharp rises in the degree of polarization with frequency (a factor of ~ 6 for the $0109+224$ data). Extrapolating from the observed frequencies the polarization would have fallen to zero below 10^{14} Hz in both cases. The observations of $0109+224$ were preceded by a number of three-frequency measurements which exhibited FDP with both $dp/d\nu > 0$ and $dp/d\nu < 0$. It is possible that a multicomponent model can explain these data but without observations at lower frequencies such an explanation cannot be tested. The observation of $0118-272$ has a peculiar spectrum due to an anomalous H flux point (see MEA). $1101+384$, $1514-241$ and $2200+420$ are located in nearby galaxies so the fluxes contain an unquantifiable amount of starlight. The observations of $2155-304$ and $1147+245$ showed FDθ as well as FDP, and so the α-parameterisation would not strictly be applicable. A likely explanation for the observed FDθ in BL Lac is a multi-component picture such as that of Holmes *et al.* (1984b) and Brindle *et al.* (1986). However the fitting of such a model requires accurate photometry of the blazar component not achieved by these data. The observation of $2254+074$ (1986 Aug. 4) showed a frequency-independent degree of polarization from H to B and a significantly higher U polarization — behaviour inconsistent with the α-parameterisation. The observations of 1987 July also showed a tendency for FDP to be more marked at the higher optical frequencies.

The cut-off model was fitted to a number of objects, selected as showing FDP with $dp/d\nu > 0$, no evidence for either FDθ and convex spectra. Also excluded were those objects which the α-parameterisation failed to explain because of the reasons given above, although the data of $0048-097$ (1986 Aug. 3), $0754+100$ (1988 Feb. 18), and $0818-128$ (1988

Feb.) were included as there was no *a posteriori* justification for the failure of the α-parameterisation. The results are tabulated in Table 9. Eight of the attempted fits could be rejected at the 5% level. The observations of $0048-097$ (1986 Aug. 3) were acceptable at the more correct 1% level. The fits to the data of $0109+224$ (1986 Aug. 7) and $0138-097$ (1987 Sep. 20) were achieved with a high value of ν_c and thus the fits were essentially a result of FDP due to the effect of the unpolarized component on the apparent behaviour.

4.4 DISCUSSION

Two pictures have been presented in the previous sections which explain the salient features of the observations. The α-parameterisation is a simple description of the expected properties of synchrotron radiation from an inhomogeneous source. The form of the flux distribution is entirely empirical. All the information contained in the flux and polarization has been removed to this parameterisation of the observed spectra. No further insights into the physics of the emission region can be obtained beyond the conclusion that the radiation is consistent with emission from an inhomogeneous source and that, to first order, equation 4 applies. SSC pictures provide a parameterisation whereby the spectrum expected from an inhomogeneous relativistic jet can be evaluated (e.g. Madau, Ghisellini & Persic 1987) but rely on observations over decades of frequency to constrain their parameters.

The cut-off picture can explain many of the examples of FDP including some that the α-parameterisation cannot. This model is attractive because an upper energy cut-off in the electron energy distribution is an expected feature of particle acceleration at shocks. This cut-off occurs because above certain energies the acceleration timescale is longer then the energy loss timescale. Biermann & Strittmatter (1987) derive a cut-off frequency between 3×10^{14} Hz and 2×10^{15} Hz. The value of the cutoff frequency is critically dependent on the assumptions made in its derivation, e.g. a Kolmogorov spectrum ($\propto k^{-5/3}$) was used to model the spectrum of the turbulent magnetic energy density responsible for the scattering. Heavens (1984) showed that a k^{-1} spectrum can give rise to a cut-off at X-ray frequencies for shocks speeds greater than 3000 km s^{-1}.

It is worth comparing the expected values with the fitted results for ν_c given in §4.2 and §4.3. For $1253-055$ the Biermann & Strittmatter (1987) upper limit corresponds to an observer's frame frequency of 1.3×10^{15} Hz. The 1986 August fits are broadly consistent with being around this upper limit, while the 1987 July and 1988 February fits are at lower frequencies. Although interpretation of ν_c for the objects in Table 9 is harder as not all the

objects have measured redshifts, most of the fits have best-fit cut-off frequencies which are either close to Biermann & Strittmatter's (1987) upper limit or higher. This is consistent with the fact that the polarization 'hump', at frequencies above ν_c, is not observed. In fact instances of $dp/d\nu < 0$ are either transient phenomena (e.g. 0109 + 224 in 1986 August) or have explanations in terms of the line emission and 'blue bump'. No significant cases also showing $d^2\alpha/d^2\nu > 0$ were seen. This is a problem for the interpretation of the observed FDP in terms of cut-offs unless the Biermann & Strittmatter (1987) model genuinely indicates the physical processes in shock acceleration produce cut-offs over a relatively restricted range of frequency.

How can the cut-off picture be placed in a framework which explains all the observed features of blazar emission? It has been shown how the cut-off picture can explain FDP where it occurs without significant FDθ . However whenever FDθ occurs, this model fails to explain the observations. The motivation for advancing the cut-off model was FDP, although many observations were characterised by power law spectra, frequency-independent degrees of polarization and frequency independent position angles of polarization. These observations can be placed in the same framework as the cut-off model in two ways. Either they could be shock components observed at frequencies much lower than ν_c or they could be the integrated emission of the quiescent jet which may be slightly polarized. If the 'best guess' model of the polarization behaviour is taken to be a cut-off component representing a shock with a steeper spectrum component representing the underlying jet, how would this relate to observations outside of the IR/optical spectral region? Rusk & Seaquist (1985) and Impey (1987) have shown that there is a tendency for preferred optical polarization position angles to be aligned along the VLBI structure. Such quiescent position angles could be speculatively assigned to a polarized jet component (Brindle *et al.* 1986). The other component would then be the shock or cut-off component, which may in principle have a different position angle. In one case the consistency of this can be checked by reference to the observations of 0851 + 202. In their two-component decomposition Holmes *et al.* (1984b) identified two distinct orientations. One appeared constant (at about 100°) and the other rotated during the observations of 1983 January. Roberts & Wardle (1987) report VLBI flux and polarization observations of this object at two epochs (1981.9 and 1982.9), which show highly polarized extensions from the moderately polarized core at a position angle around $-100°$. The polarization of the supposed constant component is close to being orientated along the jet axis, but is not quite close enough to be definitely linked with the quiescent components described above.

5 Concluding remarks

This paper has analysed the results of a programme of multi-frequency polarimetric observations of blazars. 157 observations of 44 blazars were obtained during four separate observing runs in 1986 August, 1987 July, 1987 September and 1988 February. The data consist of simultaneous observations using up to 8 different filters at infrared to optical frequencies. The major results will now be summarised.

1. In many cases the spectrum could be represented as a power law over the full range of observed frequencies, but significant spectral curvature was common. The behaviour of the polarized flux density was similar to that of the total flux density whose properties could be assumed to be representative of the synchrotron component. The spectral behaviour was inconsistent with that expected from particle acceleration at relativistic shocks unless the observations were made in the region of a high-frequency cut-off. Inhomogeneous source models can also explain the observed behaviour.

2. Frequency dependence of the degree of polarization was seen in many cases, generally with $dp/d\nu > 0$. The counter examples were often associated with the 'blue bumps' discussed in §2. Frequency dependence of the polarization position angle was a less common feature of blazar behaviour. No evidence was found to support claims that frequency dependence is associated with high levels of polarization.

3. Variability was a common feature of the observations. No simple characteristics have yet been found to describe all the variations.

4. Most of the observed frequency dependence of polarization in blazars is linked to the intrinsic curvature in the blazar flux spectrum. This suggests an inhomogeneous model for the emission region is required. An example is provided by a polarized component with a high-frequency cut-off and a second component with a steeper spectral index and no significant polarization, tentatively identified with shock accelerated electrons and a quiescent jet, respectively. This cannot simply explain the observed frequency dependence of position angles without recourse to separate polarized components.

Further work must provide a rigorous test of the cut-off model. The fits would be better constrained if flux information were available from higher and lower frequencies than those observed. This would make the empirical determination of the spectral index more secure at K, H & J and B & U. This in turn would more severely test the observed polarization behaviour at these frequencies. Polarization information at lower frequencies

where the hypothetical unpolarized (or low polarization) and steeper spectrum component will dominate would be particularly important. If on the other hand, a theoretical prediction of the observed spectral shape of a blazar is not available, then the validity of the α-parameterisation must be tested using an empirical fit to the observed flux data. In this case, the α-parameterisation would also benefit from wider frequency coverage.

Acknowledgements

We wish to thank J. Bailey and C. Brindle for assistance in making these observations and A. Heavens for useful discussions. K. Ballard and A. Mead wish to acknowledge the receipt of SERC studentships.

References

Abramowicz, M.A., Calvani, M. & Nobili, L., 1980. *Astrophys. J.*, **242**, 772.

Allen, D.A., Ward, M.J. & Hyland, A.R., 1982. *Mon. Not. R. astr. Soc.*, **199**, 969.

Bailey, J.A., Hough, J.H. & Axon, D.J., 1983. *Mon. Not. R. astr. Soc.*, **203**, 339.

Begelman, M.C., Blandford, R.D. & Rees, M.J., 1984. *Rev. Mod. Phys.*, **56**, 255.

Biermann, P.L. & Strittmatter, P.A., 1987. *Astrophys. J.*, **322**, 643.

Björnsson, C.-I., 1985. *Mon. Not. R. astr. Soc.*, **216**, 241.

Björnsson, C.-I. & Blumenthal, G.R., 1982. *Astrophys. J.*, **259**, 805.

Blandford, R.D., 1979. *Proc. A.I.P. Conf.* (La Jolla), **56**, 335.

Bregman, J.N., Lebofsky, M.J., Aller, M.F., Rieke, G.H., Aller, H.D., Hodge, P.E., Glassgold, A.E. & Huggins, P.J., 1981. *Nature*, **293**, 714.

Brindle, C., Hough, J.H., Bailey, J.A., Axon, D.J., Schulz, H., Kikuchi, S., McGraw, J.T., Wisniewski, W.J., Fontaine, G., Nadesu, D., Clayton, G., Anderson, E., Jameson, R.F., Smith, R. & Wallis, R.E., 1985. *Mon. Not. R. astr. Soc.*, **214**, 619.

Brindle, C., Hough, J.H., Bailey, J.A., Axon, D.J. & Hyland, A.R., 1986. *Mon. Not. R. astr. Soc.*, **221**, 739.

Conover, W.J., 1980. *Practical Nonparametric Statistics*, Wiley 2nd. Ed., New York.

Cotton, W.D., Wittels, J.J., Shapiro, I.I., Marcaide, J., Owen, F.N., Spangler, S.R., Rius, A., Angulo, C., Clark, T.A. & Knight, C.A., 1980. *Astrophys. J.*, **238**, L123.

Cruz–Gonzalez, I. & Huchra, J.P., 1984. *Astr. J.*, **89**, 441.

Heavens, A.F., 1984. *Mon. Not. R. astr. Soc.*, **207**, 1P.

Heavens, A.F., 1988. In: *Workshop on Hotspots in Extragalactic Radio Sources*, eds. Meisenheimer, K. & Röser, H.–J.

Heavens, A.F. & Drury, L.O'C., 1988. *Mon. Not. R. astr. Soc.*, **235**, 997.

Gear, W.K., Robson, E.I., Ade, P.A.R., Griffin, M.J., Brown, L.M.J., Smith, M.G., Nolt, I.G., Radostitz, J.V., Veeder, G., & Lebofsky, L., 1985. *Astrophys. J.*, **291**, 511.

Gear, W.K., Robson, E.I. & Brown, L.M.J., 1986. *Nature*, **324**, 546.

Ghisellini, G., Maraschi, L. & Treves, A., 1985. *Astr. Astrophys.*, **146**, 204.

Holmes, P.A., 1985. *Ph.D. Thesis*, University of Edinburgh.

Holmes, P.A., Brand, P.W.J.L., Impey, C.D. & Williams, P.M., 1984a. *Mon. Not. R. astr. Soc.*, **210**, 961.

Holmes, P.A., Brand, P.W.J.L., Impey, C.D., Williams, P.M., Smith, P., Elston, R., Balonek, T., Zeilik, M., Burns, J., Heckert, P., Barvainis, R., Kenny, J., Schmidt, G. & Puschell, J., 1984b. *Mon. Not. R. astr. Soc.*, **211**, 497.

Impey, C.D., 1987. In : *Superluminal Radio Sources*, p. 233, eds. Zensus, J.A. & Pearson, T.J., Cambridge University Press.

Impey, C.D., Brand., P.W.J.L., Wolstencroft, R.D. & Williams, P.M., 1982. *Mon. Not. R. astr. Soc.*, **200**, 19.

Impey, C.D., Brand., P.W.J.L., Wolstencroft, R.D. & Williams, P.M., 1984. *Mon. Not. R. astr. Soc.*, **209**, 245.

Kardashev, N.S., 1962. *Sov. Astr. - A.J.*, **6**, 317.

Kikuchi, S. & Mikami, Y., 1987. *Publs astr. Soc. Japan*, **39**, 237.

Kirk, J.G. & Heavens, A.F., 1989. *Mon. Not. R. astr. Soc., in press*

Kirk, J.G. & Schneider, P., 1987. *Astrophys. J.*, **315**, 425.

Königl, A., 1981. *Astrophys. J.*, **243**, 700.

Landau, R., Grolisch, B., Jones, T.J., Jones, T.W., Pedelty, J., Rudnick, L., Sitko, M.L., Kenney, J., Roellig, T., Salonen, E., Urpo, S., Schmidt, G., Neugebauer, G., Matthews, K., Elias, J.H., Impey, C.D., Clegg, P. & Harris, S., 1986. *Astrophys. J.*, **308**, 78.

Longair, M.S., 1981. *High Energy Astrophysics*, Cambridge University Press.

Madau, P., Ghisellini, G. & Persic, M., 1987. *Mon. Not. R. astr. Soc.*, **224**, 257.

Malkan, M.A. & Sargent, W.L.W., 1982. *Astrophys. J.*, **254**, 22.

Marscher, A.P., 1980. *Astrophys. J.*, **235**, 386.

Marscher, A.P. & Gear, W.K., 1985. *Astrophys. J.*, **298**, 114.

Mead, A.R.G., Brand, P.W.J.L., Hough, J.H. & Bailey, J.A., 1988. *Mon. Not. R. astr. Soc.*, **233**, 503.

Mead, A.R.G., Ballard, K.R., Brand, P.W.J.L., Hough, J.H., Bailey, J.A. & Brindle, C., 1989. *Astr. Astrophys. Suppl., in preparation.*

Meisenheimer, K. & Heavens, A.F., 1986. *Nature*, **323**, 419.

Moore, R.L., McGraw, J.T., Angel, J.R.P., Duerr, R., Lebofsky, M.J., Rieke, G.H., Wiśniewski, W.Z., Axon, D.J., Bailey, J.A., Hough, J.H., Thompson, I., Breger, M., Schulz, H., Clayton, G.C., Martin, P.G., Miller, J.S., Schmidt, G.D., Africano, J. & Miller, H.R., 1982. *Astrophys. J.*, **260**, 415.

Moore, R.L. & Stockman, H.S., 1984. *Astrophys. J.*, **279**, 465.

Nordsieck, K.H., 1976. *Astrophys. J.*, **209**, 653.

Pacholczyk, A.G., 1970. *Radio Astrophysics*, Freeman, San Francisco.

Pacholczyk, A.G., 1977. *Radio Galaxies*, Pergamon.

Puschell, J.J. & Stein, W.A., 1980. *Astrophys. J.*, **237**, 331.

Rees, M.J., 1984. *Ann. Rev. Astr. Astrophys.*, **22**, 471.

Rieke, G.H., Lebofsky, M.J. & Kinman, T.D., 1979. *Astrophys. J.*, **232**, L151.

Roberts, D.H. & Wardle, J.F.C., 1987. In: *Superluminal Radio Sources*, eds. Zensus, J.A. & Pearson, T.J., p. 193.

Rusk, R. & Seaquist, E.R., 1985. *Astr. J.*, **90**, 30.

Shields, G., 1978. *Nature*, **272**, 706.

Smith, P.S., Balonek, T.J., Elston, R. & Heckert, P.A., 1987. *Astrophys. J. Suppl.* , **64**, 459.

Figures

1, a) & b) The median and maximum values of the spectral indices at I.

2, a) & b) The median and maximum values of the spectral curvature, $\Delta\alpha_{(B-H)}$.

3, a) & b) The median and maximum values of the polarized spectral indices at I.

4, a) & b) The median and maximum values of the polarized spectral curvature, $\Delta\alpha_{p,(B-H)}$.

5, a) & b) The median and maximum values of the polarizations at I.

6, a) & b) The median and maximum values of the degree of the frequency dependence of polarization, $p(\nu_B)/p(\nu_H)$.

7, a) & b) The distributions of the I polarizations. The shaded region represents the distribution of those objects showing FDP (a) and FDθ (b) significant at the 5% level. The distributions are not significantly different.

8, a) & b) Plots of the median and maximum values of $p(\nu_B)/p(\nu_H)$ versus $p(\nu_I)$. No correlation was present here at the 5% level.

9 The flux and polarization behaviour of two superimposed synchrotron components. One component has a spectral index of 1.0, a perfectly ordered magnetic field and a sharp upper cutoff to the energy distribution. The second has a spectral index of 1.5 and is unpolarized.

10, a) & b) α-parameterisation fits to the flux and polarization data of 1986 August 5.

11, a) & b) Cutoff fits to the flux and polarization data of 1986 August 5.

12 Distribution of the fitted values of Π, the B-field ordering parameter.

Table 1: Summary of the polarimetric observations at UKIRT

IAU Name	1986 Jul./Aug.	1987 Jul.	1987 Sep.	1988 Feb.
0048 − 097	HJIRVB	KHJIRVBU	HIRVBU	
0106 + 013	HIB	HIRVBU	HIRVBU	
0109 + 224	HJIRVB	HIRVBU	HIRVBU	
0118 − 272	HJIRVB	HIRVBU	HIRVBU	
0138 − 097	HIB	HIRVBU	KHIRVBU	
0219 − 164		KHJIRVBU		
0219 + 428	HIB	HIRVBU	HIRVBU	
0235 + 164		KHJIRVBU	KHJIRVBU	
0300 + 470			HIRVBU	
0323 + 022	HIB		HIRVBU	
0336 − 019	HIB			
0338 − 214	HIB		HIRVBU	
0414 + 009			HIRVBU	HJIRVBU
0422 + 004				KHIRVBU
0735 + 178			HIRVBU	HIRVBU
0736 + 017			HIRVBU	JIRVBU
0754 + 100				KHJIRVBU.
0818 − 128				KHJIRVBU
0851 + 202				KHIRVBU
0906 + 015				HIRVBU
1101 + 384				KHJIRVBU
1147 + 245				HJIRVBU
1156 + 295				HIRVBU
1253 − 055	HJIRVBU	KHJIRVBU		HIRVBU
1413 + 135	HIB			
1418 + 546	HIB	HJIRVBU	HIRVBU	KHJIRVBU
1424 + 240				HIRVBU
1510 − 089	HIB			
1514 − 241	HIB	KHJIRVBU		
1538 + 149	HIB			
1641 + 399	KHJIRVBU	KHJIRVBU	HIRVBU	
1652 + 398			KHJIRVBU	
1717 + 178	HIB	HIRVBU	HIRVBU	
1727 + 502	HIB		HIRVBU	
1749 + 096	HIB	JIRVBU		
1921 − 293	HIB	JIRVB		
2032 + 107		JIRVBU	HIRVBU	
2155 − 304	HJIRVB	KHJIRVBU	KHJIRVBU	
2200 + 420	HJIRVB	KHJIRVBU	HIRVBU	
2208 − 137	HIB			
2223 − 052	HIB	HJIRVBU	HIRVBU	
2230 + 114	HIB			
2251 + 158	HIB	HIRVBU	HIRVBU	
2254 + 074	HJIRVBU	HIRVBU	HIRVBU	

Table 2: Objects possibly containing contaminating flux

Object Name		Date of observation	Significance Level (%)
$0106+013$	(2)	1987 July 28	2.5
$0109+224$	(1)	1986 August 4	1.0
$0118-272$	(2)	1987 July 27	0.01
$0138-097$	(1)	1986 August 5	1.0
$0735+178$	(2)	1988 February 15	5.0
$0754+100$	(1)	1988 February 18	2.5
$0818-128$	(2)	1988 February 15,16	0.01
$1418+546$	(1), (2)	1986 August 6	0.01
$1418+546$	(2)	1988 February 18	0.01
$1424+240$	(2)	1988 February 16	0.01
$1717+178$	(1)	1986 August 7	0.01
$1749+096$	(2)	1986 August 5	0.01
$1921-293$	(1)	1986 August 6	0.1
$1921-293$	(2)	1987 July 27	0.01
$2032+107$	(2)	1987 July 27	0.01
$2208-137$	(2)	1986 August 3,4 & 7	0.01
$2251+158$	(1)	1987 September 20	3.0

(1)$\equiv$ FDP with $dp/d\nu < 0$, (2)$\equiv$concave flux spectra ($d\alpha/d\nu < 0$)

Table 3: Spectral indices at I and spectral curvature parameters

Object Name	$\alpha(\nu_I)$ Median	$\alpha(\nu_I)$ Maximum	No. of Obs.	$\Delta\alpha_{(B-H)}$ Median	$\Delta\alpha_{(B-H)}$ Maximum	No. of Obs.
0048 − 097	1.32	2.29	9	0.02	0.42	7
0106 + 013	1.36	1.36	1	−0.43	−0.43	1
0109 + 224	1.24	1.55	7	0.42	0.85	5
0118 − 272	1.18	1.98	5	0.00	0.62	4
0138 − 097	1.25	1.45	7	0.45	0.70	5
0219 − 164	1.00	1.00	1	0.35	0.35	1
0219 + 428	1.21	1.44	3	0.01	0.72	3
0235 + 164	1.84	2.23	2	2.44	2.49	2
0414 + 009	1.01	1.03	2	1.09	1.09	2
0422 + 004	1.19	1.22	2	1.25	1.39	2
0735 + 178	1.55	1.62	3	0.41	0.47	3
0754 + 100	1.39	1.51	4	0.40	0.56	4
0818 − 128	1.20	1.52	3	1.29	3.37	3
0851 + 202	1.44	1.47	3	0.31	0.45	3
1101 + 384	0.62	0.62	1	1.03	1.03	1
1147 + 245	1.36	1.36	1	0.27	0.27	1
1156 + 295	1.25	1.29	3	0.06	0.11	3
1253 − 055	1.16	1.62	9	0.42	0.95	8
1418 + 546	1.15	1.59	4	0.80	1.28	4
1424 + 240	0.76	0.95	3	0.45	1.04	3
1514 − 241	0.99	0.99	1	1.99	1.99	1
1641 + 399	1.87	2.07	6	−1.46	−0.62	6
1717 + 178	1.83	1.83	1	–	–	–
1749 + 096	2.89	2.89	1	0.28	0.28	1
2155 − 304	0.62	0.71	2	0.02	0.42	2
2200 + 420	1.38	1.52	5	2.73	2.87	5
2223 − 052	1.71	1.78	3	0.28	0.50	3
2254 + 074	0.92	2.23	5	2.39	2.69	4

Table 4: The polarized flux spectral indices

Name	$\alpha_p(\nu_I)$		No. of	$\Delta\alpha_{p,(B-H)}$		No. of
	Median	Maximum	Obs.	Median	Maximum	Obs.
$0048-097$	1.16	1.27	9	1.28	1.68	7
$0106+013$	0.64	0.64	1	–2.67	–2.67	1
$0109+224$	1.40	1.59	5	–0.03	–0.03	4
$0118-272$	1.06	1.11	5	–0.39	1.08	4
$0138-097$	1.17	2.08	7	0.33	0.76	5
$0219-164$	1.07	1.07	1	0.04	0.04	1
$0219+428$	1.19	1.38	5	0.35	0.36	3
$0235+164$	2.32	3.41	2	1.60	2.50	2
$0338-214$	2.03	2.03	1	–	–	–
$0414+009$	1.71	2.19	2	–0.71	–0.38	2
$0735+178$	1.50	1.50	1	0.74	0.74	1
$0754+100$	1.51	1.55	2	0.05	0.92	2
$0818-128$	1.63	1.92	3	1.32	3.38	3
$0851+202$	1.36	1.53	2	–0.24	0.53	2
$1101+384$	0.92	0.92	1	0.44	0.44	1
$1156+295$	1.28	1.40	3	–0.08	0.34	3
$1253-055$	1.59	1.78	3	0.43	1.11	2
$1418+546$	1.35	1.61	3	0.43	0.82	2
$1424+240$	1.03	1.05	3	0.64	1.03	3
$1514-241$	1.79	1.79	1	1.33	1.33	1
$1641+399$	1.76	2.29	7	0.06	0.46	6
$1717+178$	1.62	1.62	1	–	–	–
$1727+502$	3.45	3.45	1	–	–	–
$1749+096$	1.77	2.33	4	1.86	1.86	1
$1921-293$	2.57	2.77	3	–	–	–
$2200+420$	2.66	2.66	1	–	–	–
$2223-052$	1.66	1.43	3	1.96	2.00	3
$2254+074$	1.68	1.96	6	0.59	0.93	3

Table 5: Polarization data for Figures 5 and 6. Numbers in brackets are 1σ errors.

Object Name	$p(\nu_I)/\%$ Median		$p(\nu_I)/\%$ Maximum		No. of Obs.	$p(\nu_B)/p(\nu_H)$ Median		$p(\nu_B)/p(\nu_H)$ Maximum		No. of Obs.
0048 − 097	14.55	(0.61)	21.17	(1.02)	11	1.24	(0.13)	1.64	(0.17)	10
0109 + 224	8.91	(0.85)	14.04	(0.90)	9	1.09	(0.10)	1.20	(0.05)	7
0118 − 272	16.49	(0.68)	17.82	(0.58)	7	1.17	(0.04)	1.29	(0.08)	7
0138 − 097	22.16	(1.13)	24.80	(1.08)	6	1.09	(0.15)	1.42	(0.05)	8
0219 − 164	12.45	(0.42)	12.45	(0.42)	1	0.93	(0.04)	0.93	(0.04)	1
0219 + 428	11.46	(0.84)	15.46	(0.55)	10	1.08	(0.13)	1.29	(0.06)	10
0235 + 164	13.28	(0.90)	15.52	(1.59)	2	1.52	(0.38)	2.02	(0.24)	2
0300 + 470	9.44	(1.52)	9.44	(1.52)	1	0.69	(0.52)	0.69	(0.52)	1
0323 + 022	3.84	(1.02)	3.84	(1.02)	1	–	–	–	–	–
0338 − 214	10.76	(1.05)	11.07	(1.56)	2	1.00	(0.25)	1.08	(0.13)	2
0414 + 009	7.82	(2.25)	7.82	(2.25)	1	0.63	(0.42)	0.63	(0.42)	1
0422 + 004	16.67	(0.65)	20.79	(1.12)	2	1.08	(0.13)	1.11	(0.05)	2
0735 + 178	16.57	(0.65)	21.90	(0.98)	4	1.07	(0.11)	1.15	(0.06)	4
0754 + 100	11.16	(0.39)	12.39	(0.48)	4	1.10	(0.08)	1.27	(0.03)	4
0818 − 128	23.32	(1.33)	24.73	(1.66)	2	1.29	(0.05)	1.29	(0.05)	1
0851 + 202	18.06	(0.66)	18.36	(1.22)	3	1.07	(0.05)	1.19	(0.06)	3
1101 + 384	3.73	(0.13)	3.73	(0.13)	1	1.45	(0.03)	1.45	(0.03)	1
1147 + 245	2.71	(0.67)	2.71	(0.67)	1	2.82	(0.21)	2.82	(0.21)	1
1156 + 295	26.42	(2.87)	27.27	(2.08)	3	0.91	(0.08)	0.99	(0.05)	3
1253 − 055	31.30	(0.36)	41.58	(0.55)	9	1.08	(0.01)	1.29	(0.06)	9
1418 + 546	4.62	(0.31)	15.37	(2.82)	9	1.51	(0.09)	2.93	(0.16)	7
1424 + 240	4.98	(0.66)	5.14	(0.55)	3	0.91	(0.09)	0.95	(0.09)	3
1514 − 241	3.31	(0.21)	4.76	(0.30)	2	1.53	(0.14)	1.66	(0.07)	2
1641 + 399	15.00	(0.50)	16.09	(1.14)	6	0.48	(0.16)	0.52	(0.15)	6
1652 + 398	1.56	(0.16)	1.56	(0.16)	1	2.85	(0.11)	2.85	0.11	1
1717 + 178	16.11	(1.85)	17.82	(3.62)	2	0.93	(0.50)	1.35	(0.27)	2
1727 + 502	2.48	(0.49)	2.51	(0.82)	2	–	–	–	–	–
1749 + 096	8.89	(0.58)	16.53	(0.95)	4	1.21	(0.21)	1.39	(0.13)	4
1921 − 293	7.56	(1.23)	8.13	(1.65)	2	0.41	(0.79)	0.41	(0.79)	1
2155 − 304	3.10	(0.12)	10.29	(0.23)	5	1.14	(0.06)	1.99	(0.04)	6
2200 + 420	12.02	(0.50)	14.15	(0.37)	13	1.21	(0.06)	1.88	(0.13)	13
2223 − 052	11.64	(1.87)	11.90	(1.21)	3	1.12	(0.23)	1.57	(0.14)	4
2251 + 158	4.18	(0.96)	4.18	(0.96)	1	0.47	(0.29)	0.47	(0.29)	1
2254 + 074	9.65	(1.45)	12.06	(1.26)	11	1.82	(0.16)	2.09	(0.19)	6

Table 6: The position angle data for 1253 – 055 during 1986 August.

U.T. Date	Wavebands	U.T. Time (hours)	Position angle (deg.)	
1986 August 1	HIB	6.165	120.46	(0.35)
	HIB	6.358	120.84	(0.38)
1986 August 2	HIB	6.260	FDθ	
	JVB	6.415	FDθ	
1986 August 4	HIB	5.825	125.40	(0.20)
	HIB	5.958	125.20	(0.20)
	JVB	6.072	126.06	(0.21)
	JRB	6.166	126.77	(0.16)
	JRU	6.313	128.00	(0.20)
1986 August 5	HIB	5.910	132.57	(0.29)
	HIB	5.999	131.87	(0.23)
	JVU	6.154	132.16	(0.20)
	JRU	6.280	131.45	(0.36)
1986 August 6	HIB	5.798	136.23	(0.32)
	HVB	5.997	136.85	(0.42)
	JRU	6.161	135.66	(0.20)

Table 7: The results of fits to the $1253-055$ data. $P(\chi^2)$ is the probability of obtaining the fitted value of χ^2 or greater if the model is correct and normal statistics are assumed.

α-parameterisation

	86/8/2	86/8/4	86/8/5	86/8/6	87/7/28	88/2/16	88/2/17	88/2/18
$\log S_{14}$	1.57	1.40	1.35	1.25	1.16	1.86	1.86	1.86
a	0.50	−0.17	−0.08	−0.08	−0.28	1.47	1.51	1.27
b	−0.63	−1.21	−1.21	−1.10	−1.93	0.09	−0.08	−0.33
Π	0.39	0.48	0.54	0.55	0.40	0.26	0.33	0.39
χ^2	2.96	11.7	9.60	12.0	19.5	10.7	7.28	9.27
$P(\chi^2)$	0.81	0.31	0.48	0.28	0.08	0.22	0.51	0.32

Cut-off Model

$\log S_1$	1.62	1.52	1.51	1.35	1.36	1.74	1.73	1.69
α_1	0.96	0.78	0.93	0.79	0.93	1.06	1.37	1.35
Π	0.42	0.54	0.60	0.64	0.44	0.30	0.42	0.57
ν_c	14.0	12.8	11.6	12.8	3.78	6.80	6.97	6.86
$\log S_2$	0.79	1.10	1.06	0.97	1.07	0.64	1.19	1.46
α_2	1.50	1.72	1.89	1.55	2.49	0.77	1.47	1.59
χ^2	3.92	7.50	7.21	7.27	7.51	4.71	4.16	3.28
$P(\chi^2)$	0.42	0.48	0.51	0.51	0.68	0.58	0.65	0.77

Table 8: Summary of the fits to the polarization behaviour using the α-parameterisation. Only those fits rejected at the 5% level are shown.

Name	U.T. Date	χ^2	$P(\chi^2)$	Π
$0048-097$	1986 Aug. 3	27.40	0.0006	0.20
$0048-097$	1986 Aug. 4	15.98	0.0139	0.22
$0109+224$	1986 Aug. 7	45.77	2.6×10^{-7}	0.09
$0118-272$	1986 Jul. 27	38.27	6.7×10^{-6}	0.19
$0138-097$	1987 Sep. 20	13.93	0.0304	0.32
$0235+164$	1987 Sep. 20	27.27	0.0236	0.12
$0754+100$	1988 Feb. 15	65.8	2.0×10^{-8}	0.15
$0754+100$	1988 Feb. 16	26.8	0.0028	0.15
$0818-128$	1988 Feb. 15	18.7	0.0437	0.27
$0818-128$	1988 Feb. 16	25.8	0.0040	0.28
$0818-128$	1988 Feb. 17	5.0×10^5	0.0	0.28
$1101+384$	1988 Feb. 15	67.8	8.3×10^{-8}	0.05
$1147+245$	1988 Feb. 18	43.3	4.4×10^{-4}	0.04
$1418+546$	1987 Jul. 30	62.9	1.0×10^{-8}	0.07
$1418+546$	1988 Feb. 16	31.9	0.0014	0.04
$1418+546$	1988 Feb. 17	54.7	2.0×10^{-5}	0.06
$1514-241$	1987 Jul. 27	24.44	0.0177	0.06
$2155-304$	1986 Aug. 1	30.96	2.6×10^{-5}	0.05
$2200+420$	1986 Aug. 3	57.43	1.5×10^{-9}	0.16
$2200+420$	1987 Jul. 27	124.5	7.7×10^{-21}	0.11
$2200+420$	1987 Jul. 28	91.85	2.2×10^{-13}	0.14
$2200+420$	1987 Jul. 30	41.40	1.8×10^{-6}	0.16
$2200+420$	1987 Sep. 19	54.84	4.8×10^{-9}	0.11
$2254+074$	1986 Aug. 4	75.67	3.5×10^{-12}	0.14
$2254+074$	1987 Jul. 28	28.87	0.0003	0.15
$2254+074$	1987 Jul. 30	16.94	0.0307	0.15

Table 9: A summary of the fits to the FDP of blazars, using the cut-off model outlined in §4.2 for fits to the data of 1253 − 055.

Name	U.T. Date	χ^2	$P(\chi^2)$	$\log S_1$	α_1	Π	ν_c	$\log S_2$	α_2
0048 − 097	1986 Aug. 3	16.7	0.01	0.48	1.06	0.95	11.5	1.24	1.48
0048 − 097	1986 Aug. 4	4.79	0.31	0.39	0.87	0.85	119.	1.00	1.12
0048 − 097	1986 Aug. 6	8.47	0.21	0.85	0.50	0.25	14.1	1.13	3.24
0109 + 224	1986 Aug. 7	7.19	0.30	−0.38	0.50	1.00	6.8×10^6	1.16	1.33
0118 − 272	1986 Aug. 5	7.88	0.25	0.50	0.93	1.00	12.9	1.13	1.18
0118 − 272	1987 Jul. 30	4.44	0.82	0.99	1.01	0.27	26.9	0.86	1.38
0118 − 272	1987 Sep. 21	6.53	0.16	0.99	1.04	0.28	21.9	0.76	1.51
0138 − 097	1987 Jul. 28	1.71	0.94	0.68	0.98	0.27	32.4	0.89	3.67
0138 − 097	1987 Sep. 19	10.6	0.23	0.50	0.95	0.52	15.3	0.58	1.56
0138 − 097	1987 Sep. 21	3.01	0.56	0.69	0.72	0.32	9.96	−0.62	2.01
0138 − 097	1987 Sep. 20	10.2	0.04	0.29	0.74	0.69	50.0	0.56	1.14
0235 + 164	1987 Sep. 20	23.2	0.003	0.74	0.69	0.13	2.42	0.92	3.28
0735 + 178	1988 Feb. 16	6.55	0.36	0.83	0.62	0.42	4.17	1.08	1.65
0754 + 100	1988 Feb. 18	7.84	0.45	0.91	0.62	0.24	3.89	1.08	1.33
0818 − 128	1988 Feb. 15	26.3	9.5×10^{-3}	0.51	0.50	0.30	3.52	0.17	2.22
0818 − 128	1988 Feb. 16	16.9	0.03	0.43	0.83	0.35	4.07	0.45	2.39
0818 − 128	1988 Feb. 17	17.8	0.007	0.21	1.53	0.78	16.8	0.75	1.93
0851 + 202	1988 Feb. 16	12.3	0.056	1.06	1.16	0.23	9.53	0.52	1.88
1418 + 546	1987 Jul. 30	13.3	0.10	−0.38	0.56	1.00	20.0	1.38	1.65
1749 + 096	1987 Jul. 27	29.2	5.7×10^{-5}	0.80	1.32	0.12	1.95	−4.66	−3.18
2155 − 304	1987 Jul. 27	9.40	0.40	1.72	0.50	0.21	33.3	1.56	0.86
2254 + 074	1987 Aug. 3	41.8	2.0×10^{-7}	0.68	0.84	0.17	2.87	0.46	3.25

Fig. 1a

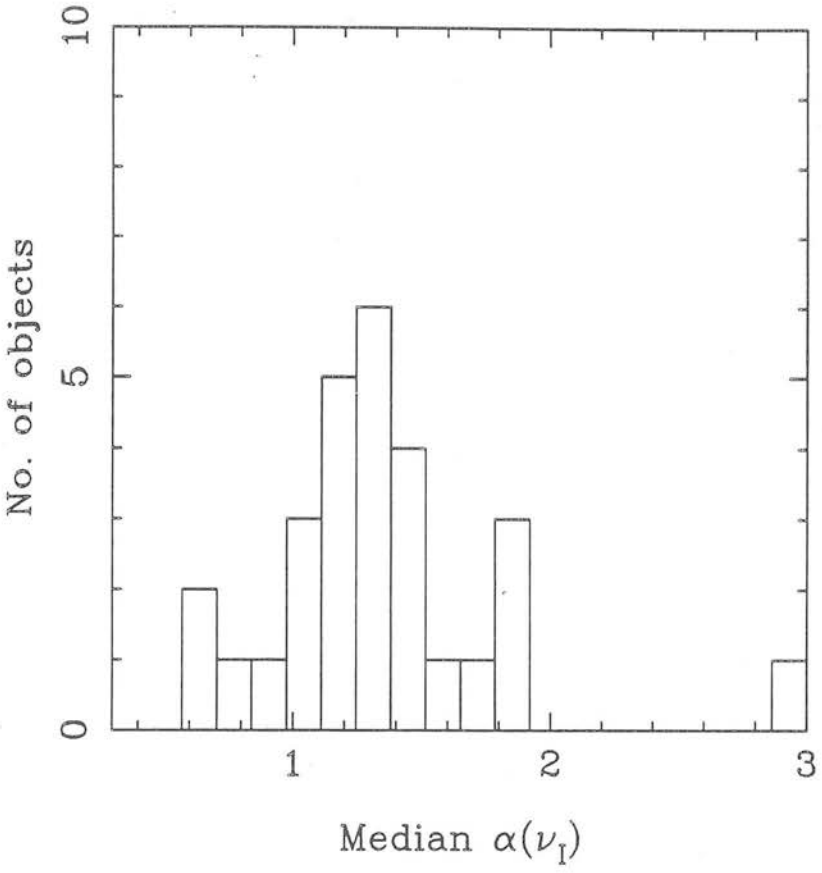
No. of objects
0
5
10
1
2
3
Median $\alpha(\nu_I)$

Fig. 1b

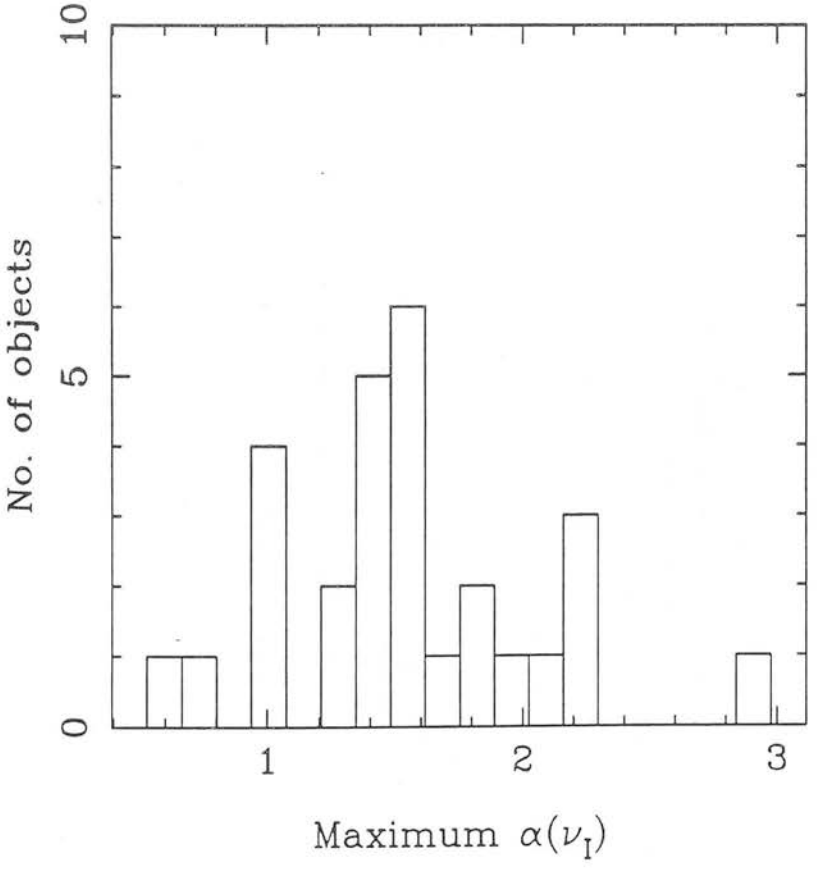
No. of objects
0
5
10
1
2
3
Maximum $\alpha(\nu_I)$

Fig. 2a

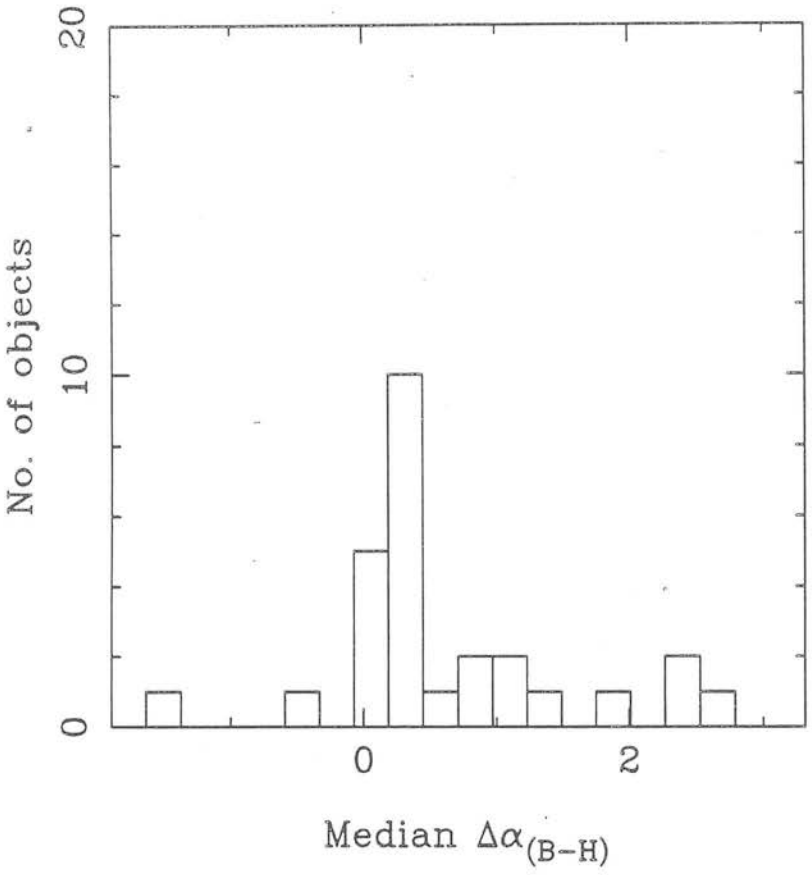
20
10
0
No. of objects
0
2
Median $\Delta\alpha_{(B-H)}$

Fig. 2b

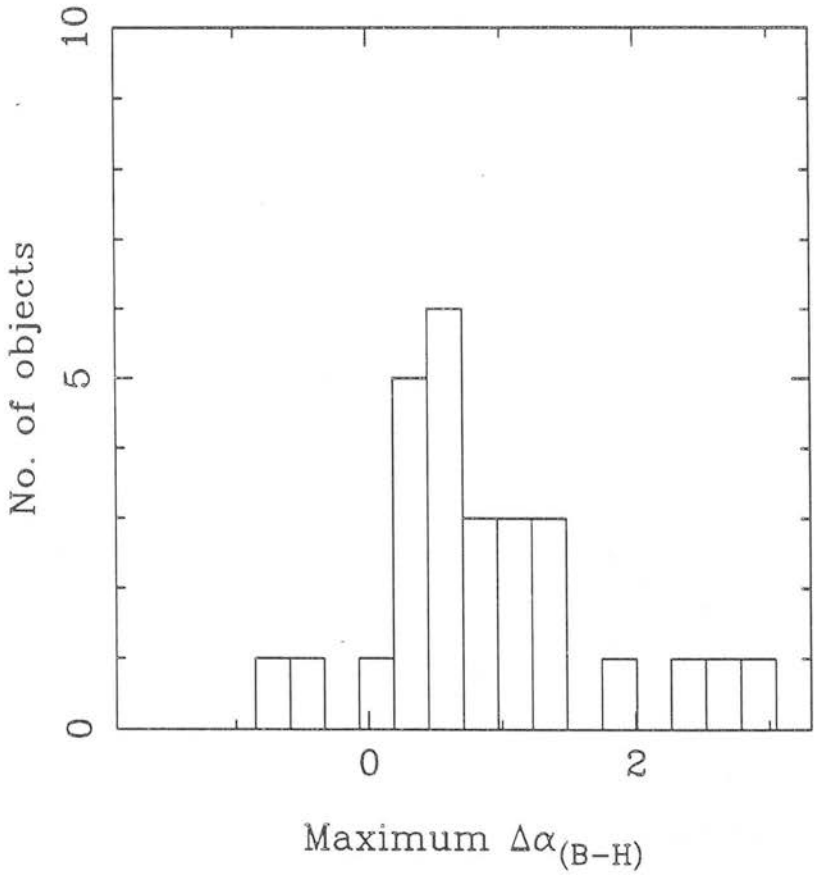
10
5
0
No. of objects
0
2
Maximum $\Delta\alpha_{(B-H)}$

Fig. 3a

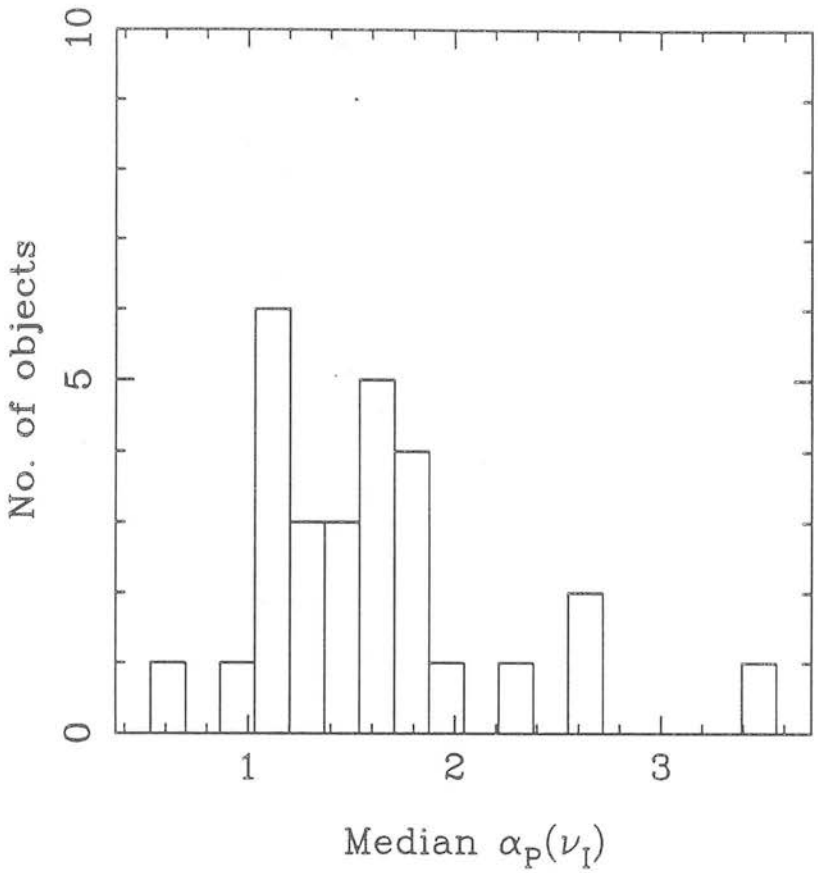
No. of objects
0
5
10
1
2
3
Median $\alpha_P(\nu_I)$

Fig. 3b

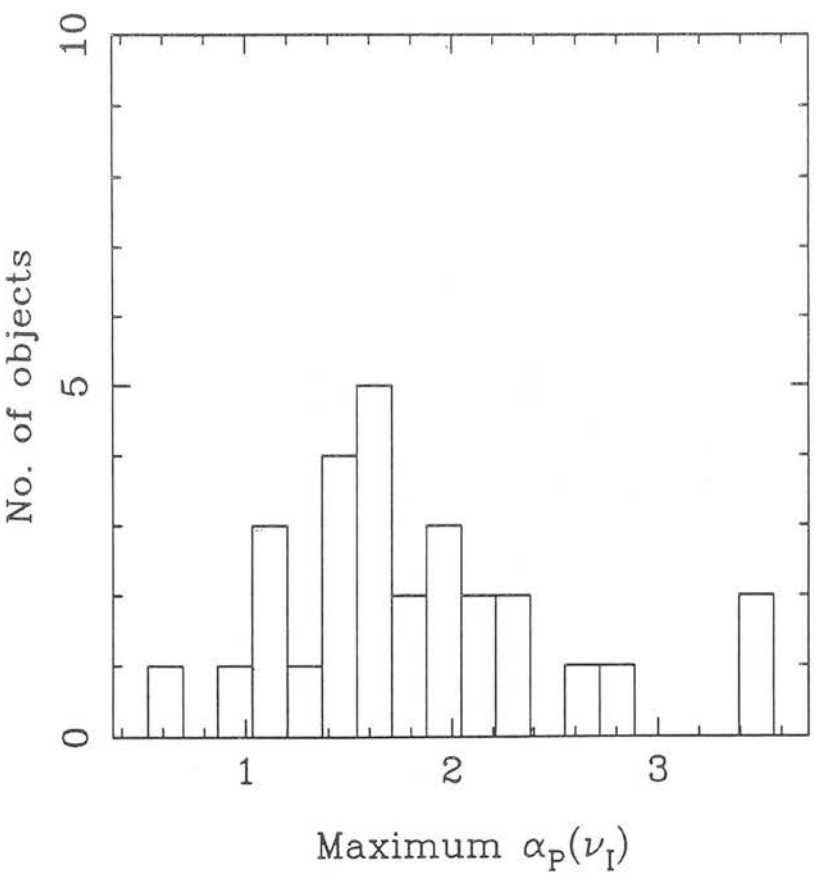
No. of objects
0
5
10
1
2
3
Maximum $\alpha_P(\nu_I)$

Fig. 4a

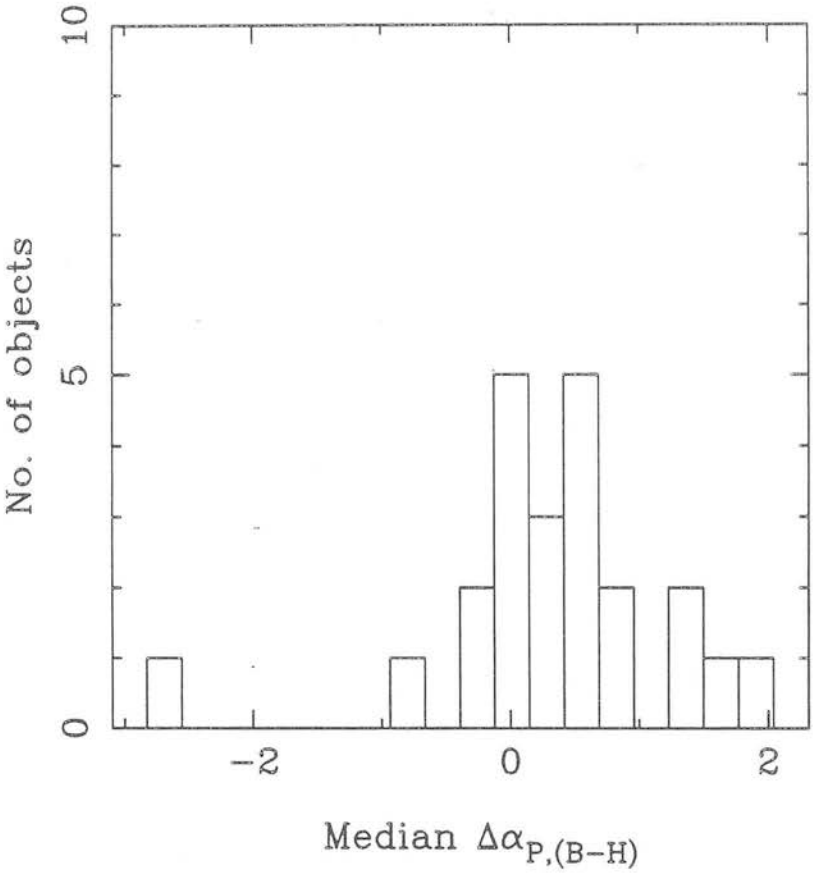
No. of objects
0
5
10
−2
0
2
Median $\Delta\alpha_{P,(B-H)}$

Fig. 4b

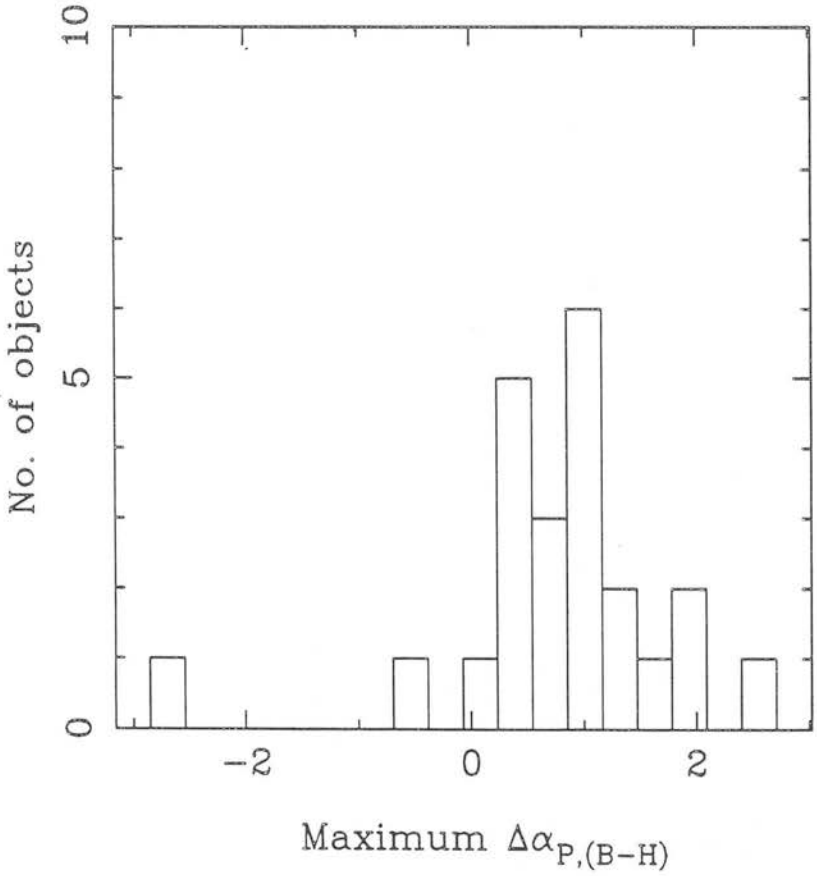
No. of objects
0
5
10
−2
0
2
Maximum $\Delta\alpha_{P,(B-H)}$

Fig. 5a

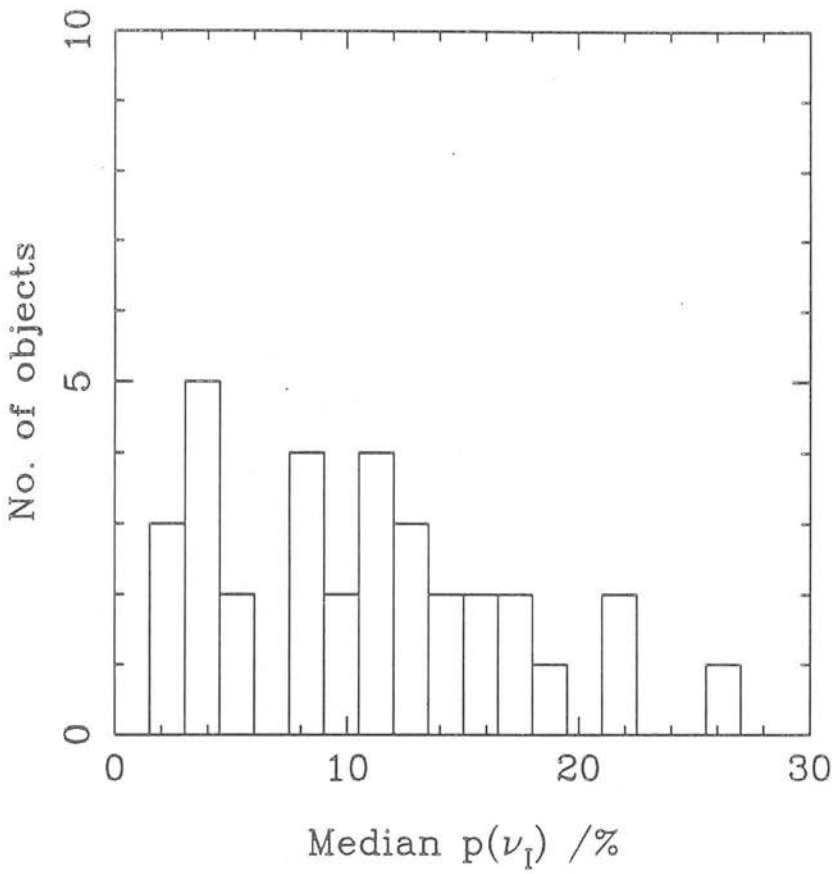
No. of objects
0
5
10
0
10
20
30
Median p(ν_I) /%

Fig. 5b

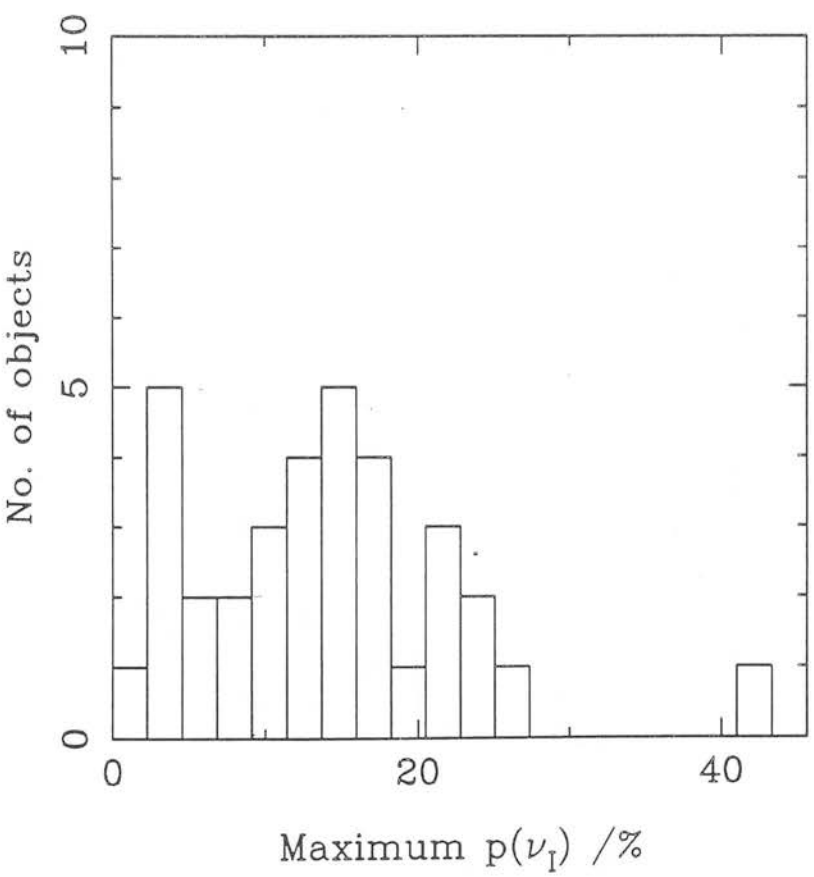
No. of objects
0
5
10
0
20
40
Maximum p(ν_I) /%

Fig. 6a

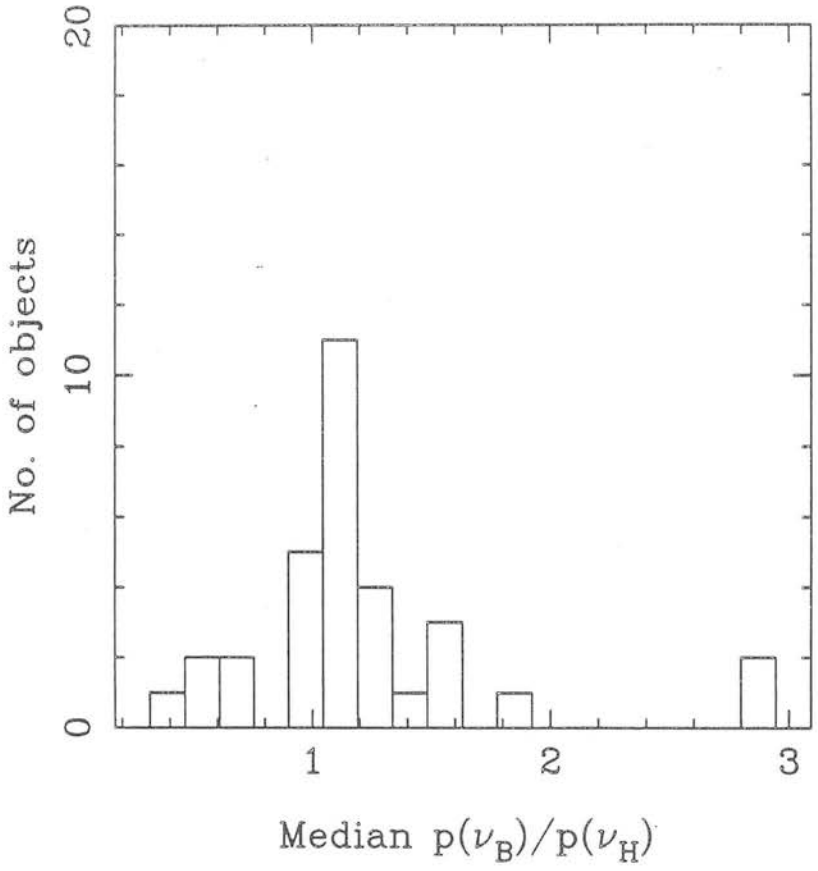
No. of objects
0
10
20
1
2
3
Median $p(\nu_B)/p(\nu_H)$

Fig. 6b

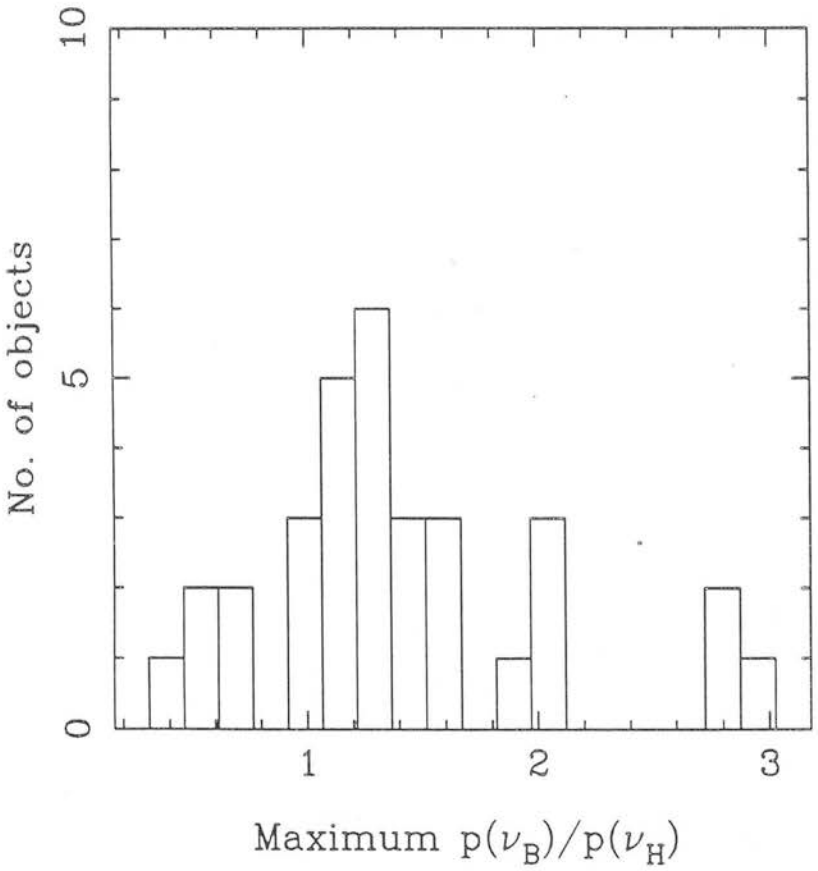
No. of objects
0
5
10
1
2
3
Maximum $p(\nu_B)/p(\nu_H)$

Fig. 7a

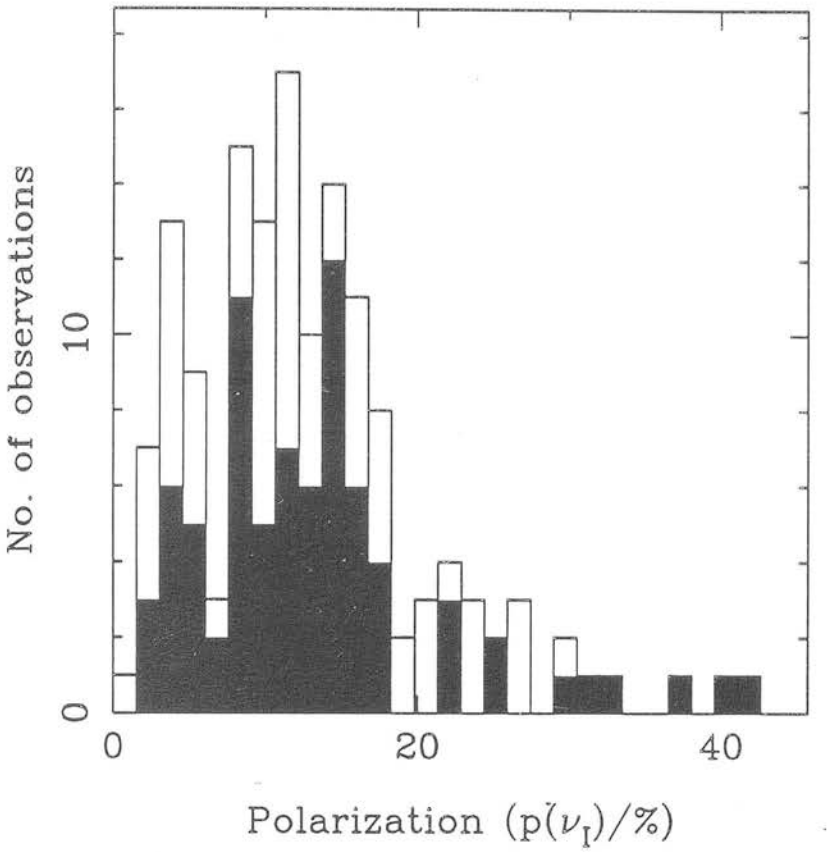
No. of observations
0
10
0
20
40
Polarization (p(ν_I)/%)

Fig. 7b

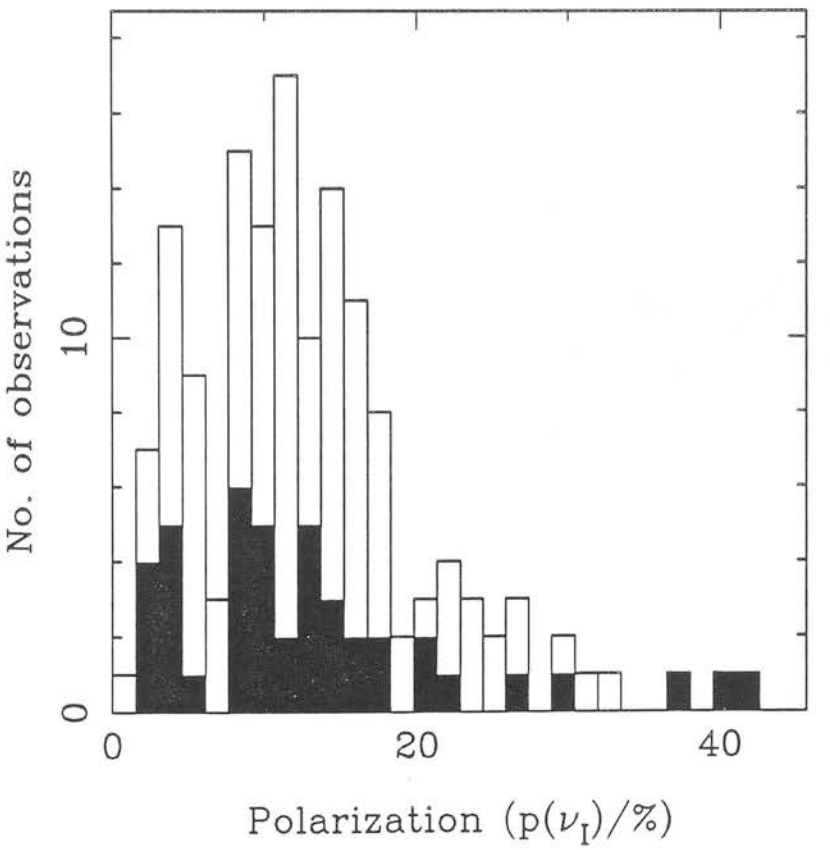
No. of observations
0
10
0
20
40
Polarization (p(ν_I)/%)

Fig. 8a

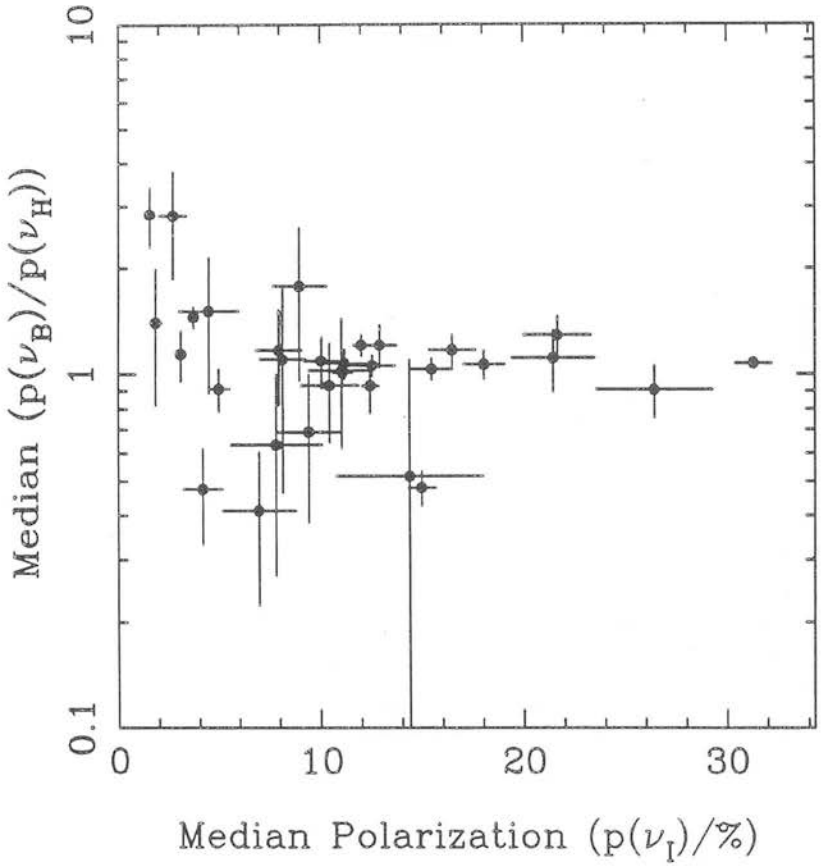
Median $(p(\nu_B)/p(\nu_H))$
10
1
0.1
0
10
20
30
Median Polarization $(p(\nu_I)/\%)$

Fig. 8b

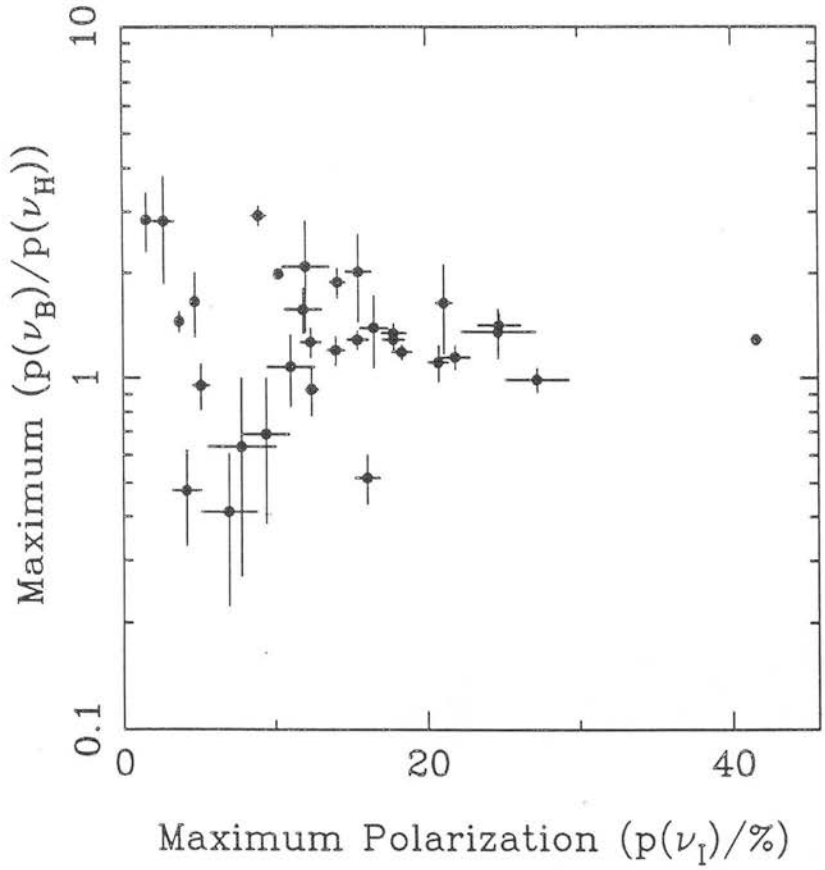
Maximum $(p(\nu_B)/p(\nu_H))$
10
1
0.1
0
20
40
Maximum Polarization $(p(\nu_I)/\%)$

Fig. 9a

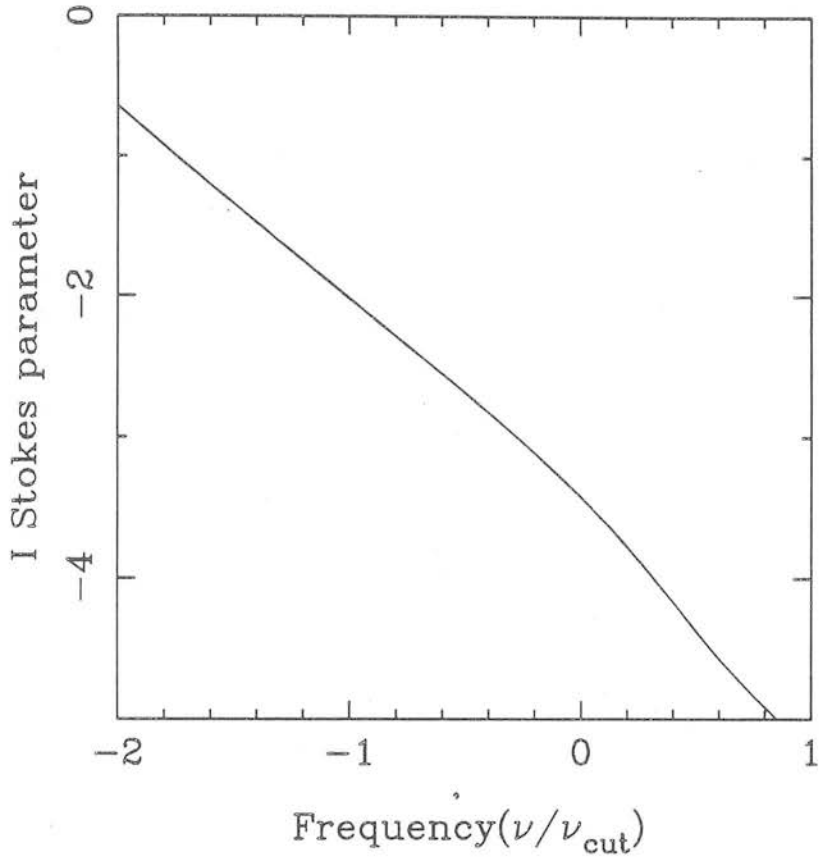
I Stokes parameter
0
−2
−4
−2
−1
0
1
Frequency(ν/ν_{cut})

Fig 9b

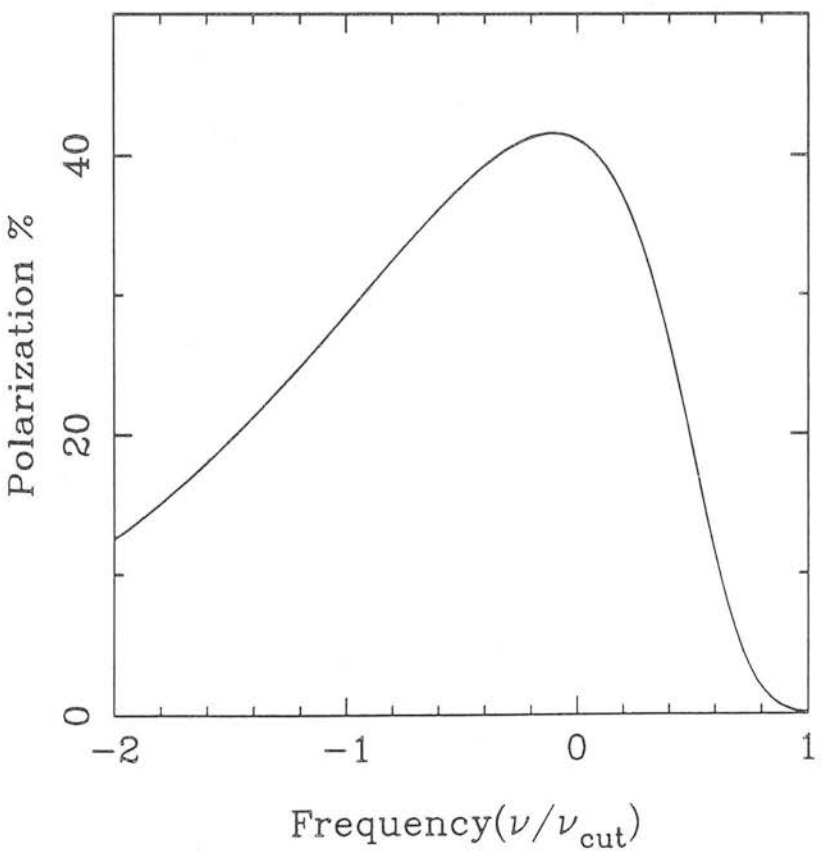
Polarization %
0
20
40
−2
−1
0
1
Frequency(ν/ν_{cut})

Fig. 10a

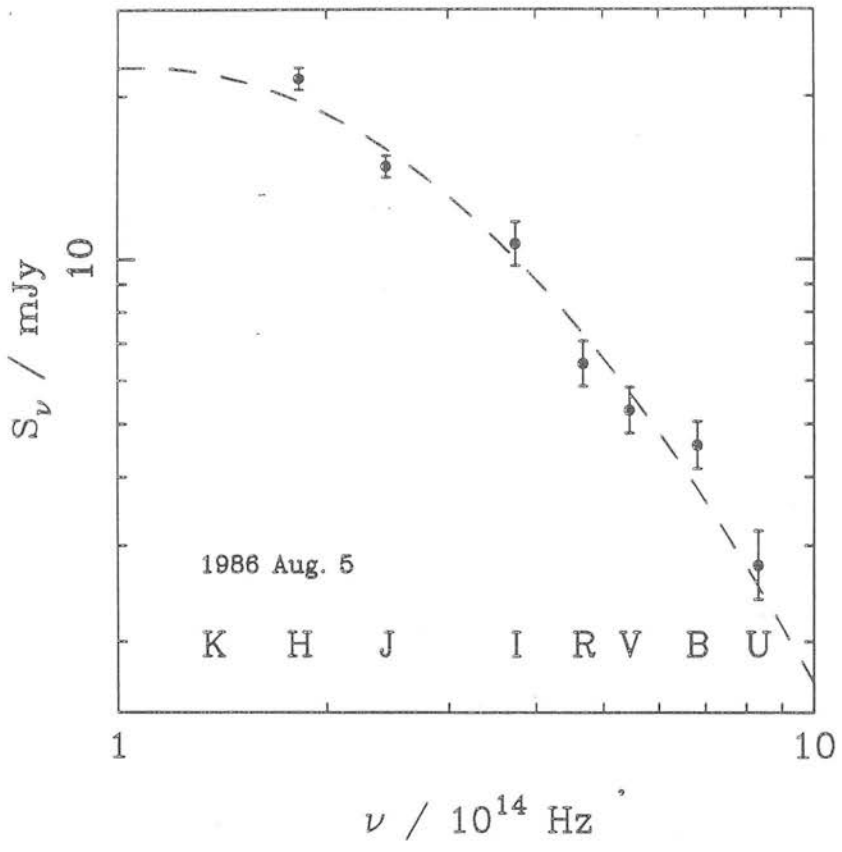

Fig. 10b

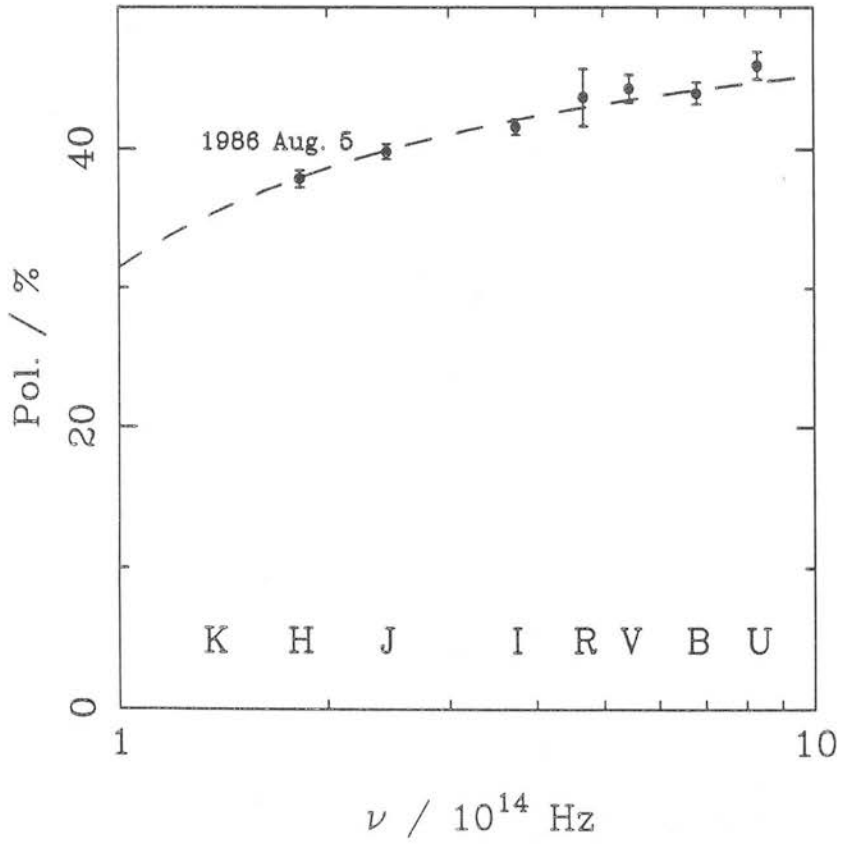

Fig. 11a

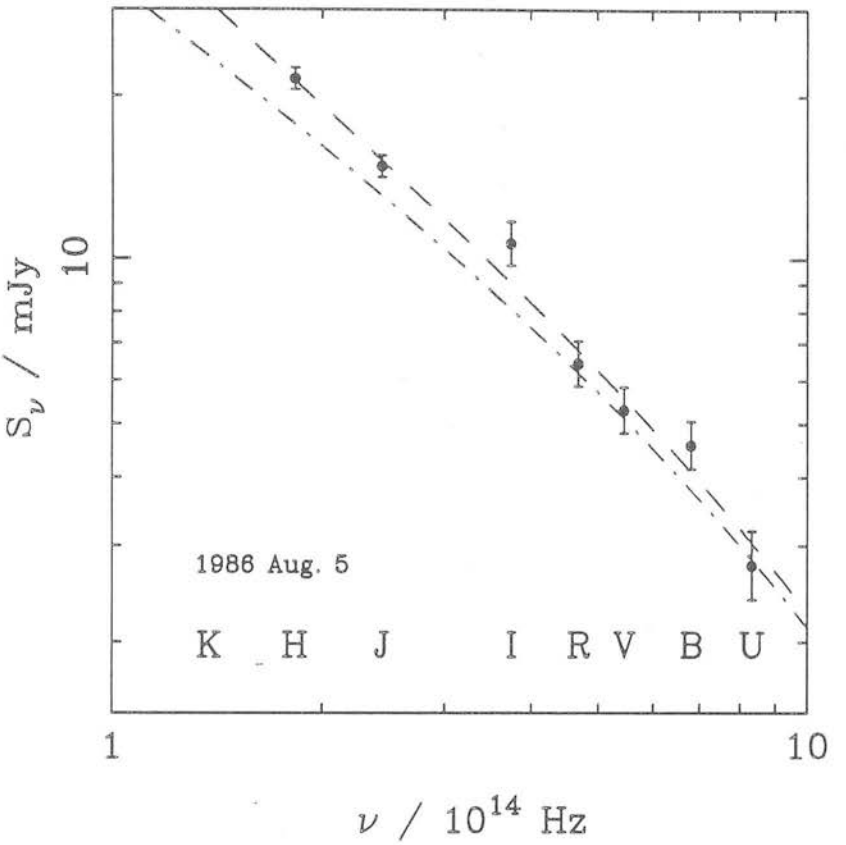

Fig. 11b

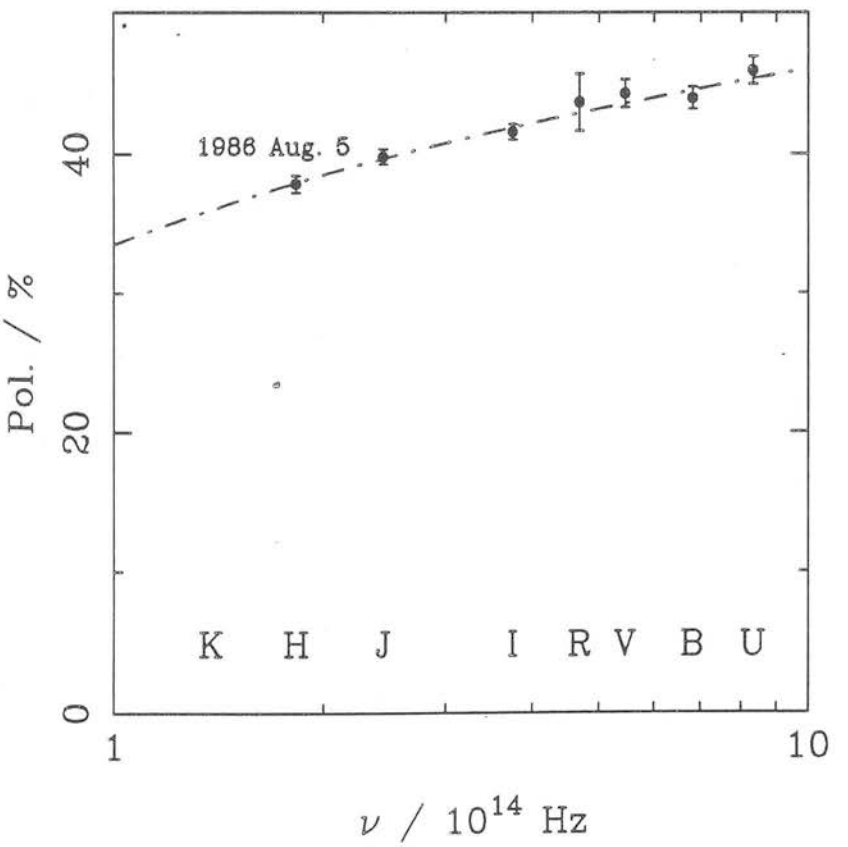

Fig. 12

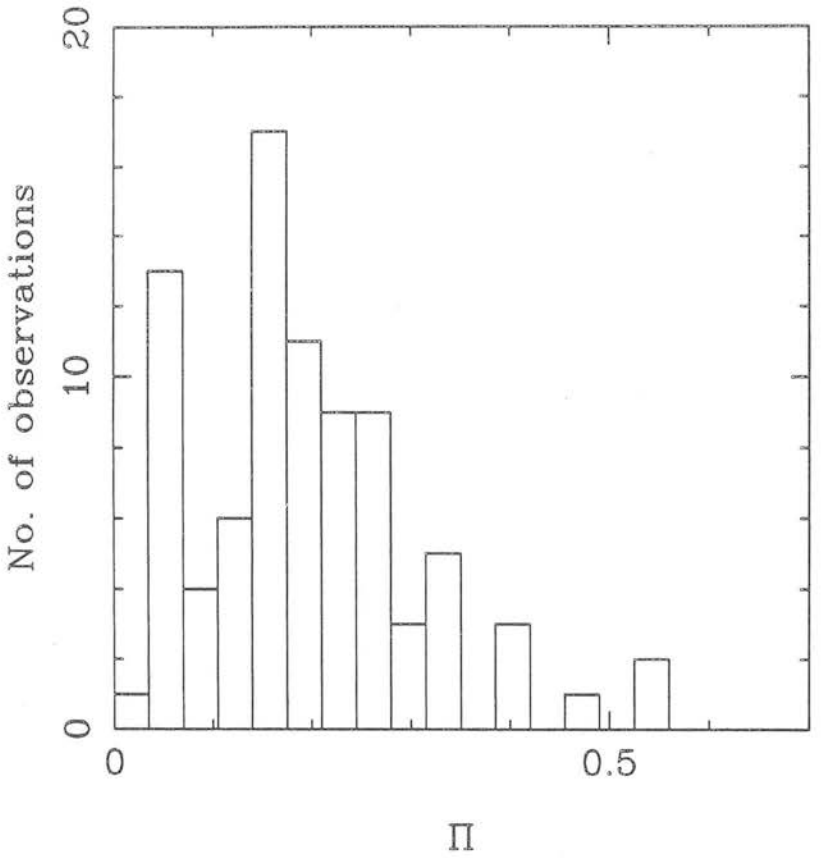

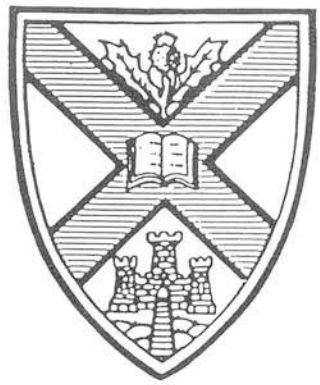

Edinburgh Astronomy Preprint

Number 29/89

December 1989

Relativistic particles in SS433

A.F. Heavens
K.R. Ballard
J.G. Kirk

University of Edinburgh Department of Astronomy
Royal Observatory, Blackford Hill, Edinburgh EH9 3HJ, Scotland
Telephone: 031-668 8100 Telex 72383

Accepted for publication
in *Monthly Notices of the Royal Astronomical Society*

Relativistic particles in SS433

A.F. Heavens and K.R. Ballard

Department of Astronomy, University of Edinburgh, Royal Observatory, Blackford Hill, Edinburgh EH9 3HJ

J.G. Kirk

Max-Planck Institut für Physik und Astrophysik, Garching, West Germany

SUMMARY

In this paper we put forward an explanation for the radio emission from the precessing jets of SS433 in terms of Fermi acceleration at shocks near the boundary of the jet material and the interstellar medium. Despite the mildly relativistic speed of the jets, we find that the spectral index is most naturally explained by particle acceleration at a non-relativistic shock. We find a consistent solution, which accounts also for the extent of the emission, provided that the density of the jet is $\gtrsim 2 \times 10^3$ times that of the ambient medium at $\sim 10^{15}$ m from the source, consistent with measurements deduced from X-ray and optical observations.

1 INTRODUCTION

SS433 has been the subject of considerable interest since its nature was revealed in 1979 (for reviews see, for example, Margon 1984, Zwitter *et al.* 1989). The optical line emission and the radio morphology are well explained by a kinematic model involving twin precessing jets (e.g. Abell & Margon 1979), which move at a speed $0.26c$ without significant deceleration.

The radio emission is characterised by a power-law flux density distribution $S_\nu \propto \nu^{-\alpha}$, with $\alpha \sim 0.6$, and a high degree of polarisation (Hjellming & Johnston 1981a).

The extended emission follows that expected from the kinematic model remarkably well (Hjellming & Johnston 1981b). It is the purpose of this paper to explain the spectrum and extent of this radio emission. Hjellming & Johnston (1988) have demonstrated that the extended emission cannot naturally be a result of relativistic electrons and magnetic field generated within the unresolved central region, since expansion losses reduce the emissivity very quickly. In order to maintain emission out to the observed $\sim$ 2 arcsec, Hjellming & Johnston postulated a period of 'slowed expansion', in which the jet does not expand freely. However, at distance greater than $\sim$ 2 from the centre, the model assumed the expansion to be free, in order to explain the observed turn-off of the radio emission. In an attempt to remove this arbitrariness we propose an alternative model in which electrons are accelerated at one of the pair of shocks near the boundary between jet material and the interstellar medium (for reviews of Fermi acceleration at shock waves, see, for example, Drury 1983 and Blandford & Eichler 1987). The shock propagating into the ambient medium has already been shown to provide a good explanation for the X-ray emission and optical emission in the inner parts of the jet (Begelman et al. 1980; hereafter BSHMA). The essence of our model is that, in the regions near the source of the jets, the shocks propagate into the jets and the ambient medium at speeds very much less than the speed of light, despite the jet speed itself being mildly relativistic. In this way, the model accounts naturally for the observed spectral index, which is close to $\alpha = 0.5$.

As the jets propagate outward along a conical surface, the angle of impact with the ambient medium increases (Section 2). For this reason, the shocks become more relativistic, and the acceleration process producing a power-law electron distribution is eventually quenched, most probably by the shock passing all the way through the jet. Additional mechanisms which may prevent particle acceleration beyond a certain point in the jet are Kelvin-Helmholtz instability of the contact discontinuity (although it is not clear whether this effect would prevent shock acceleration), and the shock becoming 'superluminal'. In this latter case, the points of intersection of magnetic field lines and the shock surface move faster than c, and particles cannot recross the shock many times, unless cross-field diffusion is efficient.

2 THE MODEL

We take as our starting point the kinematic model of Abell & Margon (1979). We assume the jets consist of fluid elements which are ejected from a central source on the surface of a cone with opening half-angle $\psi = 20°$ (Fig. 1). Each element moves outward from the centre at a constant velocity, with speed $v_j = 0.26c$.

The front surface which bounds the elements of the jet moves through the interstellar medium at an angle to the direction of flow $\beta(R)$ given by

$$\tan\beta(R) = \frac{2\pi R \sin\psi}{P v_j} \tag{1}$$

where R is the distance from the source. Thus close to the source the surface is highly oblique with respect to the fluid velocity, becoming more perpendicular further out. This behaviour is clearly visible in Fig. 1.

If the medium and the jets are sufficiently cold, then a pair of shocks will propagate away from the bounding surface, with the outer shock establishing itself as a bow shock (Fig. 2). Detailed calculations (BSHMA) show that the emission from the shocked ambient medium accounts well for the X-ray observations, and the subsequent photoexcitation of the jet material gives rise to the optical emission. The densities derived in this model at a distance $\sim 10^{13}$ m from the source are $\sim 10^{14}\mathrm{m}^{-3}$ for the ambient medium, and $\sim 10^{17}\mathrm{m}^{-3}$ for the emitting parts of the jet. The shock propagating into the jet is also suitable for exciting optical emission, but less efficiently, since the photoexcitation of an atom may be repeated many times. Letting the jet and external densities be ρ_j and ρ_e respectively, and assuming both media have a ratio of specific heats $\frac{5}{3}$, the speed of the shock propagating into the jet will have a component normal to the surface of

$$v_{shock} = \mu v_j \Delta \sin\beta \tag{2}$$

at its fastest point. For simplicity we assume that the shocks are strong and planar and $\Delta \equiv (\rho_e/\rho_j)^{1/2}$ measures the density ratio.

Matching pressures at the stagnation point gives $\mu^{-1} = 1 + \frac{3}{4}\Delta$. This result for the shock speed holds strictly only for plane shocks. We shall assume it to be accurate to within an order of magnitude for the more realistic case in which the jet surface is curved, and the shocked interstellar medium flows around it, rather like the flow of gas around a solid object (Rusanov 1976). Any uncertainty in the actual value of the shock speed will be embodied in the parameter μ, which we assume to be of order unity. The shock speed will be very much less than c close to the source, since for $R \ll \lambda \equiv Pv_j$, we have $v_{shock}/c \simeq 0.56\mu\, R\,\Delta/\lambda$. The quantity $\lambda = 1.1 \times 10^{15}$ m or 1.35 arcsec is the wavelength of the features in Fig. 1.

Thus the standard result of diffusive shock acceleration (see e.g., Drury 1983) that $\alpha \simeq 0.5$ should apply in the inner regions. Sufficiently far in, the shocks may not be strong (depending on the density ratio), owing to the heating from the X-ray gas. Thus some localised steep-spectrum emission ($\alpha > 0.5$) would not be in conflict with the model. In general the magnetic field will not be along the shock normal, and the spectral index will depend on the orientation of the field (Kirk & Heavens 1989). These authors find that significant flattening of the spectrum occurs if the speed of the shock in the de Hoffman-Teller frame (in which the magnetic field is parallel to the flow: de Hoffman & Teller 1950) exceeds about $0.1c$. Hence we would expect flatter spectra for $R/\lambda \gtrsim 0.1\,\Delta^{-1}$. If the jet density is high, this would be very hard to detect, because the emissivity decays quickly away from the source.

We do not expect the bow shock to be effective in accelerating electrons. On passing through this shock, interstellar material is deflected away from the approaching jet. Those particles which would undergo Fermi acceleration tend, as a result, to be swept along the bow shock, towards the region where it is highly oblique and weak. Eventually, after the jet has passed by, the bow shock fades away. Fermi acceleration is a diffusive process and has, as a result, a relatively long timescale, which we expect to be greater than the time during which interstellar material is close to the strong part of the bow shock. Support for this view is also provided by observations: if the bow shock were responsible for particle acceleration, the emission should not be confined to the immediate vicinity of the jet, but should come from all interstellar material which has been shocked. This would obscure

the excellent agreement between the jet kinematics and the observed emission (Fig. 1). Furthermore, a flat spectrum ($\alpha \lesssim 0.2$) would be expected much closer to the centre, at a radius $R \sim 0.2\,\lambda \sim 0.2$ arcsec, because of the relativistic effects mentioned above. This is ruled out by the observed value of $\alpha \simeq 0.5$.

3 QUENCHING OF THE PARTICLE ACCELERATION

We now turn to the question of the extent of the observed radio emission. Fermi acceleration cannot accelerate electrons to a power-law at arbitrary distances from the source, as at least three effects become important. These are (i) the shock becomes 'superluminal', (ii) the shock passes all the way through the jet, and (iii) the contact discontinuity between jet and external medium becomes unstable to the Kelvin-Helmholtz instability. We consider each of these in turn.

3.1 Superluminal shock

The Fermi acceleration process relies on particles being able to cross and recross the shock many times. Assuming that particles are not able to move easily between field lines, this means that if the point of intersection of the magnetic field line with the shock surface moves superluminally, repeated crossings cannot occur. Although the particles may undergo significant acceleration in this case (Begelman & Kirk 1990), they do not perform the multiple shock crossings required to accelerate the distribution to a power law. We can estimate at what distance the shock should become 'superluminal' in this sense, by noting that, since the fluid elements are assumed to expand freely, the component of magnetic field perpendicular to the direction of motion may be expected to become progressively more dominant, via the simple flux conservation arguments which are often applied to extragalactic jets (note that the result does not depend sensitively on this assumption). The condition for a marginally superluminal shock, $v_{shock}/\cos\beta = c$ (see, e.g., Kirk & Heavens 1989), is satisfied at a radius R_{sl} given by

$$R_{sl} = \frac{c\lambda}{2\pi \sin\psi \mu \Delta v_j} \simeq 1.8\,\mu^{-1}\,\Delta^{-1}\,\lambda \qquad (3)$$

Beyond this radius, it is unlikely that Fermi acceleration can operate, since particles cannot return to the shock once they have passed downstream. However, an alternative viewpoint is advanced by Jokipii (1982).

3.2 Shock passage through jet

We estimate the distance from the centre at which the shock will have passed through the jet by assuming that material is ejected from a precessing nozzle. If the opening angle of the nozzle is ϑ, the thickness of the jet in the radial direction is $L = \vartheta\lambda/2\pi\sin\psi$. In common with Hjellming & Johnston (1988), we estimate the opening angle from the width of the optical spectral lines to be $\vartheta \lesssim 0.1$.

The speed of the shock surface along the radial direction is $v_{shock}/\sin\beta$, so we must solve $L = \int_0^{t_c}(v_{shock}/\sin\beta)\,dt$ for the time, t_c, at which the shock passes through the jet. This requires a knowledge of the density in the jet and in the ambient medium as functions of distance from the centre. Assuming the jet expands freely (valid in the unshocked part of the jet), $\rho_j \propto R^{-2}$, and that the ambient density run is also a power-law, $\rho_e \propto R^{-a}$, we find, from (2), that the shock passage occurs at $R_c \equiv v_j t_c$, given by

$$R_c = \left[\frac{(4-a)L\lambda^{(1-a/2)}}{2\mu\Delta_\lambda}\right]^{\frac{2}{4-a}} \simeq \left[\frac{(4-a)\vartheta}{4\pi\sin\psi\mu\Delta_\lambda}\right]^{\frac{2}{4-a}}\lambda \qquad (4)$$

where $\Delta_\lambda \equiv (\rho_e/\rho_j)^{1/2}$ at $R = \lambda$. This is clearly a much tighter constraint than (3). To maintain particle acceleration out to the observed $R \sim 2\lambda$ requires $\rho_j/\rho_e \gtrsim 1.6 \times 10^3$, sensitive only to a factor of ~ 2 for a between 0 and 3.

3.3 Kelvin-Helmholtz instabilities

In this simple model, there is a contact discontinuity between the shocked jet material and the shocked interstellar medium. The fluids on either side of this surface have different tangential speeds, so there is the possibility that the Kelvin-Helmholtz instability may arise. We calculate at what radius this might occur, although whether this disrupts the

jet or not is an open question, as it will presumably depend on the nonlinear development of the instability.

Initially the shocks are extremely oblique, the tangential speeds at the contact discontinuity are highly supersonic, and the instability is suppressed, providing the magnetic field is not dynamically important (e.g. Begelman et al. 1984). As the jet progresses out, the speeds become subsonic with respect to the shocked flow, and the instability may arise. The relative transverse speed along the contact discontinuity on the jet side is $v_j \cos\beta$, and the sound speed in the shocked ambient medium is $c_s = \sqrt{5}\, v_{shock}/4$, where $v_{shock} \simeq \mu v_j \sin\beta$ from pressure balance at the stagnation point again. Hence the transverse flow becomes sonic with respect to the ambient medium at

$$R_{KH} = \frac{4\lambda}{\sqrt{5}\mu\, 2\pi \sin\psi} \tag{5}$$

For the parameters of SS433, $R_{KH} \sim \lambda$, in rough agreement with the extent of the observed emission. However, if the density ratio is large, the growth rate of the instability is small (Begelman, Blandford & Rees 1984), and it is not clear that it will affect the particle acceleration.

4 DISCUSSION

In this paper we have demonstrated that Fermi acceleration at shock waves can account for the spectrum and extent of the radio synchrotron emission from the precessing jets of SS433. Despite the mildly relativistic flow, we find that oblique non-relativistic shocks provide the most natural explanation of the radio emission observed. If the ambient density drops as a reasonable power-law with distance from the source, we find that the extent of the emission can be explained provided the jet density is $\gtrsim 2 \times 10^3$ times the ambient density. In this case, the maximum shock speed in the jet in the emission region is $\lesssim 2 \times 10^6$ m s^{-1}, so the radio spectral index is expected to be near 0.5 throughout. Assuming such a density ratio, Fig. 1 shows the points in the jet where two of the three processes discussed may lead to suppression of particle acceleration. The cross marks the

point at which the shock passes through the jet. The circle marks the point where the relative motion at the contact discontinuity becomes sonic with respect to the shocked interstellar medium. The point where the shock becomes 'superluminal' is not marked, as it lies well outside the emission region.

The results are not very sensitive to the density run of the external medium. For $\rho_e \propto R^{-a}$, the observations require a density ratio $\gtrsim$ a few $\times 10^3$ at a distance $\sim 2 \times 10^{15}$m (corresponding to the furthest extent of the radio emission), for any value of a between 0 and 3.

The main uncertainty in any comparison of the model with observation is the lack of knowledge of the jet uniformity in the outer parts. In the inner $\sim 10^{13}$m, the optical data suggest a clumpy medium (e.g. BSHMA, Kopylov *et al.* 1986), but information up to 10^{15}m from the source is lacking. We must therefore make assumptions in order to compare density determinations with those deduced from observation. The model does not depend crucially on the exact state of the jet, but the details change. For example, if the optical-emitting clouds persist to large distances, then the Fermi acceleration may take place either in the medium in which the clouds are embedded, (whose properties are unknown), or in the clouds themselves, by shocks driven by the high-pressure embedding medium. This process would rely on the long-term persistence of the clouds, which would depend on their uncertain size (see e.g. Zwitter *et al.* 1989). If the clouds are sufficiently small (dependent on the external density), they may evaporate, although the theoretical position is currently unresolved (see McKee 1988). The evaporating clouds would inject mass into the embedding jet material (cf. Hartquist *et al.* 1986). If the clouds evaporate completely, one can show that the shock speed through the embedding gas reduces to $\sqrt{4P_0/(3\rho)}$, where ρ is now the average density of the entire unshocked jet medium, and P_0 is the driving pressure. In this case, a lower limit to the density would come from including only the matter in the clouds themselves.

In another sense, comparison with determinations of density from observations is not easy, in view of the widely different states and locations of the emitting material, and the model-dependent nature of most determinations. Thus, for example, we do not make comparison with the model of Bodo *et al.*(1988), since they assume the X-ray emission

comes from the jet material; in our model, the jet shock is driven by the high pressure behind the bow shock, as proposed by BSHMA. The X-ray emission arises naturally from this hot matter. A possible upper limit for the external density at 10^{15} m comes from the absence of deceleration of the radio knots (Spencer 1984), which argues that $n_e \lesssim 10^4$ m^{-3}. However, it is not clear that the pressure in the radio knots is the dominant source of inertia. Faraday rotation and depolarisation (Zwitter *et al.* 1989 and references therein) give rather higher densities ($\sim 10^6$ m^{-3}). The *average* jet densities at 10^{13} m inferred from the optical emission are $\gtrsim 10^{14}$ m^{-3} (BSHMA), similar to the determination of $\sim 10^{13}$ m^{-3} by Kopylov *et al.* (1986), when the filling factors are taken into account. With an R^{-2} density dependence for the jet, the average jet density at 10^{15} m would be $\sim 10^9 - 10^{10}$ m^{-3}. Thus the rather uncertain determinations of the densities are at least consistent with the Fermi acceleration model presented here.

5 Acknowledgments

JGK thanks Professor M.C. Begelman for helpful discussions, and the SERC for support under a visiting fellowship scheme. KRB thanks SERC studentships for financial support.

REFERENCES

Abell, G.O., & Margon, B., 1979. *Nature*, 279, 701.
Begelman, M.C., & Kirk, J.G., 1990. *Astrophys. J.*, in press.
Begelman, M.C., Blandford, R.D., & Rees, M.J., 1984. *Rev. Mod. Phys.*, 56, 255.
Begelman, M.C., Sarazin, C.L., Hatchett, S.P., McKee, C.F., & Arons, J., 1980. *Astrophys. J.*, 238, 722 [BSHMA].
Blandford, R.D., & Eichler, D., 1987. *Phys. Rep.*, 154, 1.
Bodo, G., Ferrari, A., Massaglia, S., & Brinkmann, W., 1988. *Astrophys. Lett. and Communications*, 27, 5.
de Hoffman, F., & Teller, E., 1950. *Phys. Rev.*, 80, 692.
Drury, L.O'C., 1983. *Rep. Prog. Phys.*, 46, 973.
Hartquist, T.W., Dyson, J.E., Pettini, M., & Smith, L.J., 1986. *Mon. Not. R. astr. Soc.*, 221, 715.
Hjellming, R.M., & Johnston, K.J., 1981a. *Nature*, 290, 100.
Hjellming, R.M., & Johnston, K.J., 1981b. *Astrophys. J.*, 246, L141.
Hjellming, R.M., & Johnston, K.J., 1988. *Astrophys. J.*, 328, 600.
Jokipii, J.R., 1982. *Astrophys. J.*, 255, 716.
Kirk, J.G., & Heavens, A.F., 1989. *Mon. Not. R. astr. Soc.*, 239, 995.
Kopylov, I.M., Kumaigorodskaya, R.N., Somov, N.N., Somova, T.A. & Fabrika, S.N., 1986. *Sov. Astr.*, 30, 408.
Margon, B., 1984. *Ann. Rev. Astr. Astrophys.*, 22, 507.
McKee, C.F., 1988. In: *Supernova Remnants and the Interstellar Medium*, p.205, eds Roger, R.S. & Landecker, T.L., Cambridge University Press, Cambridge.
Rusanov, V.V., 1976. *Ann. Rev. Fluid Mech.*, 8, 377.
Zwitter, T., Calvani, M., Bodo, G., & Massaglia, S., 1989. *Fund. Cosm. Physics*, 13, 309.

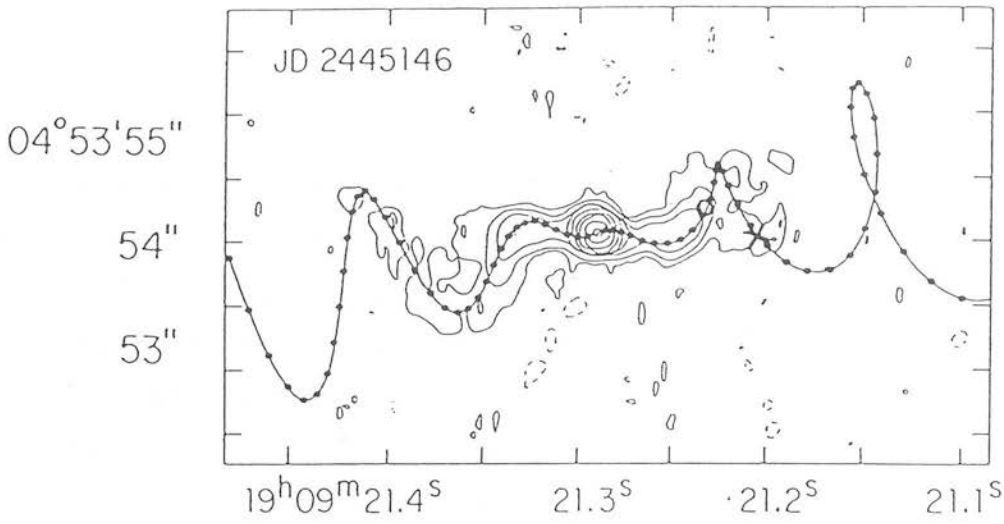

Fig. 1. The apparent position of the jets, according to the kinematic model of Abell & Margon (1979), superimposed on a high resolution 15 GHz radio map (R.M. Hjellming; reproduced with permission). The cone opening half-angle is $\psi = 20°$, and the precession period P is 164 days. The circle marks the point at which the Kelvin-Helmholtz instability may disrupt the contact surface between jet and ambient medium, and the cross marks where the shock passes through the jet. These both assume a jet/ambient medium density ratio of 2×10^3. The lack of sensitivity of these points to the assumed ambient density run is discussed in the Section 4.

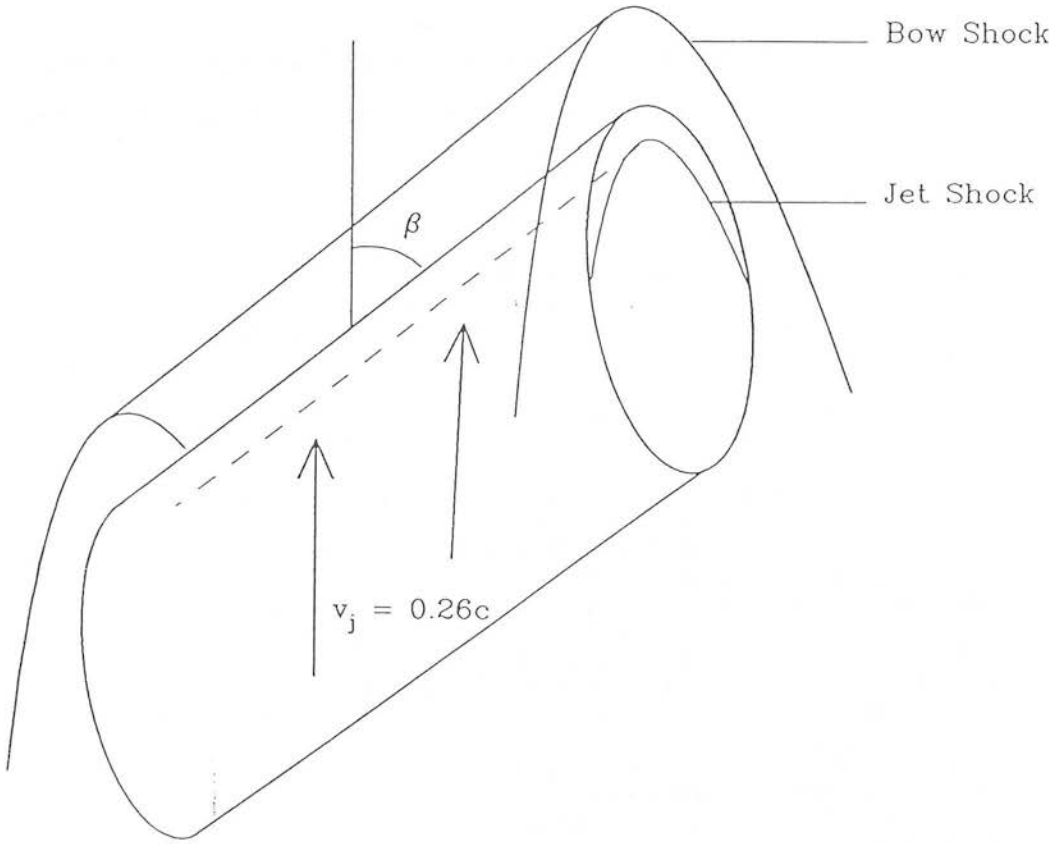

Fig. 2. A portion of the jet, showing the bow shock propagating into the ambient medium, and the jet shock, where particle acceleration is probably occuring.

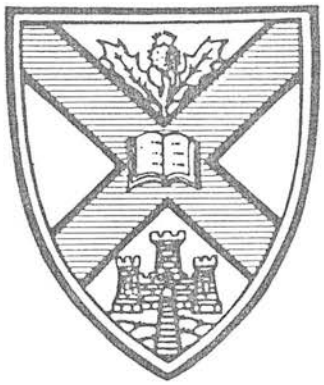

Edinburgh Astronomy Preprint

Number 7/91

April 1991

First order Fermi acceleration at oblique relativistic magnetohydrodynamic shocks

K.R. Ballard
A.F. Heavens

University of Edinburgh Department of Astronomy
Royal Observatory, Blackford Hill, Edinburgh EH9 3HJ, Scotland
Telephone: 031-668 8100 Telex 72383

Accepted for publication
in *Monthly Notices of the Royal Astronomical Society*

First order Fermi acceleration at oblique relativistic magnetohydrodynamic shocks

K.R. Ballard and A.F. Heavens

Department of Astronomy, Edinburgh University, Scotland, EH9 3HJ

SUMMARY:– In this paper we investigate first order Fermi acceleration at oblique relativistic magnetohydrodynamic (MHD) shock fronts. The jump conditions at the shock are solved using a full relativistic equation of state and allowing for various possible downstream conditions. Having obtained solutions to the jump conditions, the spectral indices of electrons accelerated by the shock front through the first order Fermi mechanism are obtained by employing two methods: a Monte Carlo simulation and the semi-analytic theory of Kirk & Heavens. Good agreement is found for the case where irregularities in the magnetic field are assumed to be small. We find that synchrotron spectral indices in the range of 0 to 0.5 are expected for oblique relativistic MHD shocks, unless the Alfvén Mach number is not much greater than unity.

1 INTRODUCTION

The theory of first order Fermi acceleration was developed initially for non-relativistic shocks with dynamically unimportant magnetic fields (Krymsky 1977; Axford, Leer & Skadron 1977; Bell 1978; Blandford & Ostriker 1978). Electrons are accelerated to high energies through scattering off magnetic irregularities on either side of a collisionless shock and, in this simple case, produce a power-law spectrum. The spectral index of the electrons then depends only on the compression ratio of the shock. The shock acceleration problem has been generalised in a number of ways, to include the back-reaction of the pressure of the accelerated particles (e.g. Drury & Völk 1981; Heavens 1984; Achterberg, Blandford & Periwal 1984) and also to relativistic shocks (Kirk & Schneider 1987a, 1987b; Heavens & Drury 1988). Usually the magnetic field is assumed to be dynamically unimportant and parallel to the shock normal, and indeed for non-relativistic shocks the magnetic field angle does not change the spectral index (Bell 1978; Drury 1983; Ostrowski 1988). However, for shocks which are even mildly relativistic, the angle which the field makes with the shock is important in determining the spectral index, the spectrum becoming harder as the

magnetic field moves away from the shock normal (Kirk & Heavens 1989; hereafter KH). In this paper we generalise still further, and investigate the effect of a dynamically important magnetic field in relativistic shock acceleration. This influences the compression ratio at the shock and thus the spectral index of the accelerated electrons. We restrict ourselves to the test-particle limit where the pressure of the accelerated particles is assumed to be negligible.

The steps involved in solving the shock acceleration problem are as follows: first, the shock structure is determined. Second, the accelerated particle distribution is obtained, either by solving the scattering equations semi-analytically, or by performing Monte Carlo simulations of the scattering and transport of the particles. The first part of the problem is completely specified by the conditions upstream of the shock front, plus assumptions about the thermodynamic state of the shocked gas. The second part of the problem is solved semi-analytically in the same way as KH, and numerically by a generalisation of the methods of Kirk & Schneider (1987b), accounting for the possibility of reflection from an oblique shock. The semi-analytic method has certain approximations in order to make the problem tractable: cross-field wandering of the electrons is neglected, assuming all particles are tied to the magnetic field lines; particles are then only scattered in pitch angle. In addition the magnetic moment is assumed to be conserved during an encounter with the shock. Without cross-field wandering, multiple shock crossing is only possible for 'subluminal' shocks where the shock front intersects the magnetic field lines at a speed less than the speed of light. Although acceleration is possible at superluminal shocks (Begelman & Kirk 1990), a power law is not a natural consequence, as it is for subluminal shocks. In this paper we shall consider only subluminal shocks. In this case it is always possible to transform to a frame where the material moves along the magnetic lines (de Hoffmann & Teller, 1950; hereafter deHT). Previous studies of oblique relativistic MHD shocks (Webb, Zank & Mackenzie 1987; Appl & Camenzind 1988) have worked in the shock frame where the fluid moves parallel to the shock normal and where there exists an electric field ($\mathbf{u} \wedge \mathbf{B} \neq 0$) which must be included in the expressions for the jump conditions. This leads to seventh-order polynomials to be solved. The method used here, transforming to the deHT frame, is considerably simpler, but is only applicable to subluminal shocks. We are concerned primarily with collisionless shocks, and so downstream of the shock the assumption of full local thermal equilibrium between the ions and electrons is not necessarily valid; in addition to this possibility it may be that full pressure is provided purely by the ions, or the electrons or indeed electron/positron pairs in the case where this is the composition of the fluid.

The layout of the remainder of this paper is as follows. In Section 2 the equation of state of the gas is considered. In Section 3 the jump conditions of the shock are calculated. Section 4 discusses the results in terms of the compression ratio and in Section 5 the spectral indices of the accelerated electrons are obtained.

The rationalized MKS system is used for electromagnetic quantities, but, for convienience, we have set the Boltzmann constant $k_B = 1$ and the speed of light $c = 1$.

2 EQUATION OF STATE

The jump conditions which will be derived in Section 3 must be accompanied by an equation of state to describe the gas. We assume that the fluid behaves according to the Synge equation of state (Synge 1957) i.e. that of a classical ideal gas composed of fully ionized hydrogen and electrons plus any electron/positron pairs produced downstream of the shock front. Summing over the different species (subscript i) we can express the pressure, energy density (including rest mass) and mass density in terms of the number density n_i, the particle rest mass m_i and temperature T_i as

$$P = \sum_i n_i T_i \tag{1}$$

$$e = \sum_i m_i n_i R(m_i/T_i) \tag{2}$$

$$\rho = \sum_i m_i n_i \tag{3}$$

These quantities are defined in the respective fluid rest frames. In SI units m/T is equivalent to $mc^2/k_B T$. $R(z)$ is defined in terms of the modified Bessel functions of order n, $K_n(z)$:

$$R(z) = \frac{3}{z} + \frac{K_1(z)}{K_2(z)} \tag{4}$$

The enthalpy is then defined as

$$w = e + P \tag{5}$$

and setting the specific enthalpy $\overline{w} = w/\rho$ etc,

$$\begin{aligned} \overline{w} &= \overline{e} + \overline{P} \\ &= \left(\sum_i m_i n_i R\left(\frac{m_i}{T_i}\right) + \sum_i n_i T_i\right) / \left(\sum_i m_i n_i\right) \end{aligned} \tag{6}$$

We now set $n_e = n_i \equiv n$, assuming overall electrical neutrality. Since we cannot be certain that the species in the downstream gas will reach thermal equilibrium, we consider three cases for the thermal state of the shocked gas.

Case 1: thermal equilibrium between electrons and ions, at temperature $T = T_e = T_i$. The temperature and enthalpy can then be written:

$$T = \frac{(m_p + m_e)}{2}\overline{P} \tag{7}$$

$$\overline{w} = \frac{m_e R\left(\frac{m_e}{T}\right) + m_p R\left(\frac{m_p}{T}\right) + 2T}{m_e + m_p} \tag{8}$$

For low temperatures the expressions for $\overline{w}$ reduce to the asymptotic expansions of $R(z)$, $z \to \infty$, $R(z) \to 1 + 3/2z$ and we obtain the non-relativistic equation of state:

$$e_i \to n_i m_i + \frac{3P_i}{2} \tag{9}$$

For high temperatures $z \to 0$ and $R(z) \to 1 + 3/z$ and $e_i \to 3P_i$, the ultra-relativistic equation of state.

Case 2. Ion pressure only. Here the electrons are unaffected by the shock and the only rôle they play is to ensure charge neutrality. This case also essentially describes a shock through an electron-positron plasma apart from corrections of order m_e/m_p and a rescaling of the temperature. In this case,

$$T = (m_p + m_e)\overline{P} \tag{10}$$

$$\overline{w} = \frac{m_e + m_p R\left(\frac{m_p}{T}\right) + T}{m_e + m_p} \tag{11}$$

Case 3. Electron pressure only.

$$T = (m_p + m_e)\overline{P} \tag{12}$$

$$\overline{w} = \frac{m_p + m_e R\left(\frac{m_e}{T}\right) + T}{m_e + m_p} \tag{13}$$

3 THE JUMP CONDITIONS

At first consider the situation as seen from the rest frame of the upstream fluid. Without loss of generality we assume that the shock front lies in the yz plane and the magnetic

field in the xy plane. In order to derive a simple set of jump conditions we now transform from this upstream frame to a frame of reference where the magnetic field lies along the streamlines. Assuming infinite conductivity the electric field vanishes in this frame, since $\mathbf{u} \wedge \mathbf{B} = \mathbf{0}$. The transformation involves a boost along the magnetic field direction of speed $\beta = \beta_s / \cos\theta$; note that β will refer to a speed throughout and we have set $c = 1$. β_s is the speed of the shock with respect to the upstream plasma and θ is the angle between the field and direction of the shock velocity. The two-dimensional Lorentz transformation from the upstream frame to the deHT frame (see Fig. 1) is given by:

$$L_{\alpha\beta} = \begin{pmatrix} \gamma & \gamma\beta_s & \gamma\beta_s \tan\theta & 0 \\ \gamma\beta_s & 1 + \frac{(\gamma-1)\beta_s^2}{\beta^2} & \frac{(\gamma-1)\beta_s^2 \tan\theta}{\beta^2} & 0 \\ \gamma\beta_s \tan\theta & \frac{(\gamma-1)\beta_s^2 \tan\theta}{\beta^2} & 1 + \frac{(\gamma-1)\beta_s^2}{\beta^2} & 0 \\ 0 & 0 & 0 & 1 \end{pmatrix} \tag{14}$$

(see Jackson 1975, p541), $\gamma = (1 - \beta^2)^{-1/2}$. Such a transformation can only be made if $\beta_s < \cos\theta$, the condition for a subluminal shock. This brings us into the deHT frame. Here the direction and magnitude of the magnetic field remain unchanged and the shock front is stationary but no longer lies in the yz plane. The rotation of the shock face can be obtained by transforming the position of shock face in the upstream frame using the above Lorentz transform. The shock is rotated through an angle α, given by:

$$\tan\alpha = \frac{\gamma\beta_s^2 \tan^4\theta + \beta_s^2 \tan^2\theta - (1 - \beta_s^2)(1 + \gamma \tan^2\theta)}{(\gamma - 1)\beta_s^2 \tan^3\theta - (\gamma - 1)(1 - \beta_s^2)\tan\theta} \tag{15}$$

The fluid velocities in the deHT frame are then:

$$\beta_{1x} = \beta_s \cos\alpha \sec\theta \tag{16}$$

$$\beta_{1y} = \beta_s \sin\alpha \sec\theta \tag{17}$$

Next, the jump conditions are obtained from the conservation equations (Licnerowicz 1967):

$$\nabla_\mu(\rho u^\mu) = 0 \tag{18}$$

$$\nabla_\mu(B^\mu u^\nu - u^\mu B^\nu) = 0 \tag{19}$$

$$\nabla_\mu(T^{\mu\nu}) = 0 \tag{20}$$

where Greek indices run from $0 - 3$ and $T^{\mu\nu}$ is the stress–energy tensor including electromagnetic terms, given by:

$$T^{\mu\nu} = (e+P)u^\mu u^\nu + Pg^{\mu\nu} + \frac{1}{\mu_0}(F^{\mu\lambda}F^\nu_\lambda - \frac{1}{4}g^{\mu\nu}F^{\lambda\sigma}F_{\lambda\sigma}) \tag{21}$$

(e.g. Ardavan 1976), where e is the energy density (including rest mass energy), P is the plasma pressure, u_ν is the four-velocity, $g^{\mu\nu}$ is the metric tensor and $F_{\mu\nu}$ is the covariant electromagnetic field tensor. In a Cartesian system,

$$F_{\mu\nu} = \begin{pmatrix} 0 & -B_z & B_y & -E_x \\ B_z & 0 & -B_x & -E_y \\ -B_y & B_x & 0 & -E_z \\ E_x & E_y & E_z & 0. \end{pmatrix} \tag{22}$$

Note that the components of the electric field E_i can be set to zero because $\mathbf{u} \wedge \mathbf{B} = \mathbf{0}$. We can now write the jump equations as given by deHT. Conservation of mass gives

$$\rho_1\beta_{1x}\gamma_1 = \rho_2\beta_{2x}\gamma_2 \tag{23}$$

where $\gamma_i = (1-\beta_i^2)^{-1/2}$. From the stress–energy tensor, conservation of momentum parallel and perpendicular to the shock normal and conservation of energy gives:

$$w_1\beta_{1x}\gamma_1^2 = w_2\beta_{2x}\gamma_2^2 \tag{24}$$

$$w_1\beta_{1x}^2\gamma_1^2 + P_1 + \frac{B_{1y}^2}{2\mu_0} = w_2\beta_{2x}^2\gamma_2^2 + P_2 + \frac{B_{2y}^2}{2\mu_0} \tag{25}$$

$$w_1 + \beta_{1x}\beta_{1y}\gamma_1^2 - \frac{B_{1x}B_{1y}}{\mu_0} = w_2 + \beta_{2x}\beta_{2y}\gamma_2^2 - \frac{B_{2x}B_{2y}}{\mu_0} \tag{26}$$

In the deHT frame the fluid flows along the magnetic field on both sides of the shock. Hence:

$$\frac{B_{1x}}{B_{1y}} = \frac{\beta_{1x}}{\beta_{1y}} \tag{27}$$

$$\frac{B_{2x}}{B_{2y}} = \frac{\beta_{2x}}{\beta_{2y}} \tag{28}$$

Finally, from $\nabla \cdot \mathbf{B} = 0$:

$$B_{1x} = B_{2x} \equiv B_x \tag{29}$$

We then substitute equations (27–29) into (24–26) and divide throughout by equation (23), setting $\overline{B_x^2} = B_x^2/\rho$, $\overline{w_1} = w_1/\rho$ etc. Defining the following constants:

$$A = \overline{w_1}\gamma_1 \tag{30}$$

$$C = \frac{\overline{B_x^2}}{\mu_0 \gamma_1 \beta_{1x}} \tag{31}$$

One obtains an expression for β_{2y}:

$$\beta_{2y} = \frac{\beta_{2x}\beta_{1y}}{\beta_{1x}} \left(\frac{A\beta_{1x} - C}{A\beta_{2x} - C} \right). \tag{32}$$

We thus obtain the following equations:

$$A\beta_{1x} + \frac{\overline{P_1}}{\gamma_1 \beta_{1x}} + \frac{C\beta_{1y}^2}{2\beta_{1x}^2} = A\beta_{2x} + \frac{\overline{P_2}\,\overline{w_2}}{A\beta_{2x}} + \frac{C}{2}\left(\frac{\beta_{1y}}{\beta_{1x}}\right)^2 \left(\frac{A\beta_{1x} - C}{A\beta_{2x} - C} \right)^2 \tag{33}$$

$$A = \overline{w_2}(1 - \beta_{2x}^2 - \beta_{2y}^2)^{-1/2} \tag{34}$$

These are the two simple simultaneous equations which express the results so far, the solutions to the jump conditions at a relativistic oblique shock. The two unknowns are essentially β_{2x} and $\overline{P_2}$. β_{2y} is estimated from (34), using (32) and $\overline{w_2}$ is a function of $\overline{P_2}$ which depends on the thermodynamic state of the downstream gas via equations (7,8), (10,11) or (12,13) for the three cases considered. In practice these were solved numerically for each set of given upstream conditions. The starting point was to take the shock speed, angle θ, between the magnetic field and shock normal, (relativistic) Alfvén Mach number, the pressure and the composition as seen from the upstream frame, Fig. 1a. These were then transformed to the deHT frame using the two-dimensional Lorentz transformation, allowing for the rotation of the shock front that results from this transformation. After solution, the variables were transformed back to the shock frame and the compression ratio, pressure, and temperature obtained. The results are outlined below.

4 SOLUTIONS TO THE JUMP CONDITIONS

Throughout the following discussion we restrict attention to the fast magnetosonic solutions to the above equations. The results of solving the jump conditions in the purely hydrodynamical limit (see Kirk, 1987) are shown in Fig. 2, which plots the downstream fluid speed, the shock compression ratio, and downstream temperature as a function of the shock speed. We have considered only shocks into cold gas, $\overline{P_1} = 0$. The three cases illustrated correspond to full local thermodynamic equilibrium (solid line), ion pressure only (dashed line) and electron pressure only, where the ions are still present and contribute to

the mass density (dot–dashed line). As is clear from Fig. 2, in both the low- and high-velocity limits, where the equations of state are fully non-relativistic and ultra-relativistic respectively, there is no difference between the compression ratios as each case is described by essentially the same equation of state with adiabatic index equal to 5/3 or 4/3 in the respective limits. The difference between the three cases considered is most apparent at intermediate velocities. This is because the protons, with their larger mass, carry a large bulk kinetic energy, which, when thermalised in a shock with $\beta \geq 0.1$ leads to relativistic thermal velocities in the electrons. The ions are only relativistic for high shock velocities, as $\beta \rightarrow 1$. Hence, there can exist states with non-relativistic shock velocities, with relativistic electrons (an adiabatic index of 13/9, and a compression ratio $\simeq 5.5$; Synge 1957).

Throughout the remainder of this paper we will be concerned primarily with the Fermi shock acceleration mechanism. Therefore it is useful to define the following parameters, of use in calculating particle pitch angles. Firstly, the compression ratio as seen in the deHT frame,

$$r = \frac{\beta_{1x}}{\beta_{2x}} \tag{35}$$

and secondly, the ratio of the magnitudes of the upstream and downstream magnetic fields,

$$b = \frac{B_1}{B_2} = \frac{\beta_1}{r\beta_2} \tag{36}$$

Note, however, that it is no longer possible to write down a simple expression for b, as in equation (4) of KH; this is because the component of fluid velocity perpendicular to the shock normal, β_y, is no longer continuous at the shock.

In Figs 3–5 the effects of increasing the magnetic pressure are displayed for a series of differing angles between the magnetic field direction and the shock normal (as seen from the upstream frame). The figures have different assumed thermodynamic states downstream, as outlined in Section 2. Here we have plotted the compression ratio, r, against shock speed, the downstream fluid temperature, T_2 in degrees Kelvin as a function of shock speed, and finally, b as a function of shock speed for several cases, as labelled. Note that the curves do not extend to $\beta = 1$ as the shock becomes superluminal when $\beta > \cos\theta$. All these figures have Alfvén Mach number, $M_A \equiv \beta_s/(B^2/\rho\mu_0)^{1/2} = \sqrt{5}$.

As the magnetic field and θ become larger, the shock becomes weaker in the sense that the compression ratio decreases (Kundt & Krotscheck, 1980), although it is apparent

that the temperature is not greatly affected by these changes. As the field becomes more oblique at a given speed the compression ratio decreases; however the component of the field perpendicular to the shock normal increases and hence the field is boosted by an increased factor. The parameter b thus decreases with increasing shock obliquity. Having solved the jump conditions, particle acceleration may be studied. This is considered next.

5 PARTICLE ACCELERATION

The jump conditions at a relativistic oblique shock have been solved for a variety of possible downstream conditions and it has been shown that increasing the magnetic pressure can significantly reduce the compression ratio at the shock. This is of manifest relevance to the process of Fermi acceleration of particles at a shock front where the spectral index of the accelerated particles is a strong function of the compression ratio. We now turn attention to the process of acceleration of electrons at a shock front. In calculating spectral indices it will been assumed that the suprathermal component has no significant back reaction upon the shock (cf. Blandford 1980; Heavens 1983; Achterberg *et al.* 1984; Heavens 1984; Drury 1989 for negligible magnetic pressure and non–relativistic shocks). We obtain the energy spectrum of the accelerated particles by two methods: we use the semi-analytic calculations of KH, and also perform some Monte Carlo simulations of the scattering process, using techniques developed by Kirk & Schneider (1987b).

5.1 Semi-analytic theory

The theory of particle acceleration at a relativistic oblique shock front was developed by KH, in the case where the magnetic pressure was negligible. This paper uses exactly the same technique as KH, and the reader is referred to that paper for full details. The method is similar to that of Kirk & Schneider (1987a) in that the problem is solved by expanding the distribution function in terms of the eigenfunctions of the scattering operator. The principal difference is that, in the oblique case, particles incident on the shock surface from the upstream side may not penetrate more than a gyroradius or so into the downstream region, being essentially reflected from the shock front. For fields which are homogeneous either side of the shock front, magnetic moment conservation in the deHT frame is a good approximation (Terasawa 1979); it is also independent of the particle or shock speed and should therefore be valid even in the relativistic limit. The downstream pitch angle cosine

$\overline{\mu_s}$ of a particle is then related to its upstream value, μ_s by:

$$1 - \mu_s^2 = b(1 - \overline{\mu}_s^2) \tag{37}$$

In this approximation there is therefore a critical pitch angle cosine:

$$\mu_0 \equiv \sqrt{1 - b} \tag{38}$$

such that particles incident with $|\mu_s| < \mu_0$ cannot penetrate downstream, and are reflected by the shock front. Particles with $|\mu_s| > \mu_0$ are transmitted to the downstream side. Particles incident from downstream are always transmitted. The method assumes that electrons do not drift across magnetic field lines. The quantities that determine the spectrum are the shock speed, magnetic field angle and the compression ratio. The method solves the steady state transport equation (KH):

$$\gamma \cos\theta(u + v\mu)\frac{\partial f}{\partial x} = \frac{\partial}{\partial \mu}\left[D_{\mu\mu}(1 - \mu^2)\frac{\partial f}{\partial \mu}\right] \tag{39}$$

where v is the particle speed, taken in practice to be unity. We choose to describe the interactions via an isotropic pitch angle scattering operator $D_{\mu\mu}$. In the parallel case, the form of the diffusion coefficient can make small changes to the spectral index in the relativistic case (Heavens & Drury 1988; Kirk 1988). Use of a pitch angle diffusion equation is appropriate to describe scattering by small magnetic irregularities. The distribution function $f(p)$ is a power-law in momentum $f(p) \propto p^{-s}$ and the spectral index s is calculated by the method. The energy spectral index, $s - 2$ is shown in Figs 6–8 for the three thermodynamic cases under consideration, for a range of values of M_A^{-2}. Also shown are the synchrotron spectral indices, $\alpha = (s - 3)/2$. For values $M_A > 10$, the effect of the magnetic field strength is negligible.

5.2 Monte Carlo Simulations

We have chosen to check the semi-analytic theory of KH by performing some numerical simulations of the scattering and shock crossing. We do not follow particle orbits, but simulate the scattering process via a diffusion equation, following the method of Kirk & Schneider (1987b). Since we also make the same assumption of magnetic moment conservation at shock encounters the test of the theory is only partially independent.

The method simulates particle acceleration by following individual particles as they

cross and re–cross the shock front and then constructing the distribution function from the number of particles at a given momentum and pitch angle. Each particle starts off with an injected fixed momentum $p_0 \gg m_0 c$ and random pitch angle μ_0 and moves away from the shock into the upstream fluid. Its subsequent motion is then followed as it undergoes scattering in pitch angle until it either crosses the shock front or is lost; the latter can only occur if the particle is in the downstream region. The key to the method is to use mixed reference frames so that spatial coordinates are measured in the shock frame, but momentum and pitch angles are measured in the appropriate fluid frame. In an electromagnetic field the scattering is governed by the relativistic transport equation:

$$\hat{L}^{\mu}_{\nu}\hat{p}^{b}\frac{\partial F_0}{\partial x^{\mu}} + \frac{e}{m}\hat{\mathcal{F}}^{a}_{\lambda}\hat{p}^{\lambda}\frac{\partial F_0}{\partial \dot{p}^{a}} = \hat{p}^{0}\hat{C} \tag{40}$$

(e.g. Riffert 1986), where F_0 is the distribution function, $\hat{\mathcal{F}}^{a}_{\lambda}$ is the electromagnetic field tensor, p is the momentum , C is the collision term. Latin indices run from $1-3$. $\hat{L}^{\mu}_{\nu}$ is the Lorentz transformation from the fluid frame to the de Hoffmann–Teller frame, and terms measured in the fluid frame are marked with a circumflex. If we assume that the distribution function is independent of the gyrophase, ϕ, and define a phase-averaged distribution function f, then the transport equation reduces to (KH):

$$\gamma\cos\theta(u+v\mu)\frac{\partial f}{\partial x} = D_{\mu\mu}\frac{\partial}{\partial\mu}(1-\mu^2)\frac{\partial f}{\partial\mu} \tag{41}$$

where we have employed an isotropic pitch angle scattering operator as the simplest case so that $D_{\mu\mu}$ is a constant. To try to treat the problem fully we would have to follow the very large number of small pitch angle deflections that a particle undergoes each time it crosses the shock front. Instead we follow the lead of Kirk & Schneider (1987b) and note that in a time Δt the particle will travel a distance $\Delta s = c\Delta t$, Δt being measured in the fluid frame; this leads to a change in position in the shock frame

$$\Delta x = \gamma(u+\mu)\Delta t \tag{42}$$

and thus one can write the transport equation as

$$\frac{\cos\theta}{D_{\mu\mu}}\frac{\partial f}{\partial \Delta t} = \frac{\partial}{\partial\mu}(1-\mu^2)\frac{\partial f}{\partial\mu} \tag{43}$$

We now follow the propagation by making a rotation, where the pitch angle μ_0' is zero and introduce the azimuthal angle ϕ, whence equation (39) becomes:

$$\frac{\cos\theta}{D_{\mu\mu}}\frac{\partial f}{\partial \Delta t} = \left[\frac{\partial^2}{\partial \mu'^2} + \frac{\partial^2}{\partial \phi^2}\right] f \tag{44}$$

The probability distribution of the pitch angle after the scattering event is then given by the Green's function,

$$P(\mu', \phi' \mid \mu'_0 = 0, \phi'_0 = 0) = \frac{\cos\theta}{4\pi \Delta t D_{\mu\mu}} \exp\left[\frac{-(\mu'^2 + \phi'^2)\cos\theta}{4\pi \Delta t D_{\mu\mu}}\right] \tag{45}$$

and the new μ' and ϕ' are random values taken from this probability distribution. This is then transformed back to the fluid frame to find the new μ,

$$\mu = (1 - \mu'^2)^{-1/2}\mu_0 \cos\phi' + \mu'(1 - \mu_0'^2)^{-1/2} \tag{46}$$

Finally, note that we must set a downstream boundary (it is clear that all particles in the upstream region must return to the shock front). From KH we note that the spatial part of the distribution is separable and decays as $\exp(-\lambda_i x/\Gamma\cos\theta)$, so that at large x the distribution function decays to its isotropic value and there is little chance of a particle returning to the shock, rather it is more likely to be advected away. We choose the position of the downstream boundary as ($\lambda_0 = 0$)

$$d = \frac{10\Gamma}{D_{\mu\mu}\lambda_1} \tag{47}$$

From KH, $\lambda_1 = 6u\Gamma$. Thus, the method we adopt is as follows. A particle is injected with momentum p_0 and pitch angle μ_0. After a time Δt it will have travelled a distance Δx, given by equation (42). At this point it is scattered to a new μ, chosen as we have described. This procedure is repeated for the next Δt and continued until either:

1. The particle crosses the predetermined downstream boundary at which point it is regarded as having no chance of returning to cross the shock front and is 'lost'. It takes no further part in the simulation.

2. Or it returns to the shock front after a finite number of scattering events. Upon reaching the shock it is added to the distribution function at its present momentum and pitch angle (in the shock frame). What happens next depends upon the value of the pitch angle. We now assume that as a particle crosses the shock front its magnetic moment is conserved. Thus all particles incident from the downstream region pass into the upstream region with a new pitch angle – measured now in the upstream frame. On the other hand, in crossing from the upstream region, a particle may be reflected by the shock and returned to the upstream region. In this case the simulation

continues as before with a reflected pitch angle.

An important point to note is that we employ the technique of particle splitting when a particle returns to the shock (Kirk & Schneider 1987b). In order to achieve a high signal-to-noise ratio in the distribution function over a large enough range of momentum it is apparent that an impractically large number of particles, each with a finite escape probability, would have to be injected into the simulation at momentum p_0. To circumvent this problem we split any particle which reaches the shock. This creates a number, N_D of daughter particles with the parent's momentum and pitch angle. This process allows us to obtain enough high energy particles to achieve the desired accuracy in the simulations. Each of the daughter particles is assigned a weighting of $1/N_D$ and is then followed throughout the simulation until it is subsequently lost. In order to retain roughly constant numbers of particles throughout the simulation we choose the number of daughters to be an integer from a Poissonian distribution with mean $\overline{N_D} = p_{esc}/(1 - p_{esc})$ (p_{esc} is the escape probability, $\sim 4u_2$ in the parallel non-relativistic limit). The value of $\overline{N_D}$ does not affect the spectral index if the particles are weighted appropriately, but it does affect the efficiency of the simulation. The weight associated with each particle as it crosses the shock is w. The increment to the distribution function at p and μ is $w/\mid \mu_s \mid$. This is because the weight w refers to the flux of particles (i.e. w particles have crossed the shock front) whereas the purpose of the simulation is to obtain the distribution function, $f(p, \mu)$.

5.3 Particle distributions

The Monte Carlo method described above returns the distribution function in a series of pitch angle and momentum bins, and this can then be plotted as a function of either. Fig. 9 shows a non-relativistic result, obtained with $\beta_{1x} = 0.2, \beta_{2x} = 0.05, \beta_{iy} = 0.0$. Fig. 10 shows the distribution obtained for a shock with $\beta_{1x} = 0.4$, $r = 4$,and $\theta = 45°$. The spectral index is $s = 3.17$, in good agreement with the result of KH. However, as can be seen from the figures, the distributions are noisy as a consequence of employing a Monte Carlo method; a large amount of computer time is required to reduce the moise to a satisfactory level. Note that, apart from a small inaccuracy around $\mu = 0$, the pitch-angle distributions show good agreement with the semi-analytic distributions in KH. These particles are travelling almost parallel to the shock front, and do not affect the momentum distributions. From the momentum distributions the spectral indices of the electron distributions are obtained using a weighted least-squares method including the Poisson noise in the momentum bins.

The simulation is terminated after obtaining the desired accuracy in the spectral index. Results for comparison with the semi–analytic method are shown as triangles in Figs 6–8 where spectral indices are plotted as a function of the parallel shock speed for a series of differing magnetic field strengths. The error on the best straight line is plotted as an error bar. The agreement is clearly very good, but it must be stressed that only part of the KH theory is being tested. The numerical method simulates the scattering, but assumes magnetic moment conservation on encounters with the shock. The upper limit to the shock speed of $\beta_{1x} = 1/\sqrt{2}$ is a result of a fixed β_s, above which the shock becomes superluminal. Although it is outside the scope of this work, it is not without interest; Jokipii (1982) has shown that superluminal shocks can accelerate particles and Begelman & Kirk (1990) have shown that, even assuming the particles do not drift across field lines and thus cannot return to the shock after having travelled further than one gyroradius away from it, the adiabatic energy gain from the shock crossings may be up to a factor of 4γ per particle.

The results of these simulations show that for values of the Alfvén Mach number of $M_A^{-2} \sim 0.05$ or larger the compression ratio of the shock may be significantly altered. This weakening of the shock strength can lead in turn to steeper spectral indices, similar to the effects of upstream pressure in hydrodynamic shocks. As high spectral indices are associated with the higher magnetic fields, the synchrotron emissivities are also high ($\propto B^2$) and one might expect regions with these magnetic fields to dominate, particularly at lower frequencies. On the other hand synchrotron lifetimes also are proportional to B^{-2} so that the source evolves more rapidly.

It is notable that at low shock speeds there is a greater range of spectral indices than at higher speeds. This is probably a result of particles being reflected more often at higher shock speeds. At the highest speeds the compression ratio at the shock decreases as the equation of state becomes fully relativistic and as a consequence of this there is a slight increase in the spectral index observed. Note that it is assumed that electrons scatter in pitch angle by collision with resonant Alfvén waves moving much more slowly than the electrons upstream of the shock, and turbulence downstream. Although we have increased the Alfvén wave speed in these simulations, it is assumed that it will still be much less than the ultrarelativistic speeds at which the electrons are moving and thus we retain the Alfvén waves as scattering centres.

6 DISCUSSION

This paper calculates the spectral indices for synchrotron radiation from mildly relativistic oblique shocks where the magnetic field is dynamically important. We demonstrate that shocks whose speeds are not greatly in excess of the upstream Alfvén speed can produce synchrotron emission with steeper spectra than $\alpha \sim 0$ which KH obtained for shocks with negligible magnetic field. The natural sites for applying these results are in blazars and in the hotspots of radio galaxies. In the latter at least mildly relativistic shock speeds are suggested, and polarisation studies indicate (presumably post-shock) magnetic fields which are preferentially perpendicular to the shock normal (e.g. Flatters & Conway 1985; Scarrott & Rolph 1989).

The parameters which are required to determine the spectral indices of the accelerated electrons are the shock speed, Alfvén number and the magnetic field inclination angle. Unfortunately, none of these is easy to determine. Heavens & Meisenheimer (1987) showed how one can use the break frequency of a synchrotron source to estimate a combination of magnetic field strength and shock speed. This method has been applied to a number of sources (Meisenheimer & Heavens 1986; Meisenheimer *et al.* 1989). Meisenheimer *et al.* showed that in those cases where there is an optical counterpart to the radio source, spectral indices are around $\alpha \sim 0.5$ in agreement with the result of Bell (1978) for non-relativistic shocks. They also attempted to constrain the shock speed using the techniques of Heavens & Meisenheimer, deducing that they are mildly relativistic. Unfortunately, although the data are consistent with such shock speeds, the method only allows a combination of field and shock speeds to be determined, and they cannot be determined individually. The magnetic field may be estimated independently from minimum energy arguments, but the uncertainties mean that the shock speed cannot be usefully constrained by this method. If we fold in the uncertainties in the density of the jet (estimated from Faraday depolarisation), we are left in the unhappy position of being unable to estimate the Alfvén number with any degree of confidence. It is not even possible to argue that the shocks are strong, in the sense of being highly super-Alfvénic. This means that weak shocks, in this sense, may provide an explanation for the observed spectra being steeper than the strong shock values of KH. It certainly appears more plausible than appealing to conventional weak shocks, with ordinary Mach numbers not much greater than unity. Such shocks would also give steep spectra, but at the expense of requiring very high pre-shock temperatures $\gtrsim 10^8$ K for shock speeds in excess of $0.01c$.

The degree of steepening is rather modest for mildly relativistic shocks, becoming more substantial as the shock speed decreases. For magnetic field angles around 45° to the shock normal, spectral indices steeper than $\alpha = 1$ are possible if the shock speed is less than $0.1c$ and the Alfvén Mach number less than about 1.8. Such weak shocks have less effect at $0.5c$, giving $\alpha \sim 0.2$. Even allowing for a steepening by $\Delta\alpha = 0.5$ from ageing, we appear to require very weak shocks to account for the steepest spectra ($\alpha \sim 2.5 - 3.0$) seen in blazars (Ballard *et al.* 1990).

Although the range of spectral indices seen in hotspot spectra can in principle be obtained from weak magnetic shocks, it is not clear that this is the correct explanation. The homogeneous geometry of the upstream magnetic field assumed in this paper is almost certainly an unrealistic idealisation. If true, there should be sources whose magnetic field directions are too close to the shock plane for Fermi acceleration to take place, if the jet speeds are even mildly relativistic. An alternative assumption, which may be more realistic, is that the magnetic field in the upstream rest frame is disordered and random. Monte Carlo simulations of particle orbits in relativistic shocks (Ballard & Heavens, in preparation) show that Fermi acceleration does take place, and produces synchrotron spectral indices which are steeper than the homogeneous field calculations of KH. All of these processes indicate that variations in physical parameters such as shock speed, magnetic field strength, orientation and degree of ordering can lead to a spread of synchrotron spectral indices in accord with that observed. On the one hand this is progress, in that we may be able to explain the observations, but it is pessimistic in that we may be unable to use the observations to tie down firmly the physical parameters in the hotspots of radio galaxies.

ACKNOWLEDGEMENT

KRB received an SERC studentship.

REFERENCES

Achterberg, A., Blandford, R.D. & Periwal, V., 1984. *Astr. Astrophys.*, **132**, 97.

Ardavan, H., 1976. *Astrophys. J.*, **206**, 822.

Appl, S. & Camenzind, M., 1988. *Astr. Astrophys.*, **206**, 258.

Axford, W.I., Leer, E. & Skadron, G., 1977. *Proc. 15th Int. Cosmic Ray Conf.*,**11**, 132.

Ballard, K.R., Mead, A.R.G., Brand, P.W.J.L. & Hough, J.H., 1990. *Mon. Not. R. astr. Soc.*, **243**, 640.

Begelman, M.C. & Kirk, J.G., 1990. *Astrophys. J.*, **353**, 66.

Bell, A.R., 1978. *Mon. Not. R. astr. Soc.*, **182**, 147.

Blandford, R.D., 1980. *Astrophys. J.*, **238**, 410.

Blandford, R.D. & Ostriker, J.P., 1978. *Astrophys. J.*, **221**, L29.

de Hoffman, F. & Teller, E., 1950. *Phys. Rev.*, **80**, 692 (deHT).

Drury, L.O'C., 1983. *Rep. Prog. Phys.*, **46**, 973.

Drury, L.O'C., 1989. *Magnetic Fields and Extragalactic Objects.* Eds Asseo, E. & Grésillon, D. Editions de Physique.

Drury, L.O'C. & Völk, H.J., 1981. *Astrophys. J.*, **248**, 344.

Flatters, C. & Conway, R.G., 1985. *Nature*, **314**, 425.

Heavens, A.F., 1983. *Mon. Not. R. astr. Soc.*, **204**, 699.

Heavens, A.F., 1984. *Mon. Not. R. astr. Soc.*, **211**, 195.

Heavens, A.F. & Meisenheimer, K., 1987. *Mon. Not. R. astr. Soc.*, **225**, 335.

Heavens, A.F. & Drury, L.O'C., 1988. *Mon. Not. R. astr. Soc.*, **235**, 997.

Jackson, J.D., 1975. *Classical Electrodynamics.* John Wiley, New York.

Jokipii, J.R., 1982. *Astrophys. J.*, **255**, 716.

Kirk, J.G., 1988. Max–Planck Institut für Astrophysik preprint No. 345.

Kirk, J.G. & Schneider, P., 1987a. *Astrophys. J.*, **315**, 425.

Kirk, J.G. & Schneider, P., 1987b. *Astrophys. J.*, **322**, 256.

Kirk, J.G. & Heavens, A.F., 1989. *Mon. Not. R. astr. Soc.*, **239**, 995 (KH).

Krymsky, G.F., 1977. *Dok. Akad. Nauk. SSSR*, **234**, 1306.

Kundt, W. & Krotscheck, E., 1980. *Astr. Astrophys.*, **83**, 1.

Licnerowicz, A., 1967. *Relativistic Hydrodynamics and Magnetohydrodynamics*, Benjamin Press, New York.

Meisenheimer, K. & Heavens, A.F., 1986. *Nature*, **323**, 419.

Meisenheimer, K., Röser, H.-J., Hiltner, P.R., Yates, M.G., Longair, M.S., Chini, R. & Perley, R.A., 1989. *Astr. Astrophys.*, **219**, 63.

Ostrowski, M., 1988. *Mon. Not. R. astr. Soc.*, **233**, 257.

Riffert, H., 1986. *Astrophys. J.*, **310**, 729.

Scarrott, S.M. & Rolph, C.D., 1989. *Mon. Not. R. astr. Soc.*, **238**, 349.

Synge, J.L., 1957. *The Relativistic Gas*, North Holland.

Terasawa, T., 1979. *Planet. Space Sci.*, **27**, 193.

Webb, G.M., Zank, G.P. & Mackenzie, J.F., 1987. *J. Plasma Physics*, **37**, 117.

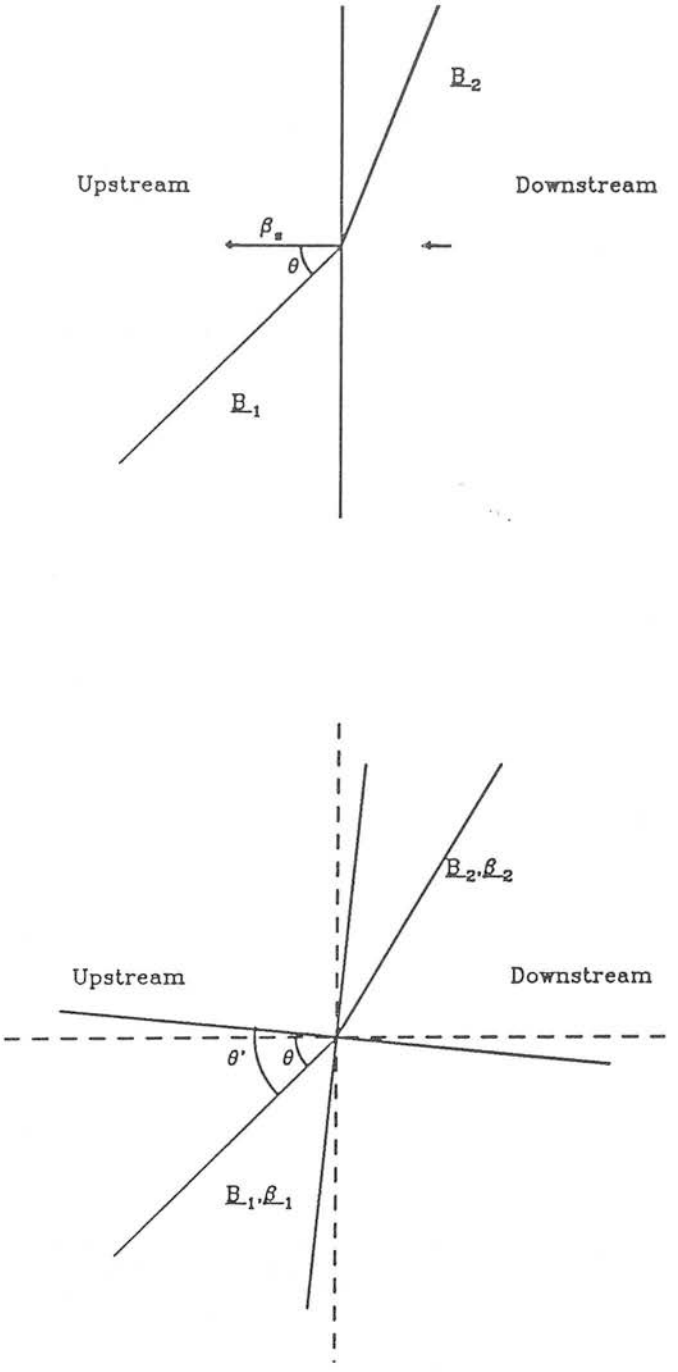

FIG 1: a) The upstream reference frame. b) The deHT frame, in which the electric field vanishes. Because the Lorentz boost is along the magnetic field direction, the shock plane is rotated.

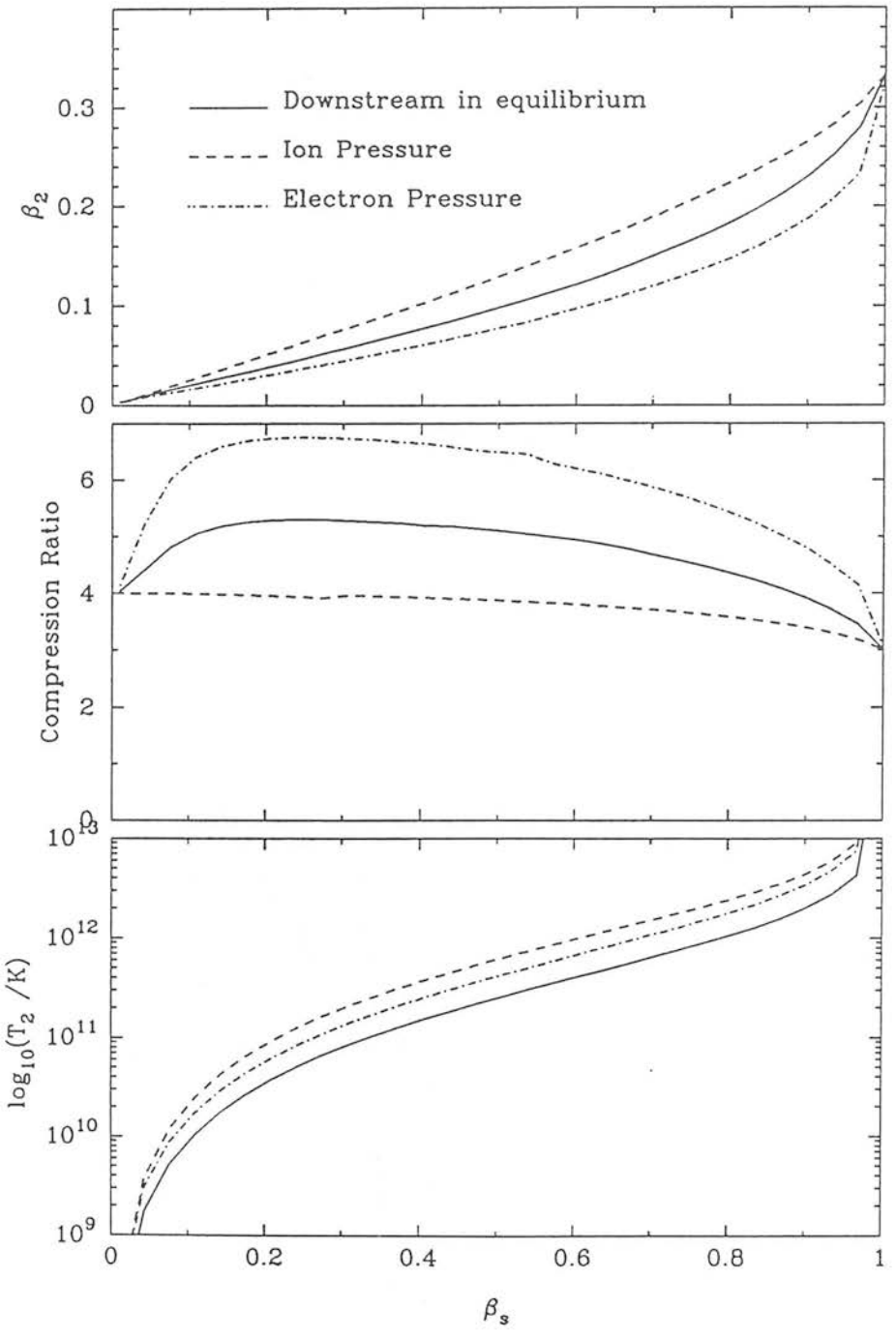

FIG 2: The solutions to the jump conditions at a relativistic strong shock in the hydrodynamic limit. The three cases of interest are with the downstream fluid in local thermodynamic equilibrium (solid line), ion pressure dominating (dashed line) and electron/positrons dominating (dot–dashed line).

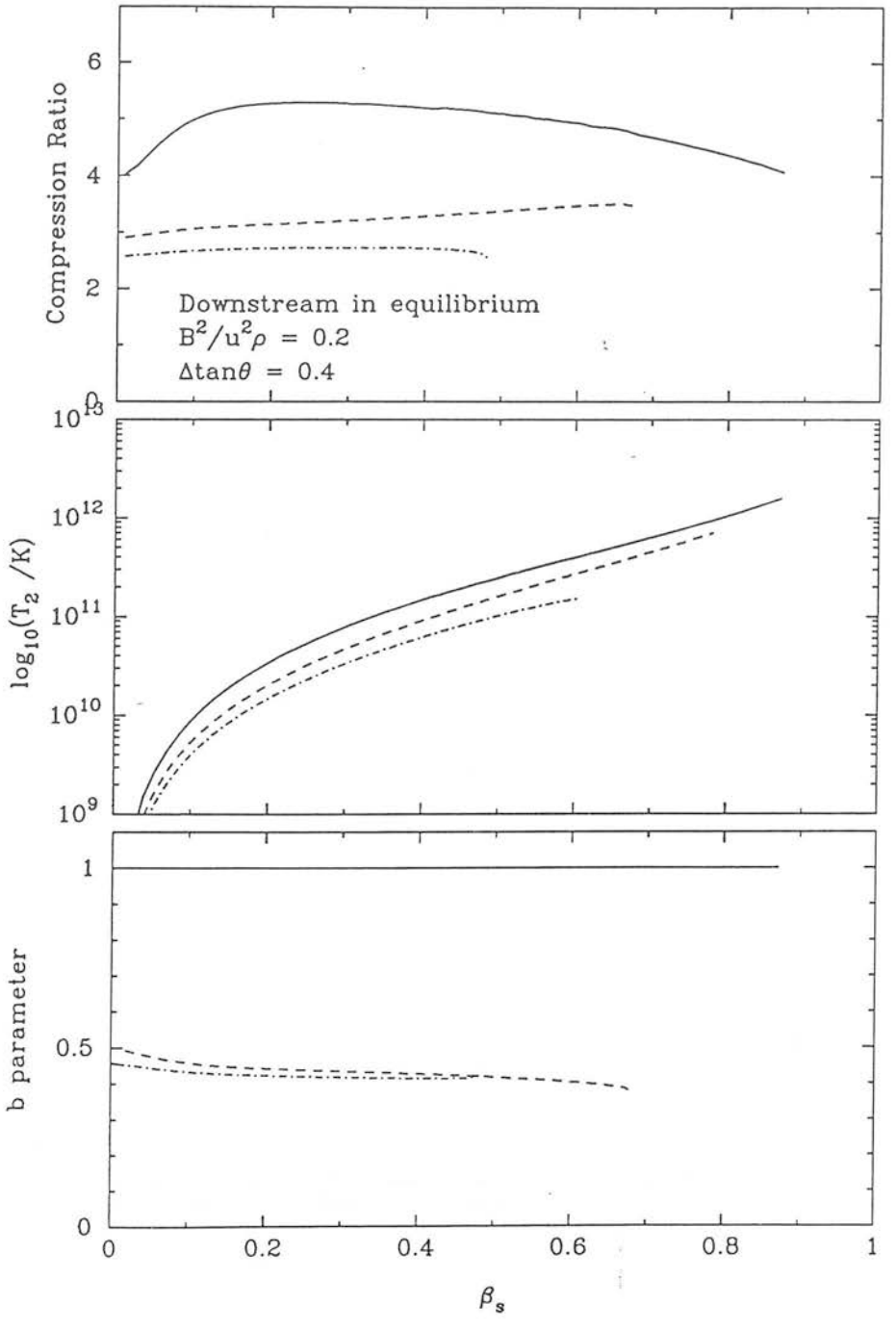

FIG 3: The solutions to the jump conditions as a function of shock speed with a dynamically important magnetic field. The downstream fluid is in equilibrium between electrons and ions. The three curves plotted correspond to $\tan\theta = 0.0, 0.4, 0.8$. As $\tan\theta$ increases the compression ratio decreases. Also shown are the downstream temperatures and b parameter.

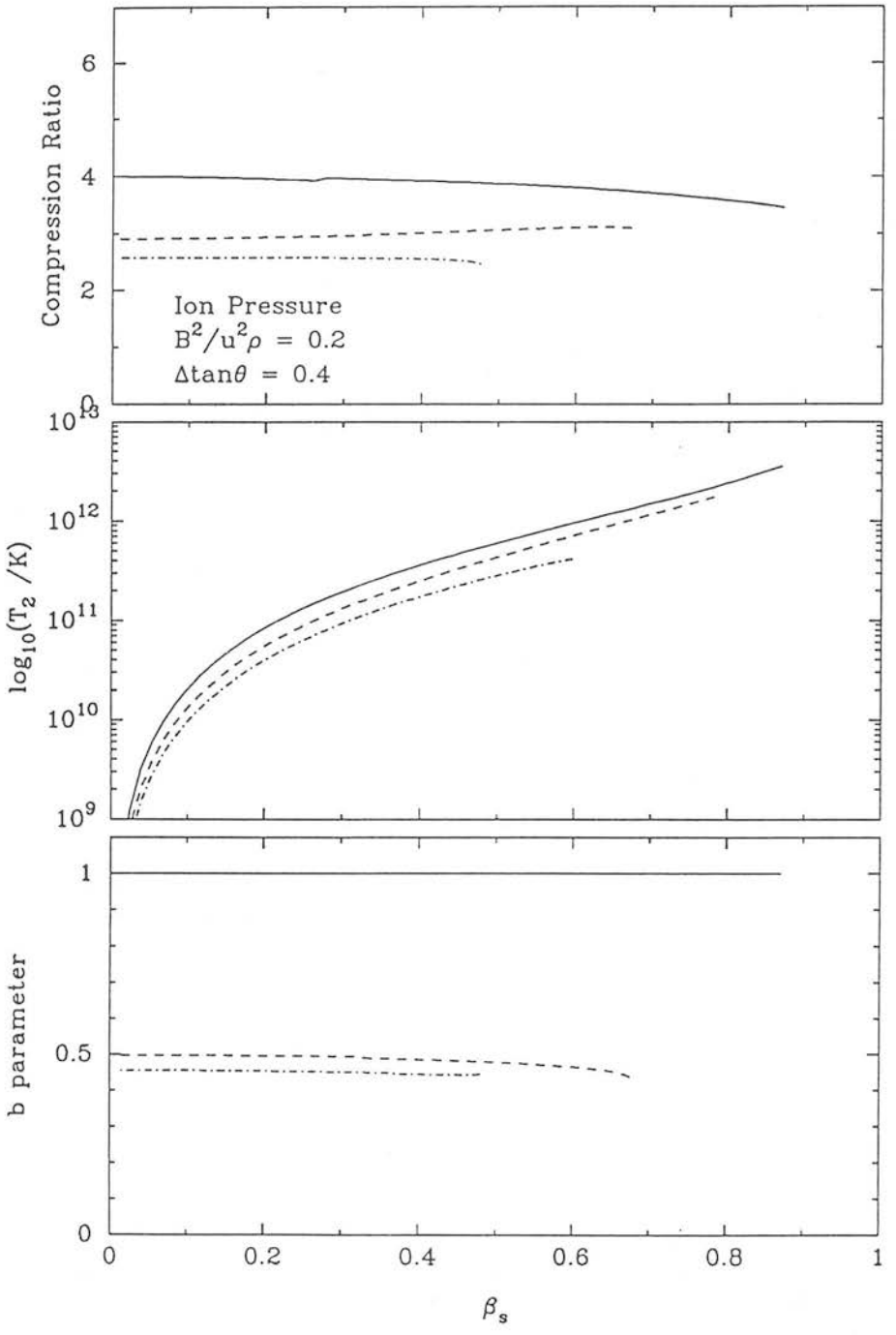

FIG 4: As Fig. 3, but with the downstream pressure provided entirely by ions.

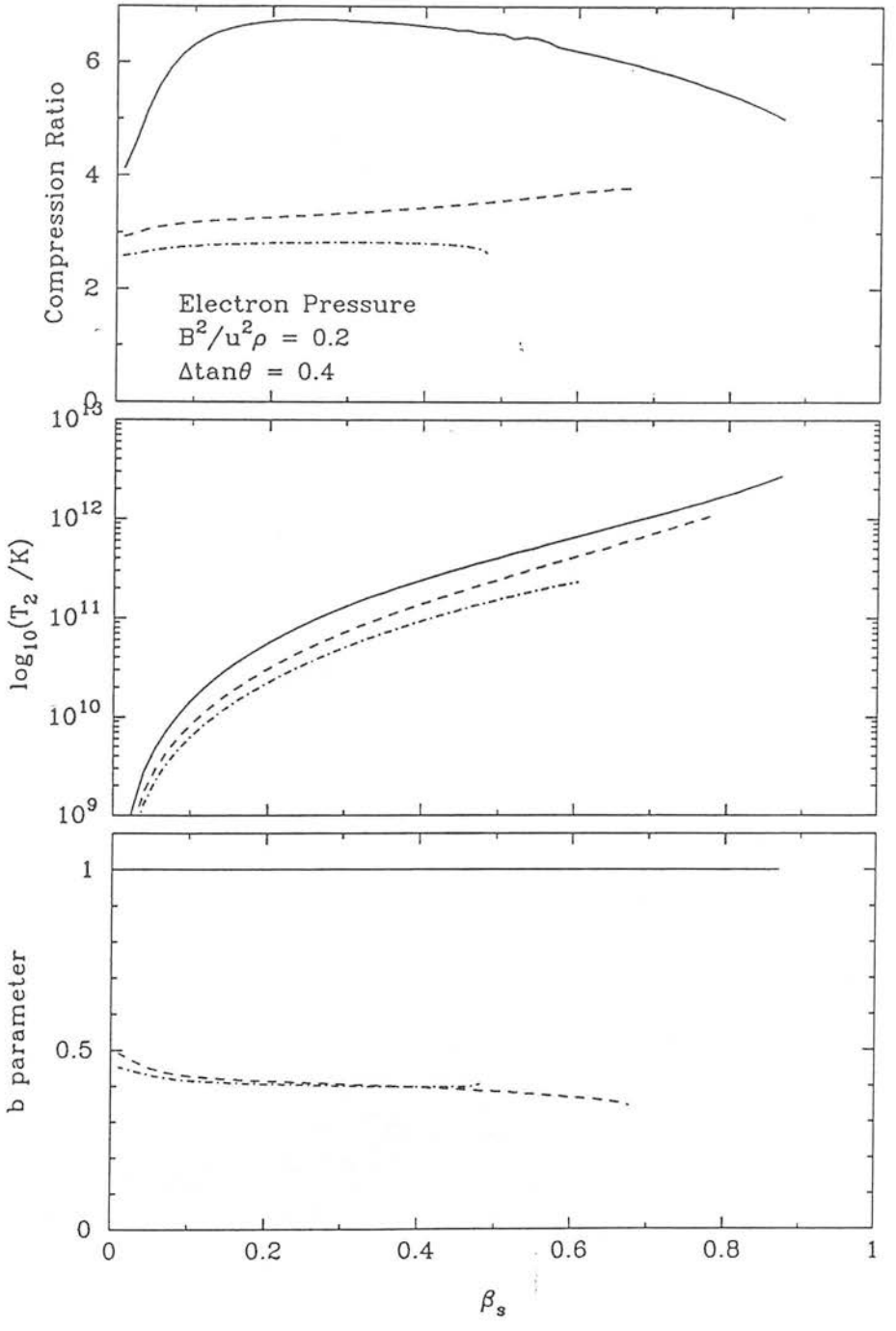

FIG 5: As Fig. 3, but with the downstream pressure provided entirely by electrons.

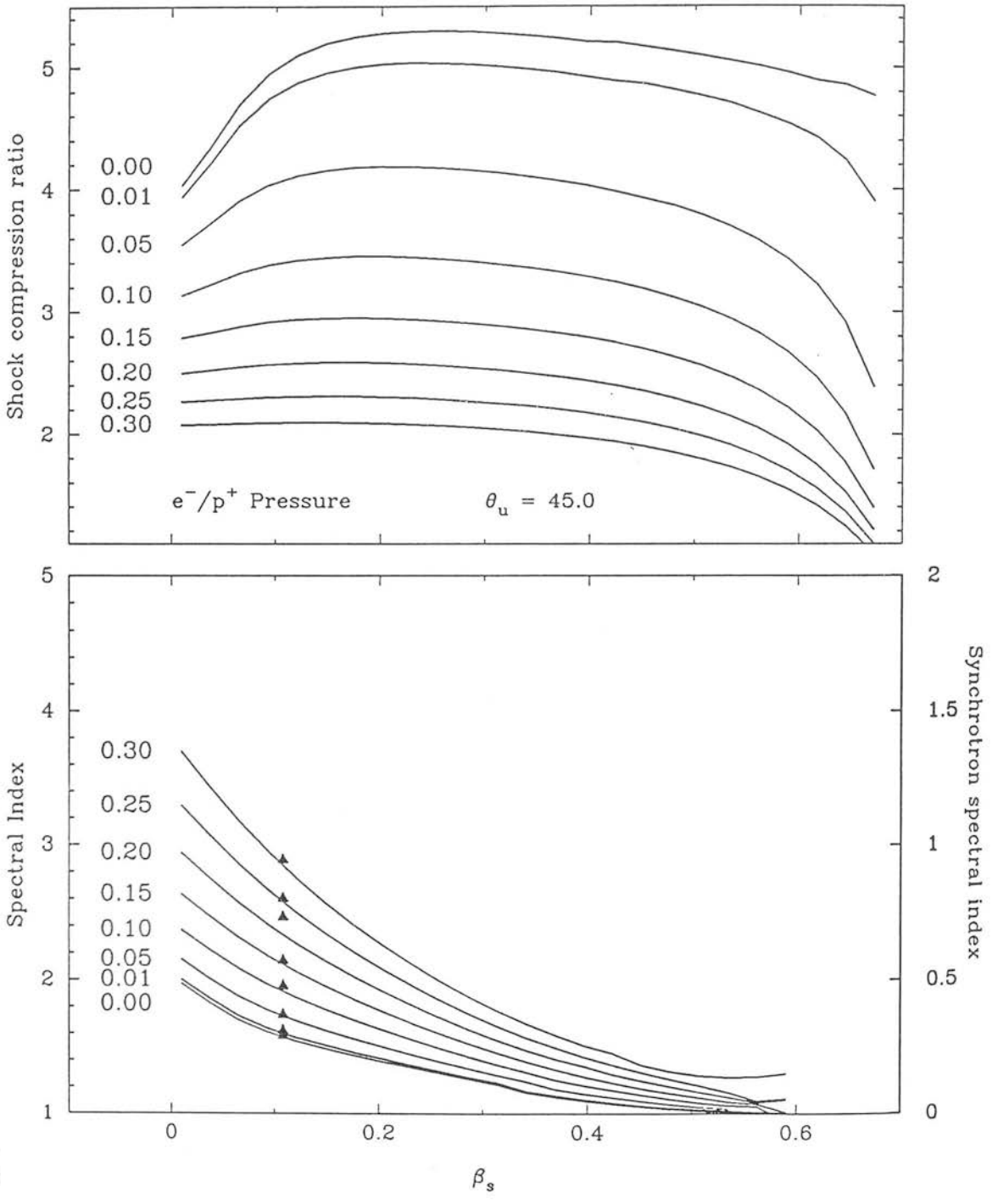

FIG 6: Comparison between the analytically derived spectral indices and the numerical results for a shock with a magnetic field at an angle $\theta = 45°$ and the downstream fluid in LTE. The different lines correspond to different values of M_A^{-2} as labelled.

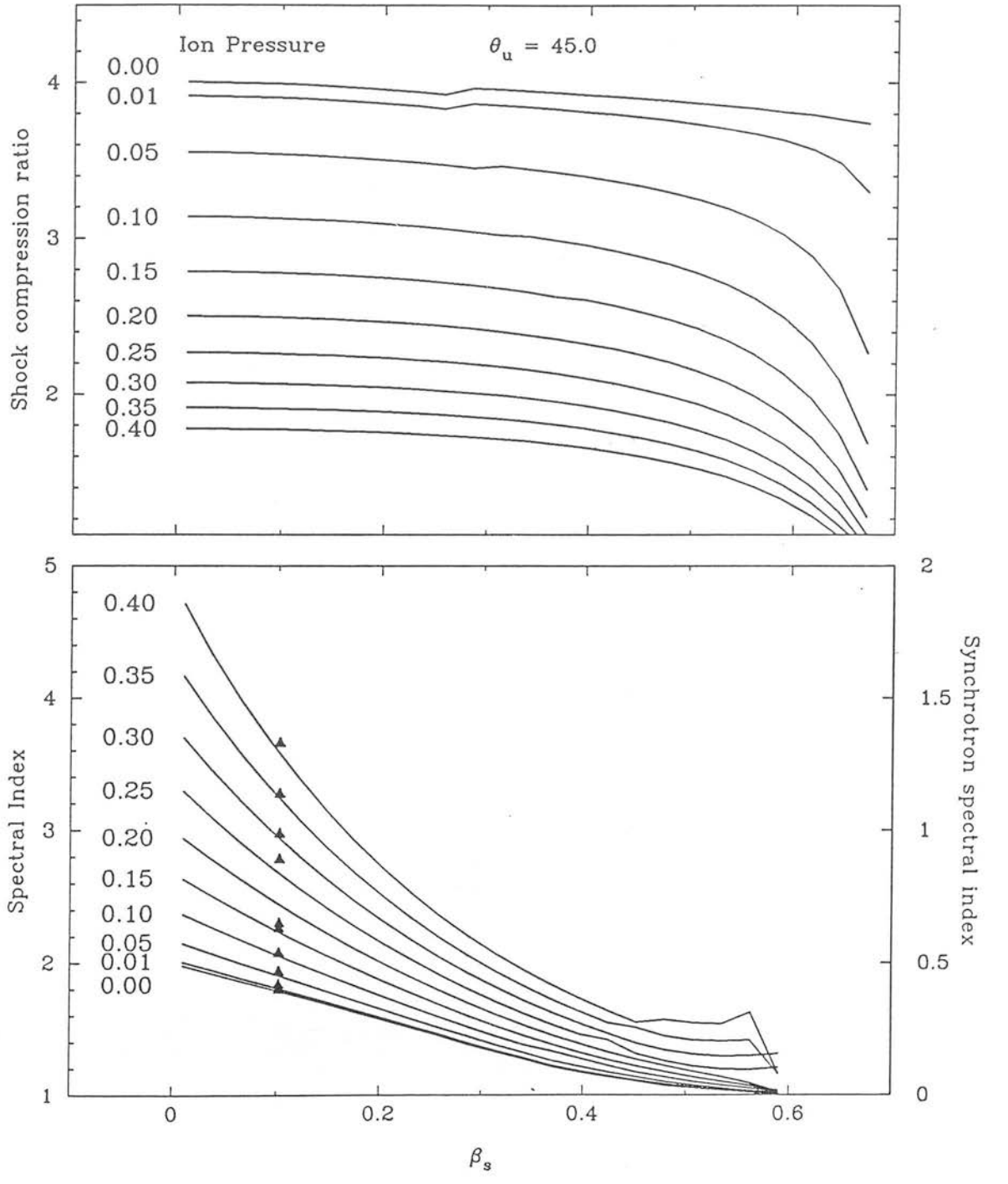

FIG 7: As Fig. 6, but with pressure provided by ions.

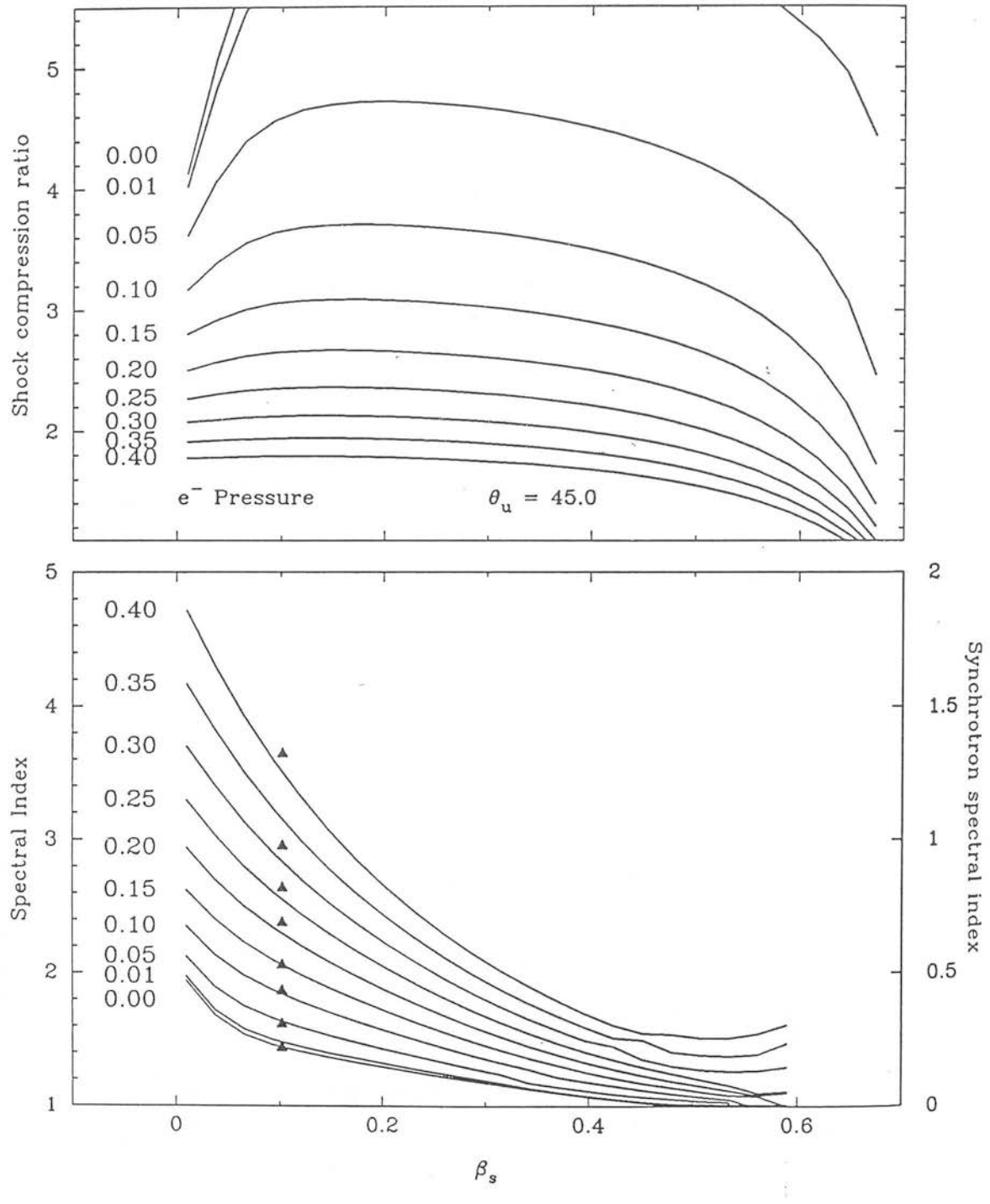

FIG 8: As Fig. 6, but with pressure provided by electrons.

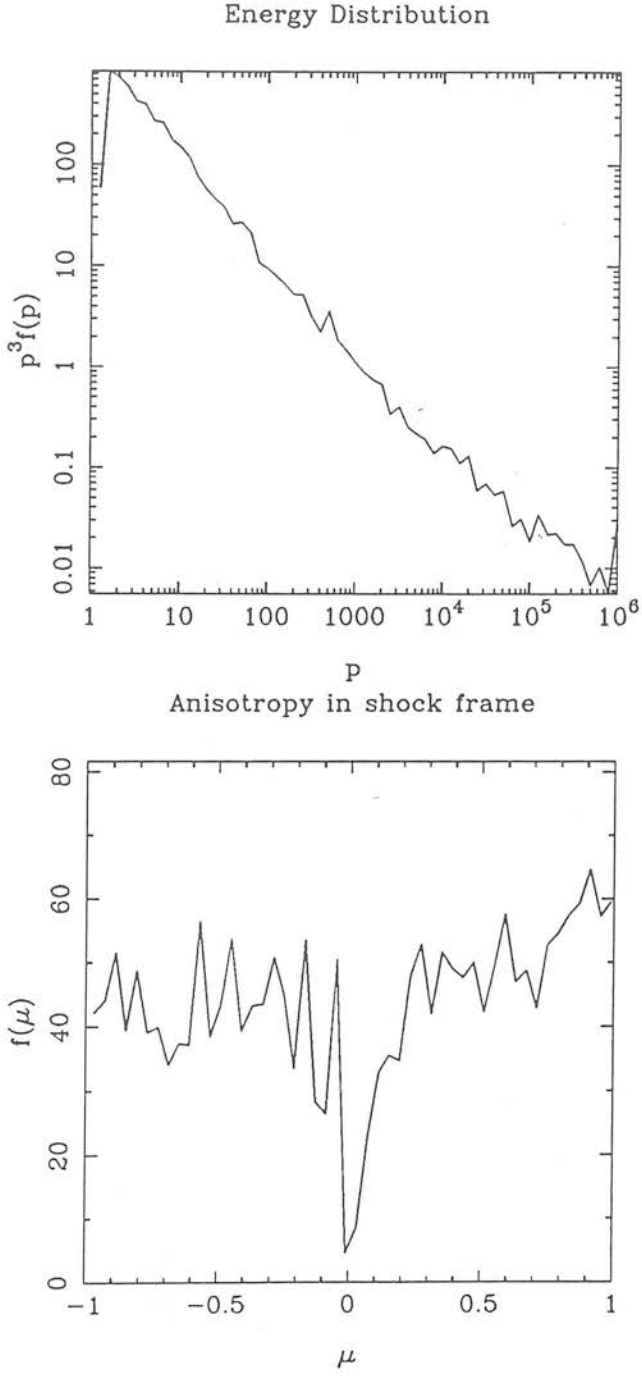

FIG 9: The distribution function at a parallel shock with speed $\beta_s = 0.2$, compression ratio 4. The spectral index is $\alpha = 0.5$.

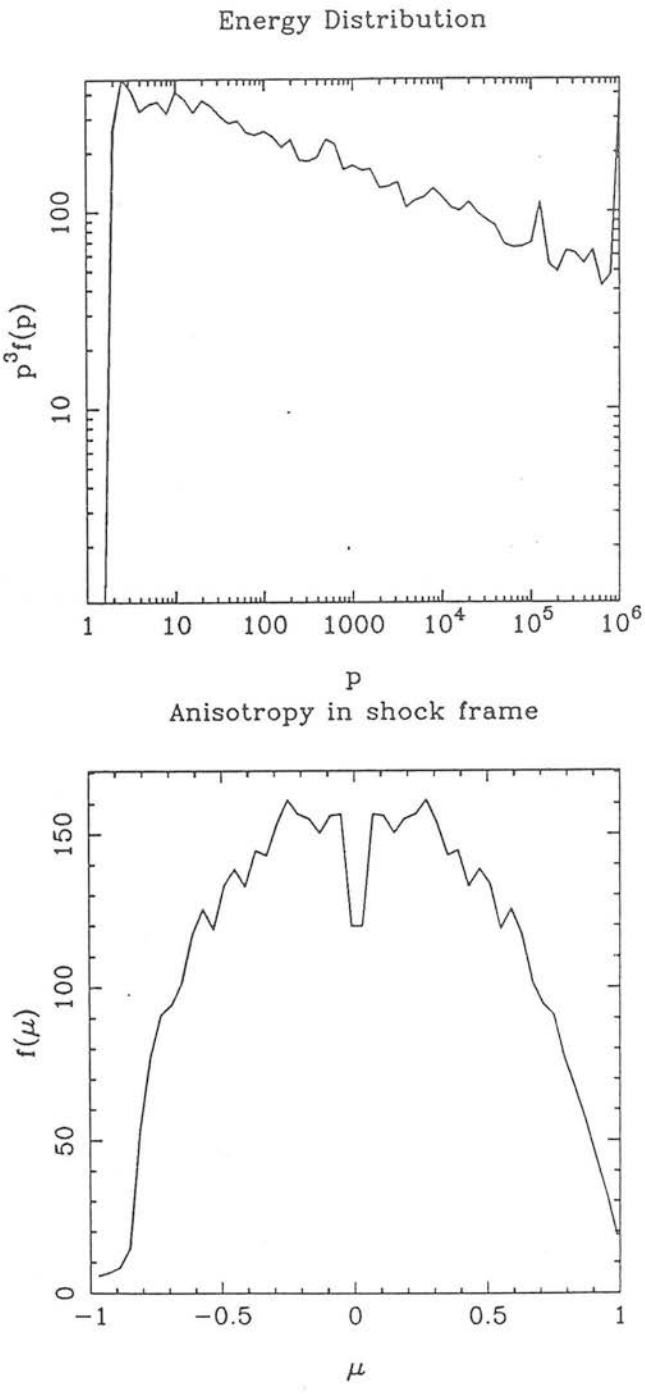

FIG 10: The distribution function at an oblique shock with speed $\beta_s = 0.4$, compression ratio 4 and a magnetic field at 45° to the shock normal. The spectral index is $\alpha = 0.057$.

Simultaneous Optical And IR Polarimetric Observations Of Blazars.

K.R.Ballard[1], *A.R.G.Mead*[1], *P.W.J.L.Brand*[1], *J.H.Hough*[2], *J.A.Bailey*[3], *C.Brindle*[2]

1: Dept of Astronomy, Edinburgh University, Scotland, EH9 3HJ.

2: Hatfield Polytechnic Observatory, Hertford, Herts, SG13 8LD.

3: Anglo-Australian Observatory, PO Box 296, Epping, NSW 2121, Australia.

ABSTRACT. We present simultaneous UBVRIJHK photometry and polarimetry for a sample of 48 Blazars covering the period 1986Aug – 1988Feb. These data were obtained as part of a continuing monitoring program at UKIRT using the MkII Hatfield Polarimeter.

Analysis of the data shows that around ~50% of objects have fluxes fitted by a power law over this wavelength range. Objects such as 3C345 which display polarization decreasing with frequency can be explained in terms of dilution of a synchrotron component by an unpolarized thermal component in the optical. Such a component cannot explain the ~40% of observations where the polarization increases with frequency. No evidence is found to support any relation between the polarization and the degree of frequency dependence of polarization. In ~30% of cases the position angle is frequency-dependent. Theoretically, wavelength-dependent behaviour proves to be a valuable tool, constraining conditions within the compact emission region of blazars and giving indications of an upper cutoff to the electron energy distribution. A frequency-dependent position angle may be evidence for emission from more than one region; the observed behaviour implies such regions must be inter-dependent.

1 Introduction.

A striking feature of blazar emission is the rapidly variable, highly polarized non-thermal continuum component which dominates the optical and infra-red emission. Blazars have long been known to exhibit such properties, which are generally assumed to be due to an incoherent synchrotron source of small extent. A successful model for the underlying physical processes must have the ability to predict the wide range of observed behaviour, including the much steeper spectral index and the variability of the optical emission. In order to set specific constraints upon models of blazar behaviour we have undertaken an observing programme, the aim of which was to obtain simultaneous multifrequency observations of flaring and quiescent blazars with high signal-to-noise.

The observations were made at the 3·8 m. U.K. Infra-red Telescope on Mauna Kea during the period 1986 August to 1988 February, using the dual-beam MkII Hatfield Polarimeter. This can measure simultaneously five optical and one IR channels covering the UBVRIJHK wavebands and is described fully by Mead (1988).

2 Results.

During the 18 months of observing described in this paper we obtained data for 48 blazars on a total of 196 occasions which will be published in full elsewhere (Mead *et al.* 1988, Ballard *et al.* 1988). Here we simply report some of the more notable behaviour and give a summary of the trends present in the sample.

2.1 Individual Objects.

1418+546 (OQ530): This object, confirmed as a BL-Lac. by Craine *et al.* , (1978) has been observed to undergo large variations in both flux and polarization. In Feb. 1988 it was observed on three occasions during which time it underwent unusual position angle behaviour. On the basis of the position angle data on the first two nights there was no evidence for anything other than a single component source with spectral curvature,

a polarization of 5% and a position angle of $\sim$ 145°. On the final night the object displayed a strong frequency-dependent position angle, which cannot be attributed to a simple single component, but rather can be explained by a two component model (Holmes *et al*, 1984). The flux for each component was modelled as:

$$\log_{10} S_\nu = \log_{10} S_{14} - \alpha \log_{10} \nu + \beta(\log_{10}(\nu))^2$$

and the polarization:

$$P = \pi \frac{\alpha+1}{\alpha+5/3}$$

Thus β represents the spectral curvature and π the degree of alignment of the B-field. The best fitting model is shown in fig. 1. It should be noted that this is just the simplest explanation for the observations, alternatives include anisotropic pitch angle distributions.

1641+399 (3C345): This strong lined HPQ was observed on 1986 Aug. 1–7 (Mead *et al.* 1988). In our data there was no evidence for significant variations in the flux or polarization over the period of the observations. The polarization decreased steadily in the optical while the spectral index flattened. The observed behaviour could not be explained in terms of simple synchrotron emission. Accordingly the behaviour was modelled using the method of Smith *et al.* (1986) who concluded that dilution by several non-polarized components could explain the results. These were estimated as: a) stellar emission – from the C model of an evolving elliptical galaxy (Bruzual, 1983). b) QSO line emission – from Grandi (1981, 1982). c) Balmer & Paschen continua – from the synthetic spectrum of Grandi (1982). d) the thermal 'blue-bump' of Malkan & Sargent (1982). The best fit finds a single black body of T$\sim$62 000 K in the emitted frame. The T$\sim$26 000 K found by Smith *et al.* could *not* be fitted satisfactorily but the possibility of the disk having varied could not be ruled out. Apart from a black body other possibilities can explain the result. Variability of the line emission and Balmer continuum was discounted as no such variations have previously been reported for 3C345. Alternatively errors in the model fits of the Fe^+ and Balmer continuum

Filter	Flux density (mJy)		Polarization (%)		Position angle (deg)	
1418+546			E(B-V) = 0.00			
17th. Feb 1988						
K	17.38	(0.32)	4.09	(0.48)	142.10	(3.71)
H	12.92	(0.25)	4.04	(0.32)	145.50	(1.85)
J	8.97	(0.18)	4.06	(0.29)	138.90	(3.07)
I	4.81	(0.11)	4.48	(0.27)	142.63	(1.88)
R	3.38	(0.09)	4.51	(0.18)	142.82	(1.09)
V	2.34	(0.08)	5.05	(0.35)	146.93	(1.91)
B	1.70	(0.07)	6.28	(0.23)	144.21	(1.11)
U	0.96	(0.05)	5.88	(0.43)	147.41	(1.86)
18th. Feb 1988						
H	14.43	(0.28)	3.38	(0.25)	132.01	(2.63)
I	5.68	(0.09)	3.56	(0.51)	140.80	(4.60)
R	4.25	(0.10)	3.11	(0.25)	146.20	(2.27)
V	2.97	(0.10)	2.96	(0.55)	142.80	(5.86)
B	2.34	(0.09)	3.20	(0.38)	150.00	(3.49)
U	1.49	(0.07)	4.05	(0.64)	156.20	(3.86)

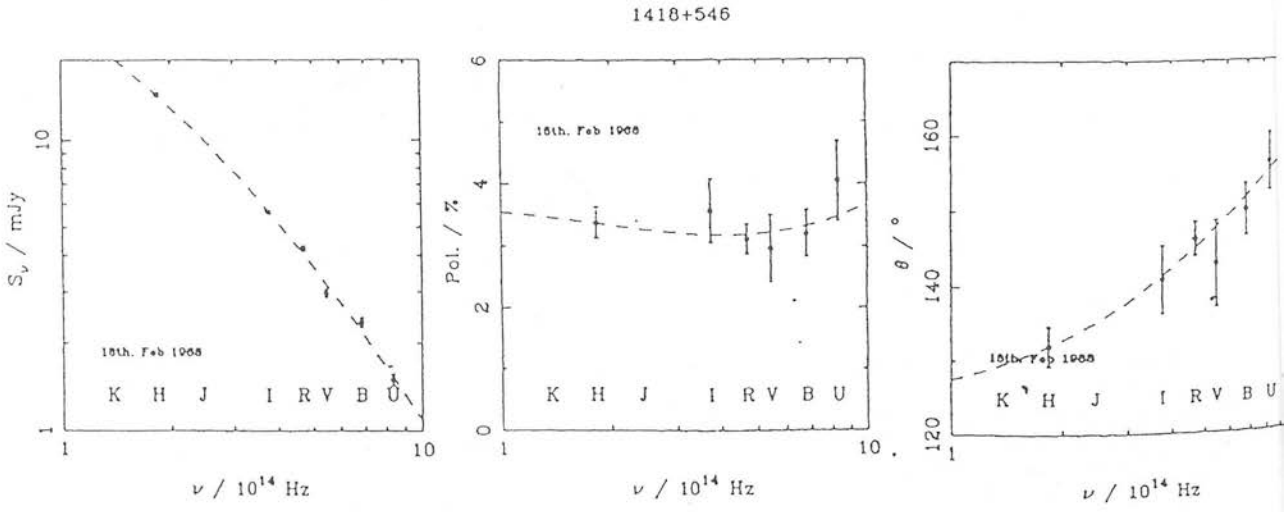

Fig. 1. This shows the best fitted values for the flux & polarization properties of 1418 + 546 on 1988 Feb 18.

could be the cause. Indeed, the model of Netzer & Wills (1983), incorporating a better estimate of the Fe^+ emission requires no black body contribution. More detailed spectropolarimetry will be needed to understand fully the emission from this object.

2.2 Trends.

The data obtained can only be treated as an *inhomogeneous* sample. The main strategy was to observe as many blazars on as many occasions as possible. In practice observations were only repeated if the results were 'interesting' (i.e. exhibited frequency dependent polarization, position angle, variability etc.), hence it would be impossible to treat individual data points independently. In order to attempt to overcome *some* of these biases we refer to maximum or median values for an object. Analysis of the data has revealed several interesting correlations, and also several non-correlations.

1) The flux data could be fitted adequately by a power-law in 50% of cases, although significant convex ($d\alpha/d\nu > 0$) spectral curvature was seen in 30% of observations. The distribution of spectral indices obtained is shown in fig. 2. Spectral indices can be used to constrain theories of particle acceleration which predict the electron energy distribution. Heavens (1988) summarizes the predictions of the most successful theory to date; acceleration at a shock front. The spectral indices observed were high enough to be inconsistent with this theory unless a high frequency cutoff is employed (in the theory of particle acceleration this occurs naturally when the time taken to accelerate a particle becomes comparable to the synchrotron loss time e.g. Blandford, 1979). Inhomogeneous jet models yield an additional explanation of steep spectral indices.

2) In the single case of the H waveband there was marginal evidence for a correlation (probability of $1 \cdot 65\%$ for the null hypothesis) between the maximum α and redshift. Such a correlation is indicative of either a) blazar evolution – e.g. at earlier epochs blazars had steeper spectral indices or b) a cutoff at a fixed frequency; for higher redshifts the cutoff is shifted towards the red yielding higher spectral indices. Clearly more data is required to resolve this point.

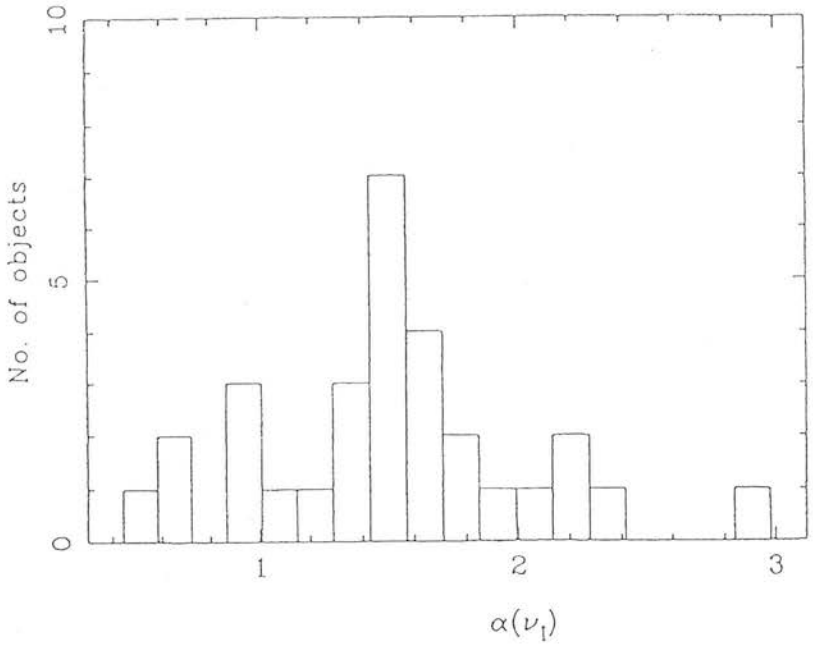

Fig. 2. The distribution of median spectral indices for the sample.

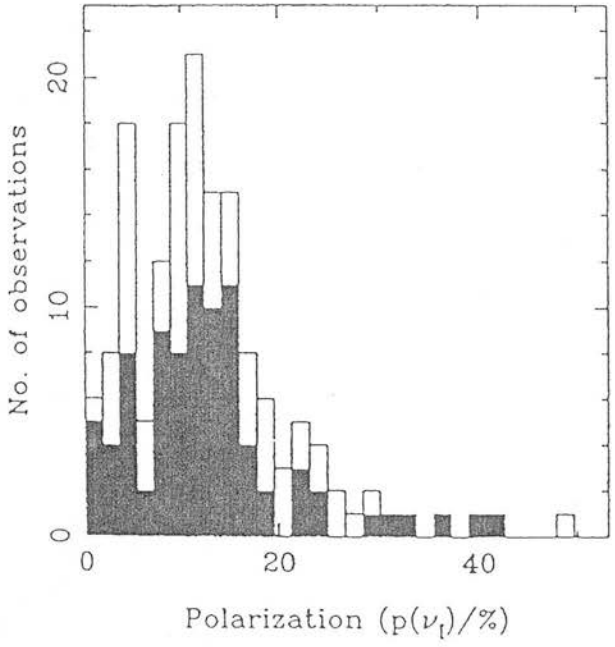

Fig. 3. The maximum polarization values observed. Objects displaying frequency-dependent polarization significant at the 5% level have been flagged. The two-sample Kolmogorov-Smirnov test was used to show that the distributions were not significantly different.

3) We describe objects not fitted by a constant polarization or position angle at the 5% level as having frequency dependent polarization (FDP) or position angle ($FD\theta$). In our sample frequency independent polarization or $dp/d\nu \geq 0$ were common, the main exceptions being objects such as 1641+399, 1921–293 and 2251+158 where contamination of the non-thermal flux by an unpolarized optical component may occur.

In the past a correlation between FDP and degree of polarization has been reported (the 'p(λ)–p' effect of Bailey, Hough & Axon (1983), Holmes *et al.* (1984)). However, in the present data this was no longer apparent. The problem was tackled in two ways. Fig 3 shows histograms of the polarizations at I in which objects displaying FDP are shaded. Under the null hypothesis that the distributions are the same the two-sample Kolmogorov-Smirnov test (Conover, 1980) was used. As an alternative test a correlation between the values of $\log(p_B/p_H)$ and p_I was sought. Neither of these were significant at the 10% level. Possible causes of this result include the fact that previously the MkI polarimeter was used which produced data of lower quality and consequently FDP at lower polarizations may have been missed. In addition $FD\theta$ was examined similarly with the result that no correlations at the 10% level were again found.

FDP can be important in determining conditions within the source. Two explanations should be considered, which can explain the majority of cases with $dp/d\nu \geq 0 \cdot 0$. Firstly, FDP may be the result of curvature within the spectrum (Björnsson & Blumenthal, 1982), which can explain the FDP in 41 of the 55 cases where it occurs. However, this empirical description does not explain the origin of the curvature. Synchrotron, Self-Compton models have had some success in fitting spectral curvature (e.g. Madau, Ghisellini & Persic, 1987) but require information over decades of frequency in order to be constrained. A second explanation is that the FDP is associated with a cutoff in the spectrum combined with an unpolarized second component with a steeper spectral index. In those cases where this model was applied the value of the cutoff was close to the upper limit postulated by Biermann & Strittmatter (1987) of $2\text{x}10^{15}$Hz. This is consistent with the fact that the polarization 'hump' (where the increasing polarization of the approximately exponentially decreasing cutoff component is swamped by the un-

polarized component) was not observed. This is a problem for the cutoff model unless this result is a consequence of a genuine restricted range of cutoff frequencies.

KRB and ARGM acknowledge the receipt of SERC studentships.

3 References.

Bailey, J.A., Hough, J.H. & Axon, D.J., 1986. *Nature*,**322**, 150.

Ballard *et al.* 1988. *in preparation.*

Biermann, P.L. & Strittmatter, P.A., 1987. *Ap.J.*, **322**, 643.

Björnsson, C.-I & Blumenthal, G.R., 1982. *Ap.J.*, **259**,805.

Blandford, R.D. 1979. *Proc. A.I.P. Conf.*(La Jolla), **56**, 335.

Bruzual, A.G., 1983. *Rev.Mex.Astr.Astrofis.*,8, 63.

Conover, W.J., 1980. *Practical Nonparametric Statistics*

Craine, E.R., Duerr, R. & Tapia, S., 1978. *Pittsburgh Conf. On BL-Lac. Objects*, Ed. Wolfe.

Grandi, S.A., 1981. *Ap.J.*,**251**, 451.

Grandi, S.A., 1982. *Ap.J.*,**255**, 25.

Heavens, A.F., 1988. in *Workshop On Hotspots In Extragalactic Radio Sources,* Ed. Meisenheimer & Röser.

Holmes, P.A., Brand, P.W.J.L., Impey, C.I., Williams, P.M., Smith, P., Elston, R., Balonek, T.J., Zeilik, M., Burns, J., Heckert, P.A., Barvainis, R., Kenny, J., Schmidt, G. & Puschell, J.J., 1984. *M.N.R.A.S.*,211, 497.

Madau, P., Ghisellini, G. & Persic, M., 1987. *M.N.R.A.S.*,**224**, 257.

Malkan, M.A. & Sargent, W.L.W., 1982. *Ap.J.*,**254**, 22.

Marscher, A.P. & Gear, W.K., 1985. *Ap.J.*,**298**, 114.

Mead, A.R.G., Brand, P.W.J.L., Hough, J.H. & Bailey, J.A., 1988. *M.N.R.A.S.*,**233**, 503.

Mead, A.R.G., 1988 *Ph.D. Thesis, University Of Edinburgh.*

Mead *et al.* 1988. *in preparation.*

Netzer, H. & Wills, B.J., 1983. *Ap.J.*,**275**, 445.

Smith, P.S., Balonek, T.J., Heckert, P.A. & Elston, R., 1986. *Ap.J.*,**305**, 484.

The high frequency properties of synchrotron radiation

Keith Ballard: *Department of Astronomy, Blackford Hill, Edinburgh, UK. EH9 3HJ.*

1: Introduction

The aim of this paper is to examine the relevance of models involving shocks to the high frequency near infrared and optical emission in BL–Lacs. A short study of the effect that losses can have upon non–thermal electron distributions is presented. This is combined with previous work relating to specific magnetic field geometries behind shock fronts to yield model spectra which can be compared to those actually observed. Agreement between the theory and observations is found only if the electrons are allowed to remain isotropic. Some of the limitations and implications for this model of the emission region are considered.

2: BL–Lac Objects

Before proceeding to consider the details of a model for the optical and infrared emission of BL–Lacs (by which we refer to those objects where there is no suspicion that the optical light has been diluted by unpolarized thermal emission) it is worth stating briefly the observational properties of the high frequency emission, which a model is required to reproduce. For these we summarize the conclusions of Mead *et al.*, (1990) and Ballard *et al.*, (1990). These papers present the results of a program of monitoring 48 blazars (BL–Lacs & HPQ's) carried out on 14 nights between 1986 and 1988 at UKIRT. The observations were made simultaneously in the UBVRIJHK wavebands.

1.) In many cases the spectrum was a power law of constant slope, often steeper than $\alpha = 2.0$. There were, however, a significant number of observations ($\sim 30\%$) where the spectrum steepened with increasing frequency. This fact, coupled with the fact that the spectrum in the optical is steeper than in the radio (where $\alpha \simeq 0.2$, Valtaoja, this volume) is strongly suggestive of losses having modified the spectrum.

2.) Frequency dependence of polarization was a common occurrence, and, with only a couple of exceptions, in the case of the BL–Lacs it always increased towards the blue end of the spectrum. The level of polarization (up to 43%) was indicative of a partially ordered magnetic field when averaged over the entire emission region — although it is possible that it could be almost uniform in smaller regions. Frequency dependence of position angle was less common. Most of the frequency dependence of polarization is associated with the intrinsic curvature of the flux via the simple parameterization of Björnsson & Blumenthal (1982) *i.e.* as the spectral index increases so does the polarization according to the relationship:

$$\mathrm{pol}(\nu) = \Pi \frac{\alpha(\nu)+1}{\alpha(\nu)+5/3} \times 100\%$$

where $\alpha(\nu)$ is the spectral index and Π is a constant representing the degree of ordering in the magnetic field.

3.) Variability was usual over timescales of a single day. No obvious characteristic patterns to the variability were apparent.

These are the principal characteristics of BL-Lacs found from a large number of observations; any model must be able to explain these in order to be taken seriously. Having achieved that, a good model should also allow for the more occasional extreme events such as those seen by Holmes *et al.*, (1984) or Moore *et al.*, (1982).

3: The Model

The remainder of this paper is devoted to the properties of shock models of BL-Lacs when losses are included. Such a study, although it does not reach any startlingly new conclusions, is instructive because it tests the limits of the applicability of models which purport to explain the blazar phenomenon.

There are two main motivations for a study of this kind. The first is simply an attempt to plug a gap in the knowledge of the properties of a simple synchrotron source. The original work in the field was published by Kardaschev (1962) who presented results for the evolution of a non-stationary synchrotron source, as the electrons lost or gained energy to various mechanisms, such as synchrotron emission, adiabatic expansion or the inverse Compton effect. Implicit in this work was the assumption that as the electrons lose energy they are tied to an element of the magnetic field and maintain their initial pitch angle with respect to the magnetic field. The only specific source fields considered were isotropic and consequently the overall electron distribution remained isotropic with time, and as there was no preferred field direction there was no polarization. The aim of this work is to evaluate any possible anisotropy which might develop in a more realistic field geometry and to investigate the effect that this has on the polarization.

The second motivation arises from observational studies of blazar emission, the interpretations placed upon the results and the necessity to adapt these to future observing programmes. Over the past decade the possibility that a shock passing along a jet represents the site of blazar emission has received much attention. Groups such as those situated in Preston and Michigan have obtained a large amount of data at millimetre and centimetre wavelengths and have shown convincingly that the day to day behaviour of the flux and polarization (Hughes, Aller & Aller, 1985) or the large flaring events in the flux around the self-absorption turnover which are periodically observed (Marscher & Gear, 1985) can be modelled by a fairly simple shock in a jet model. There is clearly a need to extend these works to higher frequencies in order to test their applicability in these regimes and to try therefore to understand the high frequency radiation. This will test the supposition that the optical emission originates in the same region as the radio emission. Furthermore, as submillimetre observations of the polarization become available it is important to be aware of the implications that they could have for our understanding of the emission region and mechanism, in particular the role played by losses in determining their properties.

In attempting to model blazars at high frequencies there are two elements which must be determined, the magnetic field and the electron distribution. Regarding the magnetic field, we have chosen in this case to extend naturally a model which has had success in the past *i.e.* that of Hughes, Aller & Aller (1985). In this model it is assumed that there is a shock passing along a jet close to the line of sight. The jet contains a magnetic field, taken to be isotropic with a uniform distribution of magnitudes upstream of the shock. Further, assume that the magnetic field is dynamically unimportant so that it plays no part in determining the jump conditions. As material passes through

the shock, it is compressed and the magnetic field perpendicular to the shock normal is enhanced by a factor of r, the compression ratio of the shock. The material then emits synchrotron radiation with the Stokes parameters:

$$I(\nu,t) = L\int_E\int_\theta\int_\phi B\sin\alpha F\left(\frac{\nu}{\nu_c}\right)N(E,\alpha,t)d\phi\sin\theta d\theta dE$$
$$\begin{matrix}Q(\nu,t)\\U(\nu,t)\end{matrix} = L\int_E\int_\theta\int_\phi B\sin\alpha G\left(\frac{\nu}{\nu_c}\right)\begin{matrix}\cos 2\chi\\\sin 2\chi\end{matrix}N(E,\alpha,t)d\phi\sin\theta d\theta dE$$
$$V(\nu,t) = 0$$

e.g. Pacholczyk, (1970). The various terms in these equations are as follows: L is the line of sight depth of the source; note that throughout this work it has been assumed that the source is optically thin as we are primarily interested in the high frequency emission where this should be a reasonable assumption. $F(x)$ and $G(x)$ are standard synchrotron functions expressing the spectrum of radiation from a single electron, E is the electron energy. The angle χ is the position angle on the sky of the radiation measured relative to some fixed direction. $B\sin\alpha$ is the magnetic field projected onto the plane of the sky as a function of α, the angle between the line of sight and the element of the magnetic field. In order to evaluate α it is necessary to take the components of the magnetic field downstream of the shock (which lies in the xy plane) in terms of the polar co-ordinates θ,ϕ where θ is the angle between the element of field and the shock normal and ϕ is the azimuthal angle, and rotate it through an angle, ϵ to the x–axis so that the electron's velocity vector lies along the new x'–axis. From this an expression for $B\sin\alpha$ can be derived:

$$B^2\sin^2\alpha = B^2(r^2\sin^2\theta\sin^2\phi + r^2\sin^2\theta\cos^2\phi\sin^2\epsilon$$
$$+\cos^2\theta cos^2\epsilon - 2r\sin\theta\cos\theta\cos\phi\sin\epsilon\cos\epsilon)$$

And then by integrating over θ,ϕ one is effectively integrating the emission from an electron over the entire magnetic field distribution. This introduces two extra parameters into the model, the shock compression ratio r and the angle between the line of sight and the shock face ϵ. Finally, one has to supply $N(E,\alpha,t)$, the distribution of electrons with energy, pitch angle and time. There are several possibilities for this which will be considered in turn in the next section.

4: Results

4.1: No scattering, Decaying source

We assume an initially isotropic distribution of electrons, with a power law energy distribution, with a cutoff at a low energy, E_b, and high energy, E_c. Also in this case assume that the electrons have a pitch angle which is constant with time. Then the decay of a simple power law source with synchrotron losses is governed by:

$$N(E,\alpha,t) = kE^{-\gamma}(1-\beta tE)^{\gamma-2}\Theta\left(\frac{E_c}{1+\beta tE_c} - E\right)$$

(Kardaschev, 1962) where the step function has been included to follow the evolution of the high energy cutoff. $\beta = (6\pi\epsilon_0 m_e^4 c^5/e^4)^{-1} B^2 \sin^2\alpha = bB^2 \sin^2\alpha$. The results of a sample integration showing flux, spectral index (the negative slope of the log(Flux)–log(ν) plot), the polarization and the position angle are shown in Fig 1.

This case, where the electron distribution becomes anisotropic can be regarded as occurring whenever the electron pitch angle remains constant for a longer time than the time it takes the lowest energy electron to lose energy, perhaps because the field is essentially uniform over large distances. The parameters chosen are $r = 4.0$ and $\epsilon = 0°$ (*i.e.* looking along the shock face). This choice maximizes the degree of polarization in order to emphasize the properties of the source. The most striking feature is the decrease in polarization and position angle rotation of 90° which develops as the spectrum evolves. There is a simple explanation for this feature. At low frequencies and early times the enhanced magnetic field perpendicular to the shock normal dominates the emission giving a polarization position angle aligned with the shock normal. As the spectrum evolves the electrons which are tied to these field lines lose more energy than those electrons lying on field lines along the shock normal. At high frequencies it is these electrons, moving around field lines along the shock normal which are left and which dominate the emission. At the frequency where the polarized fluxes are equal, there is zero polarization and the position angle rotates. The emission at the highest frequencies is characteristic of synchrotron emission around a cutoff.

However, the spectra presented in Fig 1 are dissimilar to the form of the majority of observations of blazars. There is only a single published spectrum which looks qualitatively similar, that of Holmes *et al.*, (1984) (which incidentally cannot be satisfactorily fitted by the model). Although it might be unwise to reject this model out of hand for all observations, it is clearly not relevant for the vast majority. It should also be mentioned at this point that the model so far is probably of little relevance in understanding BL–Lacs because in the first instance only a decaying source has been considered whereas one should also include the possibility of the injection of fresh energetic electrons if one is to have any hope of explaining flaring events. Secondly there is no scattering of electrons in less than the synchrotron loss timescale of the electrons considered. This necessarily precludes the possibility of the electrons being accelerated through the Fermi mechanism, or indeed any process which alters the pitch angle of the particle. It is therefore not too surprising that the results in Fig 1 bear little resemblance to the spectra which are observed. Although the results discussed above are useful in understanding the evolution of a source, an attempt to drop these restrictions should be made.

4.2: Electron scattering

We will now consider briefly the alternative limit where the electrons maintain isotropy; this corresponds to the case where the scattering timescale is much less than the synchrotron loss timescale. In deriving an electron distribution one must integrate the energy lost to an element of the magnetic field over the whole field distribution equally. One obtains a distribution of the form:

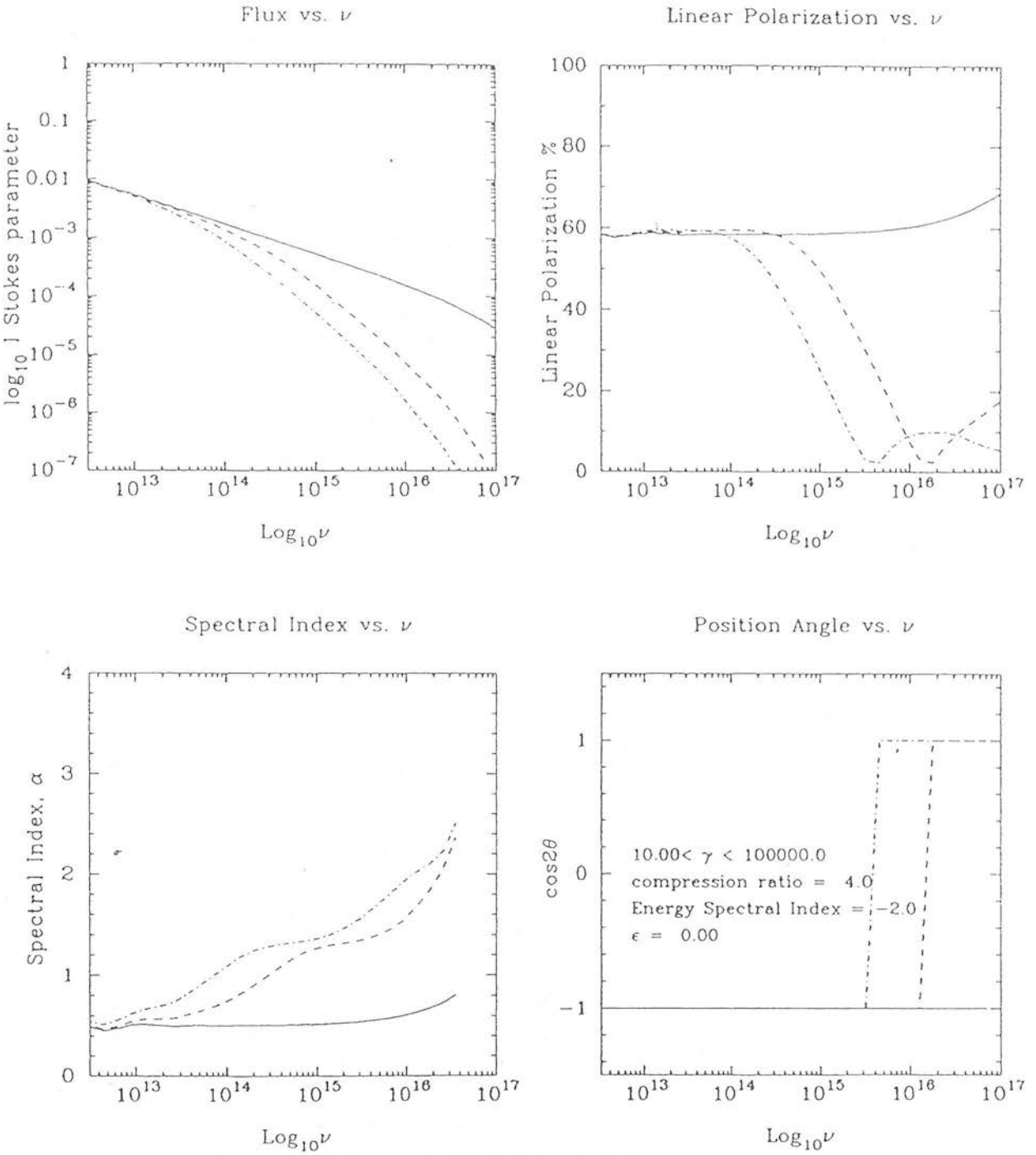

Fig 1: This shows the decay of a source with synchrotron losses & no electron scattering. The three lines are for $t = 0$ (solid) and two equally spaced later times (dashed then dot-dashed). The electrons maintain their original pitch angle and the distribution rapidly becomes anisotropic. The decrease in polarization is contrary to what is generally observed at optical wavelengths, and there is an abrupt position angle flip of 90°.

$$N(E,\alpha,t) = \frac{kE^{-\gamma+1}}{\beta(\gamma-1)}\left(\left[1-(1-\beta tE)^{\gamma-1}\right]\Theta\left(\frac{E_c}{1+\beta tE_c}-E\right)\right.$$
$$\left.+\left[1-\left(\frac{E}{E_c}\right)^{\gamma-1}\right]\Theta\left(E-\frac{E_c}{1+\beta tE_c}\right)\Theta(E_c-E)\right)$$

where $\beta = -(4\pi/9)(5r^2+1)bB^2$ and a constant injection of electrons with an isotropic power–law distribution has been included. The electron distribution is independent of pitch angle. The results of a sample integration are shown in Fig 2.

The flux is straightforward to explain; at low frequencies it rises continuously as fresh electrons are injected, at high frequencies above the break the injection is balanced by the energy loss mechanism. There is no rotation of the position angle as no anisotropies develop in the electron distribution (see Björnsson, 1985). The interesting behaviour here is the form of the polarization which increases gradually. This behaviour is quite similar qualitatively to what one actually observes for BL–Lacs, which is encouraging. The final plot included in Fig 2 is the polarization predicted by the parameterization of synchrotron radiation of Björnsson & Blumenthal (1982). The polarization changes are derived from changes in the slope of the power–law distribution of the electrons. As mentioned earlier the observed polarization could be fitted well by this parameterization in a large number of cases.

5: Discussion

We have considered the properties of the emission from two possible models of the source structure of BL–Lacs and have shown that if models which explain well the emission at radio wavelengths are correct, and are applicable to optical wavelengths, then qualitative agreement between the observations and the theory is found only if the electrons remain isotropic as they lose energy. If the electrons are scattered in the vicinity of a shock front, then the first order Fermi shock acceleration mechanism will work. Thus there is further circumstantial evidence at least that this mechanism is occurring in BL–Lacs. The Fermi mechanism is attractive because it provides us with a natural explanation of the origin of the non–thermal electrons and a prediction of their slope. In the main, calculations of the form of the particle distribution assume a uniform magnetic field, this assumption is another that should be dropped. In the case of a completely disordered magnetic field one can use numerical simulations of the orbits of electrons to obtain a value for the spectral index (Achterberg, 1988; Ballard *et al.*, in preparation); these turn out to be steeper than one would expect for an ordinary oblique shock where the electrons get trapped upstream (Kirk & Heavens, 1989). In fact the results appear to be similar to those for the simplest parallel shock case. The spectrum of electrons accelerated at a shock front with a disordered magnetic field are shown in Fig 3. In this particular case a compression ratio of $r = 4.0$ and shock speed of $u_{sh} = 0.4c$ were taken, which corresponds to a strong hydrodynamic shock with the downstream pressure provided by ions only. This example produces a non–thermal spectral index which is not the same as the value of $\alpha \simeq 0.2$ which is observed in the radio. This could be more accurately reproduced with a simulation at a shock with a higher compression ratio.

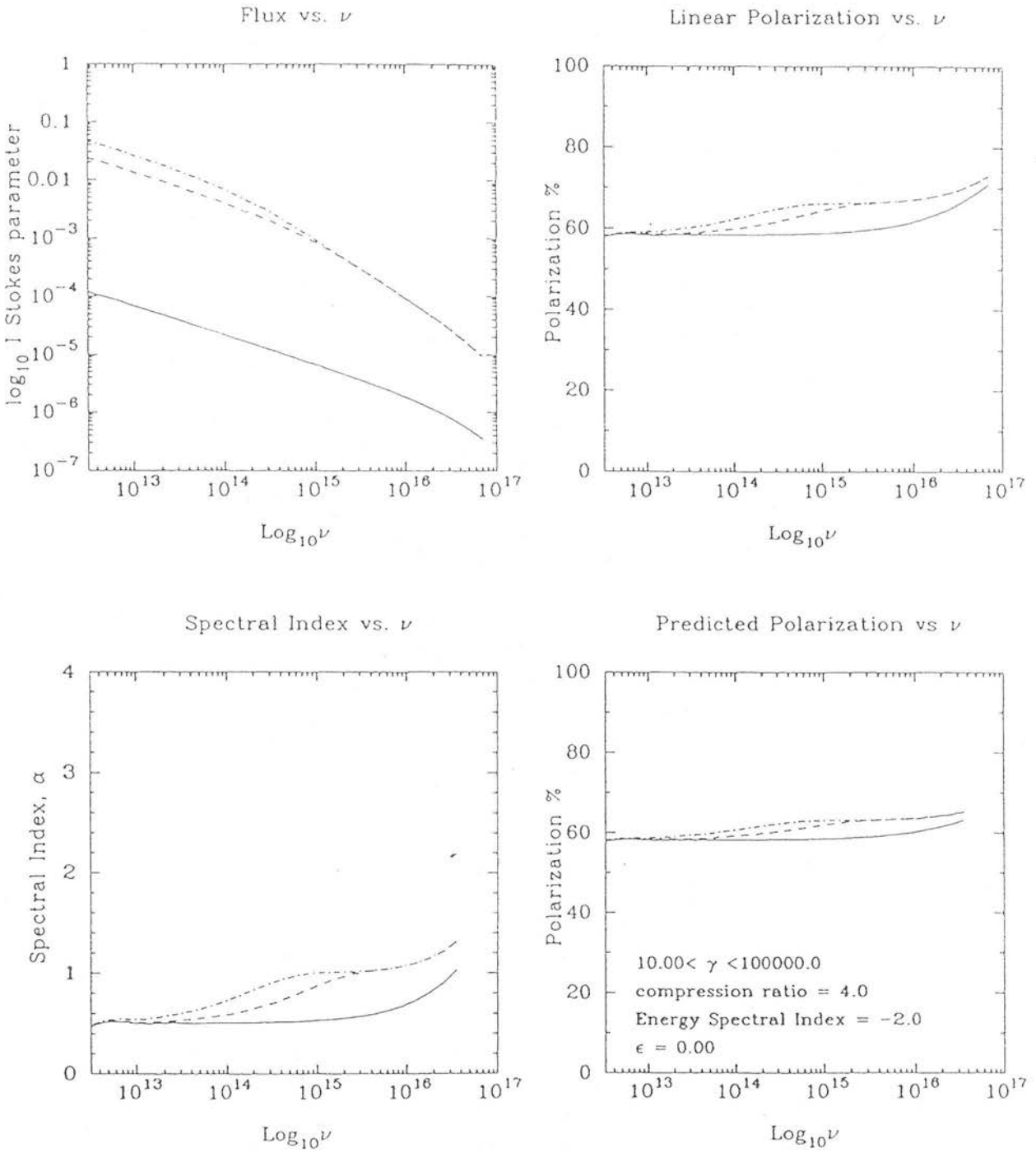

Fig 2: This shows the evolution of a source with synchrotron losses & electron scattering included, together with the steady injection of 'fresh' electrons with a power law form. The electrons now scatter in much less time than they lose energy and the distribution remains isotropic. The final plot is the polarization predicted from a parameterization of the form of equation 1.

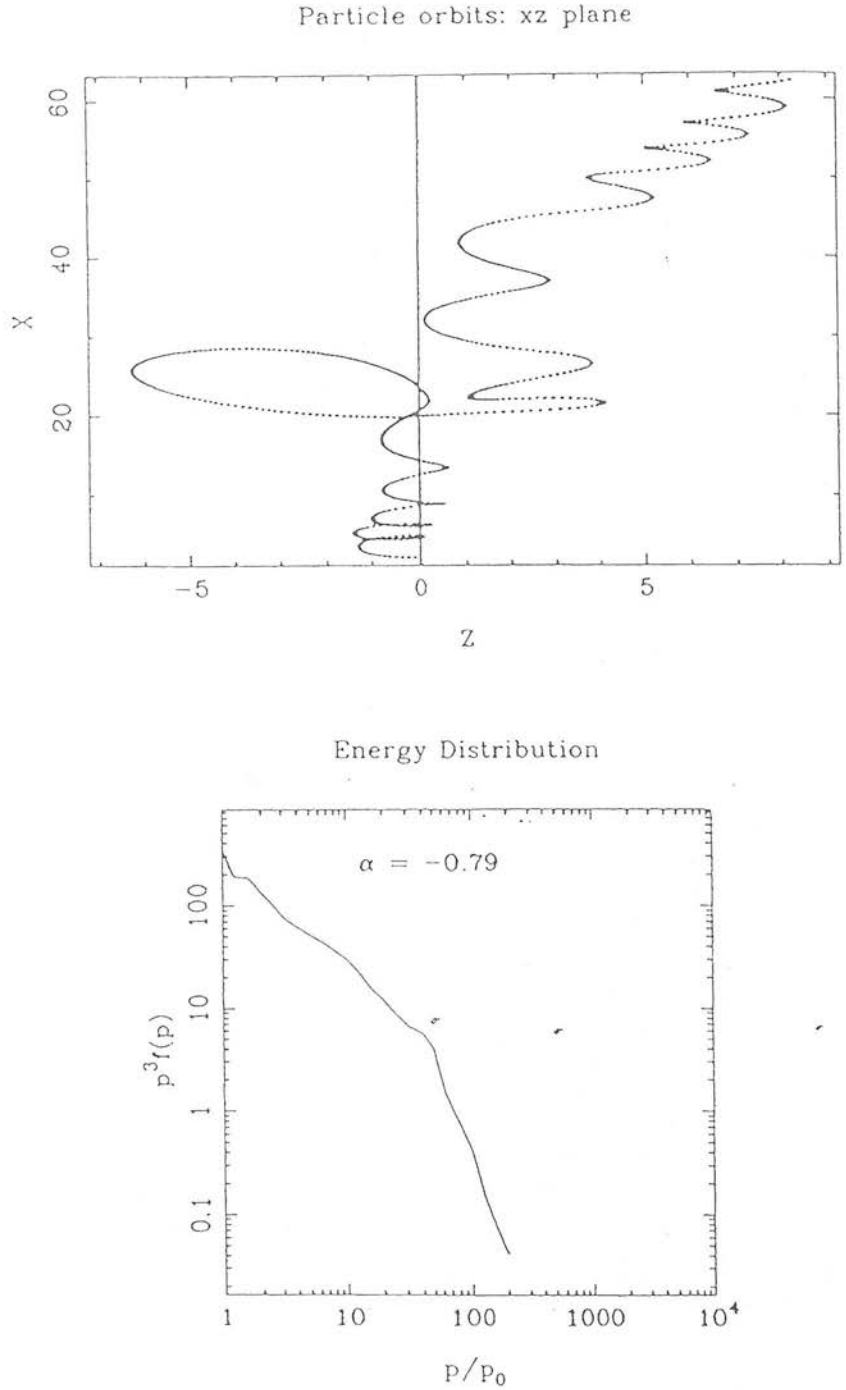

Fig 3: The top figure shows an example of an electron accelerated by the Fermi mechanism in a randomly oriented magnetic field. The electron starts from the shock front and is injected upstream (z negative). It crosses the shock repeatedly until lost from the shock vicinity. The bottom figure shows the resultant spectrum. The synchrotron spectral index is $\alpha = 0.79$ (see Ballard *et al.*, in preparation for details).

There are still considerable problems with this model of the optical emission region, for example it cannot explain the relatively common occurrence of frequency dependent position angles. One could presumably reproduce this by employing either anisotropic distributions at some level (Björnsson, 1985) or multiple component models, however unappealing that may be. However that is to miss the point of this work which is to start to explain the global properties of BL-Lacs as outlined at the beginning using a simple physical model, rather than to rely upon more empirical pictures which are less informative about the actual physics. Phenomenological models where a number of randomly oriented components are taken and passed through a shock can explain the observed correlations between the various properties of the emission and by rather artificial adjustments to the parameters can reproduce the incidence rate of frequency dependent polarization and position angle. In such a picture one would effectively be summing over a finite number of discrete cells, each containing a randomly oriented uniform magnetic field, rather than integrating over a continuous distribution of magnetic field elements. This work may be considered the limit when the number of elements is infinite. It may well be that a model with an infinite number of cells is only directly relevant to the radio where the synchrotron lifetimes are very much greater than at optical wavelengths.

Finally, the connection between the optical and radio emitting regions has not yet been established conclusively, although there are several pieces of evidence which favour this being true. Events such as that reported by Kikuchi *et al.* (1988) for OJ287 where a position angle rotation, simultaneous at both radio and optical wavelengths was observed are highly suggestive. Position angle rotations such as this may be a result either of an actual rotation of the magnetic field within the source, or of aberration effects, where the speed of the jet itself changes (Blandford & Königl, 1979). However the mere fact that it occurs suggests that the optical light is originating in the same region in space as the radio emission. In addition, the work of Landau *et al.* (1986) who find the radio to optical spectra change smoothly supports this. If the emission in the two wavebands did arise in separate regions and varied independently then the spectra would not be smooth. The fact that Landau *et al.* fitted their spectra with parabolae is not in conflict with sharp breaks in the energy distribution because of the nature of the polynomials F(x) & G(x) which represent the spectrum from a single electron and which are smooth relative to the energy distribution; hence any sharp breaks tend to be washed out, giving a much smoother flux distribution as indeed can be seen from Figs 1 and 2. Finally there is the work of Impey (1987) who has shown that the distribution of the difference between VLBI structure axis and preferred optical position angle tends to be peaked around 90°, again suggestive of underlying source structure. In this respect measurements of the polarization at submm wavelengths, would be helpful, in addition to testing the validity of the above work. These are not yet available to observers although an instrument is undergoing final tests at present at the JCMT.

Acknowlegements

KRB acknowledges the University of Edinburgh for travel assistance and the SERC for a studentship.

6: References

Achterberg, A., 1988. *Mon. Not. R. astr. Soc.*, 232, 323.
Ballard, K.R., Mead, A.R.G., Brand, P.W.J.L., Hough, J.H., 1989. *Mon. Not. R. astr. Soc.*, 243, 640.
Björnsson, C.-I., 1982. *Mon. Not. R. astr. Soc.*, 216, 241.
Björnsson, C.-I. & Blumenthal, G.R., 1982. *Astrophys. J.*, 259, 805.
Blandford, R.D. & Kõnigl, A., 1979. *Astrophys. J.*, 232, 34.
Holmes, P.A., Brand, P.W.J.L., Impey, C.D., Williams, P.M., Smith, P., Elston, R., Balonek, T., Zeilik, M., Burns, J., Heckert, P., Barvainis, R., Kenny, J., Schmidt, G. & Puschell, J., 1984. *Mon. Not. R. astr. Soc.*, 211, 497.
Hughes P.A., Aller H.D. & Aller, M.F., 1985. *Astrophys. J.*,298, 301.
Impey, C.D., 1987. In : *Superluminal Radio Sources*, p. 233, eds. Zensus, J.A. & Pearson, T.J., Cambridge University Press.
Kardashev, N.S., 1962. *Sov. Astron. - A.J.*, 6, 317.
Kikuchi, S., Inoue, M., Mikami, Y., Tabara, H. & Kato, T., 1988, *Astr. Astrophys.*, 190, L8.
Kirk, J.G. & Heavens, A.F., 1989. *Mon. Not. R. astr. Soc., in press*
Landau, R., Grolsch, B., Jones, T.J., Jones, T.W., Pedelty, J., Rudnick, L., Sitko, M.L., Kenney, J., Roellig, T., Salonen, E., Urpo, S., Schmidt, G., Neugebauer, G., Matthews, K., Elias, J.H., Impey, C.D., Clegg, P. & Harris, S., 1986. *Astrophys. J.*, 308, 78.
Marscher, A.P. & Gear, W.K., 1985. *Astrophys. J.*, 298, 114.
Mead, A.R.G., Ballard, K.R., Brand, P.W.J.L., Hough, J.H., Bailey, J.A. & Brindle, C., 1989. *Astr. Astrophys.*, 83, 183.
Moore, R.L., McGraw, J.T., Angel, J.R.P., Duerr, R., Lebofsky, M.J., Rieke, G.H., Wiśniewski, W.Z., Axon, D.J., Bailey, J.A., Hough, J.H., Thompson, I., Breger, M., Schulz, H., Clayton, G.C., Martin, P.G., Miller, J.S., Schmidt, G.D., Africano, J. & Miller, H.R., 1982. *Astrophys. J.*, 260, 415.
Pacholczyk, A.G., 1970, Radio Astrophysics, Freeman: San Francisco.